

# **Fabrication of Hybrid Nanostructured Materials and Porous Carbon for Energy Storage and Gas Adsorption Applications**

*By*

**Prajnashree Panda**

**CHEM11201804018**

**National Institute of Science Education and Research Bhubaneswar, Odisha-  
752050**

*A thesis submitted to the  
Board of Studies in Chemical Sciences  
In partial fulfilment of requirements  
for the Degree of*

**DOCTOR OF PHILOSOPHY**

*of*

**HOMI BHABHA NATIONAL INSTITUTE**


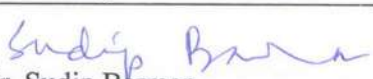
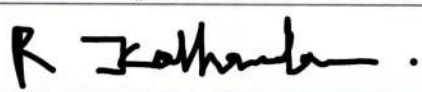
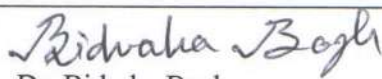
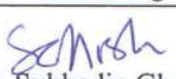
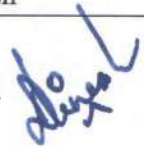


**September, 2023**

# Homi Bhabha National Institute

## Recommendations of the Viva Voce Committee

As members of the Viva Voce Committee, we certify that we have read the dissertation prepared by **Prajnashree Panda** entitled "**Fabrication of Hybrid Nanostructured Materials and Porous Carbon for Energy Storage and Gas Adsorption Applications**" and recommend that it may be accepted as fulfilling the thesis requirement for the award of Degree of Doctor of Philosophy.

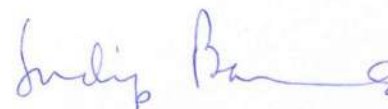
Chairman -	 Dr. Prasenjit Mal	Date: 16/2/24
Guide / Convener -	 Dr. Sudip Barman	Date: 16/02/2024
Examiner -	 R. K. Khatun	Date: 16/02/2024
Member 1 -	 Dr. Bidraha Bagh	Date: 16/02/2024
Member 2 -	 Dr. Subhadip Ghosh	Date: 16/02/2024
Member 3 -	 Dr. Dinesh Topwal	Date: 16/2/24

Final approval and acceptance of this thesis is contingent upon the candidate's submission of the final copies of the thesis to HBNI.

I/We hereby certify that I/we have read this thesis prepared under my/our direction and recommend that it may be accepted as fulfilling the thesis requirement.

Date: 16/02/2024

Place: Bhubaneswar



(Dr. Sudip Barman)

Guide

## STATEMENT BY AUTHOR

This dissertation has been submitted in partial fulfilment of requirements for an advanced degree at Homi Bhabha National Institute (HBNI) and is deposited in the Library to be made available to borrowers under rules of the HBNI.

Brief quotations from this dissertation are allowable without special permission, provided that accurate acknowledgement of source is made. Requests for permission for extended quotation from or reproduction of this manuscript in whole or in part may be granted by the Competent Authority of HBNI when in his or her judgment the proposed use of the material is in the interests of scholarship. In all other instances, however, permission must be obtained from the author.

*Prajnashree Panda*  
**Prajnashree Panda**

## DECLARATION

I, hereby declare that the investigation presented in the thesis has been carried out by me. The work is original and has not been submitted earlier as a whole or in part for a degree / diploma at this or any other Institution / University.

Prajnashree Panda  
**Prajnashree Panda**



## List of Publications arising from the thesis

### Journal Published

1. **Panda, P.**; Samanta, R.; Barman, S., Facile Synthesis of Two-Dimensional (2D) Boron Carbonitride and 2D Porous Boron Carbonitride for Excellent Energy Storage and Gas Adsorption Applications. *Energy Fuels* 2023, 37, 7, 5540–5555.
2. **Panda, P.**; Barman, S., A bottom-up fabrication for Sulphur (S), Nitrogen (N) co-Doped two-dimensional Microporous Carbon Nano-sheets for high-performance Supercapacitor and H<sub>2</sub>, CO<sub>2</sub> storage. *Sustainable Energy Fuels* 2023, 7, 2441-2454.
3. **Panda, P.**; Mishra, R.; Panigrahy, S.; Barman, S., Design of Co<sub>1</sub>Al<sub>3</sub>(OH)<sub>m</sub>/Carbon Nitride hybrid Nanostructure for Enhanced Capacitive Energy Storage in Alkaline Electrolyte. *Materials Advances*, 2021, 2, 7671.
4. **Panda, P.**; Mishra, R.; Panigrahy, S.; Barman, S., 3D Assembly of CoAl<sub>2</sub>O<sub>4</sub> Spinel Nanosheets for Energy Storage. *ACS Applied Nano Materials* 2022, 5, 4, 5176–5186.
5. 'Manna, B. K.; ' **Panda, P.**; Mishra, R.; Barman, S., One-Dimensional RuO<sub>2</sub>–Nitrogen-Doped Carbon Composite for Energy Storage Application in an Alkaline Medium. *Energy Fuels* 2023, 37, 7, 5613–5622. (! equal contribution)
6. **Panda, P.**; Mishra, R.; Barman, S., In-situ nano-engineering of amorphous MoS<sub>2</sub> nanosheets with carbon dots for enhanced

supercapacitor performances. *Int J Energy Res.* 2022; 46, 12, 17576-17589.

7. **Panda, P.**; Roy, S.; Samanta, R.; Barman, S., Ultrathin One-Dimensional Ni-Co Bimetallic MOF for High-Performance Energy Storage Application. *ACS Appl. Nano Mater.* 2023, 6, 17, 15916-15924.
8. **Panda, P.**; Roy, S.; Barman, S., Phosphorus and Nitrogen Co-doped Porous Carbon Nanosheets for Energy Storage and Gas Adsorption *ACS Appl. Nano Mater.* 2024, 7, 2, 2382-2393.

### **Journals not included in thesis**

1. Mishra, R.; **Panda, P.**; Barman, S., Synthesis of a  $\text{Co}_3\text{V}_2\text{O}_8/\text{CN}_x$  hybrid nanocomposite as an efficient electrode material for supercapacitors. *New Journal of Chemistry* 2021, 45, 5897-5906.
2. Mishra, R.; Prasad, P. R.; **Panda, P.**; Barman, S., Highly Porous Activated N-Doped Carbon as an Ideal Electrode Material for Capacitive Energy Storage and Physisorption of  $\text{H}_2$ ,  $\text{CO}_2$ , and  $\text{CH}_4$ . *Energy & Fuels* 2021, 35, 14177-14187.
3. Mishra, R.; **Panda, P.**; Barman, S., Synthesis of sulfur-doped porous carbon for supercapacitor and gas adsorption applications. *International Journal of Energy Research* 2022, 46, 2585-2600.
4. Panigrahy, S.; Mishra, R.; **Panda, P.**; Kempasiddaiah, M.; Barman, S., Carbon-Supported Ag Nanoparticle Aerogel for Electrocatalytic Hydrogenation of 5-(Hydroxymethyl) furfural to 2, 5-Hexanedione under Acidic Conditions. *ACS Applied Nano Materials* **2022**, 5, 8314-8323.

5. Panigrahy, S.; Samanta, R.; **Panda, P.**; Mishra, R.; Barman, S., RuO<sub>2</sub> as a promoter in Pt-RuO<sub>2</sub>-nanostructures/carbon composite, a pH-universal catalyst for hydrogen evolution/oxidation reactions. *International Journal of Energy Research* **2022**, *46*, 6406-6420.
6. Sahu, P.; Mishra, R.; Panigrahy, S.; **Panda, P.**; Barman, S., Constructing micropore-rich nitrogen-doped carbon for high-performance supercapacitor and adsorption of carbon dioxide. *International Journal of Energy Research* **2022**, *46*, 13556- 13569.
7. Samanta, R.; **Panda, P.**; Mishra, R.; Barman, S., IrO<sub>2</sub>-Modified RuO<sub>2</sub> Nanowires/Nitrogen-Doped Carbon Composite for Effective Overall Water Splitting in All pH. *Energy & Fuels* **2022**, *36*, 1015-1026.
8. Panigrahy, S.; **Panda, P.**; Shekhawat, A.; Barman, S., One-Dimensional Ni-MIL-77 Metal–Organic Framework as an Efficient Electrode Nanomaterial for Asymmetric Supercapacitors. *ACS Appl. Nano Mater.* **2023**, *6*, 5, 3825–3834.
9. Roy, S.; **Panda, P.**; Barman, S., Electrospun Highly Porous Carbon Nitride-Carbon Nanofibers for High Performance Supercapacitor Application. (Submitted)

## Conferences and Presentation

1. **Oral Presentation:** Recent Advances on Catalysis Science & Engineering-2021 (RACSE-2021) (26<sup>th</sup>-28<sup>th</sup> October 2021) Department of Chemistry, NIT Jamshedpur, Jharkhand, India.

2. **Poster Presentation:** International Winter School on Frontiers in Materials Science (A Hybrid event) (06<sup>th</sup>-10<sup>th</sup> December 2021) Jawaharlal Nehru Centre for Advanced Scientific Research, Jakkur, Bangalore, India.
3. **Poster Presentation:** 7<sup>th</sup> National Conference on “Recent Advancement in Material Science” (RAIMS-2022) (18<sup>th</sup>-19<sup>th</sup> November 2022) Department of Chemistry, Veer Surendra Sai University of Technology, Burla Sambalpur, Odisha, India.
4. **Poster Presentation:** 36<sup>th</sup> Annual Conference of Orissa Chemical Society & National Conference on “Advances in Materials Chemistry and Application” (AMCA-2022) (18<sup>th</sup>-19<sup>th</sup> December 2022) Department of Chemistry, Utkal University, Bhubaneswar, Odisha, India.
5. **Poster Presentation:** Emergent Materials for Energy and Environment (EMEE-2023) (04<sup>th</sup>-05<sup>th</sup> March 2023) Department of Chemistry, IIT Roorkee, Uttarakhand, India.
6. **Poster Presentation:** 1st HBNI interaction meeting in Chemical Sciences (18<sup>th</sup> -20<sup>th</sup> January 2023) School of Chemical Science, National Institute of Science Education and Research (NISER), Bhubaneswar, Odisha, India.

Prajnashree Panda  
**Prajnashree Panda**

*Dedicated*  
*To*  
*The Almighty God*  
*&*  
*My Family*

## ACKNOWLEDGEMENTS

I would like to express my profound appreciation to Dr. Sudip Barman, my research supervisor, for affording me the privilege to work under his guidance and for introducing me to the captivating realm of materials science. I extend my heartfelt thanks to him for his invaluable mentorship, unwavering support, and constant motivation throughout my research journey. I am grateful for the autonomy he granted me in selecting my research area, which allowed me to explore my interests fully. Furthermore, his constructive feedback and meticulous instructions on various scientific projects, as well as his guidance in drafting research proposals and articles have helped me a lot in this journey. His insightful input has immensely enhanced my writing skills. I am thankful for his trust in my abilities and his positive outlook towards my research endeavours in various aspects. Once again, I extend my deepest gratitude to him for his exceptional support and belief in me. His guidance and encouragement have played a pivotal role in shaping my research career, and I am truly indebted to him for the invaluable opportunities he has provided me.

I heartfelt thanks Department of Atomic Energy (DAE), India for its financial assistance during my doctoral studies. I sincerely thank the National Institute of Science Education and Research (NISER), Bhubaneswar, India, for providing research infrastructure, as well as the Homi Bhabha National Institute (HBNI), India, for academic registration. I would also like to acknowledge the Centre for Interdisciplinary Sciences (CIS) at NISER for unwavering support and provision of various experimental facilities.

I would like to thank Dr. Prasenjit Mal, Dr. Bidraha Bagh, Dr. Subhadip Ghosh, and Dr. Dinesh Topwal, members of my doctorate committee, for their assistance and insightful suggestions. I want to thank all the Ph.D. course instructors Prof. A. Srinivasan, Prof. Himansu

Sekhar Biswal, Dr. Sudip Barman, Dr. Bidraha Bagh, Dr. Moloy Sarkar, and Dr. U. Lourderaj for their valuable and informative course work.

I extend my heartfelt thanks to my past and present labmates, Dr. Mriganka Sadhukhan, Dr. Manas Kumar Kundu, Dr. Tanmay Bhowmik, Dr. Ashish Das, Dr. Ranjit Mishra, Dr. Manjunatha K., Sonali Panigrahy, Rajib Samanta, Sayak Roy, Biplab Kumar Manna, Amal, Subham, Manish, Pushp Raj, Priya, Anirudha, Suwendu, Dev, Debasis, and Sarin. This journey of my Ph.D. career has been made easier by companions of my labmates, who have created a positive atmosphere around me.

I thank Priyanka Sadangi, Amita Mohapatra, Manisha Nayak, Panisha Nayak, Rakesh R. Behera, Deepsagar Manikpuri, Dr. Kasturi Sahu, and Dr. Tanmayee Nanda for making this journey memorable.

I thank all of my NISER seniors and friends, especially Dr. Shalini Pandey, Nachiketa Sahu, Manisha Sadangi, Sourav R. Pradhan, R Vijaya Sankar, Ayendrila Das for the unforgettable moments. I would also like to thank my senior and friends from outside NISER, Dr. Subhrajit Mohanty, Milan Kumar Jena, Abhishek Garg, Tapaswini Das for their support and encouragement

Finally, I convey my heartfelt gratitude to my parents (Mrs. Subhadra Panda & Mr. Gangadhar Panda) who have always encouraged me to follow my heart and inspired my inquisitive mind throughout my childhood and study career, my grandfather Mr. Laximidhar Panda, my sister Miss Kabyashree Panda, brother Mr. Prarambha Kumar Panda, brother Mr. Pravash Dutta Sethy and Mr. Debendra Prasad Panda for their unconditional love and support.

Prajnashree Panda  
...Prajnashree Panda

# CONTENTS

<b>Title</b>	<b>Page No</b>
Summary	xvi
List of figures	xx
List of tables	xxxv
List of schemes	xxxviii
 <b>Chapter 1      Overview of sustainable electrochemical energy and gas storage applications</b>	
1.1.            Abstract	39
1.2.            Introduction	39
1.2.1.      Importance of supercapacitor (SC)	39
1.3.            Types of Energy Storage Devices (ESD)	42
Mechanical Energy Storage Device	43
Thermal Energy Storage Device	43
Chemical Energy Storage Device	43
Electrical Energy Storage Device	43
Electrochemical Energy Storage Device	44
1.4.            Types of supercapacitors according to the energy storage mechanism	45



1.4.1.	EDLCs	46
1.4.2.	Pseudocapacitors (PC)	48
1.4.3.	Hybrid SCs (HSCs)	50
1.4.3.1.	Composite SCs	50
1.4.3.2.	Asymmetry SCs (ASCs)	51
1.4.3.2.	Battery Type SCs	51
1.5.	Basic Components of SC	51
1.5.1.	Current Collector	52
1.5.2.	Electrolytes	53
1.5.3.	Binders	54
1.5.4.	Separators	54
1.5.5.	Electrode Materials	55
1.5.5.1.	EDLC Materials	55
	Activated Carbons	56
	Heteroatom doped carbon	58
	Effect of heteroatom doping into carbon	59
1.5.5.2.	Pseudocapacitive (PC) Materials	63
	Metal Oxides/Hydroxides	64
	Metal Chalcogenides/Nitrides/ Phosphides	65
1.5.5.3.	Nanocomposites based Hybrid electrodes Materials	66
1.6.	Gas Adsorption	72
1.6.1.	Importance of gas adsorption	72
1.6.2.	Heteroatom doped Porous carbon for gas storage	73

1.7.	Aims of the Present Thesis	76
1.8.	Scope of the Present Work	77
1.9.	References	77
<b>Chapter 2</b>	<b>General Experimental Methods and Techniques</b>	
2.1.	Introduction	84
2.2.	Materials	84
2.3.	Instrumental techniques	85
2.4.	References	96
<b>Chapter 3</b>	<b>Facile Synthesis of Two-dimensional (2D) Boron Carbonitride (BCN) and 2D porous BCN for excellent Energy storage and Gas Adsorption Applications</b>	
3.1.	Abstract	98
3.2.	Introduction	99
3.3.	Experimental section	104
3.4.	Results and discussions	107
3.5.	Conclusions	136
3.6.	References	137
<b>Chapter 4</b>	<b>A bottom-up fabrication for Sulphur (S), Nitrogen (N) co-Doped two-dimensional Microporous Carbon Nano-sheets for high-performance Supercapacitor and H<sub>2</sub>, CO<sub>2</sub> storage</b>	
4.1.	Abstract	146
4.2.	Introduction	147

4.3.	Experimental section	151
4.4.	Results and discussions	154
4.5.	Conclusions	182
4.6.	References	183

**Chapter 5      Phosphorous (P) and Nitrogen (N) co-doped Porous Carbon nanosheets for Energy Storage and Gas Adsorption Applications**

5.1.	Abstract	191
5.2.	Introduction	192
5.3.	Experimental section	195
5.4.	Results and discussions	198
5.5.	Conclusion	220
5.6.	References	221

**Chapter 6      Design of  $\text{Co}_1\text{Al}_3(\text{OH})_m$ /Carbon Nitride hybrid Nanostructure for Enhanced Capacitive Energy Storage in Alkaline Electrolyte**

6.1.	Abstract	231
6.2.	Introduction	232
6.3.	Experimental section	234
6.4.	Results and discussions	238
6.5.	Conclusion	255
6.6.	References	255

**Chapter 7      3D Assembly of  $\text{CoAl}_2\text{O}_4$  Spinel Nanosheets for Energy Storage**

7.1.	Abstract	265
7.2.	Introduction	266

7.3.	Experimental section	269
7.4.	Results and discussions	272
7.5.	Conclusion	289
7.6.	References	290
<b>Chapter 8</b>	<b>One-dimensional RuO<sub>2</sub>-Nitrogen doped Carbon Composite for Energy Storage Application in Alkaline Medium</b>	
8.1.	Abstract	300
8.2.	Introduction	301
8.3.	Experimental section	304
8.4.	Results and discussions	308
8.5.	Conclusion	322
8.6.	References	322
<b>Chapter 9</b>	<b>In-situ Nano-engineering of Amorphous MoS<sub>2</sub> Nanosheets with Carbon Dots for enhanced Supercapacitor performances</b>	
9.1.	Abstract	329
9.2.	Introduction	330
9.3.	Experimental section	334
9.4.	Results and discussions	337
9.5.	Conclusion	358
9.6.	References	359
<b>Chapter 10</b>	<b>Ultrathin Ni-Co Bimetallic Metal-Organic Framework Nanobelts for High-Performance Energy Storage</b>	

10.1.	Abstract	367
10.2.	Introduction	368
10.3.	Experimental section	370
10.4.	Results and discussions	375
10.5.	Conclusion	392
10.6.	References	393

## Summary

A facile synthesis method was adopted to prepare two-dimensional (2D) boron carbonitride (BCN) and 2D porous BCN (p-BCN-X) from formamide and boric acid was carried out for application in capacitive energy storage and physisorption of H<sub>2</sub>, CO<sub>2</sub>, and CH<sub>4</sub>. In 6M KOH, the resulting 2D BCN has an excellent specific capacitance value. The high porosity and surface area along with synergistic effect of B, N provide superior activity towards supercapacitor application and also good gas adsorption activity for H<sub>2</sub>, CH<sub>4</sub>, and CO<sub>2</sub> with improved CO<sub>2</sub>/N<sub>2</sub> and CO<sub>2</sub>/CH<sub>4</sub> selectivities. A highly porous B, N-doped carbon material with a surface area >3000 m<sup>2</sup> g<sup>-1</sup> was also prepared and applied in supercapacitor along with CO<sub>2</sub> & H<sub>2</sub> adsorption. The material presents a specific capacitance of 355 F g<sup>-1</sup> at 1 A g<sup>-1</sup> in 6M KOH. It also showed good H<sub>2</sub> and CO<sub>2</sub> uptake capacities with good CO<sub>2</sub>/N<sub>2</sub> and CO<sub>2</sub>/CH<sub>4</sub> selectivity.

Another approach was employed to synthesize two-dimensional (2D) S, N-doped microporous carbon nanosheets (p-CNS-X) using formamide and thiourea. These materials were also prepared with the intention of utilizing them in supercapacitor application and the uptake capability of H<sub>2</sub>, CO<sub>2</sub>, and CH<sub>4</sub> gases. In a 6M KOH solution, the resulting p-CNS-800 demonstrated exceptional specific capacitance of 615 F g<sup>-1</sup> at 0.5 A g<sup>-1</sup>. This remarkable performance is attributed to its high porosity, extensive surface area of 2847.88 m<sup>2</sup>g<sup>-1</sup>, and the synergistic effects of sulphur and

nitrogen, making it highly suitable for supercapacitor applications. Additionally, it exhibited effective gas adsorption properties for H<sub>2</sub>, CH<sub>4</sub>, and CO<sub>2</sub>, featuring improved CO<sub>2</sub>/N<sub>2</sub> and CO<sub>2</sub>/CH<sub>4</sub> selectivities.

An alternative approach was applied for the synthesis of activated N and P-doped carbon. This synthesis method involved the use of formamide and sodium hypophosphite and aimed to enable their utilization in supercapacitor applications and gas adsorption of H<sub>2</sub>, CO<sub>2</sub>, and CH<sub>4</sub>. When immersed in a 6M KOH solution, the synthesized PCN-800 displayed remarkable specific capacitance, reaching 480 F g<sup>-1</sup> at a current density of 1 A g<sup>-1</sup>. This exceptional performance can be attributed to its substantial porosity, extensive surface area measuring 2953.2 m<sup>2</sup>g<sup>-1</sup>, and the synergistic effects of heteroatoms, viz., P and N. These factors make it highly suitable for supercapacitor applications. Additionally, it exhibited effective gas adsorption properties for H<sub>2</sub>, CH<sub>4</sub>, and CO<sub>2</sub>, with enhanced selectivity for CO<sub>2</sub> over N<sub>2</sub> and CH<sub>4</sub>.

Next, a single-step synthesis of a Co<sub>1</sub>Al<sub>3</sub>(OH)<sub>m</sub>/CN<sub>x</sub> composite for supercapacitors was performed. This approach yields a smooth-surfaced, three-dimensional nanoflowes type structure formed by Co<sub>1</sub>Al<sub>3</sub>(OH)<sub>m</sub> growth on carbon nitride (CN<sub>x</sub>). The resulting composite exhibits outstanding specific capacitance, reaching 138 mAh g<sup>-1</sup> (1000 F g<sup>-1</sup>) at 1 A g<sup>-1</sup> current density, surpassing Co<sub>1</sub>Al<sub>3</sub>(OH)<sub>m</sub> alone by a factor of three. Even after 4500 cycles, it retains 84.46% of its capacitance. Moreover, when assembled into a supercapacitor, it achieves an energy density of 22.35 W h kg<sup>-1</sup> and maintains 80% capacitance after 8000 cycles at a 10 A g<sup>-1</sup> current density. The composite's excellent performance is attributed to the synergistic interaction between CN<sub>x</sub> and Co<sub>1</sub>Al<sub>3</sub>(OH)<sub>m</sub>, making it a promising supercapacitor electrode material.

The synthesis of a high-performance energy storage material through a two-step process was explored subsequently. Initially, a three-dimensional assembly of thin Co-Al spinel sheets

over carbon composite is formed by hydrothermally synthesizing CoAl layered double hydroxide (LDH) and successively heating it to create CoAl<sub>2</sub>O<sub>4</sub>/C. This composite boasts an impressive specific surface area of 102.7 m<sup>2</sup> g<sup>-1</sup>, leading to enhanced energy storage capabilities. It achieves a specific capacitance of 1394 F g<sup>-1</sup> at 1 A g<sup>-1</sup> with 87% capacitance retention after 5000 cycles. When utilized as the cathode in an asymmetric supercapacitor (ASC) alongside activated carbon (AC), the CoAl<sub>2</sub>O<sub>4</sub>/C//AC device delivers a high energy density of 76.34 W h kg<sup>-1</sup> at 750.045 W kg<sup>-1</sup> power density, maintaining 79% cyclic durability after 10,000 cycles. This improved electrochemical performance is attributed to the 3D assembly of thin 2D Co-Al spinel nanosheets, allowing efficient electron and mass transport, a high surface area, and synergistic interactions among components. Consequently, the Co-Al spinel/C composite holds promise for various energy storage applications.

Next, the focus is on one-dimensional electrode materials, which have emerged as promising candidates for supercapacitors due to their unique properties, including 1D structure with a large surface area, exceptional mechanical rigidity, cyclic stability, and excellent electrical conductivity. Here the synthesis of a one-dimensional RuO<sub>2</sub>-N-doped carbon (1D-RuO<sub>2</sub>/C) composite via a simple thermal method is presented, designed for supercapacitor applications. This composite exhibits an impressive specific capacitance of 671 F g<sup>-1</sup> at a 5 A g<sup>-1</sup> current density, with exceptional capacitance retention of 93.46% after 5000 cycles. In an asymmetric supercapacitor setup (1D-RuO<sub>2</sub>/C//AC), utilizing 1D-RuO<sub>2</sub>/C as the positive electrode and activated carbon as the negative electrode, the device achieves a specific capacitance of 53 F g<sup>-1</sup> at 1 A g<sup>-1</sup> current, delivering a power density of 751.66 W kg<sup>-1</sup> and an energy density of 16.71 W h kg<sup>-1</sup>. The ASC maintains around 98.65% of its initial value at a discharge current of 10 A g<sup>-1</sup>. The outstanding electrochemical performance of the 1D-RuO<sub>2</sub>/C composite can be attributed to

the one-dimensional morphology of RuO<sub>2</sub>, its high surface area, and synergistic interactions with the carbon support, making it a valuable material for energy storage systems.

Further, the use of amorphous materials in electrochemical energy storage was explored in this thesis. The chapter introduces a novel synthesis method involving microwave-assisted-hydrothermal techniques to create amorphous MoS<sub>2</sub>/C-dots composites, which exhibit an exceptional specific capacitance of 1368 F g<sup>-1</sup> at 1 A g<sup>-1</sup>. This surpasses both crystalline MoS<sub>2</sub> composites and amorphous MoS<sub>2</sub> without C-dots. An asymmetric supercapacitor is constructed using these composites as the cathode and activated carbon as the anode, achieving a specific capacitance of 180.82 F g<sup>-1</sup> at 1.5 V. This device provides an energy density of 56.5 W h kg<sup>-1</sup> at 750 W kg<sup>-1</sup> power density, with remarkable capacitance retention, making it a promising solution for high-performance energy storage applications.

Last section of this thesis explores the development of high-performance supercapacitors using one-dimensional (1D) nanostructured materials. Specifically, the chapter introduce synthesis of ultrathin 1D NiCo metal-organic framework (MOF) nanobelts through a solvothermal process. These nanobelts possess a distinct 1D morphology with a high specific surface area and remarkable structural stability. When incorporated into a composite, enhance the electrical conductivity and structural integrity. Electrochemical assessments reveal an outstanding specific capacitance of 1697.5 F g<sup>-1</sup> at 1 A g<sup>-1</sup> and 696.43 F g<sup>-1</sup> at 10 A g<sup>-1</sup>, coupled with excellent cyclic performance. Furthermore, an asymmetric supercapacitor configuration utilizing these nanobelts exhibits an impressive energy density of 26.56 W h Kg<sup>-1</sup> at 750 W Kg<sup>-1</sup> power density. The superior electrochemical performance can be attributed to the unique characteristics of one-dimensional nanobelt materials, such as enhanced electrochemical properties and rapid ion and electron transport. These nanobelts hold great promise for advancing high-performance supercapacitors.



# LIST OF FIGURES

Sl. No.	Figure Caption	Page No.
1	<b>Figure 1.1.</b> Statistics of the world's primary energy consumption for the last 10 years.	41
2	<b>Figure 1.2.</b> Different types of electrical energy storage systems.	44
3	<b>Figure 1.3.</b> Diagram of different types of SCs.	45
4	<b>Figure 1.4.</b> Schematic representation illustrating (a) Helmholtz model, (b) Guy-Chapman model, and (c) Guy Chapman-Stern model of EDLC supercapacitor.	47
5	<b>Figure 1.5.</b> Schematics of charge-storage mechanisms for (a) underpotential deposition, (b) redox pseudocapacitor, and (c) intercalation pseudocapacitor.	50
6	<b>Figure 1.6.</b> Scheme of the CR2032 coin cell used in the electrochemical characterization of supercapacitors.	52
7	<b>Figure 1.7.</b> Schematic representation of synthesis strategies of heteroatom doped porous carbon.	56
8	<b>Figure 1.8.</b> Schematic representation of different types of EDLC electrode materials.	58
9	<b>Figure 1.9.</b> Schematic illustration of heteroatoms self-doped porous carbon and types of (a) nitrogen, (b) sulphur, and (c) phosphorous functional groups in the carbon matrix.	61
10	<b>Figure 1.10.</b> Schematic illustration of different types of PC electrode materials.	64
11	<b>Figure 1.11.</b> Schematic illustration of the synergistic effect of TMs and carbon nanomaterials in TM/carbon hybrids.	67
12	<b>Figure 2.1.</b> Schematic representation of X-ray diffraction process.	86

13	<b>Figure 2.2.</b>	Schematic representation of Field Emission Scanning Electron Microscope (FE-SEM), adapted from ZEISS.	89
14	<b>Figure 2.3.</b>	Illustrative depiction showcasing the operational principle of X-ray Photoelectron Spectroscopy (XPS).	91
15	<b>Figure 3.1.</b>	(a) p-XRD pattern and (b) Raman spectrum of 2D BCN-X samples carbonized at different temperatures.	108
16	<b>Figure 3.2.</b>	(a-c) Low-resolution TEM images, (d) SAED pattern, (e-f) HRTEM image, (g-j) STEM image, and corresponding elemental mapping of carbonized BCN-800 composite.	110
17	<b>Figure 3.3.</b>	XPS spectrum of 2D BCN-800, (a) high-resolution spectrum, (b) B 1s, (c) C 1s, and (d) N 1s.	112
18	<b>Figure 3.4.</b>	(a) p-XRD pattern and (b) Raman spectrum of 2D porous BCN samples activated at different temperatures (p-BCN-X).	114
19	<b>Figure 3.5.</b>	(a-d) Low-resolution TEM images, (e, f) HRTEM images, (inset of (e) presents the SAED pattern), (g-k) STEM, and corresponding elemental mapping of p-BCN-800.	117
20	<b>Figure 3.6.</b>	(a) Nitrogen sorption isotherm, (b) Pore size distribution of 2D porous BCN samples activated at different temperatures (p-BCN-X).	118
21	<b>Figure 3.7.</b>	(a) CV profiles of BCN-X samples at $5 \text{ mV s}^{-1}$ (b) GCD profiles at $1 \text{ A g}^{-1}$ current for BCN-700 to 900 respectively. (c) Comparison of $C_s$ plot w.r.t different current for all the composites. (d) CV profile of differentiating diffusive and capacitive contribution at $5 \text{ mV s}^{-1}$ sweep rate. (e) Capacitive charge storage processes at different scan rates. (f) Cyclic durability test of BCN-800 at current of $7 \text{ A g}^{-1}$ in 6M KOH electrolyte.	121
22	<b>Figure 3.8.</b>	(a) CV profiles of p-BCN-X samples at $5 \text{ mV s}^{-1}$ (b) GCD plot profiles at $1 \text{ A g}^{-1}$ current for p-BCN-700 to 900 respectively. (c) Comparison plot of $C_s$ against the current for p-BCN-700 to 900 samples. (d) CV plots of p-BCN-800 at different scan rates ( $5\text{-}100 \text{ mV s}^{-1}$ ). (e) GCD plots of p-BCN-800 at diff. current ( $1\text{-}10 \text{ A g}^{-1}$ ). (f) Nyquist plot of p-BCN-X samples. (g)	123

		Contribution of a capacitive controlled process for p-BCN-800 at a scan rate of $10 \text{ mV s}^{-1}$ . (h) Capacitive charge storage processes at different scan rates ( $10$ to $60 \text{ mV s}^{-1}$ ). (i) Cyclic durability test of p-BCN-800 under $7 \text{ A g}^{-1}$ current in $6\text{M KOH}$ electrolyte.	
23	<b>Figure 3.9.</b>	(a, b) CV diagrams at $5\text{-}100 \text{ mV s}^{-1}$ & GCD plot profiles under $1\text{-}7 \text{ A g}^{-1}$ current. (c) Comparison plot of $C_s$ vs. current density. (d) Contribution of capacitive controlled process at a scan rate of $5 \text{ mV s}^{-1}$ . (e) Capacitive charge storage processes at different scan rates ( $5, 10$ , and $30 \text{ mV s}^{-1}$ ). (f) Cyclic durability test at current of $7 \text{ A g}^{-1}$ for p-BCN-800 in $1\text{M H}_2\text{SO}_4$ electrolyte.	127
24	<b>Figure 3.10.</b>	(a, b) CV and GCD profiles at different sweep rates ( $5\text{-}100 \text{ mV s}^{-1}$ ) and different current densities ( $1$ to $10 \text{ A g}^{-1}$ ). (c) $C_s$ plot w.r.t different current ( $1$ to $10 \text{ A g}^{-1}$ ). (d) The plot of energy density vs. power density and comparison to earlier reports. (e) Nyquist plot with equivalent circuit fitting. (f) Cyclic durability test for $10\text{k}$ cycles at $7 \text{ A g}^{-1}$ for the symmetric device in $6\text{M KOH}$ .	131
25	<b>Figure 3.11.</b>	(a, b) CV profiles under various potentials ranging from $1.2$ to $1.8\text{V}$ , and sweep rates of $5$ to $100 \text{ mV s}^{-1}$ . (c) GCD plots under different currents ( $1$ to $10 \text{ A g}^{-1}$ ). (d) The plot of $C_s$ w.r.t different current. (e) Nyquist plot. (f) The plot of energy density against power density for the device in $1\text{M H}_2\text{SO}_4$ .	133
26	<b>Figure 3.12.</b>	(a) CV plots at diff. voltage range of $1$ to $1.8\text{V}$ in $1\text{M Na}_2\text{SO}_4$ . (b) CV plots at different scan rates ( $5$ to $100 \text{ mV s}^{-1}$ ). (c) CD plots at different current ( $1$ to $7 \text{ A g}^{-1}$ ). (d) The $C_s$ plot under different current ( $1$ to $7 \text{ A g}^{-1}$ ). (e) ED vs. PD plot. (f) EIS spectra of p-BCN-800//p-BCN-800 device in $1\text{M Na}_2\text{SO}_4$ .	135
27	<b>Figure 3.13.</b>	(a) $\text{H}_2$ adsorption-desorption isotherms of p-BCN-700 to $900$ respectively at $77\text{K}$ , (b, c) Adsorption isotherms ( $\text{CO}_2$ ) of BCN at $0^\circ\text{C}$ and $25^\circ\text{C}$ , (d) Comparison bar plot of $\text{CO}_2$ Adsorption isotherms.	136
28	<b>Figure S3.1.</b>	FESEM images of porous (a) p-BCN-700, (a) p-BCN-800 and (a) p-BCN-900 samples.	140

29	<b>Figure S3.2.</b>	CV and GCD profiles of BCN-700.	141
30	<b>Figure S3.3.</b>	CV and GCD profiles of BCN-800.	141
31	<b>Figure S3.4.</b>	CV and GCD profiles of BCN-900.	142
32	<b>Figure S3.5.</b>	CV and GCD profiles of p-BCN-700.	142
33	<b>Figure S3.6.</b>	CV and GCD profiles of p-BCN-900.	143
34	<b>Figure S3.7.</b>	(a) H <sub>2</sub> uptake of all the samples at 77K and 1 bar pressure. (b) Change in H <sub>2</sub> uptake as a function of surface area.	143
35	<b>Figure S3.8.</b>	CO <sub>2</sub> uptake capacities of p-BCN-700 to 900 at 0 °C and 25 °C under 1 bar pressure.	144
36	<b>Figure 4.1.</b>	(a) p-XRD patterns, (b, c) TEM (low-resolution), (d, e) TEM (High-resolution) images, (f) SAED pattern, and (g-k) STEM and corresponding elemental mapping of 2D-CNS sample.	155
37	<b>Figure 4.2.</b>	(a) p-XRD patterns of p-CNS-X composites, (b-d) low-resolution TEM images, (e, f) HRTEM images (inset of (f) presents the SAED pattern), and (g-j) STEM and corresponding elemental mapping of p-CNS-800 composite.	158
38	<b>Figure 4.3.</b>	(a) Raman spectrum, (b) N <sub>2</sub> sorption isotherm, (c) Pore size distribution of p-CNS-X samples, (d) XPS survey spectra, (e) C 1s, (f) N 1s, and (g) S 2p spectrum in p-CNS-800.	162
39	<b>Figure 4.4.</b>	(a) CV diagrams of p-CNS-X compounds at 5 mV s <sup>-1</sup> . (b) CD curves of p-CNS-X at 1 A g <sup>-1</sup> . (c) C <sub>s</sub> at diff. current for all the samples of p-CNS-600 to 900. (d) CV plots of p-CNS-800 at diff. scan rates (5 to 100 mV s <sup>-1</sup> ). (e) CD profiles of p-CNS-800 at diff. current. (f) EIS plot of p-CNS-X samples. (g) Contribution of capacitive controlled process for p-CNS-800 at 10 mV s <sup>-1</sup> sweep rate. (h) Capacitive charge storage processes at different scan rates (10-60 mV s <sup>-1</sup> ). (i) Cyclic durability test of p-CNS-800 under 10 A g <sup>-1</sup> in 6M KOH electrolyte	166
40	<b>Figure 4.5.</b>	(a, b) CV plots at 5-80 mV s <sup>-1</sup> and CD diagram at 0.5-7 A g <sup>-1</sup> current for p-CNS-800. (c) Comparison of C <sub>s</sub> vs. current density. (d) Log (i) w.r.t log (v) plot. (e)	169

	Contribution of capacitive controlled process for p-CNS-800 at 5 mV s <sup>-1</sup> scan rate. (f) Capacitive charge storage processes at different scan rates (5 to 20 mV s <sup>-1</sup> ). (g) EIS spectra for p-CNS-800 in 1M H <sub>2</sub> SO <sub>4</sub> electrolyte on Ti foil. (h) Cyclic test of CNS-800 under 10 A g <sup>-1</sup> in 1M H <sub>2</sub> SO <sub>4</sub> electrolyte.	
41	<b>Figure 4.6.</b> (a) CV diagrams of a p-CNS-800// p-CNS-800 device (5 to 100 mV s <sup>-1</sup> ). (b) GCD plot under 1 to 10 A g <sup>-1</sup> current. (c) C <sub>s</sub> value plot under diff. current densities. (d) ED vs. PD plot and its comparison with previous literatures. (e) EIS plot. (f) Cyclic test for 10000 cycles under 10 A g <sup>-1</sup> in 6M KOH	173
42	<b>Figure 4.7.</b> (a, b) CV and GCD curves (c) plot of C <sub>s</sub> w.r.t current densities. (d) ED vs. PD plot for p-CNS-800// p-CNS-800 device in 1M H <sub>2</sub> SO <sub>4</sub> .	175
43	<b>Figure 4.8.</b> (a, b) CV and GCD plots under different sweep rate and current densities. (c) C <sub>s</sub> plot of device under different current (1-7 A g <sup>-1</sup> ). (d) ED versus PD plot profile of p-CNS-800// p-CNS-800 device in 1M Na <sub>2</sub> SO <sub>4</sub> .	176
44	<b>Figure 4.9.</b> (a) H <sub>2</sub> storage capacities of p-CNS-X under 1 bar pressure at 77K. (b, c) CO <sub>2</sub> uptake isotherms of p-CNS-X at 0 °C and 25 °C respectively. (d) Q <sub>st</sub> as a function of amount of CO <sub>2</sub> adsorbed for p-CNS-X. (e) CO <sub>2</sub> and N <sub>2</sub> sorption isotherms comparison plot for p-CNS-X at 25 °C. (f) The CO <sub>2</sub> /N <sub>2</sub> selectivity at 25 °C and total pressure of 1 bar for p-CNS-600 sample. (g) Adsorption selectivity for binary gas mixture of CO <sub>2</sub> /N <sub>2</sub> (15:85) at temperature of 25 °C for p-CNS-600. (h) CO <sub>2</sub> and CH <sub>4</sub> Comparison sorption isotherms of p-CNS-X measured at 25 °C. (i) Adsorption selectivity for binary mixture of CO <sub>2</sub> /CH <sub>4</sub> (50:50) at temperature of 25 °C.	181
45	<b>Figure S4.1.</b> FESEM image of (a) p-CNS-600, (b) p-CNS-700, (c) p-CNS-800, and (d) p-CNS-900 samples.	185
46	<b>Figure S4.2.</b> CV and GCD profiles of p-CNS-600.	185
47	<b>Figure S4.3.</b> CV and GCD profiles of p-CNS-700.	186
48	<b>Figure S4.4.</b> CV and GCD profiles of p-CNS-900.	186

49	<b>Figure S4.5.</b>	CV curves of a symmetric capacitor at the different potential range of 1 to 1.8 V in 1M Na <sub>2</sub> SO <sub>4</sub> .	187
50	<b>Figure S4.6.</b>	(a) H <sub>2</sub> uptake of all the samples at 77K and 1 bar pressure. (b) Change in H <sub>2</sub> uptake as a function of surface area.	187
51	<b>Figure S4.7.</b>	CO <sub>2</sub> uptake capacities of p-CNS-600 to 900 at 1 bar pressure.	188
52	<b>Figure S4.8.</b>	CO <sub>2</sub> /N <sub>2</sub> selectivities of p-CNS-X for binary mixture of ratio (15:85) under pressure of 1 bar.	188
53	<b>Figure S4.9.</b>	CO <sub>2</sub> /CH <sub>4</sub> selectivities for binary mixture of ratio (50:50) under pressure of 1 bar.	189
54	<b>Figure 5.1.</b>	(a) p-XRD patterns of PCN-x, (b, c) low-resolution TEM and HRTEM images (inset of Figure (c) represents the SAED pattern), and (d-h) STEM image and corresponding elemental mapping of PCN-800.	199
55	<b>Figure 5.2.</b>	(a) Raman spectra, (b) N <sub>2</sub> adsorption plot, (c) Pore size distribution of PCN-x, XPS high-resolution spectra (d) C 1s, (e) N 1s, and (f) P 2p in PCN-800.	202
56	<b>Figure 5.3.</b>	(a, b) CV and GCD curves at 5 mV s <sup>-1</sup> and under 1 A g <sup>-1</sup> current for PCN-x. (c) C <sub>s</sub> vs. current density for PCN-x. (d) Capacitive contribution for PCN-800 at 10 mV s <sup>-1</sup> . (e) Capacitive charge storage processes at different sweep rates (5-50 mV s <sup>-1</sup> ). (f) C <sub>s</sub> vs. number of cycles for PCN-800 at 7 A g <sup>-1</sup> in alkaline electrolyte.	205
57	<b>Figure 5.4.</b>	(a, b) CV and GCD profiles at 5-100 mV s <sup>-1</sup> and 1-10A g <sup>-1</sup> respectively. (c) Plot of C <sub>s</sub> as a function of current density. (d) Log (i) vs. log (v) profile. (e) Capacitive contribution plot for PCN-800 at 5 mV s <sup>-1</sup> . (f) Capacitive charge storage processes vs. scan rates (5-20 mV s <sup>-1</sup> ). (g) Nyquist plot of PCN-800. (h) Cycling stability performance of PCN-800 in acid electrolyte.	208
58	<b>Figure 5.5.</b>	(a, b) CV and GCD plot profile of a PCN-800//PCN-800 device. (c) C <sub>s</sub> vs. current densities plot. (d) A comparison Ragone plot with previously reported literature. (e) Nyquist plot. (f) Cycling performance for 10000 cycles in alkaline electrolyte.	211

59	<b>Figure 5.6.</b>	(a and b) CV and GCD profiles (c) $C_s$ vs. current densities. (d) Ragone plot for PCN-800//PCN-800 device in 1 M $H_2SO_4$ .	213
60	<b>Figure 5.7.</b>	(a and b) CV and GCD profiles at different scan rates and current densities. (c) Plot of $C_s$ vs currents (1-7 A $g^{-1}$ ). (d) Ragone plot of the PCN-800//PCN-800 device in 1 M $Na_2SO_4$ .	214
61	<b>Figure 5.8.</b>	(a) $H_2$ storage behaviour of PCN-x at 77 K and 1 bar pressure. (b and c) $CO_2$ adsorption curve of PCN-x at 0 °C and 25 °C, respectively. (d) $Q_{st}$ vs. amount of $CO_2$ adsorbed for PCN-x. (e) Comparison of $CO_2$ and $N_2$ sorption isotherm plot for PCN-x at 25 °C. (f) The $CO_2/N_2$ selectivity at 25 ° for PCN-900. (g) Adsorption selectivity of $CO_2/N_2$ (15: 85) at 25 °C for PCN-x. (h) $CO_2$ and $CH_4$ comparison sorption isotherms plot of PCN-x at 25 °C. (i) Adsorption selectivity of $CO_2/CH_4$ (50: 50) at 25 °C for PCN-900.	216
62	<b>Figure S5.1.</b>	FESEM images of porous (a) PCN-700, (b) PCN-800 and (c) PCN-900 samples.	223
63	<b>Figure S5.2.</b>	(a) Low resolution TEM image and (b) HRTEM image of PCN-800.	224
64	<b>Figure S5.3.</b>	XPS survey scan spectra of PCN-800 sample.	224
65	<b>Figure S5.4.</b>	CV and GCD profiles of PCN-700.	225
66	<b>Figure S5.5.</b>	CV and GCD profiles of PCN-800.	225
67	<b>Figure S5.6.</b>	CV and GCD profiles of PCN-900.	226
68	<b>Figure S5.7.</b>	EIS plot of PCN-x samples in 6M KOH electrolyte.	226
69	<b>Figure S5.8.</b>	CV curves of a symmetric capacitor at the different potential range of 1 to 1.8 V in 1M $H_2SO_4$ .	227
70	<b>Figure S5.9.</b>	CV curves of a symmetric capacitor at the different potential range of 1 to 1.6 V in 1M $Na_2SO_4$ .	227
71	<b>Figure S5.10.</b>	(a) $H_2$ uptake of all the samples at 77K and 1 bar pressure. (b) Change in $H_2$ uptake as a function of surface area.	228
72	<b>Figure S5.11.</b>	$CO_2$ uptake capacities of PCN-700 to 900 at 1 bar pressure.	228

73	<b>Figure S5.12.</b>	CO <sub>2</sub> /N <sub>2</sub> selectivities of PCN-x samples for binary mixture of ratio (15:85) under pressure of 1 bar.	229
74	<b>Figure S5.13.</b>	CO <sub>2</sub> /CH <sub>4</sub> selectivities of PCN-x samples for binary mixture of ratio (50:50) under pressure of 1 bar.	229
75	<b>Figure 6.1.</b>	XRD patterns of (a) Co <sub>1</sub> Al <sub>1</sub> (OH) <sub>m</sub> /CN <sub>x</sub> (b) Co <sub>1</sub> Al <sub>2</sub> (OH) <sub>m</sub> /CN <sub>x</sub> and (c) Co <sub>1</sub> Al <sub>3</sub> (OH) <sub>m</sub> /CN <sub>x</sub> (d) Comparison of FT-IR for Co <sub>1</sub> Al <sub>3</sub> (OH) <sub>m</sub> /CN <sub>x</sub> composite and Co <sub>1</sub> Al <sub>3</sub> (OH) <sub>m</sub> (e-f) N <sub>2</sub> adsorption-desorption isotherm and BJH pore size distribution of Co <sub>1</sub> Al <sub>3</sub> (OH) <sub>m</sub> /CN <sub>x</sub> Composite and only Co <sub>1</sub> Al <sub>3</sub> (OH) <sub>m</sub> .	239
76	<b>Figure 6.2.</b>	(a, b) FESEM images, (c-f) Low and high resolution TEM images of Co <sub>1</sub> Al <sub>3</sub> (OH) <sub>m</sub> /CN <sub>x</sub> .	242
77	<b>Figure 6.3.</b>	(a) XPS survey spectrum of Co <sub>1</sub> Al <sub>3</sub> (OH) <sub>m</sub> /CN <sub>x</sub> composite. High resolution XPS spectra of (b) Co 2p, (c) Al 2p, (d) O 1s, (e) C 1s and (f) N 1s respectively.	244
78	<b>Figure 6.4.</b>	(a) CV curves of Co <sub>1</sub> Al <sub>δ</sub> (OH) <sub>m</sub> /CN <sub>x</sub> (δ=1, 2, 3, 4) and Co <sub>1</sub> Al <sub>3</sub> (OH) <sub>m</sub> at scan rate of 30 mV/s. (b) CV curves of Co <sub>1</sub> Al <sub>3</sub> (OH) <sub>m</sub> /CN <sub>x</sub> at different sweep rate (5-100 mV/s) (c) Comparison of GCD curves of Co <sub>1</sub> Al <sub>δ</sub> (OH) <sub>m</sub> /CN <sub>x</sub> (δ=1,2,3,4) with Co <sub>1</sub> Al <sub>3</sub> (OH) <sub>m</sub> at 1 A/g current density. (d) GCD curves of Co <sub>1</sub> Al <sub>3</sub> (OH) <sub>m</sub> /CN <sub>x</sub> composite at 0.5-10 A/g current density (e) Plot of Specific capacitance of Co <sub>1</sub> Al <sub>3</sub> (OH) <sub>m</sub> /CN <sub>x</sub> with respect to current density. (f) Plot of percentage capacitance retention (%) with respect to cycling number at 10 A/g current density.	247
79	<b>Figure 6.5.</b>	(a) CV curves of Co <sub>1</sub> Al <sub>3</sub> (OH) <sub>m</sub> /CN <sub>x</sub> distinguishing both capacitive and diffusive contribution at 10 mV/s sweep rate. (b) Plot of percentage of capacitive and diffusion controlled contribution for Co <sub>1</sub> Al <sub>3</sub> (OH) <sub>m</sub> /CN <sub>x</sub> at various sweep rates. (c) Nyquist plot of Co <sub>1</sub> Al <sub>3</sub> (OH) <sub>m</sub> /CN <sub>x</sub> and Co <sub>1</sub> Al <sub>3</sub> (OH) <sub>m</sub> .	250
80	<b>Figure 6.6.</b>	(a) CV curves of AC at different sweep rate and (b) GCD plot of AC at different current densities.	252
81	<b>Figure 6.7.</b>	(a) Electrochemical behavior of ASC Co <sub>1</sub> Al <sub>3</sub> (OH) <sub>m</sub> /CN <sub>x</sub> //AC (a) CV curves of AC and Co <sub>1</sub> Al <sub>3</sub> (OH) <sub>m</sub> /CN <sub>x</sub> at a sweep rate of 10 mV/s (b) CV curves of ASC at different potential range (c) CV curves of ASC at different Sweep rate (d) GCD curves	253



at different current densities. (e) Specific capacitance at different current densities. (f) Ragone plot of  $\text{Co}_1\text{Al}_3(\text{OH})_m/\text{CN}_x//\text{AC}$  asymmetric supercapacitor. (g) Cyclic stability of the ASC at 10A/g current density (h) EIS curve of the ASC.

82	<b>Figure S6.1.</b>	p-XRD patterns of $\text{CN}_x$ .	258
83	<b>Figure S6.2.</b>	p-XRD patterns of (a) $\text{Al}(\text{OH})_x/\text{CN}_x$ and (b) $\text{Co}(\text{OH})_2/\text{CN}_x$ respectively.	258
84	<b>Figure S6.3.</b>	XRD patterns of $\text{Co}_1\text{Al}_3(\text{OH})_m$ .	259
85	<b>Figure S6.4.</b>	(a) SEM image and corresponding Elemental mapping of elements (b) C (c) N (d) Co (e) Al (f) O of $\text{Co}_1\text{Al}_3(\text{OH})_m/\text{CN}_x$ showing an uniform distribution of C, N, Co, Al and O (g) FESEM EDS profile and (h) weight percentage and atomic percentage of different elements.	260
86	<b>Figure S6.5.</b>	(a, b) SEM image of $\text{CN}_x$	261
87	<b>Figure S6.6.</b>	GCD curves of bare Ni foam at 1 A/g current density.	261
88	<b>Figure S6.7.</b>	CV curves of $\text{Co}_1\text{Al}_3(\text{OH})_3$ at diff. scan rate.	262
89	<b>Figure 7.1.</b>	(a) p-XRD pattern, (b-d) TEM images, (e) SAED pattern, (f) HRTEM image, (g) STEM image of $\text{CoAl}_2\text{O}_4/\text{C}$ , and corresponding Elemental mapping of elements (h) Co, (i) Al, (j) O, (k) C, and (l) N of $\text{CoAl}_2\text{O}_4/\text{C}$ showing the uniform distribution of Co, Al, O, C, and N respectively.	274
90	<b>Figure 7.2.</b>	(a, b) $\text{N}_2$ desorption/adsorption isotherm and pore size distribution of $\text{CoAl}_2\text{O}_4/\text{C}$ .	276
91	<b>Figure 7.3.</b>	(a) XPS wide spectrum of $\text{CoAl}_2\text{O}_4/\text{C}$ . High resolution XPS spectra of (b) Co 2p, (c) Al 2p, (d) C 1s, and (e) O 1s respectively.	278
92	<b>Figure 7.4.</b>	(a) GCD profile of $\text{CoAl}_2\text{O}_4/\text{C}$ composite ( $1-10 \text{ A g}^{-1}$ ). (b) CV profile of $\text{CoAl}_2\text{O}_4/\text{C}$ from $5-60 \text{ mV s}^{-1}$ scan rate. (c) CD profile of $\text{CoAl}_2\text{O}_4/\text{C}$ with other ratios of $\text{Co}_m\text{Al}_n\text{O}_x/\text{C}$ at $1 \text{ A g}^{-1}$ current. (d) Comparison CV profile of $\text{CoAl}_2\text{O}_4/\text{C}$ and other ratios at a sweep rate of $30 \text{ mV s}^{-1}$ (e) Plot of $C_s (\text{F g}^{-1})$ of $\text{CoAl}_2\text{O}_4/\text{C}$ with	280

		current density ( $\text{A g}^{-1}$ ). (f) Plot of cyclic durability of $\text{CoAl}_2\text{O}_4/\text{C}$ at $10 \text{ A g}^{-1}$ current.	
93	<b>Figure 7.5.</b>	(a) CV profile of $\text{CoAl}_2\text{O}_4/\text{C}$ differentiating diffusive contribution and capacitive at $5 \text{ mV s}^{-1}$ scan rate. (b) Pseudocapacitance contribution of $\text{CoAl}_2\text{O}_4/\text{C}$ by varying sweep rates. (c) EIS plot profile of $\text{Co}_m\text{Al}_n\text{O}_x/\text{C}$ in $2\text{M KOH}$ .	285
94	<b>Figure 7.6.</b>	(a, b) GCD plot of AC from $1\text{-}7 \text{ A g}^{-1}$ current and CV cycles of AC under different sweep rates ( $5\text{-}100 \text{ mV sec}^{-1}$ ).	285
95	<b>Figure 7.7.</b>	Electrochemical behavior of asymmetric supercapacitor $\text{CoAl}_2\text{O}_4/\text{C} // \text{AC}$ device (a) CD profile of $\text{CoAl}_2\text{O}_4/\text{C} // \text{AC}$ at diff. current $1$ to $10 \text{ A g}^{-1}$ . (b) CV profile of device at diff. Scan rate ( $5$ to $100 \text{ mV s}^{-1}$ ). (c) $C_s$ at diff. current densities. (d) Ragone plot of $\text{CoAl}_2\text{O}_4/\text{C} // \text{AC}$ ASC and its comparison with literature. (e) EIS spectra of the ASC (f) cyclic durability of the ASC under $10 \text{ A g}^{-1}$ current.	287
96	<b>Figure S7.1.</b>	p-XRD pattern of (a) $\text{Co}_2\text{Al}_1\text{O}_x/\text{C}$ , (b) $\text{Co}_1\text{Al}_3\text{O}_x/\text{C}$ , (c) $\text{Co}_3\text{O}_4/\text{C}$ , and (d) $\text{Al}_2\text{O}_3/\text{C}$ composites.	293
97	<b>Figure S7.2.</b>	SEM image of $\text{CoAl}_2\text{O}_4/\text{C}$ composite.	294
98	<b>Figure S7.3.</b>	SEM image of (a) $\text{Al}_2\text{O}_3/\text{C}$ and (b) $\text{Co}_3\text{O}_4/\text{C}$ .	294
99	<b>Figure S7.4.</b>	(a) p-XRD pattern, (b) SEM image, and (c, d) High and low resolution TEM image of $\text{CoAl-LDH}/\text{C}$ respectively.	294
100	<b>Figure S7.5.</b>	$\text{N}_2$ adsorption-desorption isotherm of (a) $\text{Co}_2\text{Al}_1\text{O}_x/\text{C}$ (b) $\text{Co}_1\text{Al}_1\text{O}_x/\text{C}$ (c) $\text{Co}_1\text{Al}_3\text{O}_x/\text{C}$ and (d) $\text{CoAl-LDH}/\text{C}$ composites.	295
101	<b>Figure S7.6.</b>	High resolution XPS spectra of N $1s$ .	296
102	<b>Figure S7.7.</b>	GCD curves of bare Ni foam at $1 \text{ mA}$ current.	296
103	<b>Figure S7.8.</b>	GCD curves of (a) $\text{CoAl-LDH}/\text{C}$ , and (b) only $\text{CoAl}_2\text{O}_4$ $1 \text{ A g}^{-1}$ current density.	297
104	<b>Figure S7.9.</b>	EIS spectra of only $\text{CoAl}_2\text{O}_4$ .	297
105	<b>Figure S7.10.</b>	CV curves of AC and $\text{CoAl}_2\text{O}_4/\text{C}$ spinel at a sweep rate of $5 \text{ mV s}^{-1}$ .	298

106	<b>Figure 8.1.</b>	p-XRD pattern of (a) 1D-RuO <sub>2</sub> /C composite, and Ru-NPs/C, (b) N <sub>2</sub> desorption/adsorption isotherm of 1D-RuO <sub>2</sub> /C, RuO <sub>2</sub> , and Ru-NPs/C composites.	309
107	<b>Figure 8.2.</b>	(a, b) Low-resolution SEM images, (c, d) TEM images, (e) SAED pattern, and (f) HRTEM images of 1D-RuO <sub>2</sub> /C Composites.	311
108	<b>Figure 8.3.</b>	(a) Survey scan; XPS spectra of (b) Ru 3d + C 1s and (c) O 1s of 1D-RuO <sub>2</sub> /C composite.	312
109	<b>Figure 8.4.</b>	(a, b) CV and charging/discharging curves of 1D-RuO <sub>2</sub> /C, RuO <sub>2</sub> , and N@C composites at a scan rate of 40 mV/s and 5 A/g current. (c) CV curves of 1D-RuO <sub>2</sub> /C at sweep rate 5-100 mV s <sup>-1</sup> . (d) charging/discharging curves of 1D-RuO <sub>2</sub> /C at 5-15 A/g current. (e) Specific capacitance depends on the current density for 1D-RuO <sub>2</sub> /C and RuO <sub>2</sub> composites. (f) A cyclic lifetime of 1D-RuO <sub>2</sub> /C under 10 A g <sup>-1</sup> current.	315
110	<b>Figure 8.5.</b>	(a) Log (v) vs log (i) plot for cathodic and anodic peaks. (b) CV curve of 1D-RuO <sub>2</sub> /C showing capacitive and diffusive contribution at 5 mV s <sup>-1</sup> scan rate. (c) Pseudocapacitive contribution of 1D-RuO <sub>2</sub> /C (%) at different sweep rates. (d) Nyquist plots the profile of 1D-RuO <sub>2</sub> /C composites and RuO <sub>2</sub> in 2 M KOH.	318
111	<b>Figure 8.6.</b>	(a-b) CV profiles at a sweep rate of 10-100 mV s <sup>-1</sup> and GCD cycle under 1-10 A g <sup>-1</sup> current for AC.	319
112	<b>Figure 8.7.</b>	Electrochemical behavior of asymmetric supercapacitor (a) CV plots of 1D-RuO <sub>2</sub> /C //AC ASC device, (b) GCD plots of 1D-RuO <sub>2</sub> /C //AC at different current density, (c) C <sub>s</sub> vs. current density, (d) Ragone plot for a-1D-RuO <sub>2</sub> /C //AC device, (e) Nyquist plot of the ASC, (f) Cyclic lifetime of 1D-RuO <sub>2</sub> /C //AC asymmetric device at a current of 10 A g <sup>-1</sup> .	321
113	<b>Figure S8.1.</b>	FESEM image of 1D-RuO <sub>2</sub> /C.	324
114	<b>Figure S8.2.</b>	(a) SEM image and corresponding elemental mapping of elements (b) C, (c) N, (d) O, and (e) Ru respectively indicating uniform distribution of elements in 1D-RuO <sub>2</sub> /C.	325

115	<b>Figure S8.3.</b>	SEM image of N@C.	325
116	<b>Figure S8.4.</b>	TEM image of N@C.	325
117	<b>Figure S8.5.</b>	(a, b) CV and charging/discharging curves of N@C.	326
118	<b>Figure S8.6.</b>	GCD curve of bare Ni foam at 1 mA current.	326
119	<b>Figure S8.7.</b>	FESEM image of 1D-RuO <sub>2</sub> /C after capacitance retention test.	327
120	<b>Figure S8.8.</b>	CV curves of AC and 1D-RuO <sub>2</sub> /C at a scan rate of 10 mV s <sup>-1</sup> .	327
121	<b>Figure S8.9.</b>	CV curves for ASC (1D-RuO <sub>2</sub> /C// AC) device at potential ranging from 1.2 V to 1.6 V.	328
122	<b>Figure 9.1.</b>	XRD pattern of (a) a-MoS <sub>2</sub> /C-dots, and c-MoS <sub>2</sub> /C-dots, (b) Raman spectra of a-MoS <sub>2</sub> /C-dots, and c-MoS <sub>2</sub> /C-dots, (c) Wide XPS spectrum of a-MoS <sub>2</sub> /C-dots, High-resolution XPS spectra of (d) Mo 3d, (e) S 2p, and (f) C 1s respectively, (g) N <sub>2</sub> desorption/adsorption isotherm of a-MoS <sub>2</sub> /C-dots and a-MoS <sub>2</sub> composites, and (h) photoluminescence spectra of a-MoS <sub>2</sub> /C-dots and a-MoS <sub>2</sub> excited at 240 nm.	340
123	<b>Figure 9.2.</b>	(a, b) Low-resolution TEM and, (c) HRTEM images (inset shows the SAED pattern), (d) Enlarged view of HRTEM image, (e) STEM image and corresponding elemental mapping of (f) Mo, (g) S, and (h) C in a-MoS <sub>2</sub> /C-dots Composites. (i, j) Low-resolution TEM images, (k) SAED pattern, and (l) HRTEM image of c-MoS <sub>2</sub> /C-dots Composites showing defects.	342
124	<b>Figure 9.3.</b>	(a, b) Comparison of CV and GCD plot profiles for a-MoS <sub>2</sub> /C-dots, a-MoS <sub>2</sub> , c-MoS <sub>2</sub> /C-dots, and h-MoS <sub>2</sub> /C-dots composites at sweep rate of 5 mV s <sup>-1</sup> and 1 A g <sup>-1</sup> current. (c) CV profile of a-MoS <sub>2</sub> /C-dots at different scan rates (1-50 mV s <sup>-1</sup> ). (d) GCD profile of a-MoS <sub>2</sub> /C-dots (1-10 A g <sup>-1</sup> ). (e) C <sub>s</sub> Comparison Plot of a-MoS <sub>2</sub> /C-dots, a-MoS <sub>2</sub> , c-MoS <sub>2</sub> /C-dots, and h-MoS <sub>2</sub> /C-dots composites w.r.t current. (f) Percentage capacitance retention (%) w.r.t cycling number for a-MoS <sub>2</sub> /C-dots, c-MoS <sub>2</sub> /C-dots, h-MoS <sub>2</sub> /C-dots, and a-MoS <sub>2</sub> composites at current of 15 A g <sup>-1</sup> .	344

125	<b>Figure 9.4.</b>	(a) Plot of $\log(i)$ w.r.t $\log(v)$ . (b) CV profile of a-MoS <sub>2</sub> /C-dots differentiating diffusive contribution and capacitive contribution at 1 mV s <sup>-1</sup> sweep rate. (c) Pseudocapacitive contribution of a-MoS <sub>2</sub> /C-dots by varying scan rates. (d) EIS plot profile of a-MoS <sub>2</sub> /C-dots, a-MoS <sub>2</sub> , c-MoS <sub>2</sub> /C-dots, and h-MoS <sub>2</sub> /C-dots composites in 2M KOH.	351
126	<b>Figure 9.5.</b>	(a-b) GCD profiles under 1-7 A g <sup>-1</sup> current and CV profiles at of 5-100 mV s <sup>-1</sup> sweep rate for AC.	353
127	<b>Figure 9.6.</b>	Electrochemical behavior of ASC for a-MoS <sub>2</sub> /C-dots //AC device (a) CV profiles ASC at a sweep rate of 5-40 mV s <sup>-1</sup> , (b) GCD profile of a-MoS <sub>2</sub> /C-dots //AC (1-10 A g <sup>-1</sup> ), (c) C <sub>s</sub> vs. current density, (d) Ragone plot for a-MoS <sub>2</sub> /C-dots//AC ASC, (e) EIS curve of the ASC (f) Cycling stability of ASC over 6000 GCD cycles.	355
128	<b>Figure S9.1.</b>	High resolution XPS spectra of N1s/Mo3p in a-MoS <sub>2</sub> /C-dots.	361
129	<b>Figure S9.2.</b>	UV-visible spectrum, (b) PL spectra at different wavelengths, and (c) Normalized PL spectra of C-dots excited at different wavelengths.	362
130	<b>Figure S9.3.</b>	STEM image and corresponding elemental mapping of (a) Mo, (b) S, and (c) C in c-MoS <sub>2</sub> /C-dots Composites.	362
131	<b>Figure S9.4.</b>	FESEM image of (a) a-MoS <sub>2</sub> /C-dots, (b) c-MoS <sub>2</sub> /C-dots, (c) h-MoS <sub>2</sub> /C-dots, and (d) a-MoS <sub>2</sub> .	362
132	<b>Figure S9.5.</b>	XRD pattern of (a) h-MoS <sub>2</sub> /C-dots, and (b) a-MoS <sub>2</sub> , low resolution TEM image of (c) h-MoS <sub>2</sub> /C-dots, and (d) a-MoS <sub>2</sub> .	363
133	<b>Figure S9.6.</b>	GCD curves of bare Ni foam at 1 mA current.	363
134	<b>Figure S9.7.</b>	(a) XRD and (b) FESEM image of a-MoS <sub>2</sub> /C-dots after capacitance retention test.	364
135	<b>Figure S9.8.</b>	Comparison CV profiles of a-MoS <sub>2</sub> /C-dots at scan rate 1-4 mV s <sup>-1</sup> .	364
136	<b>Figure S9.9.</b>	CV curves of AC and a-MoS <sub>2</sub> /C-dots at a scan rate of 5 mV s <sup>-1</sup> .	365

137	<b>Figure S9.10.</b>	CV curves for ASC device at potential ranging from 1-1.5 V.	365
138	<b>Figure 10.1.</b>	(a) p-XRD pattern, (b, c) TEM images of 1D NiCo-MOF-31, (d-h) STEM image and elemental mapping of 1D NiCo-MOF-31.	375
139	<b>Figure 10.2.</b>	(a) FT-IR spectrum of all the seven MOFs, (b) N <sub>2</sub> desorption/adsorption isotherm, and (c) PSD of 1D NiCo-MOF-31.	377
140	<b>Figure 10.3.</b>	High-resolution XPS spectra of (a) Ni 2p, (b) Co 2p, (c) C 1s, and (d) O 1s of 1D NiCo-MOF-31.	379
141	<b>Figure 10.4.</b>	(a, b) Comparison CV and GCD profiles of all the MOFs under 5 mV s <sup>-1</sup> sweep rate and 1 A g <sup>-1</sup> current respectively. (c, d) CV (5 to 100 mV s <sup>-1</sup> ) and GCD (1–10 A g <sup>-1</sup> ) profile of 1D NiCo-MOF-31, (e) Comparison of C <sub>s</sub> plot w.r.t current for all the MOFs. (f) Cyclic durability test of 1D NiCo-MOF-31 under 7 A g <sup>-1</sup> current.	381
142	<b>Figure 10.5.</b>	(a) log (peak current) vs. log(sweep rate) plot. (b) CV profile of 1D NiCo-MOF-31 displaying contribution area of the pseudocapacitance at a scan rate of 5 mV s <sup>-1</sup> . (c) Pseudocapacitive contribution of 1D NiCo-MOF-31 at a scan rate of 5 and 10 mV s <sup>-1</sup> . (d) EIS profile of all MOFs in 3 M KOH.	388
143	<b>Figure 10.6.</b>	(a, b) CV profile of SNAC at different sweep rates and GCD profile of SNAC at different current.	390
144	<b>Figure 10.7.</b>	(a, b) CV and GCD curves at different scan rates and different current densities. (c) Plot of C <sub>s</sub> vs. current. (d) Plot of ED vs. PD and comparison to recently reported SC devices. (e) EIS plot. (f) Cyclic stability performance for 5000 cycles under 7 A g <sup>-1</sup> for the ASC device.	392
145	<b>Figure S10.1.</b>	p-XRD pattern of all the MOFs.	395
146	<b>Figure S10.2.</b>	FESEM image of (a, b) 1D NiCo-MOF-31.	395
147	<b>Figure S10.3.</b>	FESEM image of (a) 1D NiCo-MOF-11, (b) 1D NiCo-MOF-13, (c) 1D NiCo-MOF-21, (d) 1D NiCo-MOF-41, (e) Co-MOF, and (f) Ni-MOF.	396

148	<b>Figure S10.4.</b>	(a, b) HRTEM images and (c) enlarged HRTEM images of 1D NiCo-MOF-31.	396
149	<b>Figure S10.5.</b>	(a) N <sub>2</sub> desorption/adsorption isotherm, and (b) PSDs of 1D NiCo-MOF-x.	397
150	<b>Figure S10.6.</b>	XPS survey scan of 1D NiCo-MOF-31.	397
151	<b>Figure S10.7.</b>	GCD curve of bare Ni foam at 1 mA current.	398
152	<b>Figure S10.8.</b>	(a) CV and (b) GCD profiles of 1D NiCo-MOF-11.	398
153	<b>Figure S10.9.</b>	(a) CV and (b) GCD profiles of 1D NiCo-MOF-13.	399
154	<b>Figure S10.10.</b>	(a) CV and (b) GCD profiles of 1D NiCo-MOF-41.	399
155	<b>Figure S10.11.</b>	(a) CV and (b) GCD profiles of 1D NiCo-MOF-21.	400
156	<b>Figure S10.12.</b>	(a) CV and (b) GCD profiles of Co-MOF.	400
157	<b>Figure S10.13.</b>	(a) CV and (b) GCD profiles of Ni-MOF.	401
158	<b>Figure S10.14.</b>	CV curves of SNAC and 1D NiCo-MOF-31 at a scan rate of 5 mV s <sup>-1</sup> .	401
159	<b>Figure S10.15.</b>	CV curves for ASC (1D NiCo-MOF-31// SNAC) device at potential ranging from 1 V to 1.6 V.	402

## LIST OF TABLES

Sl. No.	Table Caption	Page No.
------------	---------------	----------

1	<b>Table 2.1.</b>	Materials used for experimental work along with formula and supplier name	84
2	<b>Table 2.2.</b>	The details description of Bode and Nyquist plot	95
3	<b>Table 2.3.</b>	The components and their indication for equivalent circuit	96
4	<b>Table 3.1.</b>	Structural properties and pore analysis of p-BCN-X.	116
5	<b>Table 3.2.</b>	Performance comparison of BCN-800 and p-BCN-800 samples with other reported materials.	121
6	<b>Table 3.3.</b>	The H <sub>2</sub> adsorption capacity of p-BCN-X compared with previous reports.	136
7	<b>Table S3.1.</b>	Weight % of B, C, N, and O present in BCN-700 and p-BCN-X samples calculated from SEM EDX analysis.	144
8	<b>Table S3.2.</b>	Comparison of electrochemical performance of BCN-X samples in 6M KOH electrolyte.	144
9	<b>Table S3.3.</b>	Comparison of electrochemical performance of BCN-X samples in 6M KOH electrolyte.	145
10	<b>Table S3.4.</b>	CO <sub>2</sub> uptake capacities of carbon materials at 25 °C temperature and 1 bar pressure.	145
12	<b>Table 4.1.</b>	Detailed surface properties and pore analysis of p-CNS-X.	161
13	<b>Table 4.2.</b>	Performance comparison of p-CNS-X samples with other reported materials.	167
14	<b>Table 4.3.</b>	CO <sub>2</sub> uptake capacities of carbon materials at 25 °C temperature and 1 bar pressure.	177
15	<b>Table S4.1.</b>	Weight % of C, S, N, and O present in p-CNS-X samples calculated from SEM EDX analysis.	189
16	<b>Table S4.2.</b>	Comparison of electrochemical performance of p-CNS-X samples in 6M KOH electrolyte.	190
17	<b>Table 5.1.</b>	Detailed surface properties and pore analysis of PCN-x.	202



18	<b>Table 5.2.</b>	Electrochemical performance of PCN-800 with reported heteroatom doped porous carbon materials.	207
19	<b>Table 5.3.</b>	The H <sub>2</sub> storage capacity of PCN-900 compared with previously reported result.	217
20	<b>Table S5.1.</b>	Weight % of C, P, N, and O present in PCN-x samples calculated from SEM EDX analysis.	229
21	<b>Table S5.2.</b>	Comparison of electrochemical performance of PCN-x samples in 6M KOH electrolyte.	230
22	<b>Table S5.3.</b>	CO <sub>2</sub> uptake capacities of carbon materials at 25 °C temperature and 1 bar pressure.	230
23	<b>Table S6.1.</b>	Composition analysis of the Co <sub>1</sub> Al <sub>δ</sub> (OH) <sub>m</sub> /CN <sub>x</sub> (δ=1, 2, 3, 4) composites from elemental mapping.	262
24	<b>Table S6.2.</b>	Relative percentage of area and atomic ratio of Co <sup>+2</sup> /Co <sup>+3</sup> in Co 2p <sub>3/2</sub> and 2p <sub>1/2</sub> of Co <sub>1</sub> Al <sub>3</sub> (OH) <sub>m</sub> /CN <sub>x</sub> composite.	263
25	<b>Table S6.3.</b>	Comparison of electrochemical performance of Co <sub>1</sub> Al <sub>3</sub> (OH) <sub>m</sub> /CN <sub>x</sub> composite with previously reported literatures.	263
26	<b>Table 7.1.</b>	Comparison of electrochemical performance of CoAl <sub>2</sub> O <sub>4</sub> /C composite with previously reported literatures.	280
27	<b>Table S7.1.</b>	Composition analysis of the CoAl <sub>2</sub> O <sub>4</sub> /C and Co <sub>m</sub> Al <sub>n</sub> O <sub>x</sub> /C from ICP-OES.	298
28	<b>Table S7.2.</b>	Comparison of electrochemical performance of Co <sub>m</sub> Al <sub>n</sub> O <sub>x</sub> /C composite by varying Co/Al ratio.	299
29	<b>Table 8.1.</b>	Electrochemical properties of different composites with 1D-RuO <sub>2</sub> /C composite as electrode materials with previously reported literature.	315
30	<b>Table S8.1.</b>	Weight % of Ru, O, C, and N present in 1D-RuO <sub>2</sub> /C samples calculated from SEM EDX analysis.	328

31	<b>Table 9.1.</b>	Comparison of electrochemical performance of a-MoS <sub>2</sub> /C-dots electrode material with previously reported literature.	345
32	<b>Table S9.1.</b>	Stoichiometry of MoS <sub>2</sub> as determined by TEM EDX and XPS in a-MoS <sub>2</sub> /C-dots composite.	365
33	<b>Table S9.2.</b>	Comparison of electrochemical performance of a-MoS <sub>2</sub> /C-dots, a-MoS <sub>2</sub> , c-MoS <sub>2</sub> /C-dots, and h-MoS <sub>2</sub> /C-dots composites.	366
34	<b>Table 10.1.</b>	Electrochemical performance of 1D NiCo-MOF-31 with recently reported MOF materials.	386
35	<b>Table S10.1.</b>	1D NiCo-MOF-31 in terms of atomic percentage obtained from TEM EDS.	402
36	<b>Table S10.2.</b>	Weight percentage of Co and Ni calculated from ICP-OES.	402
37	<b>Table S10.3.</b>	Comparison of electrochemical performance of all the MOFs in 3M KOH electrolyte.	403

## LIST OF SCHEMES

Sl. No.		<b>Scheme Caption</b>	<b>Page No.</b>
1	<b>Scheme 3.1.</b>	Synthesis of 2D Boron carbonitride (BCN-X) and 2D porous Boron carbonitride (p-BCN-800).	105
2	<b>Scheme 3.2.</b>	Possible redox reactions and increased capacitance of p-BCN-800 in alkaline medium.	128
3	<b>Scheme 4.1.</b>	Synthesis of 2D S and N co-doped carbon (CNS) and 2D porous CNS-X (p-CNS-X).	152
4	<b>Scheme 4.2.</b>	Possible redox reactions of sulphur-oxo species in acidic and alkaline medium.	171
5	<b>Scheme 5.1.</b>	Scheme illustrating synthesis of PCN-x.	196
6	<b>Scheme 5.2.</b>	Possible redox reactions in acidic electrolyte.	209

7	<b>Scheme 7.1.</b>	Scheme illustrating synthesis of CoAl <sub>2</sub> O <sub>4</sub> /C.	270
8	<b>Scheme 8.1.</b>	Schematic representation for the Synthesis of 1D-RuO <sub>2</sub> /C composite.	306
9	<b>Scheme 10.1.</b>	Scheme illustrating synthesis of 1D NiCo-MOF-31.	371

## **Chapter 1**

### **Overview of sustainable electrochemical energy and gas storage applications**

#### **1.1. ABSTRACT**

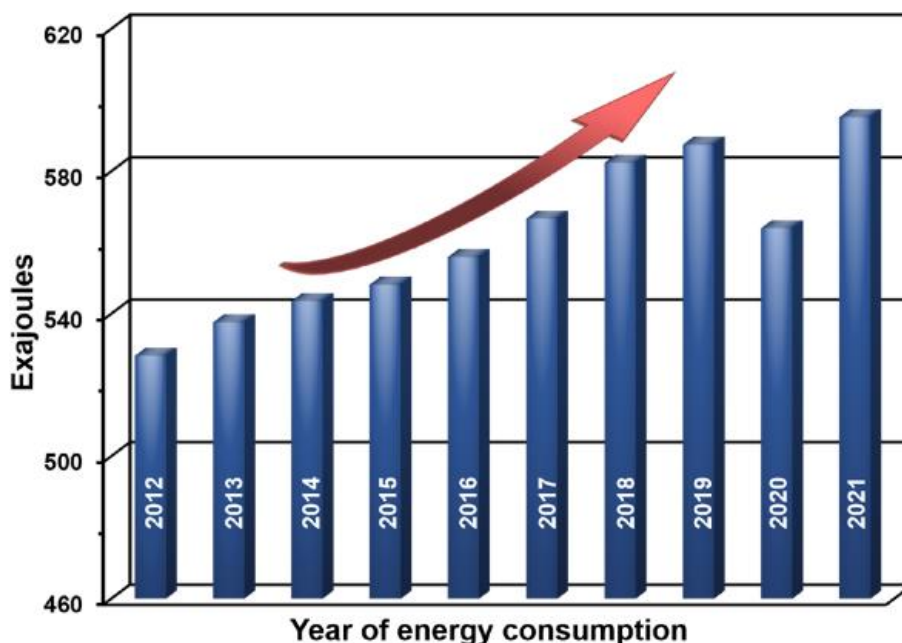
Considering the increasing energy crisis, supercapacitors (SC) are becoming increasingly popular due to the recent advancements in electronic devices. In compared to batteries, SC offer fast charging/discharging time, high power density, high energy density, and long lifespan. Herein we summarize the designing of new electrode material and fabrication of asymmetric SC (ASC) and symmetric SC device (SSC) for energy storage applications. Fundamentally, the mechanism is studied based on some in-situ characterization techniques and simulations that relate the structural properties of electrode materials to their electrochemical performances. Secondly, the basic concepts about the working principle of energy storage devices like aqueous supercapacitor. Thirdly emerging electrode materials are discussed, such as layered double hydroxide (LDH), transition metal oxide and sulphide. Fourthly heteroatom doped activated porous carbon have been studied for both energy and gas storage. Finally at the end of this chapter, we outline the goals of the current thesis.

#### **1.2. INTRODUCTION**

##### **1.2.1. Importance of Supercapacitor (SC)**

Energy storage is a pivotal component for the preservation and mobilization of energy resources, enabling their deployment for future applications. This necessity

becomes more pronounced when dealing with intermittent primary energy sources, such as renewables. Nature manifests energy in diverse forms, including electrical, thermal, chemical, nuclear, radiant, and gravitational energy, with electrical energy holding particular significance. The paramount requirement for energy storage lies in its ability to facilitate the generation of electricity on a large scale, thereby fulfilling the energy demands of contemporary society. Electricity represents the rapid flow of energy with no inherent shelf-life. Upon generation from an energy source, it is promptly consumed by energy-utilizing devices, with any surplus being dissipated. Consequently, the storage of electricity becomes crucial to ensure its availability for future utilization as and when required. Currently, scientific research is predominantly focused on the advancement of clean energy storage technologies in contrast to the consumption of fossil fuels, which has proven detrimental to society. These storage technologies hold significant importance for the future development and integration of renewable energy-based systems, hybrid electric vehicles (HEV), and portable electronic devices.



**Figure 1.1.** Statistics of the world’s primary energy consumption for the last 10 years.

With increase in energy demand, it is essential to storage energy in order to maintain the balance between energy production and consumption. With increasing global population, economic revolution, invention of machines and technologies, and modern human life style, the total energy consumption rate is growing exponentially. Based on annual BP statistical review of world energy 2022, worldwide the total amount of primary energies consumed exceeded 595 exajoules in 2021. This is 3 and 5.5% higher than in 2019 and 2020 respectively<sup>1</sup>. Figure 1.1. shows the world primary energy consumption statistics for last 10 years<sup>1</sup>. Solar and wind energy generation experiences substantial fluctuations, posing challenges for seamless integration into the power grid, which requires stable power inputs. Energy storage devices play a crucial role in addressing this issue by incorporating batteries into electrical grids, enabling easy integration with renewable energy sources. By storing excess renewable energy during peak production periods and

supplying it to the grid when demand arises, these batteries contribute to a smoother and more predictable power supply.

In regions lacking access to grid electricity, energy storage devices offer a viable solution to harness electricity from renewable sources, providing a means for electrification in remote or underserved areas.

In the realm of transportation, energy storage devices (ESD) have proven invaluable for the development of HEVs. These vehicles combine electrical storage systems with small petrol engines, resulting in reduced reliance on fossil fuels. Additionally, some HEVs implement regenerative braking, wherein the electric motor operates as a generator during braking, converting kinetic energy from the wheels into electrical energy stored in the battery. This recovered energy is then available for accelerating the vehicle, enhancing overall energy efficiency.

Lastly, the contemporary reliance on advanced electronic devices such as smartphones, iPads, iPods, cameras, and laptops is made possible through the utilization of lithium-ion batteries, which have become an integral part of modern society's technological landscape.

### **1.3. Types of Energy Storage Devices (ESD)**

Energy storage systems function by receiving and releasing electrical energy, but their primary purpose is to convert this energy into another form for storage. Various types of electrical energy storage devices have been developed, each based on a specific energy storage principle. These technologies encompass diverse processes, such as mechanical, thermal, chemical, electrical, and electrochemical

methods. This results in the existence of multiple types of electrical energy storage (EES) systems displayed in Figure 1.2<sup>2</sup>.

**Mechanical Energy Storage Device:**

Surplus electrical energy is stored using different mechanisms, including the storage of kinetic energy in flywheels, potential energy in water, and compression energy in the air. Subsequently, this stored energy is converted back into electrical energy when needed.

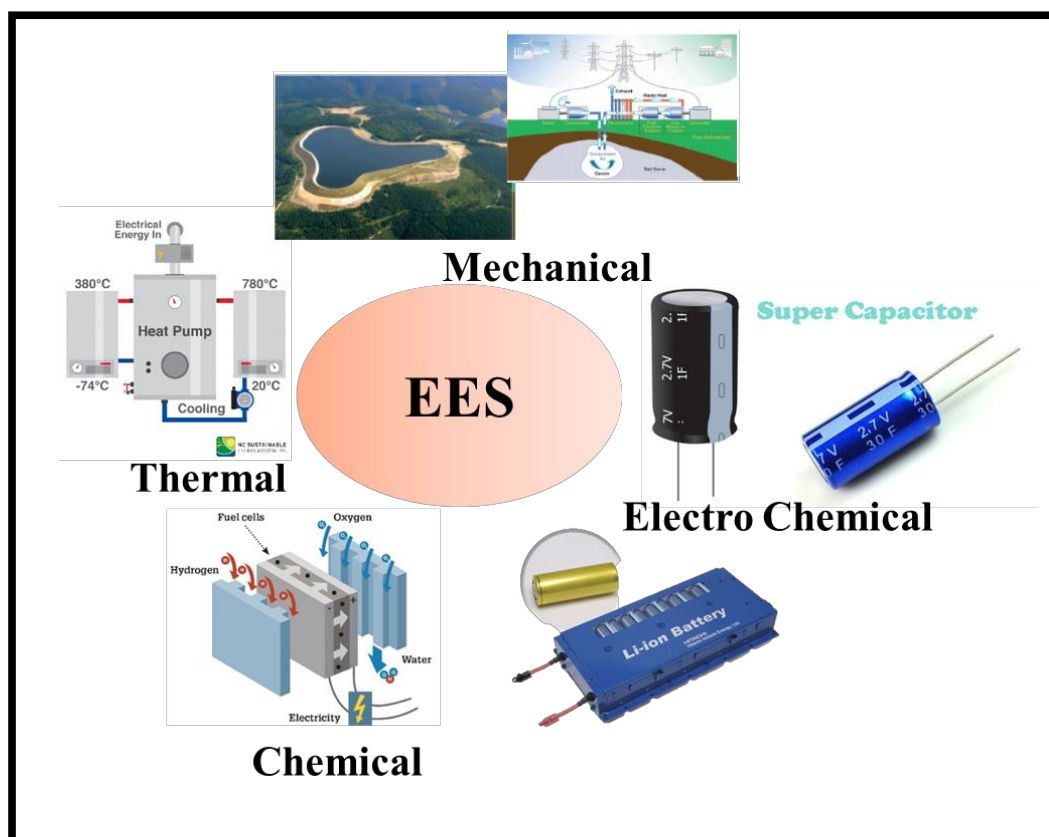
**Thermal Energy Storage Device:** A thermal ESD, exemplified by a steam boiler, generates energy through the utilization of coal, natural gas, or biomass as fuel sources. This fuel combustion produces steam, which then drives a turbine connected to a generator, thereby generating electricity.

**Chemical Energy Storage Device:** This stores energy in the form of chemical fuels, wherein  $H_2$ , a fuel variant, participates in electricity generation within a fuel cell.

**Electrical Energy Storage Device:** These devices employ electrostatic means to store electrical energy. Examples of such electrical energy storage devices include capacitors and superconducting magnetic storage, exemplified by Superconducting Magnetic Energy Storage (SMES) technology, which stores electricity from the grid within a magnetic field. A capacitor is a device that uses two conducting plates separated by a dielectric substance to store electrical charge. When the two plates are connected to a power source, a potential difference is created between them, leading to the development



of an electric field across the dielectric material and subsequent charge separation at the electrode surface. Between the two plates of the capacitor, an electric field is used to store energy.



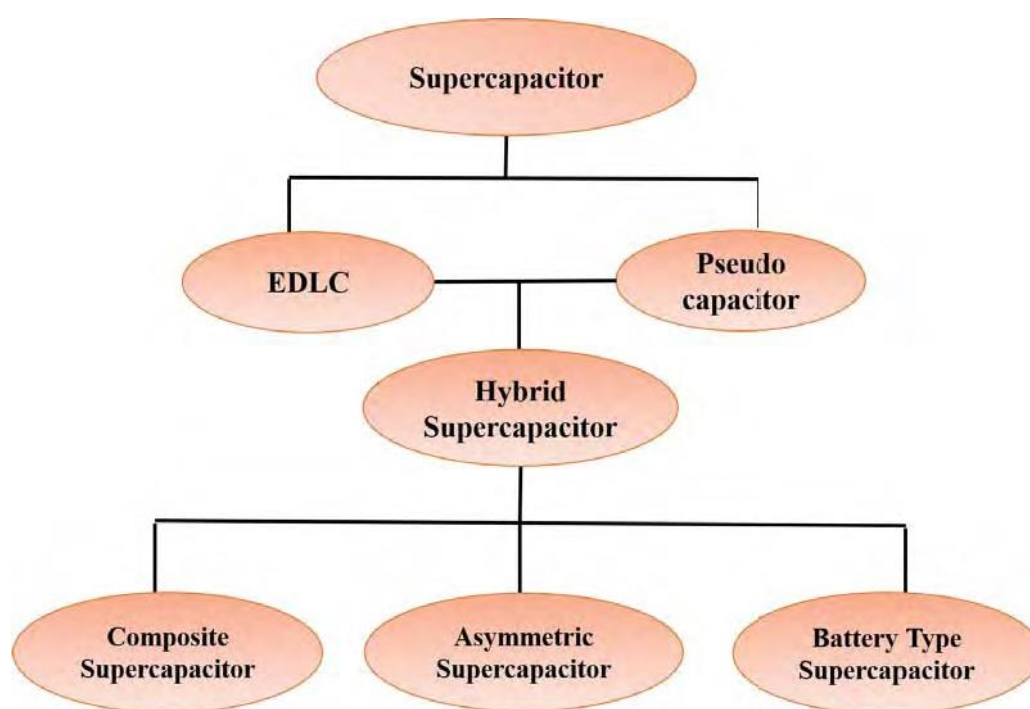
**Figure 1.2.** Different types of electrical energy storage systems<sup>2</sup>.

**Electrochemical Energy Storage Device:** The primary function shared by these devices is to store chemical energy through the electrochemical redox process and subsequently convert this chemical energy into electrical energy. Electrochemical energy storage devices encompass various types of batteries, which including secondary batteries, flow batteries, and SCs. Commonly available secondary batteries can be categorized into several groups, such as standard batteries, which include lead-acid and Ni-Cd batteries; advanced batteries, including Li-ion, Li-ion polymer, and Ni-metal hydride batteries; and special batteries, like Ag-Zn and Ni-

H<sub>2</sub> batteries. Flow batteries, such as Br<sub>2</sub>-Zn and Vanadium redox batteries, store energy directly within the electrolyte solution.

#### **1.4. Types of supercapacitors according to the energy storage mechanism**

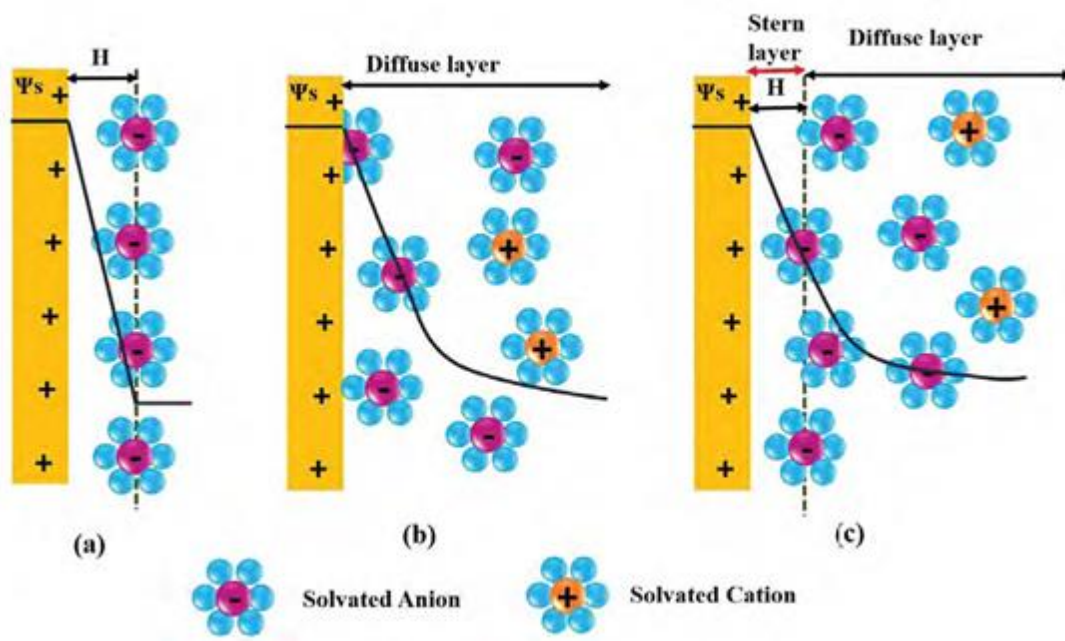
The operational foundation of a SCs relies on the electrochemical phenomenon of ion migration from the electrolyte to the electrode's surface area, facilitating energy storage and distribution. Based upon the energy storage principle, SCs are categorized into three types: EDLCs, Pseudocapacitors (PCs), and hybrid SCs as presented in Figure 1.3<sup>3</sup>.



**Figure 1.3.** Diagram of different types of SCs<sup>3</sup>.

#### **1.4.1. EDLCs**

The EDLCs store charge electrostatically or via a non-faradic process. This process includes no charge transfer of between electrolyte and electrode which is an electrostatic reversible ion adsorption process in the electrolyte onto the active material. The principle is based on the formation of a double layer having a few nanometres of thickness at the surface of the electrode to maintain electrical neutrality. The layer formed is called EDLs. This can be explained by Helmholtz model, ascribed in Figure 1.4(a)<sup>4</sup>. According to Helmholtz model hypothesis counter ions form a monolayer near the surface of the electrode. The mechanism is similar to that of conventional dielectric capacitors where the two electrodes are separated from each other by a small distance  $H$ , approximated as the ion's radius. Though the Helmholtz model was unable to elucidate the diffusion of ions in the solution and the interaction of dipole moment of the solvent molecule and the electrode. So the Helmholtz model was modified and the diffuse model of EDL was proposed by Gouy and Chapman. According to Gouy and Chapman, the ion distribution are continuous in the electrolyte solution and give the Boltzmann distribution. The Gouy-Chapman model accommodates the ion mobility in the electrolyte solution,



**Figure 1.4.** Schematic representation illustrating (a) Helmholtz model, (b) Guy-Chapman model, and (c) Guy Chapman-Stern model of EDLC supercapacitor (Adopted with permission from ref. 4 copyright © 2009 The Royal Society of Chemistry).

which arises from both ion diffusion driven by concentration gradients and electromigration due to the electric potential gradient, represented by the electric field resulting in the formation of diffusion layer presented in Figure 1.4(b)<sup>4</sup>. The overestimation of EDLC in the Gouy-Chapman model is attributed to its treatment of ions as point charges, leading to excessively high ion concentrations at the electrode surface, which are not realistic.

In 1924, a new model was proposed by Stern which is the combination of Helmholtz model and Gouy-Chapman model and explained two distinct regions. One is inner region with thickness  $H$  and termed as Stern layer and the second one is the outer layer also called the diffusion layer, as presented in Figure 1.4(c)<sup>4</sup>. The reversible electrostatic process gives the charging and discharging states of EDLC. It consist

of electrodes, electrolytes and a separator. The separator prevents the electronic contact of anode and cathode inside the electrolyte. Generally high SSA and activated carbon-based materials are used in EDLC devices. In EDLC type SC device, the specific capacitance ( $C_s$ ) dependence upon the surface area of the electrode material.

#### **1.4.2. Pseudocapacitor (PC)**

PCs stores charge via Faradic process which involves electron transfer process between the electrode and electrolyte i.e., reversible surface or near surface Faradic reactions to store charge. Upon application of potential, redox reaction takes place on the electrode material. This involves the passage of charge across the double layer, subsequent passage of Faradic current through the SC cell. Three distinct chemical processes contribute to the formation of a pseudocapacitor: firstly, the adsorption or chemisorption of ions from the electrolyte onto the electrode surface; secondly, the faradic reaction involving transition metal oxides (TMO); and finally, the reversible electrochemical doping/de-doping process occurring in conductive polymer-based electrodes. In SC applications, typical pseudocapacitive electrode materials encompass TMO, transition metal hydroxides, transition metal sulfides, and conducting polymers.

Pseudocapacitor involves different charge storage process presented in Figure 1.5.<sup>5</sup>: (i) under potential deposition, (ii) redox pseudocapacitance, (iii) intercalation pseudocapacitance, and (iv) doping pseudocapacitance<sup>6-7</sup>. In case of under potential deposition, adsorption of metal ions and hydrogen atoms takes place at the surface

of the metals like Pt, Rh, Ru, Ir etc. above their reversible redox potential i.e.,  $H^+$  or  $Pd^{2+}$  on Pt or Au. The mechanism is shown in equation (1.1) as follows:



Here  $M$  and  $A$  represents the noble metal and adsorbed atoms,  $y$ ,  $z$ , and  $yz$  are the number of adsorbed atoms, valence state of adsorbed ions, and number of transferred electron during the reaction process respectively<sup>6, 8</sup>.

In case of redox pseudocapacitance, electrochemical adsorption of cations takes place on the surface of the oxidized species ( $Ox$ ). This involves fast and reversible faradic charge transfer reactions across the electrode/electrolyte interface. The mechanism can be demonstrated by the following equation (1.2):



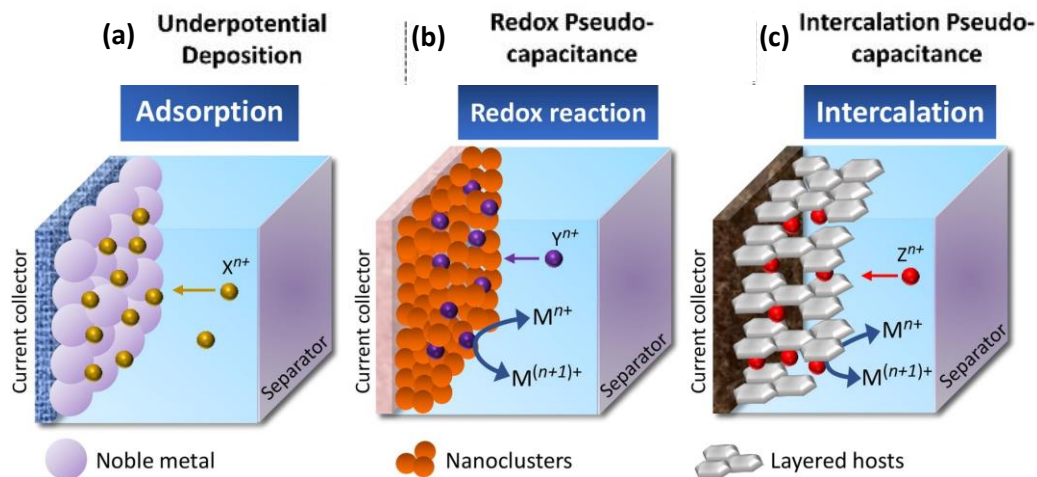
Here  $C^+$  electrolytic cation adsorbed on the surface like  $H^+$ ,  $K^+$ , and  $Na^+$  etc. and  $y$  represents the number of transferred electron<sup>8</sup>.

Intercalation pseudocapacitance involves insertion and extraction of electrolyte ions into the layered host material, accompanied by a change in the valence state of the electroactive material to maintain the charge neutrality as presented in equation (1.3):



Where  $MA_x$  and  $y$  stands for layered host material, and number of transferred electron during the electrochemical reaction respectively<sup>8</sup>.

Doping pseudocapacitance involves reversible doping and de-doping in the conducting polymers<sup>7</sup>.



**Figure 1.5.** Schematics of charge-storage mechanisms for (a) underpotential deposition, (b) redox pseudocapacitor, and (c) intercalation pseudocapacitor (Adopted with permission from ref. 5 copyright © 2022 Elsevier).

### 1.4.3. Hybrid SCs (HSCs)

EDLCs provide high PD, longer lifespan (>100k). However, Pseudocapacitor have high ED. Hybrid SC is the combination of both EDLC (high power source) and Pseudocapacitor (high energy source). The primary objective behind the design of HSCs is to enhance the overall ED and PD performance of the device by augmenting the cell voltage. The hybrid SCs are classified into three category depending upon their electrode configuration: (i) composite, (ii) asymmetric, and (iii) battery type SCs<sup>9</sup>.

#### 1.4.3.1. Composite SCs

Composite supercapacitors are fabricated by integrating carbon-based materials with pseudocapacitive electrode materials such as metal oxides/hydroxides and conducting polymers. This amalgamated electrode material is utilized within a single electrode. The charge storage mechanism in composite supercapacitors encompasses both electrostatic and chemical processes.

#### **1.4.3.2. Asymmetry SCs (ASCs)**

ASCs are a hybrid of EDLCs and pseudocapacitors. They have two electrodes with different electrochemical properties, with one electrode functioning as an EDLC and the other functioning as a pseudocapacitor. This allows for both high PD and high ED in the same device.

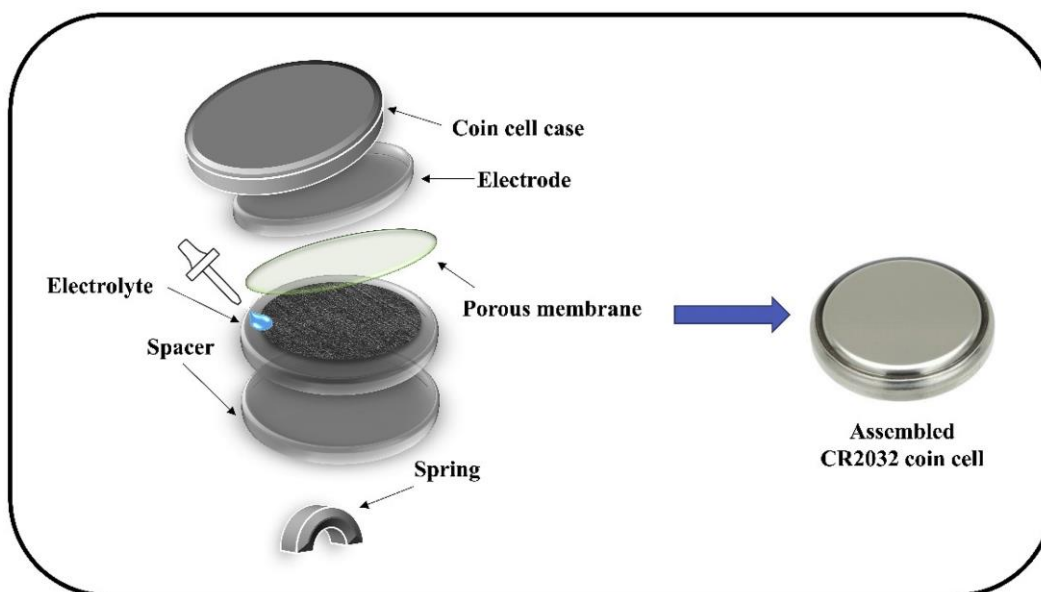
#### **1.4.3.3. Battery Type SCs**

Battery type SCs are formed by combining two different electrodes, like in the case of asymmetric hybrids. In battery type, SC electrode combined with battery type electrode. This type of arrangement was assembled to utilize the properties of both SC and battery in a single cell.

### **1.5. Basic Components of SC**

Frequently, the electrochemical assessment of supercapacitor devices can be carried out by utilizing a coin cell configuration, such as a two-electrode setup. Figure 1.6 displayed a representative illustration of a CR2032 model coin cell setup<sup>10</sup>. Different components of SC is listed below.





**Figure 1.6.** Scheme of the CR2032 coin cell used in the electrochemical characterization of supercapacitors. (Adopted with permission from ref. 8 copyright © 2020 Elsevier).

### 1.5.1. Current Collector

The choice of current collector material and design can significantly impact the overall performance and efficiency of the SC. The chemical stability of the current collector in specific electrolytes and diverse morphologies contribute significantly to the extended life cycle and improved charge storage performance of the SCs. Commonly used materials for current collectors in strong acidic electrolyte include anti-corrosion metals such as Au, indium tin oxide (ITO), and conductive carbon-based materials. In case of alkaline electrolyte, the materials used are Ni, Ti, carbon, and stainless steel etc. Among all the above materials, Ni based current collectors are generally used in alkaline medium owing to its good stability and cost effectiveness. The Ni-based current collector additionally provides pseudocapacitance behaviour owing to the formation of Ni oxide/hydroxide. Ni

foam is used as a very good current collector because of its high surface area (which can provide well exposure) towards the electrolyte for better electrochemical performance and due to its mesh like morphology. Ni, Ti, carbon based current collector (carbon cloth, ultrathin-graphite foam, carbon fibre paper), stainless steel are used as current collector in neutral electrolyte. Neutral electrolyte are more favourable for SC current collector materials due to its less corrosive nature.

### **1.5.2. Electrolytes**

The electrolyte is the foremost component in dictating the performance of a capacitor, encompassing roles such as ion supplementary, conduction of electric charge, and electrode particles adhesive. The essential characteristics the electrolyte should include is broad voltage window, low resistivity and toxicity, and high electrochemical stability etc. The electrolyte generally includes in supercapacitor devices are aqueous and organic electrolytes. Regarding electrolytic solutions, aqueous electrolytes (e.g., solutions containing KOH, H<sub>2</sub>SO<sub>4</sub>, Na<sub>2</sub>SO<sub>4</sub>, etc.) offer several advantages including elevated ionic conductivity, cost-effectiveness, non-flammability, corrosion resistance, safety, and facile assembly in ambient air<sup>11</sup>. These attributes stand in contrast to organic electrolytes, which tend to exhibit comparatively lower conductivity, increased costs, susceptibility to flammability, and elevated toxicity<sup>12</sup>. Nonetheless, these devices have constrained operating voltage range of 1V owing to the decomposition of water takes place at 1.23V<sup>13</sup>. The incorporation of redox-active entities within aqueous electrolytes can notably enhance the redox reactions between the electrode and electrolyte, as evidenced in the context of symmetric supercapacitors.

### **1.5.3. Binders**

Binders play a pivotal role in the construction of supercapacitors. The binder material is mix with the active components which provide robust adhesion that facilitate the attachment of electrode materials to the current collector. Furthermore, they establish a robust electric network between the active material and conducting carbon for easy electron transportation and ion diffusion. Usually fluorinated polymer-based binders such as polyvinylidene fluoride (PVDF) and polytetrafluoroethylene (PTFE) are extensively used owing to their widespread availability and established utility<sup>14-15</sup>. These polymers exhibit notable chemical resistance to acid and alkaline electrolytes, demonstrating high electrochemical stability.

### **1.5.4. Separators**

A separator constitutes a component positioned between two electrodes that physically separates the electronic contact between cathode and anode while facilitating the permeation of ions. Numerous parameters that should be taken into consideration when selecting a separator for a supercapacitor device. The separator must possess attributes such as porosity, chemical resistance to the electrolyte, low ionic resistance to facilitate ion transport, and substantial mechanical strength and flexibility. These characteristics collectively contribute to the longevity and compatibility of the device. Commonly, porous thin films or membranes are used as a separator<sup>16</sup>. These consist of cellulose-based materials, polymers and glass fibers. Glass fibers and certain polymer membranes PVDF and PTFE are used in alkaline electrolyte. Cellulose-based separators exhibit favorable surface

wettability in an aqueous medium and are compatible in neutral electrolyte. While both cellulose based and polymer separators are used in an organic electrolyte. The cellulose based separator suffers degradation in acidic medium<sup>17</sup>. In acidic electrolyte, Nafion@115, cellulose TF-40-30, celgard<sup>TM</sup>, celgard polypropylene separators are used. The device performance dependent upon the type of separator chosen. Presently, novel separators such as graphene oxide films and the egg shell membrane were investigated for their application in supercapacitor devices<sup>18</sup>.

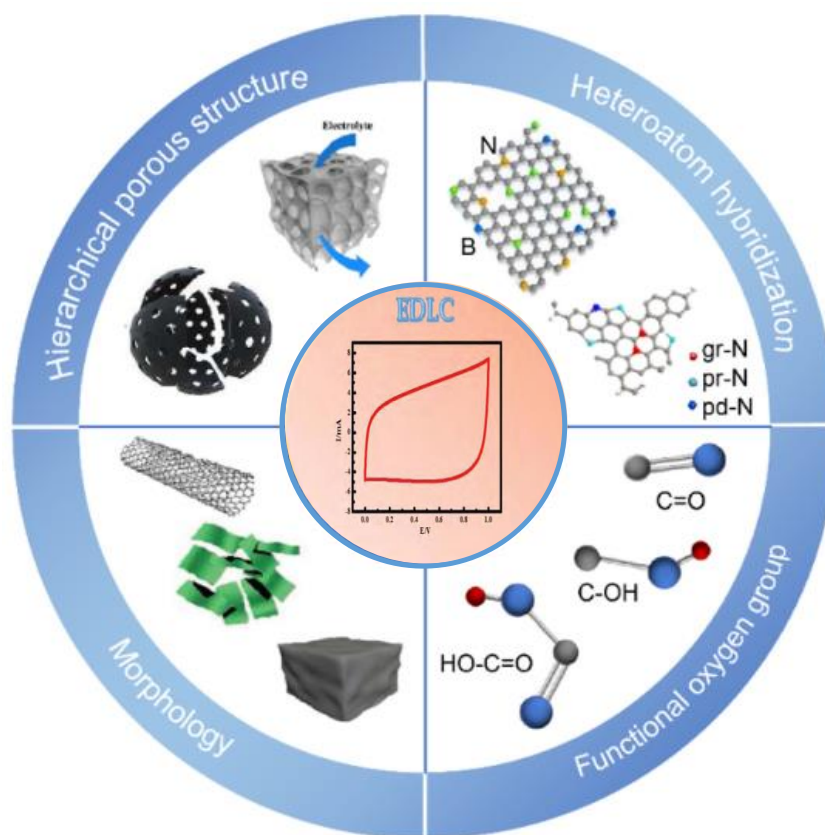
#### **1.5.5. Electrode Materials**

The capacitive performance of a SC is greatly influenced by the choice of electrode materials and their fabrication process. The electrode material must provide chemical and thermal stability, large SSA, high electrical conductivity, suitable surface wettability, cost effective, and environmental friendly etc. Besides that, the  $C_s$  of the SC device not only affected by SSA, but also some other factor including pore size distribution (PSD), pore volume, pore shape, pore size and their availability for the electrolyte ions. The electrode material is classified into two categories: EDLC and pseudocapacitive electrode material.

##### **1.5.5.1. EDLC Materials**

Carbon is the fourth most abundant element in the universe after hydrogen, helium and oxygen. Carbonaceous materials because of its high SSA, moderate cost, natural abundance, long life cycle, thermal and mechanical stability, and tunable pore structure are used for fabrication of SCs. EDLCs are three type based upon the content of carbon which involves: (i) carbon aerogels (nanopores), carbide derived carbon (tunable pore size), carbon foams (micropores), (ii) carbon nanotubes and

graphene, and (iii) Activated carbon. Figure 1.7. represents different types of EDLC electrode materials<sup>19 20</sup>. Carbon based materials worked in a wide temperature range. These are also electrochemically stable at a wide voltage range. This makes the SC of high voltage device. In case of carbon based material, the charge is stored at the electrical double layer. So, the catalytical properties greatly depends upon the surface chemistry, and porous architecture of the electrode materials.

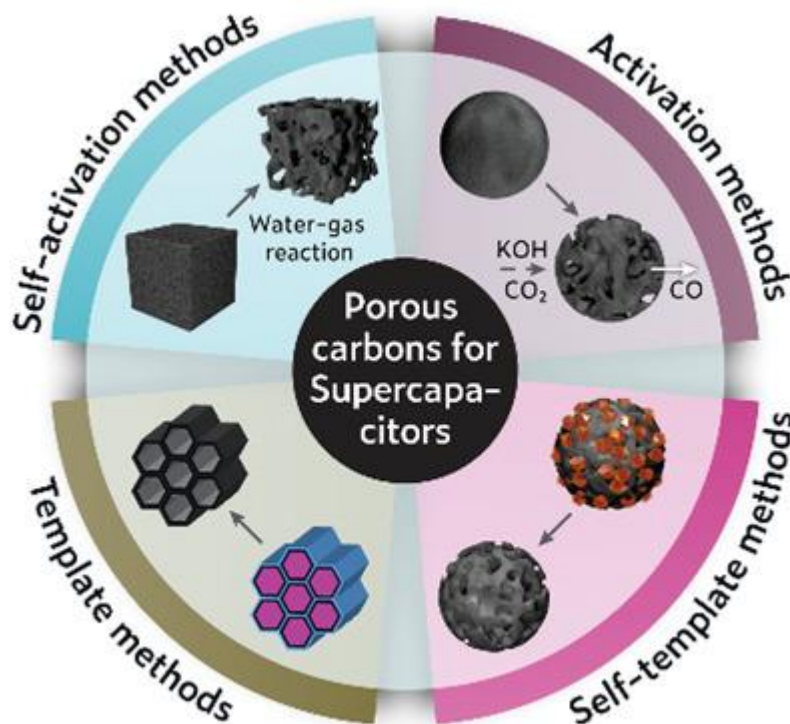


**Figure 1.7.** Schematic representation of different types of EDLC electrode materials<sup>20</sup>.

### Activated Carbons

In order to increase the capacitance of EDLC type electrode materials, development of high surface area porous carbon is needed. To increase the surface area of the

electrode, various strategies like physical and chemical activation of carbon, functionalization of the surface and heteroatom doping etc. are adopted<sup>21</sup> (Figure 1.8). Physical activation of carbon precursor takes place in presence of oxidizing agents (CO<sub>2</sub>, air, steam etc.) at a high temperature ranging from 700-1200 °C. Chemical activation process involves activating agents like NaOH, KOH, KCl, ZnCl<sub>2</sub>, H<sub>3</sub>PO<sub>4</sub> etc. at low temperature ranging from 400-700 °C. Physiochemical properties of the carbon material depends upon the activation methods and the precursors used with well-developed surface area up to 3000 m<sup>2</sup> g<sup>-1</sup>. The activation processes yielded an activated porous structure characterized by a wide PSD encompassing micropores (<2 nm), mesopores (2-50 nm), and macropores (>50 nm). The chemical activation is more preferred as it forms large SSA ranging from 1000 to 3000 m<sup>2</sup> g<sup>-1</sup> along with micro/mesopores having smooth surface area using KOH or NaOH as the activating agents, hence improving the capacitance<sup>21</sup>. Another approach to improve the capacitance is by introducing heteroatoms like N, S, B, and P into the carbon matrix.



**Figure 1.8.** Schematic representation of synthesis strategies of heteroatom doped porous carbon (Adopted with permission from ref. 19 copyright © 2020 Wiley).

### Heteroatom doped carbon

Heteroatom doping process refers to introduction of additional atoms like N, S, F, Se, O, B, P into the carbon matrix to replace part of the position of carbon atoms. Heteroatom doping to the carbon skeleton produce various structural defects, creates more active sites, introduce functional groups, and tune charge distribution for better electrical conductivity. Depending upon the number of doped heteroatoms, they are classified into single-doped porous carbon or co-doped porous carbon i.e. N/S, N/B, N/P, N/O etc. Introduction of binary atoms can enhance the physicochemical properties of carbon materials such as surface

wettability, electrical conductivity, and hence increases their electrochemical properties by synergistic effect<sup>22</sup>.

### **Effect of heteroatom doping into carbon**

Heteroatom doping improves the electrochemical performance of the electrode as:

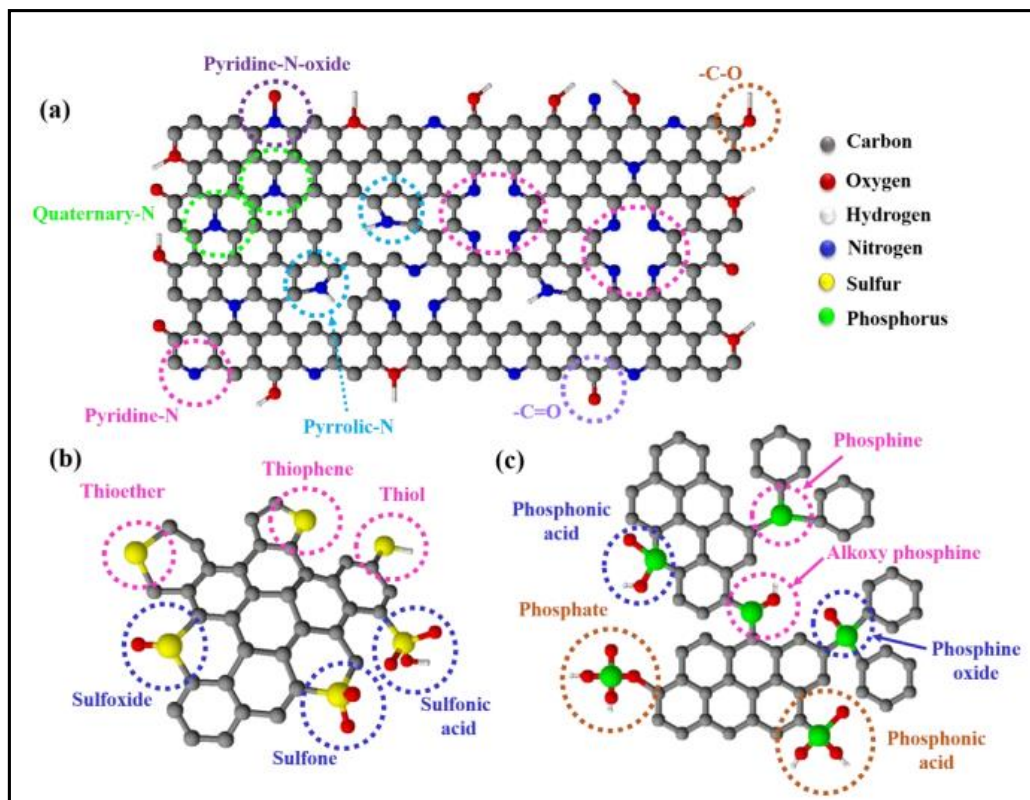
- I. Introduction of heteroatoms introduce more active and defect sites into the carbon framework create redox reactions which provides pseudocapacitance hence enhancing the specific capacitance of the electrodes.
- II. Introduction of hydrophilic functional groups improves the wettability of the electrodes.
- III. Introduction of heteroatom into the carbon skeleton enhance the electrical conductivity by regulating and controlling the charge distribution and accelerating the electron transfer.

### **Nitrogen (N) doping**

Nitrogen is the most commonly used doped atom for carbon materials. N doping to carbon framework has attracted significant attention due to the following reasons: The doped N in the carbon framework exist in four forms: pyrrolic N, pyridinic N, quaternary N (graphitic), and oxidized N<sup>23-25</sup>. The electrochemical activities of N-doped porous carbon are greatly influenced by the type of N-species present. The presence of pyrrolic and pyridinic N at the edge site of the carbon matrix is negatively charged and can transfer delocalized electrons or extra free electrons, which can participate in the pseudocapacitive reaction. This improves the capacitance of the electrode material. Furthermore, the graphitic N and pyridinic N



at the bottom of the carbon matrix are positively charged and activate the electrode surface and improve the charge transfer rate at higher current density<sup>23</sup>. In summary, N-doping to the carbon matrix is effective owing to the reasons: the electronegativity of N-atom is 3 which is higher than the C-atom (2.5), leading to positive charge density around the adjacent C-atoms<sup>26-27</sup>. The presence of extra lone pair electrons in the N atom enhances the conductivity of the N-doped electrode material. The extra lone pair on the N-atom can provide a negative charge for  $sp^2$  hybridized carbon skeleton of the delocalized  $\pi$  system, and enable the transport of the electrons<sup>27</sup>. As the N-containing functional groups are hydrophilic functional groups, they can ease the contact between the electrodes and electrolyte ions, N-doping to the carbon matrix enhance the surface hydrophilicity of the electrode<sup>28-29</sup>. The electrochemical activity of the heteroatom doped porous carbon highly depends upon the pore structure. The pore structure increases after the N-doping, hence promoting the contact between electrode and electrolyte improving the electrochemical performance<sup>30</sup>. Figure 1.9(a)<sup>31</sup> represents the heteroatoms self-doped porous carbon and types of N functional groups in the carbon matrix.



**Figure 1.9.** Schematic illustration of heteroatoms self-doped porous carbon and types of (a) nitrogen, (b) sulphur, and (c) phosphorous functional groups in the carbon matrix (Adopted with permission from ref. 29 copyright © 2020 Elsevier).

### Sulfur (S) doping

Sulfur, located in the second row of the periodic table and classified under the oxygen group, exhibits analogous functional groups (thiols, sulfides, disulfides) as oxygen (alcohols, ethers, peroxides) during carbon bonding. The incorporation of second-row atoms with a greater atomic radius than carbon induces the distortion of a planar structure, leading to the formation of defects that serve as active sites for redox reactions<sup>31</sup>. Introduction of S atom to the C=C carbon matrix ( $sp^2$  hybridized carbon framework) results in various sulfur bonding species like sulfoxide, sulfone, sulfonic acid, thiophene (aromatic sulfur), and thiol etc. in

Figure 1.9(b)<sup>31</sup>. Zhao et al. synthesized S-doped mesoporous carbon monoliths demonstrating the role of S doping and its effects on the enhanced capacitive performance<sup>32</sup>. The improved electrochemical performance is due to: (i) the faradic redox reaction takes place in presence of functional groups like sulfone and sulfoxide species in the carbon matrix where reduction of sulfone group to sulfoxide group takes place and vice versa in the reversible step, (ii) Synergistic activation with electron-rich sulfur leads to an increased electron density at the surface of carbon. Hence, introducing S-doping into the carbon framework leads to the emergence of a band gap and the incorporation of localized states, resulting in variations in electronegativity through the induction of a polarization effect. (iii) S-doping effectively modifies the distribution of spin/charge density and distorts the carbon lattice, creating significant electroactive sites<sup>31</sup>.

### **Phosphorous (P) doping**

Phosphorous, located under the nitrogen family shows similar doping features. Nevertheless, the atomic radius of P is larger than N (0.070 nm) and S (0.104 nm) resulting larger interplanar spacing. The incorporation of P into the carbon framework introduces P-O groups for the formation of a thin layer on the surface of the carbon, enhancing the electrochemical performance. The presence of  $sp^3$ -configured P atoms frequently leads to distortions and open-edge morphology, which in turn provides a greater number of active sites for storage properties. Pablo A. Denis reported that when this larger radius heteroatom is introduced into a carbon framework, it leads to a ripple effect, causing neighbouring carbon atoms to lift and resulting in a larger carbon-heteroatom bond distance protruding out of the sheet<sup>33</sup>. The modification or deviation of the  $sp^2$  carbon has significant implications

on the reactivity of these atoms, especially concerning their interaction with a large band gap. The presence of P introduces functional groups like phosphonic acid, phosphine, phosphine oxide, and phosphate which enhances the charge delocalization/asymmetric spin density and hence improving the electrochemical activity. Figure 1.9(c)<sup>31</sup> ascribes the types of phosphorous functional groups in the carbon matrix.

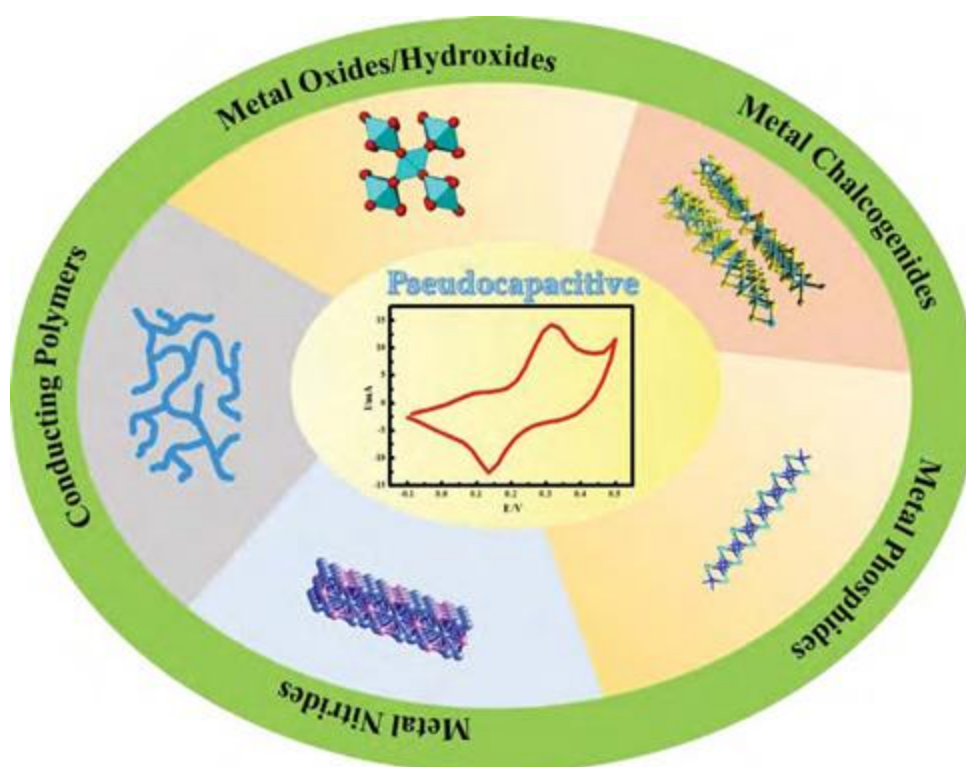
### **Boron (B) doping**

Doping of B atom into the carbon matrix is being a challenge since B species volatilize above 500 °C. According to theory, the atomic radii of B (0.082 nm) and C (0.077 nm) having similar size, resulting facile replacement of carbon atom by boron atoms<sup>34</sup>. The electronegativity of B atom is lower than the C atom. B atom act as an electron acceptor owing to its three electrons in its valence shell. So, the B atoms carrying positive charge in CB<sub>3</sub> structure have a strong interaction with the electrolyte anions. The introduction of B-doping into the carbon matrix leads to the redistribution of  $\pi$ -system, enhancing the van der Waals interaction between electrolyte cations and  $\pi$ -system<sup>35</sup>. The presence of B-C bond in the form of CB<sub>3</sub> improves the charge density and charge carriers of the nearby atoms, producing high electrical conductivity<sup>36</sup>. The B-doping improves the degree of graphitization and wettability between the electrode and the electrolyte, enhancing the electrical conductivity<sup>37</sup>.

#### **1.5.5.2. Pseudocapacitive (PC) Materials**

PC materials are the next generation SC owing to its high capacitance value. PCs store energy through a reversible Faradaic reaction that occurs at the bulk of the

electrode material. This means that electrons are transferred between the electrode and the electrolyte, which creates a charge imbalance and stores energy. Pseudocapacitors typically use transition metal hydroxides/oxides/chalcogenides or conducting polymers as the significant electrode materials, which allows higher ED compared to EDLCs. Different types of PC electrode materials are presented in Figure 1.10<sup>38</sup>.



**Figure 1.10.** Schematic illustration of different types of PC electrode materials<sup>38</sup>.

### **Metal Oxides/Hydroxides**

Compared to EDLC materials, transition/non-transition metal oxides and hydroxides are most representative active PC electrode materials. These are known for its high theoretical capacitance, natural abundance, high ED, cost effectiveness, and excellent catalytic behaviour. Metal oxide/hydroxide-based materials are

widely investigated PC materials owing to its variable oxidation number of metal atom, electrochemically stable during ion intercalation and de-intercalation process, and conducting/semiconducting nature.  $\text{RuO}_2$  extensively used as a pseudocapacitive electrode as it shows multi-oxidation states<sup>39</sup>. Similarly,  $\text{MnO}_2$  are studied as a PC material owing to its low cost, good electrical conductivity, and its abundance. Wang et al. reported mesoporous three-dimensional (3D)  $\text{MnO}_2$  having surface area  $284 \text{ m}^2 \text{ g}^{-1}$  shows a capacitance value of  $200 \text{ F g}^{-1}$  under  $1 \text{ A g}^{-1}$  current<sup>40</sup>. Layer double hydroxides (LDH) based materials sparked intense interest in SC owing to its tunability in composition and morphology. The PC properties of the LDH increases as its interlayer spacing increases, hence enhancing the electrochemical properties<sup>41</sup>. Lei et al. reported NiCo LDH with cation vacancy defect which displays a high specific capacitance of  $3200 \text{ F g}^{-1}$  under  $1 \text{ A g}^{-1}$  current<sup>42</sup>. Similarly, Kumar and co-workers synthesized NiMn-LDH hollow sphere as a promising pseudocapacitive electrode material for SC applications because of its impressive morphological features<sup>43</sup>.

### **Metal Chalcogenides/Nitrides/ Phosphides**

Transition metal chalcogenides owing to their unique electrochemical properties like multiple valence states, higher electronic conductivity, and fast ion diffusion kinetics, variable band gaps, tunable structures, and materials diversity are used as promising candidate for energy storage applications as compared to their oxide counter parts. These are the anisotropic stable crystalline material containing group 3 to 12 elements (transition metals) and group 16 elements ( $\text{S}^{2-}$ ,  $\text{Se}^{2-}$ ,  $\text{Te}^{2-}$ )<sup>5</sup>. Sulphides such as  $\text{MoS}_2$ ,  $\text{NiS}_2$ ,  $\text{Cu}_2\text{S}$ ,  $\text{WS}_2$ ,  $\text{RuS}_2$  etc. have been employed as the electrode material for SC devices because of its electrochemical active sites, good

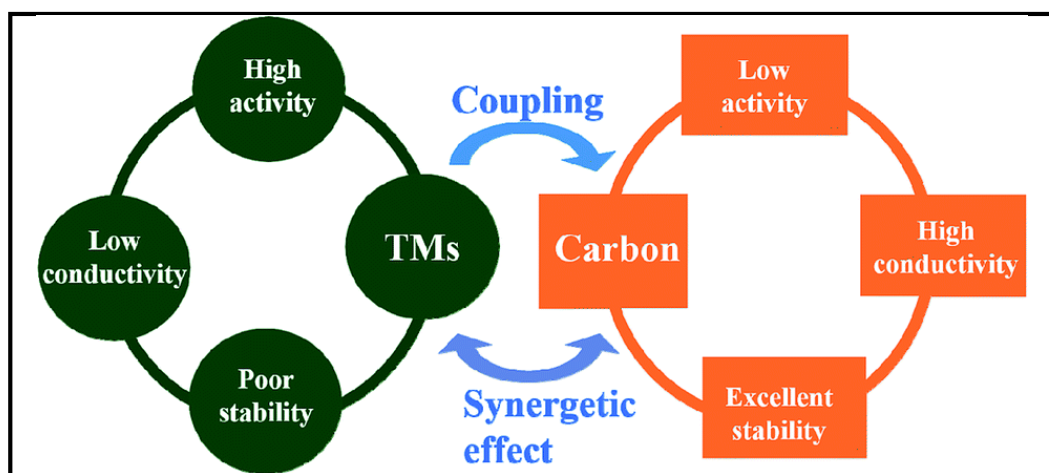
flexibility, short diffusion path-way etc. makes them a promising catalyst for SC application. However several factors like poor stability, low conductivity, low surface area, aggregation and restacking of TMC layers limits its application. Similar to metal oxides/sulfides, transition metal nitrides (TMN) and metal phosphides (TMP) qualify as suitable options for energy storage application. Compared to TMOs, TMC and TMN shows higher capacitance properties and PD<sup>44-45</sup>.

#### **1.5.5.3. Nanocomposites based Hybrid electrodes Materials**

Carbon based materials such as graphene, carbon nitride, carbon nanotubes, activated carbon, and various other carbon derivatives are widely accepted for energy storage application. Among all Graphitic carbon nitride (g-CN<sub>x</sub>) is a metal free semiconductor, used as electrode in energy storage application because of its easy synthesis method, tunable morphology, chemical and mechanical stability. g-CN<sub>x</sub> can be obtained from Formamide, urea, thiourea, melamine, cyanimide etc. by a simple thermal treatment<sup>46-48</sup>. However, its lower surface and comparatively low conductivity limits its application<sup>49-50</sup>. Various TMO such as RuO<sub>2</sub>, Co<sub>3</sub>O<sub>4</sub>, CuO, TiO<sub>2</sub>, Fe<sub>2</sub>O<sub>4</sub> etc. are previously reported for energy storage application owing to its good charge storage property, high theoretical capacity, cost effectiveness, and its abundance in nature<sup>51-52</sup>. But drawbacks like difficulty in porosity tailoring, lower conductivity, poor cyclic stability, low energy density and power density limits the use of TMO electrodes for SC device. Keeping all the advantages and disadvantages of carbon-based and TMO based electrodes in mind, combination of carbon with metal oxide were fabricated to form a composite electrode to get the desirable properties like chemical and mechanical stability, high aspect ratio, and high



surface area, high energy and power density making them a good candidate for energy storage device. This offer both physical and chemical charge storage mechanism in a single electrode. So this thesis includes a brief study on carbon based material (g-CN<sub>x</sub> and carbon dots) and transition metal hydroxides/TMC hybrid electrodes for SC applications. Figure 1.11 display the synergistic effect of TMs and carbon nanomaterials in TM/carbon hybrids<sup>53</sup>.



**Figure 1.11.** Schematic illustration of the synergistic effect of TMs and carbon nanomaterials in TM/carbon hybrids (Adopted with permission from ref. 50 copyright © 2019 Royal Society of Chemistry).

### **Properties of ideal metal oxide/Carbon composites**

For high electrochemical properties, the ideal composite electrode material required to have the properties as follows<sup>54</sup>:

- I. SSA:** High specific capacitance can be obtained by enhancing the SSA.
- II. Porosity:** By controlling/tuning the porosity of the composite materials.
- III. Electronic conductivity:** High PD and ED can be obtained by increasing the electrical conductivity.



- IV. Electroactive sites:** Desirable electroactive sites to enable the pseudocapacitance properties.
- V. Thermal and chemical stability:** It should show high thermal and chemical stability as it greatly affects the cyclic stability.
- VI. Cost:** The composite should be cost effective and should follow simple synthesis method.

#### **RuO<sub>2</sub>/Carbon hybrid**

Similar to various other TMOs, ruthenium oxide (RuO<sub>2</sub>) presents a promising option for electrode material in SCs owing to its notably higher specific capacitance, approximately 1450 F g<sup>-1</sup>. Nevertheless, the synthesis process of RuO<sub>2</sub> remains intricate. Trasatti and Buzzanca elucidated the detailed charge transfer mechanism of RuO<sub>2</sub><sup>55</sup>. Diverse carbonaceous structures were impregnated with TMOs to fabricate nanocomposites, thereby exhibiting heightened charge storage capability and improved conductivity. These nanocomposites, particularly those featuring RuO<sub>2</sub>, have garnered recognition for their viable application in SC systems. Examples include RuO<sub>2</sub>/GE/CNT nanocomposites exhibiting a specific capacitance of 502 F g<sup>-1</sup><sup>56</sup>, RuO<sub>2</sub>/GE composites demonstrating a capacitance of 570 F g<sup>-1</sup> with 97.9% capacitance retention after 1000 cycles<sup>57</sup>. Jian-Shan and co-workers reported RuO<sub>2</sub>/multi-walled carbon nano tubes (MWCNT) composites for high performance energy storage device<sup>58</sup>. The electrochemical activity of MWCNT was increased from 0.35 to 16.94 mF cm<sup>-2</sup> by modification with RuO<sub>2</sub>.

#### **Co<sub>3</sub>O<sub>4</sub>/Carbon hybrid**

Co<sub>3</sub>O<sub>4</sub> materials are highly used in energy storage application owing to its low cost, non-toxic, and environmental friendly nature. In this manner Co<sub>3</sub>O<sub>4</sub> mixed with graphene nanosheets to form a hybrid composite (Co<sub>3</sub>O<sub>4</sub>/graphene nanosheets) which shows improved electrochemical activity compared to bare Co<sub>3</sub>O<sub>4</sub><sup>59</sup>. Liang and co-workers reported in-situ fabrication of Co<sub>3</sub>O<sub>4</sub> over nanoporous carbons (NPCs) via an organometallic precursor-controlled thermolysis approach<sup>60</sup>. This shows an exceptionally high gravimetric capacitance value of 1066 F g<sup>-1</sup>.

### **Other metal oxides and hydroxide/Carbon composites**

V<sub>2</sub>O<sub>5</sub> have attracted great attention because of its predominating properties like easy synthesis, multiple oxidation states, lamellar structure, natural abundance, high theoretical capacitance and great energy density<sup>61-62</sup>. But its poor cyclic stability, low conductance, slow kinetics, morphological instability during charging/discharging process limits its application. In order to improve the electrochemical performance of V<sub>2</sub>O<sub>5</sub> electrode material, nanocomposite electrodes are fabricated because the composites provides unmatched advantages of pure materials. Viswanathan et al. reported the V<sub>2</sub>O<sub>5</sub>/rGO nanocomposite obtained by a chemical method. This V<sub>2</sub>O<sub>5</sub>/rGO composite is anticipated to support each other in mitigating their limitations and harnessing their merits to result in high energy storage<sup>63</sup>. Saravanakumar and co-workers reported V<sub>2</sub>O<sub>5</sub>/nitrogen enriched mesoporous carbon (n-MPC) sphere nanocomposite as a SC electrode material with appreciable electrochemical performance compared to pristine V<sub>2</sub>O<sub>5</sub> and n-MPC<sup>64</sup>. NiO is commonly used as electrode in electrochemical energy storage applications because of its high surface area, high specific capacitance, tunable morphology, and low cost. But pristine NiO suffers from poor conductivity, and stability limits its

application for large SCs<sup>65-67</sup>. Several methods have been implemented to tackle this problem. Kiey and co-workers synthesized porous carbon based NiO from (PC-NiO) by a simple method from banana peel waste Green and facile synthesis of nickel oxide-porous carbon composite as improved electrochemical electrodes for supercapacitor application from banana peel waste<sup>68</sup>. The PC-NiO composite shows higher electrochemical performance than PC and NiO indicating the improvement of surface properties of the composite. Gautam et al. reported NiO/PANI nanocomposites synthesized via in-situ chemical oxidative polymerization method. This acts as an efficient electrode material for SC application showing a capacitance of  $623 \text{ F g}^{-1}$  under  $1 \text{ A g}^{-1}$  current (higher than PANI and NiO) current with 92.5% capacitance retention up to 5000 cycles in  $1 \text{ M H}_2\text{SO}_4$  electrolyte. The high electrochemical performance is due to the synergistic effect between PANI and NiO. PANI plays an vital role and provides support by optimizing the pore structure and boosting the mass transfer process<sup>69</sup>.

Layered double hydroxide (LDH) received great attention as a promising catalyst for SCs because of their high tenability of cations, inorganic anion layers, multiple oxidation states, fine tuning physicochemical properties, crystal structure, ion exchange ability, and high redox activity<sup>70-73</sup>. However low specific capacitance, low ED and PD are observed because of its poor conductivity and aggregation of layers resulting great loss of active mass. Hence it is important to find an effective way in order to improve the conductivity and solve the aggregation problem. On the other hand existence of carbon support in the LDH provides a conductive support to improve the rapid Faradaic redox reactions<sup>74</sup>. Jing et al. synthesized CoAl LDH nanosheets over graphene oxide (GO) i.e. GO@CoAl LDH and only CoAl

LDH nanosheets without the support of GO<sup>74</sup>. The specific capacitance for GO@CoAl LDH is reported to be 1725.71 F g<sup>-1</sup> which is much higher than only CoAl LDH without GO support (1078.86 F g<sup>-1</sup>). Fang et al. report in-situ fabrication of NiAl LDH nanosheets/hollow carbon nanofibers (CNFs) composite showing impressive specific capacitance of 1613 F g<sup>-1</sup> which is much higher than the pristine NiAl LDH nanosheets i.e. 853 F g<sup>-1</sup> at 1 A g<sup>-1</sup> current. This confirms the contribution of CNFs in enhancing the specific capacitance which attributed to good conductivity and stable structure of the composite<sup>75</sup>.

### **Metal Chalcogenides/Carbon composites**

Transition metal chalcogenides such as MoS<sub>2</sub>, MoSe<sub>2</sub>, VS<sub>2</sub>, SnS<sub>x</sub> due to their intriguing electrochemical character like rich redox chemistry, variable valencies, high electronic conductivity compared to their oxide counter parts, fast ion diffusion, kinetics, and diverse in morphology<sup>5, 76-77</sup>. However it suffers from low conductivity, poor cyclic stability, low surface area, and agglomeration. So various modification strategies were adopted including fabrication of composite with various carbon allotropes and conducting polymers. Mahajan et al. reported biocarbon-based MoS<sub>2</sub> (Bio-C/MoS<sub>2</sub>) nanoparticles by a simple hydrothermal approach using date fruits<sup>78</sup>. Bio-C/MoS<sub>2</sub> exhibits a specific capacitance of 945 F g<sup>-1</sup> at 0.5 A g<sup>-1</sup> with outstanding capacitance retention of 92% after 10000 cycles<sup>78</sup>. Sharkawy et al. synthesized MoS<sub>2</sub>/N-doped carbon quantum dots (NCD) composite nanospheres as electrode materials for high performance SC<sup>79</sup>. The specific capacitance were calculated to be 77.23 F g<sup>-1</sup> and 250.55 F g<sup>-1</sup> for pristine MoS<sub>2</sub> and MoS<sub>2</sub>/NCDs electrode material, respectively, demonstrating the positive effect

of CDs in improving the capacitance of MoS<sub>2</sub>. This may be attributed to the enhanced conductivity of the composite upon the addition of CDs as only pristine MoS<sub>2</sub> suffers from poor conductivity. Also, the incorporation of CDs seems to offer fast electron transfer ability.

## **1.6. Gas Adsorption:**

### **1.6.1. Importance of gas adsorption**

Large-scale discharge of CO<sub>2</sub> into the environment leads to serious environmental concerns like the greenhouse effect, global warming, and anthropogenic climate change. To reduce greenhouse gas emissions and global warming, the development of the technique for CO<sub>2</sub> uptake and storage is highly necessary. The global energy consumption has exhibited consistent annual growth as a consequence of both economic advancement and population expansion. In 2018, the increase surpassed the average increment observed since 2010 by a margin of 70%. In spite of persistent endeavours directed towards the substitution of fossil fuels with renewable energy alternatives like solar and wind power, a report disseminated in the year 2020 indicates that fossil fuel reservoirs continue to serve as the predominant global energy reservoir<sup>80</sup>. As a direct consequence, carbon dioxide (CO<sub>2</sub>) emissions experienced an escalation to 33.1 gigatons in the year 2018. Concurrently, the atmospheric CO<sub>2</sub> concentration surpassed the threshold of 400 parts per million (ppm), and these numerical values exhibit a perpetual upward trend in tandem with economic expansion<sup>81</sup> (Increase of the atmospheric CO<sub>2</sub> concentration measured during 1958–2015 at the Mauna Loa (Hawaii)). Owing to the alarming situation, a globally initiative was initiated in 2010 to decrease

worldwide carbon emissions by 45% before 2030 and achieving zero net carbon by 2050<sup>82-83</sup>. Global energy demand

in 2020 recorded a 6% decline for the first time in 70 years, but efforts to decrease carbon emissions still must be maintained and increased as one of main reasons of the decline seems to be due to the COVID-19 pandemic situations<sup>84</sup>. The design of a better adsorbent for storage and separation of CO<sub>2</sub> and H<sub>2</sub> is very essential, as it is an energy source of fuel cell vehicles. Many solid adsorbents such as porous silica, calcium oxide, metal-organic framework, porous carbon, porous polymers, zeolites, and hybrid composites are developed because of their low cost, large SSA, adjustable pore size, and chemical stability. Among them, porous carbon materials have gained intense interest for gas capture due to their high SSA, tunable porous morphology, tunable pore volume, low density and resistivity, thermo-mechanical stability, and facile synthesis methods<sup>85</sup>.

### **1.6.2. Heteroatom doped Porous carbon for gas storage**

The worldwide trajectory of energy utilization has exhibited a consistent annual increase driven by both economic progression and population expansion. This inexorable trend has given rise to significant CO<sub>2</sub> emissions, thereby consequently augmenting the atmospheric concentration of this greenhouse gas in tandem with economic progress. The mitigation of CO<sub>2</sub> emissions has led to the development of diverse methodologies, although persistent challenges remain to be addressed. In recent times, nanoporous carbons have garnered substantial interest as an appealing class of functional porous materials, owing to their distinctive attributes. These materials have acquired a pivotal role across a spectrum of modern scientific and industrial applications, including but not limited to water and air purification,

catalysis, gas separation, and energy storage/conversion. This versatile utility emanates from their pronounced chemical and thermal stability, coupled with their exceptional electronic conductivity, synergistically combined with substantial specific surface areas. Nanoporous carbons can be harnessed for the adsorption of environmental pollutants and small gaseous molecules like CO<sub>2</sub>, as well as for empowering electrochemical energy storage devices for example batteries and fuel cells. In all these domains, the pore architecture and electrical characteristics of these materials can be tailored to suit specific objectives.

Porous carbon materials, such as activated carbons or template carbons, have been have garnered considerable attention owing to their high thermal/chemical stabilities, exhibiting hydrophobic characteristics, remarkable cost-effectiveness, and sustainable synthesis using various carbon precursors. Their adsorption properties can be improved when heteroatoms like N, O, S, P etc. are introduced. The introduction of heteroatoms leads to alterations in the surface's electrical properties. High SSA, ample pore volumes, expansive pore sizes, and appropriate interactions with adsorbate components make porous carbons a promising contender to replace alternative porous substances. Due to the considerable energy demands associated with the regeneration of chemisorptive interactions and exhibits vapour sensitivity, the physisorption of CO<sub>2</sub> gas in porous substrates is a more promising and attractive approach owing to its lower adsorption enthalpy, heightened reversibility, and the lower energy needed for regeneration process. The materials should show specific criteria to be used as adsorbents in CO<sub>2</sub> adsorption. These criteria encompass high selectivity over the other gas species from the mixture of gases, high adsorption capacity for CO<sub>2</sub> in the atmosphere of adsorption

as well as, easy regeneration under low pressure and temperature swings, remarkable resistance against moistures and impurities, and fast adsorption kinetics in relation to the contact duration with the gas mixture.

Efficient extraction of CO<sub>2</sub> from the atmosphere demands high selectivity of CO<sub>2</sub> over N<sub>2</sub> and/or O<sub>2</sub> owing to its scant concentration of approximately 400 ppm. The selectivity of CO<sub>2</sub>/N<sub>2</sub> can be accomplished through simple volumetric physisorption experiments, employing the ideal adsorption solution theory (IAST). The CO<sub>2</sub>/N<sub>2</sub> are usually comparable, CO<sub>2</sub>/N<sub>2</sub> is generally used as a reference. Highly selective CO<sub>2</sub> adsorption depends upon two important parameters. The first one is the thermodynamic principles where the polarizability is the foremost factor of significance. The second one is based on kinetic principles, in which the pore size plays a vital role. In short, for selective CO<sub>2</sub> adsorption, designing a heteroatom doped porous carbon material not just for the porosity for the CO<sub>2</sub> capacity and the diffusion of the adsorbate, but the surface chemical composition for easy regeneration and CO<sub>2</sub> capacity should also be considered. The microspore structure provides more favourable sites for gas adsorptions. The introduction of basic groups into the carbon framework improves the performance of selective adsorption of CO<sub>2</sub>. N doping to the carbon framework increases the surface active-redox sites and hence increases the energy storage capacity as well as CO<sub>2</sub> capture. S and N co-doping into the carbon matrix can improve the adsorption properties of acidic gases<sup>86</sup>. Microporous 2D carbon nanomaterials with nanometer thickness is also attracted importance due to their wonderful potential applications in different fields such as energy storage, gas storage/separation, catalysis, etc. The high SSA, plenty



of accessible active sites, and the 2D porous morphology allow easy mass/heat transport overcoming the problems faced by traditional bulk porous compounds. It was predicted<sup>87</sup> that the capacitance of carbon-based 2D porous materials can be enhanced if pores size distribution is sub-nanometre (<1nm).

### **1.7. Aim of the present thesis:**

- I. To synthesize hybrid nanostructure electrode material and heteroatom doped highly porous carbon nanosheets through sustainable and facile strategy.
2. To develop composite materials enhancing electrochemical performance and heteroatom doped porous carbon nanosheets for both energy storage and gas (CO<sub>2</sub>, CH<sub>4</sub>, and H<sub>2</sub>) adsorption applications and their selectivity over other gases.
3. To study the effect of doping on morphology, characteristics, and electrochemical properties.
4. To fabricate hybrid SC and doped porous carbon electrodes for high-performance aqueous-based SC devices.
5. To examine the mechanistic pathways associated with the electrocatalytic behaviours of various SC electrode materials.
6. This thesis offers a comprehensive examination of heteroatom doped nanoporous carbons, encompassing both synthetic methodologies and application perspectives. The interplay between pore architecture, atomic construction, and the adsorption properties of nanoporous heteroatom doped carbon materials are investigated.

## **1.8. Scope of the Present Work:**

SCs have emerged as a highly promising class of energy storage devices due to their rapid charge-discharge kinetics. Their specific power output surpasses that of lithium-ion batteries, while their superior energy density is comparable to conventional capacitors. Based on the energy storage mechanisms SCs are categorized as carbon-based EDLC materials and pseudocapacitive materials. Among these, EDLC-based SCs have attained prominence within market share, due to their prevalent efficacy over alternative constituents. Notably, g-CN<sub>x</sub> and heteroatom doped porous carbon are prominent EDLC materials, and have garnered attention for its capacity to deliver elevated specific capacitance compared to other carbon derivatives, thereby facilitating superior power density performance. In contrast, pseudocapacitive electrode materials exhibit heightened specific capacitance due to their swift faradaic processes, consequently enhancing ED performance. Nevertheless, addressing challenges such as charge transfer resistance, conductivity enhancement, and material stability remains pivotal. In this regard, the integration of porous carbon with pseudocapacitive materials emerges as a prospective pathway to mitigate these concerns. The main focus of this thesis is to design, develop, and characterize hybrid nanostructured materials and heteroatom doped porous carbon and their applications in energy and gas storage.

## **1.9. References:**

- (1) Islam, M. S.; Mubarak, M.; Lee, H.-J. Hybrid Nanostructured Materials as Electrodes in Energy Storage Devices *Inorganics* [Online], 2023.
- (2) Sripadmanabhan Indira, S.; Aravind Vaithilingam, C.; Oruganti, K. S.; Mohd, F.; Rahman, S. Nanogenerators as a Sustainable Power Source: State of Art, Applications, and Challenges *Nanomaterials* [Online], 2019.
- (3) Iro, Z. S.; Subramani, C.; Dash, S. A brief review on electrode materials for supercapacitor. *Int. J. Electrochem. Sci* **2016**, *11* (12), 10628-10643.

- (4) Zhang, L. L.; Zhao, X. S. Carbon-based materials as supercapacitor electrodes. *Chemical Society Reviews* **2009**, 38 (9), 2520-2531, DOI: 10.1039/B813846J.
- (5) Dahiya, Y.; Hariram, M.; Kumar, M.; Jain, A.; Sarkar, D. Modified transition metal chalcogenides for high performance supercapacitors: Current trends and emerging opportunities. *Coordination Chemistry Reviews* **2022**, 451, 214265, DOI: <https://doi.org/10.1016/j.ccr.2021.214265>.
- (6) Kumar, A.; Rathore, H. K.; Sarkar, D.; Shukla, A. Nanoarchitected transition metal oxides and their composites for supercapacitors. *Electrochemical Science Advances* **2022**, 2 (6), e2100187, DOI: <https://doi.org/10.1002/elsa.202100187>.
- (7) Noori, A.; El-Kady, M. F.; Rahmanifar, M. S.; Kaner, R. B.; Mousavi, M. F. Towards establishing standard performance metrics for batteries, supercapacitors and beyond. *Chemical Society Reviews* **2019**, 48 (5), 1272-1341, DOI: 10.1039/C8CS00581H.
- (8) Shao, Y.; El-Kady, M. F.; Sun, J.; Li, Y.; Zhang, Q.; Zhu, M.; Wang, H.; Dunn, B.; Kaner, R. B. Design and Mechanisms of Asymmetric Supercapacitors. *Chemical Reviews* **2018**, 118 (18), 9233-9280, DOI: 10.1021/acs.chemrev.8b00252.
- (9) Iro, Z. S.; Subramani, C.; Dash, S. S. A Brief Review on Electrode Materials for Supercapacitor. *International Journal of Electrochemical Science* **2016**, 11 (12), 10628-10643, DOI: <https://doi.org/10.20964/2016.12.50>.
- (10) Da Silva, L. M.; Cesar, R.; Moreira, C. M. R.; Santos, J. H. M.; De Souza, L. G.; Pires, B. M.; Vicentini, R.; Nunes, W.; Zanin, H. Reviewing the fundamentals of supercapacitors and the difficulties involving the analysis of the electrochemical findings obtained for porous electrode materials. *Energy Storage Materials* **2020**, 27, 555-590, DOI: <https://doi.org/10.1016/j.ensm.2019.12.015>.
- (11) Sajjad, M.; Khan, M. I.; Cheng, F.; Lu, W. A review on selection criteria of aqueous electrolytes performance evaluation for advanced asymmetric supercapacitors. *Journal of Energy Storage* **2021**, 40, 102729, DOI: <https://doi.org/10.1016/j.est.2021.102729>.
- (12) Zhao, C.; Zheng, W. A Review for Aqueous Electrochemical Supercapacitors. *Frontiers in Energy Research* **2015**, 3, DOI: 10.3389/fenrg.2015.00023.
- (13) Ruiz, V.; Roldán, S.; Villar, I.; Blanco, C.; Santamaría, R. Voltage dependence of carbon-based supercapacitors for pseudocapacitance quantification. *Electrochimica Acta* **2013**, 95, 225-229, DOI: <https://doi.org/10.1016/j.electacta.2013.02.056>.
- (14) Zhu, Z.; Tang, S.; Yuan, J.; Qin, X.; Deng, Y.; Qu, R.; Haarberg, G. M. Effects of Various Binders on Supercapacitor Performances. *International Journal of Electrochemical Science* **2016**, 11 (10), 8270-8279, DOI: <https://doi.org/10.20964/2016.10.04>.
- (15) Bresser, D.; Buchholz, D.; Moretti, A.; Varzi, A.; Passerini, S. Alternative binders for sustainable electrochemical energy storage – the transition to aqueous electrode processing and bio-derived polymers. *Energy & Environmental Science* **2018**, 11 (11), 3096-3127, DOI: 10.1039/C8EE00640G.
- (16) Li, J.; Jia, H.; Ma, S.; Xie, L.; Wei, X.-X.; Dai, L.; Wang, H.; Su, F.; Chen, C.-M. Separator Design for High-Performance Supercapacitors: Requirements, Challenges, Strategies, and Prospects. *ACS Energy Letters* **2023**, 8 (1), 56-78, DOI: 10.1021/acsenenergylett.2c01853.
- (17) Verma, K. D.; Sinha, P.; Banerjee, S.; Kar, K. K.; Ghorai, M. K. Characteristics of Separator Materials for Supercapacitors. In *Handbook of Nanocomposite Supercapacitor Materials I: Characteristics*; Kar, K. K., Ed.; Springer International Publishing: Cham, 2020; pp 315-326.
- (18) Ahankari, S.; Lasrado, D.; Subramaniam, R. Advances in materials and fabrication of separators in supercapacitors. *Materials Advances* **2022**, 3 (3), 1472-1496, DOI: 10.1039/D1MA00599E.

- (19) Najib, S.; Erdem, E. Current progress achieved in novel materials for supercapacitor electrodes: mini review. *Nanoscale Advances* **2019**, *1* (8), 2817-2827, DOI: 10.1039/C9NA00345B.
- (20) Liu, Q.; Zhang, H.; Xie, J.; Liu, X.; Lu, X. Recent progress and challenges of carbon materials for Zn-ion hybrid supercapacitors. *Carbon Energy* **2020**, *2* (4), 521-539, DOI: <https://doi.org/10.1002/cey2.69>.
- (21) Yin, J.; Zhang, W.; Alhebshi, N. A.; Salah, N.; Alshareef, H. N. Synthesis Strategies of Porous Carbon for Supercapacitor Applications. *Small Methods* **2020**, *4* (3), 1900853, DOI: <https://doi.org/10.1002/smtd.201900853>.
- (22) Zheng, Y.; Chen, K.; Jiang, K.; Zhang, F.; Zhu, G.; Xu, H. Progress of synthetic strategies and properties of heteroatoms-doped (N, P, S, O) carbon materials for supercapacitors. *Journal of Energy Storage* **2022**, *56*, 105995, DOI: <https://doi.org/10.1016/j.est.2022.105995>.
- (23) Gao, Y.; Wang, Q.; Ji, G.; Li, A.; Niu, J. Doping strategy, properties and application of heteroatom-doped ordered mesoporous carbon. *RSC Advances* **2021**, *11* (10), 5361-5383, DOI: 10.1039/D0RA08993A.
- (24) Zeng, K.; Su, J.; Cao, X.; Zheng, X.; Li, X.; Tian, J.-H.; Jin, C.; Yang, R. B. N Co-Doped ordered mesoporous carbon with enhanced electrocatalytic activity for the oxygen reduction reaction. *Journal of Alloys and Compounds* **2020**, *824*, 153908, DOI: <https://doi.org/10.1016/j.jallcom.2020.153908>.
- (25) Wang, J.-G.; Liu, H.; Sun, H.; Hua, W.; Wang, H.; Liu, X.; Wei, B. One-pot synthesis of nitrogen-doped ordered mesoporous carbon spheres for high-rate and long-cycle life supercapacitors. *Carbon* **2018**, *127*, 85-92, DOI: <https://doi.org/10.1016/j.carbon.2017.10.084>.
- (26) Jiang, T.; Wang, Y.; Wang, K.; Liang, Y.; Wu, D.; Tsiakaras, P.; Song, S. A novel sulfur-nitrogen dual doped ordered mesoporous carbon electrocatalyst for efficient oxygen reduction reaction. *Applied Catalysis B: Environmental* **2016**, *189*, 1-11, DOI: <https://doi.org/10.1016/j.apcatb.2016.02.009>.
- (27) Sheng, X.; Daems, N.; Geboes, B.; Kurttepel, M.; Bals, S.; Breugelmans, T.; Hubin, A.; Vankelecom, I. F. J.; Pescarmona, P. P. N-doped ordered mesoporous carbons prepared by a two-step nanocasting strategy as highly active and selective electrocatalysts for the reduction of O<sub>2</sub> to H<sub>2</sub>O<sub>2</sub>. *Applied Catalysis B: Environmental* **2015**, *176-177*, 212-224, DOI: <https://doi.org/10.1016/j.apcatb.2015.03.049>.
- (28) Qiu, Z.; Zhao, K.; Liu, J.; Xia, S. Nitrogen-doped mesoporous carbon as an anode material for high performance potassium-ion batteries. *Electrochimica Acta* **2020**, *340*, 135947, DOI: <https://doi.org/10.1016/j.electacta.2020.135947>.
- (29) Du, J.; Liu, L.; Yu, Y.; Zhang, Y.; Lv, H.; Chen, A. N-doped ordered mesoporous carbon spheres derived by confined pyrolysis for high supercapacitor performance. *Journal of Materials Science & Technology* **2019**, *35* (10), 2178-2186, DOI: <https://doi.org/10.1016/j.jmst.2019.05.029>.
- (30) Matter, P. H.; Zhang, L.; Ozkan, U. S. The role of nanostructure in nitrogen-containing carbon catalysts for the oxygen reduction reaction. *Journal of Catalysis* **2006**, *239* (1), 83-96, DOI: <https://doi.org/10.1016/j.jcat.2006.01.022>.
- (31) Gopalakrishnan, A.; Badhulika, S. Effect of self-doped heteroatoms on the performance of biomass-derived carbon for supercapacitor applications. *Journal of Power Sources* **2020**, *480*, 228830, DOI: <https://doi.org/10.1016/j.jpowsour.2020.228830>.
- (32) Zhao, X.; Zhang, Q.; Chen, C.-M.; Zhang, B.; Reiche, S.; Wang, A.; Zhang, T.; Schlögl, R.; Sheng Su, D. Aromatic sulfide, sulfoxide, and sulfone mediated mesoporous carbon monolith for use in supercapacitor. *Nano Energy* **2012**, *1* (4), 624-630, DOI: <https://doi.org/10.1016/j.nanoen.2012.04.003>.

- (33) Denis, P. A. Band gap opening of monolayer and bilayer graphene doped with aluminium, silicon, phosphorus, and sulfur. *Chemical Physics Letters* **2010**, 492 (4), 251-257, DOI: <https://doi.org/10.1016/j.cplett.2010.04.038>.
- (34) Chen, D. D.; He, Z. Q.; Wang, M.; Wu, D.; Chen, X. Y.; Zhang, Z. J. Boron doping and structure control of carbon materials for supercapacitor application: the effect of freeze-drying and air-drying for porosity engineering. *Journal of Solid State Electrochemistry* **2020**, 24 (3), 641-654, DOI: 10.1007/s10008-020-04498-1.
- (35) Sun, F.; Qu, Z.; Gao, J.; Wu, H. B.; Liu, F.; Han, R.; Wang, L.; Pei, T.; Zhao, G.; Lu, Y. In Situ Doping Boron Atoms into Porous Carbon Nanoparticles with Increased Oxygen Graft Enhances both Affinity and Durability toward Electrolyte for Greatly Improved Supercapacitive Performance. *Advanced Functional Materials* **2018**, 28 (41), 1804190, DOI: <https://doi.org/10.1002/adfm.201804190>.
- (36) Su, J.; Cao, X.; Wu, J.; Jin, C.; Tian, J.-H.; Yang, R. One-pot synthesis of boron-doped ordered mesoporous carbons as efficient electrocatalysts for the oxygen reduction reaction. *RSC Advances* **2016**, 6 (29), 24728-24737, DOI: 10.1039/C6RA01296E.
- (37) Wang, T.; Zhang, C.; Sun, X.; Guo, Y.; Guo, H.; Tang, J.; Xue, H.; Liu, M.; Zhang, X.; Zhu, L.; Xie, Q.; He, J. Synthesis of ordered mesoporous boron-containing carbon films and their corrosion behavior in simulated proton exchange membrane fuel cells environment. *Journal of Power Sources* **2012**, 212, 1-12, DOI: <https://doi.org/10.1016/j.jpowsour.2012.03.068>.
- (38) Chen, R.; Yu, M.; Sahu, R. P.; Puri, I. K.; Zhitomirsky, I. The Development of Pseudocapacitor Electrodes and Devices with High Active Mass Loading. *Advanced Energy Materials* **2020**, 10 (20), 1903848, DOI: <https://doi.org/10.1002/aenm.201903848>.
- (39) Guduru, R. K.; Icaza, J. C.; Pudi, S. K. Electrochemical characterization of RuO<sub>2</sub> and activated carbon (AC) electrodes using multivalent Ni(NO<sub>3</sub>)<sub>2</sub> electrolyte for charge storage applications. *Journal of Energy Storage* **2021**, 34, 102170, DOI: <https://doi.org/10.1016/j.est.2020.102170>.
- (40) Wang, Y.-T.; Lu, A.-H.; Zhang, H.-L.; Li, W.-C. Synthesis of Nanostructured Mesoporous Manganese Oxides with Three-Dimensional Frameworks and Their Application in Supercapacitors. *The Journal of Physical Chemistry C* **2011**, 115 (13), 5413-5421, DOI: 10.1021/jp110938x.
- (41) Li, X.; Du, D.; Zhang, Y.; Xing, W.; Xue, Q.; Yan, Z. Layered double hydroxides toward high-performance supercapacitors. *Journal of Materials Chemistry A* **2017**, 5 (30), 15460-15485, DOI: 10.1039/C7TA04001F.
- (42) Lei, G.; Chen, D.; Li, Q.; Liu, H.; Shi, Q.; Li, C. NiCo-layered double hydroxide with cation vacancy defects for high-performance supercapacitors. *Electrochimica Acta* **2022**, 413, 140143, DOI: <https://doi.org/10.1016/j.electacta.2022.140143>.
- (43) Kumar, J.; Neiber, R. R.; Abbas, Z.; Soomro, R. A.; BaQais, A.; Amin, M. A.; El-Bahy, Z. M. Hierarchical NiMn-LDH Hollow Spheres as a Promising Pseudocapacitive Electrode for Supercapacitor Application *Micromachines* [Online], 2023.
- (44) Zhong, Y.; Xia, X.; Shi, F.; Zhan, J.; Tu, J.; Fan, H. J. Transition Metal Carbides and Nitrides in Energy Storage and Conversion. *Advanced Science* **2016**, 3 (5), 1500286, DOI: <https://doi.org/10.1002/advs.201500286>.
- (45) Zong, Q.; Liu, C.; Yang, H.; Zhang, Q.; Cao, G. Tailoring nanostructured transition metal phosphides for high-performance hybrid supercapacitors. *Nano Today* **2021**, 38, 101201, DOI: <https://doi.org/10.1016/j.nantod.2021.101201>.
- (46) Santos, R. S.; Suresh Babu, R.; Devendiran, M.; Haddad, D. B.; Barros, A. L. F. d. Facile synthesis of transition metal (M = Cu, Co) oxide grafted graphitic carbon nitride nanosheets for high performance asymmetric supercapacitors. *Materials Letters* **2022**, 308, 131156, DOI: <https://doi.org/10.1016/j.matlet.2021.131156>.

- (47) Peng, X.; Peng, L.; Wu, C.; Xie, Y. Two dimensional nanomaterials for flexible supercapacitors. *Chemical Society Reviews* **2014**, 43 (10), 3303-3323, DOI: 10.1039/C3CS60407A.
- (48) Sridharan, K.; Kuriakose, T.; Philip, R.; Park, T. J. Transition metal (Fe, Co and Ni) oxide nanoparticles grafted graphitic carbon nitrides as efficient optical limiters and recyclable photocatalysts. *Applied Surface Science* **2014**, 308, 139-147, DOI: <https://doi.org/10.1016/j.apsusc.2014.04.121>.
- (49) Ashritha, M. G.; Hareesh, K. A review on Graphitic Carbon Nitride based binary nanocomposites as supercapacitors. *Journal of Energy Storage* **2020**, 32, 101840, DOI: <https://doi.org/10.1016/j.est.2020.101840>.
- (50) Kazemi, S. H.; Kiani, M. A.; Ghaemmaghami, M.; Kazemi, H. Nano-architected MnO<sub>2</sub> Electrodeposited on the Cu-decorated Nickel Foam substrate as Supercapacitor Electrode with Excellent Areal Capacitance. *Electrochimica Acta* **2016**, 197, 107-116, DOI: <https://doi.org/10.1016/j.electacta.2016.03.063>.
- (51) Li, Z.; Wu, L.; Wang, L.; Gu, A.; Zhou, Q. Nickel cobalt sulfide nanosheets uniformly anchored on porous graphitic carbon nitride for supercapacitors with high cycling performance. *Electrochimica Acta* **2017**, 231, 617-625, DOI: <https://doi.org/10.1016/j.electacta.2017.02.087>.
- (52) Liu, L.; Zhao, Q.; Zhou, S.; Zhao, M. Modulating interfacial dilatational properties by electrostatic sodium caseinate and carboxymethylcellulose interactions. *Food Hydrocolloids* **2016**, 56, 303-310, DOI: <https://doi.org/10.1016/j.foodhyd.2015.11.028>.
- (53) Hu, Q.; Li, G.; Han, Z.; Wang, Z.; Huang, X.; Yang, H.; Zhang, Q.; Liu, J.; He, C. Recent progress in the hybrids of transition metals/carbon for electrochemical water splitting. *Journal of Materials Chemistry A* **2019**, 7 (24), 14380-14390, DOI: 10.1039/C9TA04163J.
- (54) Abbas, Q.; Olabi, A. G.; Raza, R.; Gibson, D. Carbon/Metal Oxide Composites as Electrode Materials for Supercapacitors Applications. In *Reference Module in Materials Science and Materials Engineering*; Elsevier: 2018.
- (55) Trasatti, S.; Buzzanca, G. Ruthenium dioxide: A new interesting electrode material. Solid state structure and electrochemical behaviour. *Journal of Electroanalytical Chemistry and Interfacial Electrochemistry* **1971**, 29 (2), A1-A5, DOI: [https://doi.org/10.1016/S0022-0728\(71\)80111-0](https://doi.org/10.1016/S0022-0728(71)80111-0).
- (56) Wang, W.; Guo, S.; Lee, I.; Ahmed, K.; Zhong, J.; Favors, Z.; Zaera, F.; Ozkan, M.; Ozkan, C. S. Hydrous Ruthenium Oxide Nanoparticles Anchored to Graphene and Carbon Nanotube Hybrid Foam for Supercapacitors. *Scientific Reports* **2014**, 4 (1), 4452, DOI: 10.1038/srep04452.
- (57) Wu, Z.-S.; Wang, D.-W.; Ren, W.; Zhao, J.; Zhou, G.; Li, F.; Cheng, H.-M. Anchoring Hydrous RuO<sub>2</sub> on Graphene Sheets for High-Performance Electrochemical Capacitors. *Advanced Functional Materials* **2010**, 20 (20), 3595-3602, DOI: <https://doi.org/10.1002/adfm.201001054>.
- (58) Ye, J.-S.; Cui, H. F.; Liu, X.; Lim, T. M.; Zhang, W.-D.; Sheu, F.-S. Preparation and Characterization of Aligned Carbon Nanotube–Ruthenium Oxide Nanocomposites for Supercapacitors. *Small* **2005**, 1 (5), 560-565, DOI: <https://doi.org/10.1002/sml.200400137>.
- (59) Lakra, R.; Kumar, R.; Sahoo, P. K.; Sharma, D.; Thatoi, D.; Soam, A. Facile synthesis of cobalt oxide and graphene nanosheets nanocomposite for aqueous supercapacitor application. *Carbon Trends* **2022**, 7, 100144, DOI: <https://doi.org/10.1016/j.cartre.2021.100144>.
- (60) Liang, Y.; Schwab, M. G.; Zhi, L.; Mugnaioli, E.; Kolb, U.; Feng, X.; Müllen, K. Direct Access to Metal or Metal Oxide Nanocrystals Integrated with One-Dimensional



- Nanoporous Carbons for Electrochemical Energy Storage. *Journal of the American Chemical Society* **2010**, 132 (42), 15030-15037, DOI: 10.1021/ja106612d.
- (61) Qu, Q. T.; Shi, Y.; Li, L. L.; Guo, W. L.; Wu, Y. P.; Zhang, H. P.; Guan, S. Y.; Holze, R. V2O5·0.6H2O nanoribbons as cathode material for asymmetric supercapacitor in K2SO4 solution. *Electrochemistry Communications* **2009**, 11 (6), 1325-1328, DOI: <https://doi.org/10.1016/j.elecom.2009.05.003>.
- (62) Chao, D.; Xia, X.; Liu, J.; Fan, Z.; Ng, C. F.; Lin, J.; Zhang, H.; Shen, Z. X.; Fan, H. J. A V2O5/Conductive-Polymer Core/Shell Nanobelt Array on Three-Dimensional Graphite Foam: A High-Rate, Ultrastable, and Freestanding Cathode for Lithium-Ion Batteries. *Advanced Materials* **2014**, 26 (33), 5794-5800, DOI: <https://doi.org/10.1002/adma.201400719>.
- (63) Viswanathan, A.; Shetty, A. N. Reduced graphene oxide/vanadium pentoxide nanocomposite as electrode material for highly rate capable and durable supercapacitors. *Journal of Energy Storage* **2020**, 27, 101103, DOI: <https://doi.org/10.1016/j.est.2019.101103>.
- (64) Saravanakumar, B.; Purushothaman, K. K.; Muralidharan, G. V2O5 / nitrogen enriched mesoporous carbon spheres nanocomposite as supercapacitor electrode. *Microporous and Mesoporous Materials* **2018**, 258, 83-94, DOI: <https://doi.org/10.1016/j.micromeso.2017.09.010>.
- (65) Du, D.; Hu, Z.; Liu, Y.; Deng, Y.; Liu, J. Preparation and characterization of flower-like microspheres of nano-NiO as electrode material for supercapacitor. *Journal of Alloys and Compounds* **2014**, 589, 82-87, DOI: <https://doi.org/10.1016/j.jallcom.2013.11.176>.
- (66) Wang, Y.; Guo, J.; Wang, T.; Shao, J.; Wang, D.; Yang, Y.-W. Mesoporous Transition Metal Oxides for Supercapacitors *Nanomaterials* [Online], 2015, p. 1667-1689.
- (67) Cao, F.; Pan, G. X.; Xia, X. H.; Tang, P. S.; Chen, H. F. Synthesis of hierarchical porous NiO nanotube arrays for supercapacitor application. *Journal of Power Sources* **2014**, 264, 161-167, DOI: <https://doi.org/10.1016/j.jpowsour.2014.04.103>.
- (68) Al Kiey, S. A.; Hasanin, M. S. Green and facile synthesis of nickel oxide-porous carbon composite as improved electrochemical electrodes for supercapacitor application from banana peel waste. *Environmental Science and Pollution Research* **2021**, 28 (47), 66888-66900, DOI: 10.1007/s11356-021-15276-5.
- (69) Gautam, K. P.; Acharya, D.; Bhatta, I.; Subedi, V.; Das, M.; Neupane, S.; Kunwar, J.; Chhetri, K.; Yadav, A. P. Nickel Oxide-Incorporated Polyaniline Nanocomposites as an Efficient Electrode Material for Supercapacitor Application *Inorganics* [Online], 2022.
- (70) Chen, S.; Mao, M.; Liu, X.; Hong, S.; Lu, Z.; Sang, S.; Liu, K.; Liu, H. A high-rate cathode material hybridized by in-site grown Ni-Fe layered double hydroxides and carbon black nanoparticles. *Journal of Materials Chemistry A* **2016**, 4 (13), 4877-4881, DOI: 10.1039/C6TA00842A.
- (71) Li, M.; Cheng, J. P.; Wang, J.; Liu, F.; Zhang, X. B. The growth of nickel-manganese and cobalt-manganese layered double hydroxides on reduced graphene oxide for supercapacitor. *Electrochimica Acta* **2016**, 206, 108-115, DOI: <https://doi.org/10.1016/j.electacta.2016.04.084>.
- (72) Tang, D.; Liu, J.; Wu, X.; Liu, R.; Han, X.; Han, Y.; Huang, H.; Liu, Y.; Kang, Z. Carbon Quantum Dot/NiFe Layered Double-Hydroxide Composite as a Highly Efficient Electrocatalyst for Water Oxidation. *ACS Applied Materials & Interfaces* **2014**, 6 (10), 7918-7925, DOI: 10.1021/am501256x.
- (73) Sanati, S.; Rezvani, Z. g-C3N4 nanosheet@CoAl-layered double hydroxide composites for electrochemical energy storage in supercapacitors. *Chemical Engineering Journal* **2019**, 362, 743-757, DOI: <https://doi.org/10.1016/j.cej.2019.01.081>.

- (74) Jing, C.; Huang, Y.; Xia, L.; Chen, Y.; Wang, X.; Liu, X.; Dong, B.; Dong, F.; Li, S.; Zhang, Y. Growth of cobalt-aluminum layered double hydroxide nanosheets on graphene oxide towards high performance supercapacitors: The important role of layer structure. *Applied Surface Science* **2019**, *496*, 143700, DOI: <https://doi.org/10.1016/j.apsusc.2019.143700>.
- (75) He, F.; Hu, Z.; Liu, K.; Zhang, S.; Liu, H.; Sang, S. In situ fabrication of nickel aluminum-layered double hydroxide nanosheets/hollow carbon nanofibers composite as a novel electrode material for supercapacitors. *Journal of Power Sources* **2014**, *267*, 188-196, DOI: <https://doi.org/10.1016/j.jpowsour.2014.05.084>.
- (76) Palchoudhury, S.; Ramasamy, K.; Han, J.; Chen, P.; Gupta, A. Transition metal chalcogenides for next-generation energy storage. *Nanoscale Advances* **2023**, *5* (10), 2724-2742, DOI: 10.1039/D2NA00944G.
- (77) Theerthagiri, J.; Karuppasamy, K.; Durai, G.; Rana, A. U.; Arunachalam, P.; Sangeetha, K.; Kuppusami, P.; Kim, H.-S. Recent Advances in Metal Chalcogenides (MX; X = S, Se) Nanostructures for Electrochemical Supercapacitor Applications: A Brief Review *Nanomaterials* [Online], 2018.
- (78) Mahajan, H.; Mohanan, K. U.; Cho, S. Facile Synthesis of Biocarbon-Based MoS<sub>2</sub> Composite for High-Performance Supercapacitor Application. *Nano Letters* **2022**, *22* (20), 8161-8167, DOI: 10.1021/acs.nanolett.2c02595.
- (79) El Sharkawy, H. M.; Dhmees, A. S.; Tamman, A. R.; El Sabagh, S. M.; Aboushahba, R. M.; Allam, N. K. N-doped carbon quantum dots boost the electrochemical supercapacitive performance and cyclic stability of MoS<sub>2</sub>. *Journal of Energy Storage* **2020**, *27*, 101078, DOI: <https://doi.org/10.1016/j.est.2019.101078>.
- (80) 2020, G. E. R. <https://www.iea.org/reports/global-energy-review-2020>.
- (81) Oschatz, M.; Antonietti, M. A search for selectivity to enable CO<sub>2</sub> capture with porous adsorbents. *Energy & Environmental Science* **2018**, *11* (1), 57-70, DOI: 10.1039/C7EE02110K.
- (82) Union, T. E. Communication from the Commission to the European parliament, The council, The European economic and social committee and the committee of the regions. <https://eur-lex.europa.eu/legal-content/EN/TXT/?uri=CELEX%3A52020DC0562> (accessed 17.9.2020).
- (83) capture, A. c. Irlam, L., Global costs of carbon capture and storage. Global CCS Institute, Melbourne, Australia
- (84) Global Energy Review 2020 <https://www.iea.org/reports/global-energy-review-2020>.
- (85) Daulbayev, C.; Lesbayev, B.; Bakbolat, B.; Kaidar, B.; Sultanov, F.; Yeleuov, M.; Ustayeva, G.; Rakhymzhan, N. A mini-review on recent trends in prospective use of porous 1D nanomaterials for hydrogen storage. *South African Journal of Chemical Engineering* **2022**, *39*, 52-61, DOI: <https://doi.org/10.1016/j.sajce.2021.11.008>.
- (86) Shahtalebi, A.; Mar, M.; Guérin, K.; Bhatia, S. K. Effect of fluorine doping on structure and CO<sub>2</sub> adsorption in silicon carbide-derived carbon. *Carbon* **2016**, *96*, 565-577, DOI: <https://doi.org/10.1016/j.carbon.2015.09.105>.
- (87) Chmiola, J.; Yushin, G.; Gogotsi, Y.; Portet, C.; Simon, P.; Taberna, P. L. Anomalous Increase in Carbon Capacitance at Pore Sizes Less Than 1 Nanometer. *Science* **2006**, *313* (5794), 1760-1763, DOI: 10.1126/science.1132195.



## Chapter 2

### General Experimental Methods and Techniques

#### 2.1. INTRODUCTION

In this chapter, we present a comprehensive overview of the essential instruments employed in the current thesis and provide a concise discussion of the experimental methodologies utilized for various experiments.

#### 2.2. Materials:

The precursors and synthetic mixtures used in this thesis were obtained using commercial materials available for purchase without additional purification. **Table 2.1** contains a list of the chemicals used in the thesis, together with their formulas.

**Table 2.1.** Materials used for experimental work along with formula and supplier name.

Name of Chemicals	Chemical formula	Company name
Formamide	HCONH <sub>2</sub>	Merck
Boric Acid	H <sub>3</sub> BO <sub>4</sub>	Spectrochem
Thiourea	CH <sub>4</sub> N <sub>2</sub> S	Spectrochem
Sodium hypophosphite	NaPO <sub>2</sub> H <sub>2</sub>	Sigma-Aldrich
Aluminum nitrate nonahydrate	Al (NO <sub>3</sub> ) <sub>3</sub> · 9H <sub>2</sub> O	Merck
Cobalt nitrate hexahydrate	Co (NO <sub>3</sub> ) <sub>2</sub> · 6H <sub>2</sub> O	Merck
Hydrochloric acid	HCl	CDH
Potassium hydroxide	KOH	CDH
Sulphuric acid	H <sub>2</sub> SO <sub>4</sub>	CDH
Hexamethylenetetramine	HMT	Thermo Fisher scientific
Urea	NH <sub>2</sub> CONH <sub>2</sub>	Thermo Fisher scientific

Ammonium fluoride	NH <sub>4</sub> F	HI Media
Ammonium tetrathiomolybdate	(NH <sub>4</sub> ) <sub>2</sub> MoS <sub>4</sub>	Sigma Aldrich
Hydrazine hydrate	N <sub>2</sub> H <sub>4</sub> .4H <sub>2</sub> O	Spectrochem
N, N dimethylformamide	DMF	Spectrochem
Ruthenium chloride hydrate	RuCl <sub>3</sub> .xH <sub>2</sub> O	Sigma Aldrich
Sodium borohydride	NaBH <sub>4</sub>	Sigma Aldrich

## 2.3. INSTRUMENTAL TECHNIQUES

### X-ray diffraction (XRD)<sup>1</sup>:

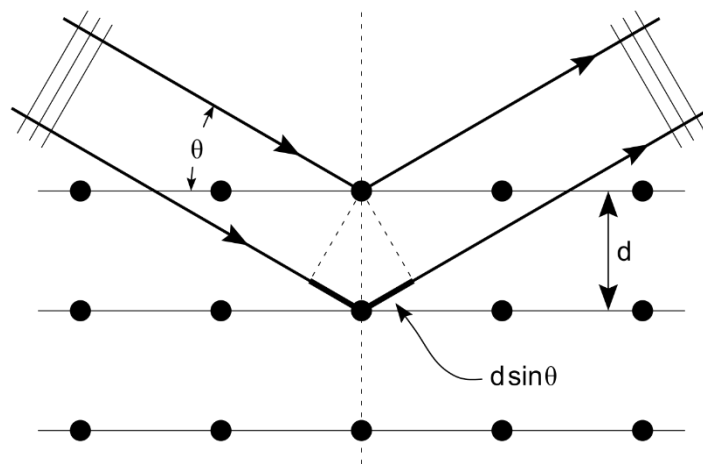
The XRD setup consists of an X-ray tube, which serves as the source of X-rays. The tube comprises a heated tungsten filament enclosed within a transparent ceramic vessel acting as the cathode, and a cooled copper foil serving as the anode. Electrons emitted from the tungsten filament are accelerated towards the copper anode, causing the ejection of electrons from the internal shells of copper atoms. This process leads to the relaxation of valence electrons into lower energy states, resulting in the generation of X-rays. The copper target produces two distinct X-ray wavelengths: Cu K $\alpha$  ( $\lambda = 0.154$  nm) and Cu K $\beta$  ( $\lambda = 0.139$  nm). To ensure monochromatic X-ray emission, a nickel filter is employed, allowing only Cu K $\beta$  radiation to pass through.

During the experiment, the X-ray beam is directed towards the sample, and the scattered X-rays are detected. The angle of  $2\theta$  is measured, which represents the angle between the incident and diffracted beams. By utilizing Bragg's diffraction equation, the interplanar distance (d-spacing) between two crystal lattice planes can be determined:

$$n\lambda = 2d \sin\theta$$

Here,  $n$  represents the interference order,  $\lambda$  is the wavelength of the incident X-ray beam,  $d$  is the interplanar distance, and  $\theta$  is the angle between the incident beam and the lattice plane.

XRD analysis provides crucial information about the crystalline phases present in the sample, their relative abundance, and the lattice parameters. By interpreting the diffraction pattern, valuable insights into the crystal structure, grain size, preferred orientation, and presence of any structural defects can be obtained, facilitating the characterization and understanding of the material's properties.



**Figure 2.1.** Schematic representation of X-ray diffraction process (adopted from Wikipedia).

For this thesis, the X-ray diffraction analyses were conducted using a Bruker DAVINCI D8 ADVANCE diffractometer. During these experiments, the Cu K $\alpha$  radiation of wavelength of  $\lambda = 0.154$  nm was used.

### **Transmission Electron Microscope (TEM)<sup>2-3</sup>:**

Transmission Electron Microscopy (TEM) is a widely used technique in materials science for the study of various nanostructures, including nanowires, quantum dots, and nanoparticles, as well as their size, shape, and density. It is also employed to investigate the composition and defects present in semiconductors. TEM operates on the principles similar to a microscope, but instead of using light, it utilizes electrons.

In TEM, a monochromatic electron beam is generated by an electron gun. The condenser lenses focus this beam into a coherent and narrow stream. The aperture of the condenser restricts the beam, eliminating high-angle electrons. As the electron beam interacts with the specimen, a portion of its energy is transmitted, depending on the specimen's thickness and transparency. The transmitted electrons are then converted into an image by the objective lens. The image is magnified as it is transmitted through intermediate and projection lenses along the column. Finally, the image is detected by a fluorescent screen, which produces light. Darker regions in the image indicate fewer electrons reaching that area, while brighter regions correspond to more frequent electron interactions.

TEM can be operated in different modes, depending on the desired outcome, such as imaging or diffraction. In the case of High-Resolution TEM (HRTEM), both transmitted and scattered electron beams are utilized to generate an interference pattern, providing a detailed image of the sample. This technique enables the characterization of point defects, dislocations, surface structures, and precise analysis of crystal lattice defects in various materials at the atomic scale. The selected area electron diffraction (SAED) pattern, obtained from a specific region of the sample, can be used to determine the crystal's d-spacing. The diffraction pattern also reveals information about the sample's crystallinity. According to Bragg's law, crystal planes parallel to the path of the electron beam will undergo diffraction. The periodic potential of the electrons undergoes a Fourier transformation to produce the diffraction pattern, and the interference between the diffracted electrons and the primary electrons results in a back transformation (inverse Fourier transform) that generates an image.

In this thesis, the morphologies of materials were examined using a Transmission Electron Microscope (TEM) with the model name JEOL F200, operating at a voltage of 200 kV. The TEM allowed for detailed investigation and characterization of the materials' structures at the nanoscale.

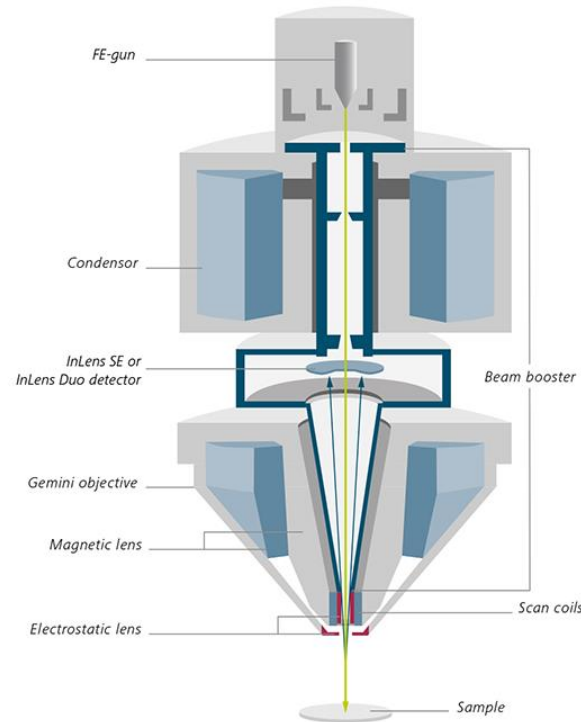
### **Field Emission Scanning Electron Microscope (FESEM)<sup>4-5</sup>:**

Field-Emission Scanning Electron Microscopy (FESEM) is employed to generate high-resolution three-dimensional images of the sample morphology. The cathode of the electron gun emits electrons, which are subsequently accelerated by the anode within a high vacuum environment. The vacuum ensures that atoms and molecules within the column do not interact with the electron beam, thus preserving image quality. The condenser lenses focus the electron beam, while the generated magnetic field causes the beam to deflect back and forth.

To obtain a detailed surface image, the electron beam is directed in a raster pattern over the sample surface after being focused to a very small area (1-5 nm) by the objective lens. This scanning process allows for the examination of relatively small surface areas. During the interaction between the primary electron and the atoms on the sample surface, secondary emissions are generated. These secondary electrons are recorded and utilized to construct an image. The angle and velocity of the secondary electron beam provide valuable information about the surface structure of the sample.

FESEM enables the visualization and analysis of surface topography with exceptional resolution and depth. By utilizing a combination of electron beam scanning and secondary electron detection, this technique provides valuable insights into the

microstructural features and surface characteristics of the examined materials. We have used Carl Zeiss, Germany (Model:  $\Sigma$ igma) instrument to perform FESEM measurements.



**Figure 2.2.** Schematic representation of Field Emission Scanning Electron Microscope (FE-SEM), adapted from ZEISS.

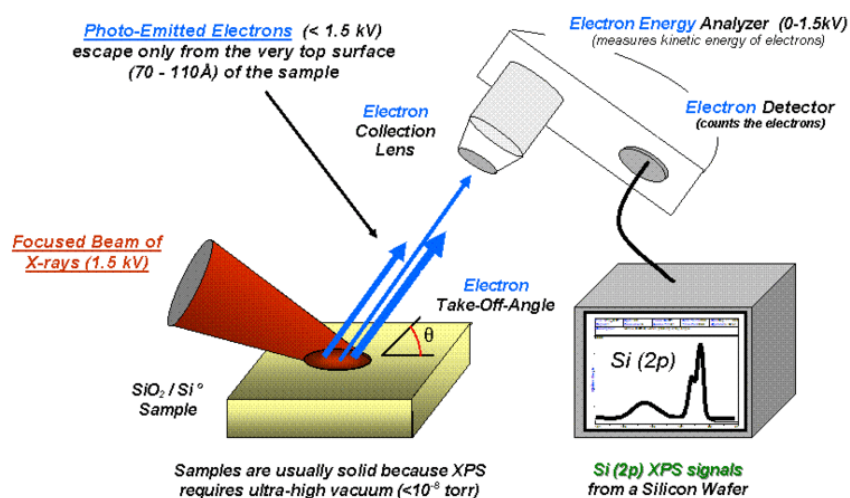
### **Energy-Dispersive X-ray spectroscopy (EDS):**

Energy-Dispersive X-ray Spectroscopy (EDS), also known as Energy-Dispersive X-ray Analysis (EDX), is a technique commonly used in conjunction with electron microscopes to analyse the elemental composition of a sample. EDS works based on the principle that when a high-energy electron beam interacts with a sample, it causes the sample's atoms to emit characteristic X-rays. The energies of these X-rays are specific to the elements present in the sample. By detecting and analysing the energies of these emitted X-rays, it's possible to determine the elemental composition of the sample. Including the

composition, EDS can also provide spatial information. By scanning the electron beam over the sample's surface, elemental maps can be generated which give the information of the distribution of different elements within the sample.

**X-ray photoelectron spectroscopy (XPS)<sup>6-7</sup>:**

XPS is a useful technique for conducting surface analysis, which involves gathering qualitative and chemical information from materials. This technique enables the determination of the empirical formula, elemental composition, and electronic configuration of the compound. The generation of photoelectron emission from the sample surface is facilitated by the utilization of Al K $\alpha$  X-rays as the emission source. By gauging the photoelectron energy (binding energy) and the intensity of the photoelectron peak, it becomes feasible to ascertain both the chemical state and quantity of an element. The insights provided by XPS measurements originate from a depth of about 10 nm, as these photoelectrons originate from within this specific depth. Here, X-ray Photoelectron Spectroscopy (XPS) analyses were conducted within an environment of ultra-high vacuum, employing the Kratos Axis Ultra and VG Microtech instruments equipped with a monochromatic X-ray source utilizing Al K radiation.



**Figure 2.3.** Illustrative depiction showcasing the operational principle of X-ray Photoelectron Spectroscopy (XPS) (adopted from Wikipedia).

### Raman Spectroscopy<sup>8-9</sup>:

Fourier Transform Infra-red Spectroscopy (FTIR) serves as a highly sensitive technique primarily employed for identifying the functional groups within a molecule. FT-IR spectra are generated by utilizing electromagnetic radiation in the infrared region. The absorption patterns correspond predominantly to the vibrational movements of the bonds within the molecule. The measurable frequency ranges generally span from 4000 to 400  $\text{cm}^{-1}$ . Initially, it is necessary to measure the background emission spectrum of the IR source, followed by the emission spectrum of the sample. The ratio between the sample and background spectra directly correlates to the sample's absorption spectrum. Notably, the prominent advantages of FT-IR spectroscopy include its minimal sample requirements and remarkable sensitivity. All FT-IR spectra presented in this thesis were acquired using the Perkin Elmer RXI FT-IR spectrophotometer.

### Inductive Coupled Plasma-Optical Emission Spectroscopy (ICP-OES)<sup>10-11</sup>:

This technique serves the purpose of revealing constituent elements and is exclusively utilized as an analytical method. Detecting minute quantities of metals within various



substances, including food and water, holds significant utility. Fundamentally, it employs a flame-based approach with a temperature range for the flame between 6000 and 10,000 K. Within the ICP-OES instrument, both the atomizer and the analyzer play crucial roles. The atomization process is carried out by inductively coupled plasma (ICP), while optical emission spectroscopy serves as the analytical component. As per the emission theory, when argon, previously utilized as a carrier gas to traverse a differential vacuum interface, cools down, it emits characteristic radiation. This emitted radiation is directed into the optical emission chamber based on the wavelength of the photons being measured. The identification of an element is determined by the location of the photon signals, whereas the quantity is ascertained through the intensity of the emitted photons. ICP-OES measurements offer numerous advantages compared to other experimental approaches, including:

- (a) Many elements can be simultaneously measured.
- (b) Minimal ionisation and chemical interference.
- (c) Very sensitive and can detect down to parts per billion.
- (d) It can result in a fairly steady outcome.

ICP-OES was carried out using the iCAP 7000 Series for this thesis (Thermo Scientific).

### **Elemental Analysis<sup>12</sup>:**

Elemental analysis aims to determine the elemental composition of a compound, typically expressed as a weight percentage. CHNS analysis focuses on quantifying the concentrations of carbon, hydrogen, nitrogen, and sulfur. This involves subjecting the sample to combustion at elevated temperatures in the presence of ultra-high purity oxygen. The resulting combustion gases, encompassing carbon dioxide, water, nitrogen gas or nitrogen oxides, and sulfur dioxide, are then subjected to a process of ballast collation to achieve balanced proportions. Subsequently, the combustion gases are

isolated, and carbon and hydrogen concentrations are measured using infrared spectroscopy. These gases are subsequently mixed uniformly in a chamber under specific temperature and pressure conditions. The concentrations of nitrogen are then determined from this homogeneous mixture as it passes through multiple thermal conductivity detectors. In this thesis, we have used a EuroEA Elemental Analyzer for CHNS analysis.

**Electrochemical measurement:**

A conventional three-electrode configurations were employed for all electrochemical performance evaluations. Data acquisition was conducted using an electrochemical workstation (CorrTest Electrochemical Workstation [Model: CS350]). The counter and reference electrodes consisted of platinum wire/mesh and Ag/AgCl immersed in 3 M KCl solution, along with Hg/HgO in 1 M KOH solution. The working electrode was a metal foam electrode (such as Ni foam) for alkaline electrolyte and a Ti foil for acidic electrolyte. In preparation for electrochemical investigations, oxide layers were removed by washing Ni foam in 3M HCl for 30 min, followed by washing in water and ethanol and dried. Several commonly utilized methods are enumerated below:

**Voltammetry:**

Voltammetry entails the controlled alteration of potential at a predefined rate while simultaneously measuring the resulting current. This technique is characterized by its sensitivity to the surface of the material being studied. It offers insights into the extent of charge exchange transpiring at the interfaces between the electrode and the electrolyte. In Cyclic Voltammetry (CV) approach, potential changes take place directly from an initial potential (V1) to a subsequent potential (V2), and subsequently from (V2) back to (V1), forming a cyclic pattern.

**Chronoamperometry (CA):**

In the CA method, current is monitored over time at a fixed potential. Using this technique, the electrocatalysts' stability may be assessed. Tafel slope may also be measured with the use of this method. By integrating the current over a predetermined period of time, quantitative information may be retrieved, such as the total quantity of charges that have gone through the electrode.

### **Galvanostatic charge discharge (GCD):**

With the GCD method, the charging and discharging times are measured using a set potential range and a constant current. For the purpose of calculating specific capacitance values, GCD is helpful. Energy density and power density values can be determined using the GCD data.

### **Impedance spectroscopy<sup>13</sup>:**

Electrical resistance,  $R$ , is connected with circuit components' resistance to electrical current flow. According to Ohm's law, the resistance is equal to the product of the output current,  $I$ , and the input voltage,  $E$ .

Impedance, like resistance, shows how resistant the circuit is to electrical current flow. It is represented by actual parts, but it also contains an imagined impedance component that corresponds to the circuit's capacity to store electrical energy. Impedance fits into this description in both direct and alternating current. The relationship between impedance and frequency-dependent resistance in a real circuit may be expressed as:

$$Z_{\omega} = \frac{E_{\omega}}{I_{\omega}}$$

Where  $Z_{\omega}$  is the impedance,  $E_{\omega}$  is the frequency dependent potential and  $I_{\omega}$  is frequency dependent AC current.

For a sinusoidal perturbation of potential of fixed frequency and corresponding measurement AC current are also in the same frequency but in different phase.

The potentials response signal is

$$E(t) = E_0 \sin(\omega t)$$

Where the radial frequency  $\omega = 2\pi f$ .

The corresponding AC current signal follows as:

$$I(t) = I_0 \sin(\omega t + \varphi)$$

Where  $\varphi$  is phase difference and  $I_0$  is the response signal amplitude. Now in according to the impedance ( $Z_\omega$ )-

$$Z_\omega = \frac{E_0 \sin(\omega t)}{I_0 \sin(\omega t + \varphi)} = Z_0 \frac{\sin(\omega t)}{\sin(\omega t + \varphi)} = Z_0 \{\cos(\varphi) + i \sin(\varphi)\} = Z_{real} + Z_{imag}$$

**Table 2.2.** The details description of Bode and Nyquist plot.

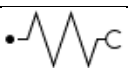


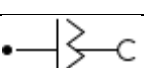
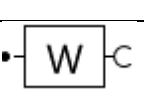
Parameter	Bode plot	Nyquist plot
<b>Process</b>	The individual electron transfer process was describes	The individual electron transfer process was describes
<b>Frequency</b>	Frequency was well defined.	Frequency was not well defined.
<b>Nature</b>	Both small and large impedance was defined simultaneously.	In presence of large impedance, small impedance was not well defined.

As a result, total impedance is a complicated number with two counterparts, one of which is the real and the other is the imagination. A compound's EIS can be shown in one of two ways: (a) by charting the real component on the x-axis and the imaginary portion's negative value on the y-axis to create a Nyquist plot. (b) The Bode Plot was created by taking the x-axis and y-axis logarithms.

Table 2.2 provides a detailed description of the Bode and Nyquist plot. If the capacitive and resistance components of a given circuit are parallel to one another, the Nyquist plot for that circuit would resemble the one where low frequency data is presented on the right side and high frequency data is plotted on the left. Equivalent circuits are network

frames of passive electrical components that can mimic an electrochemical cell. In Table 2.3, the corresponding circuit's components are listed.

**Table 2.3.** The components and their indication for equivalent circuit.

Equivalent	Impedance	Indication
Resistance	R	
Capacitance	C	
Inductance	L	
Constant phase element	Q	
Warburg Impedence	W	

## 2.4. References:

1. Bragg, W. H.; Bragg, W. L., Proceedings of the Royal Society of London. Series A, Containing Papers of a Mathematical and Physical Character **1997**, *88*, 428-438.
2. Saka, H., Chapter 14 - Transmission Electron Microscopy. In *Carbon Alloys*, Yasuda, E.-i.; Inagaki, M.; Kaneko, K.; Endo, M.; Oya, A.; Tanabe, Y., Eds. Elsevier Science: Oxford, 2003; pp 223-238.
3. Pennycook, S. J., Transmission Electron Microscopy. In *Encyclopedia of Condensed Matter Physics*, Bassani, F.; Liedl, G. L.; Wyder, P., Eds. Elsevier: Oxford, 2005; pp 240-247.
4. Singh, M. K.; Singh, A., Chapter 17 - Scanning electron microscope. In *Characterization of Polymers and Fibres*, Singh, M. K.; Singh, A., Eds. Woodhead Publishing: 2022; pp 387-419.
5. de Assumpção Pereira-da-Silva, M.; Ferri, F. A., 1 - Scanning Electron Microscopy. In *Nanocharacterization Techniques*, Da Róz, A. L.; Ferreira, M.; de Lima Leite, F.; Oliveira, O. N., Eds. William Andrew Publishing: 2017; pp 1-35.
6. Defosse, C.; Rouxhet, P. G. In *Introduction to X-Ray Photoelectron Spectroscopy*, Advanced Chemical Methods for Soil and Clay Minerals Research, Dordrecht, 1980//; Stucki, J. W.; Banwart, W. L., Eds. Springer Netherlands: Dordrecht, 1980; pp 169-203.
7. Wagner, C. D.; Wagner, C. D.; Muilenberg, G. E., *Handbook of X-ray Photoelectron Spectroscopy: A Reference Book of Standard Data for Use in X-ray Photoelectron Spectroscopy*. Perkin-Elmer: 1979.
8. John, N.; George, S., Chapter 5 - Raman Spectroscopy. In *Spectroscopic Methods for Nanomaterials Characterization*, Thomas, S.; Thomas, R.; Zachariah, A. K.; Mishra, R. K., Eds. Elsevier: 2017; pp 95-127.
9. Wolverson, D., Chapter 17 - Raman Spectroscopy. In *Characterization of Semiconductor Heterostructures and Nanostructures (Second Edition)*, Lamberti, C.; Agostini, G., Eds. Elsevier: Oxford, 2013; pp 753-802.

10. Hou, X.; Amais, R. S.; Jones, B. T.; Donati, G. L., Inductively Coupled Plasma Optical Emission Spectrometry. In *Encyclopedia of Analytical Chemistry*, 2016; pp 1-25.
11. He, M.; Hu, B.; Chen, B.; Jiang, Z., **2017**, 2.
12. Hollas, J. M., *Modern Spectroscopy*. Fourth Edition ed.; 2003.
13. Lazanas, A. C.; Prodromidis, M. I., *ACS Measurement Science Au* **2023**, 3, 162-193.

## Chapter 3

### Facile Synthesis of Two-dimensional (2D) Boron Carbonitride (BCN) and 2D porous BCN for excellent Energy storage and Gas Adsorption Applications

#### 3.1. ABSTRACT

The development of two-dimensional (2D) carbon nanosheets and microporous 2D carbon-nanosheets with high specific surface area (SSA), large pore volume, and high conductivity is important for energy storage and gas storage applications. Traditional microporous carbon materials have several disadvantages such as low accessibility of active sites and poor mass transport due to large diffusion pathways. The nanometer-thick 2D microporous carbon-nanosheets permit easy mass/heat transport leading to overcoming the drawbacks of bulk-porous-materials. Herein, we demonstrate facile synthesis of 2D boron carbonitride (BCN) and 2D porous BCN for energy and gas storage applications. The 2D BCN showed excellent supercapacitor (SC) application with a specific capacitance ( $C_s$ ) of  $273 \text{ F g}^{-1}$  under  $1 \text{ A g}^{-1}$ . Most importantly, 2D porous BCN (p-BCN) were prepared by KOH-activation at high temperatures. The optimized 2D porous BCN with highly concentrated micropores and a considerable amount of mesopores provide a high SSA ( $3310.4 \text{ m}^2 \text{ g}^{-1}$ ) and pore volumes of  $1.75 \text{ cc g}^{-1}$ . The combined effect of unique porous nanosheets and optimum doping of heteroatoms allow easy electrolyte/ion diffusions, electron conduction, faradic reactions, etc. The p-BCN-800 electrode showed superior  $C_s$  of 406 and  $355 \text{ F g}^{-1}$  under  $1 \text{ A g}^{-1}$  in  $\text{H}_2\text{SO}_4$ , and KOH electrolytes respectively. Moreover, symmetric p-BCN-800//p-BCN-800 device showed high energy and power densities ( $17 \text{ W h Kg}^{-1}$  and  $4000 \text{ W kg}^{-1}$ ) with high cycling stability. The 2D porous BCN showed excellent  $\text{H}_2$  and  $\text{CO}_2$  adsorption capacity. The  $\text{H}_2$  uptake of 2D porous BCN is 2.91 wt % at 77 K under 1 bar pressure, whereas  $\text{CO}_2$

uptakes are 3.96 mmol g<sup>-1</sup> and 2.39 mmol g<sup>-1</sup> at 0 and 25 °C respectively. This chapter demonstrates an efficient way to produce 2D BCN and 2D porous BCN for energy storage and gas uptake applications.

## 3.2. INTRODUCTION

The quest to develop energy storage and conversion systems has been burgeoning with approaching the time of the energy crisis<sup>1</sup>. Carbon-based materials is a forefront candidate for various applications like energy storage, gas storage, and catalysis because of their convenient synthesis method and high electrochemical performance<sup>2-3</sup>. Mainly, the 2D carbon framework plays a pivotal role in various industrial and environmental applications but overlapping and restacking of the Vander Waals sheets limits its application in the energy storage system as it lowers its SSA (leading to limits its effective electrochemical surface) and hence limits its ion transport (lengthens the ion transport channel<sup>4</sup>) across the sheets<sup>5</sup>. However, tuning of structural and physicochemical properties is still required to enhance electrochemical energy storage. Zealous efforts have been made to boost the energy storage performance of 2D carbon nanosheets. The pore engineering of 2D carbon nanosheets has received a lot of attention in reports. The holey carbon nanosheets with meso and micropores show much better ionic diffusion/transportation, and electron transport path and increase the (SSA)<sup>6</sup> of carbon, i.e. the contact area between the carbon and electrolyte interface, the reversible desorption/adsorption of charged ions from electrolytes into highly porous electrode materials becomes favorable. The modification of porosity leads to a higher electroactive surface area<sup>7</sup>, providing space for transportation which is essential for the enhancement of high-charge storage. Compared to activated carbon, hierarchical porous carbon has a greater capacitance and much better rate capability as a result of its interconnected micro–meso–macropores that act as adsorption sites, ion transport paths, or ion



reservoirs. This is owing to the higher utilization of micropores with nanometers of ion transport distance from adjacent macropores and mesopores<sup>8</sup>. Contrarily, consistently ordered mesoporous carbon with uniform mesopores can also promote ion transport, depending on the ratio of mesopore length to diameter. The lesser ratios (short length, large pores) would improve ion transport behavior but would result in a smaller SSA and density, which is related to less energy in terms of gravimetric and volumetric<sup>6, 9</sup>. To overcome the above-mentioned issues, engineering 2D porous carbon materials such as making pores, crumping, and solvating are employed to avoid surface area loss and allow ion transport across the electrode materials. Compared to traditional porous carbon sheets, 2D porous carbon nanosheets with interlinked hierarchical porous structure and high utilization of micropores in the interconnected hierarchical porous structure are very good candidates for energy storage applications owing to their high aspect ratio for electron transport, ion transport capability across the electrodes<sup>10</sup>. Pore size plays a vital role in improved capacitance performance. Pore size lesser than 2nm can improve capacitance which results in increasing the energy density (ED)<sup>11</sup>. In addition, it shortens the distance of the electrolyte ions to access the interior of the material<sup>12</sup>. Although a few approaches are developed for the synthesis of 2D porous carbon with better ion transport properties and desirable pore size but very few reports are there for the same with sub-nanometer (<1nm) pores as 2D porous carbon with pores <1nm is generally difficult to prepare.

Further, heteroatom like boron (B)<sup>13</sup>, nitrogen (N)<sup>14</sup>, sulfur (S)<sup>15</sup>, selenium (Se)<sup>16</sup>, phosphorous (P)<sup>17</sup>, and fluorine (F)<sup>18</sup> doping has been proven to be the most favorable technique to improve the activity of the carbon material. Doping of heteroatom results in the enhancement of electrical conductivity and wettability of the surface ultimately

increasing the availability of the more active site and hence the  $C_s$  of carbon materials<sup>19</sup>. N doping to the carbon framework improves the charge mobility on the carbon surface including the wettability of the carbon materials<sup>20</sup> while P doping results in higher oxidation resistance of the electrode<sup>21</sup>. Further, S doping with carbon framework combines EDLCs with pseudocapacitance owing to its easy polarizable lone pair electrons and large size with better charge distribution over the carbon surface and improves the capacitive performance through a faradic process. Boron doping to the carbon framework can substitute the carbon and act as an electron acceptor because of its three valence electrons resulting in the Fermi level to the conduction band and modifying the electronic structure of doped carbon<sup>22-23</sup>. Though mono heteroatom doping significantly improves the capacitive performance, recently it is observed that co-doping such as N and S, N and O, N and B etc. has been more efficient<sup>7, 15</sup>. Boron doping has a very low efficiency by boric acid due to its poor reactivity and  $H_3BO_3$  is a green boron dopant because of its low toxicity. So it's difficult to dope boron into carbon framework at temperature below 1500 °C<sup>24-25</sup>. So doping of boron directly to the carbon framework at lower activation temperature remains a challenge. But few reports are there for synthesis of boron doped carbon using boric acid as B source at lower activation temperature. For instance, Liu Yang et al. reported B/N doped Carbon Nanosheets from boric acid and amino acids by a pregelation and carbonization activation approach with good SC performance<sup>26</sup>.

In recent times, not only the energy crisis, but large-scale CO<sub>2</sub> emission is also a serious environmental issue since it can lead to the greenhouse effect, global warming, anthropogenic climate change, and so on. Hence, it is imperative to develop different techniques for CO<sub>2</sub> capture and storage. So, designing a better adsorbent is required for

the storage and separation of CO<sub>2</sub> and H<sub>2</sub> which can be used as an energy source for fuel cell vehicles. Nowadays, porous silica, calcium oxide, metal-organic framework, porous carbon, and porous polymers, zeolites, hybrid composites have been used as adsorbents owing to their low cost, large specific surface area, adjustable pore size, and chemical stability. But, the high SSA, tunable porous morphology, tunable pore volume, low density and resistivity, thermo-mechanical stability, and facile synthesis methods of porous carbon materials pave the way for real-world application. Additionally, the performance of selective adsorption of CO<sub>2</sub> can be improved by the introduction of basic groups into the carbon framework. Mainly, the N doping enhances the energy storage capacity and CO<sub>2</sub> capture by increasing the surface-active redox sites, while the heteroatom doping can improve the adsorption properties of acidic gases. Recent theoretical and experimental research has shown that 2D porous nanostructured boron nitrides have high H<sub>2</sub> storage capacity because of the strong interactions with the H<sub>2</sub> molecule caused by the dipole moment of the B-N bonds and the surface local curvature. Controlling the composition of B, N, and C can provide an additional way to control the H<sub>2</sub> storage property<sup>27</sup>. Therefore, it is believed that controlling the composition of B, N, and C can provide an additional way to control the gas storage property as this allows modifying the nature and energy of the bond between the H<sub>2</sub> molecule and surface.

The hetero atom doping and designing of micropore-enriched structures mainly depend only on the raw materials and synthesis route. Pre- and post-decoration treatments are the primary techniques to dope hetero atoms in the carbon framework. In the pre-decoration method, chemical substances rich in hetero atoms are used as gas components for surface activation. On the other hand, the post-decoration method involves direct

preparation and uniform distribution of heteroatoms which increases the stability and hence a more preferred method. However, hetero atom doping precursor needs a sophisticated synthetic method and expensive monomer reagent. Hence, it is more important to prepare a binary heteroatom doping carbon framework for gas adsorption and storage which can be easily synthesized at low-cost and on large scale. For N and B doping, inexpensive chemicals such as formamide and boric acid are widely used, allowing the formation of an in-situ binary heteroatom-doped porous carbon framework for high-performance energy storage and H<sub>2</sub> uptake.

Herein we have prepared 2D heteroatom doped nanosheets by the solvothermal method in the first step followed by calcination by varying the temperatures. In the second step, 2D porous nanosheets consisting of micro-, and mesopores were prepared by the KOH-activated pyrolysis method. A series of N and B co-doped 2D nanosheets and binary heteroatom-doped porous carbon materials were prepared by varying the temperature. The unique microporous carbon sheets with optimal doping of B/N activated at 800°C show a high SSA of 3300 m<sup>2</sup>g<sup>-1</sup> and pore volume of 1.75 cc g<sup>-1</sup>. Microspores are concentrated at 2 nm including plenty of microspores with a size of less than 1nm (sub-nanometer scale). First, we studied the electrochemical performance of 2D BCN prepared by carbonization at 800 °C. This shows a C<sub>s</sub> value of 273 F g<sup>-1</sup> under 1 A g<sup>-1</sup> in 6M KOH electrolyte. The 2D porous BCN activated at 800°C (p-BCN-800) show great potential as electrode material in base, acidic, as well as in neutral electrolytes for energy storage applications. The doping engineering and activation strategy are of great importance in altering the electronic conductivity, structural defects, and energy storage performance of carbonaceous materials. The symmetric device formed by assembling two p-BCN-800 electrodes (p-BCN-800//p-BCN-800) shows a C<sub>s</sub> value of 307.7 F g<sup>-1</sup> at

1 A g<sup>-1</sup> in 6M KOH. The device shows an energy density of 10.69 W h kg<sup>-1</sup> along with 2500 W kg<sup>-1</sup> power densities. Furthermore, 2D porous BCN (p-BCN-X) act as good adsorbents for H<sub>2</sub> and CO<sub>2</sub> gasses. The heteroatom-doped porous carbon shows CO<sub>2</sub> uptake of 3.96 mmol g<sup>-1</sup> at 273 K and 2.39 mmol g<sup>-1</sup> at 298 K respectively and H<sub>2</sub> uptake of 2.91 wt % at 77 K under 1 bar pressure. Hence incorporation of B and N into the 2D porous nanosheets is a very effective and reasonable method for energy storage and CO<sub>2</sub> adsorption.

### **3.3. EXPERIMENTAL SECTION:**

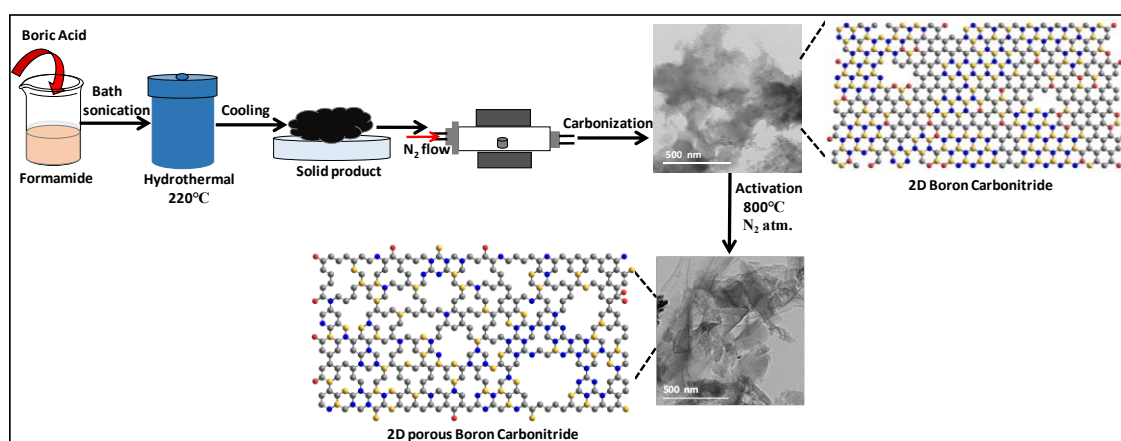
#### **3.3.1. Materials:**

Formamide was purchased from Merck, India. Boric Acid was purchased from Spectrochem PVT. LTD. Mumbai (India). Potassium Hydroxide (KOH), Hydrochloric acid (HCl), and Sulphuric acid (H<sub>2</sub>SO<sub>4</sub>) were purchased from CDH chemicals, India. PTFE binder was purchased from MTI corporation. Deionized water was used to carry out all experiments.

#### **3.3.2. Synthesis of 2D Boron carbonitride (BCN-X) and 2D porous BCN (p-BCN-X)**

The synthesis of heteroatom-doped 2D porous BCN was carried out in two steps. In the first step, 30 ml of Formamide (as a C and N source) was taken in a 50 ml beaker and 4 g of boric acid was added as a boron source and ultrasonically dispersed in a beaker for 1hr in a bath sonicator. Then the homogeneous mixture was transferred into a 100 ml autoclave and allowed to heat at 220 °C for 48 hrs. The solid product obtained was heated in a tube furnace at three different temperatures with a heating rate of 5 °C min<sup>-1</sup> (700 °C, 800 °C, and 900 °C) for 2 hrs under a nitrogen flow of 700 mL/min. The solid product obtained was a 2D boron carbonitride denoted as BCN-X (X= 700,800 and 900) and was

further used to characterize. In the second step, the product obtained from carbonization at 800 °C was soaked in 6M KOH maintaining a KOH and C weight ratio of 2:1 and dried in an oven at 150 °C. Then the sample was activated at a different temperature from 700-900 °C and the samples obtained are 2D porous boron carbonitride denoted as p-BCN-X (X= 700, 800, and 900) accordingly. The soluble impurities are removed by washing the synthesized p-BCN-X materials with 0.2M HCl and DI water multiple times. The material obtained was then dried for 12 hrs at 100 °C to remove the adsorbed solvents to obtain a black-colour solid product. A detailed synthesis illustrating the synthesis of 2D BCN-X and p-BCN-X is presented in Scheme 3.1.



**Scheme 3.1.** Synthesis of 2D Boron carbonitride (BCN-X) and 2D porous Boron carbonitride (p-BCN-800).

### 3.3.3. Electrode Fabrication:

Fabrication of electrodes was carried out by mixing PTFE binder, conductive carbon, and active material (BCN-X and p-BCN-X) with a mass ratio of 10:10:80 (*N*-Methyl-2-pyrrolidone (NMP)) followed by coating over Nickel foam (1\*1 cm<sup>2</sup>) and Ti foil (current collector) for the base and acid medium respectively. The electrodes were dried at 85 °C in a vacuum. The mass loading of each electrode was close to 1 mg. The single electrode Performance was measured in the electrolyte of 6M KOH and 1M H<sub>2</sub>SO<sub>4</sub> in a three-

electrode system configuration with Hg/HgO reference electrode (Ag/AgCl in 1M H<sub>2</sub>SO<sub>4</sub>) and platinum mesh as counter electrode while the symmetric device was tested in the two-electrode system. The symmetric device was prepared using glass microfibre filter paper as a separator in a CR2032 coin cell configuration. 1M Na<sub>2</sub>SO<sub>4</sub> was used as an electrolyte for the test in a neutral medium. From a single electrode, the specific capacitance ( $C_s$ ) Calculation was carried out from Galvanostatic Charge discharge (GCD) curves using the following equation:

$$C_s = \frac{I\Delta t}{m(V_f - V_i)} \quad (3.1)$$

Specific capacitance ( $C_s$ ) can be calculated from the CV curve by using the following equation:

$$C_s = \frac{\int I dV}{2m\Delta V u} \quad (3.2)$$

Where  $C_s$  = specific capacitance

$I$  = current applied (A)

$\Delta t$  = discharge time (sec)

$m$  = mass of the active material (g)

$V_f - V_i$  = Voltage window (V)

$\int I dv$  = area under the CV curve

$u$  = scan rate (mV s<sup>-1</sup>).

For a symmetric supercapacitor device, the calculation was done using the following equations.

$$C_s = \frac{2I\Delta t}{m(V_f - V_i)} \quad (3.3)$$

$$ED = \frac{C_{cell}\Delta V^2}{2 \times 3.6} = \frac{C_s\Delta V^2}{8 \times 3.6} \quad (3.4)$$

$$PD = \frac{E \times 3600}{t} \quad (3.5)$$

Where  $C_s$  = specific capacitance, ED = Energy density, and PD = power density.

### **3.3.4 Material Characterization:**

The powder x-ray diffraction patterns (p-XRD) of samples were measured by Bruker X-ray diffractometer (DAVINCI D8 ADVANCE equipped with Cu K $\alpha$  source of wavelength 0.154 nm). The morphological characterization was investigated by a Field-emission scanning electron microscope (FESEM) system (Model-Sigma, Carl Zeiss, Germany) and Transmission Electron Microscopy (TEM) instrument operated at 200 kV (F200, JEOL). XPS measurement was done using AXIS ULTRA (Kratos) instrument where a monochromated Al-K $\alpha$  source was used. XPS was taken from the sample deposited on the silicon wafer. The CO<sub>2</sub> and N<sub>2</sub> physisorption isotherms were collected using AUTOSORB-1 (Quantachrome). The pore size distribution (PSD) was calculated using the nonlocal density functional theory (NLDFIT) model while the micropore analysis was carried out using the t-plot method. LabRAM HR Evolution, Horiba Scientific, and Raman Spectrometer were used for Raman analysis using a 532 nm laser source. Electrochemical measurements were performed using CS310 Electrochemical Workstation (Corrtest Instruments).

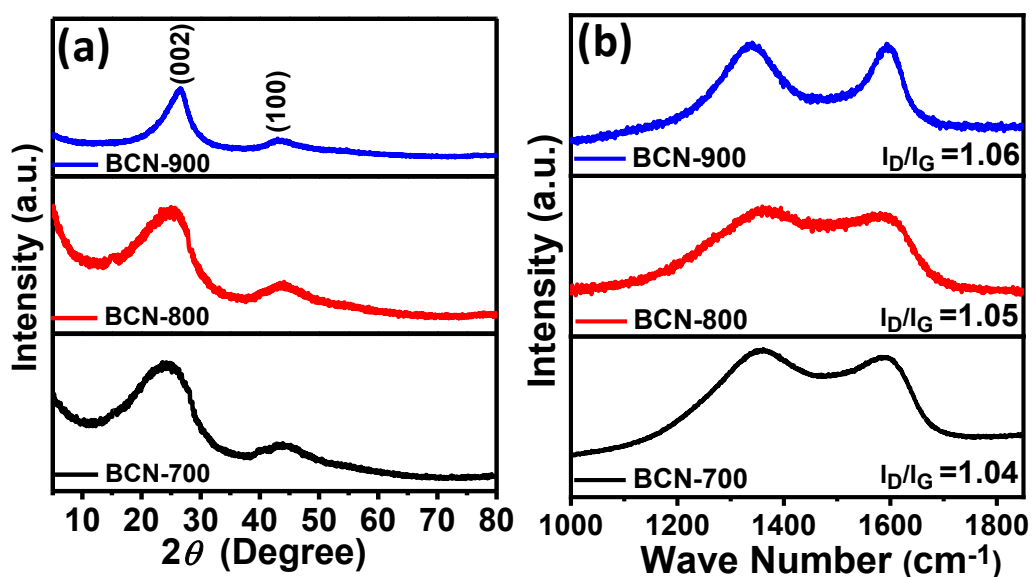
## **3.4 RESULTS AND DISCUSSIONS:**

### **3.4.1 Morphology and characterization**

Electrochemical performance depends on the morphology, heteroatom doping, and SSA of carbon materials. In this study, all the BCN-X and p-BCN-X samples were prepared via hydrothermal synthesis followed by pyrolysis and activation by KOH at different temperatures in presence of N<sub>2</sub> flow and to regulate the boron content and porosity. During the calcination process in the N<sub>2</sub> atmosphere, H<sub>3</sub>BO<sub>3</sub> can be transformed into



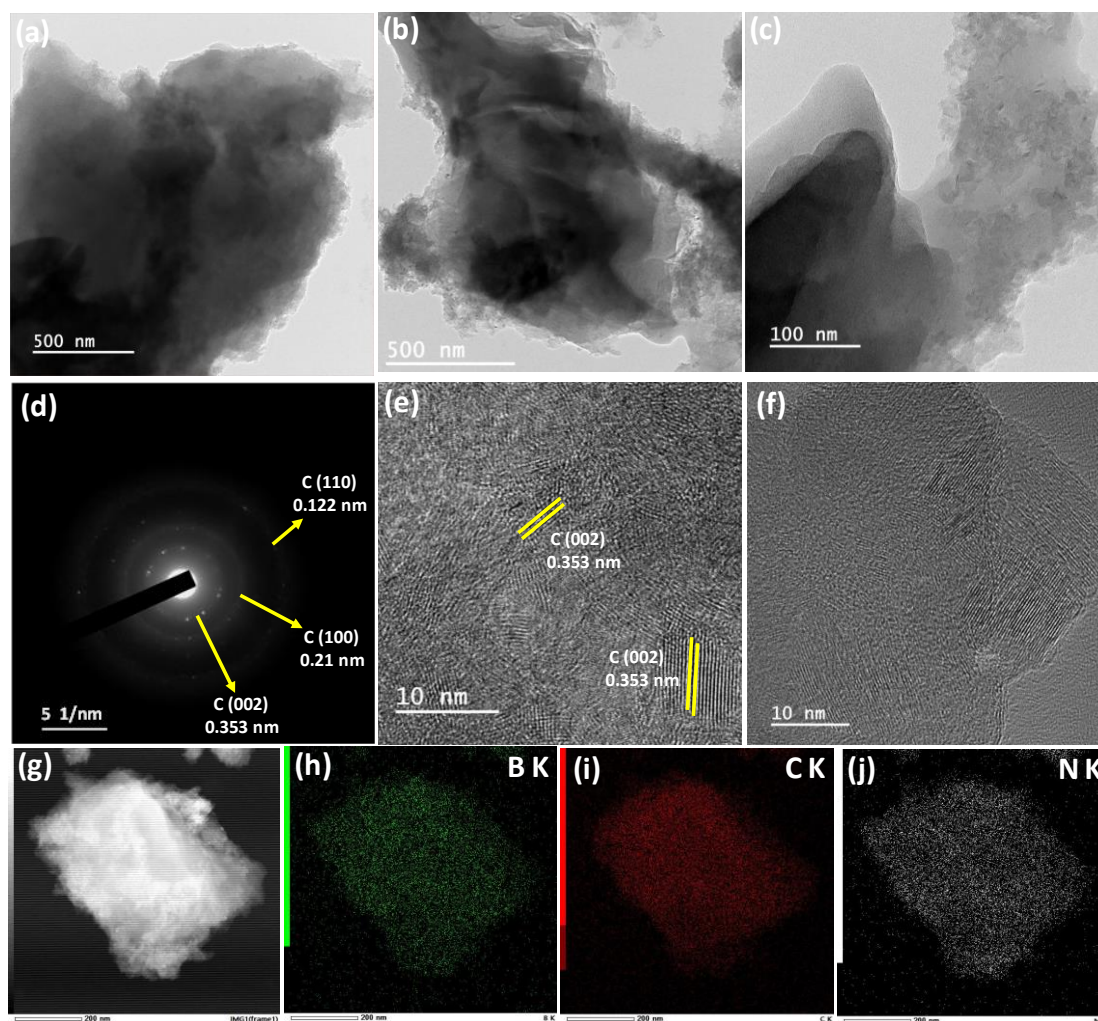
B<sub>2</sub>O<sub>3</sub>, and the boron atoms therein enter the carbon skeleton through the reaction  $2\text{B}(\text{OH})_3 \rightarrow \text{B}_2\text{O}_3 + 3\text{H}_2\text{O}$ ,  $3\text{B}_2\text{O}_3 + 9\text{C} \rightarrow \text{BC}_3 + \text{BC}_2\text{O} + 4\text{BCO}_2$ . In addition, volatile gasses like CO<sub>2</sub>, CO, and H<sub>2</sub>O are generated to form the micropores, which result from the interaction between the carbon atoms and oxygen groups and the dehydration of H<sub>3</sub>BO<sub>3</sub>. The removal of B<sub>2</sub>O<sub>3</sub> (by pyrolysis) produces mesopores and micropores<sup>28</sup>. All the synthesized materials are characterized by p-XRD pattern. Figure 3.1(a) represents the powder X-ray diffraction (p-XRD) pattern of 2D BCN-X samples before the activation process. Two broad and weak peaks at  $2\theta$  values 25.32 and 43.73° indexed to (002) and (100) crystal planes of graphite carbon respectively representing the formation of the disordered carbon structure.



**Figure 3.1.** (a) p-XRD pattern and (b) Raman spectrum of 2D BCN-X samples carbonized at different temperatures.

Figure 3.1(b) depicts the Raman spectrum of 2D BCN-X samples, showing two distinct peaks located at 1339 and 1597 cm<sup>-1</sup> corresponding to D and G bands, respectively. The D band demonstrates the existence of disordered or defective structure (sp<sup>3</sup>-hybridized carbon) and the G band demonstrates the crystalline graphitic structure (sp<sup>2</sup>-carbon) in

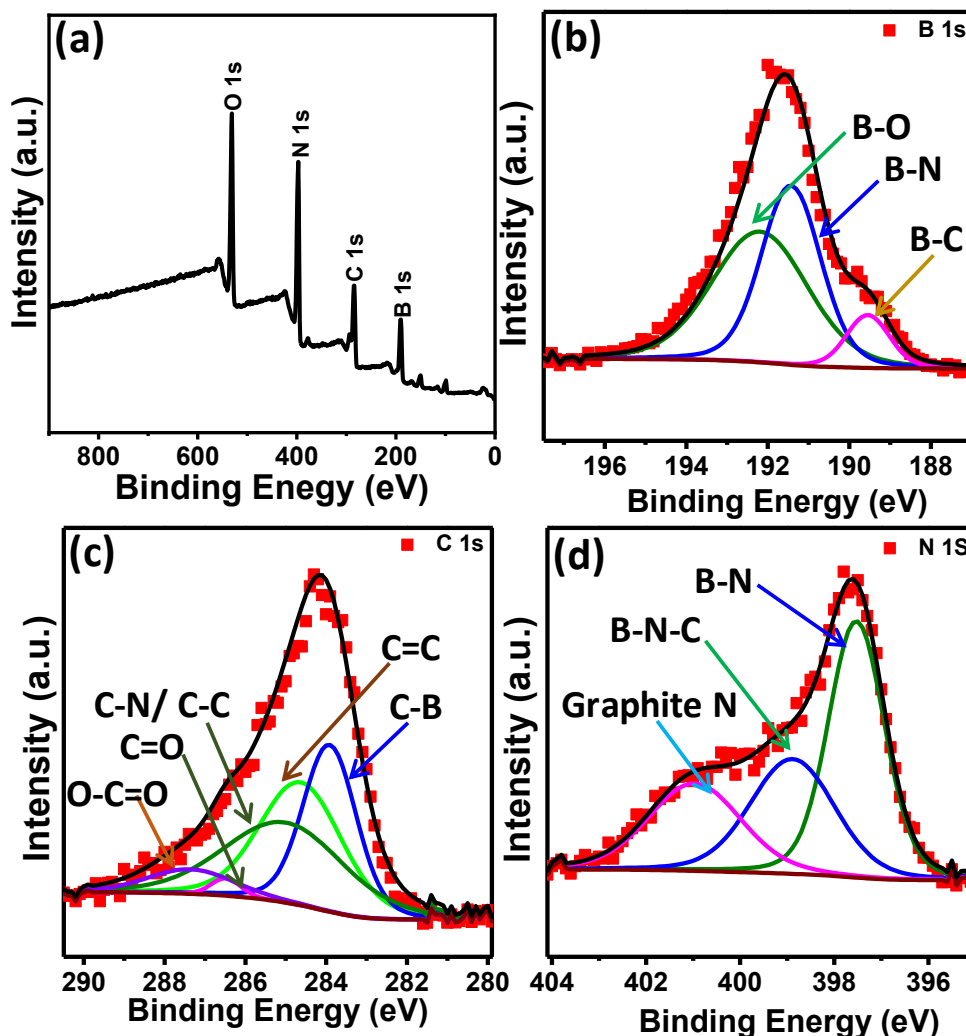
BCN-X samples. The  $I_D/I_G$  (D and G band integral intensity ratios) for BCN-X was calculated to be in the range of 1.04-1.06 suggesting a lower degree of graphitization with an increase in annealing temperature from 700 to 900 °C. The morphology of the 2D BCN-800 sample was further characterized by transmission electron microscopy (TEM). Figure 3.2(a-c) represents the low-resolution TEM images of the BCN-800 sample. The TEM images show that the 2D nanosheets are crumpled and contain entangled wrinkles. The crumple-like structure may arise due to local stresses caused by lattice defects, such as vacancies, boron, and nitrogen dopants<sup>29</sup>. The SAED image of carbonized BCN-800 (Figure 3.2(d)) shows three very faded circles with some bright spots on them, which suggest the presence of both defective and graphitized carbon in the composite. The high-resolution (HR) TEM images of the catalysts are presented in Figure 3.2(e) and (f). The HRTEM image of carbonized BCN-800 shows the (002) planes of graphitized carbon with few irregular fragments in some places suggesting the presence of graphitized as well as disordered carbon in the composite, which is in good agreement with the SAED finding. Figure 3.2(g-j) presents the STEM image and corresponding elemental mapping of carbonized BCN-800 material. These show the homogeneous distribution of atoms and the presence of a significant amount of B, C, and N respectively in the compounds.



**Figure 3.2.** (a-c) Low-resolution TEM images, (d) SAED pattern, (e-f) HRTEM image, (g-j) STEM image, and corresponding elemental mapping of carbonized BCN-800 composite.

X-ray photoelectron spectroscopy (XPS) measurement was used to interpret the successful doping of B element into the carbon framework, chemical states, and composition in carbonized BCN-800 sample. The survey scan was performed to reveal the existence of B, C, N, and O elements in the composites. Figure 3.3(a) represents the detailed scan spectrum of the BCN-800 compound. As depicted in Figure 3.3(b), the high-resolution XPS spectrum of the B1s peak can be deconvoluted into three peaks,

revealing the different states of B. The peak at bond energy of 189.53 eV was observed which is attributed to the bond B–C in BC<sub>3</sub>. The peaks at binding energy 191.45 and 192.22 eV correspond to bonds B–N and B–O (indicate surface defects) respectively<sup>1</sup>. The high-resolution C1s peak presented in Figure 3.3(c) can be fitted into five peaks. The peak at binding energy 283.96 eV and 284.17 eV is assigned to C–B and the C=C bonds in the sample. The peak centered at 285.12, 286.47, and 287.5 eV were indexed to the C–C/C–N bond, C=O, and O–C=O bond respectively<sup>30</sup>. Figure 3.3(d) depicts the N1s peak fitted into three peaks centered at 397.56, 398.92 and 400.98 eV binding energy related to B–N bond, B–N–C bonding and graphitic N respectively<sup>31</sup>. Overall, the XPS measurement demonstrated that all the C–C, B–C, B–N, and C–N bonds were present in the final product. The presence of oxygen peaks was associated with surface contamination.



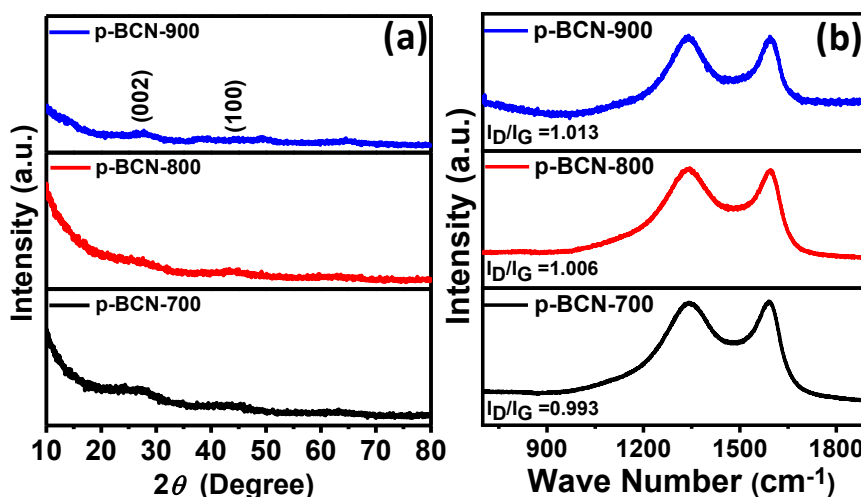
**Figure 3.3.** XPS spectrum of 2D BCN-800, (a) high-resolution spectrum, (b) B 1s, (c) C 1s, and (d) N 1s.

Figure 3.4(a) shows the XRD patterns of B-doped hierarchical porous carbon samples (p-BCN-X) obtained through the KOH activation process. The low-intense but broad hump located at  $24.3^\circ$  and  $43.73^\circ$  ( $2\theta$ ) corresponds to (002) and (100) planes of carbons. This outcome reveals the amorphous nature of p-BCN-X materials. The relatively low peak intensity of the (100) plane indicates the non-uniform graphitization of the samples which arises due to the lower activation temperature used during the synthesis method since the activation temperature significantly influences the degree of graphitization of

the samples. Moreover, B-doping has a minor impact on the p-XRD patterns of p-BCN-X samples. Raman analysis was further carried out to get more information about the degree of graphitization and physical structure of the samples (p-BCN-X). For p-BCN-X,  $I_D/I_G$  ratio was obtained to be in the range of 0.993-1.013 indicating the presence of defects and the amorphous nature of the porous carbon samples (Figure 3.4(b)). The  $I_D/I_G$  ratio for p-BCN-700 is 0.993 which is slightly lower than p-BCN-800 suggesting more degree of defect in p-BCN-800 due to the pyrolysis at higher activation temperature. The higher the value of  $I_D/I_G$  ratio reflects the lower degree of graphitization and defects into the carbon framework by boron doping<sup>32</sup>.

To know the structure, phase, and morphology of the catalysts p-BCN-X field emission scanning electron microscopy (FESEM) and transmission electron microscopy (TEM) was carried out. Figure S3.1 presents FESEM images of p-BCN-X samples. All images show a 2D porous sheet-like structure of the composites. It is also observed that the activated p-BCN-X samples are more porous compared to carbonized 2D BCN-800. A comparison table containing the weight % of all the elements (boron, carbon, nitrogen, and oxygen) for 2D BCN-800 and p-BCN-800 is presented in Table S3.1. The carbon, nitrogen, and boron content rose to 41.8, 18.3, and 18.3% respectively for 2D BCN-800 samples. The content of C is 34.2 wt% and B is 17.6 wt% for the p-BCN-800 sample. This indicates that the activation temperature significantly affects the chemical content of N and B. The Low-resolution TEM images of p-BCN-800 are presented in Figure 3.5(a-d). This shows the 2D porous morphology of the activated p-BCN-800 composite. While activating a boron, nitrogen-doped carbon composite with KOH, the formation of  $K_2CO_3$  takes place ( $2C + 6KOH \rightarrow 2K_2CO_3 + 2K + 3H_2$ ), which can further decompose to  $K_2O$  and  $CO_2$  at a temperature higher than 600 °C. Thus, the porosity of the composite

also increases accordingly. These porous materials can easily pass the electrolyte through them, therefore, increasing the power density of the material. HRTEM image of p-BCN-800 shows mostly irregular fragments with 0.353 nm lattice spacing value suggesting that the composite was very low crystallinity in nature (Figure 3.5 (e and f)). Abundant nanopores are observed which are marked as a circle in Figure 3.5(f). To know more about the crystallinity of these materials, selected area electron diffraction (SAED) analysis was also carried out. The inset of Figure 3.5(e) presents the SAED images of p-BCN-800. The SAED image of p-BCN-800 shows two faded circles that are indexed to the (002) and (100) planes of carbon. This suggests very poor crystallinity of the composite. Figure 3.5(g-k) shows the STEM image and elemental mapping of the p-BCN-800 indicating the homogeneous distribution of B, C, N, and O respectively in the activated compound. The annealing and activation temperature also has some effects on the 2D BCN nanosheets.



**Figure 3.4.** (a) p-XRD pattern and (b) Raman spectrum of 2D porous BCN samples activated at different temperatures (p-BCN-X).



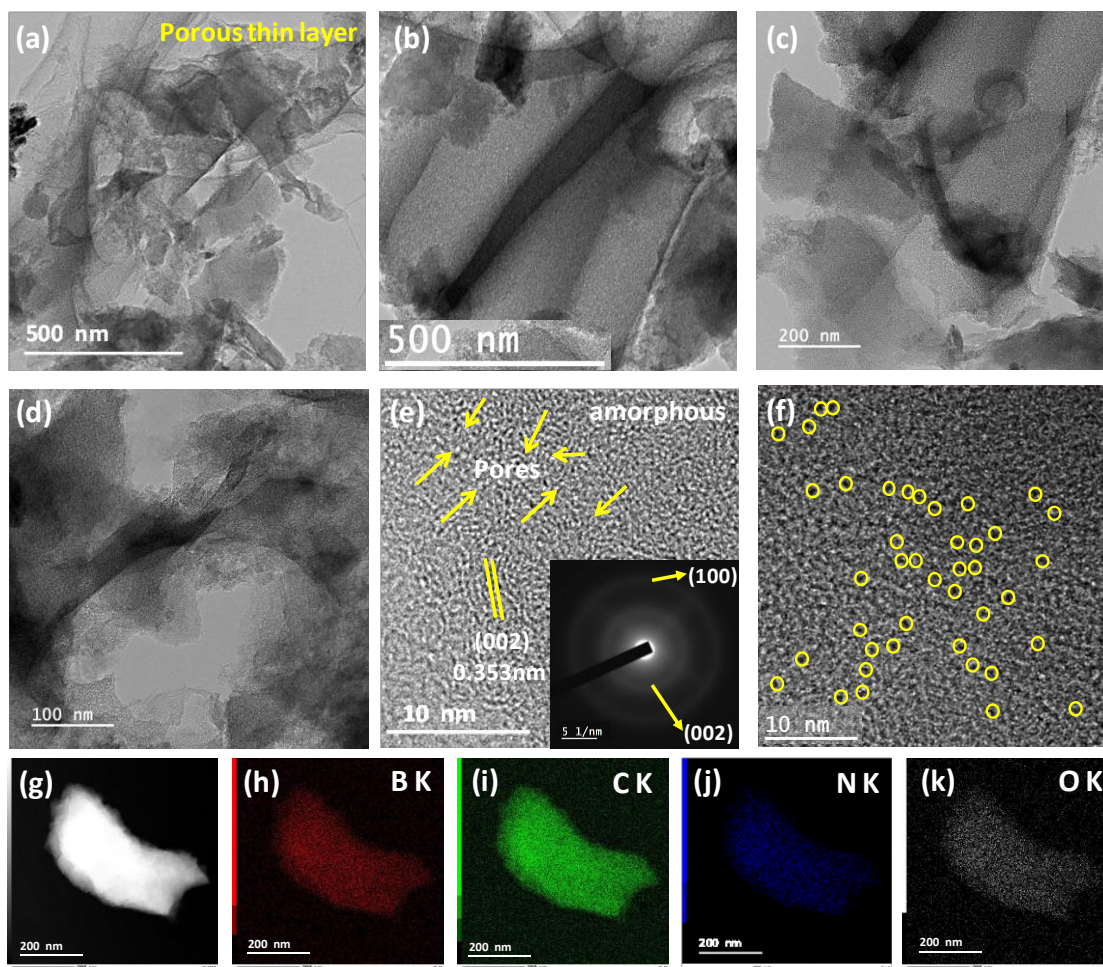
The pore structures of all the carbon materials (p-BCN-X) were further characterized by N<sub>2</sub> adsorption-desorption isotherm at 77K. All the p-BCN-X composites show type-I isotherm curves at low-pressure regions with narrow hysteresis loops, characteristics of microporous structure which is depicted in Figure 3.6(a). The co-existence of mesoporous and microporous structure of the prepared samples is confirmed as the N<sub>2</sub> adsorption curve steady rise after the pressure range of 0.1. The BET SSA ( $S_{\text{BET}}$ ) is obtained to be 1213.7, 2680.7, and 3310.4 m<sup>2</sup> g<sup>-1</sup>, and total pore volume are obtained to be 1.001, 1.75, and 2.016 cc g<sup>-1</sup> for p-BCN-700, p-BCN-800, and p-BCN-900 respectively. A sharp increase in  $S_{\text{BET}}$  value for p-BCN-800 (2680.660 m<sup>2</sup> g<sup>-1</sup>) than p-BCN-700 (1213.651 m<sup>2</sup> g<sup>-1</sup>) samples resulted upon increasing the activation temperature, which has a significant effect when the temperature rises from 700 to 800 °C. The rapid increase may be due to the peak activity of KOH around this temperature<sup>33</sup>. All the BET results ( $S_{\text{BET}}$ ,  $S_{\text{micro}}$ , micropore volume ( $V_{\text{micro}}$ ), average pore radius ( $R_a$ ), and total pore volume ( $V_t$ ) are presented in Table 3.1. The total surface area was determined by using the BET technique and the microporous surface area was obtained by the t-plot technique. The total pore volume ( $V_t$ ) for p-BCN-800 is obtained to be 1.75 cc g<sup>-1</sup> which is higher than the p-BCN-700 sample (1.001 cc g<sup>-1</sup>). Figure 3.6(b) shows the pore size distribution (PSD) plots of the samples suggesting narrow PSD in the p-BCN-800 sample compared to p-BCN-700. The PSD patterns also indicate the presence of plenty of micropores in the samples. The pores of p-BCN-800 are mainly concentrated on five pore sizes (0.72, 1.13, 1.42, 1.77, and 2.65 nm). Out of these pores, sub-nanometer micropores with sizes below 1 nm significantly improved the capacitance behavior of carbon materials due to the pore confinement effect<sup>34</sup>. High  $S_{\text{BET}}$  value of activated B and N co-doped porous carbon at 800 temperatures resulting in a high capacitive charge



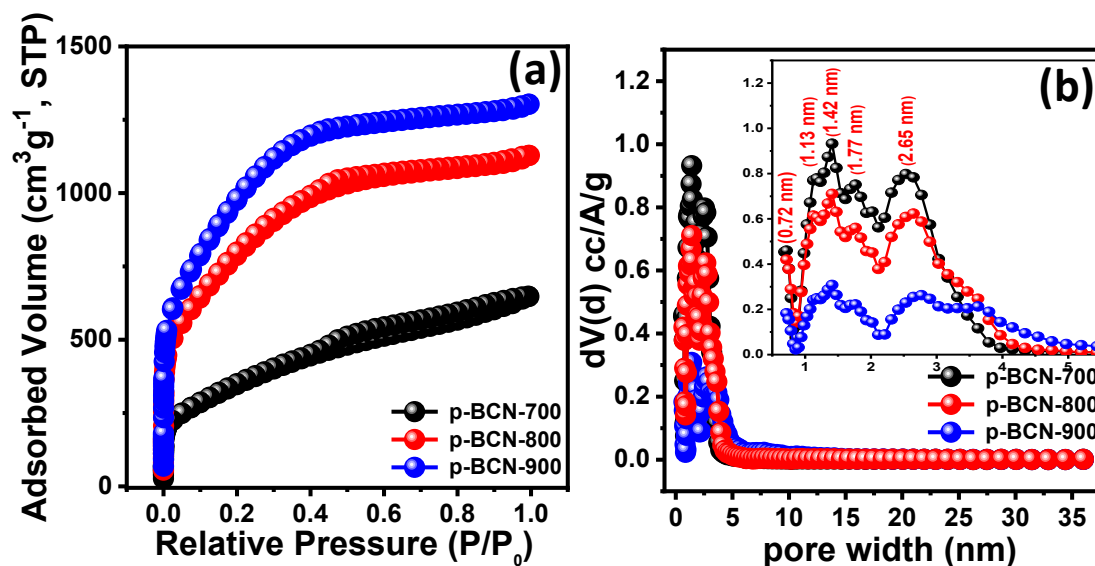
storage mechanism and the formation pore provides more defect sites and hence increases the diffusion of electrolyte ions on the surface of the electrode materials.

**Table 3.1.** Structural properties and pore analysis of p-BCN-X.

Sample	BET SSA ( $S_{\text{BET}}$ ) ( $\text{m}^2 \text{g}^{-1}$ )	Micropore surface area ( $S_{\text{micro}}$ ) ( $\text{m}^2 \text{g}^{-1}$ )	Total pore volume ( $V_t$ ) ( $\text{cc g}^{-1}$ )	Micropor e volume ( $V_{\text{micro}}$ ) ( $\text{cc g}^{-1}$ )	Average pore radius ( $R_a$ ) ( $\text{\AA}$ )
p-BCN-700	1213.7	279.318	1.001	0.114	18.542
p-BCN-800	2680.7	1128.889	1.75	0.475	17.522
p-BCN-900	3310.4	1867.426	2.016	0.794	14.835



**Figure 3.5.** (a-d) Low-resolution TEM images, (e, f) HRTEM images, (inset of (e) presents the SAED pattern), (g-k) STEM, and corresponding elemental mapping of p-BCN-800.



**Figure 3.6.** (a) Nitrogen sorption isotherm, (b) Pore size distribution of 2D porous BCN samples activated at different temperatures (p-BCN-X).

### 3.4.2. Electrochemical Analysis

#### Electrochemical Performance in a three-electrode system

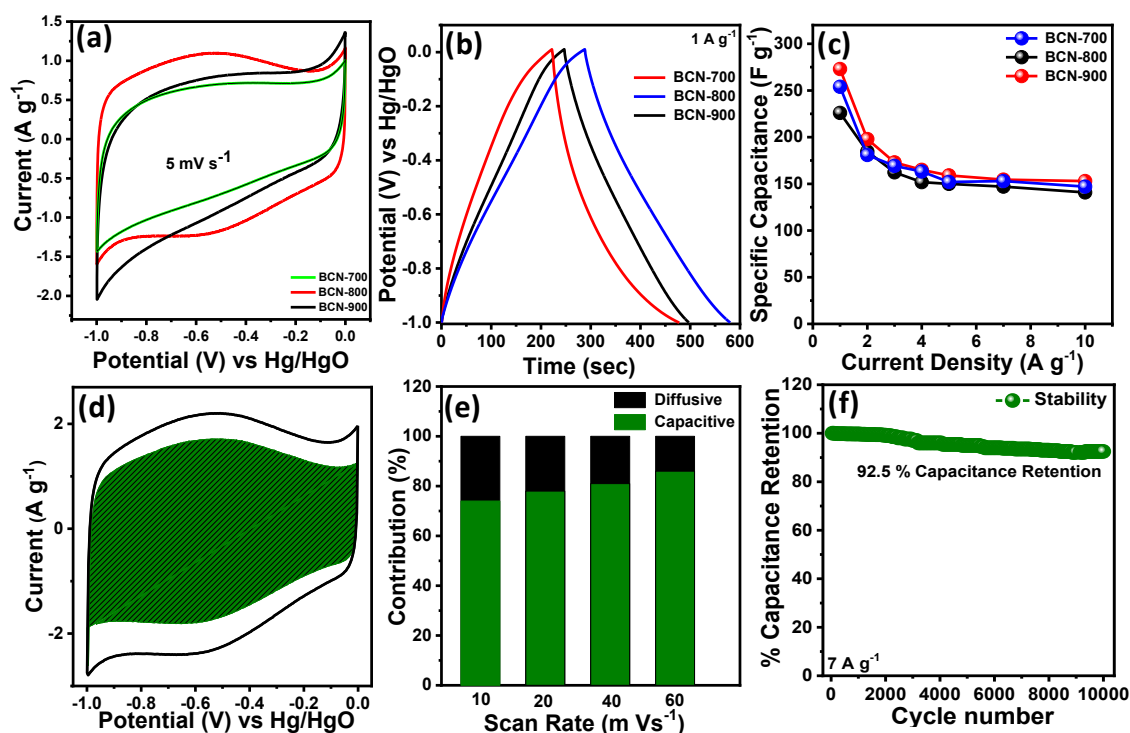
The effects of heteroatom doping on the electrochemical performance of the boron-doped materials are investigated by Cyclic voltammetry (CV), galvanostatic charge-discharge (GCD), and EIS measurement with a three-electrode system in 6 M KOH. We first studied the electrochemical performance of 2D BCN-X materials. Figure 3.7(a) depicts comparison CV plots of the 2D BCN-X samples at a sweep rate of  $5 \text{ mV s}^{-1}$  and a potential ranging from -1 to 0V. All the samples are quasi-rectangular in shape indicating an electrochemical double-layer (EDLC) structure owing to the presence of redox-active O and N containing functional groups<sup>35</sup> and electron deficiency of the boron atom, which attracts more anions ( $\text{OH}^-$ ) in the aqueous electrolyte. Among all the CV curves, the area under the CV curve is higher in BCN-800 showing the highest capacitance value. The specific capacitance for samples BCN-700, 800, and 900 are calculated from the area

under the CV curves and are obtained to be 127.4, 193.71, and 158.4 F g<sup>-1</sup> under 5 mV s<sup>-1</sup> (equation 3.2). Comparison GCD curves for all three samples at 1 A g<sup>-1</sup> current are presented in Figure 3.7(b). All the GCD plots show quasi-symmetrical triangles rather than completely symmetrical. This deviation of GCD plots from a symmetrical triangular shape is owing to the presence of hetero atoms and functional groups in the carbon. The N species, -OH and -COOH groups present in BCN-X samples lead to pseudocapacitance, and doping of B into the carbon framework act as an electron acceptor which modifies the electronic structure of the material, and the presence of boron functional groups enhances the pseudocapacitance nature of the material<sup>26</sup>. The C<sub>s</sub> of BCN-700, 800, and 900 are calculated by using equation 3.1 and are obtained to be 226, 273, and 254 F g<sup>-1</sup> respectively under 1 A g<sup>-1</sup> current. It can be noted that BCN-800 shows the highest capacitance value compared to the other two samples prepared at two different carbonization temperatures. The capacitance retention of the BCN-800 electrode is 56% as the current rises from 1 to 10 A g<sup>-1</sup>. The BCN-800 sample is an excellent charge storage electrode material for supercapacitor, as evidenced by the CV curve results. Table S3.2 shows a comparison of BCN-800 with other 2D boron carbonitride. Figure S3.2 represents the CV and GCD profile of the BCN-700 sample showing 62% capacitance retention of the initial value after 10 A g<sup>-1</sup> current. CV and GCD for BCN-800 and BCN-900 are depicted in Figure S3.3 and S3.4 respectively. Figure 3.7(c) represents the comparison of the specific capacitance of BCN-X samples with different current densities implying the BCN-800 sample shows superior electrochemical performance. The charge storage mechanism of the BCN-800 electrode was analyzed by using the CV curves measured at different sweep rates. Moreover, Dunn's method is used to differentiate diffusive and EDLC type contribution to quantify

their contributions (to calculate their contribution to total capacitance). The capacitive contribution can be quantitatively analyzed according to equation 3.6:

$$i(V) = k_2 v^{1/2} + k_1 v \quad (3.6)$$

$i(V)$  presents the current at potential  $V$ .  $v$  stands for sweep rate,  $k_1$  and  $k_2$  are the constants,  $k_2 v^{1/2}$  and  $k_1 v$  represent the diffusive and capacitive current respectively. The capacitive contribution of BCN-800 at  $5 \text{ mV s}^{-1}$  was calculated, presented in Figure 3.7(d). Capacitive contributions at different sweep rates ( $10\text{-}60 \text{ mV s}^{-1}$ ) are depicted in Figure 3.7(e) showing 85% capacitive contribution at a sweep rate of  $60 \text{ mV s}^{-1}$ . Cyclic performance test of BCN-800 for 10k discharging/charging cycles at  $7 \text{ A g}^{-1}$  current is presented in Figure 3.7(f) showing 92.5 % capacitance retention of its initial value.



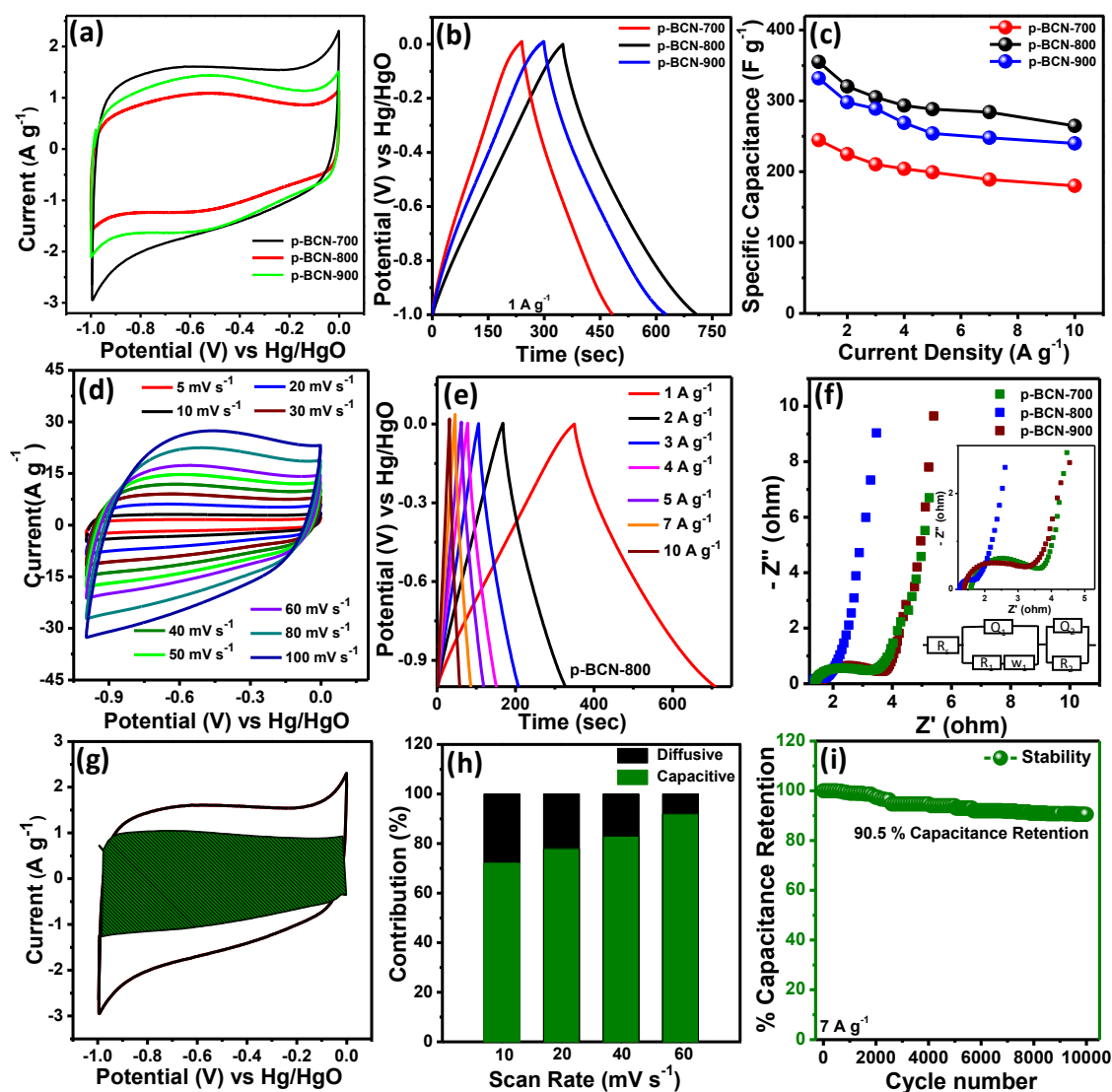
**Figure 3.7.** (a) CV profiles of BCN-X samples at  $5 \text{ mV s}^{-1}$  (b) GCD profiles at  $1 \text{ A g}^{-1}$  current for BCN-700 to 900 respectively. (c) Comparison of  $C_s$  plot w.r.t different current for all the composites. (d) CV profile of differentiating diffusive and capacitive contribution at  $5 \text{ mV s}^{-1}$  sweep rate. (e) Capacitive charge storage processes at different scan rates. (f) Cyclic durability test of BCN-800 at current of  $7 \text{ A g}^{-1}$  in 6M KOH electrolyte.

**Table 3.2.** Performance comparison of BCN-800 and p-BCN-800 samples with other reported materials.

Compound	Specific capacitance ( $\text{F g}^{-1}$ )	Electrolyte	References
Boron doped carbon fiber	309.0 ( $0.25 \text{ A g}^{-1}$ )	1M $\text{Li}_2\text{SO}_4$	36

CPSM-900	400 (0.6 A g <sup>-1</sup> )	1 M H <sub>2</sub> SO <sub>4</sub>	37
Nitrogen-doped mesoporous graphene nanoflakes	175 (0.05 A g <sup>-1</sup> )	Tetraalkylammonium bis(trifluoromethylsul fonyl) imide ionic liquids	38
Nitrogen-doped mesoporous carbon	295 (0.5 A g <sup>-1</sup> )	6M KOH	39
B,N-codoped chitosan derived porous carbon	306 (0.1 A g <sup>-1</sup> )	1M H <sub>2</sub> SO <sub>4</sub>	40
Boron and nitrogen codoped porous carbon	304 (0.1 A g <sup>-1</sup> )	1M H <sub>2</sub> SO <sub>4</sub>	25
B,N-codoped porous graphitic carbon	313 (1.0 A g <sup>-1</sup> )	6M KOH	41
BNPC	402 (0.5 A g <sup>-1</sup> )	6M KOH	30
AMT-B-Fe	437(0.5 A g <sup>-1</sup> )	6M KOH	42
B/N-CNS	423 (0.2 A g <sup>-1</sup> )	1M H <sub>2</sub> SO <sub>4</sub>	43
BCN-700	130.7 (0.2 A g <sup>-1</sup> )	1M H <sub>2</sub> SO <sub>4</sub>	44
CS/His-B	478 (0.5 A g <sup>-1</sup> )	6M KOH	26
Bean shell	119 (0.5 A g <sup>-1</sup> )	6M KOH	45
BNC-20	188 (0.5 A g <sup>-1</sup> )	6M KOH	46
B-AIAC	285.6 (1 A g <sup>-1</sup> )	3M KOH	47
BCN-800	273 (1 A g <sup>-1</sup> )	6M KOH	This work
p-BCN-800	355 (1 A g <sup>-1</sup> )	6M KOH	This work
	406 (1 A g <sup>-1</sup> )	1M H <sub>2</sub> SO <sub>4</sub>	This work





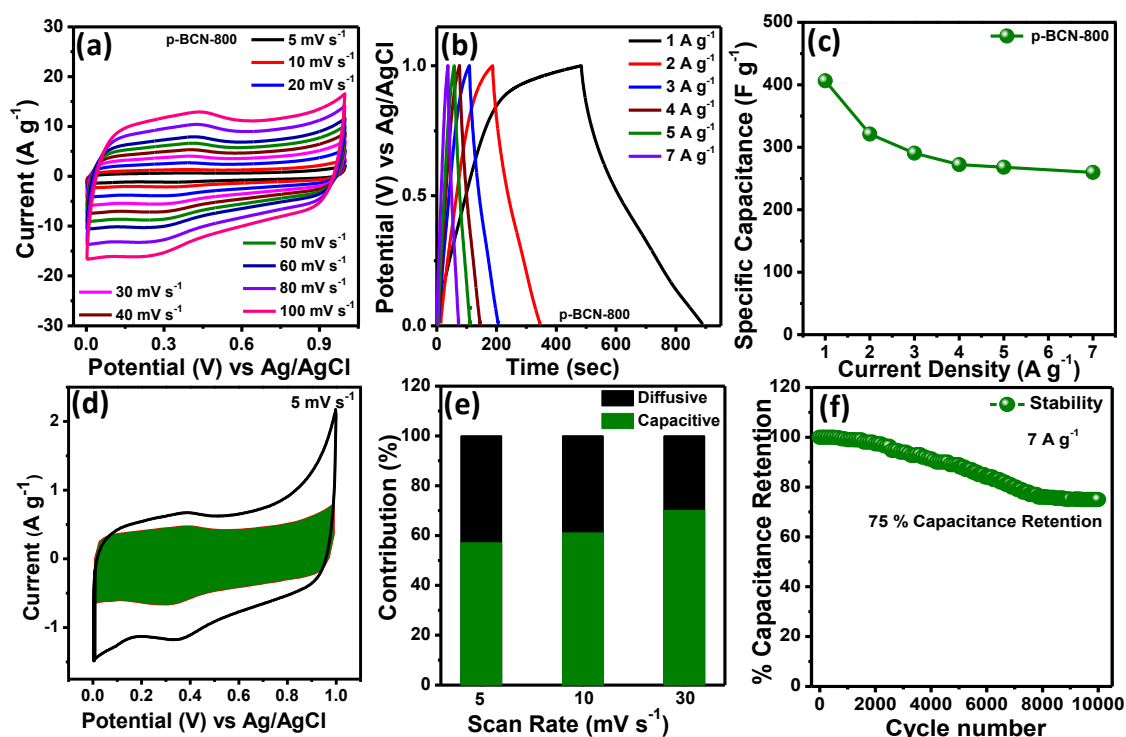
**Figure 3.8.** (a) CV profiles of p-BCN-X samples at  $5\text{ mV s}^{-1}$  (b) GCD plot profiles at  $1\text{ A g}^{-1}$  current for p-BCN-700 to 900 respectively. (c) Comparison plot of  $C_s$  against the current for p-BCN-700 to 900 samples. (d) CV plots of p-BCN-800 at different scan rates ( $5\text{--}100\text{ mV s}^{-1}$ ). (e) GCD plots of p-BCN-800 at diff. current ( $1\text{--}10\text{ A g}^{-1}$ ). (f) Nyquist plot of p-BCN-X samples. (g) Contribution of a capacitive controlled process for p-BCN-800 at a scan rate of  $10\text{ mV s}^{-1}$ . (h) Capacitive charge storage processes at different scan rates ( $10\text{ to }60\text{ mV s}^{-1}$ ). (i) Cyclic durability test of p-BCN-800 under  $7\text{ A g}^{-1}$  current in 6M KOH electrolyte.



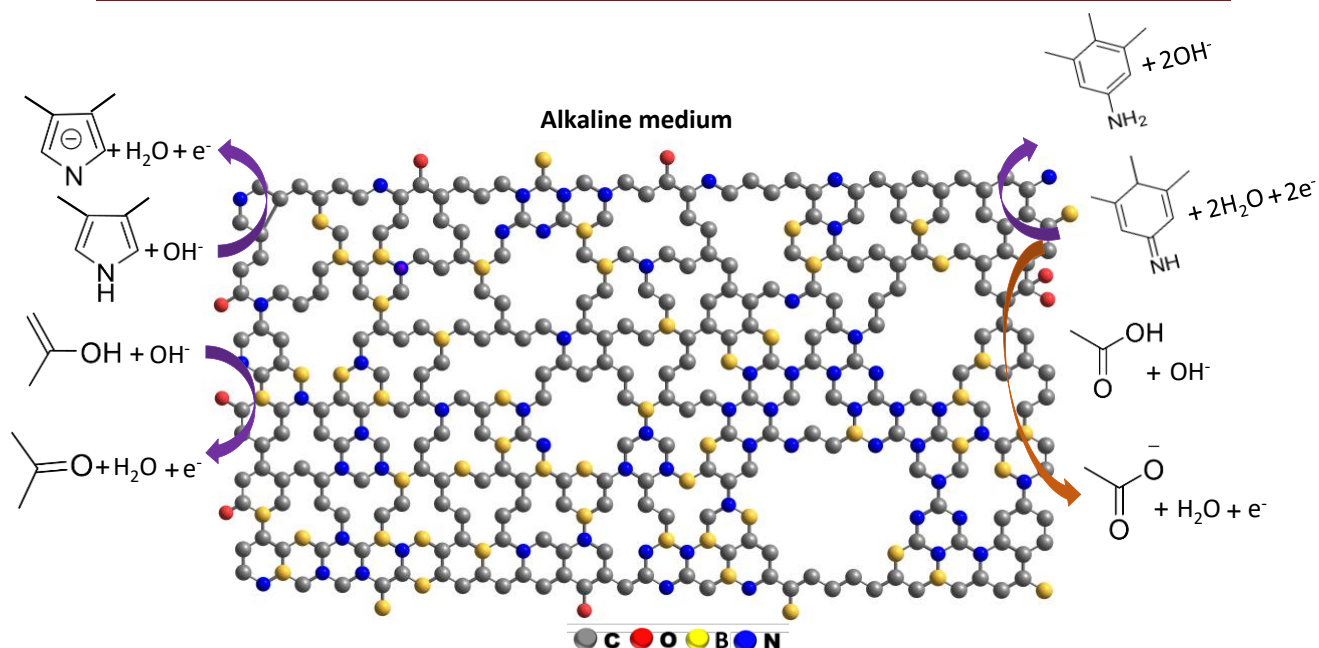
The BCN-X sample carbonized at 800 °C is activated by KOH at three different temperatures to make them porous and is denoted as p-BCN-X (X=700,800 and 900). Comparison CV curves for p-BCN-700, 800, and 900 are presented in Figure 3.8 (a) in the voltage window varying from 0 to -1V (SCE). The quasi-rectangular nature of the CV curves indicates higher capacitive behavior of the prepared samples, which is primarily due to the electric double layers structure arising from the existence of redox-active N and O containing functional group<sup>35</sup>. The area under the CV curves for p-BCN-800 is higher compared to other activation temperatures resulting highest capacitance value as the integral area of the CV profile is directly proportional to the  $C_s$  value. Figure 3.8 (b) presents the comparison GCD profiles for all the samples at 1 A g<sup>-1</sup> current. All the plots represent symmetrical triangular shapes indicating excellent reversibility of Faradic redox reaction during the charging/discharging process. p-BCN-800 shows the highest discharge time suggesting the highest capacitance among all the three composites. The  $C_s$  for p-BCN-700 and p-BCN-900 is calculated to be 247, and 332 F g<sup>-1</sup> under 1 A g<sup>-1</sup> current respectively which is presented in Table S3.3. For sample p-BCN-800, the  $C_s$  of the material are calculated to be 355 F g<sup>-1</sup> at 1 A g<sup>-1</sup> which is higher than those of the reported heteroatom-doped electrode. The excellent electrochemical performance of p-BCN-800 was due to the porous morphology (as the presence of meso and micropores content improves the rate capability and specific capacitance), very high SSA, presence of higher content of B compared to other synthesized carbon material (confirmed from SEM-EDS analysis) and doping with heteroatoms i.e. B and N which increases the surface wettability of the electrode material and increases the contact area between the electrode surface and electrolyte material. The comparison table for the specific capacitance of p-BCN-800 with other reported literature is presented in

Table 3.2. Figure 3.8(c) presents the plot of  $C_s$  w.r.t different currents for all three samples demonstrating the highest capacitance of p-BCN-800 compared to the other samples prepared by varying the temperature. The p-BCN-800 sample shows initial capacitance retention of 74.5 % at  $10 \text{ A g}^{-1}$  current. The CV plots for p-BCN-800 at sweep rates varying from  $5\text{-}100 \text{ mV s}^{-1}$  are presented in Fig.8 (d). The characteristics EDLCs nature of the CV curves were confirmed by the quasi-rectangular behavior. GCD curves for p-BCN-800 at different currents from  $1\text{-}10 \text{ A g}^{-1}$  were presented in Fig.8 (e). For samples p-BCN-700, and p-BCN-900, the CV and GCD plots are presented in Figure S3.5, and S3.6 respectively. The CV cures at sweep rates ranging from  $10\text{-}100 \text{ mV s}^{-1}$  and GCD plots at  $1\text{-}10 \text{ A g}^{-1}$  current densities are presented in Figure S3.5 for the p-BCN-700 electrode. The  $C_s$  value of p-BCN-700 was calculated to be  $247 \text{ F g}^{-1}$  under  $1 \text{ A g}^{-1}$  current and it shows 72.8 % capacitance retention from its initial capacitance value after  $10 \text{ A g}^{-1}$  current. For p-BCN-900 material, the CV plots at scan rates ranging from  $10\text{-}100 \text{ mV s}^{-1}$  and GCD profiles at  $1\text{-}10 \text{ A g}^{-1}$  current density are presented in Fig.S6. The specific capacitance for p-BCN-900 was calculated to be  $332 \text{ F g}^{-1}$  under  $1 \text{ A g}^{-1}$  and it shows capacitance retention of 72.3 % from its initial capacitance after  $10 \text{ A g}^{-1}$  current. Electron transport in the p-BCN-X samples was well analyzed by Nyquist plots (EIS). Figure 3.8(f) represents the comparison Nyquist plot of p-BCN-X electrodes between  $0.1 \text{ Hz}\text{-}100 \text{ kHz}$  frequency range under AC amplitude of  $5 \text{ mV s}^{-1}$ . A straight line in the low-frequency region (approximately parallel to the Y axis) gives information about the electrode/electrolyte interface interaction and ion diffusion process. The intercept of the X-axis and the curve in the high-frequency region represents the equivalent series resistance (ESR), and the diameter of the semicircle represents the charge transfer resistance ( $R_{ct}$ ). The ESR values for p-BCN-700, p-BCN-800, and p-BCN-900 are

1.29  $\Omega$ , 1.17  $\Omega$  and 1.54  $\Omega$  and  $R_{ct}$  values are 1.95  $\Omega$ , 0.63  $\Omega$  and 2.02  $\Omega$  respectively showing very low  $R_{ct}$  values, indicating fast ion diffusion transfer rate and good conductivity of the p-BCN-800 electrode compared to other electrodes (Figure 3.8(f)). It can be found that p-BCN-800 has excellent electrolyte transport ability, which can be attributed to the unique 2D porous network structure of p-BCN-800 material. The pseudocapacitance contribution of the p-BCN-800 sample is calculated by using equation 3.6. According to the calculation, the contribution rate of p-BCN-800 is 63% at 5  $\text{mV s}^{-1}$  (Figure 3.8 (g)). The capacitive contribution of p-BCN-800 at different sweep rates was calculated, presented in Figure 3.8 (h). The EDLC proportion of p-BCN-800 increases to 92% at 60  $\text{mV s}^{-1}$  sweep rate. The higher electrochemical performance of the p-BCN-800 electrode is due to the presence of boron accelerating the redox reaction of the nitrogen functional group and hence improving the pseudocapacitance and nitrogen functional group ensures steady pseudocapacitance, possibly ascribed to amine group redox reactions. The pseudocapacitance was further improved due to the presence of boron heteroatom, which accelerates the redox reaction of O and N functional groups<sup>48</sup>. In the carbon materials lattice, boron substitute the carbon resulting in a downward shift of the Fermi level which increases the charge storage and charge transfer within the doped porous carbon matrix<sup>48</sup>. Possible redox reactions and increased capacitance of p-BCN-800 in the alkaline medium are presented in Scheme 3.2. A cyclic durability test is necessary for the commercial SC. Figure 3.8 (i) present the cyclic performance test of p-BCN-800 for 10k cycles at 7  $\text{A g}^{-1}$  current with 90.5 % capacitance retention of its initial value.



**Figure 3.9.** (a, b) CV diagrams at 5-100 mV s<sup>-1</sup> & GCD plot profiles under 1-7 A g<sup>-1</sup> current. (c) Comparison plot of C<sub>s</sub> vs. current density. (d) Contribution of capacitive controlled process at a scan rate of 5 mV s<sup>-1</sup>. (e) Capacitive charge storage processes at different scan rates (5, 10, and 30 mV s<sup>-1</sup>). (f) Cyclic durability test at current of 7 A g<sup>-1</sup> for p-BCN-800 in 1M H<sub>2</sub>SO<sub>4</sub> electrolyte.



**Scheme 3.2.** Possible redox reactions and increased capacitance of p-BCN-800 in alkaline medium.

The electrochemical activity of p-BCN-800 was investigated in 1M H<sub>2</sub>SO<sub>4</sub> electrolyte in a three-electrode system. Figure 3.9 (a) depicts the CV profile of p-BCN-800 at different sweep rates in a potential between 0 and 1 V (vs. Ag/AgCl electrode). All the CV profiles for p-BCN-800 exhibit a quasi-rectangular shape with a pair of redox peaks (small ‘humps’ in the CV plots) indicating reversible faradic pseudocapacitance owing to B and N heteroatom electrochemical polarization (associated with electrochemically active functionalities)<sup>43-44</sup>. Pseudocapacitance nature may be due to the presence of B and N atoms. Furthermore, the nature of the CV plots remains unchanged as we increase the sweep rate from 5-100 mV s<sup>-1</sup> indicating the faradic response and fast electrochemical double layer formation over the B and N co-doped porous carbon framework<sup>43</sup>. Figure 3.9 (b) represents the GCD plots at various currents ranging from 1 to 7 A g<sup>-1</sup> in the same potential range as mentioned above. The specific capacitance was calculated to be 406, 321, 290.4, 272.12, 268, and 259.7 F g<sup>-1</sup> at 1, 2, 3, 4, 5, and 7 A g<sup>-1</sup> current respectively.

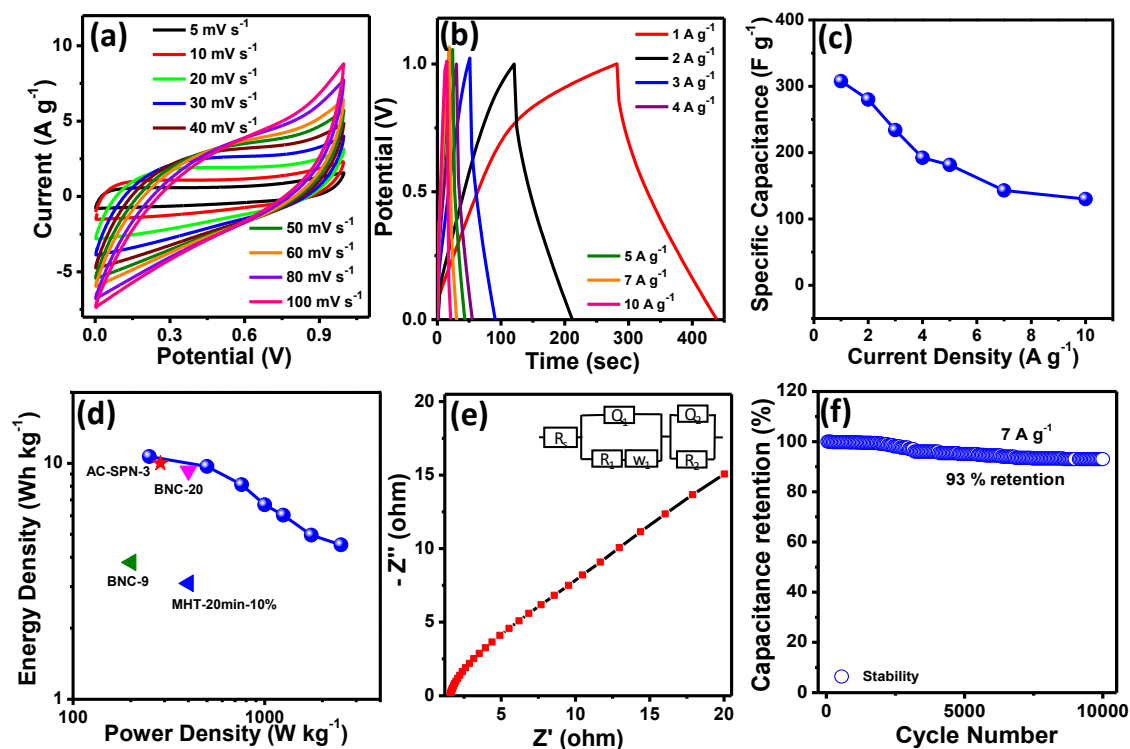
The  $C_s$  against the current densities are presented in Figure 3.9 (c). The capacitive contribution can be quantitatively analyzed according to equations 3.6 and Figure 3.9 (d) shows the contribution curve at  $5 \text{ mV s}^{-1}$ . Capacitive contributions at different sweep rates ranging from  $5\text{--}30 \text{ mV s}^{-1}$  are presented in Figure 3.9 (e) showing 57 % capacitive contribution at a sweep rate of  $5 \text{ mV s}^{-1}$ . This suggests the high rate capability of the material. 10000 charging-discharging cycles are carried out to test the cyclic stability performance in  $1 \text{ M H}_2\text{SO}_4$  electrolyte (Figure 3.9 (f)) showing 75% capacitance retention of the electrode material. Thus, an appreciable amount of N and B incorporated into the carbon matrix can boost electrochemical performance.

The high specific capacitance value of the p-BCN-800 electrode can be due to the following reasons:

- (1) Unique 2D porous nanosheets with a high SSA of  $3310.4 \text{ m}^2/\text{g}$  increase the contact between active sites and electrolyte ions. This shortens the distance of the electrolyte ion to access the interior of the electrode material. In addition to that, the presence of sub-nanometer microspores ( $<1 \text{ nm}$ ) significantly improved the capacitance activity due to the pore confinement effect.
- (2) Doping of B and N to the carbon matrix is also another reason for the enhancement of the activity because of the synergistic interaction of unsaturated carbon atoms with B and N atoms. This enhances the conductivity and lowers the charge transfer resistance. Also, the redox behavior of the O and N-containing functional groups helps to improve the supercapacitor behaviors.
- (3) The substitutions of carbon with boron in the carbon materials lattice cause a downward shift to the Fermi level, thereby enhancing charge storage and transfer within the structure of doped carbon materials.

### **Electrochemical Behavior of symmetrical supercapacitor**

To more precisely assess the capacitive performance of the p-BCN-800 electrode, a symmetric device was assembled by using p-BCN-800 in a two-electrode system. Figure 3.10 (a) shows the CV cycles of the symmetric device at sweep rates varying from 5-100  $\text{mV s}^{-1}$ . The quasi-rectangular type nature of the CV plots without any distortion at a higher scan rate implies the EDLC-type behavior of the electrode. GCD curves of the symmetric device at different current densities are depicted in Figure 3.10 (b). Figure 3.10 (c) represents the variation of  $C_s$  (calculated by using equation 3.3) w.r.t current density of 1-10  $\text{A g}^{-1}$ . The  $C_s$  value of 307.7  $\text{F g}^{-1}$  was obtained under 1  $\text{A g}^{-1}$  current and it maintains a  $C_s$  value retention of 41 % from its initial value after 10  $\text{A g}^{-1}$  current for the symmetric device. Figure 3.10 (d) represents the Ragone plot for a symmetric capacitor (calculated by using equations 3.4 and 3.5) and its comparison with previous reports<sup>9, 45, 49-51</sup>. The device shows maximum ED of 10.69  $\text{W h kg}^{-1}$  and PD of 2500  $\text{W kg}^{-1}$ . The EIS spectra of the symmetric device show a vertical line at low-frequency region indicating the excellent electrochemical performance of the symmetric device. The  $R_s$  and  $R_{ct}$  values were obtained to be 1.53  $\Omega$  and 9.85  $\Omega$  (Figure 3.10 (e)). The low  $R_{ct}$  values indicate the low resistance and high conductivity of the material. The cyclic stability of 10k cycles was performed at 7  $\text{A g}^{-1}$  current as presented in Figure 3.10 (f) indicating the device maintains a capacitance of 93 % of its initial measured value.

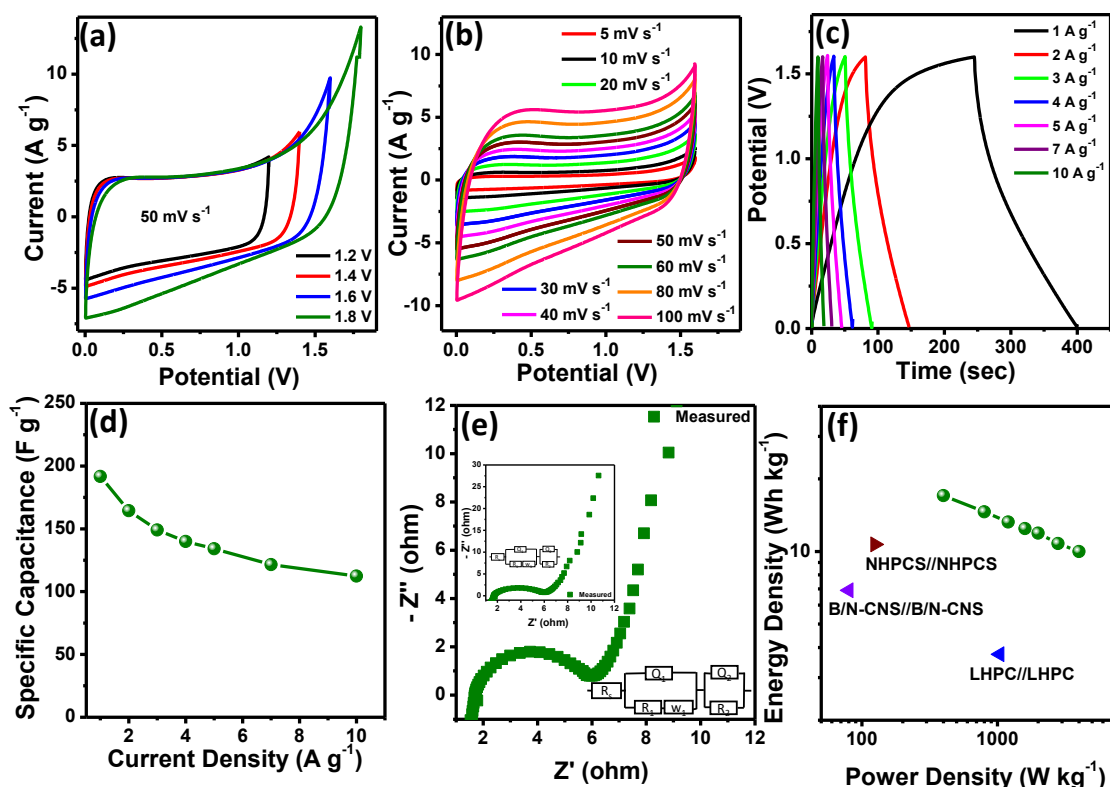


**Figure 3.10.** (a, b) CV and GCD profiles at different sweep rates (5-100 mV s<sup>-1</sup>) and different current densities (1 to 10 A g<sup>-1</sup>). (c) C<sub>s</sub> plot w.r.t different current (1 to 10 A g<sup>-1</sup>). (d) The plot of energy density vs. power density and comparison to earlier reports. (e) Nyquist plot with equivalent circuit fitting. (f) Cyclic durability test for 10k cycles at 7 A g<sup>-1</sup> for the symmetric device in 6M KOH.

To check the actual device characteristics in 1 M H<sub>2</sub>SO<sub>4</sub>, CV, GCD, and EIS measurements were investigated in a two-electrode system using p-BCN-800 as both cathode and anode. Figure 3.11 (a) depicts the CV plots for symmetric SC runs under 50 mV s<sup>-1</sup> at a different voltage range of 0–1.8 V. It is obvious that the nature of the CV plots remains unaffected up to potential 0-1.6 V and when we applied the potential 1.8 V, the nature of the CV plot changes suggesting reversible capacity can be obtained at applied voltage of 0-1.6 V. CV and GCD plot profiles are shown in Figure 3.11(b) and (c) in the voltage ranging from 0–1.6 V. The rectangular nature of the CV plots reflects



ideal double-layer charge storage. The  $C_s$  obtained is  $191 \text{ F g}^{-1}$  at  $1 \text{ A g}^{-1}$ , which decreases to  $112.4 \text{ F g}^{-1}$  at  $10 \text{ A g}^{-1}$  retaining 58.8 % of its initial capacitance. The difference of the device capacitance from the three-electrode system may be attributed to the asymmetry in the adsorption of negative/ positive ions. Another reason may be due to the capacitance of the p-BCN-800// p-BCN-800 device based on the full cell including two electrodes are theoretically 1/4 of the value of a single electrode<sup>52</sup>. Furthermore, in the two-electrode cell, Ti foil and microfiber filter paper were used as current collectors and separators, respectively, which may increase the impedance and reduce the ion diffusions as well. Moreover, the lower capacitance value may be related to the high mass loading of the electrodes used<sup>53</sup>. Figure 3.11(d) represents the variation of  $C_s$  w.r.t current. Nyquist plots of the device with equivalent circuit fitting are presented in Figure 3.11(e) showing  $R_{ct}$  and  $R_s$  values  $1.7 \text{ } \Omega$  and  $0.51 \text{ } \Omega$  respectively. The low  $R_{ct}$  values indicate low resistance and high conductivity of the material. Ragone plot for p-BCN-800//p-BCN-800 symmetric device shows PD of  $4000 \text{ W kg}^{-1}$  and ED of  $17 \text{ W h kg}^{-1}$ , presented in Figure 3.11(f)<sup>54-55</sup>.



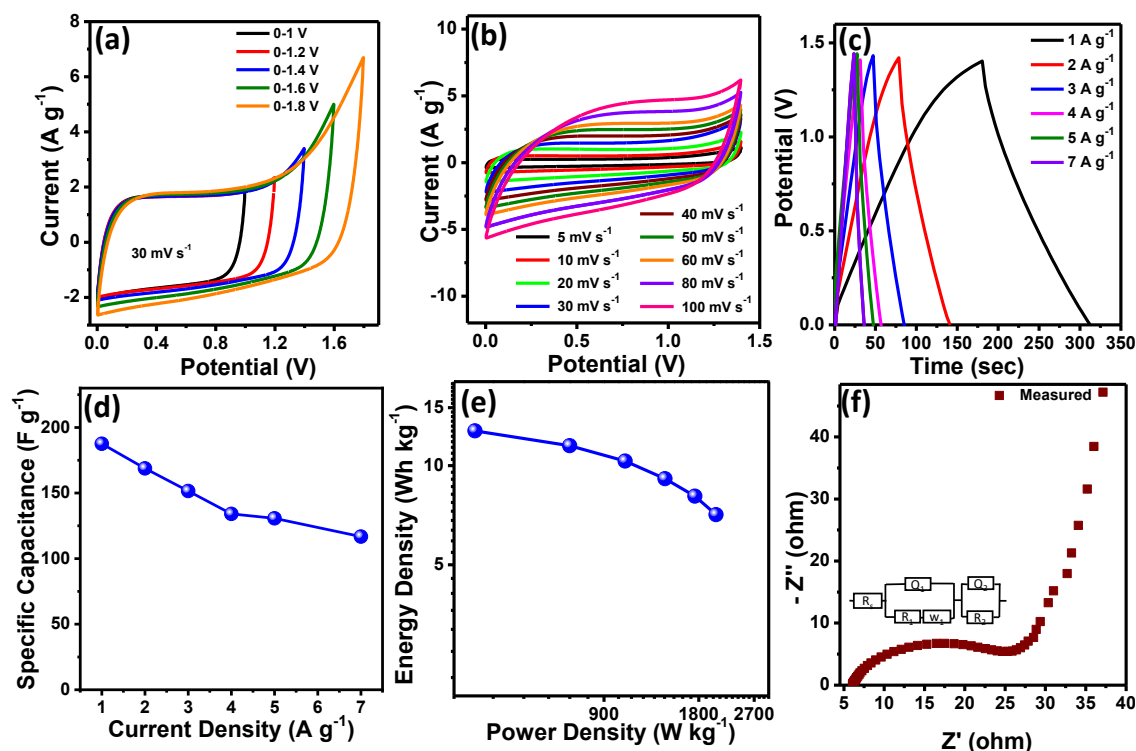
**Figure 3.11.** (a, b) CV profiles under various potentials ranging from 1.2 to 1.8V, and sweep rates of 5 to 100  $\text{mV s}^{-1}$ . (c) GCD plots under different currents (1 to 10  $\text{A g}^{-1}$ ). (d) The plot of  $C_s$  w.r.t different current. (e) Nyquist plot. (f) The plot of energy density against power density for the device in 1M  $\text{H}_2\text{SO}_4$ .

The feasibility of the p-BCN-800 electrode was tested in the neutral medium as it provides a large voltage window for practical application. Therefore, we evaluated the performance of the symmetric device in 1M  $\text{Na}_2\text{SO}_4$ . Figure 3.12(a) represents the CV plots at the potential window of 0-1.8V at a 30  $\text{mV s}^{-1}$  scan rate. A sharp rise in CV current due to the decomposition of electrolyte is shown as potential approaches to 1.8 V. Therefore, we fix the voltage window at 1.4 V, and a voltage range of 0 to 1.4 V was used for all measurements. Figure 3.12(b) depicts the CV profiles from 5-100  $\text{mV s}^{-1}$

scan rates. Rectangular shapes of the CV curves at higher scan rates demonstrate outstanding rate performance of the symmetric device. The linearly symmetric charge/discharge profiles at a potential of 0-1.4 V indicate high capacitive reversibility (Figure 3.12(c)). The  $C_s$  value against the different currents is presented in Figure 3.12(d) which is obtained from the GCD plots. The  $C_s$  were obtained to be  $187.3 \text{ F g}^{-1}$  under  $1 \text{ A g}^{-1}$  current using equation 3.3 with an outstanding rate of 62.4 % at  $7 \text{ A g}^{-1}$ . Figure 3.12(e) represents the ED and PD, obtained from the  $C_s$  values. The assembled symmetric capacitor provides an excellent energy density of nearly  $12.75 \text{ W h kg}^{-1}$  and a power density of  $2450 \text{ W kg}^{-1}$ . The EIS spectra of the symmetric device show a vertical line at the low-frequency region indicating the outstanding capacitance of the p-BCN-800// p-BCN-800 device. The  $R_{CT}$  and  $R_s$  values were obtained to be  $5.92 \text{ } \Omega$  and  $18.948 \text{ } \Omega$  (Figure 3.12(f)).

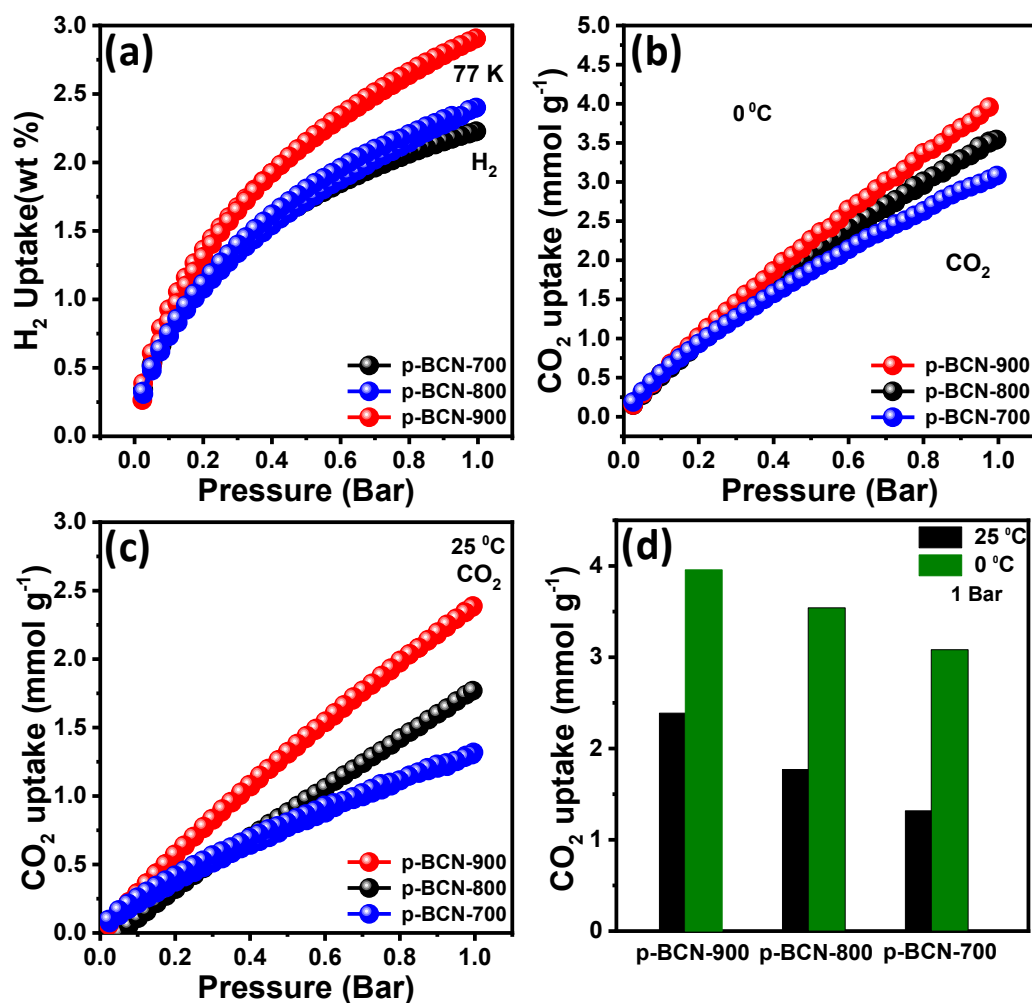
### 3.4.3. Gas Adsorption Behavior

Hydrogen adsorption isotherm performance was studied using isothermal adsorption/desorption at 77K with pressure from 0-1 bar for all the samples synthesized at different activated temperatures are presented in Figure 3.13(a). All the samples have a broad knee indicating the continuous rise in  $\text{H}_2$  storage capacities up to 1 bar pressure. With the rise in activation temperature, the  $\text{H}_2$  adsorption capacities increases due to the increase in large pore volume and SSA. For sample p-BCN-900, the highest  $\text{H}_2$  storage capacity was observed to be 2.91 wt%. The hydrogen uptake capacity of p-BCN-X samples increases from 2.27 % for p-BCN-700 to 2.91 % for p-BCN-900. The bar plot for the  $\text{H}_2$  uptake of all the samples is depicted in Figure S3.7 (a).



**Figure 3.12.** (a) CV plots at diff. voltage range of 1 to 1.8V in 1M Na<sub>2</sub>SO<sub>4</sub>. (b) CV plots at different scan rates (5 to 100 mV s<sup>-1</sup>). (c) CD plots at different current (1 to 7 A g<sup>-1</sup>). (d) The C<sub>s</sub> plot under different current (1 to 7 A g<sup>-1</sup>). (e) ED vs. PD plot. (f) EIS spectra of p-BCN-800// p-BCN-800 device in 1M Na<sub>2</sub>SO<sub>4</sub>.

Figure S3.7 (b) presents the change in H<sub>2</sub> uptake as a function of SSA. A comparison of the H<sub>2</sub> uptake of various porous carbon materials with this work is presented in Table 3.3. In addition to H<sub>2</sub> adsorption, two different temperatures (25 °C and 0 °C) were used to analyze the CO<sub>2</sub> desorption/adsorption isotherm of the prepared materials in the pressure range of up to 1 bar. The CO<sub>2</sub> adsorption capacities of p-BCN-900 samples are found to be 3.96 mmol g<sup>-1</sup> at 273 K and 2.39 mmol g<sup>-1</sup> at 298 K, presented in Figure 3.13(b). The high CO<sub>2</sub> adsorption capacities of p-BCN-X materials are related to their high SSA. Figure 3.13(b, c) represents the CO<sub>2</sub> adsorption isotherm of p-BCN-X materials at 25 °C and 0 °C.



**Figure 3.13.** (a) H<sub>2</sub> adsorption-desorption isotherms of p-BCN-700 to 900 respectively at 77K, (b, c) Adsorption isotherms (CO<sub>2</sub>) of BCN at 0 °C and 25 °C, (d) Comparison bar plot of CO<sub>2</sub> Adsorption isotherms.

**Table 3.3.** The H<sub>2</sub> adsorption capacity of p-BCN-X compared with previous reports.

Adsorbent	H <sub>2</sub> uptake (wt %)	Pressure	References
microporous	2.84	1 bar	56
oxygen-doped			
carbons			

Nitrogen-doped porous carbon	2.71	1 bar	57
Nanoporous Boron Carbon Nitrides	1.07	1 bar	27
Hexagonal boron nitride	2.3	1 bar	58
NC-3800	2.81	1 bar	59
p-BCN-900	2.91	1 bar	This work

Figure S3.8 presents the comparison plot for CO<sub>2</sub> uptake capacities of p-BCN-700 to 900 at 0 °C and 25 °C under 1 bar pressure and Figure 3.13(d) represents the corresponding bar plot for the same. A comparison table for CO<sub>2</sub> uptake of various porous carbon materials with this work is presented in Table S3.4.

### 3.5. CONCLUSIONS

In this chapter, we reported a facile, effective way to synthesize 2D boron carbonitride (BNP-X) and 2D porous boron carbonitride (p-BCN-X) derived from formamide as the nitrogen source and boric acid as both boron source and template. The B/N doped nanometer thick 2D nanosheets are formed by hydrothermal followed by carbonization at 800 °C. 2D porous nanosheets are produced from 2D BCN by KOH activation at high temperatures. The unique porous structures have a majority of micro-pores (< 2nm) with a significant number of sub-nanometer pores (<1nm). These porous 2D sheets possess a high SSA of 3300 m<sup>2</sup>/g and a high pore volume of 1.75 cc g<sup>-1</sup>. Owing to the unique pore structure and optimal B/N doping, the 2D porous nanosheets show exceptional supercapacitor performance with a C<sub>s</sub> value of 355 F g<sup>-1</sup> at 1 A g<sup>-1</sup> in 6M KOH with an

outstanding rate capability of 90.5 % after 10k cycles and 406 F g<sup>-1</sup> (1 A g<sup>-1</sup>) in 1M H<sub>2</sub>SO<sub>4</sub> electrolyte. The H<sub>2</sub> uptake of these 2D porous BCN was found to be 2.91 wt % at 77 K under 1 bar pressure and CO<sub>2</sub> uptake of 3.96 mmol g<sup>-1</sup> and 2.39 mmol g<sup>-1</sup> at 273 and 298 K respectively. The higher performance of this is due to high SSA and unique nanometer thick porous morphology, optimal B/N doping. This work aims to provide a facile synthesis strategy of 2D porous materials for energy storage and gas adsorption applications.

### 3.6. REFERENCES

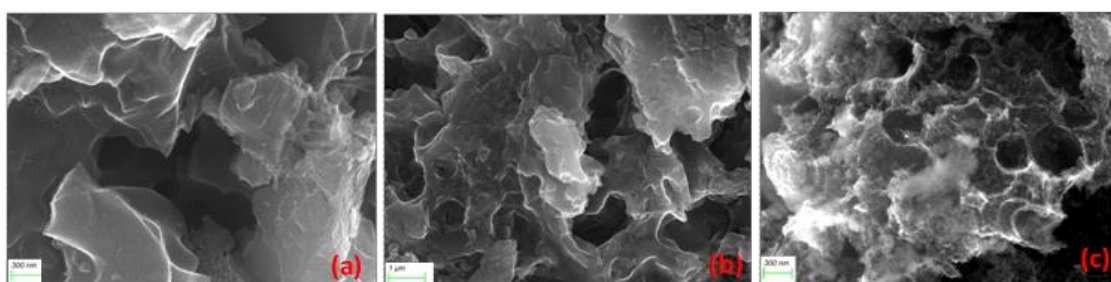
- (1) Li, S.; Zhang, L.; Zhang, L.; Guo, Y.; Chen, X.; Holze, R.; Tang, T. *New Journal of Chemistry* **2021**, *45*, 16011-16018.
- (2) Lee, Y.-H.; Lee, Y.-F.; Chang, K.-H.; Hu, C.-C. *Electrochemistry Communications* **2011**, *13*, 50-53.
- (3) Li, S.; Zhang, L.; Guo, Y.; Zhang, Q.; Aleksandrak, M.; Mijowska, E.; Chen, X. *New Journal of Chemistry* **2022**, *46*, 6319-6329.
- (4) Lei, W.; Guo, J.; Wu, Z.; Xuan, C.; Xiao, W.; Wang, D. *Science Bulletin* **2017**, *62*, 1011-1017.
- (5) Xu, Y.; Sprick, R. S.; Brownbill, N. J.; Blanc, F.; Li, Q.; Ward, J. W.; Ren, S.; Cooper, A. I. *Journal of Materials Chemistry A* **2021**, *9*, 3303-3308.
- (6) Jiang, H.; Lee, P. S.; Li, C. *Energy & Environmental Science* **2013**, *6*, 41-53.
- (7) Zhang, D.; Hao, Y.; Zheng, L.; Ma, Y.; Feng, H.; Luo, H. *Journal of Materials Chemistry A* **2013**, *1*, 7584-7591.
- (8) Zheng, X.; Luo, J.; Lv, W.; Wang, D.-W.; Yang, Q.-H. *Advanced Materials* **2015**, *27*, 5388-5395.
- (9) Li, S.; Zhang, L.; Zhang, L.; Zhang, J.; Zhou, H.; Chen, X.; Tang, T. *New Journal of Chemistry* **2021**, *45*, 1092-1099.
- (10) Yao, L.; Lin, J.; Yang, H.; Wu, Q.; Wang, D.; Li, X.; Deng, L.; Zheng, Z. *Nanoscale* **2019**, *11*, 11086-11092.
- (11) Chmiola, J.; Yushin, G.; Dash, R.; Gogotsi, Y. *Journal of Power Sources* **2006**, *158*, 765-772.
- (12) Xiang, S.; Yang, X.; Lin, X.; Chang, C.; Que, H.; Li, M. *Journal of Solid State Electrochemistry* **2017**, *21*, 1457-1465.
- (13) Zhou, J.; Li, N.; Gao, F.; Zhao, Y.; Hou, L.; Xu, Z. *Scientific Reports* **2014**, *4*, 6083.
- (14) Hou, J.; Cao, C.; Idrees, F.; Ma, X. *ACS Nano* **2015**, *9*, 2556-2564.
- (15) *Acs Applied Materials and Interfaces* **2014**, *6*, 2657-2665.
- (16) Chen, J.; Lin, C.; Zhang, M.; Jin, T.; Qian, Y. *ChemElectroChem* **2020**, *7*, 3311-3318.
- (17) Shang, T. X.; Cai, X. X.; Jin, X. J. *RSC Advances* **2015**, *5*, 16433-16438.
- (18) Gao, Y.; Cui, P.; Liu, J.; Sun, W.; Chen, S.; Chou, S.; Lv, L.-P.; Wang, Y. *ACS Applied Energy Materials* **2021**, *4*, 4519-4529.
- (19) Wen, Z.; Wang, X.; Mao, S.; Bo, Z.; Kim, H.; Cui, S.; Lu, G.; Feng, X.; Chen, J. *Advanced Materials* **2012**, *24*, 5610-5616.
- (20) Nazir, G.; Rehman, A.; Park, S.-J. *Journal of CO2 Utilization* **2020**, *42*, 101326.

- (21) Zhao, L.; Fan, L.-Z.; Zhou, M.-Q.; Guan, H.; Qiao, S.; Antonietti, M.; Titirici, M.-M. *Advanced Materials* **2010**, *22*, 5202-5206.
- (22) Wang, D.-W.; Li, F.; Chen, Z.-G.; Lu, G. Q.; Cheng, H.-M. *Chemistry of Materials* **2008**, *20*, 7195-7200.
- (23) Zhang, J.; Nie, N.; Liu, Y.; Wang, J.; Yu, F.; Gu, J.; Li, W. *ACS Applied Materials & Interfaces* **2015**, *7*, 20134-20143.
- (24) Abbas, Q.; Raza, R.; Shabbir, I.; Olabi, A. G. *Journal of Science: Advanced Materials and Devices* **2019**, *4*, 341-352.
- (25) Chen, H.; Xiong, Y.; Yu, T.; Zhu, P.; Yan, X.; Wang, Z.; Guan, S. *Carbon* **2017**, *113*, 266-273.
- (26) Yang, L.; Wu, D.; Wang, T.; Jia, D. *ACS Applied Materials & Interfaces* **2020**, *12*, 18692-18704.
- (27) Portehault, D.; Giordano, C.; Gervais, C.; Senkovska, I.; Kaskel, S.; Sanchez, C.; Antonietti, M. *Advanced Functional Materials* **2010**, *20*, 1827-1833.
- (28) Wang, C.; Zhang, X.; Wang, J.; Ma, Y.; Lv, S.; Xiang, J.; Chu, M.; Sun, T.; Qin, C. *Journal of The Electrochemical Society* **2018**, *165*, A856.
- (29) Jin, J.; Pan, F.; Jiang, L.; Fu, X.; Liang, A.; Wei, Z.; Zhang, J.; Sun, G. *ACS Nano* **2014**, *8*, 3313-3321.
- (30) Guo, D.; Ding, B.; Hu, X.; Wang, Y.; Han, F.; Wu, X. *ACS Sustainable Chemistry & Engineering* **2018**, *6*, 11441-11449.
- (31) Saha, S.; Jana, M.; Khanra, P.; Samanta, P.; Koo, H.; Murmu, N. C.; Kuila, T. *ACS Applied Materials & Interfaces* **2015**, *7*, 14211-14222.
- (32) Zhang, K.; Liu, M.; Zhang, T.; Min, X.; Wang, Z.; Chai, L.; Shi, Y. *Journal of Materials Chemistry A* **2019**, *7*, 26838-26848.
- (33) Wang, J.; Kaskel, S. *Journal of Materials Chemistry* **2012**, *22*, 23710-23725.
- (34) Raymundo-Piñero, E.; Kierzek, K.; Machnikowski, J.; Béguin, F. *Carbon* **2006**, *44*, 2498-2507.
- (35) Mai, L.-Q.; Minhas-Khan, A.; Tian, X.; Hercule, K. M.; Zhao, Y.-L.; Lin, X.; Xu, X. *Nature Communications* **2013**, *4*, 2923.
- (36) Wu, M.; Zhao, X.; Gao, J.; Guo, J.; Xiao, J.; Chen, R. *Surfaces and Interfaces* **2022**, *31*, 101983.
- (37) Pal, A.; Ghosh, S.; Singha, D.; Nandi, M. *ACS Applied Energy Materials* **2021**, *4*, 10810-10825.
- (38) Kim, T.; Jung, G.; Yoo, S.; Suh, K. S.; Ruoff, R. S. *ACS Nano* **2013**, *7*, 6899-6905.
- (39) Ubaidullah, M.; Al-Enizi, A. M.; Ahamad, T.; Shaikh, S. F.; Al-Abdrabalnabi, M. A.; Samdani, M. S.; Kumar, D.; Alam, M. A.; Khan, M. *Journal of Energy Storage* **2021**, *33*, 102125.
- (40) Ling, Z.; Wang, G.; Zhang, M.; Fan, X.; Yu, C.; Yang, J.; Xiao, N.; Qiu, J. *Nanoscale* **2015**, *7*, 5120-5125.
- (41) Sun, L.; Fu, Y.; Tian, C.; Yang, Y.; Wang, L.; Yin, J.; Ma, J.; Wang, R.; Fu, H. *ChemSusChem* **2014**, *7*, 1637-1646.
- (42) Ren, X.; Yuan, Z.; Ma, Y.; Zhang, C.; Qin, C.; Jiang, X. *Energy & Fuels* **2022**, *36*, 2841-2850.
- (43) Hao, J.; Wang, J.; Qin, S.; Liu, D.; Li, Y.; Lei, W. *Journal of Materials Chemistry A* **2018**, *6*, 8053-8058.
- (44) Dou, S.; Huang, X.; Ma, Z.; Wu, J.; Wang, S. *Nanotechnology* **2015**, *26*, 045402.
- (45) Zhou, Y.; Yan, W.; Yu, X.; Chen, T.; Wang, S.; Zhao, W. *Journal of Energy Storage* **2020**, *32*, 101706.
- (46) Luo, L.; Zhou, Y.; Yan, W.; Wu, X.; Wang, S.; Zhao, W. *Electrochimica Acta* **2020**, *360*, 137010.
- (47) Poornima, B. H.; Vijayakumar, T. *Inorganic Chemistry Communications* **2022**, *145*, 109953.
- (48) Wang, Y.; Wang, D.; Li, Z.; Su, Q.; Wei, S.; Pang, S.; Zhao, X.; Liang, L.; Kang, L.; Cao, S. Preparation of Boron/Sulfur-Codoped Porous Carbon Derived from Biological Wastes and Its Application in a Supercapacitor *Nanomaterials* [Online], 2022.
- (49) Wang, C.; Wu, D.; Wang, H.; Gao, Z.; Xu, F.; Jiang, K. *Journal of Power Sources* **2017**, *363*, 375-383.
- (50) Guo, H.; Gao, Q. *Journal of Power Sources* **2009**, *186*, 551-556.



- (51) Xu, J.; Gao, Q.; Zhang, Y.; Tan, Y.; Tian, W.; Zhu, L.; Jiang, L. *Scientific Reports* **2014**, *4*, 5545.
- (52) Hao, Q.; Xia, X.; Lei, W.; Wang, W.; Qiu, J. *Carbon* **2015**, *81*, 552-563.
- (53) Ling, Z.; Wang, Z.; Zhang, M.; Yu, C.; Wang, G.; Dong, Y.; Liu, S.; Wang, Y.; Qiu, J. *Advanced Functional Materials* **2016**, *26*, 111-119.
- (54) Wang, C.; Wu, D.; Wang, H.; Gao, Z.; Xu, F.; Jiang, K. *Journal of Colloid and Interface Science* **2018**, *523*, 133-143.
- (55) Zhang, W.; Lin, H.; Lin, Z.; Yin, J.; Lu, H.; Liu, D.; Zhao, M. *ChemSusChem* **2015**, *8*, 2114-2122.
- (56) Hu, W.; Zhang, W.; Zheng, M.; Xiao, Y.; Dong, H.; Liang, Y.; Hu, H.; Liu, Y. *International Journal of Hydrogen Energy* **2021**, *46*, 896-905.
- (57) Wang, Z.; Sun, L.; Xu, F.; Zhou, H.; Peng, X.; Sun, D.; Wang, J.; Du, Y. *International Journal of Hydrogen Energy* **2016**, *41*, 8489-8497.
- (58) Naresh Muthu, R.; Rajashabala, S.; Kannan, R. *Renewable Energy* **2016**, *85*, 387-394.
- (59) Hu, W.; Huang, J.; Yu, P.; Zheng, M.; Xiao, Y.; Dong, H.; Liang, Y.; Hu, H.; Liu, Y. *ACS Sustainable Chemistry & Engineering* **2019**, *7*, 15385-15393.
- (60) Jin, Z.-e.; Wang, J.-l.; Zhao, R.-j.; Guan, T.-t.; Zhang, D.-d.; Li, K.-x. *New Carbon Materials* **2018**, *33*, 392-401.
- (61) Plaza, M. G.; González, A. S.; Pis, J. J.; Rubiera, F.; Pevida, C. *Applied Energy* **2014**, *114*, 551-562.
- (62) Jin, C.; Sun, J.; Chen, Y.; Guo, Y.; Han, D.; Wang, R.; Zhao, C. *Separation and Purification Technology* **2021**, *276*, 119270.
- (63) Saha, D.; Deng, S. *Journal of Colloid and Interface Science* **2010**, *345*, 402-409.
- (64) Ullah, R.; Atilhan, M.; Aparicio, S.; Canlier, A.; Yavuz, C. T. *International Journal of Greenhouse Gas Control* **2015**, *43*, 22-32.
- (65) Wu, Q.; Li, W.; Liu, S.; Jin, C. *Applied Surface Science* **2016**, *369*, 101-107.
- (66) Manmuanpom, N.; Thubsuang, U.; Dubas, S. T.; Wongkasemjit, S.; Chaisuwan, T. *Journal of Environmental Management* **2018**, *223*, 779-786.
- (67) Thubsuang, U.; Manmuanpom, N.; Chokaksornsan, N.; Sommut, C.; Singhawat, K.; Payaka, A.; Wongkasemjit, S.; Chaisuwan, T. *Applied Surface Science* **2023**, *607*, 155120.

## Appendix A



**Figure S3.1.** FESEM images of porous (a) p-BCN-700, (b) p-BCN-800 and (c) p-BCN-900 samples.

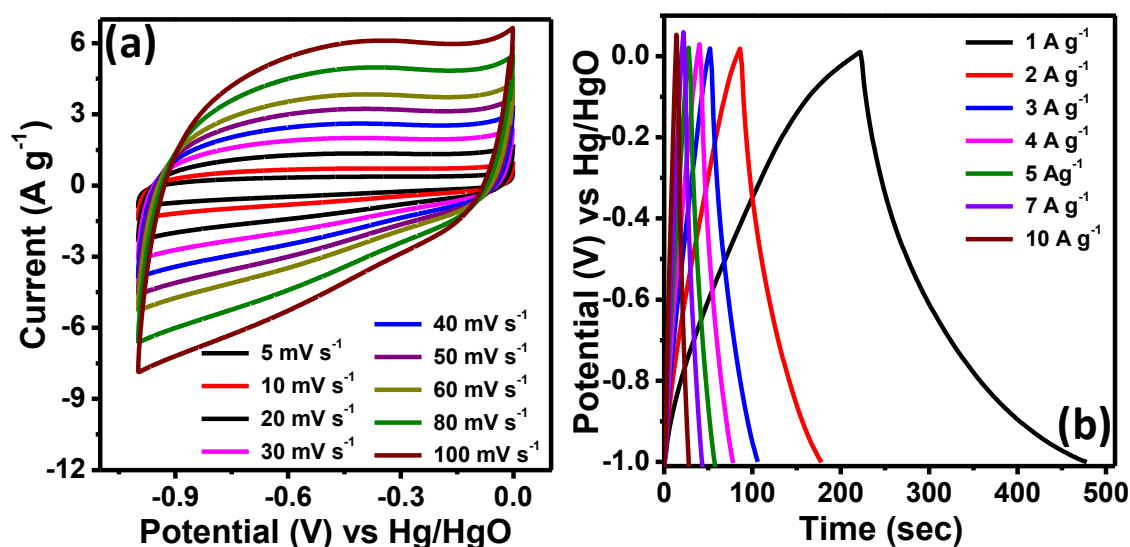


Figure S3.2. CV and GCD profiles of BCN-700.

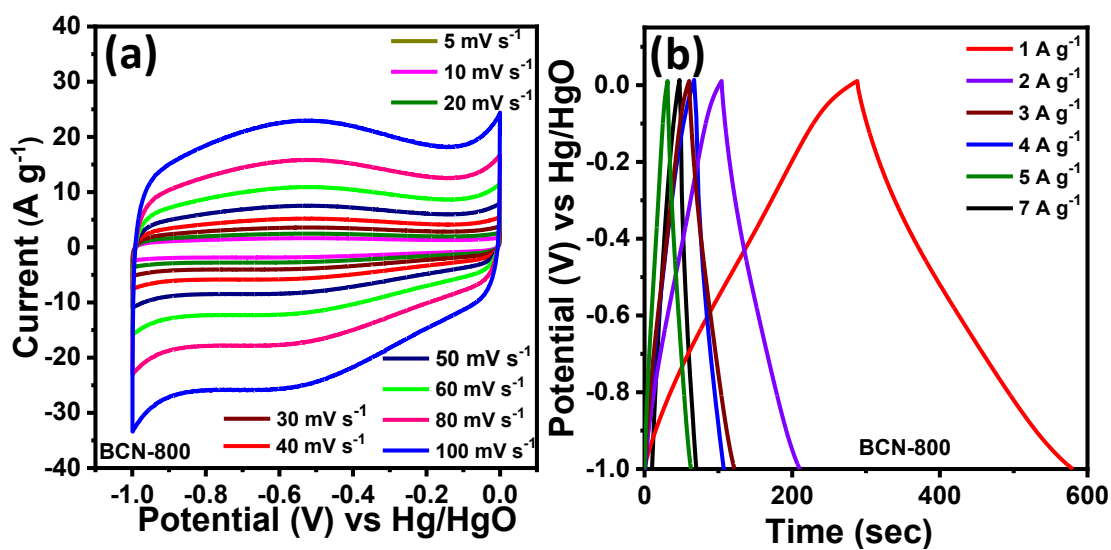


Figure S3.3. CV and GCD profiles of BCN-800.

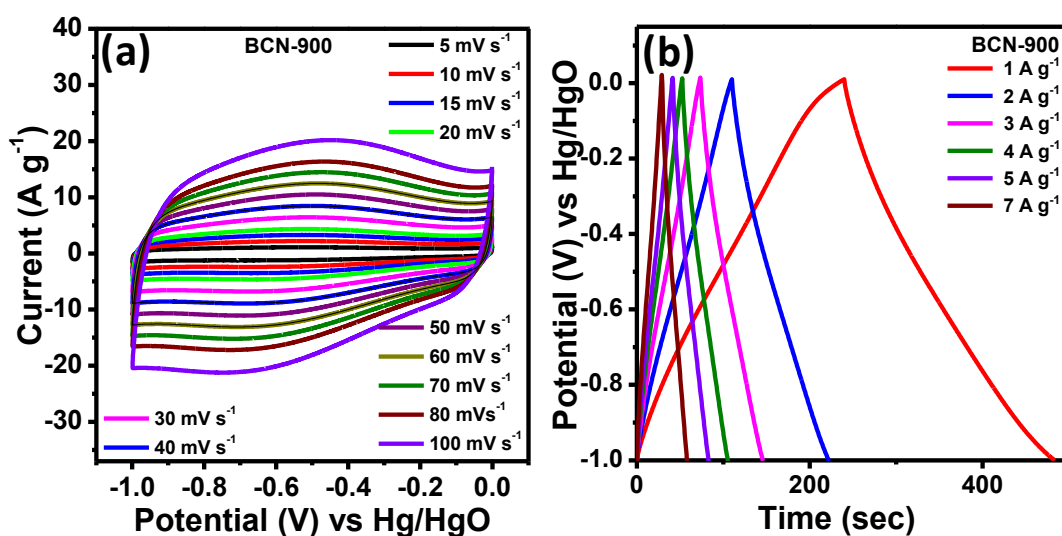


Figure S3.4. CV and GCD profiles of BCN-900.

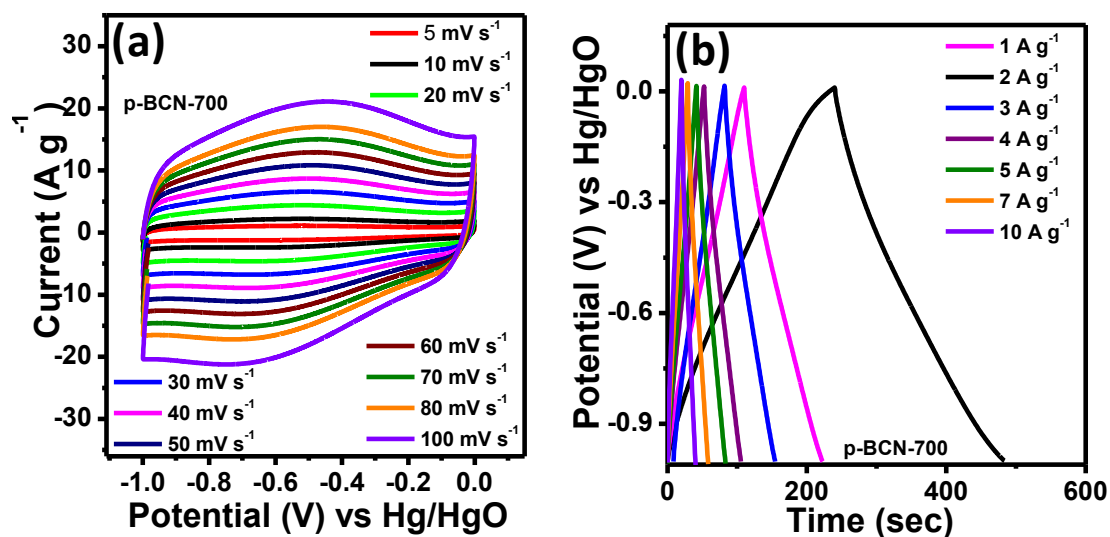


Figure S3.5. CV and GCD profiles of p-BCN-700.

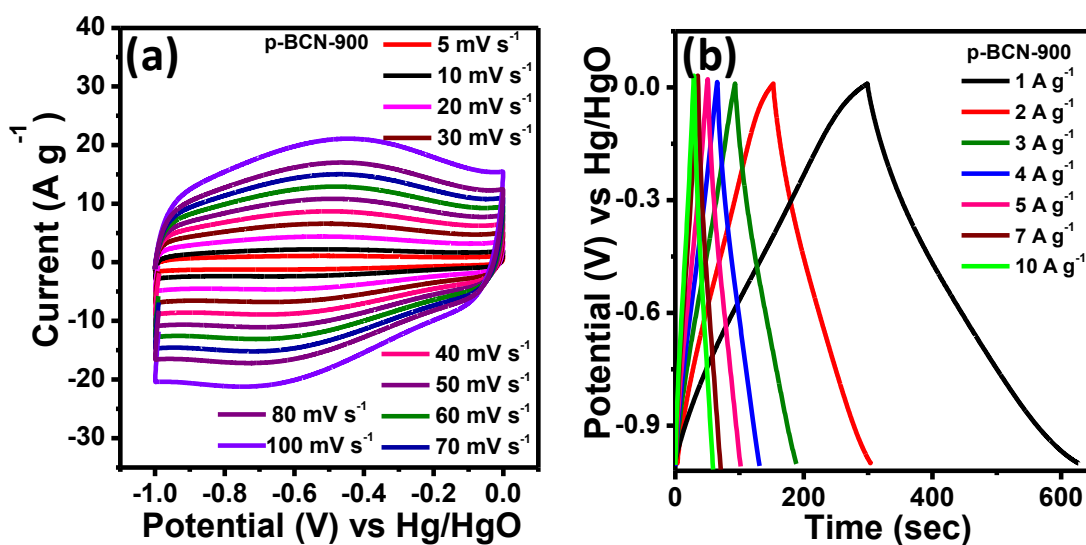


Figure S3.6. CV and GCD profiles of p-BCN-900.

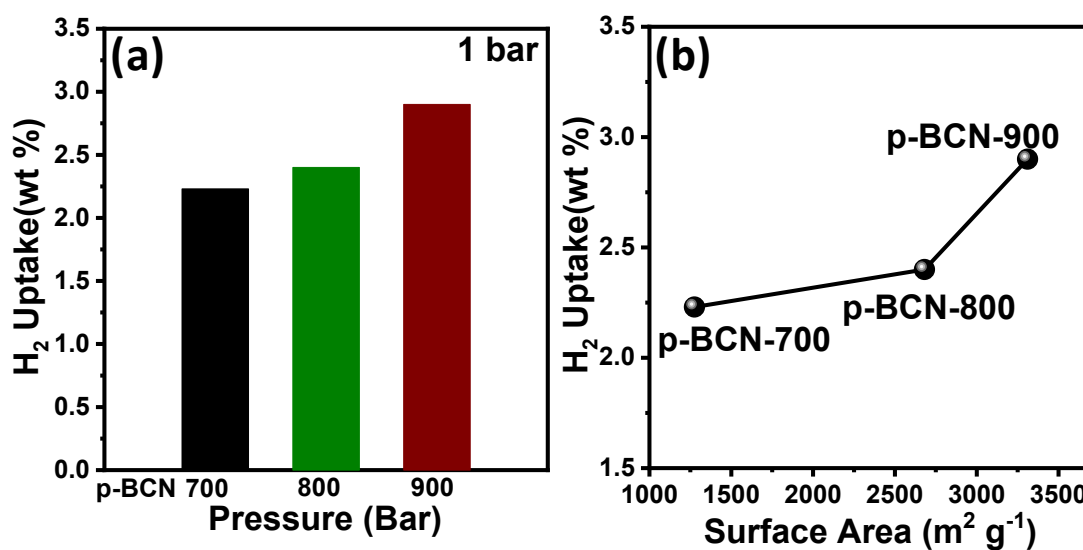
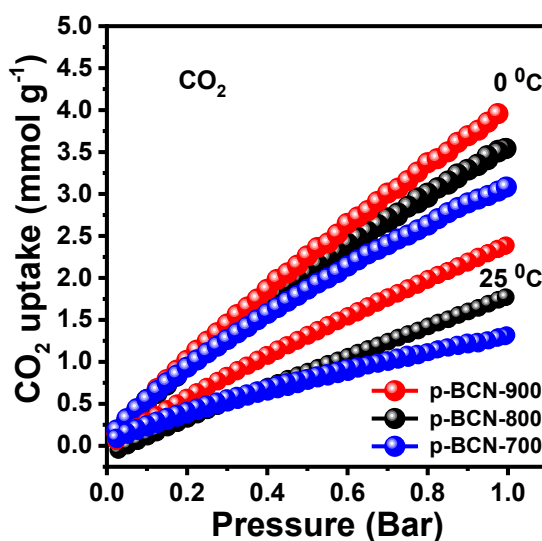


Figure S3.7. (a) H<sub>2</sub> uptake of all the samples at 77K and 1 bar pressure. (b) Change in H<sub>2</sub> uptake as a function of surface area.



**Figure S3.8.** CO<sub>2</sub> uptake capacities of p-BCN-700 to 900 at 0 °C and 25 °C under 1 bar pressure.

**Table S3.1.** Weight % of B, C, N, and O present in BCN-700 and p-BCN-X samples calculated from SEM EDX analysis.

Sample Name	C (%)	B (%)	N (%)	O (%)
BCN-800 (2D nanosheets)	41.80	18.50	18.30	21.50
p-BCN-800(2D porous nanosheets)	34.20	17.60	10.30	37.90

**Table S3.2.** Comparison of electrochemical performance of BCN-X samples in 6M KOH electrolyte.

Sample Name	Specific capacitance (F g <sup>-1</sup> ) at 1 A g <sup>-1</sup> current density (6M KOH electrolyte)
BCN-700	226
BCN-800	273
BCN-900	254

**Table S3.3.** Comparison of electrochemical performance of p-BCN-X samples in 6M KOH electrolyte.

Sample Name	Specific capacitance (F g <sup>-1</sup> ) at 1 A g <sup>-1</sup> current density (6M KOH electrolyte)
p-BCN-700	247
p-BCN-800	355
p-BCN-900	332

**Table S3.4.** CO<sub>2</sub> uptake capacities of carbon materials at 25 °C temperature and 1 bar pressure.

Adsorbent	CO <sub>2</sub> uptake (mmol g <sup>-1</sup> )	Pressure	Temperature	References
SNPC-c	2.01	1 bar	25 °C	60
A-3-650-150	2.11	1 bar	25 °C	61
SPC-E20	2.36	1 bar	25 °C	62
Meso-Carbon	1.5	1 bar	25 °C	63
MSBA-15	1.6164	1 bar	25 °C	64
CS <sub>0.2</sub> -950	1.89	1 bar	25 °C	65
AC-800	1.86	1 bar	30 °C	66
C40%Si-600	2.27	1 bar	30 °C	67
p-BCN	2.39	1 bar	25 °C	This work

## Chapter 4

### **A bottom-up fabrication for Sulphur (S), Nitrogen (N) co-Doped two-dimensional Microporous Carbon Nano-sheets for high-performance Supercapacitor and H<sub>2</sub>, CO<sub>2</sub> storage**

#### 4.1. ABSTRACT

The synthesis of two-dimensional (2D) carbon sheets with sub-nanometer pore-rich microporous morphology and an understanding of the structure-performance relationship is important to develop an advanced device for supercapacitors and gas adsorption. The 2D microporous carbon nanosheets with nanometer thickness allow easy mass/ions transport and overcome the problem faced by traditional porous materials. This chapter report a bottom-up method to form 2D S, N-doped microporous carbon nanosheets from simple organic molecules for supercapacitor and gas adsorption. The optimized microporous carbon nanosheets prepared at 800 °C (p-CNS-800), possesses an average-micropore size of ~2.2 nm with plenty of sub-nanometer micropores (>1 nm) and provide a high surface area (2847.8 m<sup>2</sup>g<sup>-1</sup>) with pore volume (1.32 cc g<sup>-1</sup>). These unique 2D microporous carbon nanosheets and optimal S, N doping allow easy ions diffusion, electron transport, and ions/gas storage. The p-CNS-800 showed ultra-high specific capacitance of 935 F g<sup>-1</sup> and 615 F g<sup>-1</sup> at 0.5 A g<sup>-1</sup> in 1M H<sub>2</sub>SO<sub>4</sub> and 6M KOH respectively. The symmetric (p-CNS-800//p-CNS-800) device delivers specific capacitance of 297.4 F g<sup>-1</sup> (H<sub>2</sub>SO<sub>4</sub>) and 296.12 F g<sup>-1</sup> (KOH) and 247.2 F g<sup>-1</sup> (Na<sub>2</sub>SO<sub>4</sub>) with excellent cyclic stability. The symmetric device delivers an excellent energy density of 31.01W h kg<sup>-1</sup> and a power density of 1720.36 W kg<sup>-1</sup>. Moreover, S, N doped 2D-nanosheets showed excellent H<sub>2</sub> and CO<sub>2</sub> uptake. The H<sub>2</sub> uptake of 2D microporous carbon sheets is 2.6 wt% at 77 K under 1 bar pressure

whereas CO<sub>2</sub> uptakes are 5.5 mmol g<sup>-1</sup> and 2.75 mmol g<sup>-1</sup> at 273 and 298 K with selectivity for CO<sub>2</sub>/N<sub>2</sub> and CO<sub>2</sub>/CH<sub>4</sub> are 21.8 and 2.6 respectively.

## 4.2. INTRODUCTION

With increasing energy demands the energy storage/conversion or gas storage system based on porous carbon-based compounds snatched great attention owing to their convenient synthesis method and high electrochemical performance<sup>1</sup>. Based on their pore size, porous materials can be classified as mesoporous, microporous, or macroporous. Microporous material is a porous material with a pore diameter of < 2 nm and possesses surface areas usually higher than 200 m<sup>2</sup> g<sup>-1</sup>. There are several disadvantages of microporous materials such as (i) the mass transport of molecules is generally poor owing to the long diffusion length between micropores, (ii) high-pressure drop is due to high resistance at a high flow rate (iii) separation selectivity is poor because of random arrangement of pores. The recent development in nano-meter thick 2D microporous materials with plenty of porous morphology with a high aspect ratio can overcome these disadvantages. However, these 2D porous materials are not used in practical applications due to the limitation of ion diffusion in the porous framework. Several strategies have been employed to increase the electrochemical energy storage activity of the carbon-based materials for example (i) exploring the SSA<sup>2</sup>, (ii) modifying the porosity of the carbon material<sup>3</sup>, (iii) by functionalizing carbon materials by hetero atoms like boron<sup>4</sup>, nitrogen<sup>5</sup>, sulphur<sup>6</sup>, selenium<sup>7</sup>, phosphorous<sup>8</sup>, and fluorine<sup>9</sup>. The SSA of carbon material can provide more contact area to the electrolyte-carbon interface owing to the reversible desorption/adsorption of charged ions from the electrolyte into the highly porous surface area of the electrode



materials<sup>10</sup>. The porosity of the carbon material can be modified by optimization of electroactive surface area<sup>11</sup>, providing space for transportation which is essential for the enhancement of high charge storage. The porous morphology not only enhances the contact between active sites and electrolyte ions but also shortens the distance of the electrolyte ion accessing the interior of the material<sup>12</sup>. Heteroatom doping is a most favourable technique to enhance the performance of the carbon material. Heteroatom doping used to improve the electrical conductivity and wettability of the surface and hence enhances availability of more active sites and increasing the specific capacitance ( $C_s$ ) of the carbon materials. Doping carbon materials with hetero-atoms improve the conductivity, influence the SSA and pore size. N doping to the carbon framework improves the electronic conductivity i.e. charge mobility on the carbon surface as well as wettability of the carbon materials<sup>13</sup>, P doping enhances the oxidation resistance of carbon electrode and S doping with carbon framework, combines EDLCs with pseudocapacitance due to its easy polarization of lone pair electrons and large size with better charge distribution over the carbon surface and improving the capacitance through the faradic process. Nowadays more research has been focused on binary doping of hetero atoms such as O and N, S and N, etc. Doping with N and O improves the  $C_s$  value of the material by the faradic redox process. S and N co-doping to carbon framework further enhance the  $C_s$  value and electrical conductivity due to the synergistic effects of sulfur with nitrogen<sup>6, 11</sup>. Abd El-Moneim et al. reported that S, N dual doped reduced graphene oxide (rGO) shows a 2.5 times capacitance behavior than that of only N- doped rGO<sup>14</sup>.

Large-scale discharge of CO<sub>2</sub> into the environment leads to serious environmental concerns like the greenhouse effect, global warming, and anthropogenic

climate change. To reduce greenhouse gas emissions and global warming, the development of the technique for CO<sub>2</sub> uptake and storage is highly necessary. The design of a better adsorbent for storage and separation of CO<sub>2</sub> and H<sub>2</sub> is very essential, as it is an energy source of fuel cell vehicles. Many solid adsorbents such as porous silica, calcium oxide, metal-organic framework, porous carbon, porous polymers, zeolites, and hybrid composites are developed because of their low cost, large SSA, adjustable pore size, and chemical stability. Among them, porous carbon materials have gained intense interest for gas capture due to their high SSA, tunable porous morphology, tunable pore volume, low density and resistivity, thermo-mechanical stability, and facile synthesis methods<sup>15</sup>. The microspore structure provides more favourable sites for gas adsorptions. The introduction of basic groups into the carbon framework improves the performance of selective adsorption of CO<sub>2</sub>. N doping to the carbon framework increases the surface active-redox sites and hence increases the energy storage capacity as well as CO<sub>2</sub> capture. S and N co-doping into the carbon matrix can improve the adsorption properties of acidic gases<sup>16</sup>.

Recently, 2D nanomaterials such as graphene, carbon nitride, boron nitride, boron carbon nitride, etc. have received so much attention due to their unique structure, interesting properties, and their applications in a variety of fields such as sensors, energy conversion and storage, gas storage/separation, electronic devices, etc<sup>17-18</sup>. Another type of 2D material, microporous 2D carbon nanomaterials with nanometer thickness is also attracted importance due to their wonderful potential applications in different fields such as energy storage, gas storage/separation, catalysis, etc. The high SSA, plenty of accessible active sites, and the 2D porous morphology allow easy mass/heat transport overcoming the problems faced by traditional bulk porous

compounds. It was predicted<sup>19</sup> that the capacitance of carbon-based 2D porous materials can be enhanced if pores size distribution is sub-nanometre (<1 nm), but 2D porous Carbon with sub-nanometer pores is generally difficult to prepare.

Herein, a facile bottom-up technique for the synthesis of 2D S, N-doped microporous carbon nanosheets for electrochemical energy storage and gas storage applications is reported. First, 2D carbon nano-sheets with nanometer thickness are formed from hydrothermal heating of simple organic molecules-thiourea and formamide and then calcination at 700 °C. In the second step, 2D carbon sheets were activated by KOH at different temperatures (600–900 °C) to form 2D microporous carbon nano-sheets. The unique microporous carbon sheets with optimal doping of N/S, activated at 800°C, show a high SSA of 2847.8 m<sup>2</sup>g<sup>-1</sup> and pore volume of 1.32 cc g<sup>-1</sup> and microspores are concentrated at 2 nm including plenty of microspores with size less than 1nm. The combined effect of microporous structure and dual S/N doping, the 2D microporous N, S sheets showed high excellent supercapacitor (SC) and gas adsorptions. The unique porous carbon sheets allow accessing the surface active site for the electrolytes and ions storage, high conductivity due to the presence of partial graphitic nature and hetero doping in carbon sheets. The p-CNS-800 show remarkable supercapacitor performance with a C<sub>s</sub> of 935 F g<sup>-1</sup> under 0.5 A g<sup>-1</sup> current (1M H<sub>2</sub>SO<sub>4</sub>). Furthermore, a p-CNS-800//p-CNS-800 symmetric device shows high energy density (ED) as well as high power densities (PD). Furthermore, 2D-porous carbon sheets show excellent H<sub>2</sub> and CO<sub>2</sub> adsorption with excellent CO<sub>2</sub>/N<sub>2</sub> selectivity. The high supercapacitor and gas adsorption performance of p-CNS-800 sheets can be explained due to the unique porous morphology of carbon sheets which allows to access the surface active site for

the electrolytes and ions storage, high conductivity due to the presence of hetero-doping in carbon sheets.

### **4.3. EXPERIMENTAL SECTION:**

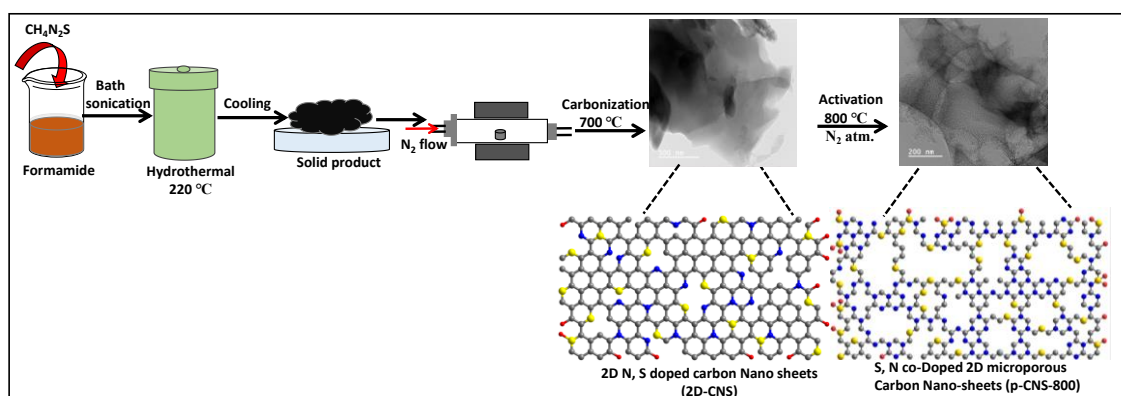
#### **4.3.1. Materials:**

Formamide was purchased from Merck, India. Thiourea was purchased from Spectrochem PVT. LTD. Mumbai (India). Potassium Hydroxide (KOH), Hydrochloric acid (HCl), and Sulphuric acid (H<sub>2</sub>SO<sub>4</sub>) were purchased from CDH chemicals, India. PTFE binder was purchased from MTI corporation. Deionized water was used to carry out all experiments.

#### **4.3.2. Synthesis of 2D S and N co-doped carbon (CNS) and 2D porous CNS-X (p-CNS-X)**

The microporous 2D N/S doped carbon nano-sheets are produced by a two-step facile bottom-up synthesis method from simple organic molecules. In the first step, nanometer thick 2D N, S-co-doped thin carbon nanosheets are formed by hydrothermal heating of formamide and thiourea and then carbonization at 700 °C. For this, 30 ml of formamide was taken in a 50 ml beaker, and 4 g of thiourea was added to it and allowed to dissolve by sonicating it in a bath sonicator. Then the solution was transferred into a 100 ml autoclave and allowed to heat at 220 °C for 48 hrs. The solid product obtained was heated in a tube furnace at 700 °C for 2 hrs under a nitrogen flow of 700 mL/min to form 2D thin microporous N, S doped carbon nano-sheets, denoted as 2D-CNS. In the second step, 2D microporous N, S co-doped Carbon nano-sheets are formed by KOH activation of these 2D-CNS at different temperatures (600 to 900 °C). The N, S doped 2D carbon sheets were soaked in 6M KOH maintaining a KOH and C

weight ratios of 2:1, and dried in an oven at 150 °C. Then it was activated at different temperatures from 600-900 °C to form 2D microporous N, S doped carbon nanosheets and the obtained samples are named p-CNS-X (X= 600,700, 800, and 900) accordingly. The as-synthesized p-CNS-X was washed several times with 0.2M HCl and deionized (DI) H<sub>2</sub>O to remove the soluble impurities. Scheme 4.1 presents a detailed synthesis scheme illustrating the synthesis of 2D-CNS and p-CNS-X.



**Scheme 4.1.** Synthesis of 2D S and N co-doped carbon (CNS) and 2D porous CNS-X (p-CNS-X).

### 4.3.3. Electrode Fabrication:

Fabrication of electrodes was carried out by mixing polyvinylidene fluoride (PVDF) binder, conductive carbon, and p-CNS-X with a mass ratio of 10:10:80 (in *N*-Methyl-2-pyrrolidone (NMP)) followed by coating over Nickel foam (1\*1 cm<sup>2</sup>) and Ti foil (current collector) for the base and acid medium respectively. The electrodes were dried at 85 °C in a vacuum. The mass loading of each electrode was close to 1 mg. The single electrode performance was measured in the electrolyte of 6M KOH and 1M H<sub>2</sub>SO<sub>4</sub> in a three-electrode system configuration with Hg/HgO reference electrode (Ag/AgCl in 1M H<sub>2</sub>SO<sub>4</sub>) and platinum mesh as counter electrode while the symmetric device was tested in the two-electrode system. The symmetric device was prepared

using glass microfibre filter paper as a separator in a CR2032 coin cell configuration. The thickness of the working electrode was measured from FESEM cross sectional area and is calculated to be 75-100  $\mu\text{m}$ . 1M Na<sub>2</sub>SO<sub>4</sub> was used as an electrolyte for the test in a neutral medium. From a single electrode, the specific capacitance ( $C_s$ ) Calculation was carried out from Galvanostatic Charge discharge (GCD) curves using the following equation:

$$C_s = \frac{I\Delta t}{m(V_f - V_i)} \quad (4.1)$$

Specific capacitance ( $C_s$ ) can be calculated from the CV curve by using the following equation:

$$C_s = \frac{\int I dV}{2m\Delta V u} \quad (4.2)$$

Where  $C_s$  = specific capacitance

$I$  = current applied (A)

$\Delta t$  = discharge time (sec)

$m$  = mass of the active material (g)

$V_f - V_i$  = Voltage window (V)

$\int I dv$  = area under the CV curve

$u$  = scan rate ( $\text{mV s}^{-1}$ ).

For a symmetric supercapacitor device, the calculation was done using the following equations.

$$C_s = \frac{2I\Delta t}{m(V_f - V_i)} \quad (4.3)$$

$$ED = \frac{C_{cell}\Delta V^2}{2 \times 3.6} = \frac{C_s \Delta V^2}{8 \times 3.6} \quad (4.4)$$

$$PD = \frac{E \times 3600}{t} \quad (4.5)$$

Where  $C_s$  = specific capacitance, ED = Energy density, and PD = power density.

#### **4.3.4. Material Characterization:**

The powder x-ray diffraction patterns (p-XRD) of samples were measured by Bruker X-ray diffractometer (DAVINCI D8 ADVANCE equipped with Cu K $\alpha$  source of wavelength 0.154 nm). The morphological characterization was investigated by a Field-emission scanning electron microscope (FESEM) system (Model- $\Sigma$ igma, Carl Zeiss, Germany) and Transmission Electron Microscopy (TEM) instrument operated at 200 kV (F200, JEOL). XPS measurement was done using AXIS ULTRA (Kratos) instrument where a monochromated Al-k $\alpha$  source was used. XPS was taken from the sample deposited on the silicon wafer. The CO<sub>2</sub> and N<sub>2</sub> physisorption isotherms were collected using AUTOSORB-1 (Quantachrome). The pore size distribution (PSD) was calculated using the nonlocal density functional theory (NLDFT) model while the micropore analysis was carried out using the t-plot method. LabRAM HR Evolution, Horiba Scientific, and Raman Spectrometer were used for Raman analysis using a 532 nm laser source. Electrochemical measurements were performed using CS310 Electrochemical Workstation (Corrtest Instruments).

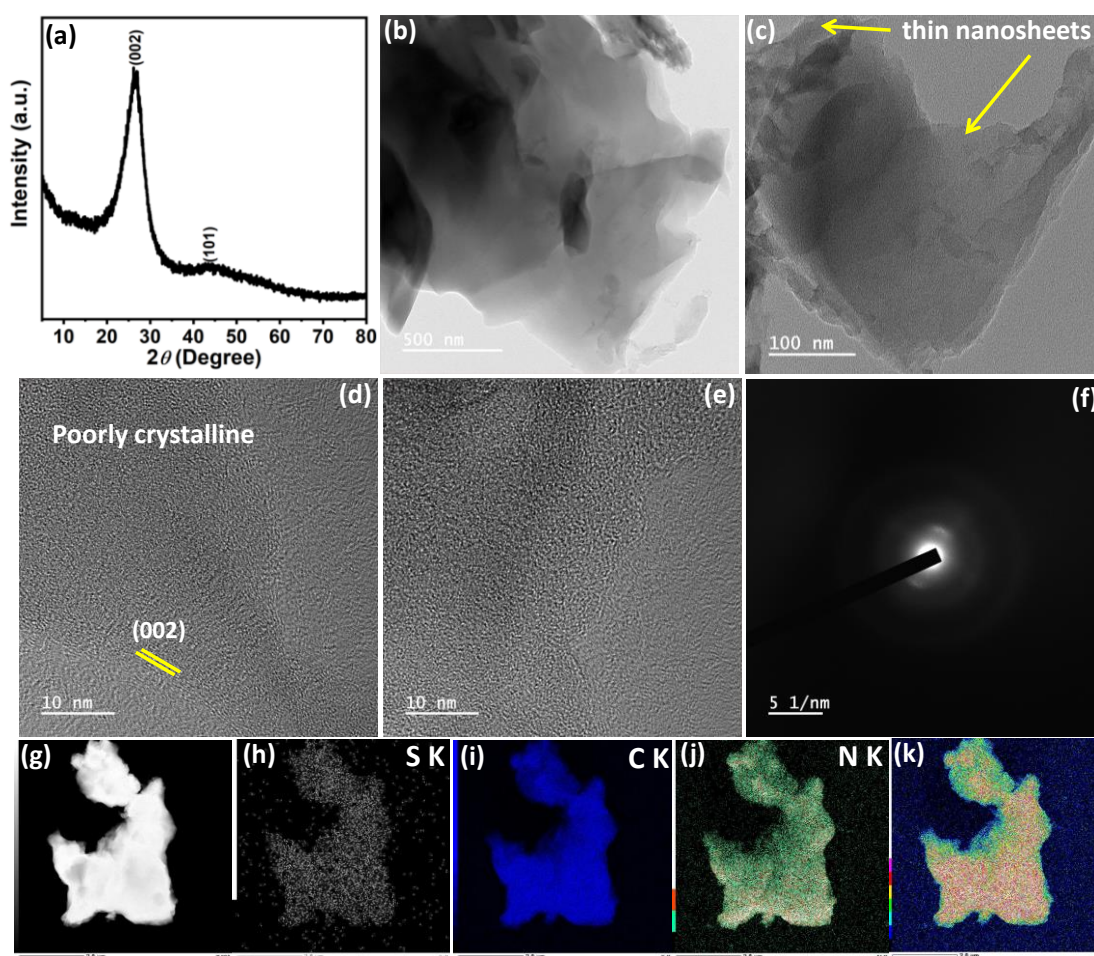
### **4.4. RESULTS AND DISCUSSIONS:**

#### **4.4.1. Morphology and characterization**

The 2D N, S doped carbon nano-sheets are formed by a simple bottom-up synthesis (hydrothermal heating of simple organic molecules followed by calcination at 700 °C). Figure 4.1(a) represents the powder X-ray diffraction (p-XRD) pattern of 2D-CNS. A broad peak indexed at  $2\theta$  values of 26.5 and 43.2 ° corresponds to the graphitic (002) and (101) planes. The low-resolution TEM and HRTEM images of 2D-CNS are presented in Figure 4.1 (b-e). HRTEM images show amorphous carbon sheets with



very few lattice fringes having a d-spacing of 0.32 nm at the edges. The TEM image shows the thin 2D carbon nanosheets. SAED images (Figure 4.1(f)) show the diffuse ring suggesting the amorphous nature of the prepared 2D N, S doped carbon nanosheets. STEM images and corresponding elemental mapping of 2D sheets are presented in Figure 4.1(g-k) showing the homogeneous distribution of C, N, and S in the sheets.



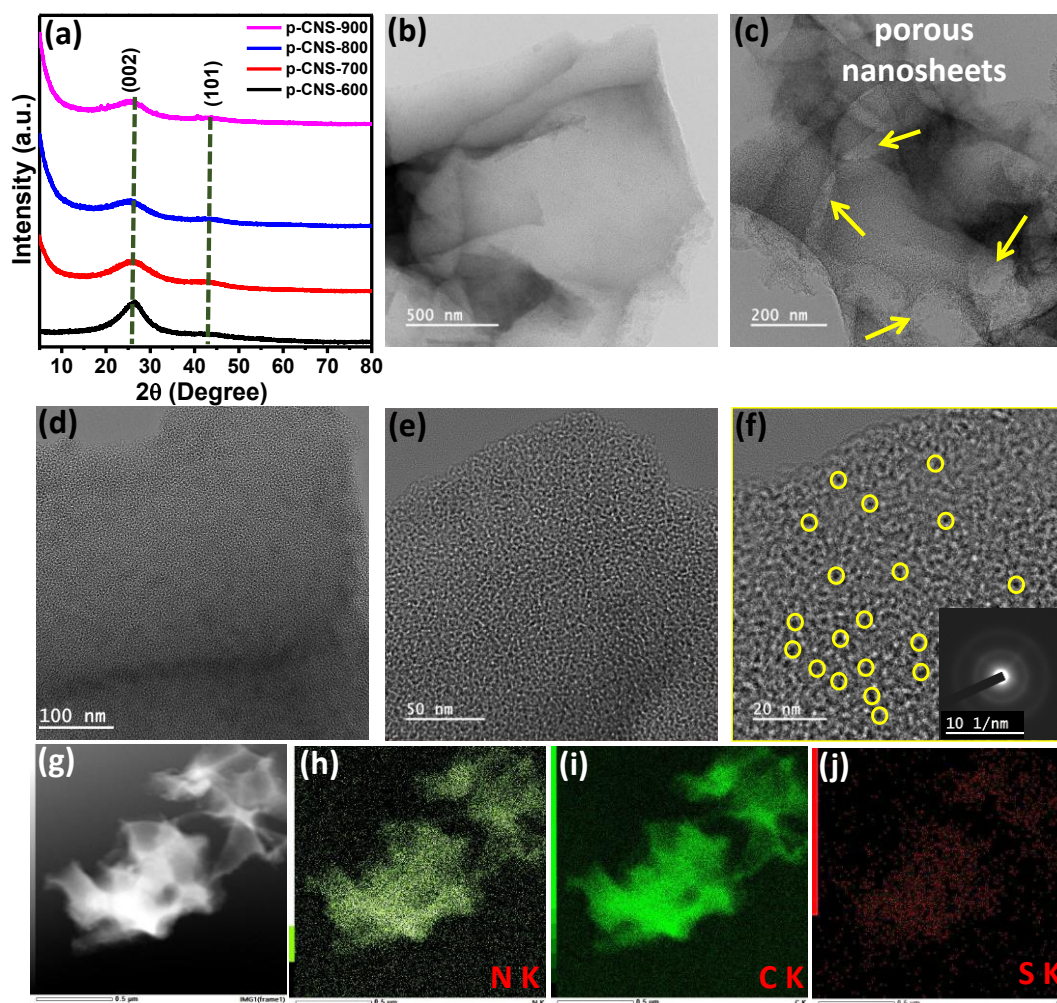
**Figure 4.1.** (a) p-XRD patterns, (b, c) TEM (low-resolution), (d, e) TEM (High-resolution) images, (f) SAED pattern, and (g-k) STEM and corresponding elemental mapping of 2D-CNS sample.

The 2D microporous N, S carbon nano-sheets were synthesized by KOH activation of these 2D carbon sheets at different temperatures in presence of KOH under N<sub>2</sub> flow.



During the activation process, complete consumption of KOH was taking place, represented as  $2C + 6KOH \Rightarrow 2K_2CO_3 + 2K + H_2$ . At a temperature higher than 600 °C,  $K_2CO_3$  significantly decomposes into  $K_2O$  and  $CO_2$  resulting in maximum porosity<sup>20</sup>. Figure 4.2(a) represents the p-XRD pattern of p-CNS-X samples. Two dominant broad peaks centred at  $2\theta$  values 25.48 and 43.86 ° indexed to the planes (002) and (101) of graphitic carbon representing the formation of the disordered amorphous carbon structure. With an increase in annealing temperature, the diffraction peak (002) decreases indicating defects and amorphous structures that are formed during the carbonization and activation process. In addition, there is no impurity peaks are observed in the p-XRD patterns reflecting all potassium-containing impurities are removed by washing with HCl and DI water. The morphology and porous structure of p-CNS-X were analysed by SEM analysis. Figure S4.1. displays porous sheet-like morphology of p-CNS-X samples. Effective doping of S and N into the activated carbon was confirmed from the SEM EDX result. A comparison table containing the weight % of all the elements (carbon, Sulphur, Nitrogen, and Oxygen) for all four p-CNS-X samples is presented in Table S4.1. The carbon, nitrogen, and sulfur content rose to 61, 8.5, and 7.2 % respectively for p-CNS-600 samples. It is observed that the activation temperature significantly affects the chemical content of N and S. The content of N and S decreases with increasing activation temperature. The microporous structure and porous morphology of p-CNS-800 were investigated by TEM and HRTEM (Figure 4.2(b-f)). There is no obvious long-range ordered structure in the HRTEM image indicating the amorphous structure of the sample which is consistent with p-XRD results. Abundant nanopores are observed which are marked as a circle in Figure 4.2(f). Such nanopores are the number of channels allowing the electrolyte ions

to enter through the structure and transport electrolyte ions between the electrolyte/electrode interfaces. The SAED image (Inset of Figure 4.2(f) of p-CNS-800 shows a faded circle with some bright spots on it, which indicates the existence of both defective and graphitized carbon in the composite, which is a good agreement with the HRTEM finding. Figure 4.2(g-j) presents the STEM image and their corresponding elemental mapping suggesting the uniform distribution of C, N, and S elements all through the porous carbon nanosheets. The homogeneous distribution of N, and S atoms is favourable for the faradic reaction occurring in entire CNS nanosheets. Raman analysis is performed to characterize the micropore structure of the prepared samples. As presented in Figure 4.3(a) two peaks centred at 1347 and 1594 cm<sup>-1</sup> indexed to the D and G bands respectively. D band is a result of out-of-plane vibrations and is sensitive to structural defects and disorder associated with heteroatom (S, N) doping and structural defects caused by carbonization and activation process whereas the G band arises owing to in-plane vibration of sp<sup>2</sup>-hybridized graphitic carbon respectively<sup>21</sup>. The degree of disorderness and defectiveness can be obtained by taking the intensity ratio I<sub>D</sub>/I<sub>G</sub> (characteristic peaks of D and G band). The I<sub>D</sub>/I<sub>G</sub> ratio for p-CNS-X was calculated to be in the range of 0.96-1.01 indicating the presence of defects and the amorphous nature of the porous nanocarbon samples, which are consistent with the p-XRD and TEM results. The I<sub>D</sub>/I<sub>G</sub> ratio for p-CNS-700 is obtained to be 0.97, which is slightly higher than the p-CNS-600 and lower than p-CNS-800 suggesting an increase in defect sites in p-CNS-800 than p-CNS-700 due to the pyrolysis at higher activation temperature. The higher the value of I<sub>D</sub>/I<sub>G</sub> ratio reflects the higher will be the degree of defects in the carbon structure.



**Figure 4.2.** (a) p-XRD patterns of p-CNS-X composites, (b-d) low-resolution TEM images, (e, f) HRTEM images (inset of (f) presents the SAED pattern), and (g-j) STEM and corresponding elemental mapping of p-CNS-800 composite.

N<sub>2</sub> desorption/adsorption isotherm was performed to analyse the SSA and pore-size distribution (PSD) of p-CNS-X samples. All the compounds show type-I isotherm curves (IUPAC classification) indicating hierarchical porous nanostructures, with coexisting micropores and mesopores which are depicted in Figure 4.3(b). For developing a better electrode material, the presence of both meso and micropores plays an essential role. In general, micropores account for high C<sub>s</sub> values, and mesopores as

good ion channels and it is essential for the retention of rate capacity. The presence of a significant amount of micropores in the compounds was confirmed, as there is a sharp uptake in the N<sub>2</sub> adsorption at the 0-0.1 pressure range. The co-existence of the mesoporous and microporous structure of the prepared samples is confirmed as the N<sub>2</sub> adsorption curve steadily rises after the pressure range of 0.1 which implies that the sample contains plenty of meso and micropores. It has been reported that the C<sub>s</sub> of carbon material can be significantly improved by increasing SSA as well as the pore size in the sub-nanometer scale<sup>22</sup>. The high SSA was obtained by increasing activation temperature and KOH: C ratio, demonstrating the role of activation temperature which affects the formation of a large number of micropores<sup>20</sup>. When KOH: C ratio is low the inaccessible pore opening, as well as the formation of new pores, takes place, and when KOH: C ratio increases the expansion of the existing pore occurs. Similarly when the temperature is raised from 600 °C to 900 °C the percentage of S<sub>micro</sub> decreases. The total surface area was calculated by using the BET method and the microporous surface area was calculated by the t-plot technique. The p-CNS-600 sample has lowest SSA value compared to other samples prepared at different temperature. The SSA for p-CNS-600, p-CNS-700, p-CNS-800, and p-CNS-900 is obtained to be 2181.6, 2538.58, 2847.8, and 2872.78 m<sup>2</sup>/g. Among these four compounds, the highest microporous surface area (2135.55 m<sup>2</sup> g<sup>-1</sup>), microporous volume (0.95 cm<sup>3</sup> g<sup>-1</sup>), the high microporous volume ratio of 75%, and smallest average pore size (2.2 nm). The high microporous surface area is valuable for capacitance. The increase in S<sub>BET</sub> value for p-CNS-800 than other samples resulted from the activation temperature, which has a significant effect when the temperature rises from 600 to 800 °C. The total pore volume (V<sub>t</sub>) is highest for p-CNS-800 and lowest for p-CNS-600 with values of 1.32 and 0.99 cc g<sup>-1</sup> respectively.

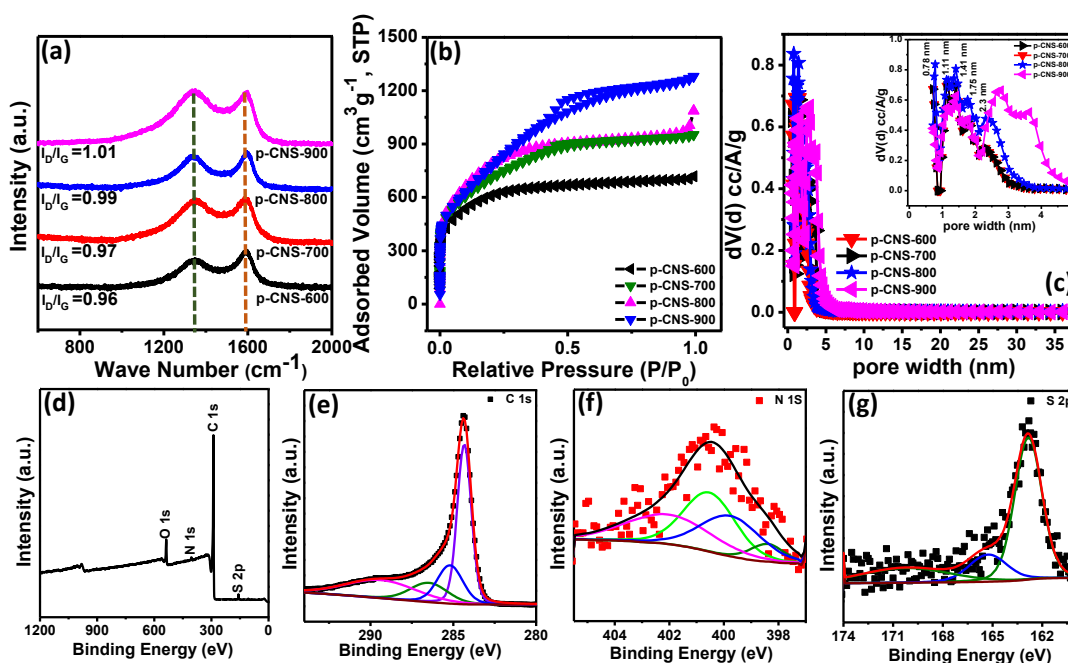
The presence of plenty of micropore SSA and high  $S_{\text{BET}}$  value of p-CNS-800 sample among all four samples suggest high capacitive charge storage performance of the sample. The formation of porous architecture not only increases the diffusion of electrolytes on the surface of the electrode material but also provides more and more defect sites. The pore size distribution of p-CNS-X samples is presented in Figure 4.3(c). Table 4.1 presents the  $S_{\text{BET}}$ ,  $S_{\text{micro}}$ , micropore volume ( $V_{\text{micro}}$ ), average pore radius ( $R_a$ ), total pore volume ( $V_t$ ), and percentage of micropore surface area ( $S_{\text{micro}}/S_{\text{BET}}$ ). The PSD of porous carbon samples strongly affects the surface area and is important for the high  $C_s$  value of porous carbon materials. The pores of all these S/N-doped carbon materials are predominantly micropores. In the p-CNS-600, p-CNS-700, and p-CNS-800 compounds the PSD was from 0.7 to 3.0 nm suggesting the presence of some mesopores in these compounds. The pores of p-CNS-800 are mainly concentrated on five pore sizes (0.78, 1.11, 1.41, 1.75, and 2.3 nm). Out of these pores, sub-nanometer micropores with sizes below 1 nm significantly improved the capacitance behavior of carbon materials due to the pore confinement effect<sup>23</sup>. In addition to material porosity, surface chemistry plays a major role in the wettability of electrolytes. The surface wettability and electronic conductivity of the materials are modified by introducing heteroatoms into the carbon structure. The S and N atoms are doped into the carbon framework to optimize the structure of the pores and hence modify electronic properties.

**Table 4.1.** Detailed surface properties and pore analysis of p-CNS-X.

Sample	BET	Micropore	Total	Micropore	Average	Percentage
	surface	surface	pore	volume	pore	of
	area	area (S <sub>micro</sub> )	volume	(V <sub>micro</sub> )	radius	S <sub>micro</sub> /S <sub>BET</sub>
	(S <sub>BET</sub> )	(m <sup>2</sup> /g)	(V <sub>t</sub> )	(cc/g)	(R <sub>a</sub> ) (Å)	(%)
	(m <sup>2</sup> /g)		(cc/g)			
p-CNS-600	2181.6	1821.6	0.99	0.81	14.87	83.49
p-CNS-700	2538.6	1228	1.15	0.55	12.12	48.4
p-CNS-800	2847.8	2135.6	1.32	0.95	11.18	74.99
p-CNS-900	2872.8	598.6	1.99	0.24	18.60	20.84

To further explore the chemical composition and surface oxidation state of the p-CNS-800 sample, an X-ray photoelectron spectroscopy (XPS) measurement was performed. Figure 4.3(d) shows the XPS survey scan of p-CNS-800 elucidating the co-existence of C, S, N, and O. The high-resolution XPS spectra of C 1s can be readily fitted into 4 peaks (Figure 4.3(e)). The peaks at 284.3, 285.2, 286.5, and 289.7 eV are indexed to C=C bonds (sp<sup>2</sup> hybridized C), C-N/C-O bonds, C-S/C-O bond, and O-C-N/O-C=C components respectively<sup>24</sup>. N 1s spectrum (Figure 4.3(f)), can be fitted into pyridinic-N, pyrrolic-N, graphitic quaternary-N, and oxidized N species corresponding to 398.4,

399.98, 400.9, and 402.12 eV respectively<sup>25</sup>. Furthermore, as shown in Figure 4.3(g) the S 2p spectrum can be fitted into three peaks indexed at 163.8, 165.15, and 168.5 eV. The two peaks at 163.8 and 165.15 eV can be assigned to S 2p<sub>3/2</sub>, and S 2p<sub>1/2</sub> of C-S-S of thiophene moiety whereas the peak at 168.5 eV is due to oxidized sulfur of C-SO<sub>x</sub>-C group<sup>24</sup>. The S atoms in the compound can enhance electrical conductivity and it also increases polarizability resulting from large sulfur lone pairs. The enhanced polarizability favours oxygen interactions with active oxygen atoms leading to enhance abilities of ions capture and pseudocapacitance performance<sup>26</sup>.



**Fig. 4.3.** (a) Raman spectrum, (b) N<sub>2</sub> sorption isotherm, (c) Pore size distribution of p-CNS-X samples, (d) XPS survey spectra, (e) C 1s, (f) N 1s, and (g) S 2p spectrum in p-CNS-800.



#### 4.4.2 Electrochemical Analysis

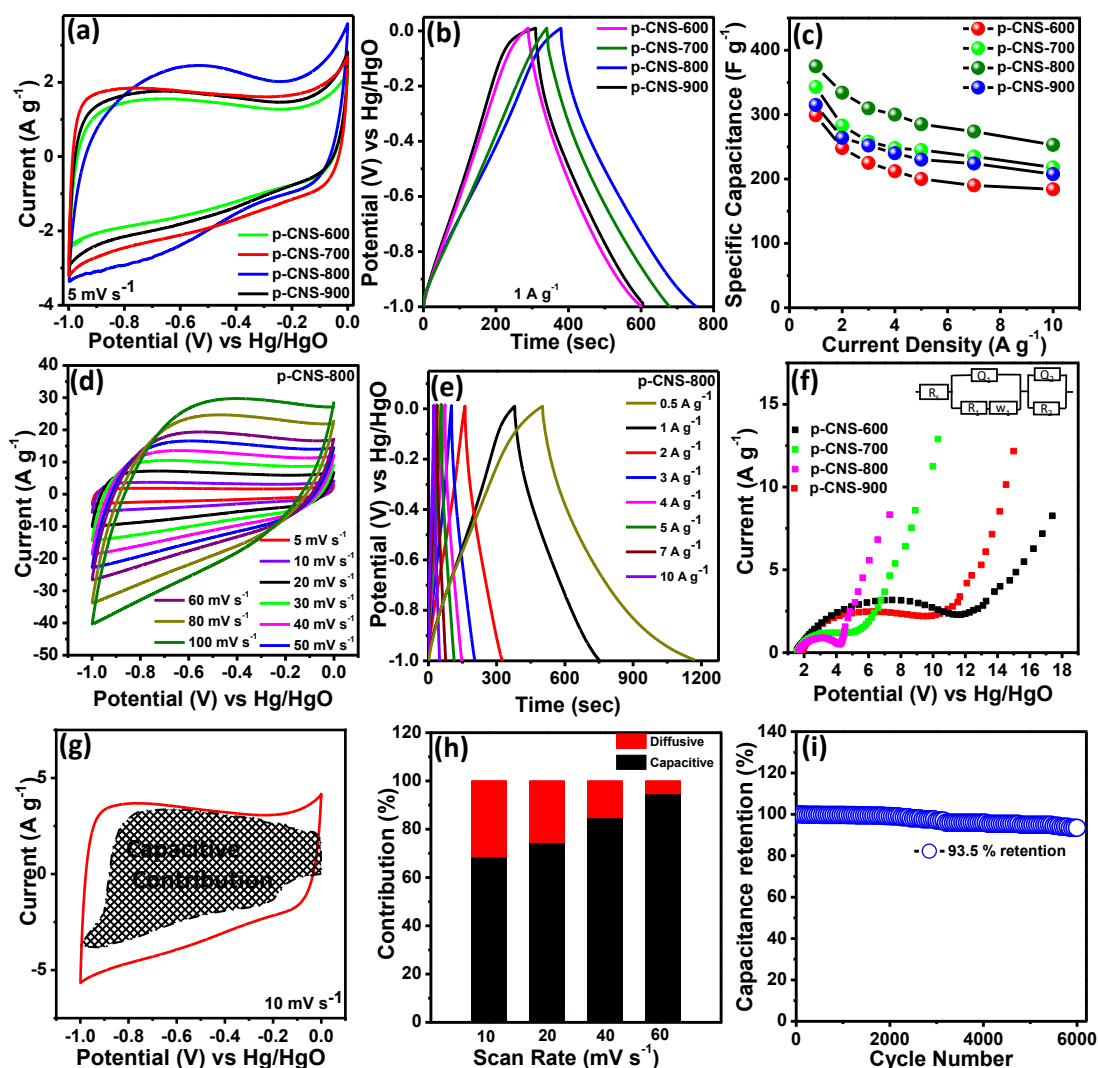
##### Electrochemical Performance in a three-electrode system

The electrochemical performance of p-CNS-X for supercapacitor electrode materials is dependent on the hetero atoms containing functional groups in the carbon framework and the choice of electrolyte. First, the prepared samples were tested in a three-electrode system using both cyclic voltammetry (CV) and Galvanostatic charge-discharge (GCD) measurements in a 6M KOH aqueous solution electrolyte. Alkaline solutions are used as an electrolyte for the facile generation of small and fast-moving OH<sup>-</sup> ions. Comparison CV curves for p-CNS-600, p-CNS-700, p-CNS-800, and p-CNS-900 are presented in Figure 4.4(a) at a sweep rate of 5 mV s<sup>-1</sup> and potential range varying from 0 to -1 V. Symmetrical and quasi rectangular nature of the CV curves indicating higher capacitive nature of the prepared samples. The area under the CV curves for p-CNS-800 is higher compared to other activation temperatures resulting highest capacitance value. Figure 4.4(b) depicts the comparison GCD plots for all four samples at 1 A g<sup>-1</sup> current. All the curves presents triangular shape indicating an electrical double-layer capacitance. The p-CNS-800 shows the highest discharge time indicating the highest capacitance among all samples. The C<sub>s</sub> values for p-CNS-600, p-CNS-700, p-CNS-800, and p-CNS-900 is calculated to be 299, 343, 375, and 315 F g<sup>-1</sup> under 1 A g<sup>-1</sup> current respectively as presented in Table S4.2. For the p-CNS-800 electrode, the C<sub>s</sub> of the material is obtained to be 615 F g<sup>-1</sup> at 0.5 A g<sup>-1</sup> which is superior than the reported heteroatom-doped electrode. The good electrochemical activity of p-CNS-800 was due to the porous morphology and optimal doping with heteroatoms i.e., S and N, which increases the surface wettability of the electrode and increases the contact area between the electrode surface and electrolyte material. The



comparison table for the  $C_s$  value of p-CNS-800 with other reported literature is presented in Table 4.2. Figure 4.4(c) display the  $C_s$  vs. current density plot for all four samples indicating the highest capacitance of p-CNS-800 compared to the other samples prepared by varying the activation temperature. The existence of micro and mesopores enhance the rate capability and  $C_s$  value of the heteroatom-doped porous carbon materials. There is a significant amount of sub-nano-meter pore present in the microporous structure of p-CNS-800. The highest electrochemical activity of p-CNS-800 is possibly due to 2D porous structure, high SSA, the presence of a significant amount of sub-nano pores along with micro-pores, optimal S, N doping in p-CNS-800, etc. The p-CNS-800 sample shows initial capacitance retention of 67.5 % at 10 A g<sup>-1</sup> current. The CV profiles at sweep rates ranging from 5-100 mV s<sup>-1</sup> are presented in Figure 4.4(d). The characteristics EDLCs nature of the CV profiles were confirmed by the symmetrical rectangular behaviour. GCD plots for p-CNS-800 at different current densities from 1-10 A g<sup>-1</sup> were presented in Figure 4.4(e). For samples p-CNS-600, p-CNS-700, and p-CNS-900, the CV and GCD curves are presented in Figures S4.2, S4.3, and S4.4 respectively. The CV plots at sweep rates varying from 5-100 mV s<sup>-1</sup> and GCD profiles at 1-10 A g<sup>-1</sup> current are presented in Figure S4.2 for the p-CNS-600 sample. The  $C_s$  value for p-CNS-600 was calculated to be 299 F g<sup>-1</sup> under 1 A g<sup>-1</sup> and then it shows 61.5 % capacitance retention from its initial capacitance after 10 A g<sup>-1</sup> current, presented in Figure S4.2(b). Figure S4.3 shows CV and GCD curves at various sweep rates and current for p-CNS-700 and the  $C_s$  value were obtained to be 343 F g<sup>-1</sup> under 1 A g<sup>-1</sup> current (Figure S4.3(b)). CV and GCD profiles for the p-CNS-900 sample were presented in Figure S4.4. The  $C_s$  value of p-CNS-900 was calculated to be 315 F g<sup>-1</sup> under 1 A g<sup>-1</sup> current, presented in Figure S4.4(b). The internal resistance of the electrode and the resistance between the electrode and electrolyte were analysed by

EIS (Electrochemical Impedance Spectroscopy) measurement. The EIS measurement was performed between 0.1 Hz-100 kHz frequency range under an AC amplitude of 5 mV s<sup>-1</sup>. Figure 4.4(f) depicts the EIS spectra of p-CNS-600 to 900. The half semi-circle at the higher frequency region and a straight line in the lower frequency region gives information about the serial resistance ( $R_s$ ) and Charge transfer resistance ( $R_{CT}$ ). The  $R_s$  values obtained are 1.49, 1.55, 1.36, and 1.77  $\Omega$ , and the  $R_{CT}$  values are obtained to be 9.93, 3.203, 2.62, and 7.35  $\Omega$  for samples p-CNS-600, p-CNS-700, p-CNS-800, and p-CNS-900 respectively. The lowers  $R_s$  value for p-CNS-800 compared to others indicates the fast electric responses and fast charge transfer kinetics. In addition, the lower  $R_{ct}$  values suggest the good conductivity of the electrochemical system. Hence, EIS data confirms the good supercapacitive application of p-CNS-800 electrode material. In the incorporation of heteroatoms i.e. sulfur and nitrogen into the carbon material, the nitrogen and sulfur electrons were localized into the carbon framework and under an external altering electric field, it is well polarized which provides negative permittivity property<sup>27-28</sup>. Overall, the introduction of heteroatoms into the carbon frame promotes the conductivity of the materials i.e. ions can easily pass through the electrical double layer and hence improving the wettability of the electrode material in the electrolyte solution. The faradic contribution includes both redox reactions on the surface of the material and the intercalation of ions. For better evolution of electrochemical performance, the separation of the diffusion-controlled process from the non-faradic process is needed. Diffusion control current linearly varies with  $v^{1/2}$  and EDLCs contribution varies linearly with  $v$ .



**Figure 4.4.** (a) CV diagrams of p-CNS-X compounds at 5 mV s<sup>-1</sup>. (b) CD curves of p-CNS-X at 1 A g<sup>-1</sup>. (c) C<sub>s</sub> at diff. current for all the samples of p-CNS-600 to 900. (d) CV plots of p-CNS-800 at diff. scan rates (5 to 100 mV s<sup>-1</sup>). (e) CD profiles of p-CNS-800 at diff. current. (f) EIS plot of p-CNS-X samples. (g) Contribution of capacitive controlled process for p-CNS-800 at 10 mV s<sup>-1</sup> sweep rate. (h) Capacitive charge storage processes at different scan rates (10-60 mV s<sup>-1</sup>). (i) Cyclic durability test of p-CNS-800 under 10 A g<sup>-1</sup> in 6M KOH electrolyte.

**Table 4.2.** Performance comparison of p-CNS-X samples with other reported materials.

Compound	Specific capacitance (F g <sup>-1</sup> )	Electrolyte	References
ACGL (Carbon from ginkgo leaves)	364 (0.5 A g <sup>-1</sup> )	6 M KOH	29
N,S-PCNs1-1 (carbon from catkin)	298 (0.5 A g <sup>-1</sup> )	6 M KOH	30
FCC slurry	291 (1 A g <sup>-1</sup> )	6 M KOH	31
CS-HPGC	332 (0.5 A g <sup>-1</sup> )	6 M KOH	32
S-PCNS	312 (0.5 A g <sup>-1</sup> )	6 M KOH	33
Asn-5-NaHCO <sub>3</sub>	148 (0.5A g <sup>-1</sup> )	6 M KOH	34
porous carbon nanosheets	150.4(0.05A g <sup>-1</sup> )	6 M KOH	35
N, S co-doped PCFF	250 (0.5 A g <sup>-1</sup> )	6 M KOH	36
S-DG <sub>DMSO</sub>	261.43 (10 mVs <sup>-1</sup> ) 337.16 (10 mVs <sup>-1</sup> ) 280.06 (10 mVs <sup>-1</sup> )	1 M Na <sub>2</sub> SO <sub>4</sub> 1 M H <sub>2</sub> SO <sub>4</sub> 1.5 M NaOH	37
S-containing activated C	195 240	6 M LiCl 1 M HCl	38
CNOs/4-ABA	<34.44	0.1 M H <sub>2</sub> SO <sub>4</sub>	39
oz-CNOs	43.40	Na <sub>2</sub> SO <sub>4</sub>	40
CNOs/PDDA	20-30	0.1 M H <sub>2</sub> SO <sub>4</sub>	41
C-700	695 (50 mA g <sup>-1</sup> )	1 M H <sub>2</sub> SO <sub>4</sub>	42
p-CNS-800	375 (1 A g <sup>-1</sup> ) 615 (0.5 A g <sup>-1</sup> ) 515 (1 A g <sup>-1</sup> )	6 M KOH 6 M KOH 1M H <sub>2</sub> SO <sub>4</sub>	This work This work This work

935 (0.5 A g <sup>-1</sup> )	1M H <sub>2</sub> SO <sub>4</sub>	This work
------------------------------	-----------------------------------	-----------

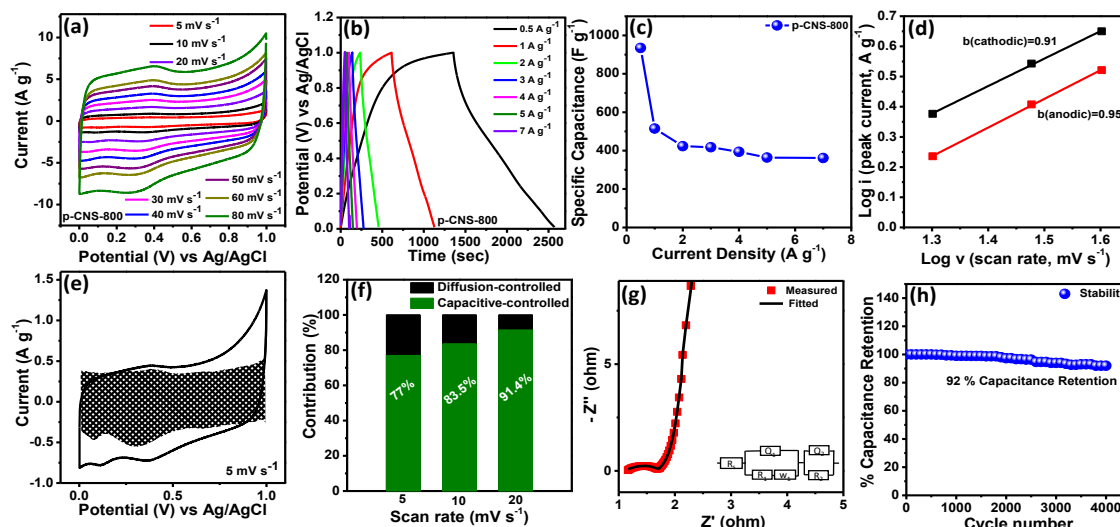
Dunn's method is used to differentiate diffusive and EDLC type contribution by using the equation 4.6:

$$i(V) = av^b \quad (4.6)$$

Here a and b are adjustable parameters obtained by plotting log v vs. log i. The b-value provides insight into charge storage kinetics. The current is capacitive when b approaches to 1 then and the current is diffusion limited when b is close to 0.5. Moreover, the capacitive contribution can be quantitatively analyzed according to equation 4.7.

$$i(V) = k_2v^{1/2} + k_1v \quad (4.7)$$

i (V) presents the current at potential V. v stands for scan rate, k<sub>1</sub> and k<sub>2</sub> are the constants, and k<sub>2</sub>v<sup>1/2</sup> and k<sub>1</sub>v represent the diffusive and capacitive current respectively. The capacitive contribution of p-CNS-800 at 10 mV s<sup>-1</sup> was calculated, presented in Figure 4.4(g). Capacitive contributions at different sweep rates varying from 10-60 mV s<sup>-1</sup> are presented in Figure 4.4(h) showing 95% capacitive contribution at a scan rate of 60 mV s<sup>-1</sup>. For the commercialization of supercapacitor, a cyclic durability test is necessary. The Cyclic performance test was performed in a three-electrode system for p-CNS-800 at 10 A g<sup>-1</sup> current density. Figure 4.4(i) presents the cyclic performance test of p-CNS-800 for 6k cycles under 10 A g<sup>-1</sup> current with 93.5 % capacitance retention of its initial value.

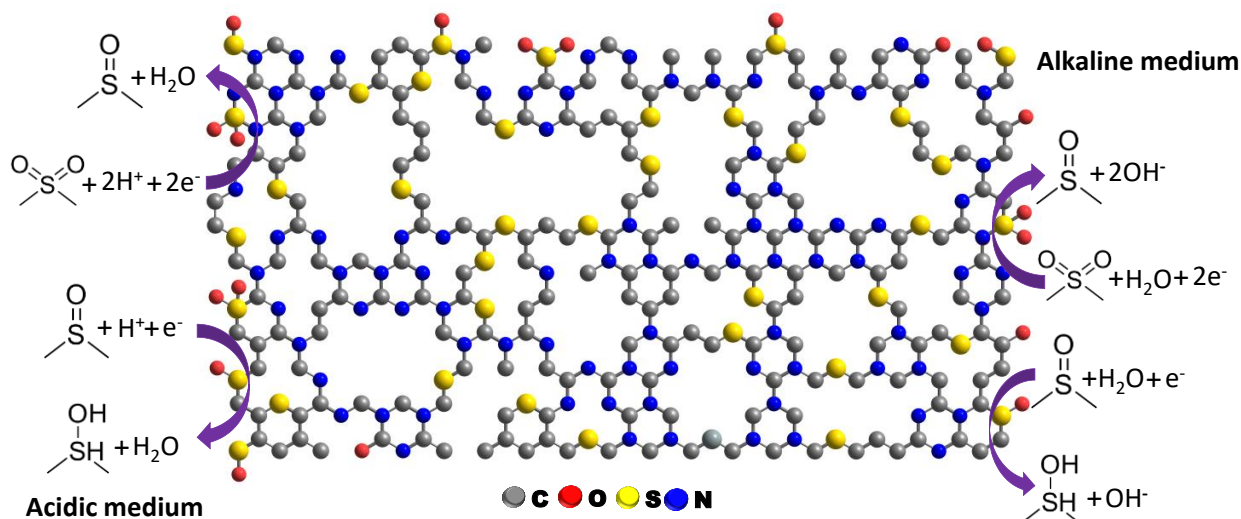


**Figure 4.5.** (a, b) CV plots at 5-80 mV s<sup>-1</sup> and CD diagram at 0.5-7 A g<sup>-1</sup> current for p-CNS-800. (c) Comparison of C<sub>s</sub> vs. current density. (d) Log (i) w.r.t log (v) plot. (e) Contribution of capacitive controlled process for p-CNS-800 at 5 mV s<sup>-1</sup> scan rate. (f) Capacitive charge storage processes at different scan rates (5 to 20 mV s<sup>-1</sup>). (g) EIS spectra for p-CNS-800 in 1M H<sub>2</sub>SO<sub>4</sub> electrolyte on Ti foil. (h) Cyclic test of CNS-800 under 10 A g<sup>-1</sup> in 1M H<sub>2</sub>SO<sub>4</sub> electrolyte.

In addition to that, the electrochemical performance of p-CNS-800 was carried out in 1M H<sub>2</sub>SO<sub>4</sub> electrolyte. Figure 4.5(a) represents the CV plots at different scan rates varying from 5-80 mV s<sup>-1</sup> in a voltage range of 0-1 V. All CV profiles show a pseudocapacitive behaviour of p-CNS-800 electrode material as two reversible peaks are observed in CV curves and triangles in the charging-discharging profiles are not exactly symmetrical in acid electrolyte. Redox reactions involving sulphone groups can contribute to pseudocapacitance through sulfur functionalities. The following reactions are proposed. The first step involves the reduction of sulphones to sulfoxides (Reaction (1)). It is reversible to reduce sulfoxide groups to sulfenic acid<sup>38</sup> (Reaction (2)). Yushin G. et al. reported that, in an acidic electrolyte i.e. 1M H<sub>2</sub>SO<sub>4</sub>, the distinct redox peaks in the voltammograms are due to the reduction of -SO<sub>x</sub> groups of sulfur-containing

activated carbon<sup>37-38</sup>. The capacitance from the CV curves is calculated by using equation 4.2 and was obtained to be 206 F g<sup>-1</sup> under 5 mV s<sup>-1</sup> scan rate. The GCD profiles measured at different current densities are presented in Figure 4.5(b) showing nonlinear sloping potential profiles. This suggests that the Faradaic reactions take place on the surface of p-CNS-800, which is in good agreement with the CV results. Figure 4.5(c) shows capacitance with different current densities. The p-CNS-800 exhibits a very high C<sub>s</sub> value of 935 F g<sup>-1</sup> under 0.5 A g<sup>-1</sup> whereas the C<sub>s</sub> value were 515, 423, 417, 393.6, 364, and 361.8 F g<sup>-1</sup> under 1, 2, 3, 4, 5, and 7 A g<sup>-1</sup> current. An excellent retention of 70.3 % of its initial capacitance value was observed at a higher discharging rate of 7 A g<sup>-1</sup> compared to 1 A g<sup>-1</sup> current. The capacitive contribution can be quantitatively analyzed by Dunn's method according to equation 4.6. The b-value provides valuable insight into charge storage kinetics. The plot of log i vs. log (v) is shown in Figure 4.5(d). The b value of anodic and cathodic peaks is found to be 0.95 and 0.91 (very close to 1), revealing the capacitive nature of the charge transfer processes. Figure 4.5(e) shows the contribution plot at 5 mV s<sup>-1</sup>. The capacitive/diffusion contribution at different scan rates from 5-20 mV s<sup>-1</sup> are presented in Figure 4.5(f). The diffusion contribution of p-CNS-800 at a low sweep rate of 5 mV s<sup>-1</sup> is ~23% whereas it is ~8.4% at a sweep rate of 20 mV s<sup>-1</sup>. The very high electrochemical performance of p-CNS-800 under this low current density of 0.5 A g<sup>-1</sup> can be attributed to the favourable reversible faradic reaction at low current densities. The diffusion contribution arises owing to the presence of N and S atoms in the carbon matrix, which is favourable for reversible faradic reactions at low current densities whereas capacitive contribution is dominated at high current densities. Figure 4.5(g) displays the Nyquist plot for the prepared electrode material in a three-electrode configuration. The capacitance retention after the fast charge- discharge

condition is possible if the system has a very fast diffusion of ions. The  $R_s$  and  $R_{CT}$  are obtained to be 1.17 and 0.51  $\Omega$  showing fast diffusion of electrolyte ions. 4k charging-discharging cycles are carried out to test the cyclic stability performance in 1M H<sub>2</sub>SO<sub>4</sub> electrolyte (Figure 4.5(h)) showing a 92% capacitance retention of the electrode material.



**Scheme 4.2.** Possible redox reactions of sulphur-oxo species in acidic and alkaline medium.

The very high supercapacitive performances of p-CNS-800 can be attributed to the synergetic effect originating from unique microporous 2D carbon sheets and optimal heteroatoms (S, N) doping in the carbon matrix. Scheme 4.2 demonstrates the mechanism for the high capacitance of p-CNS-800. The 2D porous carbon sheets with nano-meter thickness facilitate easy ion/mass transport. The presence of nitrogen atoms in the carbon matrix could enhance capacitance, possibly due to redox reactions of N-containing functional groups. The S atoms in the carbon matrix contributed to enhancing electrochemical performances. The higher charge transfer process in CNS material may be due to the synergistic interaction of unsaturated carbon atoms with the

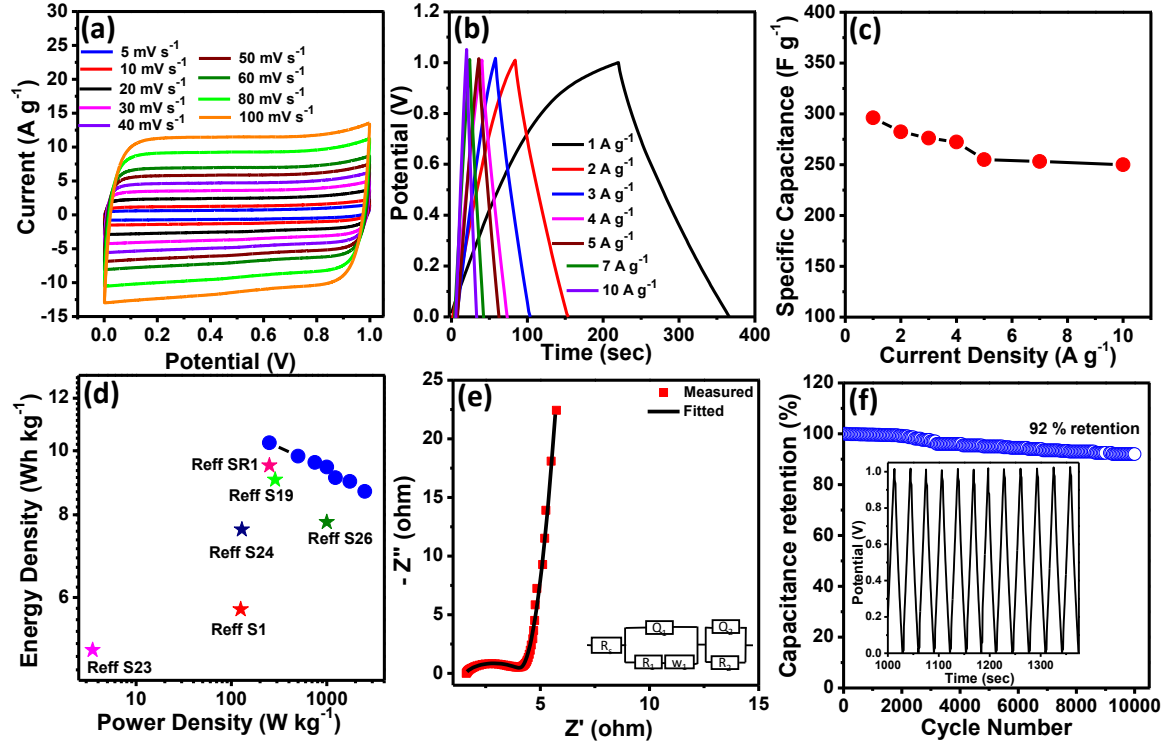


electron-rich S atoms. The presence of C-S in the carbon matrix modifies the surface as the n-type S dopant provides more polarized surfaces<sup>43</sup>. Several reversible faradic reactions take place in the CNS matrix due to the presence of sulfone and sulfoxide species.

### **Electrochemical Behaviour of symmetrical supercapacitor**

For practical application, the symmetric device was assembled by using p-CNS-800 in a CR2032 coin cell. All the CV and GCD measurements were performed with 6M KOH electrolyte in a voltage range of 0-1 V. Figure 4.6(a) despite the CV cycles of the symmetric device at sweep rate ranging from 5-100 mV s<sup>-1</sup>. The quasi-rectangular type nature of the CV plots without any distortion at a higher sweep rate implies the EDLC nature of the electrode. The excellent reversibility nature of the samples was confirmed by the symmetrical and liner charging-discharging GCD curves (Figure 4.6(b)). Figure 4.6(c) represents the variation of C<sub>s</sub> value (calculated by using equation 4.3) vs. current density of 1-10 A g<sup>-1</sup>. A C<sub>s</sub> value of 296.12 F g<sup>-1</sup> was obtained at 1 A g<sup>-1</sup> current and it maintains a capacitance retention of 92.89 % from its early value after 10 A g<sup>-1</sup> current for the symmetric device. Figure 4.6(d) represents the Ragone plot for a symmetric capacitor (calculated by using equations 4.4 and 4.5) and its comparison with previous reports<sup>25, 42, 44-48</sup>. The device shows maximum ED of 10.28 W h kg<sup>-1</sup> and PD of 2500 W kg<sup>-1</sup>. The EIS spectra of the symmetric device show a vertical line at the low-frequency region indicating the outstanding capacitance of the p-CNS-800// p-CNS-800 device. The R<sub>CT</sub> and R<sub>s</sub> values were obtained to be 1.57 Ω and 2.48 Ω (Figure 4.6(e)). The low R<sub>ct</sub> values indicate the low resistance and high conductivity of the material. The cyclic stability of 10k cycles was performed at 10 A g<sup>-1</sup> current density as presented in

Figure 4.6(f) indicating the device maintains a capacitance of 92 % of its initial measured value. The inset of Figure 4.6(f) represents the CD cycles showing symmetrical charging-discharging time and good capacitive behaviour of the material.

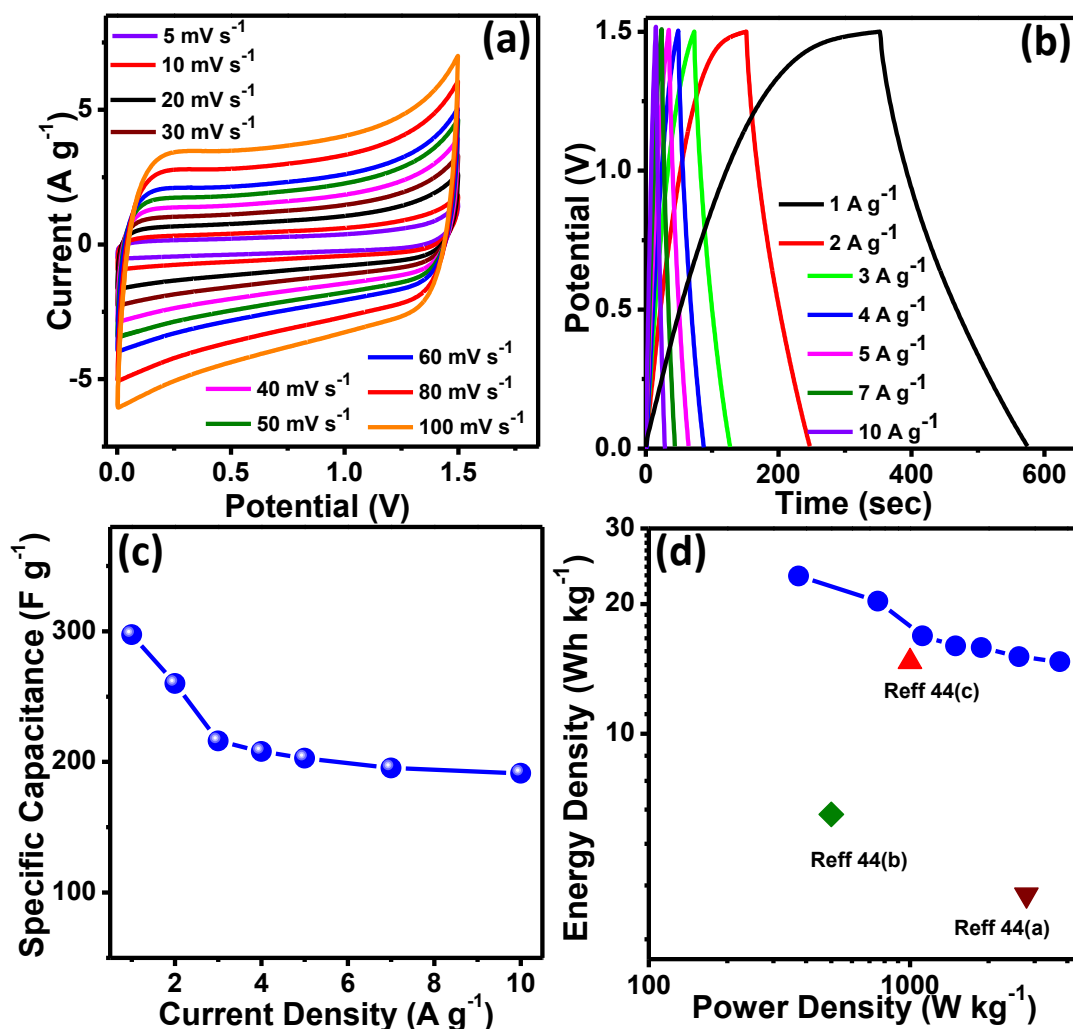


**Figure 4.6.** (a) CV diagrams of a p-CNS-800// p-CNS-800 device (5 to 100 mV s<sup>-1</sup>). (b) GCD plot under 1 to 10 A g<sup>-1</sup> current. (c) C<sub>s</sub> value plot under diff. current densities. (d) ED vs. PD plot and its comparison with previous literatures. (e) EIS plot. (f) Cyclic test for 10000 cycles under 10 A g<sup>-1</sup> in 6M KOH.

In order to verify the real device characteristics, CV measurements in 1 M H<sub>2</sub>SO<sub>4</sub> were performed on two-electrode cells. CV and CD curves are presented in Figure 4.7(a) and (b) in 0–1.5 V voltage range. The rectangular shape in the CV pattern represents perfect double-layer charge storage. The C<sub>s</sub> value of p-CNS-800// p-CNS-800 device is 297.4 F g<sup>-1</sup> under 1 A g<sup>-1</sup>, which decreases to 191.34 F g<sup>-1</sup> under 10 A g<sup>-1</sup> retaining 64.34 % of its initial C<sub>s</sub> value. The difference of the device capacitance from the three-

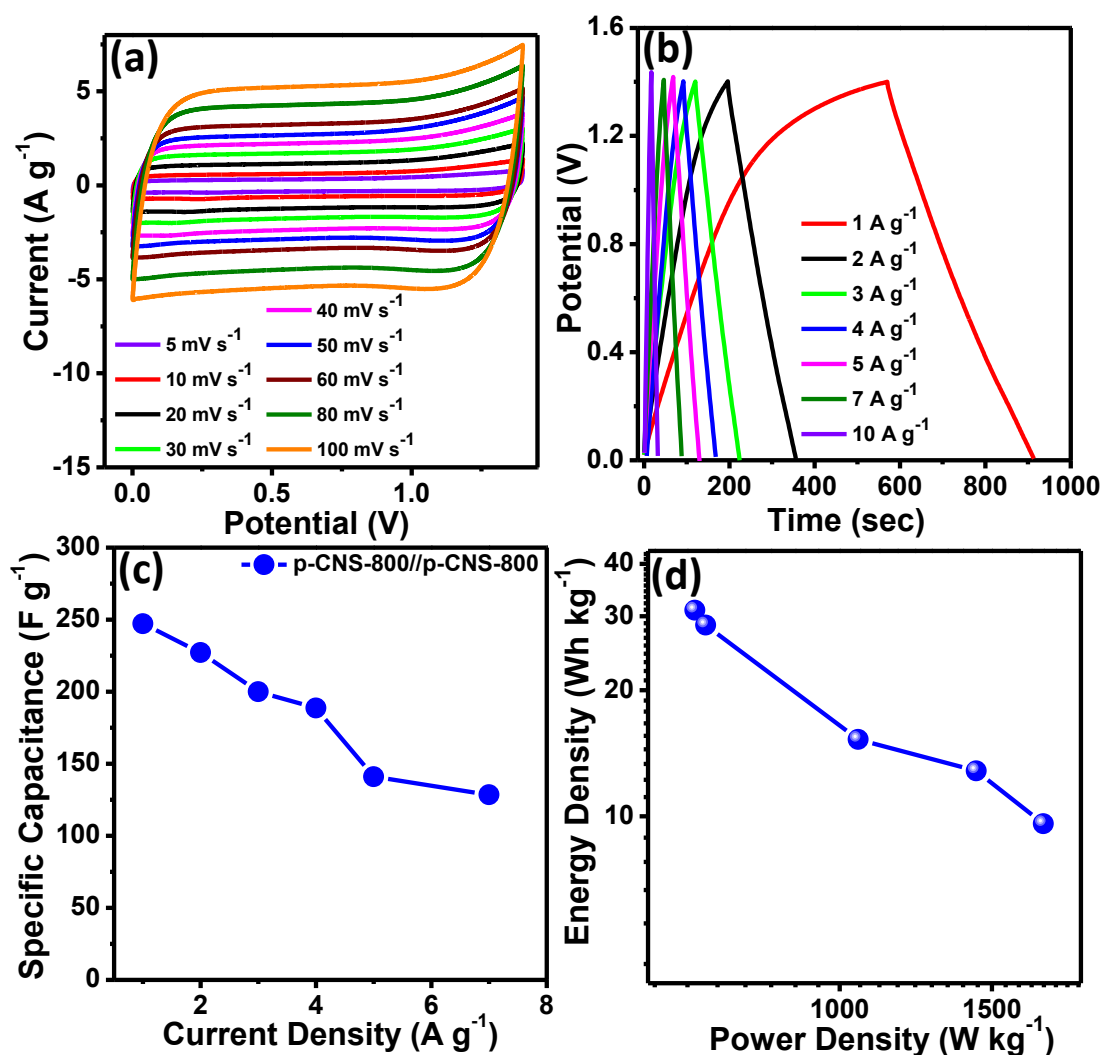
electrode system is due to the asymmetry in the adsorption of negative/positive ions. Another reason may be due to the capacitance of the p-CNS-800// p-CNS-800 device based on the full cell including two electrodes are theoretically 1/4 of the value of a single electrode<sup>49</sup>. Furthermore, in two-electrode cell, Ti foil and microfiber filter paper were used as current collectors and separators, respectively. As a result, the impedance may increase and diffusion of ions may be reduced. In addition to that, the electrode mass loading is also responsible for the decreased capacitance. Figure 4.7(c) shows the variation of  $C_s$  value with current density. Figure 4.7(d) displays the Ragone plot for the p-CNS-800// p-CNS-800 symmetric device with the calculated PD of 3750.13 W kg<sup>-1</sup> and ED of 23.234 W h kg<sup>-1</sup> and comparison with literature<sup>50-52</sup>. As a result of the asymmetry in charge storage, the electrode material may not perform to its full potential in a working symmetric cell capacitors and distinctly superior to that of activated carbons.

In light of practical applications, it is necessary to evaluate how electrode materials behave in a neutral medium because neutral electrolytes allow supercapacitors to extend their working potential window, which directly improves their energy density. Therefore, we evaluated the performance of the CNS-800// p-CNS-800 device in 1M Na<sub>2</sub>SO<sub>4</sub> electrolyte. The CV plots of a symmetric capacitor at 30 mV s<sup>-1</sup> sweep rate under the different potential windows are shown in Figure S4.5. When the potential approaches 1.8 V, the CV current rises sharply as the electrolyte decomposition takes place. So we fix the voltage range at 1.4 V and the potential window of 0-1.4 V was used for all measurements. Figure 4.8(a) represents the CV profile under the sweep rate of 5-100 mV s<sup>-1</sup>. All the CV curves present nearly symmetrical quasi-rectangular shapes.



**Figure 4.7.** (a, b) CV and GCD curves (c) plot of  $C_s$  w.r.t current densities. (d) ED vs. PD plot for p-CNS-800// p-CNS-800 device in 1M H<sub>2</sub>SO<sub>4</sub>.

The device offers a  $C_s$  of 247 F g<sup>-1</sup> at a current of 1 A g<sup>-1</sup> and retention of 52% capacitance from its initial value after 7 A g<sup>-1</sup> current. The plot of the  $C_s$  with respect to current density is depicted in Figure 4.8(c). Both ED and PD were calculated from the above  $C_s$  values. The symmetric device offers an exceptional ED of nearly 31.01 W h kg<sup>-1</sup> and a PD of 1720.36 W kg<sup>-1</sup> (Figure 4.8(d)).



**Figure 4.8.** (a, b) CV and GCD plots under different sweep rate and current densities. (c)  $C_s$  plot of device under different current (1-7 A g<sup>-1</sup>). (d) ED versus PD plot profile of p-CNS-800// p-CNS-800 device in 1M Na<sub>2</sub>SO<sub>4</sub>.

#### 4.4.3. Gas Adsorption Behaviour

Hydrogen adsorption isotherms at 77K with pressure from 0 to 1 bar for all four samples synthesized at different activated temperatures are presented in Figure 4.9(a).

All the samples have a broad knee indicating the continuous rise in H<sub>2</sub> storage

capacities up to 1 bar pressure. With a rise in activation temperature, the H<sub>2</sub> adsorption capacities increases due to the increase in large pore volume and SSA. For sample p-CNS-900, the highest H<sub>2</sub> storage capacity was observed to be 2.6 wt%. The hydrogen uptake capacity of p-CNS-X samples increases from 2.35 % for p-CNS-600 to 2.6 % for p-CNS-900. The bar plot for all the samples is depicted in Figure S4.6(a). Figure S4.6(b) represents the change in H<sub>2</sub> uptake as a function of SSA. For sample p-CNS-600, the decrease in the H<sub>2</sub> storage capacity is due to the small microspore size and low SSA. This indicates that the porous carbon has a great significance and microspore volume and SSA plays an important role in hydrogen storage capacity. In addition to H<sub>2</sub> adsorption, two different temperatures (25<sup>0</sup>C and 0 <sup>0</sup>C) were used to analyse the CO<sub>2</sub> desorption/adsorption isotherm of the prepared materials in the pressure range up to 1 bar. The CO<sub>2</sub> uptake capacities of p-CNS-600 samples are found to be 4.5 mmol/g at 273 K and 2.73 mmol g<sup>-1</sup> at 298K, presented in Figure 4.9(b). The high CO<sub>2</sub> adsorption capacities of p-CNS-600 are related to its high SSA of 2184.6 m<sup>2</sup>/g. Figure 4.9(b, c) represents the CO<sub>2</sub> adsorption isotherm of p-CNS-X materials at 0 <sup>0</sup>C and 25<sup>0</sup>C. The CO<sub>2</sub> uptake capacity of samples p-CNS-600, 700, 800, and 900 were obtained to be 2.74, 2.7, 2.12, and 2.16 mmol g<sup>-1</sup> at 25 <sup>0</sup>C and 4.5, 4.26, 3.8, and 3.72 mmol g<sup>-1</sup> at 0 <sup>0</sup>C respectively. A comparison of the CO<sub>2</sub> uptake of various porous carbon materials with this work is provided in table 4.3.

**Table 4.3.** CO<sub>2</sub> uptake capacities of carbon materials at 25 <sup>0</sup>C temperature and 1 bar pressure.

Sample	CO <sub>2</sub> Uptake (mmol g <sup>-1</sup> )	Pressure	References
--------	---	----------	------------

Microporous oxygen-doped carbons	2.84	1 bar	53
Nitrogen-doped polyimine-based carbons	3.10	1 bar	54
N,S co-doped carbon for glucose and thiourea	3.4	1 bar	55
Poplar catkin- based Nitrogen- Doped Porous Carbon	4.05	1 bar	56
N, O-doped biocarbon	2.8	1 bar	57
S,N co-doped carbon polybenzoxazine	4.55	1 bar	58
N, O-co-doped porous carbon/carbon nanotube composite derived from coal	3.7	1 bar	59
p-CNS-600	4.5	1 bar	This work

The both presence of sulfur content and textural properties play a very important role in the uptake of CO<sub>2</sub>. The presence of sulfur (oxidized sulfur) in the porous carbon material increases the CO<sub>2</sub> uptake capacity<sup>60-61</sup>. The sulfur content is highest up to 7.2 wt% for the p-CNS-600 sample and the sulfur content decreases as the temperature rises from 600 to 900 °C in the carbon samples owing to the formation of volatile sulfur species at higher temperature<sup>62</sup>. The strength of interaction between adsorbents and

CO<sub>2</sub> molecule also called CO<sub>2</sub> adsorption energy i.e. isosteric heat of adsorption ( $Q_{st}$ ) for heteroatom doped carbon materials were calculated using CO<sub>2</sub> sorption isotherms measured at 25 °C and 0 °C by using Clausius-Clapeyron equation<sup>62</sup>. Figure 4.9(d) shows the plot of  $Q_{st}$  as a function of CO<sub>2</sub> uptake for all four samples. Initially, the  $Q_{st}$  for p-CNS-X samples at low CO<sub>2</sub> uptake varies in the range of 30.56-21 kJ mol<sup>-1</sup>. The highest  $Q_{st}$  values result from the strong interaction between S-doped porous carbon and CO<sub>2</sub> molecules. The adsorption of CO<sub>2</sub> on the carbon surface may be not only due to the formation of strong base-acid interaction between basic S and C functional groups and acidic CO<sub>2</sub> molecules but also due to the strong pole-pole interaction between polar sites of functional groups present in sulfur and quadrupole moments created by CO<sub>2</sub> molecules. The highest sulfur-containing sample p-CNS-600 exhibits the highest  $Q_{st}$  value of 30.56 kJ mol<sup>-1</sup> at higher coverage. Samples containing intermediate S content but having higher total and microporous surface area have comparable  $Q_{st}$  of 21 kJ mol<sup>-1</sup> at high coverage. All the result suggest that the presence of the S functional group not only play a vital role in determining the interaction between the porous carbon material and CO<sub>2</sub> but also the textural property are crucial for the higher CO<sub>2</sub> coverage. For the separation of flue gas, evaluation of the selective uptake of CO<sub>2</sub> over other gases like methane and nitrogen is a key parameter for concern. So for all the samples prepared at four different activation temperatures, the adsorption selectivity was measured. The selectivity of the binary gas mixture was obtained by using IAST (Ideal Adsorption Solution Theory) method<sup>63</sup>. Figure 4.9(e) shows the CO<sub>2</sub> and N<sub>2</sub> sorption isotherms comparison plot for p-CNS-X samples at 25 °C and 1 bar pressure.

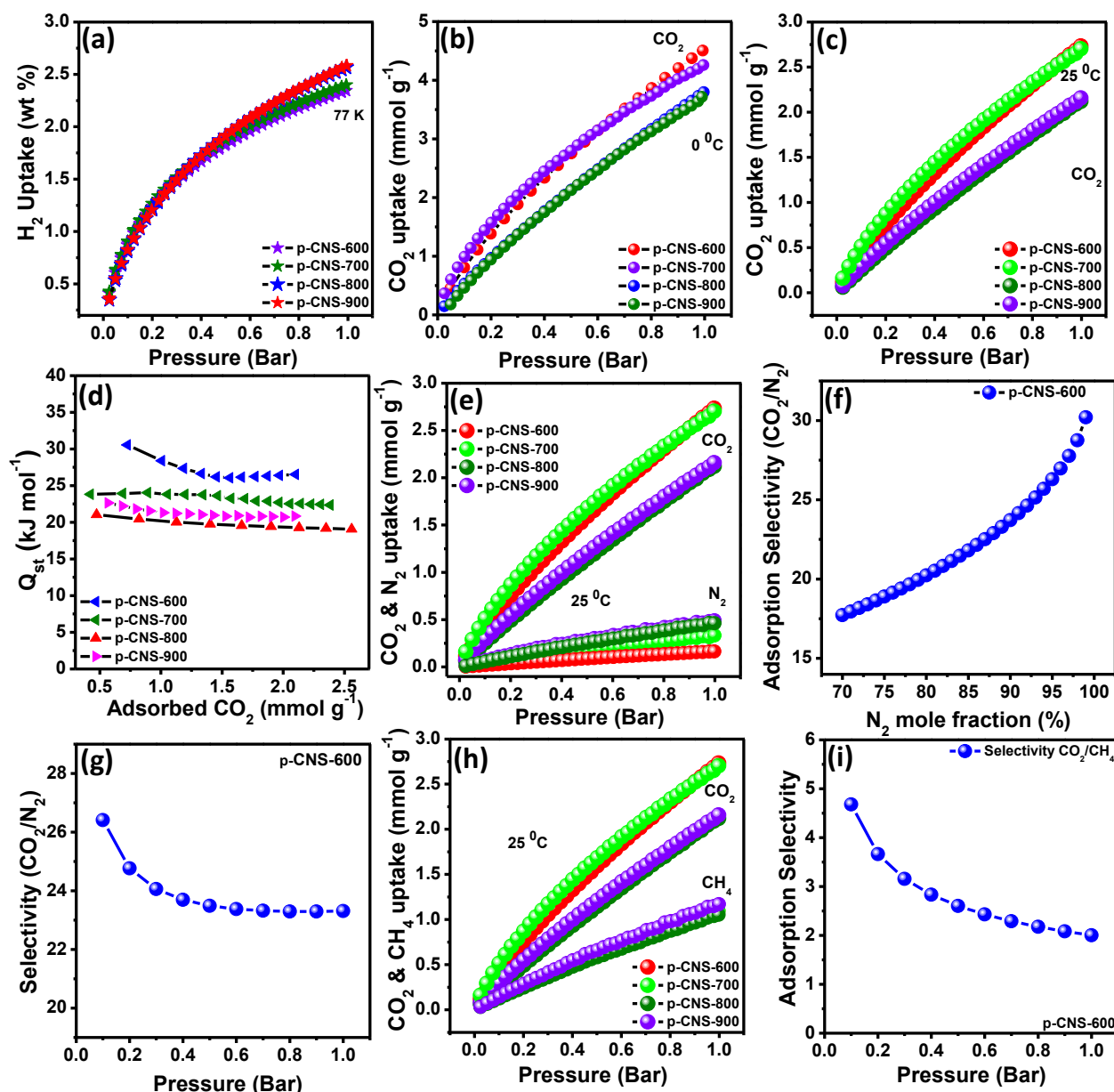


$$S = \frac{P_2 q_1}{P_1 q_2}$$

Where  $P_1$  and  $P_2$  stand for partial pressure and  $q_1$  and  $q_2$  refer to molar absolute adsorption capacities of components denoted as 1 and 2 respectively.

Selectivity for CO<sub>2</sub>/N<sub>2</sub> are calculated for a binary mixture ratio of 15:85 under a total pressure of 1 bar. The plot for selectivity of CO<sub>2</sub>/N<sub>2</sub> are presented in Figure 4.9(f) showing maximum selectivity of 21.8 for p-CNS-600 and selectivity continuously decreases for the samples activated at high temperatures. Selectivity values of CO<sub>2</sub>/N<sub>2</sub> for p-CNS-700, p-CNS-800, and p-CNS-900 are calculated to be 19.2, 11.3, and 9.1 respectively. The decrease in the selectivity value of CO<sub>2</sub>/N<sub>2</sub> with an increase in activation temperature may be due to the decrease in sulfur content and increase in pore size of the synthesized porous carbon materials. A comparison plot for N<sub>2</sub> and CO<sub>2</sub> adsorption isotherm of p-CNS-X samples are measured at 25 °C presented in Figure S4.7. Changes in the adsorption selectivity of CO<sub>2</sub>/N<sub>2</sub> with respect to pressure are presented in Figure 4.9(g). Figure S4.8 represents the selectivity of CO<sub>2</sub>/N<sub>2</sub> for binary mixture in a 15:85 ratio under the pressure of 1 bar. A rise in selectivity was observed by moving from 1 bar pressure to a lower pressure region. Selectivity of CO<sub>2</sub>/CH<sub>4</sub> is also calculated at 25 °C under 1 bar pressure with a mole fraction of 50:50. A comparison of CO<sub>2</sub> and CH<sub>4</sub> sorption isotherms for p-CNS-X is measured at 25 °C which is presented in Figure 4.9(h). Figure S4.9 shows the bar plot for the selectivity of CO<sub>2</sub>/CH<sub>4</sub> for binary mixture in a 50:50 ratio under the pressure of 1 bar. The maximum selectivity of CO<sub>2</sub>/CH<sub>4</sub> is observed for p-CNS-600 and the selectivity value is 2.64 while for p-CNS-700, 800, and 900, the values are obtained to be 2, 1.98, and 2.16 respectively. Adsorption selectivity predicted from the IAST for a binary mixture of CO<sub>2</sub>/CH<sub>4</sub> (50:50) at a temperature of 25 °C were presented in Figure 4.9(i). Maximum

selectivity was obtained at low pressure whereas, with an increase in pressure to 1 bar, the selectivity decreases to 2. The above-mentioned selectivity for CO<sub>2</sub>/CH<sub>4</sub> and CO<sub>2</sub>/N<sub>2</sub> makes the hetero atom doped porous carbon an advanced gas separator.



**Figure 4.9.** (a) H<sub>2</sub> storage capacities of p-CNS-X under 1 bar pressure at 77K. (b, c) CO<sub>2</sub> uptake isotherms of p-CNS-X at 0 °C and 25 °C respectively. (d) Q<sub>st</sub> as a function of amount of CO<sub>2</sub> adsorbed for p-CNS-X. (e) CO<sub>2</sub> and N<sub>2</sub> sorption isotherms of amount of CO<sub>2</sub> adsorbed for p-CNS-X. (f) CO<sub>2</sub> and N<sub>2</sub> sorption isotherms of amount of CO<sub>2</sub> adsorbed for p-CNS-X. (g) CO<sub>2</sub> and N<sub>2</sub> sorption isotherms of amount of CO<sub>2</sub> adsorbed for p-CNS-X. (h) CO<sub>2</sub> and CH<sub>4</sub> sorption isotherms of amount of CO<sub>2</sub> adsorbed for p-CNS-X. (i) CO<sub>2</sub> and CH<sub>4</sub> sorption isotherms of amount of CO<sub>2</sub> adsorbed for p-CNS-X.

comparison plot for p-CNS-X at 25 °C. (f) The CO<sub>2</sub>/N<sub>2</sub> selectivity at 25 °C and total pressure of 1 bar for p-CNS-600 sample. (g) Adsorption selectivity for binary gas mixture of CO<sub>2</sub>/N<sub>2</sub> (15:85) at temperature of 25 °C for p-CNS-600. (h) CO<sub>2</sub> and CH<sub>4</sub> Comparison sorption isotherms of p-CNS-X measured at 25 °C. (i) Adsorption selectivity for binary mixture of CO<sub>2</sub>/CH<sub>4</sub> (50:50) at temperature of 25 °C.

## 4.5. CONCLUSIONS

In summary, facile bottom-up synthesis for two-dimensional N/S co-doped carbon sheets and 2D microporous N/S co-doped carbon sheets are reported. The S/N doped nano-meter thick 2D carbon sheets are formed by hydrothermal heating of organic molecules/carbonization at 700 °C. Finally, microporous 2D carbon sheets are produced from 2D sheets by KOH activation at high temperatures. The unique porous structures have a majority of micro-pores (<2 nm) with a significant number of sub-nanometer pores (>1 nm). These porous 2D sheets possess a high SSA of 2847.8 m<sup>2</sup>/g and a high pore volume of 1.9 cc g<sup>-1</sup>. Owing to the unique pore structure and optimal S/N doping, the 2D-microporous-carbon nano-sheets show exceptional supercapacitor performance with a C<sub>s</sub> value of 935 F g<sup>-1</sup> at 0.5 A g<sup>-1</sup> in 1M H<sub>2</sub>SO<sub>4</sub> electrolyte. It also shows a C<sub>s</sub> value of 375 F g<sup>-1</sup> at 1 A g<sup>-1</sup> in 6M KOH with an outstanding rate capability of 95% after 10k cycles. A symmetric supercapacitor device, p-CNS-800//p-CNS-800 shows outstanding energy densities and power densities. The S, N doped porous carbon nano-sheets show CO<sub>2</sub> uptake of 4.5 mmol g<sup>-1</sup> and 2.73 mmol g<sup>-1</sup> at 273 and 298 K respectively with selectivity for CO<sub>2</sub>/N<sub>2</sub> and CO<sub>2</sub>/CH<sub>4</sub> found to be 21.8 and 2.6 respectively. The H<sub>2</sub> uptake of these 2D porous carbon sheets is also found to be 2.6 wt % at 77 K under 1 bar pressure. This work aims to provide a facile bottom-up

synthesis strategy to form S, N co-doped 2D carbon nano-sheets and porous 2D carbon sheets for supercapacitor and gas adsorption applications.

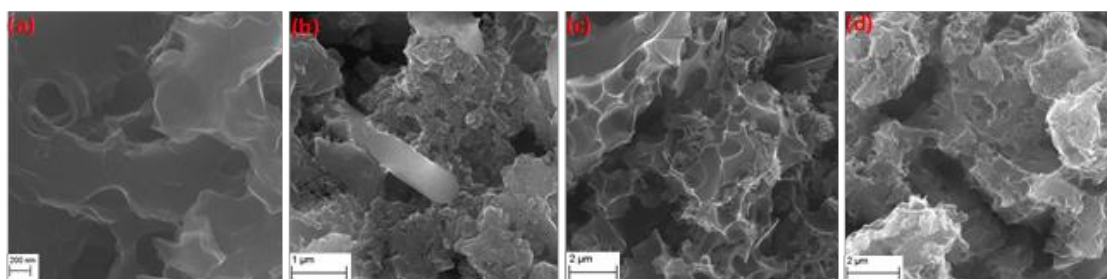
## 4.6 REFERENCES

- (1) Lei, W.; Guo, J.; Wu, Z.; Xuan, C.; Xiao, W.; Wang, D. *Science Bulletin* **2017**, 62, 1011-1017.
- (2) Jiang, H.; Lee, P. S.; Li, C. *Energy & Environmental Science* **2013**, 6, 41-53.
- (3) Wang, Q.; Yan, J.; Wang, Y.; Wei, T.; Zhang, M.; Jing, X.; Fan, Z. *Carbon* **2014**, 67, 119-127.
- (4) Zhou, J.; Li, N.; Gao, F.; Zhao, Y.; Hou, L.; Xu, Z. *Scientific Reports* **2014**, 4, 6083.
- (5) Hou, J.; Cao, C.; Idrees, F.; Ma, X. *ACS Nano* **2015**, 9, 2556-2564.
- (6) *Acs Applied Materials and Interfaces* **2014**, 6, 2657-2665.
- (7) Chen, J.; Lin, C.; Zhang, M.; Jin, T.; Qian, Y. *ChemElectroChem* **2020**, 7, 3311-3318.
- (8) Shang, T. X.; Cai, X. X.; Jin, X. J. *RSC Advances* **2015**, 5, 16433-16438.
- (9) Gao, Y.; Cui, P.; Liu, J.; Sun, W.; Chen, S.; Chou, S.; Lv, L.-P.; Wang, Y. *ACS Applied Energy Materials* **2021**, 4, 4519-4529.
- (10) Candelaria, S. L.; Shao, Y.; Zhou, W.; Li, X.; Xiao, J.; Zhang, J.-G.; Wang, Y.; Liu, J.; Li, J.; Cao, G. *Nano Energy* **2012**, 1, 195-220.
- (11) Zhang, D.; Hao, Y.; Zheng, L.; Ma, Y.; Feng, H.; Luo, H. *Journal of Materials Chemistry A* **2013**, 1, 7584-7591.
- (12) Xiang, S.; Yang, X.; Lin, X.; Chang, C.; Que, H.; Li, M. *Journal of Solid State Electrochemistry* **2017**, 21, 1457-1465.
- (13) Nazir, G.; Rehman, A.; Park, S.-J. *Journal of CO<sub>2</sub> Utilization* **2020**, 42, 101326.
- (14) Hamed, A.; Hessein, A.; Abd El-Moneim, A. *Applied Surface Science* **2021**, 551, 149457.
- (15) Daulbayev, C.; Lesbayev, B.; Bakbolat, B.; Kaidar, B.; Sultanov, F.; Yeleuov, M.; Ustayeva, G.; Rakhymzhan, N. *South African Journal of Chemical Engineering* **2022**, 39, 52-61.
- (16) Shahtalebi, A.; Mar, M.; Guérin, K.; Bhatia, S. K. *Carbon* **2016**, 96, 565-577.
- (17) Kim, J.; Han, J.; Ha, D.; Kang, S. *Journal of Materials Chemistry A* **2014**, 2, 16645-16651.
- (18) Sevilla, M.; Valle-Vigón, P.; Fuertes, A. B. *Advanced Functional Materials* **2011**, 21, 2781-2787.
- (19) Chmiola, J.; Yushin, G.; Gogotsi, Y.; Portet, C.; Simon, P.; Taberna, P. L. *Science* **2006**, 313, 1760-1763.
- (20) Wang, J.; Kaskel, S. *Journal of Materials Chemistry* **2012**, 22, 23710-23725.
- (21) Wu, D.; Cheng, J.; Wang, T.; Liu, P.; Yang, L.; Jia, D. *ACS Sustainable Chemistry & Engineering* **2019**, 7, 12138-12147.
- (22) Jäckel, N.; Simon, P.; Gogotsi, Y.; Presser, V. *ACS Energy Letters* **2016**, 1, 1262-1265.
- (23) Raymundo-Piñero, E.; Kierzek, K.; Machnikowski, J.; Béguin, F. *Carbon* **2006**, 44, 2498-2507.
- (24) Chen, H.; Yu, F.; Wang, G.; Chen, L.; Dai, B.; Peng, S. *ACS Omega* **2018**, 3, 4724-4732.
- (25) Chang, C.; Yang, X.; Xiang, S.; Lin, X.; Que, H.; Li, M. *Journal of The Electrochemical Society* **2017**, 164, A1601.
- (26) Paraknowitsch, J. P.; Thomas, A. *Energy & Environmental Science* **2013**, 6, 2839-2855.
- (27) Jiang, Y.; Fu, X.; Tian, R.; Zhang, W.; Du, H.; Fu, C.; Zhang, Z.; Xie, P.; Xin, J.; Fan, R. *Journal of Materials Science* **2020**, 55, 5832-5842.
- (28) Xie, P.; Li, Y.; Hou, Q.; Sui, K.; Liu, C.; Fu, X.; Zhang, J.; Murugadoss, V.; Fan, J.; Wang, Y.; Fan, R.; Guo, Z. *Journal of Materials Chemistry C* **2020**, 8, 3029-3039.

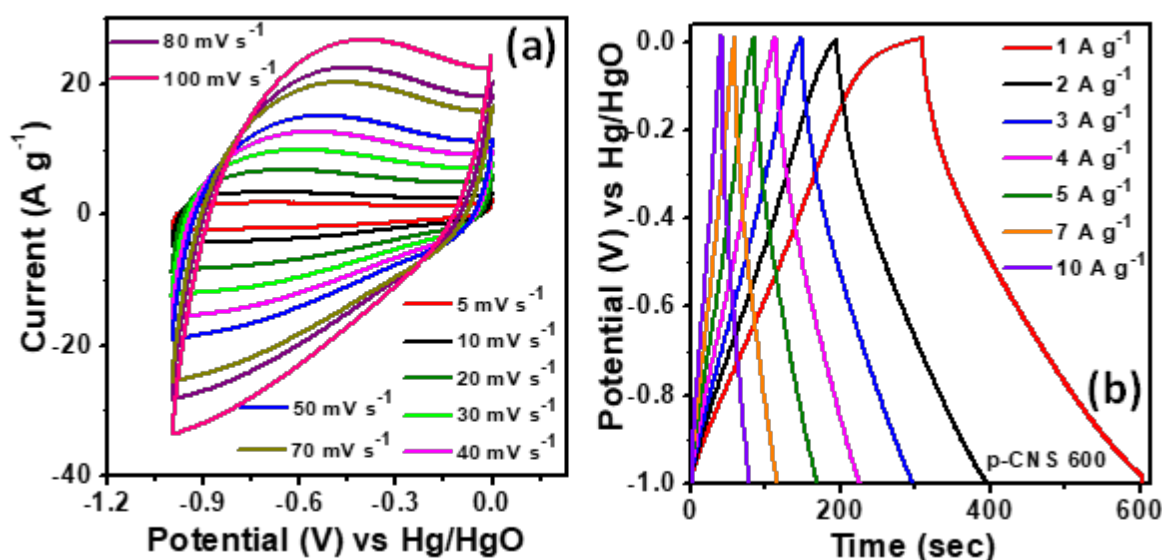
- (29) Hao, E.; Liu, W.; Liu, S.; Zhang, Y.; Wang, H.; Chen, S.; Cheng, F.; Zhao, S.; Yang, H. *Journal of Materials Chemistry A* **2017**, *5*, 2204-2214.
- (30) Li, Y.; Wang, G.; Wei, T.; Fan, Z.; Yan, P. *Nano Energy* **2016**, *19*, 165-175.
- (31) Zhao, F.; Song, F.; Chen, Q. *Applied Surface Science* **2021**, *561*, 150063.
- (32) Gong, Y.; Li, D.; Fu, Q.; Zhang, Y.; Pan, C. *ACS Applied Energy Materials* **2020**, *3*, 1585-1592.
- (33) Deng, W.; Zhang, Y.; Yang, L.; Tan, Y.; Ma, M.; Xie, Q. *RSC Advances* **2015**, *5*, 13046-13051.
- (34) Zhou, H.; Zhou, Y.; Wu, S.; Li, L.; Li, Y.; Guo, M.; Qi, Z.; Feng, C. *Journal of Alloys and Compounds* **2020**, *829*, 154549.
- (35) Zhang, W.; Lin, M.; Cheng, R.; Li, L.; Sun, Y.; Ran, S.; Lv, Y.; Ma, L. *Diamond and Related Materials* **2021**, *113*, 108278.
- (36) Chen, L.; Wen, Z.; Chen, L.; Wang, W.; Ai, Q.; Hou, G.; Li, Y.; Lou, J.; Ci, L. *Carbon* **2020**, *158*, 456-464.
- (37) Maity, S.; Banerjee, D.; Bhattacharya, G.; Roy, S. S.; Dhar, B. B. *ACS Applied Nano Materials* **2022**, *5*, 3548-3557.
- (38) Gu, W.; Sevilla, M.; Magasinski, A.; Fuertes, A. B.; Yushin, G. *Energy & Environmental Science* **2013**, *6*, 2465-2476.
- (39) Plonska-Brzezinska, M. E.; Mazurczyk, J.; Palys, B.; Breczko, J.; Lapinski, A.; Dubis, A. T.; Echegoyen, L. *Chemistry – A European Journal* **2012**, *18*, 2600-2608.
- (40) Plonska-Brzezinska, M. E.; Lapinski, A.; Wilczewska, A. Z.; Dubis, A. T.; Villalta-Cerdas, A.; Winkler, K.; Echegoyen, L. *Carbon* **2011**, *49*, 5079-5089.
- (41) Breczko, J.; Winkler, K.; Plonska-Brzezinska, M. E.; Villalta-Cerdas, A.; Echegoyen, L. *Journal of Materials Chemistry* **2010**, *20*, 7761-7768.
- (42) Gao, F.; Qu, J.; Zhao, Z.; Wang, Z.; Qiu, J. *Electrochimica Acta* **2016**, *190*, 1134-1141.
- (43) Zhao, X.; Zhang, Q.; Chen, C.-M.; Zhang, B.; Reiche, S.; Wang, A.; Zhang, T.; Schlögl, R.; Sheng Su, D. *Nano Energy* **2012**, *1*, 624-630.
- (44) Li, L.; Hu, X.; Guo, N.; Chen, S.; Yu, Y.; Yang, C. *Journal of Materials Research and Technology* **2021**, *15*, 6918-6928.
- (45) Jia, H.; Wang, S.; Sun, J.; Yin, K.; Xie, X.; Sun, L. *Journal of Alloys and Compounds* **2019**, *794*, 163-170.
- (46) Mishra, R.; Prasad, P. R.; Panda, P.; Barman, S. *Energy & Fuels* **2021**, *35*, 14177-14187.
- (47) Chang, C.; Yang, X.; Xiang, S.; Lin, X.; Que, H.; Li, M. *Journal of The Electrochemical Society* **2017**, *164*, A1601-A1607.
- (48) Wahid, M.; Puthusseri, D.; Phase, D.; Ogale, S. *Energy & Fuels* **2014**, *28*, 4233-4240.
- (49) Hao, Q.; Xia, X.; Lei, W.; Wang, W.; Qiu, J. *Carbon* **2015**, *81*, 552-563.
- (50) Yu, H.; Wu, J.; Lin, J.; Fan, L.; Huang, M.; Lin, Y.; Li, Y.; Yu, F.; Qiu, Z. *ChemPhysChem* **2013**, *14*, 394-399.
- (51) Mohapatra, D.; Dhakal, G.; Sayed, M. S.; Subramanya, B.; Shim, J.-J.; Parida, S. *ACS Applied Materials & Interfaces* **2019**, *11*, 8040-8050.
- (52) Hu, W.; Xu, D.; Sun, X. N.; Xiao, Z. H.; Chen, X. Y.; Zhang, Z. J. *ACS Sustainable Chemistry & Engineering* **2017**, *5*, 8630-8640.
- (53) Hu, W.; Zhang, W.; Zheng, M.; Xiao, Y.; Dong, H.; Liang, Y.; Hu, H.; Liu, Y. *International Journal of Hydrogen Energy* **2021**, *46*, 896-905.
- (54) Wang, J.; Senkovska, I.; Oschatz, M.; Lohe, M. R.; Borchardt, L.; Heerwig, A.; Liu, Q.; Kaskel, S. *Journal of Materials Chemistry A* **2013**, *1*, 10951-10961.
- (55) Cui, H.; Xu, J.; Shi, J.; Yan, N.; Zhang, C.; You, S. *Journal of the Taiwan Institute of Chemical Engineers* **2022**, *138*, 104441.
- (56) Chang, B.; Shi, W.; Yin, H.; Zhang, S.; Yang, B. *Chemical Engineering Journal* **2019**, *358*, 1507-1518.
- (57) Singh, G.; Bahadur, R.; Ruban, A. M.; Davidraj, J. M.; Su, D.; Vinu, A. *Green Chemistry* **2021**, *23*, 5571-5583.

- (58) Jin, Z.-e.; Wang, J.-l.; Zhao, R.-j.; Guan, T.-t.; Zhang, D.-d.; Li, K.-x. *New Carbon Materials* **2018**, 33, 392-401.
- (59) Hao, J.; Wang, X.; Wang, Y.; Lai, X.; Guo, Q.; Zhao, J.; Yang, Y.; Li, Y. *Nanoscale Advances* **2020**, 2, 878-887.
- (60) Sun, Y.; Zhao, J.; Wang, J.; Tang, N.; Zhao, R.; Zhang, D.; Guan, T.; Li, K. *The Journal of Physical Chemistry C* **2017**, 121, 10000-10009.
- (61) Seema, H.; Kemp, K. C.; Le, N. H.; Park, S.-W.; Chandra, V.; Lee, J. W.; Kim, K. S. *Carbon* **2014**, 66, 320-326.
- (62) Xia, Y.; Zhu, Y.; Tang, Y. *Carbon* **2012**, 50, 5543-5553.
- (63) Yue, L.; Rao, L.; Wang, L.; Sun, Y.; Wu, Z.; DaCosta, H.; Hu, X. *Energy & Fuels* **2018**, 32, 2081-2088.

## Appendix B



**Figure S4.1.** FESEM image of (a) p-CNS-600, (b) p-CNS-700, (c) p-CNS-800, and (d) p-CNS-900 samples.



**Figure S4.2.** CV and GCD profiles of p-CNS-600.



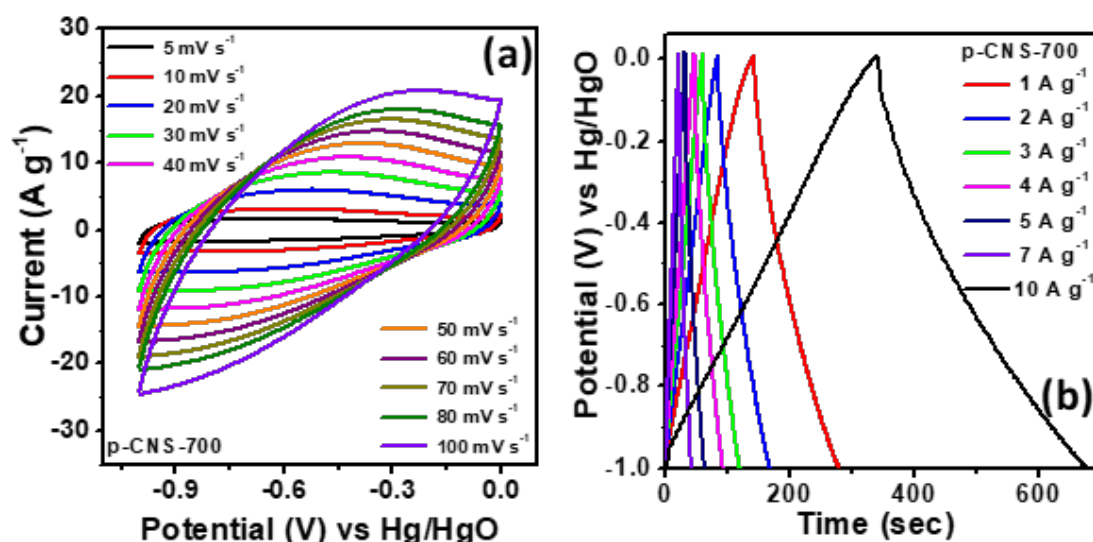


Figure S4.3. CV and GCD profiles of p-CNS-700.

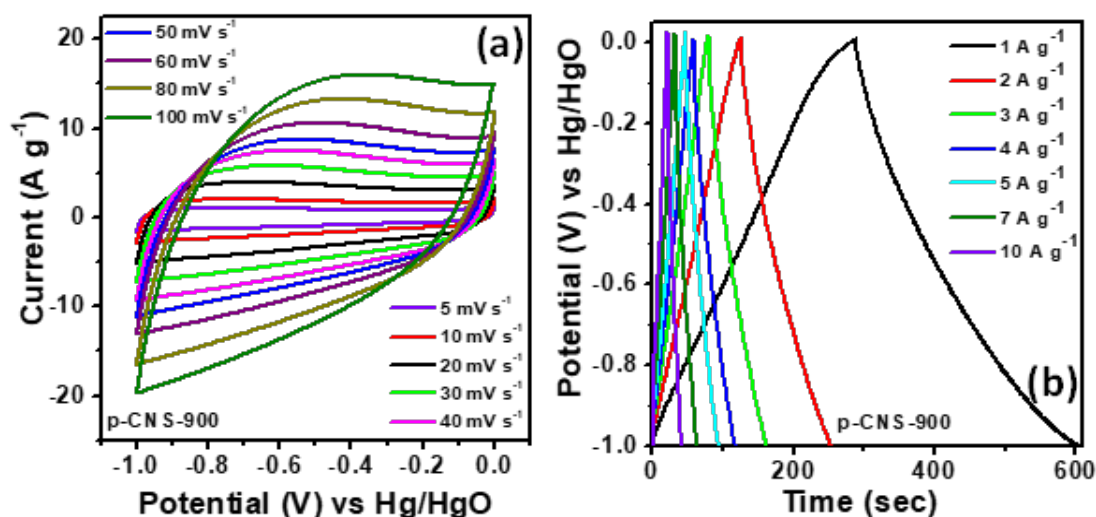
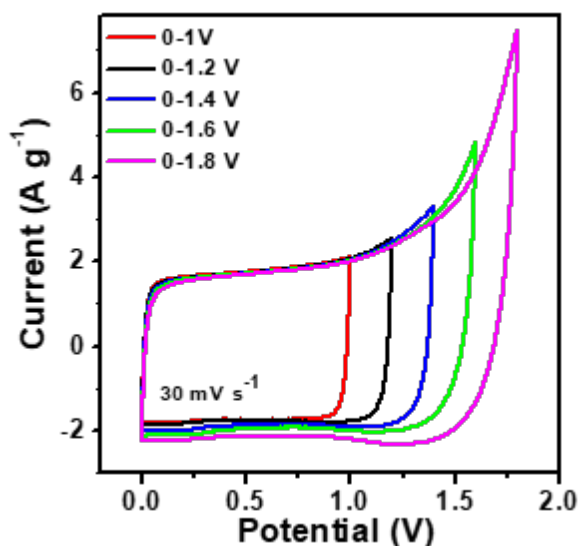
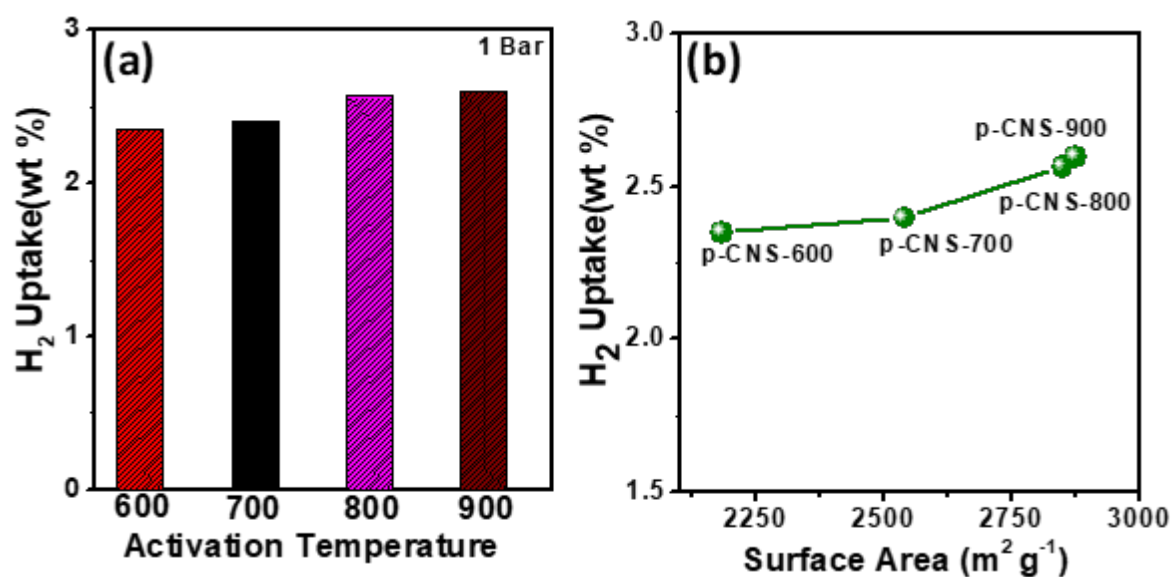


Figure S4.4. CV and GCD profiles of p-CNS-900.

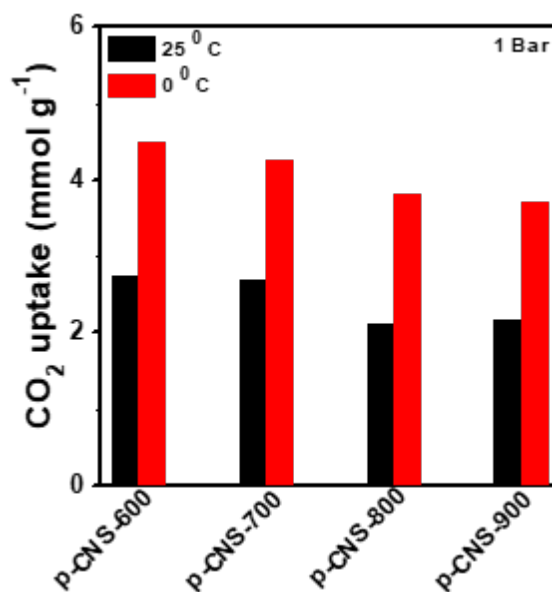


**Figure S4.5.** CV curves of a symmetric capacitor at the different potential range of 1 to 1.8 V in 1M Na<sub>2</sub>SO<sub>4</sub>.

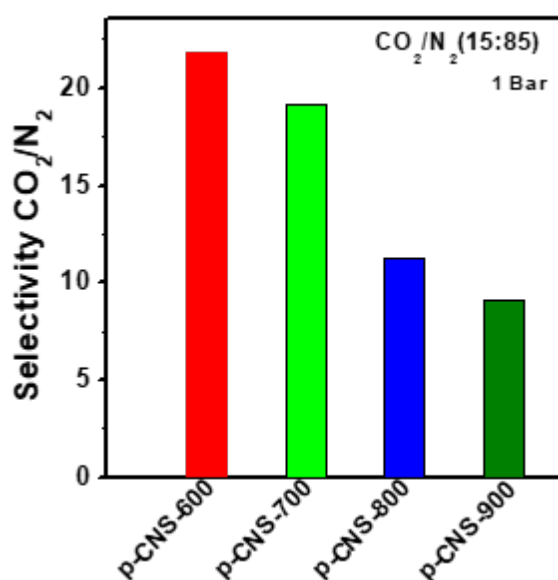


**Figure S4.6.** (a) H<sub>2</sub> uptake of all the samples at 77K and 1 bar pressure. (b) Change in H<sub>2</sub> uptake as a function of surface area.

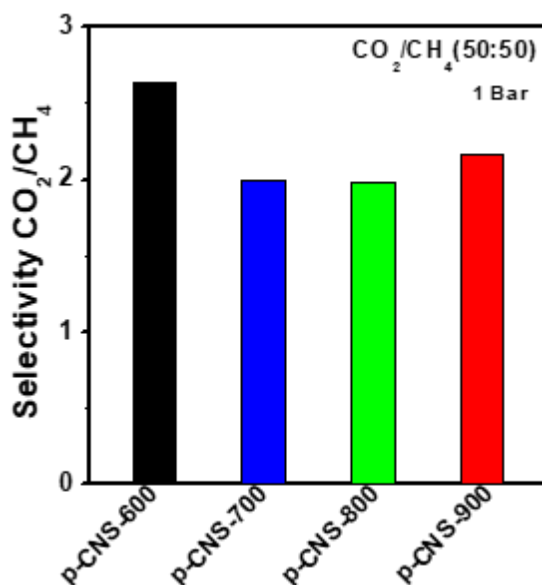




**Figure S4.7.** CO<sub>2</sub> uptake capacities of p-CNS-600 to 900 at 1 bar pressure.



**Figure S4.8.** CO<sub>2</sub>/N<sub>2</sub> selectivities of p-CNS-X for binary mixture of ratio (15:85) under pressure of 1 bar.



**Figure S4.9.** CO<sub>2</sub>/CH<sub>4</sub> selectivities for binary mixture of ratio (50:50) under pressure of 1 bar

**Table S4.1.** Weight % of C, S, N, and O present in p-CNS-X samples calculated from SEM EDX analysis.

Sample Name	C (%)	S (%)	N (%)	O (%)
p-CNS-600	60.60	7.40	10.80	21.20
p-CNS-700	82.70	3.10	3.20	11.00
p-CNS-800	85.10	1.1	3.70	10.09
p-CNS-900	89.00	0.20	3.50	7.30

**Table S4.2.** Comparison of electrochemical performance of p-CNS-X samples in 6M KOH electrolyte.

<b>Sample Name</b>	<b>Specific capacitance (F g<sup>-1</sup>) at 1 A g<sup>-1</sup> current density (6M KOH electrolyte)</b>
p-CNS-600	299
p-CNS-700	343
p-CNS-800	375
p-CNS-900	315

## Chapter 5

### Phosphorus and Nitrogen Co-doped Porous Carbon Nanosheets for Energy Storage and Gas Adsorption

#### 5.1. ABSTRACT

Heteroatom-doped porous carbon has emerged as a promising applicant for capacitive energy and gas storage applications because of its abundant availability and cost-effectiveness. In this study, a solvothermal strategy was adopted to synthesize Phosphorous (P) and Nitrogen (N) co-doped activated carbon (PCN-x) with an abundance of micropores, which can be utilized in both energy storage and gas (such as H<sub>2</sub> and CO<sub>2</sub>) adsorption applications. The optimized P and N co-doped porous carbon activated at 800 °C (PCN-800) shows a very high specific capacitance ( $C_s$ ) of 575.15 F g<sup>-1</sup> in an acid medium and the  $C_s$  value was calculated to be 477.63 F g<sup>-1</sup> under 1 A g<sup>-1</sup> current in an alkaline medium. The symmetric device performance shows an excellent energy density (ED) of 10.61 W h kg<sup>-1</sup> at a power density (PD) of 250 W kg<sup>-1</sup> along with capacitance retention of 91.23 % up to 10000 cycles in alkaline medium. The P and N co-doped porous carbon activated at 900 °C (PCN-900) shows a high specific surface area (SSA) of 2953.2 m<sup>2</sup> g<sup>-1</sup> with a high micropore volume of 0.77 cc g<sup>-1</sup>. It also shows a good H<sub>2</sub> storage capacity of 3.26 wt% at 77 K and 1 bar pressure. The CO<sub>2</sub> adsorption capacities were calculated to be 5.98 mmol g<sup>-1</sup> at 0 °C and 3.61 mmol g<sup>-1</sup> at 25 °C with good selectivity of CO<sub>2</sub>/N<sub>2</sub> and CO<sub>2</sub>/CH<sub>4</sub>. The incorporation of P and N co-doped species into porous carbon nanosheets presents a promising avenue for improving the performance of energy and gas storage applications. The synergistic effects of P, N doping and porous morphology, high SSA contribute to improved electrochemical

performance, enabling higher energy and power densities in supercapacitor devices along with good H<sub>2</sub> and CO<sub>2</sub> uptake capacities.

## 5.2. INTRODUCTION

The development of multifunctional materials has great influence owing to their flexibility in many applications<sup>1-2</sup>. Heteroatom doped porous carbon are considered to be one of the best promising candidates because of its application in various field such as electrochemical energy storage<sup>3</sup>, gas storage<sup>3-4</sup>, separation<sup>5-6</sup>, and adsorption<sup>5</sup>, etc. owing to its high SSA, tunable porosity, high conductivity, structural/chemical stability, and physical/chemical inertness<sup>7-9</sup>. Nowadays heteroatom doping to the porous carbon matrix has gained more attention as it leads to an increase in the number of active sites, offers more anisotropic distribution of charges, and introduces more defects at the surface of the electrode material<sup>10</sup>. The difference in size and charge of the base material and heteroatoms results in a change in the charge density of the material and hence introduce a defect in the carbon matrix. N doping to porous carbon increase the surface polarity, electric conductivity, and affinity for electron donation. It involves pseudocapacitance by enhancing the charge mobility of negatively charged particles on the surface of the carbon matrix and hence increasing the capacitance value<sup>11-12</sup>. Predominantly the existence of pyridinic and pyrrolic N in the porous carbon matrix possesses a negative charge which functions as basic and faradic reaction sites. And also in particular, the presence of pyridinic N atoms in the carbon increases the catalytic activity as well as the function of the material<sup>13</sup>. The portion of active N content can be controlled by pyrolyzing the commercially available monomers or biomass products by varying temperatures. But at high pyrolysis temperatures, the limitation of this approach is the restricted N content. However, compared to the direct pyrolysis method, the synthesis of

highly cross-linked polymers followed by pyrolyzing at different high temperatures can offer more N content on the porous carbon matrix. Fluorine (F) doping increases the electrical conductivity and hence enhance the electrochemical performance<sup>14</sup>. The wettability of the carbon material can be enhanced by doping heteroatoms like O and P, as the electrolyte ions can easily spread on the surface of the carbon matrix<sup>15</sup>. Moreover, co-doping of N with another heteroatom (B, P, O, and S) enhances their energy storage properties. This improved energy storage and gas adsorption can be due to the synergistic effect between the doped heteroatoms<sup>16</sup>. P shows properties similar to N since both of them are group 15 elements. Compared to N, P atoms have larger atomic radius than the C atom creating vacancy defects that greatly influence the electronic structure. This is owing to its difference in atomic size, electronegativity and addition of more functional groups<sup>10, 17</sup>. The presence of lone pair electrons induces the Faradic reactions along with EDLC, increasing the  $C_s$  value of the electrode material. The incorporation of P into the carbon framework along with the existence of a large amount of oxygen functional groups on the surface improves capacitive performance of the supercapacitor. Incorporating P functional groups into the carbon matrix prevents oxidation of carbon electrodes and hence boosts the operating potential window, cyclic durability, and ED of supercapacitors<sup>18</sup>. Besides the heteroatom doping to the carbon matrix, the porous structure has a great influence on energy as well as gas storage applications. The porous carbon having meso and micropores along with subnanometer pore size plays an important role in ion transport channels (promotes the electrolyte transportation and increases the contact area between the electrolyte and electrode material), and charge adsorption carrier. Besides the use of porous carbon in energy storage application, it can also be used in gas adsorption application owing to its rich porosity, large SSA, and

presence of multiple functional groups. However the structural and chemical properties of carbon materials can be enhanced by modification. Several research have been carried out and it has been proved that doping of heteroatoms like N, P, S etc. into the carbon framework can enhance the chemical and physical properties of the materials<sup>19-20</sup>. The heteroatom doped porous carbon materials are used as good gas adsorbents for CO<sub>2</sub> uptake as emission of CO<sub>2</sub> gases has a major contribution for the global warming. H<sub>2</sub> adsorption was also greatly affected by pore size as well as SSA of the materials. Various research have shown the addition of dopants like P and N can boost the CO<sub>2</sub> and H<sub>2</sub> adsorption capacity due to the existence of active N and P species, high SSA, well developed micropores, synergistic effects between the heteroatoms, and well-formed porous structure<sup>21</sup>.

In this chapter, we have synthesized PCN-x in two step methods: (i) the first step involves the solvothermal synthesis followed by carbonization and (ii) the second step comprises of activation of the carbonized product at three different temperatures to produce the heteroatom doped porous carbon. The P and N co-doped porous carbon obtained at 800 °C activation temperature (PCN-800) displays highest C<sub>s</sub> of 477.63 F g<sup>-1</sup> under 1 A g<sup>-1</sup> current which shows cyclic durability of 90 % over 5000 cycles. Higher SSA, abundant micropores and optimum P/N doping in PCN-800 are advantageous for higher electrochemical activity of PCN-800. The optimized P and N co-doped porous carbon activated at 900 °C (PCN-900) shows higher H<sub>2</sub> storage capacity of 3.26 wt% at 77 K and the CO<sub>2</sub> uptake was obtained to be 5.98 and 3.61 mmol g<sup>-1</sup> at 0 and 25 °C respectively. The CO<sub>2</sub>/N<sub>2</sub> and CO<sub>2</sub>/CH<sub>4</sub> selectivity were calculated to be 13.78 and 4.7 respectively at 25 °C.

### **5.3. EXPERIMENTAL SECTION:**

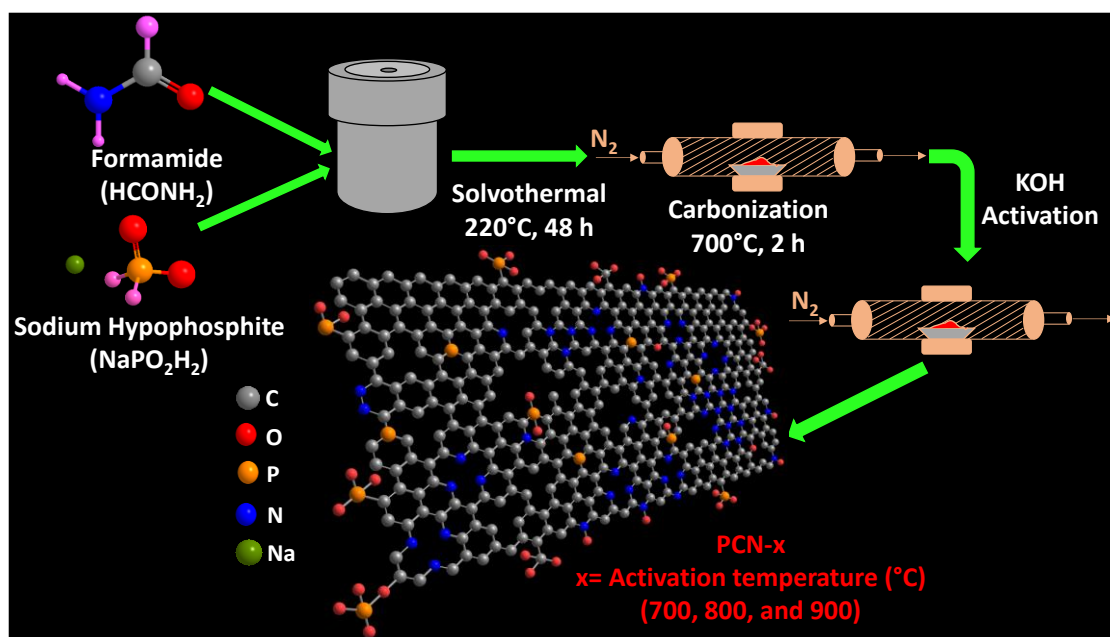
#### **5.3.1. Materials:**

Formamide was purchased from Merck, India. Sodium hypophosphite was purchased from Sigma-Aldrich. Potassium Hydroxide (KOH), Hydrochloric acid (HCl), and Sulphuric acid (H<sub>2</sub>SO<sub>4</sub>) were purchased from CDH chemicals, India. PVDF binder was purchased from MTI Corporation. Deionized H<sub>2</sub>O was used to carry out all experiments.

#### **5.3.2. Synthesis of P and N co-doped Porous Carbon (PCN-x)**

PCN-x was synthesized from Formamide and sodium hypophosphite in a two-step method. First, 20 ml of Formamide and 5g of sodium hypophosphite was mixed to form a homogeneous mixture. The solution was put into a 100 ml autoclave and subjected to heating at 220 °C for 48 h, resulting in the formation of a black colour solid product. The solid product was carbonized at 700 °C for 2h in N<sub>2</sub> atmosphere (700 mL min<sup>-1</sup>), heating rate of 5 °C min<sup>-1</sup> subsequently activation at three different temperatures (700, 800 and 900 °C) by keeping carbon: KOH ratio 1:2. Then it was washed with 0.2 M HCl and H<sub>2</sub>O several times to obtain the desired product. The product obtained were named as PCN-x (x signifies the activation temperatures i.e. 700, 800 and 900 °C). A detailed method for the synthesis of PCN-x is provided in Scheme 5.1.





**Scheme 5.1.** Scheme illustrating synthesis of PCN-x.

### 5.3.3. Electrode Fabrication:

Fabrication of electrodes was carried out by mixing PVDF binder, conductive carbon, and PCN-x with a mass ratio of 10:10:80 followed by coating over Nickel foam (1\*1 cm<sup>2</sup>) and Ti foil (current collector) for the base and acid medium respectively. The electrodes were dried at 85 °C in a vacuum. The mass loading of each electrode was close to 1 mg. The single electrode Performance was measured in the electrolyte of 6M KOH and 1M H<sub>2</sub>SO<sub>4</sub> in a three-electrode system configuration with Hg/HgO reference electrode (Ag/AgCl in 1M H<sub>2</sub>SO<sub>4</sub>) and platinum mesh as counter electrode while the symmetric device was tested in the two-electrode system. The symmetric device was prepared using glass microfibre filter paper as a separator in a CR2032 coin cell configuration. 1M Na<sub>2</sub>SO<sub>4</sub> was used as an electrolyte for the test in a neutral medium. From a single electrode, the specific capacitance ( $C_s$ ) Calculation was carried out from Galvanostatic Charge discharge (GCD) curves using the following equation:

$$C_s = \frac{I\Delta t}{m(V_f - V_i)} \quad (6.1)$$

Specific capacitance ( $C_s$ ) can be calculated from the CV curve by using the following equation:

$$C_s = \frac{\int I dv}{2m\Delta V u} \quad (6.2)$$

Where  $C_s$  = specific capacitance

$I$  = current applied (A)

$\Delta t$  = discharge time (sec)

$m$  = mass of the active material (g)

$V_f - V_i$  = Voltage window (V)

$\int I dv$  = area under the CV curve

$u$  = scan rate ( $\text{mV s}^{-1}$ ).

For a symmetric supercapacitor device, the calculation was done using the following equations.

$$C_s = \frac{2I\Delta t}{m(V_f - V_i)} \quad (6.3)$$

$$ED = \frac{C_{cell}\Delta V^2}{2 \times 3.6} = \frac{C_s\Delta V^2}{8 \times 3.6} \quad (6.4)$$

$$PD = \frac{E \times 3600}{t} \quad (6.5)$$

Where  $C_s$  = specific capacitance, ED = Energy density, and PD = power density.

#### **5.3.4. Material Characterization:**

The powder x-ray diffraction patterns (p-XRD) of samples were measured by Bruker X-ray diffractometer (DAVINCI D8 ADVANCE equipped with Cu  $K\alpha$  source of wavelength 0.154 nm). The morphological characterization was investigated by a Field-emission scanning electron microscope (FESEM) system (Model-Sigma, Carl Zeiss, Germany) and Transmission Electron Microscopy (TEM) instrument operated at 200 kV (F200, JEOL). XPS measurement was done using AXIS ULTRA (Kratos) instrument

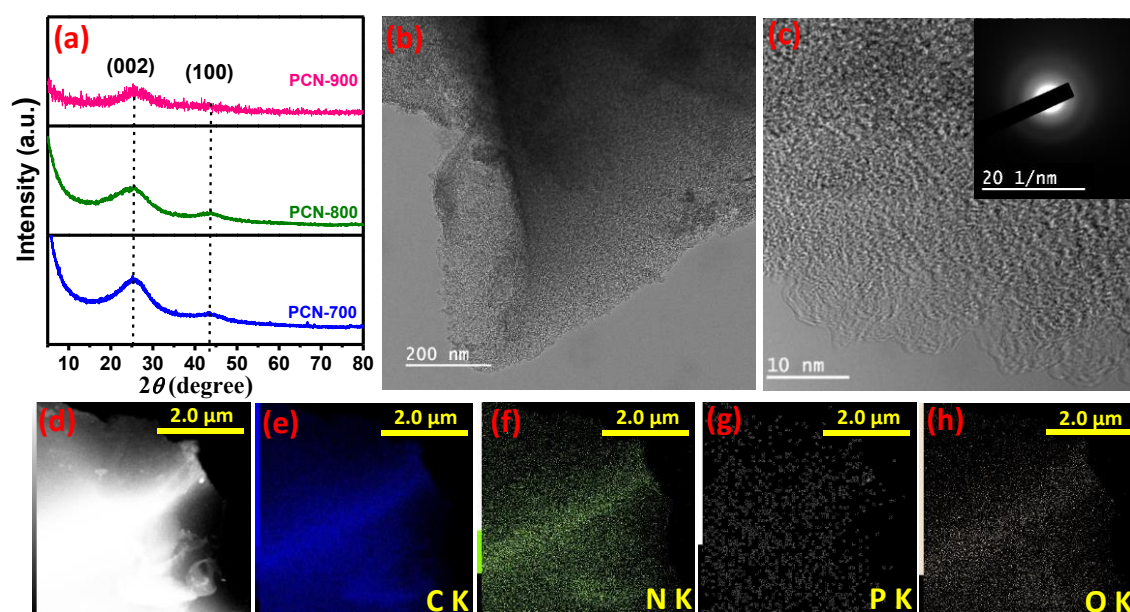
where a monochromated Al-K $\alpha$  source was used. XPS was taken from the sample deposited on the silicon wafer. The CO<sub>2</sub> and N<sub>2</sub> physisorption isotherms were collected using AUTOSORB-1 (Quantachrome). The pore size distribution (PSD) was calculated using the nonlocal density functional theory (NLDFT) model while the micropore analysis was carried out using the t-plot method. LabRAM HR Evolution, Horiba Scientific, and Raman Spectrometer were used for Raman analysis using a 532 nm laser source. Electrochemical measurements were performed using CS310 Electrochemical Workstation (Corrtest Instruments).

## **5.4 RESULTS AND DISCUSSIONS:**

### **5.4.1 Structural and morphological characterizations**

The structural properties of the PCN-x materials were characterized by using p-XRD pattern as shown in Figure 5.1(a). The peak at 2 $\theta$  value 25.26 and 43.1° represents the (002) and (100) crystal planes of graphitic carbon matrix. The broad diffraction peak indicates the formation of low crystalline carbon (amorphous nature of carbon). The morphology of PCN-x were studied by Scanning Electron Microscopy (SEM). SEM image of PCN-800 reveals formation of carbon nanosheets having bulk morphology with a rough surface, attributed to the activation process as depicted in Figure S5.1. (b). The SEM images of PCN-700 and PCN-900 are presented in Figure S5.1. (a, c). Table S5.1 display the wt% of C, P, N, and O existing in PCN-x samples calculated from SEM EDX. The formation of porous nanosheets was confirmed by Transmission Electron Microscopy (TEM) images. Figures 5.1(b-c) and S5.2. shows the TEM images of PCN-800 revealing the sheet like structure. The High Resolution TEM (HRTEM) shows the formation of pores in regular intervals over the nanosheets. HRTEM images display the alternative dark and bright regions at the edge of the nanosheets depicting the formation

of microporous structures (marked as circle in Figure S5.2 (b)). The synthesis method (KOH activation process) and introduction of heteroatoms (N and P) results in formation of defects in PCN-800 sample<sup>22</sup>. Notably, the porous structure improves the surface wettability and conductivity of the material. As a result synthesized PCN-x can be widely used in both energy and gas storage applications. Inset of Figure 5.1(c) displays the SAED pattern of PCN-800. The STEM image showing elemental mapping indicating uniform distribution of C, N, O and P over the surface of the porous carbon nanosheets, ascribed in Figure 5.1(d-h). The Raman spectra was conducted to analyse the extent of graphitization in PCN-x displayed in Figure 5.2(a). All the samples show a pair of peaks around 1340 and 1592  $\text{cm}^{-1}$ , which correspond to D and G bands respectively. The D band is related with the structural disorderness ( $\text{sp}^3$ -hybridized carbon) and G band represents graphitized nature ( $\text{sp}^2$ -carbon) of the carbon respectively.



**Figure 5.1.** (a) p-XRD patterns of PCN-x, (b, c) low-resolution TEM and HRTEM images (inset of Figure (c) represents the SAED pattern), and (d-h) STEM image and corresponding elemental mapping of PCN-800.

The D band intensity increases with the presence of disorderness of carbon. The  $I_D/I_G$  ratio (intensity ratio of D and G band) indicate the level of disorderness of the material. As the number of defects increases, intensity of D band increases. The incorporation of P, and N into the carbon matrix introduces surface edge defects in the samples, resulting in the formation of D band. The  $I_D/I_G$  ratio was calculated to be 1.02 for PCN-700 which increases to 1.04 for PCN-900. This shows with increase in temperature the degree of defect and disorderness present in carbon increases which is helpful in enhancing the adsorption of CO<sub>2</sub> molecules and improves the energy storage capacity<sup>23</sup>.

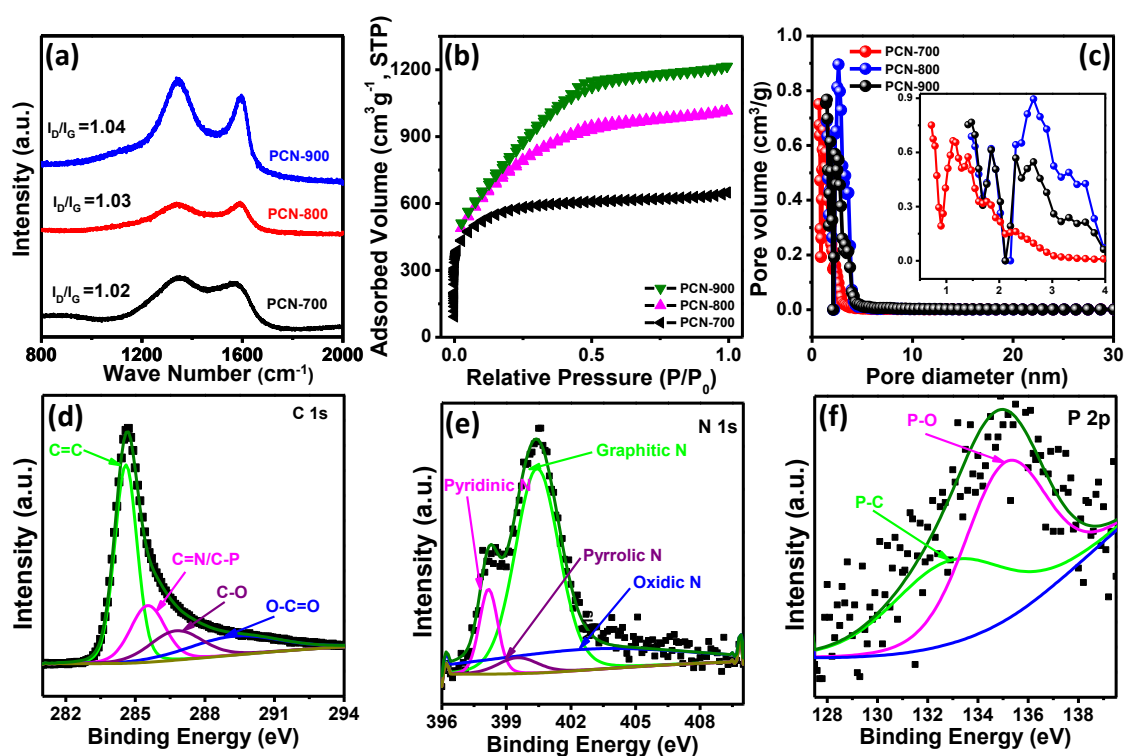
The Brunauer-Emmett-Teller (BET) measurements were employed to analyze the porous structure and textural properties of PCN-x, as materials with well-developed pore structures have greater contact with electrolyte ions. Figure 5.2(b) depicts the N<sub>2</sub> sorption isotherm for all the samples indicating typical type-I isotherms feature for microporous materials as the adsorption capacity of N<sub>2</sub> sharply increase in low relative pressure<sup>24</sup>. The SSA and micropore surface area were obtained from BET method and t-plot method. The SSA and total pore volume ( $V_t$ ) are obtained to be 2069.8, 2704.6, and 2953.2 m<sup>2</sup> g<sup>-1</sup> and 1.01, 1.57 and 1.88 cc g<sup>-1</sup> for PCN-700, PCN-800 and PCN-900 respectively. This suggests that degree of carbonization and activation process are crucial for the formation of micropores. Higher the activation temperature, the volatilization of gas becomes faster indicating the increase in SSA with increase in activation temperature. The pore size distribution (PSD) analysis of PCN-x are presented in Figure 5.2(c), calculated from NLDT model. The pores for PCN-800 is mainly combination of micropores (<2 nm), and mesopores (>2 nm) which is beneficial for easy penetration of aqueous electrolyte ions hence increasing the capacitance value<sup>4</sup>. The porous structure parameters indicates that a large percentage of the total pore volume is occupied by micropores. The average

pore diameter ( $D_a$ ) of the samples decreases with an increase in SSA as the activation temperature rises. The increased number of micropores caused by the etching of KOH is thought to be the cause of this phenomena<sup>25</sup>. Mesopores have major role for the transportation pathway of electrolyte ions. The detailed parameters are listed in Table 5.1. The SSA for PCN-900 is  $2953.2 \text{ m}^2 \text{ g}^{-1}$ , slightly greater than SSA of PCN-800 ( $2704.6 \text{ m}^2 \text{ g}^{-1}$ ). This may be because of the emptying of space occupied by the polyphosphates owing to thermal decomposition and reduction of phosphates to elemental phosphorus<sup>16</sup>. Higher SSA, abundant micropores and N, P and O doping in PCN-800 are helpful in transport and adsorption of electrolyte ions. X-ray photoelectron spectroscopy (XPS) analysis were recorded to assess the surface composition of PCN-800. The survey spectrum shows the existence of P, C, N, and O in the material, presented in Figure S5.3. This result aligns with the findings in the EDS spectra. The high resolution C 1s peak can be deconvoluted into four peaks. The peaks centered at binding energy 284.59, 285.53, 286.85 and 289.31 eV can be attributed to C=C, C-P/C=N, C-O, and O-C=O respectively, presented in Figure 5.2(d)<sup>26</sup>. Figure 5.2(e) presents the high resolution spectrum of N 1s, deconvoluted into four peaks<sup>26</sup>. The peaks centered at 398.16, 399.5, 400.4 and 401.9 eV correspond to pyridinic N, pyrrolic N, graphitic N and N-O bond (oxidic N) respectively<sup>26</sup>. The existence of pyrrolic and pyridinic N can improve the faradic reactive sites to provide pseudocapacitor and enhance the capacitive performance of the carbon material. High resolution P 2p peak possesses two peaks. The peak observed at binding energy 133.1 eV corresponds to P-C and the peak centered at 135.32 eV is associated with P-O bonding respectively shown in Figure 5.2(f)<sup>27</sup>. This reveals P was effectively doped into the carbon matrix, providing more active sites and

higher wettability which promotes the contact between electrode and electrolyte, consequently improving the electrochemical behavior of the synthesized material.

**Table 5.1.** Detailed surface properties and pore analysis of PCN-x

Material	BET SSA ( $S_{\text{BET}}$ ) ( $\text{m}^2 \text{g}^{-1}$ )	Micropore surface area ( $S_{\text{micro}}$ ) ( $\text{m}^2 \text{g}^{-1}$ )	Total pore volume ( $V_{\text{t}}$ ) ( $\text{cc g}^{-1}$ )	Micropore volume ( $V_{\text{micro}}$ ) ( $\text{cc g}^{-1}$ )	Average pore diameter ( $D_{\text{a}}$ ) (nm)	Percent of $S_{\text{micro}}/S_{\text{BET}}$
PCN-700	2069.8	598.5	1.01	0.22	2.22	28.9
PCN-800	2704.6	1329.8	1.57	0.58	2.52	49.2
PCN-900	2953.2	1798.3	1.88	0.77	2.42	60.9





**Figure 5.2.** (a) Raman spectra, (b) N<sub>2</sub> adsorption plot, (c) Pore size distribution of PCN-x, XPS high-resolution spectra (d) C 1s, (e) N 1s, and (f) P 2p in PCN-800.

#### 5.4.2. Electrochemical Analysis

##### Electrochemical Performance in a three-electrode system

The electrochemical behavior of PCN-x were studied in a three electrode setup with a 6M KOH electrolyte. Figure 5.3(a) presents comparison CV plots of PCN-x at 5 mV s<sup>-1</sup> sweep rate at a voltage window -1 to 0 V. All the CV curves show quasi rectangular nature indicating the charge can be quickly reassembled by turning the voltage. This finding suggests excellent rate capability of the electrode material. There is a vertical change in the current density on altering the electrode polarity near at 0 V and -1 V potential suggesting very low internal cell resistance for PCN-x electrodes. This finding is owing to the uniformly ordered mesopores, allowing easy flow of electrolyte ions into the active surface of the electrodes. The increase in current density for PCN-800 compared to the other two samples at same scan rate indicating superior charge storage abilities of PCN-800 electrode. This may be attributed to the high SSA, micropore volume and the doping of P, and N atoms. Figure 5.3(b) represents the comparison GCD curves. The discharge time for PCN-800 is highest which depicts the higher C<sub>s</sub> value compared to others, consistent with the CV results. The C<sub>s</sub> value were calculated to be 349.3, 477.63 and 456.53 F g<sup>-1</sup> under 1 A g<sup>-1</sup> for PCN-700, PCN-800 and PCN-900 respectively. Table S5.2 displays the comparison of electrochemical activity of all the three PCN-x samples in 6M KOH electrolyte. All GCD profile shows symmetrical triangle curve resulting high rate and cyclic performance. However the GCD curve is not perfectly symmetrical because of the presence of heteroatom doping (N and P). The CV at different sweep rate and GCD profile at different current density for PCN-700,



PCN-800 and PCN-900 are depicted in Figure S5.4, S5.5 and S5.6 respectively. With increase in sweep rate the area under the CV curves as well as current densities increases for all the samples. The electrode PCN-800 shows up to 63.18% capacitance retention at 10 A g<sup>-1</sup> current. All the PCN-x signifies decrease in C<sub>s</sub> value with increase in current density, presented in Figure 5.3(c). Owing to the high SSA, and high microporous volume of PCN-800, the C<sub>s</sub> value of the electrode gets improved. Figure S5.7 represents the Nyquist spectra of PCN-x consisting of a semicircle and a linear vertical line at high and low frequency region respectively. The semicircle shows charge transfer resistance from electrolyte/electrode interface (R<sub>ct</sub>) and the perpendicular straight line indicates the solution resistance (R<sub>s</sub>). Smaller the semicircle faster is the charge transfer process and more perpendicular the straight line, better is the capacitive performance of the electrode material. The presence of smaller circle implies the pseudocapacitive nature of the carbon material. The semicircle was owing to the interface redox reactions of impurities and surface functional groups<sup>28</sup>. As presented in Figure S5.7, the semicircle of PCN-800 is smaller than that of PCN-700, and PCN-900 indicating better capacitance performance. For practical use, cyclic stability of the single electrode was performed up to 5000 cycles resulting 90 % capacitance retention of its initial cycle.

Power Law is used to more accurately describe the impact of diffusion controlled and capacitive contribution based on the expression as follows:

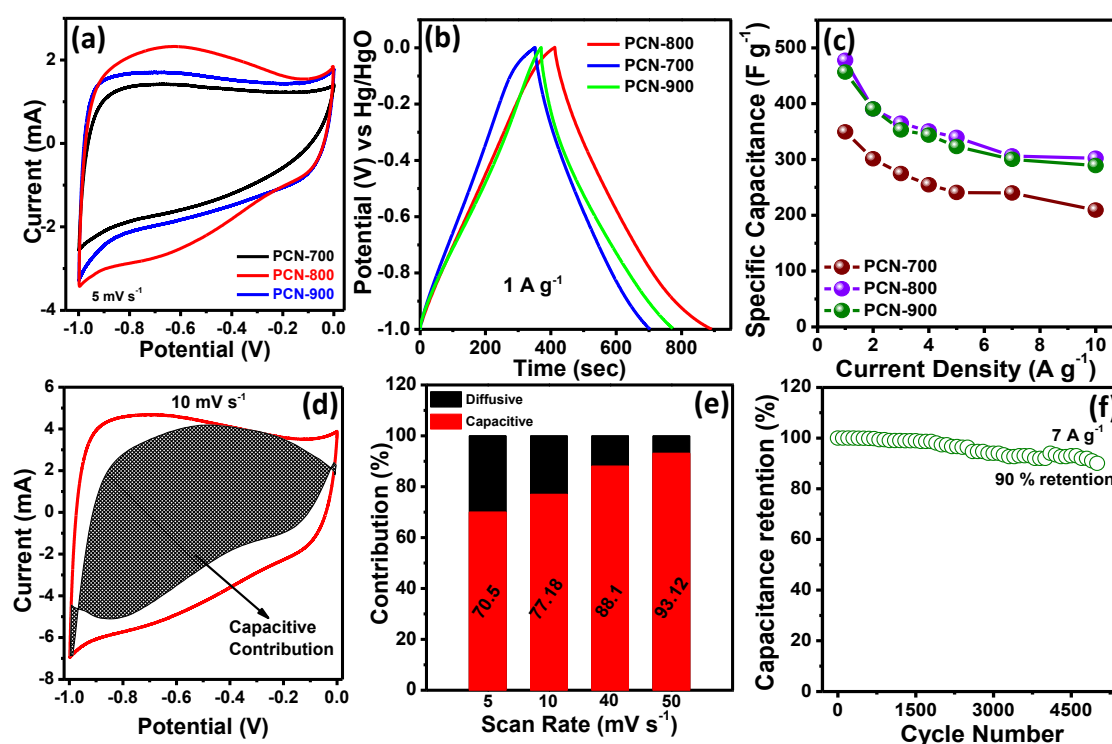
$$i(V) = av^b \quad (5.6)$$

Here *i* stands for current, *v* is the sweep rate, *a* and *b* are adjustable parameters respectively.

To quantify the diffusive and capacitive controlled contribution, we have used Dunn method according to the following expression 5.7:

$$i(V) = k_2 v^{1/2} + k_1 v \quad (5.7)$$

Here  $i(V)$  and  $v$  states the current density and sweep rate respectively,  $k_1$  and  $k_2$  are the constant calculated from current response at a certain potential. Figure 5.3(d) represents the capacitive contribution curve of PCN-800 demonstrating 70.5 % capacitance and 29.5 % diffusion-controlled contribution at  $10 \text{ mV s}^{-1}$ . Figure 5.3(e) represents the bar plot displaying the capacitive contribution of the electrode material increases with rise in scan rate indicating EDLC nature of the electrode in alkaline medium. Capacitive contribution rates of all the electrodes are calculated to be 70.5, 88.1, and 93.12 % at 5, 40 and 50  $\text{mV s}^{-1}$  scan rate. The capacitive contribution is higher than 50 % signifying its electrochemical kinetics are determined by capacitive behavior<sup>29</sup>.



**Figure 5.3.** (a, b) CV and GCD curves at  $5 \text{ mV s}^{-1}$  and under  $1 \text{ A g}^{-1}$  current for PCN-x.

(c)  $C_s$  vs. current density for PCN-x. (d) Capacitive contribution for PCN-800 at  $10 \text{ mV}$

s<sup>-1</sup>. (e) Capacitive charge storage processes at different sweep rates (5-50 mV s<sup>-1</sup>). (f) C<sub>s</sub> vs. number of cycles for PCN-800 at 7 A g<sup>-1</sup> in alkaline electrolyte.

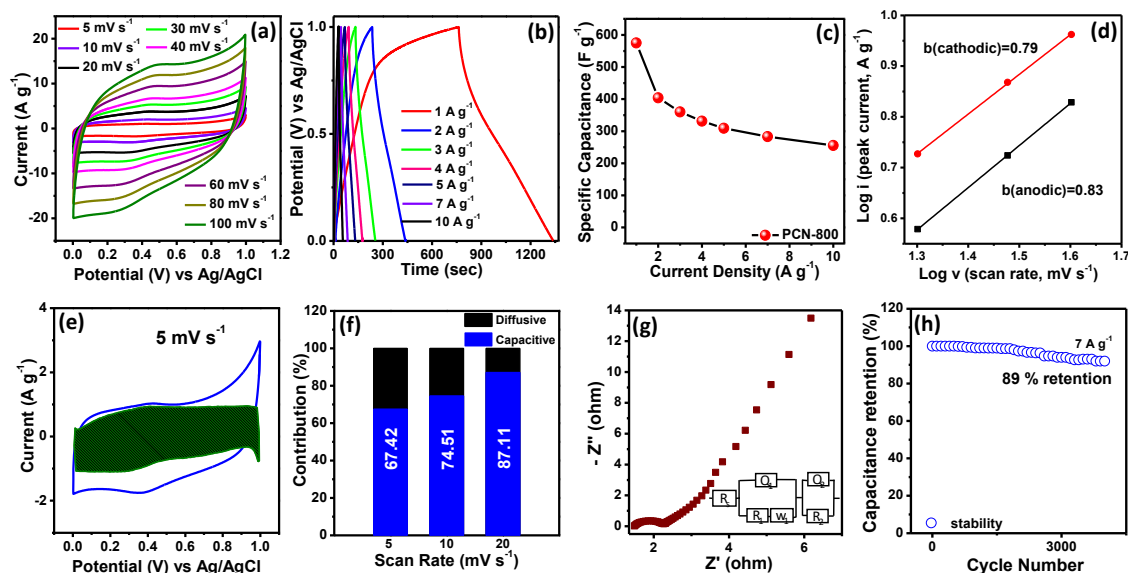
The electrochemical behavior of PCN-800 was again examined in 1M H<sub>2</sub>SO<sub>4</sub> solution in a three electrode setup. All the CV curves at different sweep rate (5-100 mV s<sup>-1</sup>) display quasi rectangular nature having a small pair of humps indicate predominant EDL formation. The weak reversible redox peaks imply the pseudocapacitance contribution of PCN-800, which is an additional mechanism of energy storage besides the double layer mechanism (Figure 5.4(a)). This indicates the co-existence of EDLC as well as pseudocapacitance behavior. The EDLC behavior of the electrode is due to the doping of P into the porous carbon matrix and the pseudocapacitance nature arises owing to the redox reaction (Faradic reaction) taking place on the surface (presence of surface oxygen, and nitrogen functional group) of the electrode. Faradic redox reaction responsible for pseudocapacitance are shown in scheme 5.2<sup>30</sup>. Figure 5.4(b) displays the GCD profiles under different current densities indicating nonlinear sloping voltage. This suggest that faradic reactions are occurring on the electrode surface, matches with the CV findings. Equation S1 was used to calculate the C<sub>s</sub> value and are obtained to be 575.15, 403.86, 360.24, 331.4, 309.1, 283.15 and 255.6 F g<sup>-1</sup> at 1, 2, 3, 4, 5, 7 and 10 A g<sup>-1</sup> current respectively. Figure 5.4(c) shows comparison curve of specific capacitance w.r.t different current density of our finding. At higher discharge rate of 10 A g<sup>-1</sup>, PCN-800 maintenance 44.44% retention of capacitance of its initial one. Figure 5.4(d) depicts the plot of log (i) as a function of log (v) and the b-value for anodic and cathodic peaks are calculated to be 0.83 and 0.79 revealing the charge transfer processes are both capacitive and diffusive. The capacitive and diffusive current was calculated by using Dunn's

method. Figure 5.4(e) represents the contribution plot at  $5 \text{ mV s}^{-1}$ . The bar plot at different sweep rate are depicted in Figure 5.4(f). The capacitive contribution were calculated to be 67.42, 74.51 and 87.11 at 5, 10 and  $20 \text{ mV s}^{-1}$  scan rate respectively. Figure 5.4(g) depicts the EIS plot and the  $R_s$  and  $R_{ct}$  are found to be 1.51 and  $0.66 \Omega$  indicating fast diffusion of electrolyte ions. The cyclic stability plot shows the capacitance remain 89% up to 5000 cycles, depicted in Figure 5.4(h). The higher  $C_s$  value is owing to the presence of significantly larger pores compared to the size of electrolyte ions and their surrounding solvation layers are essential for achieving greater capacitance values. The presence of micropores within the size range of 0.70 to 1.8 nm, for instance, enables full accessibility to hydronium ions (0.36 to 0.42 nm) and hydrated bisulphate ions (0.53 nm)<sup>4</sup>.

**Table 5.2.** Electrochemical performance of PCN-800 with reported heteroatom doped porous carbon materials.

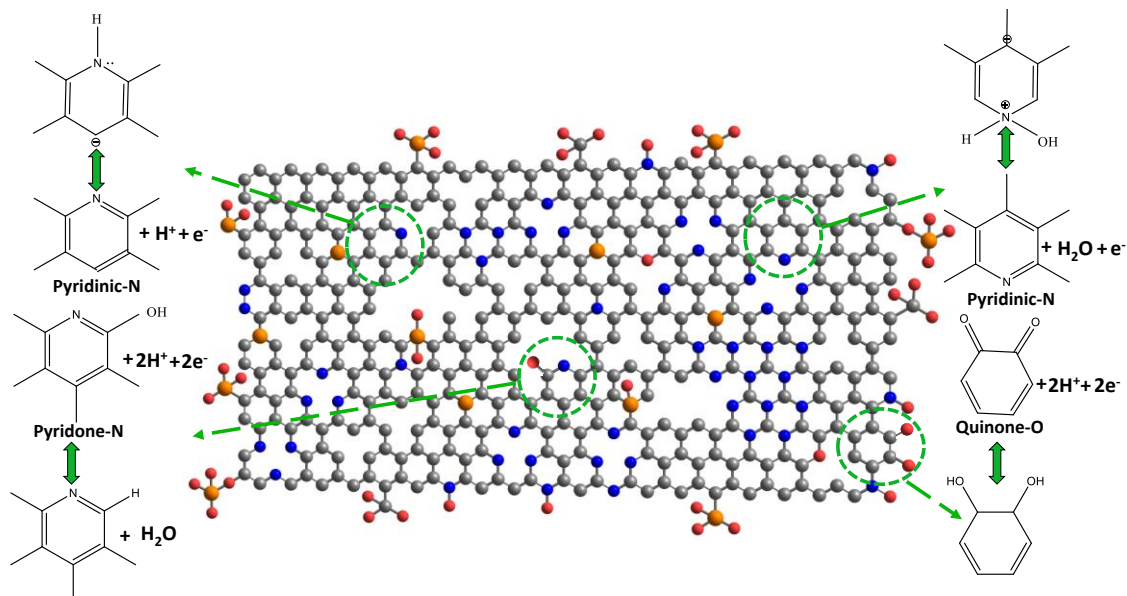
Material	$C_s$ of single Electrode ( $\text{F g}^{-1}$ )	Capacitance retention (%) (Cycle Number)	Electrolyte	Ref.
NPHCMs-65-700	208 ( $0.5 \text{ A g}^{-1}$ )	89 (5000)	6M KOH	31
HCSs-700	210 ( $0.5 \text{ A g}^{-1}$ )	95.6 (1000)	6M KOH	32
G/SWCNHs	206 ( $0.1 \text{ A g}^{-1}$ )	99 (1000)	1M KOH	33
$\text{H}_3\text{PO}_4/\text{C}-500$	260 ( $0.05 \text{ A g}^{-1}$ )	71.3 (1000)	6M KOH	34
PN-ECB-950	265 ( $0.5 \text{ A g}^{-1}$ )	94 (5000)	6M KOH	35
DAC-700	299.1 ( $0.5 \text{ A g}^{-1}$ )	99.6 (4000)	6M KOH	36

P-PC	253 (1 A g <sup>-1</sup> )	95 (10000)	6M KOH	37
A-TDP-12	172.7 (1 A g <sup>-1</sup> )	96.1 (4000)	6M KOH	17
NPPC-800	297.62 (0.5 A g <sup>-1</sup> )	-	6M KOH	29
P-TRG	115 (0.05 A g <sup>-1</sup> )	-	1M H <sub>2</sub> SO <sub>4</sub>	38
ETC-900	385 (0.2 A g <sup>-1</sup> )	71 (2000)	1M H <sub>2</sub> SO <sub>4</sub>	4
20PNG	359 (0.5 A g <sup>-1</sup> )	90.2	6M KOH	22
	351 (0.5 A g <sup>-1</sup> )	(20000)	1M H <sub>2</sub> SO <sub>4</sub>	
NP-rGO <sub>2</sub>	416 (1 A g <sup>-1</sup> )	94.63 (10000)	6M KOH	39
NPCHSs	232 (1 A g <sup>-1</sup> )	89.1 (5000)	6M KOH	40
PCN-800	477.63 (1 A g <sup>-1</sup> )	90 (5000)	6M KOH	This
	575.15 (1 A g <sup>-1</sup> )	89 (5000)	1M H <sub>2</sub> SO <sub>4</sub>	work



**Figure 5.4.** (a, b) CV and GCD profiles at 5-100 mV s<sup>-1</sup> and 1-10 A g<sup>-1</sup> respectively. (c) Plot of  $C_s$  as a function of current density. (d) Log (i) vs. log (v) profile. (e) Capacitive contribution plot for PCN-800 at 5 mV s<sup>-1</sup>. (f) Capacitive charge storage processes vs.

scan rates (5-20 mV s<sup>-1</sup>). (g) Nyquist plot of PCN-800. (h) Cycling stability performance of PCN-800 in acid electrolyte.



**Scheme 5.2.** Possible redox reactions in acidic electrolyte.

The high electrochemical performance of PCN-800 is due to:

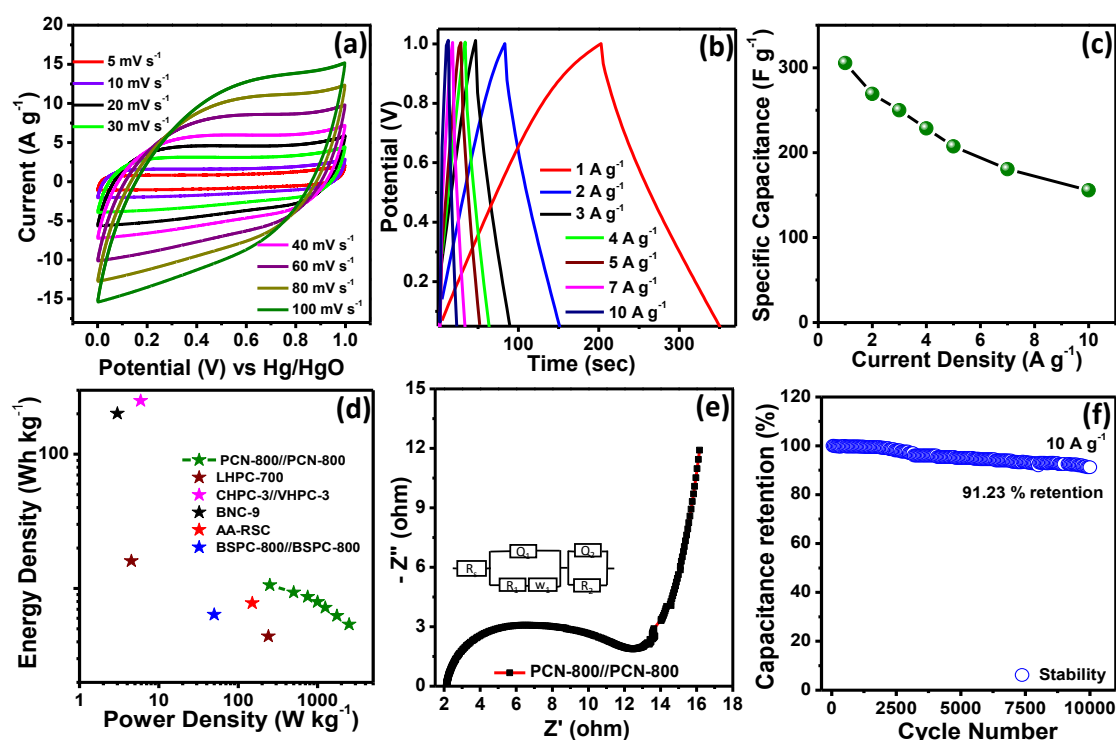
1. Unique 2D porous nanosheets with a high SSA of 3310.4 m<sup>2</sup>/g increase the high SSA offer active sites for easy diffusion of electrolyte ions on the surface of the material. Presence of mesopores and micropores increases the catalytic activity as presence of mesopores increases the capacitance and that of micropores enhances the rate capability of the electrode. The porous structure provide more active sites and higher wettability which promotes the interaction between electrode and electrolyte, consequently improving the electrochemical activity of the material. Although the SSA for PCN-900 is slightly higher than PCN-800 but the higher electrochemical activity of PCN-800 is because of the presence of optimal  $S_{\text{meso}}/S_{\text{micro}}$  (1.05 %) which facilitating fast transmission of electrolyte ions.

2. Heteroatom doping (P and N) to the carbon matrix increases the surface functionalities (surface P, N and O functional group) hence increasing the electrochemical properties of the material. The improved electrochemical stability and reversibility of PCN-800 can be owing to the synergetic effect of P, N and O containing functional groups<sup>16-21</sup>.
3. Another reason for high electrochemical behaviour is optimal P/N doping and porous structure formed at 800 °C activation temperature. As the activation temperature continues to rise, the heteroatoms are reduced because of the formation of volatile heteroatom species at higher temperature.

### **Electrochemical Behavior of symmetrical supercapacitor**

A symmetrical SC device in 6M KOH electrolyte was assembled by using PCN-800 in two electrode system. The CV curves of the PCN-800// PCN-800 device are depicted in Figure 5.5(a) at different sweep rate. The nature of the CV plots remains unaltered (approximately rectangular) indicating the material have good capacitance performance. With rise in sweep rate the CV curves maintains the shape of rectangular without any distortion. Figure 5.5(b) represents the GCD curve of the symmetrical device at different current densities. These shows nearly symmetrical triangle shape suggesting high reversible charge/discharge behavior of the device. The  $C_s$  was found to be 305.64 F g<sup>-1</sup> at 1 A g<sup>-1</sup> current. The  $C_s$  value under 10 A g<sup>-1</sup> decreases to 155.56 F g<sup>-1</sup> from its initial value indicating high capacitance retention of 50.9%, presented in Figure 5.5(c). Furthermore, the quality of the symmetric device depends upon the ED and PD parameters to determine the practical application of the device. Figure 5.5(d) depicts the Ragone plot for the device with other recently reported literature. The ED and PD were

obtained by using equation S4 and S5 and are found to be  $10.61 \text{ W h Kg}^{-1}$  and  $2500 \text{ W Kg}^{-1}$  respectively, which are higher than recently reported heteroatom doped carbon based literature such as LHPC-700<sup>25</sup>, CHPC-3//CHPC-3<sup>41</sup>, BNC-9<sup>42</sup>, AA-RSC<sup>43</sup> and BSPC-800//BSPC-800<sup>44</sup>. The enhanced ED and PD are may be because of porous carbon structure and incorporation of heteroatoms (N and P) into the porous carbon matrix. From the EIS spectra, the  $R_s$  and  $R_{ct}$  are obtained to be 1.9 and 9.7, presented in Figure 5.5(e). The inset of Figure 5.5(e) represents the circuit diagram related to the EIS circuit fit. The cyclic stability plot shows, the capacitance remain 91.23% over 10000 cycles measured at  $10 \text{ A g}^{-1}$  current.



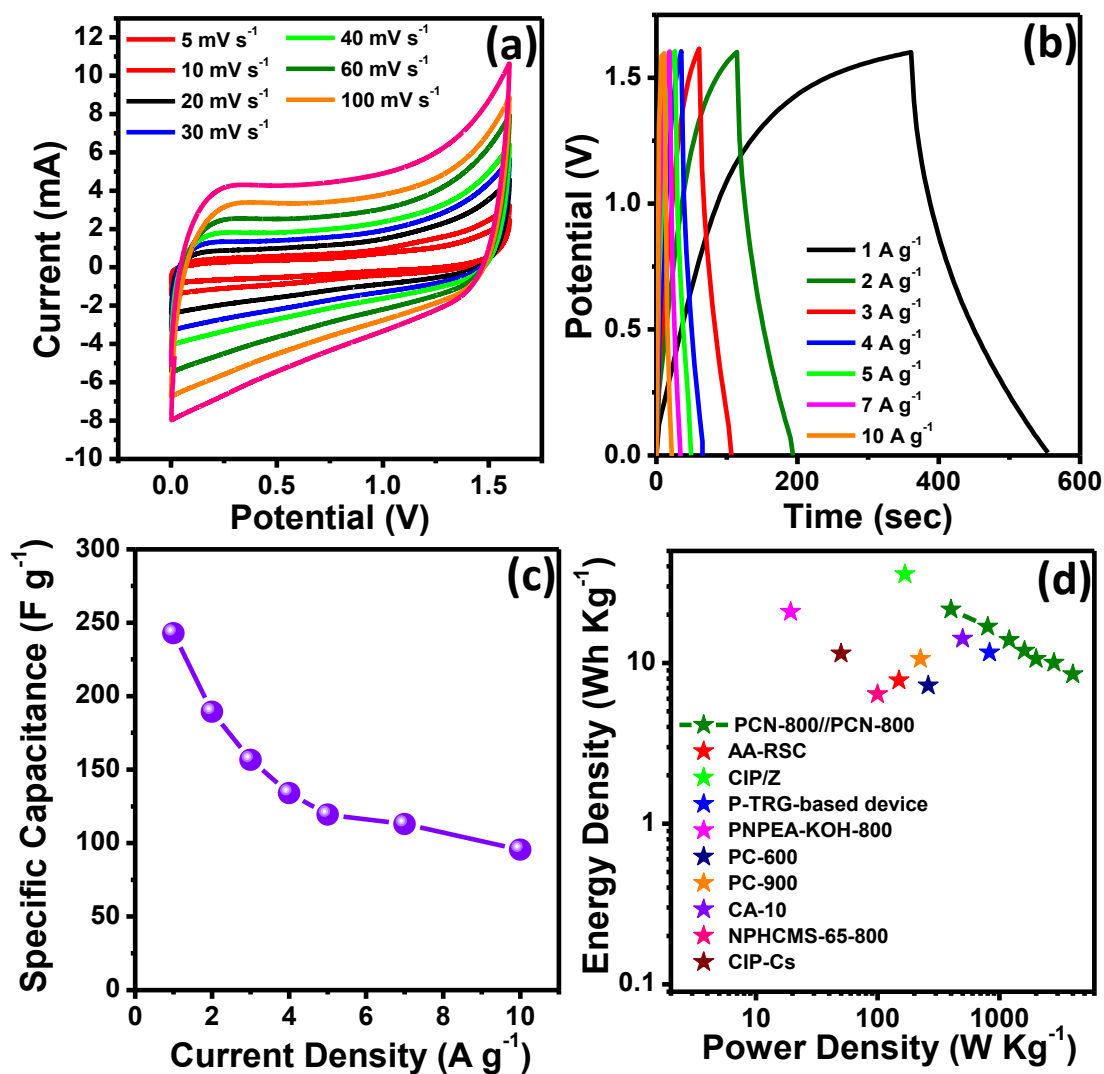
**Figure 5.5.** (a, b) CV and GCD plot profile of a PCN-800//PCN-800 device. (c)  $C_s$  vs. current densities plot. (d) A comparison Ragone plot with previously reported literature. (e) Nyquist plot. (f) Cycling performance for 10000 cycles in alkaline electrolyte.

The electrochemical behavior of the device (PCN-800//PCN-800) was further evaluated in  $1 \text{ M H}_2\text{SO}_4$  electrolyte. Figure S5.8 displays the CV plot at different voltage ranging

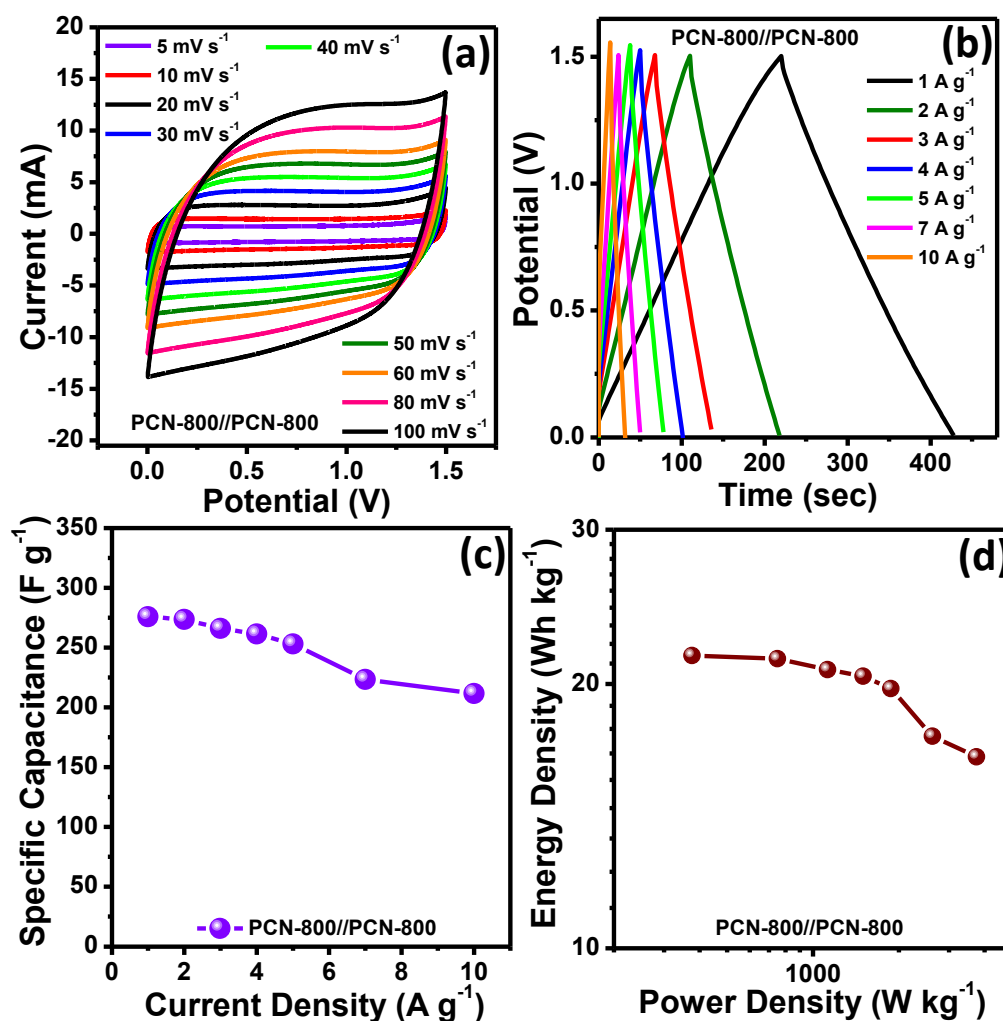


from 1-1.8 V. A sharp rise in current after 1.8 V potential indicates the decomposition of  $\text{H}_2\text{O}$  in an aqueous electrolyte<sup>4</sup>. So we restrict the device potential up to 0-1.6 V. It is

reported by several group that the widening of voltage window is attributed to the existence of phosphorous containing groups on the surface of the material which block electrochemically unstable active oxidation sites, and minimize the process of deterioration of the capacitance associated with free oxygen atoms (i.e. reduction of electrochemical active oxidation sites which are replaced by phosphorous groups)<sup>45-46</sup>. All the CV and GCD curves are obtained within this voltage window. Figure 5.6(a) depicts the CV curve at different sweep rate. A weak pair of redox peak in the CV plot suggest the high rate capability and cyclic reversibility of the PCN-800// PCN-800 device in acid electrolyte owing to high electrical conductivity of the electrode. The GCD curves of the PCN-800// PCN-800 supercapacitor at different current densities ( $1-10 \text{ A g}^{-1}$ ) are presented in Figure 5.6(b). Little distortion in shape of the GCD curve (asymmetric triangular nature) may be due to the existence of P and N heteroatoms, which also improves the activity. The  $C_s$  value of the device in acid medium was calculated to be 242.8, 189.31, 156.59, 133.92, 119.31, 112.88 and 95.55  $\text{F g}^{-1}$  under 1, 2, 3, 4, 5, 7 and 10  $\text{A g}^{-1}$  current respectively. The  $C_s$  value vs. current are represented in Figure 5.6(c) indicating high rate capability and cyclic reversibility.



**Figure 5.6.** (a and b) CV and GCD profiles (c)  $C_s$  vs. current densities. (d) Ragone plot for PCN-800//PCN-800 device in 1 M H<sub>2</sub>SO<sub>4</sub>.



**Figure 5.7.** (a and b) CV and GCD profiles at different scan rates and current densities. (c) Plot of  $C_s$  vs currents (1-7 A g<sup>-1</sup>). (d) Ragone plot of the PCN-800//PCN-800 device in 1 M Na<sub>2</sub>SO<sub>4</sub>.

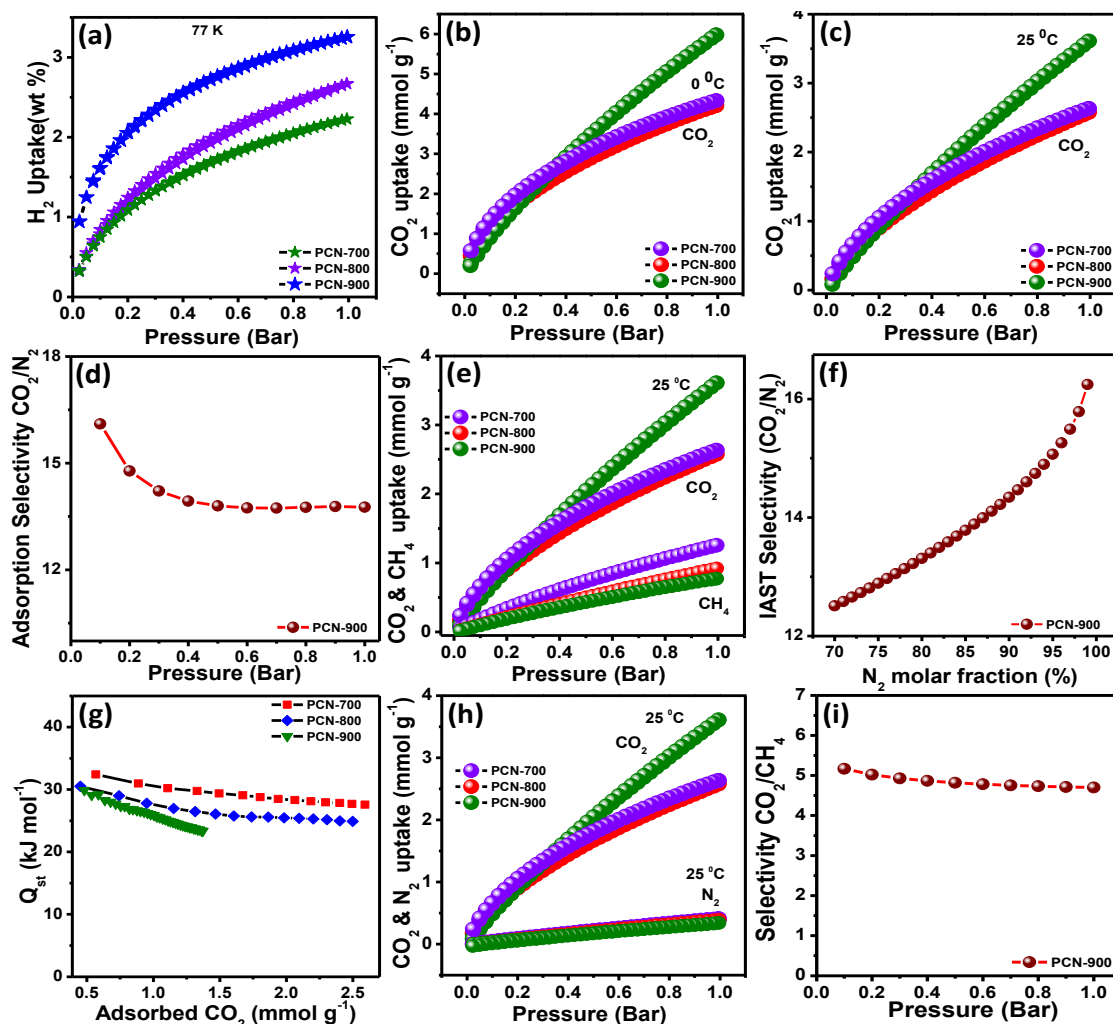
The Ragone plot (ED vs. PD plot) is presented in Figure 5.6(c) in comparison to the other recent references device performance. The device displays PD of 4001.86 W Kg<sup>-1</sup> and the ED was obtained to be 21.58 W h Kg<sup>-1</sup>. The symmetric device performance was also investigated in 1M Na<sub>2</sub>SO<sub>4</sub> solution to examine the practical potential application. Neutral electrolyte are important as they provide large potential window hence

significantly enhancing the ED as well as PD of the device<sup>29</sup>. Figure S5.9 represents the CV cycles by varying the voltage from 1 V to 1.6 V at a sweep rate of 30 mV s<sup>-1</sup>. A sudden rise in the current was observed in the 1.6 V potential range. So we fix the device potential up to 1.5 V and all the CV and GCD profiles are obtained within this voltage range. Figure 5.7(a) displays the CV curve at different sweep rates i.e. from 5-100 mV s<sup>-1</sup>. The CV plots of the device demonstrate quasi-rectangular shape and having no deformation suggesting good rate performance owing to the porous structure and presence of mesopores. The GCD plots at different current densities are depicted in Figure 5.7(b). The GCD curves displays a symmetric triangular nature. The C<sub>s</sub> was calculated to be 275.85 F g<sup>-1</sup> at 1 A g<sup>-1</sup> which decreased to 211.47 F g<sup>-1</sup> at 1 A g<sup>-1</sup> indicating 76.66% capacitance retention. Figure 5.7(c) shows the Ragone plot. The PD is calculated to be 3750.1 W Kg<sup>-1</sup> and ED is 21.55 W h Kg<sup>-1</sup> which is significantly greater than the previously reported heteroatom doped porous carbon.

### 5.4.3. Gas Adsorption Behavior

The hydrogen adsorption isotherms of PCN-x were measured at 77 K temperature from 0 to 1 bar pressure, as depicted in Figure 5.8(a). As presented in the Figure, the broad knee for all the samples reveals the rise in H<sub>2</sub> uptake with increase in activation temperature. The hydrogen uptake of PCN-700, PCN-800 and PCN-900 are obtained to be 2.23, 2.67, and 3.26 wt% respectively at 1 bar pressure. A bar plot presenting the H<sub>2</sub> uptake of PCN-x samples with increasing activation temperature are shown in Figure S5.10 (a). The relationship between the SSA and H<sub>2</sub> uptake are presented in Figure S5.10 (b). Figure S5.10 shows with increase in activation temperature, SSA increases from 700 to 900 °C activation temperature and H<sub>2</sub> storage also increases. The increase in H<sub>2</sub> storage may be due to the increase in micropore surface area and micropore volume with increase

in activation temperature<sup>47-48</sup> and hence PCN-900 have higher H<sub>2</sub> uptake capacity than the other two. Table 5.3 shows the comparison of H<sub>2</sub> storage for PCN-900 with some previously reported heteroatom doped carbon literature indicating PCN-900 is one of the best catalyst for H<sub>2</sub> uptake.



**Figure 5.8.** (a) H<sub>2</sub> storage behaviour of PCN-x at 77 K and 1 bar pressure. (b and c) CO<sub>2</sub> adsorption curve of PCN-x at 0 °C and 25 °C, respectively. (d) Q<sub>st</sub> vs. amount of CO<sub>2</sub> adsorbed for PCN-x. (e) Comparison of CO<sub>2</sub> and N<sub>2</sub> sorption isotherm plot for PCN-x at 25 °C. (f) The CO<sub>2</sub>/N<sub>2</sub> selectivity at 25 ° for PCN-900. (g) Adsorption selectivity of CO<sub>2</sub>/N<sub>2</sub> (15: 85) at 25 °C for PCN-x. (h) CO<sub>2</sub> and CH<sub>4</sub> comparison sorption isotherms plot of PCN-x at 25 °C. (i) Adsorption selectivity of CO<sub>2</sub>/CH<sub>4</sub> (50: 50) at 25 °C for PCN-900.

**Table 5.3.** The H<sub>2</sub> storage capacity of PCN-900 compared with previously reported result.

Adsorbent	H <sub>2</sub> uptake (wt %)	Pressure	References
P-PC	1.75	100 bar	<sup>37</sup>
CA-4700	1.2	30 bar	<sup>49</sup>
JUTE-700, 1:3	1.2	40 bar	<sup>50</sup>
MDC-1	3.25	1 bar	<sup>51</sup>
HPC-650	2.03	1 bar	<sup>47</sup>
NC-3800	2.81	1 bar	<sup>52</sup>
PCN-900	3.26	1 bar	This work

CO<sub>2</sub> adsorption isotherms were measured at two different temperature, at 273K and 298K and 1 bar pressure. CO<sub>2</sub> adsorption behavior of all the PCN-x samples are displayed in Figure 5.8(b, c). PCN-900 shows highest adsorption capacity of 5.98 mmol g<sup>-1</sup> under 273 K temperature and atmospheric pressure. It has been reported in various literature that SSA and micropores are vital for CO<sub>2</sub> adsorption<sup>53-54</sup>. With increase in activation temperature the SSA and micropores increases and hence the CO<sub>2</sub> adsorption capacity is highest for PCN-900. The CO<sub>2</sub> uptake for PCN-700 and PCN-800 are calculated to be 4.33 and 4.21 mmol g<sup>-1</sup> respectively under 273 K and 2.63 and 2.58 mmol g<sup>-1</sup> respectively under 298 K temperature (Figure 5.8(b, c)). As the pressure increases adsorption of CO<sub>2</sub> was followed by capillary condensation, micropore filling and liquefaction<sup>55</sup>. The CO<sub>2</sub> adsorption performance also greatly depends upon the presence of oxygen-containing functional groups. The presence of O-C=O was confirmed from XPS findings revealing

the existence of oxygen functional group as oxygen containing group have a positive effect on CO<sub>2</sub> capture. In this study, activation at higher temperature was conducive for the formation of high SSA, leading to high CO<sub>2</sub> adsorption. Figure S5.11 displays the comparison bar plot for CO<sub>2</sub> adsorption of PCN-x samples at two different temperatures (273 K and 298 K) indicating PCN-900 shows higher CO<sub>2</sub> uptake capacity compared to other two samples. Table S5.3 represents a comparison of the CO<sub>2</sub> uptake capacities of various reported porous carbon materials at 0 °C and 1 bar pressure.

In order to estimate the interaction strength between PCN-x samples and CO<sub>2</sub>, the isosteric heat of adsorption ( $Q_{st}$ ) were calculated by using Clausius-Clapeyron equation on the basis of CO<sub>2</sub> uptake at 273 K and 298 K temperature.  $Q_{st}$  values gives information about the binding affinity between carbon and CO<sub>2</sub>. Higher  $Q_{st}$  value indicates stronger interaction. A plot for  $Q_{st}$  vs. adsorbed CO<sub>2</sub> for all the three PCN-x samples are displayed in Figure 5.8(d). The  $Q_{st}$  value varies in the range of 29.87 to 32.41 kJ mol<sup>-1</sup> at low CO<sub>2</sub> uptake. The higher initial  $Q_{st}$  values reveals that there is a strong interaction between the CO<sub>2</sub> molecules and pores of PCN-x samples<sup>56</sup>. Meanwhile, the heteroatom doping plays an key role in the initial interaction of CO<sub>2</sub> adsorption because of the formation of strong pole-pole interaction between the quadrupole moment of CO<sub>2</sub> molecules and the polar sites corresponding to the heteroatom functional group and strong acid-base interaction between the acidic CO<sub>2</sub> molecules and basic nitrogen containing functional groups<sup>56-57</sup>. The  $Q_{st}$  for PCN-x decreased to 27.56-23.34 kJ mol<sup>-1</sup>. The  $Q_{st}$  values are in the range of 23.34-29.87 kJ mol<sup>-1</sup> for PCN-900, 30.51-24.91 kJ mol<sup>-1</sup> for PCN-800, and 32.41-27.56 kJ mol<sup>-1</sup> for PCN-700 respectively. These  $Q_{st}$  values are lower than the energy required to cleavage of CO<sub>2</sub> bond i.e. 749 kJ mol<sup>-1</sup>, suggesting the adsorption process between the CO<sub>2</sub> molecules and adsorbents are physisorption<sup>58-59</sup>. Landfill and flue gas are the

mixture of CO<sub>2</sub>/CH<sub>4</sub> and CO<sub>2</sub>/N<sub>2</sub> respectively. So removal of CO<sub>2</sub> from N<sub>2</sub> and CH<sub>4</sub> are of great practical significance. So the selectivity performance of CO<sub>2</sub>/CH<sub>4</sub> and CO<sub>2</sub>/N<sub>2</sub> are calculated by using ideal adsorbed solution theory (IAST). The selectivity of CO<sub>2</sub>/N<sub>2</sub> and CO<sub>2</sub>/CH<sub>4</sub> gas mixture are calculated by using the following equation<sup>60</sup>:

$$S = \frac{P_2 q_1}{P_1 q_2}$$

Here ‘S’ represents the selectivity, P<sub>1</sub> and P<sub>2</sub> are the partial pressure of component 1 and 2, q<sub>1</sub> and q<sub>2</sub> stand for amount of component 1 and 2 adsorbed respectively.

To investigate the CO<sub>2</sub>/N<sub>2</sub> selectivity, CO<sub>2</sub> and N<sub>2</sub> adsorption isotherm were collected at 298 K and 1 bar pressure. Figure 5.8(e) displays the comparison plot of CO<sub>2</sub> and N<sub>2</sub> uptake isotherm for all the PCN-x samples. The IAST calculations were used to calculate the adsorption equilibrium for the following binary mixtures: CO<sub>2</sub>/N<sub>2</sub>:15/85 and CO<sub>2</sub>/CH<sub>4</sub>:50/50 respectively. The selectivity results of CO<sub>2</sub>/N<sub>2</sub> for PCN-900 is displayed in Figure 5.8(f) resulting maximum selectivity of 13.78. Selectivity bar plot of CO<sub>2</sub>/N<sub>2</sub> binary mixture in a 15:85 ratio and 1 bar pressure for PCN-x samples are presented in Figure S5.12. The selectivity for PCN-700 and PCN-800 are obtained to be 13.57 and 12.73 respectively. Figure 5.8(g) represents the change in adsorption selectivity of CO<sub>2</sub>/N<sub>2</sub> vs. pressure. Microporosity and surface chemistry of the materials play a leading role for the increase in selectivity of PCN-900 than PCN-700 and PCN-800<sup>60</sup>. The CO<sub>2</sub>/CH<sub>4</sub> selectivity with a mole fraction of 50:50 for all the samples are calculated at 298 K under 1 bar pressure. Figure 5.8(h) displays the comparison selectivity plot of CO<sub>2</sub>/CH<sub>4</sub> for all the three samples. Figure S5.13 represents the bar plot of PCN-x samples showing the CO<sub>2</sub>/CH<sub>4</sub> selectivity for binary mixture of ratio (50:50) under pressure of 1 bar. Adsorption selectivity of PCN-900 for CO<sub>2</sub>/CH<sub>4</sub> binary mixture (50:50) at 298 K temperature and 1 bar pressure is displayed in Figure 5.8(i). Highest selectivity of 5.1



was achieved at low pressure (0.1 bar), and with rise in pressure to 1 bar, the selectivity decreased to 4.7 for PCN-900. Selectivity of CO<sub>2</sub>/CH<sub>4</sub> for PCN-700 and PCN-800 are calculated to be 2.43 and 3.32 at pressure of 1 bar. The IAST selectivity of CO<sub>2</sub>/N<sub>2</sub> is higher than the selectivity of CO<sub>2</sub>/CH<sub>4</sub> corresponding to higher uptake capacity and the polarity of its methane molecules<sup>61</sup>.

## 5.5. CONCLUSIONS

P and N co-doped porous carbon were synthesized through KOH activation method with formamide as carbon and nitrogen source and sodium hypophosphite as phosphorous source. The P and N co-doped porous carbon activated at 800 °C (PCN-800) displays a very high C<sub>s</sub> of 575.15 and 477.63 F g<sup>-1</sup> at 1 A g<sup>-1</sup> current in acid and alkaline electrolytes respectively. The symmetric device performance shows an excellent ED of 10.61 W h kg<sup>-1</sup> at a PD of 250 W kg<sup>-1</sup> along with 91.23 % cyclic stability over 10000 cycles. Higher SSA, abundant micropores and optimum P/N doping of PCN-800 are advantageous in transport and adsorption of electrolyte ions resulting higher electrochemical activity of PCN-800. The P and N co-doped porous carbon activated at 900 °C (PCN-900) shows a good H<sub>2</sub> uptake of 3.26 wt% at 77K and 1 bar pressure. The CO<sub>2</sub> uptake capacities were obtained to be 5.98 and 3.61 mmol g<sup>-1</sup> at 0 and 25 °C temperatures respectively with good CO<sub>2</sub>/N<sub>2</sub> and CO<sub>2</sub>/CH<sub>4</sub> selectivity. This result demonstrate the P and N co-doping strategy could enhances the electrochemical performance and it is of great potential for gas adsorption application.

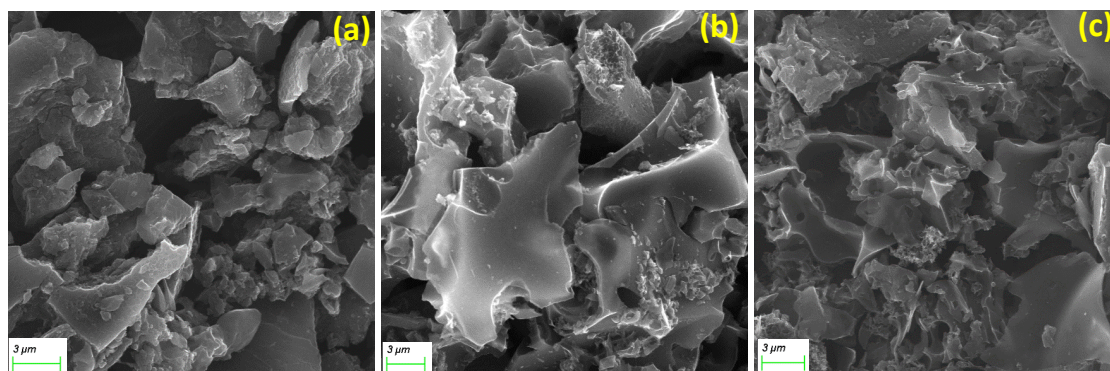
## 5.6. REFERENCES

- (1) Rana, M.; Subramani, K.; Sathish, M.; Gautam, U. K. *Carbon* **2017**, *114*, 679-689.
- (2) Huang, Y.; Wang, Y.; Tang, C.; Wang, J.; Zhang, Q.; Wang, Y.; Zhang, J. *Advanced Materials* **2019**, *31*, 1803800.
- (3) Abbas, Q.; Raza, R.; Shabbir, I.; Olabi, A. G. *Journal of Science: Advanced Materials and Devices* **2019**, *4*, 341-352.
- (4) Nirosha, B.; Selvakumar, R.; Jeyanthi, J.; Vairam, S. *New Journal of Chemistry* **2020**, *44*, 181-193.
- (5) Rehman, A.; Nazir, G.; Yop Rhee, K.; Park, S.-J. *Chemical Engineering Journal* **2021**, *420*, 130421.
- (6) Ashourirad, B.; Arab, P.; Verlander, A.; El-Kaderi, H. M. *ACS Applied Materials & Interfaces* **2016**, *8*, 8491-8501.
- (7) Zhang, J.; Qiao, Z.-A.; Mahurin, S. M.; Jiang, X.; Chai, S.-H.; Lu, H.; Nelson, K.; Dai, S. *Angewandte Chemie International Edition* **2015**, *54*, 4582-4586.
- (8) Choi, M.; Ryoo, R. *Journal of Materials Chemistry* **2007**, *17*, 4204-4209.
- (9) Kou, T.; Yao, B.; Liu, T.; Li, Y. *Journal of Materials Chemistry A* **2017**, *5*, 17151-17173.
- (10) Rawal, S.; Kumar, Y.; Mandal, U. K.; Kumar, A.; Tanwar, R.; Joshi, B. *SN Applied Sciences* **2021**, *3*, 141.
- (11) Subramanian, N.; Viswanathan, B. *RSC Advances* **2015**, *5*, 63000-63011.
- (12) Shi, Q.; Zhang, R.; Lv, Y.; Deng, Y.; Elzatahrya, A. A.; Zhao, D. *Carbon* **2015**, *84*, 335-346.
- (13) Rashidi, N. A.; Yusup, S. *Journal of Energy Storage* **2020**, *32*, 101757.
- (14) Jung, M.-J.; Jeong, E.; Kim, S.; Lee, S. I.; Yoo, J.-S.; Lee, Y.-S. *Journal of Fluorine Chemistry* **2011**, *132*, 1127-1133.
- (15) Hulicova-Jurcakova, D.; Puziy, A. M.; Poddubnaya, O. I.; Suárez-García, F.; Tascón, J. M. D.; Lu, G. Q. *Journal of the American Chemical Society* **2009**, *131*, 5026-5027.
- (16) Huang, C.; Puziy, A. M.; Poddubnaya, O. I.; Hulicova-Jurcakova, D.; Sobiesiak, M.; Gawdzik, B. *Electrochimica Acta* **2018**, *270*, 339-351.
- (17) Wang, Y.; Xiao, J.; Wang, H.; Zhang, T. C.; Yuan, S. *Journal of Materials Science & Technology* **2022**, *99*, 73-81.
- (18) Moreno-Fernández, G.; Gómez-Urbano, J. L.; Enterría, M.; Cid, R.; López del Amo, J. M.; Mysyk, R.; Carriazo, D. *Electrochimica Acta* **2020**, *361*, 136985.
- (19) Liu, S.; Yang, Z.; Li, M.; Liu, L.; Wang, Y.; Lv, W.; Qin, Z.; Zhao, X.; Zhu, P.; Wang, G. *Electrochimica Acta* **2018**, *265*, 221-231.
- (20) Zeng, H.; Wang, W.; Li, J.; Luo, J.; Chen, S. *ACS Applied Materials & Interfaces* **2018**, *10*, 8721-8729.
- (21) Bing, X.; Wei, Y.; Wang, M.; Xu, S.; Long, D.; Wang, J.; Qiao, W.; Ling, L. *Journal of Colloid and Interface Science* **2017**, *488*, 207-217.
- (22) Li, G.; Li, Y.; Deng, J.; Lin, H.; Hou, X.; Jia, L. *Materials Chemistry Frontiers* **2020**, *4*, 2704-2715.
- (23) Xiao, J.; Wang, Y.; Zhang, T. C.; Ouyang, L.; Yuan, S. *Journal of Power Sources* **2022**, *517*, 230727.
- (24) Meng, F.; Gong, Z.; Wang, Z.; Fang, P.; Li, X. *Fuel* **2019**, *251*, 562-571.
- (25) Yang, H.; Sun, X.; Zhu, H.; Yu, Y.; Zhu, Q.; Fu, Z.; Ta, S.; Wang, L.; Zhu, H.; Zhang, Q. *Ceramics International* **2020**, *46*, 5811-5820.
- (26) Yang, C.; Li, P.; Wei, Y.; Wang, Y.; Jiang, B.; Wu, W. Preparation of Nitrogen and Phosphorus Doped Porous Carbon from Watermelon Peel as Supercapacitor Electrode Material *Micromachines* [Online], 2023.

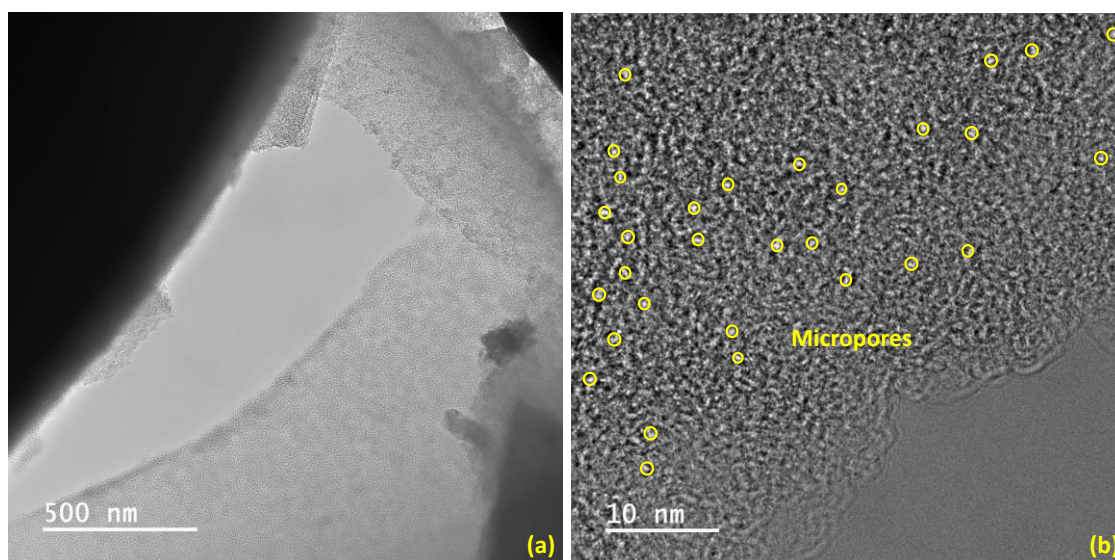
- (27) Huo, S.; Zhao, Y.; Zong, M.; Liang, B.; Zhang, X.; Khan, I. U.; Li, K. *Electrochimica Acta* **2020**, 353, 136523.
- (28) Nian, Y.-R.; Teng, H. *Journal of Electroanalytical Chemistry* **2003**, 540, 119-127.
- (29) Zhang, H.; Song, Y.; Liu, Y.; Zhao, J.; Li, Y. *Electrochimica Acta* **2022**, 431, 141131.
- (30) Nasini, U. B.; Bairi, V. G.; Ramasahayam, S. K.; Bourdo, S. E.; Viswanathan, T.; Shaikh, A. U. *Journal of Power Sources* **2014**, 250, 257-265.
- (31) Zhang, N.; Liu, F.; Xu, S.-D.; Wang, F.-Y.; Yu, Q.; Liu, L. *Journal of Materials Chemistry A* **2017**, 5, 22631-22640.
- (32) Yuan, C.; Liu, X.; Jia, M.; Luo, Z.; Yao, J. *Journal of Materials Chemistry A* **2015**, 3, 3409-3415.
- (33) Annamalai, K. P.; Gao, J.; Liu, L.; Mei, J.; Lau, W.; Tao, Y. *Journal of Materials Chemistry A* **2015**, 3, 11740-11744.
- (34) Qu, J.; Geng, C.; Lv, S.; Shao, G.; Ma, S.; Wu, M. *Electrochimica Acta* **2015**, 176, 982-988.
- (35) Jin, J.; Qiao, X.; Zhou, F.; Wu, Z.-S.; Cui, L.; Fan, H. *ACS Applied Materials & Interfaces* **2017**, 9, 17317-17325.
- (36) Jin, T.; Su, J.; Luo, Q.; Zhu, W.; Lai, H.; Huang, D.; Wang, C. *ACS Omega* **2022**, 7, 37564-37571.
- (37) Ariharan, A.; Ramesh, K.; Vinayagamoorthi, R.; Rani, M. S.; Viswanathan, B.; Ramaprabhu, S.; Nandhakumar, V. *Journal of Energy Storage* **2021**, 35, 102185.
- (38) Wen, Y.; Wang, B.; Huang, C.; Wang, L.; Hulicova-Jurcakova, D. *Chemistry – A European Journal* **2015**, 21, 3520-3520.
- (39) Cheng, H.; Yi, F.; Gao, A.; Liang, H.; Shu, D.; Zhou, X.; He, C.; Zhu, Z. *ACS Applied Energy Materials* **2019**, 2, 4084-4091.
- (40) Lv, B.; Li, P.; Liu, Y.; Lin, S.; Gao, B.; Lin, B. *Applied Surface Science* **2018**, 437, 169-175.
- (41) Hui, S.; Ying, Z.; Lin, X.; Sun, J.; Wang, Y.; Fu, Q.; Li, J. *Journal of Alloys and Compounds* **2020**, 846, 156235.
- (42) Guo, H.; Gao, Q. *Journal of Power Sources* **2009**, 186, 551-556.
- (43) Sudhan, N.; Subramani, K.; Karnan, M.; Ilayaraja, N.; Sathish, M. *Energy & Fuels* **2017**, 31, 977-985.
- (44) Li, J.; Zan, G.; Wu, Q. *RSC Advances* **2016**, 6, 57464-57472.
- (45) Yan, X.; Liu, Y.; Fan, X.; Jia, X.; Yu, Y.; Yang, X. *Journal of Power Sources* **2014**, 248, 745-751.
- (46) Liu, C.; Shi, G.; Wang, G.; Mishra, P.; Jia, S.; Jiang, X.; Zhang, P.; Dong, Y.; Wang, Z. *RSC Advances* **2019**, 9, 6898-6906.
- (47) Zhao, Z.-Q.; Xiao, P.-W.; Zhao, L.; Liu, Y.; Han, B.-H. *RSC Advances* **2015**, 5, 73980-73988.
- (48) Chen, Q.; Luo, M.; Hammershøj, P.; Zhou, D.; Han, Y.; Laursen, B. W.; Yan, C.-G.; Han, B.-H. *Journal of the American Chemical Society* **2012**, 134, 6084-6087.
- (49) Blankenship, L. S.; Balahmar, N.; Mokaya, R. *Nature Communications* **2017**, 8, 1545.
- (50) Ramesh, T.; Rajalakshmi, N.; Dhathathreyan, K. S. *Renew. Energy Environ. Sustain.* **2017**, 2.
- (51) Yang, S. J.; Kim, T.; Im, J. H.; Kim, Y. S.; Lee, K.; Jung, H.; Park, C. R. *Chemistry of Materials* **2012**, 24, 464-470.
- (52) Hu, W.; Huang, J.; Yu, P.; Zheng, M.; Xiao, Y.; Dong, H.; Liang, Y.; Hu, H.; Liu, Y. *ACS Sustainable Chemistry & Engineering* **2019**, 7, 15385-15393.
- (53) Quan, C.; Wang, H.; Jia, X.; Gao, N. *Journal of the Energy Institute* **2021**, 97, 92-99.
- (54) Jang, E.; Choi, S. W.; Hong, S.-M.; Shin, S.; Lee, K. B. *Applied Surface Science* **2018**, 429, 62-71.
- (55) Wang, H.; Li, X.; Cui, Z.; Fu, Z.; Yang, L.; Liu, G.; Li, M. *Journal of Colloid and Interface Science* **2020**, 578, 491-499.
- (56) Wang, Y.; Wang, M.; Wang, Z.; Wang, S.; Fu, J. *Applied Surface Science* **2020**, 507, 145130.
- (57) Hao, G.-P.; Li, W.-C.; Qian, D.; Lu, A.-H. *Advanced Materials* **2010**, 22, 853-857.
- (58) Li, J.; Chen, X.; Gong, J.; Zhu, J.; Mijowska, E. *Diamond and Related Materials* **2020**, 105, 107802.

- (59) Li, J.; Michalkiewicz, B.; Min, J.; Ma, C.; Chen, X.; Gong, J.; Mijowska, E.; Tang, T. *Chemical Engineering Journal* **2019**, 360, 250-259.
- (60) Ojeda-López, R.; Vilarrasa-García, E.; C. S. Azevedo, D.; Felipe, C.; Cecilia, J. A.; Rodríguez-Castellón, E. *Fuel* **2022**, 324, 124242.
- (61) Hong, L.; Ju, S.; Liu, X.; Zhuang, Q.; Zhan, G.; Yu, X. *Energy & Fuels* **2019**, 33, 11454-11464.
- (62) Guo, X.; Zhang, G.; Wu, C.; Liu, J.; Li, G.; Zhao, Y.; Wang, Y.; Xu, Y. *Journal of Environmental Chemical Engineering* **2021**, 9, 105165.
- (63) Abdelmoaty, Y. H.; Tessema, T.-D.; Norouzi, N.; El-Kadri, O. M.; Turner, J. B. M.; El-Kaderi, H. M. *ACS Applied Materials & Interfaces* **2017**, 9, 35802-35810.
- (64) Periyasamy, T.; Asrafali, S. P.; Kim, S.-C. Heteroatom-Enhanced Porous Carbon Materials Based on Polybenzoxazine for Supercapacitor Electrodes and CO<sub>2</sub> Capture *Polymers* [Online], 2023.
- (65) Ma, X.; Li, L.; Chen, R.; Wang, C.; Li, H.; Wang, S. *Applied Surface Science* **2018**, 435, 494-502.
- (66) Cui, H.; Xu, J.; Shi, J.; Yan, N.; Liu, Y. *Energy* **2019**, 187, 115936.
- (67) Tian, W.; Zhang, H.; Sun, H.; Suvorova, A.; Saunders, M.; Tade, M.; Wang, S. *Advanced Functional Materials* **2016**, 26, 8651-8661.

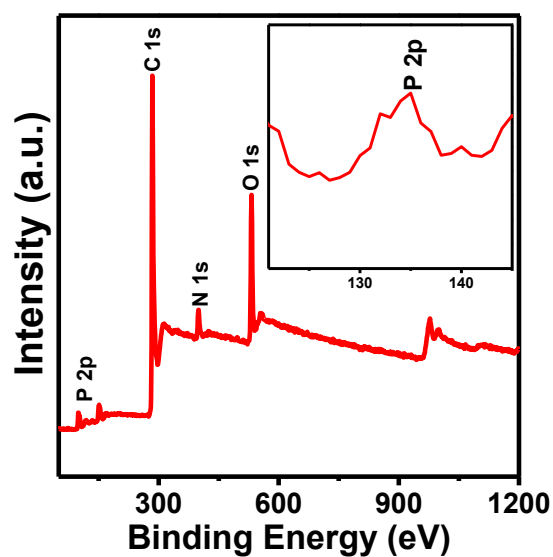
## Appendix C



**Figure S5.1.** FESEM images of porous (a) PCN-700, (b) PCN-800 and (c) PCN-900 samples.



**Figure S5.2.** (a) Low resolution TEM image and (b) HRTEM image of PCN-800.



**Figure S5.3.** XPS survey scan spectra of PCN-800 sample.



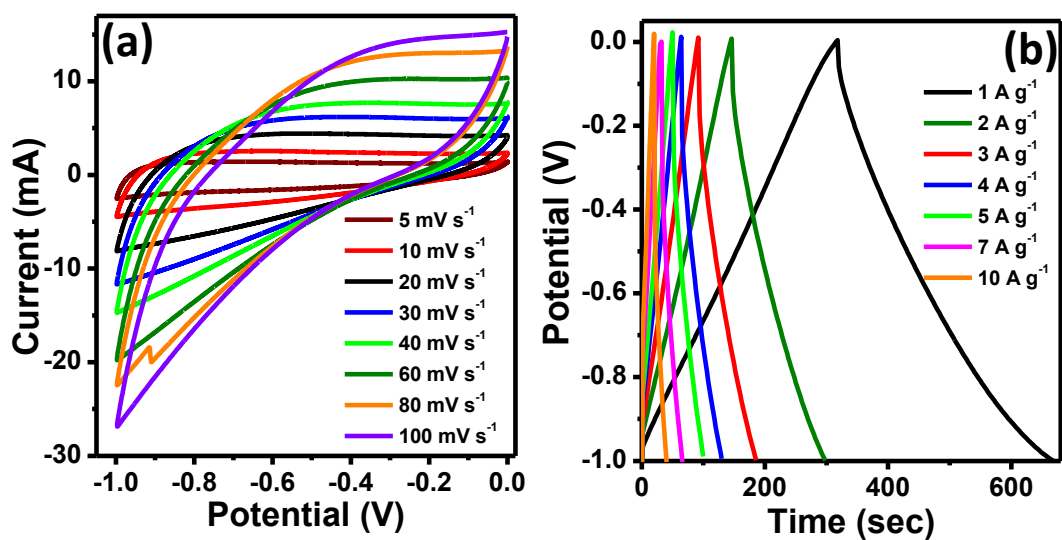


Figure S5.4. CV and GCD profiles of PCN-700.

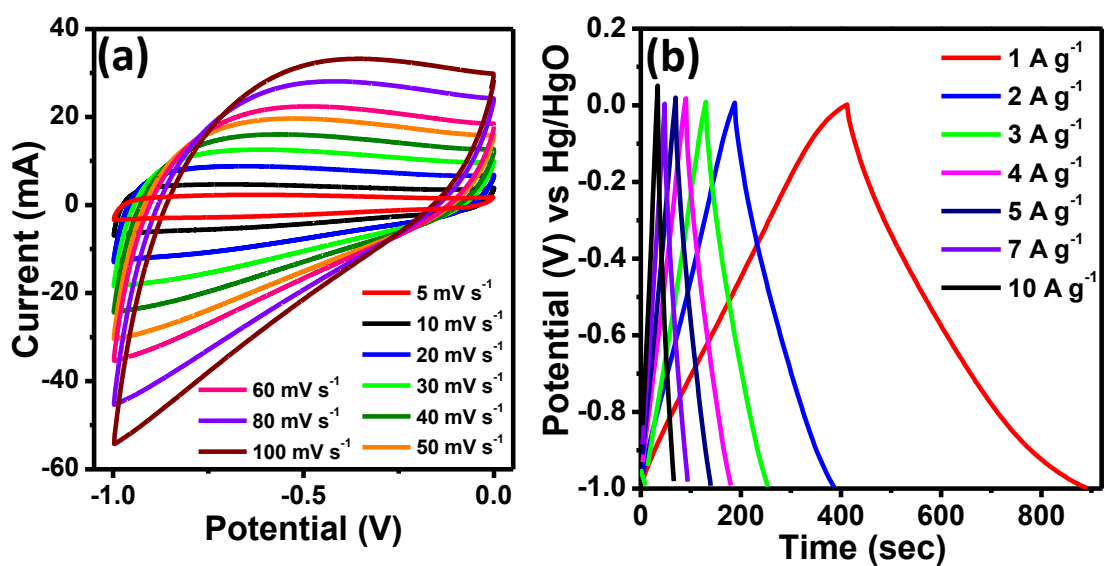


Figure S5.5. CV and GCD profiles of PCN-800.

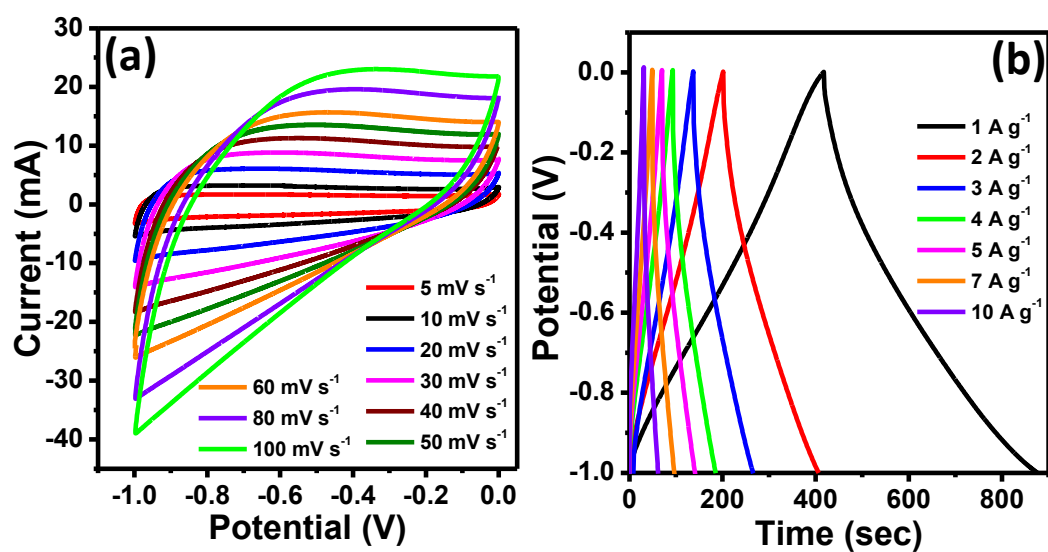


Figure S5.6. CV and GCD profiles of PCN-900.

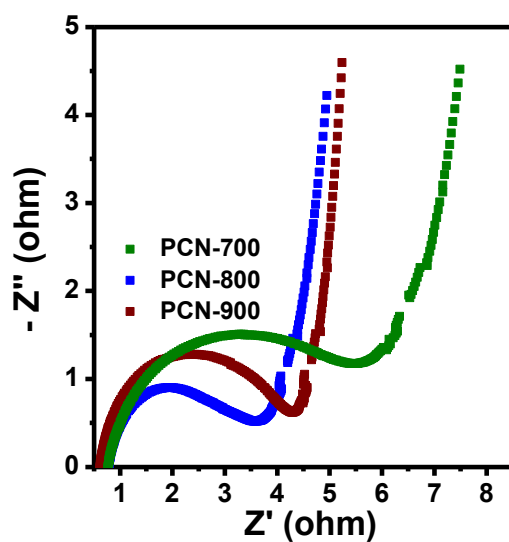
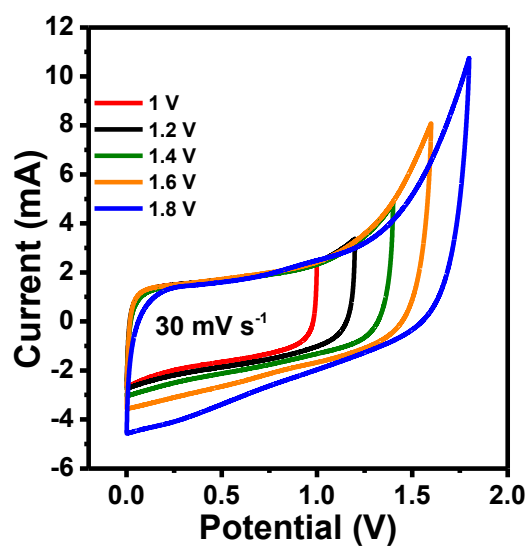
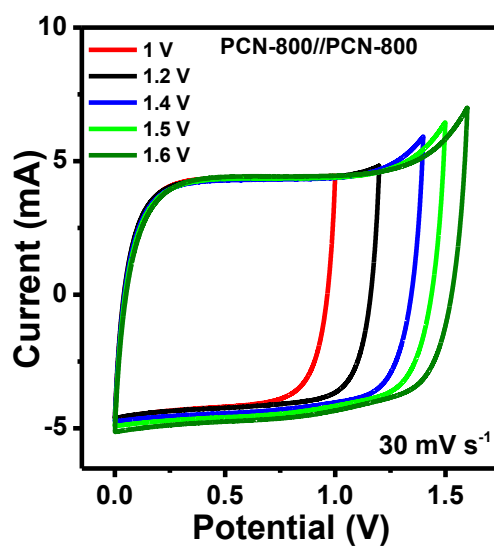


Figure S5.7. EIS plot of PCN-x samples in 6M KOH electrolyte.



**Figure S5.8.** CV curves of a symmetric capacitor at the different potential range of 1 to 1.8 V in 1M H<sub>2</sub>SO<sub>4</sub>.



**Figure S5.9.** CV curves of a symmetric capacitor at the different potential range of 1 to 1.6 V in 1M Na<sub>2</sub>SO<sub>4</sub>.



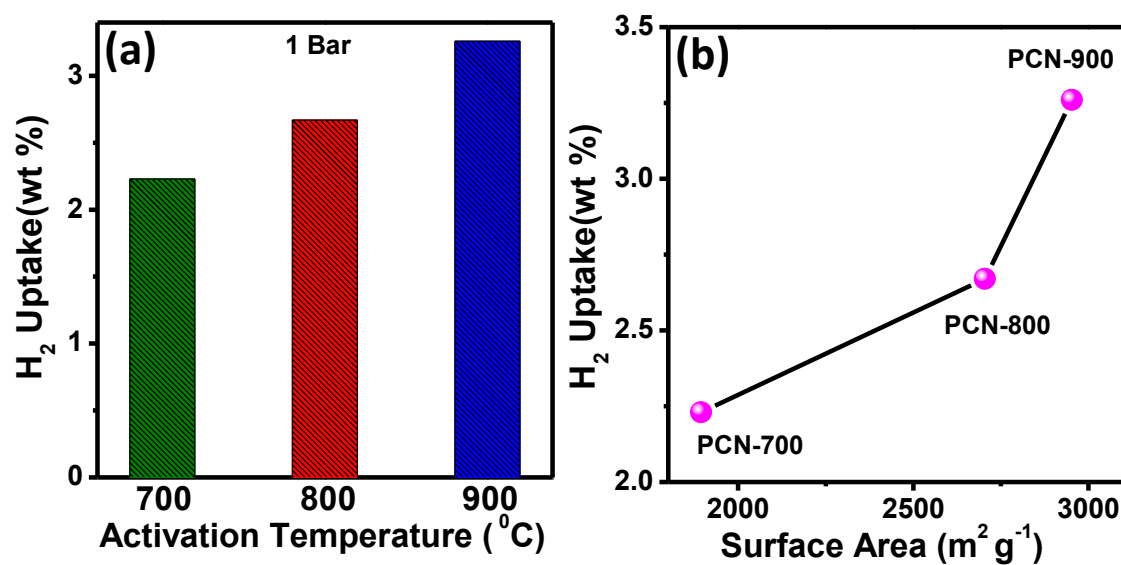


Figure S5.10. (a) H<sub>2</sub> uptake of all the samples at 77K and 1 bar pressure. (b) Change in H<sub>2</sub> uptake as a function of surface area.

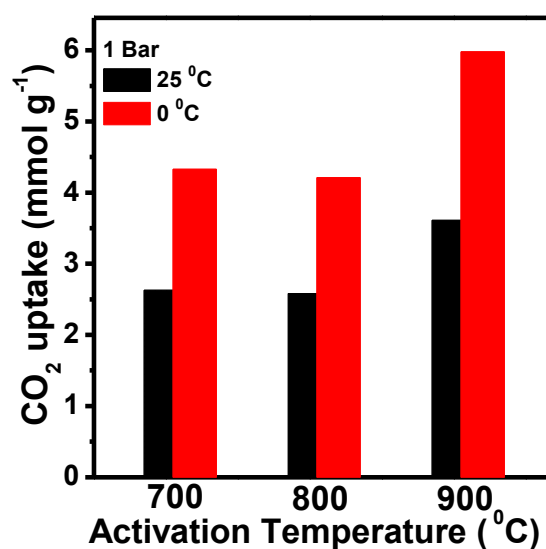
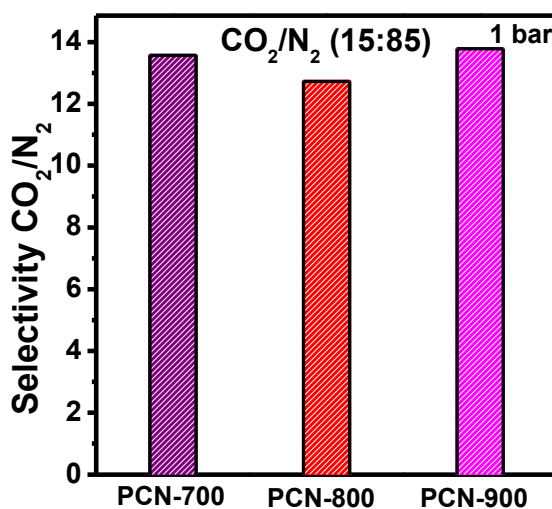
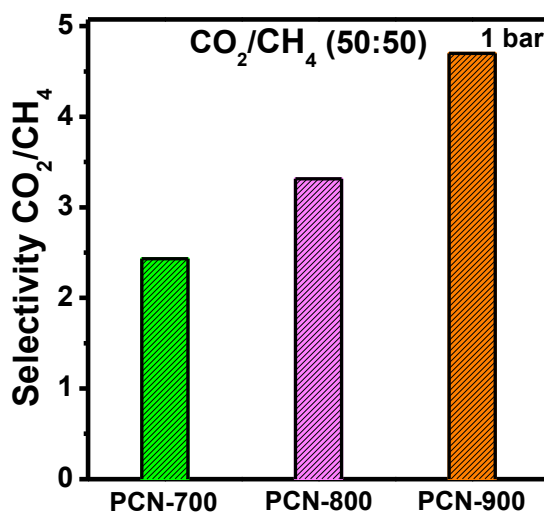


Figure S5.11. CO<sub>2</sub> uptake capacities of PCN-700 to 900 at 1 bar pressure.



**Figure S5.12.** CO<sub>2</sub>/N<sub>2</sub> selectivities of PCN-x samples for binary mixture of ratio (15:85) under pressure of 1 bar.



**Figure S5.13.** CO<sub>2</sub>/CH<sub>4</sub> selectivities of PCN-x samples for binary mixture of ratio (50:50) under pressure of 1 bar

**Table S5.1.** Weight % of C, P, N, and O present in PCN-x samples calculated from SEM EDX analysis.

Sample Name	C (%)	P (%)	N (%)	O (%)
PCN-700	87.10	1.10	2.10	9.70
PCN-800	86.20	2.1	3.10	8.60
PCN-900	87.20	0.80	1.70	10.40

**Table S5.2.** Comparison of electrochemical performance of PCN-x samples in 6M KOH electrolyte.

<b>Sample Name</b>	<b>Specific capacitance (<math>\text{F g}^{-1}</math>) at 1 A <math>\text{g}^{-1}</math> current density (6M KOH electrolyte)</b>
PCN-700	349.3
PCN-800	477.63
PCN-900	456.53

**Table S5.3.** CO<sub>2</sub> uptake capacities of carbon materials at 25 °C temperature and 1 bar pressure.

<b>Adsorbent</b>	<b>CO<sub>2</sub> uptake (<math>\text{mmol g}^{-1}</math>)</b>	<b>Pressure</b>	<b>References</b>
PCSK-2-3-80	5.61	1 bar	62
PYDC-550-2	3.714	0.15 bar	63
NRPC 800	3.6	1 bar	64
MUC900	3.7	1 atm	65
P0	5.12	1 bar	66
NSC	4.7	1 bar	67
NPPC-0.75-600	3.02	100 kPa	23
PCN-900	5.98	1 bar	This work

## Chapter 6

### Design of Co<sub>1</sub>Al<sub>3</sub>(OH)<sub>m</sub>/Carbon Nitride hybrid Nanostructure for Enhanced Capacitive Energy Storage in Alkaline Electrolyte

#### 6.1. ABSTRACT

Over the past few years, layered double hydroxide (LDH) nanostructures attracted the attention of scientific community owing to their facile synthesis, interesting structure, and morphology and have been promising in the fields of energy storage applications. In this chapter, CoAl LDH over graphitic carbon nitride (CN<sub>x</sub>) surface was synthesized by varying the ratio of Co:Al and among them, Co<sub>1</sub>Al<sub>3</sub>(OH)<sub>m</sub>/CN<sub>x</sub> composite was found to have maximum electrochemical behaviour for supercapacitor application in alkaline electrolytes. Interestingly, it exhibits 3D nano flower-like structure which provides a high specific capacitance (C<sub>s</sub>) value of 138 mAh/g (1000 F/g) at 1 A/g current density and cyclic durability of approximately 84.46 % after 4500 cycles at 10 A/g current density. In addition, we obtained a specific capacitance of 71.5 F/g at 1 A/g current density along with long-term cyclic stability for the asymmetric supercapacitor (ASC) Co<sub>1</sub>Al<sub>3</sub>(OH)<sub>m</sub>/CN<sub>x</sub>//AC assembled with Co<sub>1</sub>Al<sub>3</sub>(OH)<sub>m</sub>/CN<sub>x</sub> as positive and activated carbon (AC) as negative electrodes respectively. Furthermore, an energy density of 22.35 W h kg<sup>-1</sup> is obtained at 750.2 W kg<sup>-1</sup> power densities in ASC. The enhanced charge storage property of the aforementioned material can be attributed to the high surface area of the composite and the synergetic interaction between CN<sub>x</sub> and CoAl-LDH. Moreover, this facile synthesis method is promising for designing a novel and cost-effective electrode material for supercapacitor applications.

## 6.2. INTRODUCTION

The depletion of fossil fuels and the rising environmental concerns have made it crucial for the development of sustainable and clean energy sources<sup>1-3</sup>. The ever-increasing demand for modern electric vehicles and electronic devices promotes the growth of highly efficient energy storage devices with high energy density as well as high power density. Out of several energy storage devices, supercapacitors have gained enormous attention owing to their long life cycles, high power density and safe operation<sup>2, 4</sup>. Compared to conventional secondary batteries, supercapacitors offer promising power efficiency to meet the demand of practical applications. Based on the energy storage mechanism, general supercapacitors are classified as Electrical double-layer capacitors (EDLCs) and pseudocapacitors<sup>5-6</sup>. In fact, EDLCs work through the adsorption of electrolytic ions on the electrode surface and pseudocapacitors work on the existence of faradaic redox reactions during the charge-discharge process<sup>7-8</sup>. Examples of EDLCs include carbon-based materials while pseudocapacitors include metal oxides, hydroxides and sulfides etc<sup>9-10</sup>. Therefore, designing better supercapacitors relies on developing electrode materials with noticeable capacity values.

In electrochemical applications, Layered double hydroxides (LDHs) have appeared as promising material towards applications like water electrolysis and supercapacitors<sup>2, 11</sup>. LDHs are composed of both divalent and trivalent metal cations with a general formula of  $[M(II)_{1-x}M(III)_x(OH)_2]^{x+}[A^{n-}]_{x/n} \cdot zH_2O$ , where A is an anion. Also, LDHs can intercalate and exchange anions. Since LDHs can provide many electrochemical active sites, they can be the potential materials to improve the capacity of modern electrochemical capacitors. However, the low rate of diffusion of mass and electron transfer restricts the high charge-discharge capability of LDHs<sup>1</sup>. Nowadays, several

efforts have been exploited to design LDH based supercapacitor electrodes using non-precious metals and different strategies like designing porous morphology, controlling the size of the Nanocomposite, amorphization of materials, synthesizing oxygen-deficient materials or defect-rich materials and tuning the composition of LDH have been adopted for enhanced capacitive behaviour<sup>12</sup>. Previously it has been reported that the molar ratio of trivalent and divalent ion affects the morphology, structure and charge storage capacity of LDHs. Recently, Wu et al. used NiAl-LDH as electrode material for supercapacitor and investigated the impact of change in molar feeding ratio of Ni and Al on the capacitive performance of the LDH<sup>13</sup>. The result revealed that the LDH with Ni/Al ratio of 3 provides maximum specific capacitance value along with a stable lifecycle. The introduction of aluminium broadened the inter-layer spacing and improved ion diffusion kinetics of LDH. Recently some other reports have also explored that the change in molar ratio of Co/Ni can change the morphology of the NiCo LDH<sup>14</sup>. Moreover, tuning of metal ion composition in LDHs can be crucial for improving the capacitive behaviour of the material and the electronic behaviour of active electrode materials can be enhanced via doping low-cost other metals like Al and Cu etc.

In addition, the performance of LDHs can be optimized via preparing hybrid composites with two-dimensional carbon-based materials (graphene, carbon nanotube and carbon nitride etc.) which can provide better charge transfer, electronic conductivity and high surface area to the composite material arising from the synergistic interactions between the components<sup>9</sup>. Recently nitrogen-doped carbon materials have gained attention towards energy storage applications as the presence of nitrogen provides electron pairs to the carbon materials which results in enhanced electronic conductivity<sup>15</sup>. Recently

Tian et al synthesized hybrid composite of NiAl LDH and nitraime-N doped graphene which showed enhanced capacitive performance<sup>16</sup>. The presence of N improved the electrostatic interaction between carbon sheets and NiAl LDH and also enhanced the amount of Ni (III) ion in the material. The composite material provide increased electrochemical active sites and better electron transport during the redox reaction at electrode-electrolyte interface. Also, graphitic carbon nitride could specifically enhance the pseudocapacitive property of composites through its high nitrogen content providing surface polarity and better electron donor capacity. Although few reports of  $\text{CN}_x$  supported LDHs have been published in recent times, but there is a need for research in  $\text{CN}_x$  supported hybrid nanocomposites for supercapacitor application<sup>17</sup>.

In this chapter, a single step one pot synthesis of  $\text{Co}_1\text{Al}_3(\text{OH})_m/\text{CN}_x$  composite for supercapacitor application was proposed. The growth and in situ nucleation of  $\text{Co}_1\text{Al}_3(\text{OH})_m$  over carbon nitride results in the formation of 3D nanoflower type structure having a smooth surface. The  $\text{Co}_1\text{Al}_3(\text{OH})_m/\text{CN}_x$  composite showed a superior specific capacitance value along with long term cyclic stability.

## **6.3. EXPERIMENTAL SECTION**

### **6.3.1. Materials:**

$\text{Al}(\text{NO}_3)_3 \cdot 9\text{H}_2\text{O}$  (aluminum (III) nitrate nonahydrate) and  $\text{Co}(\text{NO}_3)_2 \cdot 6\text{H}_2\text{O}$  (Cobalt (II) nitrate hexahydrate) were purchased from Merck (India). Hexamethylenetetramine (HMT),  $\text{NH}_2\text{CONH}_2$  (Urea) and KOH (potassium hydroxide) were obtained from Thermo Fisher scientific India.  $\text{NH}_4\text{F}$  (Ammonium fluoride) was purchased from HI Media India. All the chemicals were used directly without any additional purification.

Deionized water (DI H<sub>2</sub>O) was obtained from an ultrafiltration system (Milli-Q) at room temperature with a resistivity of 19.0 M  $\Omega$  cm.

### **6.3.2. Synthesis of CN<sub>x</sub>:**

Carbon nitride was synthesized from urea using a modified procedure similar to reported literature<sup>18-19</sup>. 5g urea was taken in a porcelain crucible and covered with a petridish followed by heating at a temperature of 500°C for three hours in a muffle furnace. The resulting yellow colour product was washed several times with ethanol to remove the unwanted residues and allowed it to dry to get the desired product.

### **6.3.3. Synthesis of Co<sub>1</sub>Al<sub>3</sub>(OH)<sub>m</sub>/CN<sub>x</sub> Composites:**

In a typical procedure, 35 mg of CN<sub>x</sub> was added to a beaker containing 20 mL of DI H<sub>2</sub>O and allowed to sonicate for 15 min. Into this, Co(NO<sub>3</sub>)<sub>2</sub>·6H<sub>2</sub>O and Al(NO<sub>3</sub>)<sub>3</sub>·9H<sub>2</sub>O were added varying in a molar ratios of 1:1, 1:2, 1:3 and 1:4 in order to attain a total molarity of 40 mM. To this above mixture solution, 214 mmol of HMT and 135 mmol of NH<sub>4</sub>F were added and stirred to get a homogeneous mixture. Then the mixture solutions were sealed into a 50 mL Stainless steel autoclave reactor and allow to heat at 120°C for 6 h. After the heating was completed, the autoclave reactor was allowed to cool naturally to room temperature. Then the obtained precipitates were centrifuged at 1000 rpm and washed with DI H<sub>2</sub>O followed by ethanol several times to obtain Co<sub>1</sub>Al<sub>3</sub>(OH)<sub>m</sub>/CN<sub>x</sub>. The Co<sub>1</sub>Al<sub>3</sub>(OH)<sub>m</sub>/CN<sub>x</sub> was named according to their Co/Al molar ratio. Also, only Co<sub>1</sub>Al<sub>3</sub>(OH)<sub>m</sub> was synthesized using the procedure same as above except using CN<sub>x</sub>.

### **6.3.4. Electrode Fabrication:**

Fabrication of working electrode was carried out on a piece of Ni foam of area 1×1 cm<sup>2</sup>. In order to wipe off the oxide layers, the electrode was washed in 3M HCl for 30 min



and then cleaned with DI H<sub>2</sub>O and then ethanol followed by drying. Homogenous slurry was prepared using polyvinylidene fluoride (PVDF) binder in N-methyl-2-pyrrolidone (NMP), conductive carbon (CC) and active materials in 10:10:80 weight percent and coated on the 1×1 cm<sup>2</sup> Ni foam and dried. The weight of the active material on the Ni foam in single electrode was 1 mg. For the designing of ASC, active material was used as cathode, activated carbon (AC) as anode and cellulose paper as separator. Before the electrochemical performance the separator was soaked in 2M KOH. From the calculation, mass loading of positive and negative electrodes was taken to be 1 mg and 5.4 mg and the weight ratio of positive and negative electrodes was found to be 0.185.

#### **6.3.5. Characterizations:**

The x-ray diffraction data (p-XRD) of as prepared samples were conducted by Bruker DAVINCI D8 ADVANCE diffractometer equipped with a monochromatic radiation source of Cu K $\alpha$  ( $\lambda$ = 0.15406). The composition and morphology of the material was recorded by Field-emission scanning electron microscope (FESEM) system (Carl Zeiss, Germany make, Model: Sigma) and Transmission Electron Microscopy (TEM, JEOL F200) and High-Resolution TEM (HRTEM). VG Microtech was used to record the XPS data with monochromatic Mg K $\alpha$  X-ray as the source. IR data was collected by using Perkin Elmer RXI FT-IR spectrophotometer. All electrochemical measurements were performed by using CorrTest Electrochemical Workstation [Model: CS350]. Quantachrome Instruments (AutosorbiQ-XR-XR (2 Stat.)) Viton was used to determine the Specific surface area by N<sub>2</sub> adsorption-desorption isotherm. ICP-OES data was collected on iCAP 7000 Series (Thermo Scientific). Before experiment, pH of the working solution was measured by Hanna (HI 2209) pH meter.

### **Electrochemical measurements:**

Cyclic voltammetry (CV), galvanostatic charging-discharging (GCD) tests and EIS were performed by using CorrTest Electrochemical Workstation [Model: CS350]. EIS measurements were conducted in the frequency range of 0.1 to 100 kHz with 5 mV AC amplitude under open circuit potential. All electrochemical measurements were performed in 2M KOH aqueous solution at room temperature. For half-cell configuration platinum wire, Ag/AgCl and active material coated on 1×1 cm<sup>2</sup> Ni foam was used as counter, reference and working electrode respectively. Cyclic voltammetry curves were recorded in a potential range of 0-0.55V at scan rate ranging from 5-100 mV/sec.

Specific capacitance of the as synthesized material was calculated by using equation 6.1<sup>20-21</sup>

$$C_s = \frac{I\Delta t}{m\Delta V} \quad (6.1)$$

$$\Delta V \times C_s = \frac{I\Delta t}{m} = Q \quad (6.1(a))$$

Specific capacitance ( $C_s$ ) can be calculated from the CV curve by using the equation 6.2

$$C_s = \frac{\int I dv}{2m\Delta V u} \quad (6.2)$$

Where  $C_s$  is the specific capacitance (F/g),  $Q$  is the specific capacitance (mAh/g)  $I$  is the current applied (mA),  $\Delta t$  is the discharge time (sec),  $m$  is the mass of active material (mg),  $\Delta V$  is the operating potential window (V),  $\int I dv$  is the area under the CV curve and  $u$  denotes the scan rate (mV/s).

For Asymmetric supercapacitor (ASC) cell the as prepared material (active material) act as cathode and commercial AC act as anode. The full cell is represented as Co<sub>1</sub>Al<sub>3</sub>(OH)<sub>m</sub>/CN<sub>x</sub>//AC. In order to balance the charge storage the mass ratio of Co<sub>1</sub>Al<sub>3</sub>(OH)<sub>m</sub>/CN<sub>x</sub> and AC was calculated by using equation 6.3

$$\frac{m_- - C_+ \Delta V_+}{m_+ - C_- \Delta V_-} \quad (6.3)$$

Where  $m_+$  was the mass (mg),  $C_+$  and  $C_-$  were the specific capacitance of active material and AC respectively,  $\Delta V_+$  and  $\Delta V_-$  is the voltage window of cathode and anode electrode respectively and  $m_-$  was the mass of anode.

$$E = \frac{C_s (\Delta V)^2}{7.2} \quad (6.4)$$

$$P = \frac{E}{\Delta t} \times 3600 \quad (6.5)$$

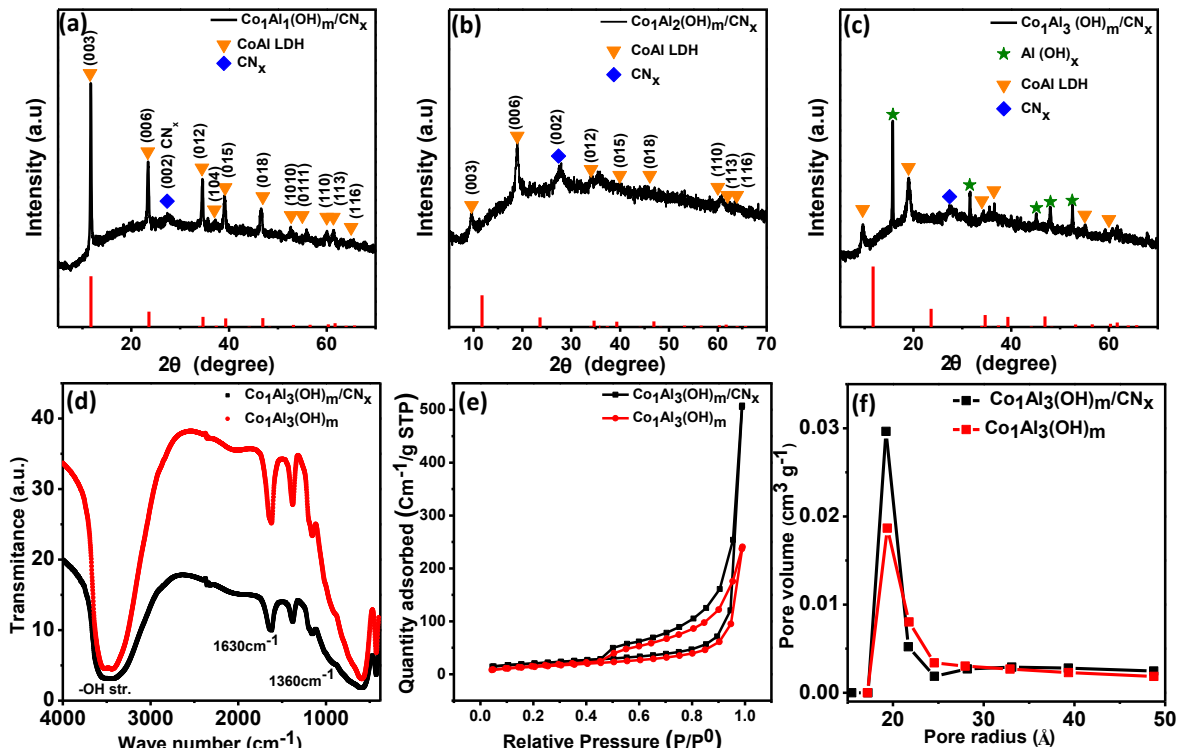
Where  $\Delta V$  is the voltage window (V),  $C_s$  is the capacitance of ASC (F/g) and  $\Delta t$  is the discharge time (sec).

## 6.4. RESULTS AND DISCUSSIONS

### 6.4.1. Structural and morphological characterizations

The crystal structure of as synthesized Co<sub>1</sub>Al<sub>δ</sub>(OH)<sub>m</sub>/CN<sub>x</sub> ( $\delta=1, 2, 3, 4$ ), Al(OH)<sub>x</sub>/CN<sub>x</sub> and Co(OH)<sub>2</sub>/CN<sub>x</sub> composites were characterized by using powder X-ray diffraction (p-XRD). Figure 6.1(a-c) shows the diffraction pattern of Co<sub>1</sub>Al<sub>1</sub>(OH)<sub>m</sub>/CN<sub>x</sub>, Co<sub>1</sub>Al<sub>2</sub>(OH)<sub>m</sub>/CN<sub>x</sub> and Co<sub>1</sub>Al<sub>3</sub>(OH)<sub>m</sub>/CN<sub>x</sub> composites respectively. The XRD peaks of Co<sub>1</sub>Al<sub>1</sub>(OH)<sub>m</sub>/CN<sub>x</sub> and Co<sub>1</sub>Al<sub>2</sub>(OH)<sub>m</sub>/CN<sub>x</sub> composite at 11.74°, 23.6°, 34.67°, 37.39°, 39.32°, 46.92°, 60.37°, 61.69°, and 65.7° correspond to the (003), (006), (012), (104), (015), (018), (110), (113), and (116) planes of CoAl LDH structure (PDF 04-014-8855) and the peak at 27.3° corresponds to (002) plane of CN<sub>x</sub>. The (003) diffraction peak at  $2\theta$  value 11.74° corresponding to the d-spacing 0.75 nm indicate the presence of CO<sub>3</sub><sup>2-</sup> ions and H<sub>2</sub>O molecule in the interlayer space<sup>22</sup>. As displayed in Figure 6.1(c), in the XRD pattern of Co<sub>1</sub>Al<sub>3</sub>(OH)<sub>m</sub>/CN<sub>x</sub> along with the peaks of LDH Figure 6.1(d) shows the Fourier transform infrared (FTIR) spectra of Co<sub>1</sub>Al<sub>3</sub>(OH)<sub>m</sub> and Co<sub>1</sub>Al<sub>3</sub>(OH)<sub>m</sub>/CN<sub>x</sub> composites. A broad peak at around 3485 cm<sup>-1</sup> in both the sample is due to the structural

–OH group stretching vibrations of water molecule. The band at  $1630\text{ cm}^{-1}$  is due to the bending vibrations of  $\text{H}_2\text{O}$  and the band at  $1360\text{ cm}^{-1}$  indicates the presence of the interlayered  $\text{CO}_3^{2-}$  ion (C-O vibrations). The absorption bands below wavelength of structure, additional peaks of  $\text{Al}(\text{OH})_x$  was observed. On moving from  $\text{Co}_1\text{Al}_1(\text{OH})_m/\text{CN}_x$  to  $\text{Co}_1\text{Al}_3(\text{OH})_m/\text{CN}_x$ , the left shift of XRD peak corresponding to (003) plane is due to the increasing amount of Co/Al ratio<sup>12-13, 23</sup>.



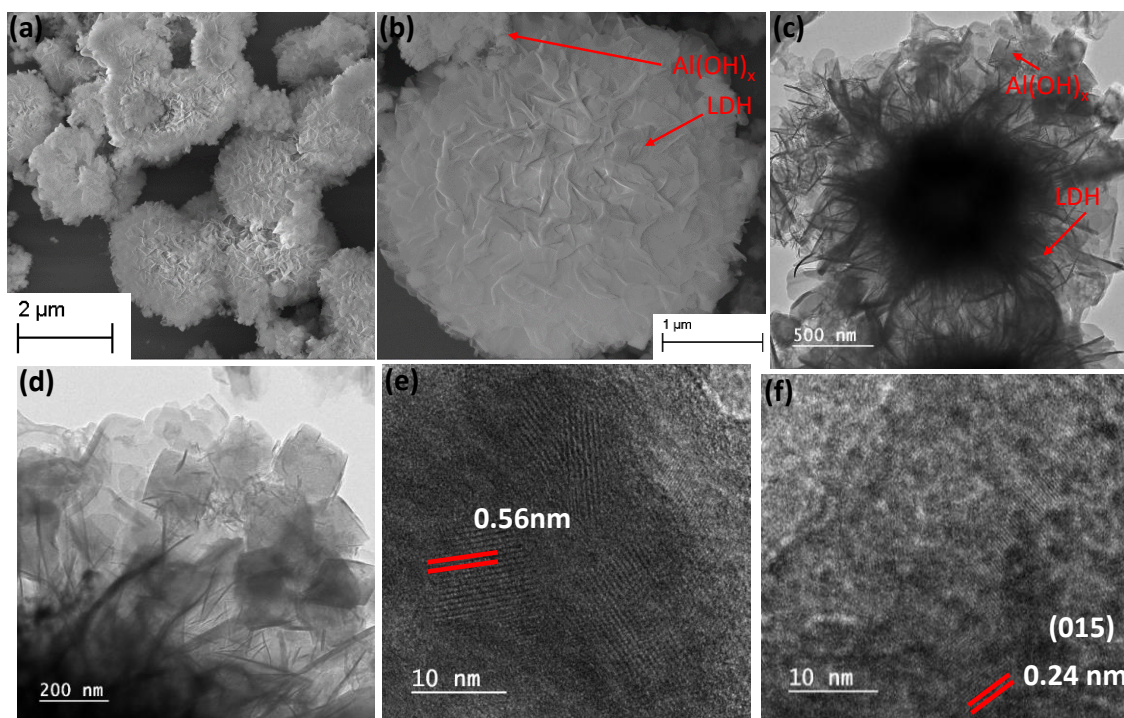
**Figure 6.1.** XRD patterns of (a)  $\text{Co}_1\text{Al}_1(\text{OH})_m/\text{CN}_x$  (b)  $\text{Co}_1\text{Al}_2(\text{OH})_m/\text{CN}_x$  and (c)  $\text{Co}_1\text{Al}_3(\text{OH})_m/\text{CN}_x$  (d) Comparison of FT-IR for  $\text{Co}_1\text{Al}_3(\text{OH})_m/\text{CN}_x$  composite and  $\text{Co}_1\text{Al}_3(\text{OH})_m$  (e-f)  $\text{N}_2$  adsorption-desorption isotherm and BJH pore size distribution of  $\text{Co}_1\text{Al}_3(\text{OH})_m/\text{CN}_x$  Composite and only  $\text{Co}_1\text{Al}_3(\text{OH})_m$ .

The peak corresponding to (003) plane moves from  $2\theta$  value  $11.74^\circ$  to  $9.62^\circ$  and  $9.5^\circ$  for  $\text{Co}_1\text{Al}_1(\text{OH})_m/\text{CN}_x$ ,  $\text{Co}_1\text{Al}_2(\text{OH})_m/\text{CN}_x$ , and  $\text{Co}_1\text{Al}_3(\text{OH})_m/\text{CN}_x$  respectively. This indicates with increasing amount of Co/Al ratio the interlayer spacing increases<sup>13</sup>. In case of  $\text{Co}_1\text{Al}_3(\text{OH})_m/\text{CN}_x$  the peaks at  $2\theta$  value of  $15.79^\circ$ ,  $31.56^\circ$ ,  $45.08^\circ$ ,  $48^\circ$  and  $52.59^\circ$  corresponds to (111), (222), (422), (511) and (440) plane of  $\text{Al}(\text{OH})_x$  (PDF-00-060-0273). The XRD pattern of  $\text{CN}_x$  is shown in Figure S6.1 which shows typical diffraction peak at  $2\theta$  value of  $27.3^\circ$  indexed to the plane (002) of graphitic carbon nitride. The p-XRD patterns of only  $\text{Al}(\text{OH})_x/\text{CN}_x$ ,  $\text{Co}(\text{OH})_2/\text{CN}_x$  and  $\text{Co}_1\text{Al}_3(\text{OH})_m$  are shown in Figure S6.2 (a, b) and S3 respectively. The average grain size was calculated by using Scherrer's equation,  $D=(k\lambda)/(\beta \cos \theta)$ , where  $D$  is the grain size,  $k$  is the shape factor with a typical value of 0.94,  $\lambda$  is the X-ray wavelength (0.154 nm),  $\beta$  is the full width at half maximum (fwhm),  $\theta$  is Bragg's angle. The average crystallite sizes of the  $\text{Co}_1\text{Al}_1(\text{OH})_m/\text{CN}_x$ ,  $\text{Co}_1\text{Al}_2(\text{OH})_m/\text{CN}_x$  and  $\text{Co}_1\text{Al}_3(\text{OH})_m/\text{CN}_x$ , composite material are found to be 35.05, 24.40 and 15.05 nm respectively.

Figure 6.1(d) shows the Fourier transform infrared (FTIR) spectra of  $\text{Co}_1\text{Al}_3(\text{OH})_m$  and  $\text{Co}_1\text{Al}_3(\text{OH})_m/\text{CN}_x$  composites. A broad peak at around  $3485 \text{ cm}^{-1}$  in both the sample is due to the structural  $-\text{OH}$  group stretching vibrations of water molecule. The band at  $1630 \text{ cm}^{-1}$  is due to the bending vibrations of  $\text{H}_2\text{O}$  and the band at  $1360 \text{ cm}^{-1}$  indicates the presence of the interlayered  $\text{CO}_3^{2-}$  ion (C-O vibrations). The absorption bands below wavelength of  $800 \text{ cm}^{-1}$  indicates the stretching as well as bending modes of metal oxygen (M-O) bond in the hydrotalcite structure<sup>24</sup> of LDH.

The specific surface area (SSA) as well as the porosity are considered as crucial aspects for the improvement of electrochemical activities of the supercapacitor electrode materials. The  $\text{N}_2$  adsorption-desorption isotherms were used to determine the SSA as well as the average pore size distribution (PSD) of  $\text{Co}_1\text{Al}_3(\text{OH})_m/\text{CN}_x$  and  $\text{Co}_1\text{Al}_3(\text{OH})_m$

composite. Figure 6.1(e) represents a type IV adsorption/desorption isotherm with an obvious type-H3 hysteresis loops ( $P/P_0 > 0.4$ ) indicating the typical mesoporous nature<sup>17, 25</sup> of  $\text{Co}_1\text{Al}_3(\text{OH})_m/\text{CN}_x$  composite. Total BET SSA values of  $\text{Co}_1\text{Al}_3(\text{OH})_m/\text{CN}_x$  and  $\text{Co}_1\text{Al}_3(\text{OH})_m$  composites were found to be  $72.78 \text{ m}^2/\text{g}$  and  $52.051 \text{ m}^2/\text{g}$  which indicates that the SSA for  $\text{Co}_1\text{Al}_3(\text{OH})_m/\text{CN}_x$  is much higher than that of  $\text{Co}_1\text{Al}_3(\text{OH})_m$ . This high SSA of the  $\text{Co}_1\text{Al}_3(\text{OH})_m/\text{CN}_x$  composite is believed to provide a large electrolyte-electrode interface for accumulation of charge electrostatically and the transportation of ions are facilitated by increasing electrical contact as well as by shortening the diffusion path<sup>17</sup>. The average pore radius of the samples are determined from the Barrett-Joyner-Halenda (BJH) pore size distribution analysis and the average pore radius of the composites are lying below  $40 \text{ \AA}$ . The average pore radius of the  $\text{Co}_1\text{Al}_3(\text{OH})_m/\text{CN}_x$  and  $\text{Co}_1\text{Al}_3(\text{OH})_m$  composites are found to be  $19.36 \text{ \AA}$  and  $19.2 \text{ \AA}$  respectively which indicates the  $\text{Co}_1\text{Al}_3(\text{OH})_m$  composite has smaller mesopores than the  $\text{Co}_1\text{Al}_3(\text{OH})_m/\text{CN}_x$  composite which is shown in Figure 6.1(f). From the above obtained results, it can be stated that the introduction of  $\text{CN}_x$  in the LDH plays an vital role for the improvement of the dispersibility of LDH as well as formation of mesopore structure of  $\text{Co}_1\text{Al}_3(\text{OH})_m/\text{CN}_x$  composite<sup>26</sup> which also suggests that the participation of the small amount of  $\text{CN}_x$  relieves the agglomeration in the LDH layers<sup>27</sup>.



**Figure 6.2.** (a, b) FESEM images, (c-f) Low and high resolution TEM images of  $\text{Co}_1\text{Al}_3(\text{OH})_m/\text{CN}_x$

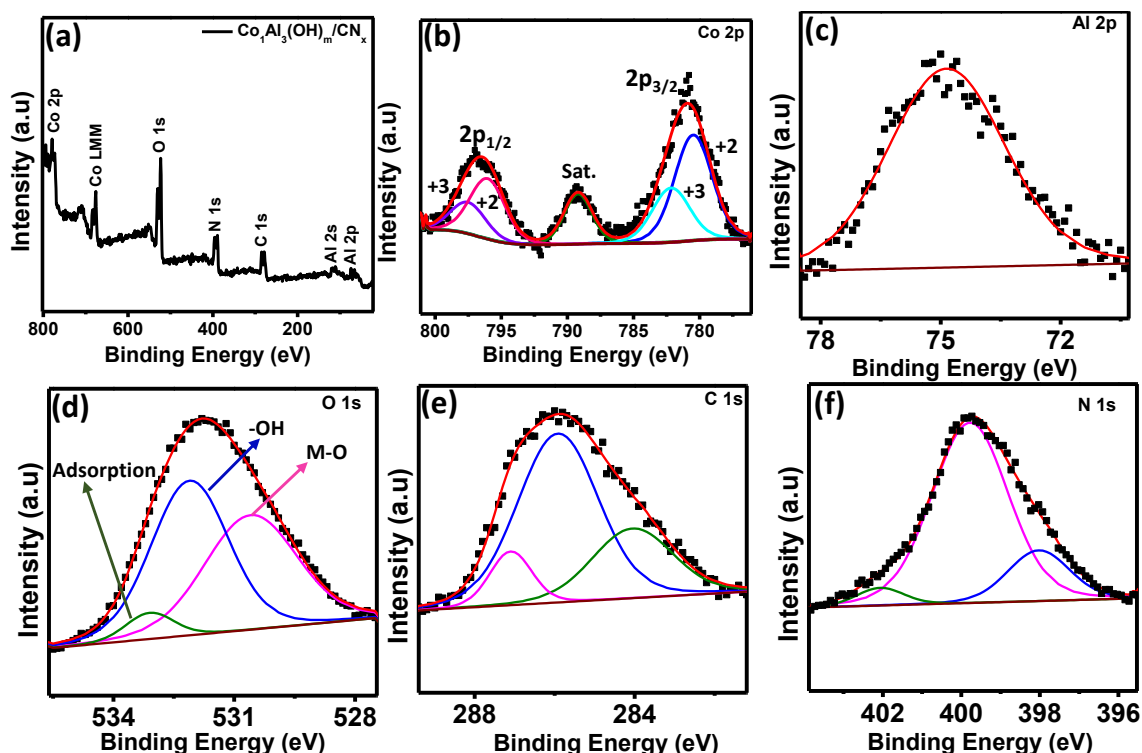
The Scanning electron microscopy (SEM) and transmission electron microscopy (TEM) analysis were performed to characterize the morphological features of  $\text{Co}_1\text{Al}_3(\text{OH})_m/\text{CN}_x$  composite at different magnifications. Figure 6.2(a, b) shows the FESEM images of  $\text{Co}_1\text{Al}_3(\text{OH})_m/\text{CN}_x$ . The 2D nanosheets were self- assembled to form 3D nanoflowers type structure having a smooth surface to provide sufficient surface area which allows an easy passage of electrolytes through the nanosheets resulting high capacitive performance<sup>28</sup>. From the EDAX analysis, presence of all the elements in  $\text{Co}_1\text{Al}_\delta(\text{OH})_m/\text{CN}_x$  ( $\delta=1, 2, 3, 4$ ) were confirmed. Figure S6.4 (a-f) presents the FESEM image and corresponding elemental mappings of C, N, Co, Al and O which clearly shows the uniform distribution of elements over the nanocomposite structure of  $\text{Co}_1\text{Al}_3(\text{OH})_m/\text{CN}_x$  and Figure S6.4 (g) shows the corresponding EDAX spectra. From



elemental mapping, percentage of elements were calculated which are shown in Figure S6.4 (h). Atomic percentage of Al and Co were found to be 15.70 % and 5.40% respectively with a ratio of 2.9 which is close to the precursor ratio taken during synthesis. Atomic percentage of Co and Al present in all the composites of Co<sub>1</sub>Al<sub>δ</sub>(OH)<sub>m</sub>/CN<sub>x</sub> (δ=1, 2, 3, 4) are shown in Table S6.1 which is in good accordance with amount of precursor used during synthesis. SEM images of CN<sub>x</sub> is shown in Figure S6.5 (a-b) which shows the sheet type morphology of CN<sub>x</sub>. Figure 6.2(c and d) represents the low resolution transmission electron microscopy images of Co<sub>1</sub>Al<sub>3</sub>(OH)<sub>m</sub>/CN<sub>x</sub> composite which shows presence of nanosheets of LDH structure along with some amount of cubic aluminium hydroxides distributed over the sheets. High resolution transmission electron microscopy (HRTEM) images of Co<sub>1</sub>Al<sub>3</sub>(OH)<sub>m</sub>/CN<sub>x</sub> are displays in Figure 6.2 (e, f) and the lattice fringes with interplanar distance of 0.56 nm and 0.24 nm were indexed to the (111) and (015) planes of aluminium hydroxide and CoAl LDH structure respectively which is well consistent with the p-XRD data.

The ICP-OES measurement was carried out to determine the more accurate composition of the composite and to calculate the metal ion content of Co<sub>1</sub>Al<sub>3</sub>(OH)<sub>m</sub>/CN<sub>x</sub>. The Co<sub>1</sub>Al<sub>3</sub>(OH)<sub>m</sub>/CN<sub>x</sub> composite contains 23.3 % of Al and 7.9% of Co while the Al/Co atomic ratio was obtained to be 2.95:1 which is very close to the SEM EDAX analysis data of Co<sub>1</sub>Al<sub>3</sub>(OH)<sub>m</sub>/CN<sub>x</sub>. In addition to this, the CHN analysis of CN<sub>x</sub> and Co<sub>1</sub>Al<sub>3</sub>(OH)<sub>m</sub>/CN<sub>x</sub> composite was performed to determine the percentage of nitrogen and carbon present in it. From the CHN analysis the N/C ratio in only CN<sub>x</sub> is found to be 1.75 where for Co<sub>1</sub>Al<sub>3</sub>(OH)<sub>m</sub>/CN<sub>x</sub> composite the N/C ratio was 1.68. The ratio N/C in CN<sub>x</sub> was higher than Co<sub>1</sub>Al<sub>3</sub>(OH)<sub>m</sub>/CN<sub>x</sub> composite which might be because of the loss of nitrogen-containing groups during hydrothermal synthesis<sup>3</sup>.





**Figure 6.3.** (a) XPS survey spectrum of Co<sub>1</sub>Al<sub>3</sub>(OH)<sub>m</sub>/CN<sub>x</sub> composite. High resolution XPS spectra of (b) Co 2p, (c) Al 2p, (d) O 1s, (e) C 1s, and (f) N 1s respectively.

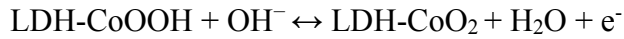
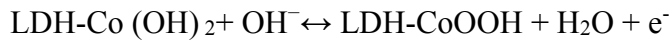
X-ray Photoelectron spectroscopy (XPS) measurement was performed for better analysis of surface oxidation state of Co<sub>1</sub>Al<sub>3</sub>(OH)<sub>m</sub>/CN<sub>x</sub> composite. XPS studies were carried out using monochromatic Mg K $\alpha$  as a source. The XPS spectra were charge corrected with respect to C 1s peak. Figure 6.3(a) presents the XPS survey scan of Co<sub>1</sub>Al<sub>3</sub>(OH)<sub>m</sub>/CN<sub>x</sub> composite that confirms the presence of Co, Al, O, N and C elements with binding energy ranging from 0 to 800 eV. The high resolution XPS spectra of Co 2p is shown in Figure 6.3 (b) which appears in the spectrum as a doublet of 2p<sub>3/2</sub> and 2p<sub>1/2</sub>. The 2p<sub>3/2</sub> and 2p<sub>1/2</sub> spectra of Co were decomposed to four peaks. The Co 2p<sub>3/2</sub> peak was deconvoluted into two peaks at 780.48 eV and 782.24 eV corresponding to Co<sup>2+</sup> and Co<sup>3+</sup> oxidation state. An additional peak at 789.2 eV is a satellite peak. Similarly Co 2p<sub>1/2</sub> was also

deconvoluted into two peaks at 796.03 eV and 797.5 eV due to the presence of Co<sup>2+</sup> and Co<sup>3+</sup> oxidation state. This confirms the coexistence of Co<sup>2+</sup> and Co<sup>3+</sup> species. Relative percentage area of Co<sup>+2</sup> and Co<sup>+3</sup> and the atomic ratio of Co<sup>+2</sup>/Co<sup>+3</sup> for 2p<sub>3/2</sub> and 2p<sub>1/2</sub> are provided in Table S6.2. The atomic ratio of Co<sup>+2</sup>/Co<sup>+3</sup> was obtained by integrating the area of deconvoluted Co<sup>+2</sup> and Co<sup>+3</sup> peak and was found to be nearly 1.95. It has been reported that presence of Co<sup>3+</sup> enhances the conductivity of CoAl LDH structure. Hence the presence of Co<sup>3+</sup> could be one of the possible factors for better electrochemical behaviour of the electrode material. The high resolution XPS spectra of Al 2p is provided in Figure 6.3 (c) and a singlet peak centred at 74.28 eV can be ascribed to Al<sup>3+</sup> oxidation state. The XPS spectra of O 1s is given in Figure 6.3 (d) and it is deconvoluted into three peaks centred at 530.54, 531.9 and 532.72 eV which can be assigned to metal-hydroxyl bond, adsorbed H<sub>2</sub>O and C-O bond respectively. The high resolution 1s XPS peaks of carbon, shown in Figure 6.3(e) can be deconvoluted into three peaks. The peak at 284.2 eV is because of C–C bond whereas the peaks at 285.5 eV and 286.9 eV are because of C–OH bonds and C=C bonds indicating the presence of CO<sub>3</sub><sup>2-</sup> intercalated anion in the LDH<sup>12</sup>. The Figure 6.3(f) displays the high resolution N 1s XPS spectra which can be deconvoluted into three different peaks. The peak position at 398.3 eV refers to graphitic nitrogen whereas the peaks at 398.9 eV and 402.2 eV are assigned for pyridinic nitrogen and pyrrolic nitrogen respectively<sup>29-30</sup>.

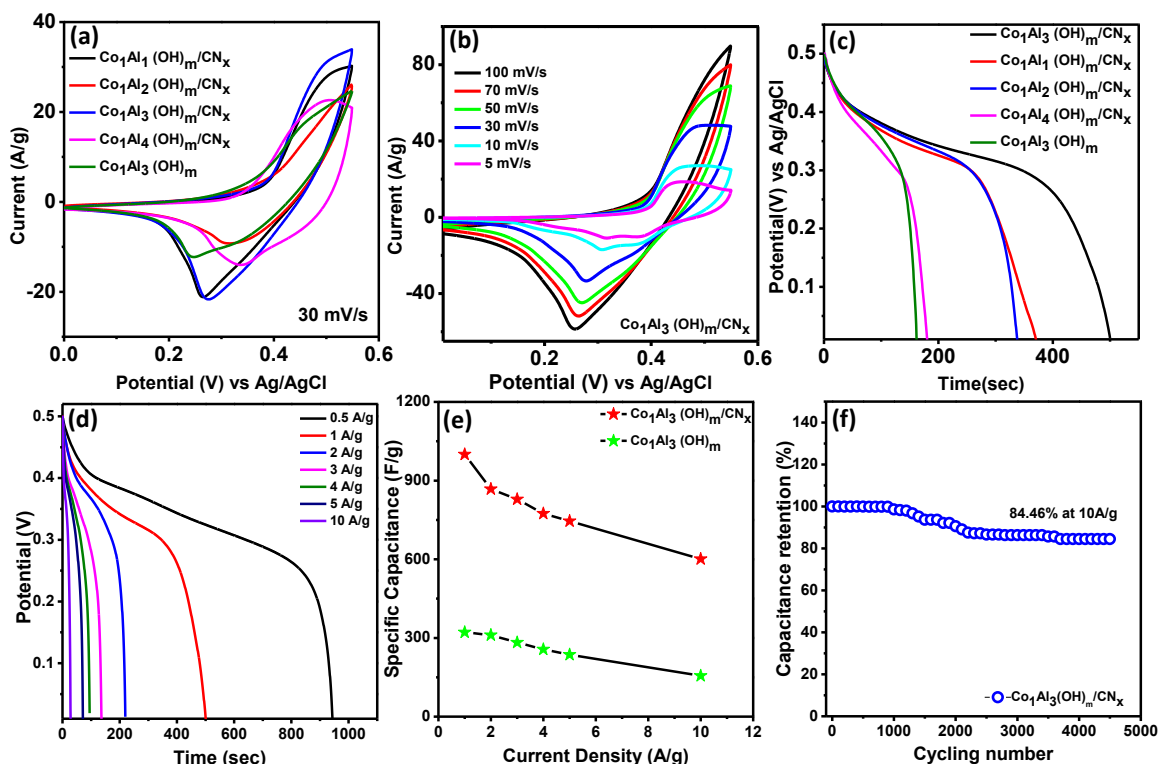
#### **6.4.2. Electrochemical Analysis**

The electrochemical measurements of Co<sub>1</sub>Al<sub>δ</sub>(OH)<sub>m</sub>/CN<sub>x</sub> (δ=1, 2, 3, 4) and Co<sub>1</sub>Al<sub>3</sub>(OH)<sub>m</sub> composites were investigated in a standard three-electrode system through Cyclic voltammetry(CV), galvanostatic charge discharge (GCD) and electrochemical impedance spectroscopy (EIS) measurements at a voltage range of 0-0.55 V in 2M KOH.

The preparation method of the electrodes are briefly explained in the electrode fabrication section. Figure 6.4 (a) displays the comparison of CV curve of Co<sub>1</sub>Al<sub>δ</sub>(OH)<sub>m</sub>/CN<sub>x</sub> (δ=1, 2, 3, 4) and only Co<sub>1</sub>Al<sub>3</sub>(OH)<sub>m</sub> at a sweep rate of 30 mV/s. All the CV curves exhibits similar shapes and for each CV cycle there is a pair of redox peak which is due to the reversible reaction occurring between Co<sup>+2</sup> to Co<sup>+3</sup> and vice-versa present in Co<sub>1</sub>Al<sub>3</sub>(OH)<sub>m</sub> LDH. The CV integral area for Co<sub>1</sub>Al<sub>3</sub>(OH)<sub>m</sub>/CN<sub>x</sub> composite is much larger than other composites. The Co<sub>1</sub>Al<sub>3</sub>(OH)<sub>m</sub>/CN<sub>x</sub> composite shows the reversible cathodic and anodic peak at 0.47 and 0.27 volt respectively which are shifted from the initial value compared to Co<sub>1</sub>Al<sub>3</sub>(OH)<sub>m</sub> composite. This shift in peak position may be attributed due to the presence of CN<sub>x</sub><sup>22</sup>. The redox peaks for Co<sub>1</sub>Al<sub>3</sub>(OH)<sub>m</sub>/CN<sub>x</sub> are because of the faradic redox reaction occurring between LDH-Co-OH and LDH-Co-O-O-H which can be represented as follow<sup>13, 17, 31-32</sup>.



During the redox reaction, Al<sup>+3</sup> is non electroactive but this promotes the oxidation of Co<sup>+2</sup> to Co<sup>+3</sup> which improve the electrochemical activity of Co<sub>1</sub>Al<sub>3</sub>(OH)<sub>m</sub>/CN<sub>x</sub> composite<sup>31, 33</sup>.

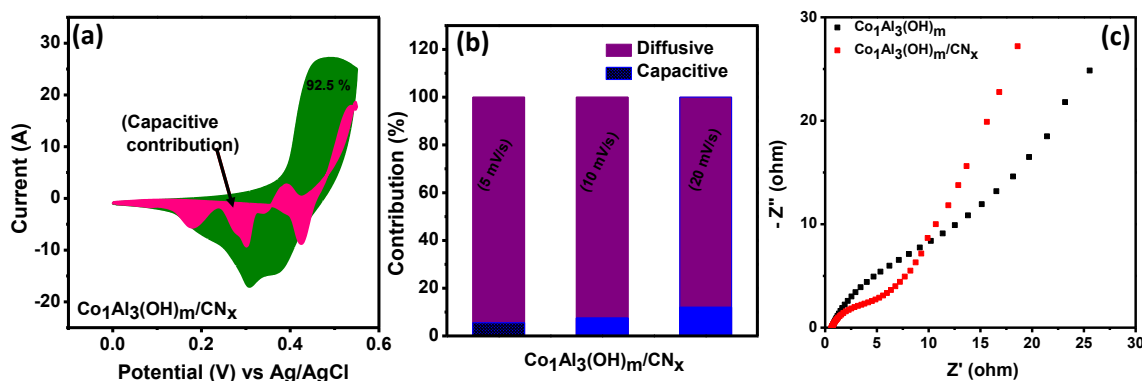


**Figure 6.4.** (a) CV curves of  $\text{Co}_1\text{Al}_\delta(\text{OH})_m/\text{CN}_x$  ( $\delta=1, 2, 3, 4$ ) and  $\text{Co}_1\text{Al}_3(\text{OH})_m$  at scan rate of 30 mV/s. (b) CV curves of  $\text{Co}_1\text{Al}_3(\text{OH})_m/\text{CN}_x$  at different sweep rate (5-100 mV/s) (c) Comparison of GCD curves of  $\text{Co}_1\text{Al}_\delta(\text{OH})_m/\text{CN}_x$  ( $\delta=1, 2, 3, 4$ ) with  $\text{Co}_1\text{Al}_3(\text{OH})_m$  at 1 A/g current density. (d) GCD curves of  $\text{Co}_1\text{Al}_3(\text{OH})_m/\text{CN}_x$  composite at 0.5-10 A/g current density (e) Plot of Specific capacitance of  $\text{Co}_1\text{Al}_3(\text{OH})_m/\text{CN}_x$  with respect to current density. (f) Plot of percentage capacitance retention (%) with respect to cycling number at 10 A/g current density.

Due to the introduction of  $\text{Al}^{+3}$  in LDH, the crystallinity and hydrophilicity of LDHs are improved which is useful to improve charge transport and utilization of electrolyte<sup>31, 34-35</sup>. The CV curves of the  $\text{Co}_1\text{Al}_3(\text{OH})_m/\text{CN}_x$  composite at different sweep rate 5 mV/s to 100 mV/s in a voltage window varying from 0-0.55 V are displayed in Figure 6.4(b). With increase in scan rate, the potential difference between the cathodic and anodic peak

increases<sup>36-37</sup> and current also increases gradually with increase in sweep rate indicating the good electrochemical responses of Co<sub>1</sub>Al<sub>3</sub>(OH)<sub>m</sub>/CN<sub>x</sub> composite<sup>38</sup>. Area under the CV curve at different sweep rate for Co<sub>1</sub>Al<sub>3</sub>(OH)<sub>m</sub>/CN<sub>x</sub> is much larger than that for only Co<sub>1</sub>Al<sub>3</sub>(OH)<sub>m</sub> which indicates Co<sub>1</sub>Al<sub>3</sub>(OH)<sub>m</sub>/CN<sub>x</sub> shows higher specific capacitance<sup>36</sup>. The specific capacitance value for Co<sub>1</sub>Al<sub>3</sub>(OH)<sub>m</sub>/CN<sub>x</sub> composite was found to be 821.81 F/g and 594.73 F/g at a sweep rate of 5 mV/s and 10 mV/s respectively and for Co<sub>1</sub>Al<sub>3</sub>(OH)<sub>3</sub> it was found to be 611.87 F/g and 549.09 F/g which are calculated from area under the CV curve. Presence of CN<sub>x</sub> promotes the SSA as well as conductivity of Co<sub>1</sub>Al<sub>3</sub>(OH)<sub>m</sub>/CN<sub>x</sub> composite enhancing the electrochemical behaviour of the material. High SSA is one of the important factors for increased faradic reaction between electrolyte and electrode material and the increase in conductivity promotes the transfer of electron in redox reaction. Moreover the synergic interaction between LDH and CN<sub>x</sub> promotes the electrochemical performance<sup>27</sup> of the Co<sub>1</sub>Al<sub>3</sub>(OH)<sub>m</sub>/CN<sub>x</sub> composite. Table S6.3 presents the comparison of electrochemical performance of Co<sub>1</sub>Al<sub>3</sub>(OH)<sub>m</sub>/CN<sub>x</sub> composite with previously reported literatures. Figure 6.4(c) presents the comparison of non-linear GCD curves of Co<sub>1</sub>Al<sub>δ</sub>(OH)<sub>m</sub>/CN<sub>x</sub> (δ=1, 2, 3, 4) and only Co<sub>1</sub>Al<sub>3</sub>(OH)<sub>m</sub> in the potential window of 0-0.5 V at 1 A/g current density. In order to show the electrochemical contribution of bare Ni foam, the GCD measurement was carried out which shows a negligible contribution towards electrochemical performance as shown in Figure S6.6. From the discharge curve, the specific capacitance of Co<sub>1</sub>Al<sub>δ</sub>(OH)<sub>m</sub>/CN<sub>x</sub> (δ=1, 2, 3, 4) composites and Co<sub>1</sub>Al<sub>3</sub>(OH)<sub>m</sub> were calculated to be 102.8 mAh/g (739 F/g), 93.7 mAh/g (674.18 F/g), 138 mAh/g (1000 F/g), and 50 mAh/g (321 F/g) respectively under 1 A/g current density which implies the specific capacitance of the hybrid materials are enhanced compared to other control samples and also pure Co<sub>1</sub>Al<sub>3</sub>(OH)<sub>m</sub>. The non-

linear GCD profiles of the composite obtained at 1 to 10 A/g demonstrate the faradic behaviour of the electrodes<sup>24, 28</sup>. Figure 6.4(d) shows the GCD curve of Co<sub>1</sub>Al<sub>3</sub>(OH)<sub>m</sub>/CN<sub>x</sub> composite at current density ranging from 0.5 to 10 A/g and the corresponding specific capacitance were calculated to be 138 mAh/g (1000 F/g), 122 mAh/g (884 F/g), 96 mAh/g (690.66 F/g) and 78 mAh/g (560 F/g) under 1, 2, 5 and 10 A/g current densities respectively. The specific capacitance value increases with decrease in current density as the diffusion of electrolyte ions gain access to maximum electrode surface area at low current density resulting high specific capacitance. In case of higher current density, the decrease in capacitance is due to the reduction of effective interaction between the electrolyte ions and electrode<sup>27</sup>. The composite Co<sub>1</sub>Al<sub>3</sub>(OH)<sub>m</sub>/CN<sub>x</sub> retains 69% of its initial specific capacitance at current density of 5 A/g. Figure 6.4 (e) shows the specific capacitance (F/g) plot as a function of current densities (A/g) for Co<sub>1</sub>Al<sub>3</sub>(OH)<sub>m</sub>/CN<sub>x</sub> and Co<sub>1</sub>Al<sub>3</sub> (OH)<sub>m</sub> composites. The specific capacitance of only Co<sub>1</sub>Al<sub>3</sub>(OH)<sub>m</sub> is lower than that of Co<sub>1</sub>Al<sub>3</sub>(OH)<sub>m</sub>/CN<sub>x</sub> and the high specific capacitance of Co<sub>1</sub>Al<sub>3</sub> (OH)<sub>m</sub>/CN<sub>x</sub> correlates with CV results, high SSA and average pore size distribution results. Figure 6.4 (f) represents the cyclic durability of the single electrode which shows an excellent 84.46 % capacitance retention of initial value after 4500 cycles at 10 A/g current density.



**Figure 6.5.** (a) CV curves of  $\text{Co}_1\text{Al}_3(\text{OH})_m/\text{CN}_x$  distinguishing both capacitive and diffusive contribution at 10 mV/s sweep rate. (b) Plot of percentage of capacitive and diffusion controlled contribution for  $\text{Co}_1\text{Al}_3(\text{OH})_m/\text{CN}_x$  at various sweep rates. (c) Nyquist plot of  $\text{Co}_1\text{Al}_3(\text{OH})_m/\text{CN}_x$  and  $\text{Co}_1\text{Al}_3(\text{OH})_m$ .

In order to give a better explanation for the charge storage mechanism of the electrode material, differentiation of capacitive contribution and diffusive contribution to the total capacitance is important. Capacitive current arises from the Electrical double layer (surface ion adsorption/desorption process) which is directly proportional to the sweep rate while diffusion-controlled current arises from the diffusion of electrolyte ions from and into the electrode<sup>39</sup>. At a fixed potential (V), the current (i) can be calculated by using the following equation 6.6<sup>11, 40-42</sup>

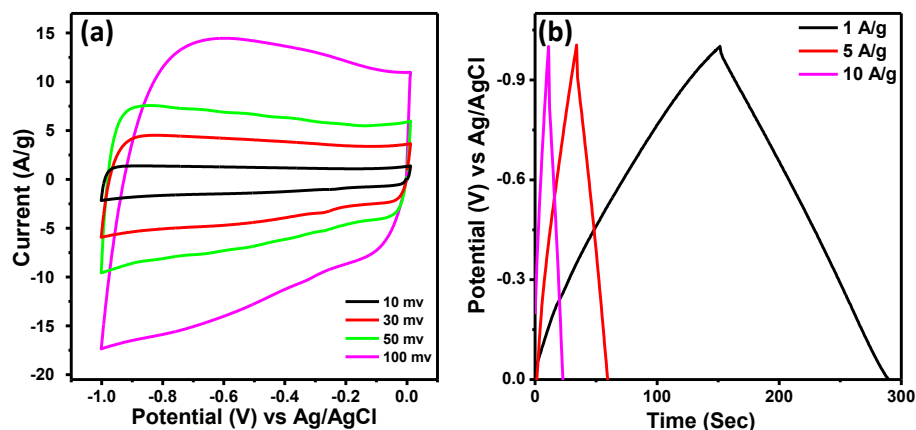
$$i(V) = k_1 v + k_2 v^{1/2} \quad (6.6)$$

Where  $k_1 v$  and  $k_2 v^{1/2}$  represents the capacitive current and diffusion controlled current respectively,  $k_1$  and  $k_2$  are constant and  $v$  is the scan rate. The slope ( $k_1$ ) can be obtained by plotting  $i$  against  $v^{1/2}$ . Figure 6.5(a) presents the fractional area of capacitive contribution of  $\text{Co}_1\text{Al}_3(\text{OH})_m/\text{CN}_x$  at sweep rate of 10 mV/s. The capacitive contribution for  $\text{Co}_1\text{Al}_3(\text{OH})_m/\text{CN}_x$  sample was calculated to be 5.47 at 5 mV/s and it increases to 7.56 at a scan rate of 10 mV/s as shown in Figure 6.5(b).

EIS measurements were performed under open circuit potential in the frequency window of 100 kHz to 0.1 Hz for better evaluation of electrochemical performance of Co<sub>1</sub>Al<sub>3</sub>(OH)<sub>m</sub>/CN<sub>x</sub> composite. The Nyquist plot for Co<sub>1</sub>Al<sub>3</sub>(OH)<sub>m</sub>/CN<sub>x</sub> and Co<sub>1</sub>Al<sub>3</sub>(OH)<sub>m</sub> are shown in Figure 6.5 (c). The Co<sub>1</sub>Al<sub>3</sub>(OH)<sub>m</sub>/CN<sub>x</sub> composite shows a lower Equivalent series resistance ( $R_s$ ) value of 0.64  $\Omega$  and also lower charge transfer resistance value than Co<sub>1</sub>Al<sub>3</sub>(OH)<sub>m</sub> ( $R_s$  = 0.67  $\Omega$ ). The more vertical nature of EIS plot of Co<sub>1</sub>Al<sub>3</sub>(OH)<sub>m</sub>/CN<sub>x</sub> than only Co<sub>1</sub>Al<sub>3</sub>(OH)<sub>m</sub> in the low frequency region signifies that the Co<sub>1</sub>Al<sub>3</sub>(OH)<sub>m</sub>/CN<sub>x</sub> composite has high electrochemical capacitive performance than Co<sub>1</sub>Al<sub>3</sub>(OH)<sub>m</sub>.

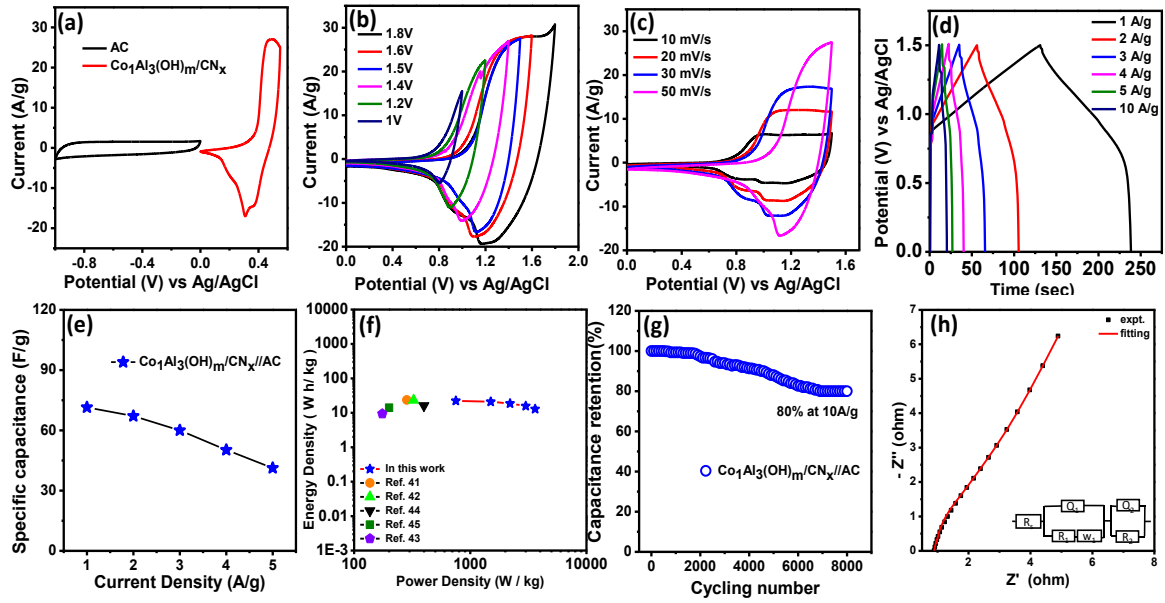
Before assembling the asymmetric supercapacitor (ASC), the capacitive performance of Activated Carbon (AC) was evaluated as AC was used as negative electrode in the device. Figure 6.6 (a) represents the CV curves of AC at different sweep rate while GCD curves at different current densities under a voltage range of 0 to -1 V are provided in Figure 6.6(b). The rectangular shape of the CV curves having no redox peaks and the symmetrical GCD curves indicate the EDLC type behaviour of the AC<sup>17</sup>. From CV curves, the specific capacitance values for AC were found to be 260 F/g and 220 F/g at sweep rate of 10 and 100 mV/s respectively while from the GCD curve, it was found to be 135 F/g at 1 A/g current density.





**Figure 6.6.** (a) CV curves of AC at different sweep rate and (b) GCD plot of AC at different current densities.

For the practical application of  $\text{Co}_1\text{Al}_3(\text{OH})_m/\text{CN}_x$  composite, the Asymmetric Supercapacitor (ASC) device was assembled with  $\text{Co}_1\text{Al}_3(\text{OH})_m/\text{CN}_x$  and AC as cathode and anode respectively. All the electrochemical measurements of the ASC device were performed in 2M KOH. Figure 6.7(a) shows the CV curves of both AC and  $\text{Co}_1\text{Al}_3(\text{OH})_m/\text{CN}_x$  at a scan rate of 10 mV/s. Figure 6.7 (b) shows the CV curves of the ASC device measured by varying the potential range from 1V to 1.8V. With increase in potential from 1 V to 1.6 V, the nature of CV curve does not change, which indicates that the ASC device can work steadily in the potential range of 1.6 V. The specific capacitance vs. current density for  $\text{Co}_1\text{Al}_3(\text{OH})_m/\text{CN}_x//\text{AC}$  ASC is plotted in the Figure 6.7 (e). As the energy density and power density are important parameters for supercapacitors, their evaluation is very much important. Figure 6.7 (f) represents the Ragone plot for  $\text{Co}_1\text{Al}_3(\text{OH})_m/\text{CN}_x//\text{AC}$  which shows the variation of energy density with change in power density.



**Figure 6.7.** (a) Electrochemical behavior of ASC  $\text{Co}_1\text{Al}_3(\text{OH})_m/\text{CN}_x//\text{AC}$  (a) CV curves of AC and  $\text{Co}_1\text{Al}_3(\text{OH})_m/\text{CN}_x$  at a sweep rate of 10 mV/s (b) CV curves of ASC at different potential range (c) CV curves of ASC at different Sweep rate (d) GCD curves at different current densities. (e) Specific capacitance at different current densities. (f) Ragone plot of  $\text{Co}_1\text{Al}_3(\text{OH})_m/\text{CN}_x//\text{AC}$  asymmetric supercapacitor. (g) Cyclic stability of the ASC at 10A/g current density (h) EIS curve of the ASC.

A energy density value of  $22.35 \text{ W h kg}^{-1}$  was obtained at a power density of  $750.2 \text{ W kg}^{-1}$  while the power density was found to be  $3613.36 \text{ W kg}^{-1}$  at energy density of  $12.89 \text{ W h kg}^{-1}$  which is much higher than LDH or Co-based ASC devices reported in the literature such as  $\text{Ni}_x\text{Co}_{1-x} \text{ LDH-ZTO//AC}$  ( $23.7 \text{ W h kg}^{-1}$ ,  $284.2 \text{ W kg}^{-1}$ )<sup>43</sup>,  $\text{NiCo}_2\text{O}_4\text{-rGO//AC}$  ( $23.32 \text{ W h kg}^{-1}$ ,  $324.9$ )<sup>44</sup>,  $\text{NiCo}_2\text{O}_4/\text{MnO}_2//\text{AG}$  ( $9.4 \text{ W h kg}^{-1}$ ,  $175 \text{ W kg}^{-1}$ )<sup>45</sup>,  $\text{Co-Fe LDHs-CFC//AC}$  ( $16.1 \text{ W h kg}^{-1}$ ,  $399 \text{ W kg}^{-1}$ )<sup>46</sup>,  $\text{C-MnO}_2$ 12h ( $14 \text{ W h kg}^{-1}$ ,  $200 \text{ W kg}^{-1}$ )<sup>47</sup>. The cycling stability of the  $\text{Co}_1\text{Al}_3(\text{OH})_m/\text{CN}_x//\text{AC}$  ASC device was performed at 10 A/g current density for 8000 cycles and the capacitance retention was

found to be 80% which is shown in Figure 6.7(g). EIS spectra was measured at a frequency range of 0.1 Hz to 100 kHz and Figure 6.7(h) presents the EIS plot of Co<sub>1</sub>Al<sub>3</sub>(OH)<sub>m</sub>/CN<sub>x</sub>//AC ASC along with the equivalent circuit.  $R_s$ ,  $R_{ct}$ , CPE and W represent the equivalent series resistance, charge transfer resistance, constant phase element and Warburg impedance respectively. The  $R_s$  for ASC was obtained to be 0.89  $\Omega$  and the  $R_{ct}$  value was found to be 1.18  $\Omega$  which were calculated by fitting experimental data with equivalent circuit. The low value of  $R_{ct}$  signifies the low resistance and high charge transfer property of the material.

The high capacitance of Co<sub>1</sub>Al<sub>3</sub>(OH)<sub>m</sub>/ CN<sub>x</sub> composite can be attributed to the following factors:

- (i) Presence of CN<sub>x</sub> in Co<sub>1</sub>Al<sub>3</sub>(OH)<sub>m</sub> LDH composite improves the dispersability of the LDH and hence improves the charge transfer property of material which in turn improves the electrochemical performance.<sup>1, 48-51</sup>
- (ii) It prevents the rapid agglomeration of layered materials and hence provides high structural and chemical stability during electrochemical process<sup>1, 48, 50</sup>.
- (iii) Introduction of Al in the LDH increases the formation of more Co<sup>3+</sup> ion in the interlayer of LDH composite which enhances the conductivity and electrochemical performance of the material<sup>31-33, 35</sup>
- (iv) The synergetic interaction of the CN<sub>x</sub> and Co<sub>1</sub>Al<sub>3</sub>(OH)<sub>m</sub> LDH is another possible factor for increased electrochemical performances of the Co<sub>1</sub>Al<sub>3</sub>(OH)<sub>m</sub>/CN<sub>x</sub> electrode material where CN<sub>x</sub> provides a large active surface area for effective transfer of electrons and restrict the stacking of the LDH<sup>27</sup>. Hence the interfacial contact can be enhanced by anchoring CN<sub>x</sub> on

the layered material resulting fast and smooth ion diffusion through the layered structure.

- (v) High SSA of the Co<sub>1</sub>Al<sub>3</sub>(OH)<sub>m</sub>/CN<sub>x</sub> composite compared to Co<sub>1</sub>Al<sub>3</sub>(OH)<sub>m</sub> provides a large interface between electrolyte-electrode for electrostatic charge accumulation and it facilitates the transport of ions by increasing electrical contact as well as by shortening the diffusion path<sup>17</sup>.

## 6.5. CONCLUSION

In this chapter Co<sub>1</sub>Al<sub>3</sub>(OH)<sub>m</sub>/CN<sub>x</sub> composite was synthesised by one-pot hydrothermal method for supercapacitor applications. The as synthesised composite shows a 3D nanoflower type structure having a smooth surface which is believed to improve the electrochemical performance of the composite. The maximum specific capacitance for Co<sub>1</sub>Al<sub>3</sub>(OH)<sub>m</sub>/CN<sub>x</sub> was obtained to be 138 mAh/g (1000 F/g) at current density of 1 A/g (approximately 3 times higher than that of Co<sub>1</sub>Al<sub>3</sub>(OH)<sub>m</sub>) and capacitance retention of 84.46 % even after 4500 cycles. Furthermore the ASC provides an energy density of 22.35 W h kg<sup>-1</sup> at a power density of 750.2 W kg<sup>-1</sup> with 80% capacitive retention even after 8000 cycle at 10 A/g current density. The synergetic interaction between CN<sub>x</sub> and Co<sub>1</sub>Al<sub>3</sub>(OH)<sub>m</sub> LDH provides large electroactive surface providing faster ion diffusion through LDH structure. Moreover Co<sub>1</sub>Al<sub>3</sub>(OH)<sub>m</sub>/CN<sub>x</sub> composite having superior capacitance along with long term stability makes it a promising electrode material for supercapacitor applications.

## 6.6 REFERENCES

- (1) Jing, C.; Dong, B.; Zhang, Y. *ENERGY & ENVIRONMENTAL MATERIALS* **2020**, 3, 346-379.
- (2) Li, X.; Du, D.; Zhang, Y.; Xing, W.; Xue, Q.; Yan, Z. *Journal of Materials Chemistry A* **2017**, 5, 15460-15485.

- (3) Bhowmik, T.; Mishra, R.; Barman, S. *Energy & Fuels* **2021**, 35, 5206-5216.
- (4) Wulan Septiani, N. L.; Kaneti, Y. V.; Fathoni, K. B.; Wang, J.; Ide, Y.; Yulianto, B.; Nugraha; Dipojono, H. K.; Nanjundan, A. K.; Golberg, D.; Bando, Y.; Yamauchi, Y. *Nano Energy* **2020**, 67, 104270.
- (5) Wang, K.-B.; Xun, Q.; Zhang, Q. *EnergyChem* **2020**, 2, 100025.
- (6) Li, Y.; Henzie, J.; Park, T.; Wang, J.; Young, C.; Xie, H.; Yi, J. W.; Li, J.; Kim, M.; Kim, J.; Yamauchi, Y.; Na, J. *Bulletin of the Chemical Society of Japan* **2019**, 93, 176-181.
- (7) Wang, K.-B.; Bi, R.; Wang, Z.-K.; Chu, Y.; Wu, H. *New Journal of Chemistry* **2020**, 44, 3147-3167.
- (8) Tang, J.; Salunkhe, R. R.; Zhang, H.; Malgras, V.; Ahamad, T.; Alshehri, S. M.; Kobayashi, N.; Tominaka, S.; Ide, Y.; Kim, J. H.; Yamauchi, Y. *Scientific Reports* **2016**, 6, 30295.
- (9) Mishra, R.; Panda, P.; Barman, S. *New Journal of Chemistry* **2021**, 45, 5897-5906.
- (10) Cha, J.-H.; Park, E. B.; Han, S. W.; Kim, Y. D.; Jung, D.-Y. *Chemistry – An Asian Journal* **2019**, 14, 446-453.
- (11) Li, C.; Zhou, Y.; Li, X.; Wang, H.; Huo, P.; Wang, X. *Applied Surface Science* **2021**, 536, 147780.
- (12) Wang, G.; Jin, Z. *Journal of Materials Chemistry C* **2021**, 9, 620-632.
- (13) Li, G.; Zhang, X.; Qiu, D.; Liu, Z.; Yang, C.; Cockreham, C. B.; Wang, B.; Fu, L.; Zhang, J.; Sudduth, B.; Guo, X.; Sun, H.; Huang, Z.; Qi, J.; Sun, J.; Ha, S.; Wang, Y.; Wu, D. *Advanced Electronic Materials* **2019**, 5, 1900215.
- (14) Wang, T.; Zhang, S.; Yan, X.; Lyu, M.; Wang, L.; Bell, J.; Wang, H. *ACS Applied Materials & Interfaces* **2017**, 9, 15510-15524.
- (15) Xu, X.; Tang, J.; Qian, H.; Hou, S.; Bando, Y.; Hossain, M. S. A.; Pan, L.; Yamauchi, Y. *ACS Applied Materials & Interfaces* **2017**, 9, 38737-38744.
- (16) Tian, H.; Bao, W.; Jiang, Y.; Wang, L.; Zhang, L.; Sha, O.; Wu, C.; Gao, F. *Chemical Engineering Journal* **2018**, 354, 1132-1140.
- (17) Sanati, S.; Rezvani, Z. *Chemical Engineering Journal* **2019**, 362, 743-757.
- (18) Zheng, Y.; Zhang, Z.; Li, C. *Journal of Photochemistry and Photobiology A: Chemistry* **2017**, 332, 32-44.
- (19) Zhang, Y.; Liu, J.; Wu, G.; Chen, W. *Nanoscale* **2012**, 4, 5300-5303.
- (20) Zhai, X.; Gao, J.; Xu, X.; Hong, W.; Wang, H.; Wu, F.; Liu, Y. *Journal of Power Sources* **2018**, 396, 648-658.
- (21) Wang, K.; Lv, B.; Wang, Z.; Wu, H.; Xu, J.; Zhang, Q. *Dalton Transactions* **2020**, 49, 411-417.
- (22) Masikhwa, T. M.; Madito, M. J.; Momodu, D. Y.; Dangbegnon, J. K.; Guellati, O.; Harat, A.; Guerioune, M.; Barzegar, F.; Manyala, N. *RSC Advances* **2016**, 6, 46723-46732.
- (23) Wang, H.; Xiang, X.; Li, F. *Journal of Materials Chemistry* **2010**, 20, 3944-3952.
- (24) Fang, J.; Li, M.; Li, Q.; Zhang, W.; Shou, Q.; Liu, F.; Zhang, X.; Cheng, J. *Electrochimica Acta* **2012**, 85, 248-255.
- (25) Yang, W.; Gao, Z.; Wang, J.; Ma, J.; Zhang, M.; Liu, L. *ACS Applied Materials & Interfaces* **2013**, 5, 5443-5454.
- (26) Zhang, L.; Ou, M.; Yao, H.; Li, Z.; Qu, D.; Liu, F.; Wang, J.; Wang, J.; Li, Z. *Electrochimica Acta* **2015**, 186, 292-301.
- (27) Patil, B.; Park, C.; Ahn, H. *RSC Advances* **2019**, 9, 33643-33652.
- (28) Li, T.; Li, G. H.; Li, L. H.; Liu, L.; Xu, Y.; Ding, H. Y.; Zhang, T. *ACS Applied Materials & Interfaces* **2016**, 8, 2562-2572.
- (29) Arif, M.; Yasin, G.; Shakeel, M.; Mushtaq, M. A.; Ye, W.; Fang, X.; Ji, S.; Yan, D. *Materials Chemistry Frontiers* **2019**, 3, 520-531.
- (30) Arif, M.; Yasin, G.; Shakeel, M.; Fang, X.; Gao, R.; Ji, S.; Yan, D. *Chemistry – An Asian Journal* **2018**, 13, 1045-1052.
- (31) Li, J.; Zhang, P.; Zhao, X.; Chen, L.; Shen, J.; Li, M.; Ji, B.; Song, L.; Wu, Y.; Liu, D. *Journal of Colloid and Interface Science* **2019**, 549, 236-245.
- (32) Scavetta, E.; Ballarin, B.; M. Gazzano; Tonelli, D. *Electrochimica Acta* **2009**, 54, 1027-1033.

- (33) Zhang, Q.; Zhao, B.; Wang, J.; Qu, C.; Sun, H.; Zhang, K.; Liu, M. *Nano Energy* **2016**, *28*, 475-485.
- (34) Wang, X.; Lin, Y.; Su, Y.; Zhang, B.; Li, C.; Wang, H.; Wang, L. *Electrochimica Acta* **2017**, *225*, 263-271.
- (35) Qian, L.; Lu, Z.; Xu, T.; Wu, X.; Tian, Y.; Li, Y.; Huo, Z.; Sun, X.; Duan, X. *Advanced Energy Materials* **2015**, *5*, 1500245.
- (36) Zhang, A.; Wang, C.; Xu, Q.; Liu, H.; Wang, Y.; Xia, Y. *RSC Advances* **2015**, *5*, 26017-26026.
- (37) Shakir, I.; Shahid, M.; Rana, U. A.; Nashef, I. M. A.; Hussain, R. *Electrochimica Acta* **2014**, *129*, 28-32.
- (38) Jing, C.; Huang, Y.; Xia, L.; Chen, Y.; Wang, X.; Liu, X.; Dong, B.; Dong, F.; Li, S.; Zhang, Y. *Applied Surface Science* **2019**, *496*, 143700.
- (39) Wang, K.; Bi, R.; Huang, M.; Lv, B.; Wang, H.; Li, C.; Wu, H. **2020**, *59*, 6808-6814.
- (40) Yang, Q.; Liu, Y.; Xiao, L.; Yan, M.; Bai, H.; Zhu, F.; Lei, Y.; Shi, W. *Chemical Engineering Journal* **2018**, *354*, 716-726.
- (41) Wang, K.; Li, Q.; Ren, Z.; Li, C.; Chu, Y.; Wang, Z.; Zhang, M.; Wu, H.; Zhang, Q. *Small* **2020**, *16*, 2001987.
- (42) Wang, K.; Wang, S.; Liu, J.; Guo, Y.; Mao, F.; Wu, H.; Zhang, Q. *ACS Applied Materials & Interfaces* **2021**, *13*, 15315-15323.
- (43) Wang, X.; Sumboja, A.; Lin, M.; Yan, J.; Lee, P. S. *Nanoscale* **2012**, *4*, 7266-7272.
- (44) Wang, X.; Liu, W. S.; Lu, X.; Lee, P. S. *Journal of Materials Chemistry* **2012**, *22*, 23114-23119.
- (45) Kuang, M.; Wen, Z. Q.; Guo, X. L.; Zhang, S. M.; Zhang, Y. X. *Journal of Power Sources* **2014**, *270*, 426-433.
- (46) Ma, K.; Cheng, J. P.; Liu, F.; Zhang, X. *Journal of Alloys and Compounds* **2016**, *679*, 277-284.
- (47) Mane, V. J.; Malavekar, D. B.; Ubale, S. B.; Lokhande, V. C.; Lokhande, C. D. *Inorganic Chemistry Communications* **2020**, *115*, 107853.
- (48) Wu, J.; Zhang, Q. e.; Wang, J.; Huang, X.; Bai, H. *Energy & Environmental Science* **2018**, *11*, 1280-1286.
- (49) Mondal, S.; Rana, U.; Malik, S. *Chemical Communications* **2015**, *51*, 12365-12368.
- (50) Ghaemmaghami, M.; Mohammadi, R. *Sustainable Energy & Fuels* **2019**, *3*, 2176-2204.
- (51) Luo, Y.; Yan, Y.; Zheng, S.; Xue, H.; Pang, H. *Journal of Materials Chemistry A* **2019**, *7*, 901-924.
- (52) Lobinsky, A. A.; Tolstoy, V. P.; Gulina, L. B. *Applied Surface Science* **2014**, *320*, 609-613.
- (53) Long, Y.-W.; Zeng, H.-Y.; Li, H.-B.; Zou, K.-M.; Xu, S.; Cao, X.-J. *Electrochimica Acta* **2020**, *361*, 137098.
- (54) Huang, Z.; Wang, S.; Wang, J.; Yu, Y.; Wen, J.; Li, R. *Electrochimica Acta* **2015**, *152*, 117-125.
- (55) Wang, L.; Wang, D.; Dong, X. Y.; Zhang, Z. J.; Pei, X. F.; Chen, X. J.; Chen, B.; Jin, J. *Chemical Communications* **2011**, *47*, 3556-3558.
- (56) Han, J.; Dou, Y.; Zhao, J.; Wei, M.; Evans, D. G.; Duan, X. *Small* **2013**, *9*, 98-106.
- (57) Li, J.; Chen, D.; Wu, Q. *Journal of Energy Storage* **2019**, *23*, 511-514.
- (58) Deng, J.; Kang, L.; Bai, G.; Li, Y.; Li, P.; Liu, X.; Yang, Y.; Gao, F.; Liang, W. *Electrochimica Acta* **2014**, *132*, 127-135.

## Appendix D

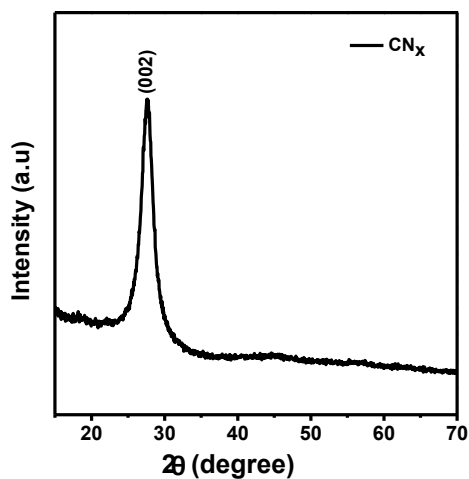


Figure S6.1. p-XRD patterns of  $\text{CN}_x$ .

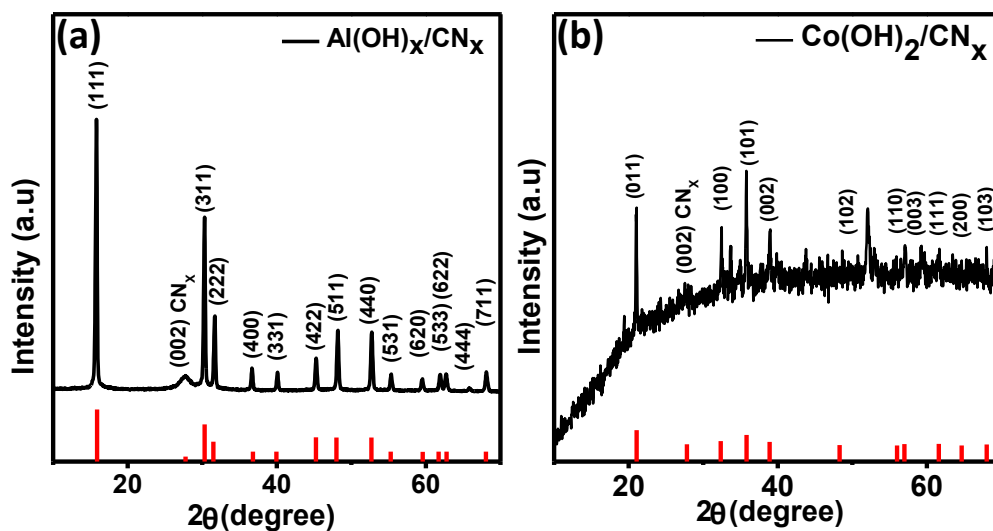
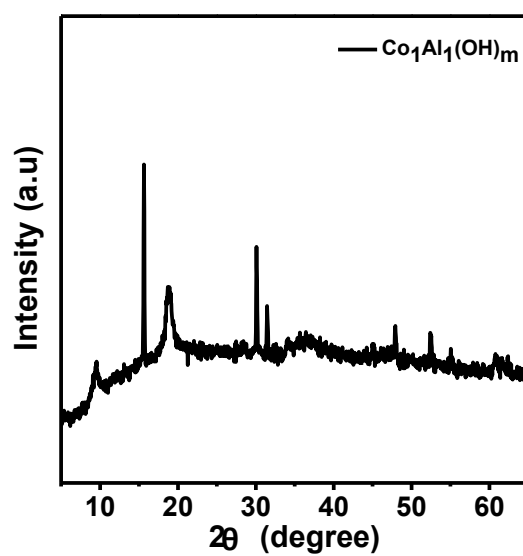
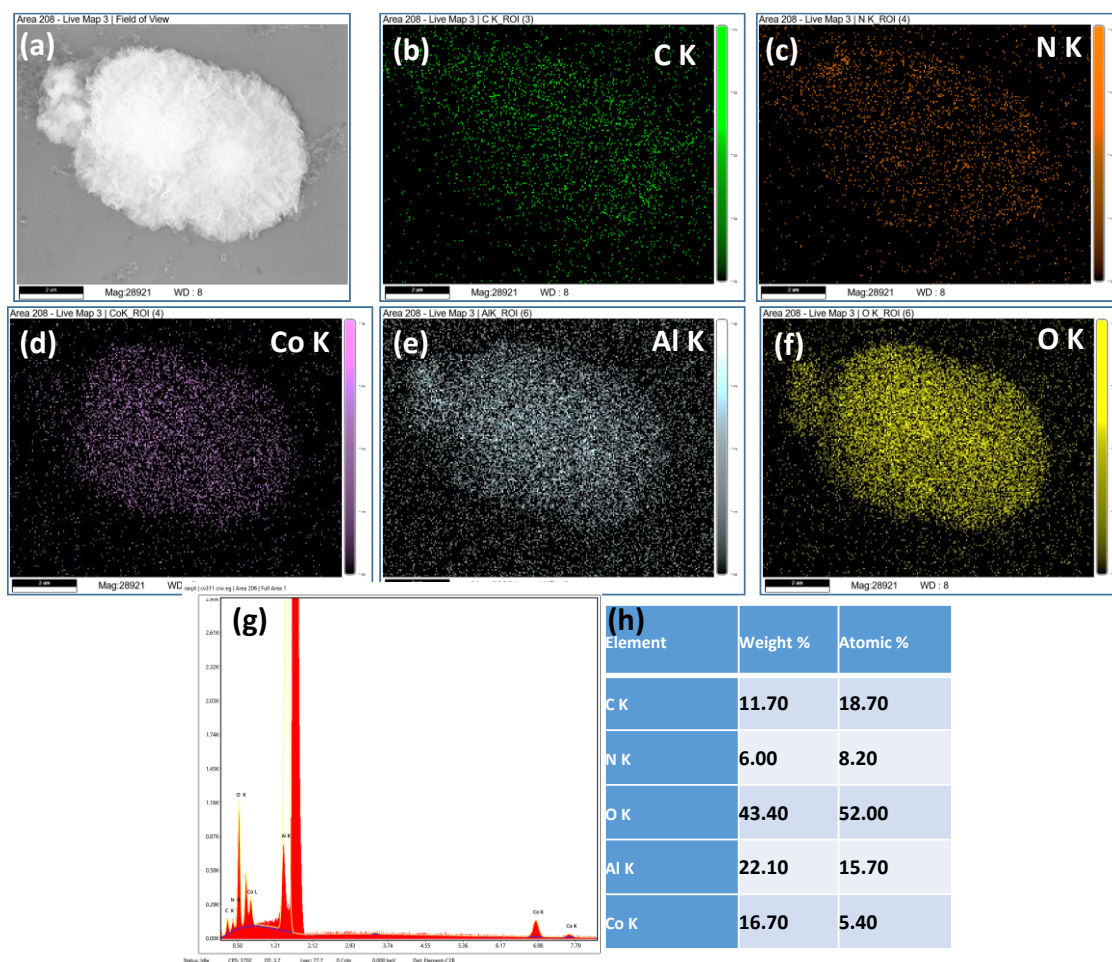


Figure S6.2. p-XRD patterns of (a)  $\text{Al(OH)}_x/\text{CN}_x$  and (b)  $\text{Co(OH)}_2/\text{CN}_x$  respectively.

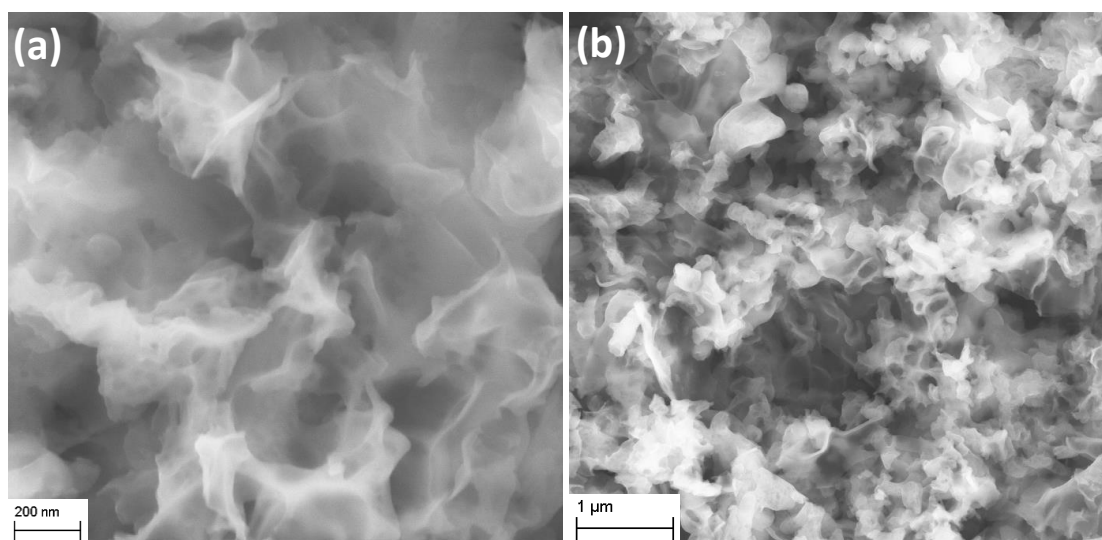


**Figure S6.3.** XRD patterns of  $\text{Co}_1\text{Al}_3(\text{OH})_m$ .

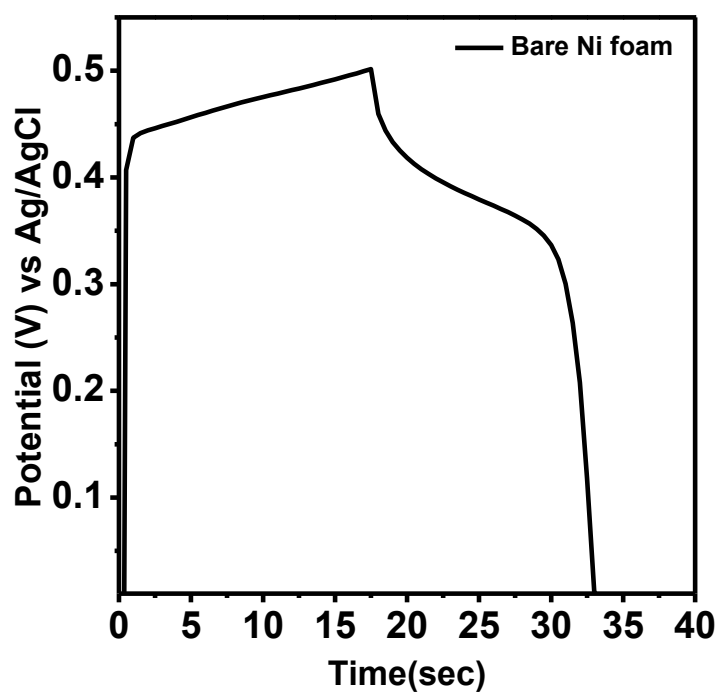




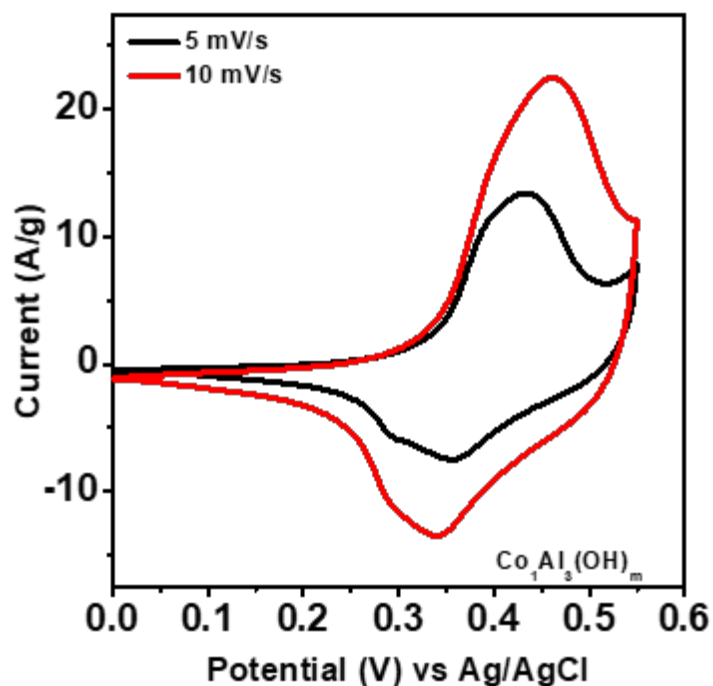
**Figure S6.4.** (a) SEM image and corresponding Elemental mapping of elements (b) C (c) N (d) Co (e) Al (f) O of  $\text{Co}_1\text{Al}_3(\text{OH})_m/\text{CN}_x$  showing an uniform distribution of C, N, Co, Al and O (g) FESEM EDS profile and (h) weight percentage and atomic percentage of different elements.



**Figure S6.5.** (a, b) SEM image of CN<sub>x</sub>.



**Figure S6.6.** GCD curves of bare Ni foam at 1 A/g current density.



**Figure S6.7.** CV curves of Co<sub>1</sub>Al<sub>3</sub>(OH)<sub>3</sub> at different scan rate.

**Table S6.1.** Composition analysis of the Co<sub>1</sub>Al<sub>δ</sub> (OH)<sub>m</sub>/CN<sub>x</sub> (δ=1, 2, 3, 4) composites from elemental mapping

Composite	Amount of Co and Al (Atomic %) (EDS)	
	Co	Al
Co <sub>1</sub> Al <sub>1</sub> (OH) <sub>m</sub> /CN <sub>x</sub>	4.3	3.6
Co <sub>1</sub> Al <sub>2</sub> (OH) <sub>m</sub> /CN <sub>x</sub>	2.4	4.6
Co <sub>1</sub> Al <sub>3</sub> (OH) <sub>m</sub> /CN <sub>x</sub>	5.4	15.7
Co <sub>1</sub> Al <sub>4</sub> (OH) <sub>m</sub> /CN <sub>x</sub>	3.9	16.5

**Table S6.2.** Relative percentage of area and atomic ratio of Co<sup>+2</sup>/Co<sup>+3</sup> in Co 2p<sub>3/2</sub> and 2p<sub>1/2</sub> of Co<sub>1</sub>Al<sub>3</sub>(OH)<sub>m</sub>/CN<sub>x</sub> composite

Peak	Relative area (%) of Co <sup>+2</sup>	Relative area (%) of Co <sup>+3</sup>	Co <sup>+2</sup> /Co <sup>+3</sup>
Co 2p <sub>3/2</sub>	679.5	349.4	1.95
Co 2p <sub>1/2</sub>	365	189.5	1.93

**Table S6.3.** Comparison of electrochemical performance of Co<sub>1</sub>Al<sub>3</sub>(OH)<sub>m</sub>/CN<sub>x</sub> composite with previously reported literatures.

Electrode material	Specific capacitance of single electrode	Capacitance retention after cycling stability	No. of cycles	Ref.
CoAl-LDH/GF	101.4 F/g (0.5 A/g)	-	-	22
Co-Al LDH/GHA	640 F/g (1 A/g)	97	10000	36
Co-Al LDH/rGO-3	1492 F/g (1 A/g)	94.3	5000	31
g-C <sub>3</sub> N <sub>4</sub> nanosheet@CoAl-LDH	343.3 F/g (5 A/g)	95.28	6000	17
CoAl LDHs-0.5	799.2 F/g (1 A/g)	82	5000	12
Co <sub>2</sub> Al(OH) <sub>7-2x</sub> (CO <sub>3</sub> ) <sub>x</sub> .nH <sub>2</sub> O	900 F/g (1 A/g)	100	1000	52
CoAl-S8	1150.6 F/g (1 A/g)	97.8	1000	53
CAN-LDH-NS-rGO	1296 F/g (1 A/g)	90.5	1000	54
Co-Al LDH-NS/GO	1031 F/g (1 A/g)	100	6000	55
CoAl LDH@PEDOT	672 F/g (1 A/g)	63.1	5000	56
CoS-20	365 F/g (10 A/g)	91.2	1300	57
Co <sub>3</sub> O <sub>4</sub> /CoO	362.8 F/g (0.2 A/g)	78.7	1000	58
NiFRS	198 C/g (1 A/g)	46	-	41

FeSCl	683.2 C/g (1 A/g)	-	-	42
$\text{Co}_1\text{Al}_3(\text{OH})_m/\text{CN}_x$	1000 F/g (1 A/g)	84.46	4500	This work

## Chapter 7

### 3D Assembly of CoAl<sub>2</sub>O<sub>4</sub> Spinel Nanosheets for Energy Storage

#### 7.1. ABSTRACT

Two-dimensional (2D) materials have attracted attention for electrochemical energy storage applications owing to their unique physical and chemical properties. However, the facile synthesis of thin 2D sheets remains a challenge. Herein, this chapter demonstrate the formation of 3D assembly of thin Co-Al spinel sheets and Carbon composite through a facile two steps process: hydrothermal synthesis of CoAl Layered double hydroxide (LDH) followed by heating of this LDH at high temperature to form CoAl<sub>2</sub>O<sub>4</sub>/C. This composite with a high specific surface area (SSA) of 102.7 m<sup>2</sup> g<sup>-1</sup> showed enhanced energy storage application. The CoAl<sub>2</sub>O<sub>4</sub>/C is capable of delivering specific capacitance of 1394 F g<sup>-1</sup> under 1 A g<sup>-1</sup> current density with 87% capacitance retention after 5k cycles. For asymmetric supercapacitor (ASC), the CoAl<sub>2</sub>O<sub>4</sub>/C and Activated Carbon (AC) were used as cathode and anode respectively. The device CoAl<sub>2</sub>O<sub>4</sub>/C//AC exhibits a high energy density of 76.34 W h kg<sup>-1</sup> at a power density of 750.045 W kg<sup>-1</sup> with good cyclic durability of 79 % after 10k cycles. The improved electrochemical activity may be due to the 3D assembly of thin 2D Co-Al spinel nanosheets that allows easy electron and mass transport, high surface area, synergistic interaction among different components, etc. for which Co-Al spinel/C composite will find application in energy storage.

## 7.2 INTRODUCTION

To deal with the ever-rising energy crisis arising from heavy use of non-renewable fossil fuels, renewable resource technologies for instance biomass energy, fuel cells, metal air batteries, and hydroelectricity are used as alternatives for energy conversion and storage<sup>1</sup>. Owing to its high specific capacitance, cycling stability, extraordinary power density, and high energy density, supercapacitors have emerged as attractive energy storage devices among all types of energy storage systems<sup>2</sup>. In general, according to their charge storage phenomenon supercapacitors are classified as Electrical double layer capacitors (EDLCs) and pseudocapacitors<sup>3</sup>. EDLCs store charge in an electrode-electrolyte interface which is based on adsorption-desorption mechanism and their examples include especially conductive carbon based materials such as AC, graphene oxide, polyaniline (PANI), carbon aerogels, graphene hydrogels, and carbon nanotubes, etc. having very high surface area and porosity<sup>3</sup>. Pseudocapacitors store charge electrostatically via fast reversible redox process on electrode surface resulting in high specific capacitance compared to EDLCs<sup>4</sup>. Pseudocapacitor-type materials mainly include transition metal oxides (TMO), oxyhydroxides, chalcogenides, and phosphides,<sup>5</sup> etc. Although pseudocapacitors have high specific capacitance compared to EDLCs, they suffer from issues like electrochemical cyclic stability and rate performance. To overcome these issues, hybrid composites combining both EDLCs and battery (pseudo) type electrode materials can be preferable electrode materials that will provide better stability and rate capacity to the storage device<sup>6</sup>.

A well-defined morphology of electrode material can provide promising electrochemical performance compared to its bulk counterpart. Two dimensional (2D) and three dimensional (3D) materials with high surface areas have gained considerable attention

and proved that these materials can be beneficial for effective ion diffusion and electron transport that boost the performance of energy storage devices<sup>7</sup>. Notable research has been carried out on TMOs because of their low-cost, high theoretical specific capacitance value, excellent energy density, and redox ability, but their poor ion diffusion and electron transfer properties in their bulk state have been the reason behind low capacitive performance<sup>8</sup>. For the last several years, TMOs for example Co<sub>3</sub>O<sub>4</sub>, MnO<sub>2</sub>, Fe<sub>3</sub>O<sub>4</sub>, NiCo<sub>2</sub>O<sub>4</sub>, and NiO along with conductive supports are used as supercapacitor electrodes materials<sup>9</sup>. Among TMOs, Cobalt-based spinels are widely used in applications like catalysis, magnetism, electricity, and energy storage devices<sup>10</sup>. Compared to traditional bulk materials, 2D cobaltites can offer good ion diffusion and complete use of active sites for electrochemical reactions through their high surface area<sup>11</sup>. However, 2D electrode materials suffer from several aggregation issues during the practical application, which results in loss of active sites in the material<sup>12</sup>. Therefore, the construction of 3D hierarchical structures based on 2D nanosheets can be an effective strategy to resolve the above-mentioned problems<sup>13</sup>. To date, several works have reported 3D hierarchical structured materials and their applications in energy storage and conversion system. For example, P. Wang et al. prepared a 3D assembly of layered MoS<sub>2</sub> nanosheets for enhanced lithium-ion storage<sup>12</sup>. R. Kumar et al. reported a one-step synthesis of self-assembled 3D interconnected Fe<sub>3</sub>O<sub>4</sub>/rGO nanosheets for supercapacitor application with a specific capacitance value of 455 F g<sup>-1</sup> at the scan rate of 8 mV s<sup>-1</sup><sup>14</sup>. Q. Jing et al. prepared self-assembled 3D cobalt organic phosphate which displayed a specific capacitance of 274.32 F g<sup>-1</sup> under 0.5 A g<sup>-1</sup> current<sup>15</sup>. Several strategies have also been reported on the preparation of cobalt based spinels for supercapacitor applications and substantial focus has been given to offer more environmental-friendly



and moderately rationable alternative metals have been used for partial substitution of Cobalt for the synthesis of ternary spinel cobaltites which collaboratively provide superior reversible capacities, preferred electrical conductivity, and interesting redox chemistry. For example, Abbasi et al. reported hierarchical arrays of ultrathin  $\text{CuCo}_2\text{O}_4$  nanosheets by controlling the synthesis time, precursor types and investigated the effect of morphology on electrochemical performance achieving a high specific capacitance of  $1330 \text{ F g}^{-1}$  under current density of  $2 \text{ A g}^{-1}$  along with 70% capacitance retention under  $60 \text{ A g}^{-1}$  current<sup>16</sup>. Similarly, Xiao et al. prepared mesoporous nanosheets of  $\text{ZnCo}_2\text{O}_4$  which showed a good capacity value of  $835.26 \text{ F g}^{-1}$  under current of  $1.0 \text{ A g}^{-1}$  along with 73.28% retention of cycling stability after 1000 charging-discharging cycles under  $8 \text{ A g}^{-1}$  current<sup>17</sup>. Several metals like Cu, Al, Zn, Mn, and Fe have been incorporated into the cobaltite structure to study the synergistic interaction between metals and their effect on electrochemical behavior<sup>3</sup>. Among all the elements, Al can be a promising candidate for incorporation into oxide materials because of its low cost and nontoxic nature. Previous reports also have shown that Al doping can effectively tune the electronic structure of material for electrochemical applications. For example, X.-W. Lv et al. reported an increase in oxygen vacancy ion  $\text{Co}_3\text{O}_4$  via doping of Al into it and applied it in electrochemical water splitting and batteries<sup>18</sup>. Similarly, Chen et al. reported nanosheets array of Aluminium doped NiO for supercapacitor application and showed an increase in conductivity in the material through Al doping<sup>19</sup>. Metal aluminate spinels have been used in applications like electrochemical water splitting, photochemical water oxidations<sup>20</sup>. For example, T. Kanazawa et. al reported  $\text{CoAl}_2\text{O}_4$  spinel for photocatalytic water oxidation<sup>21</sup>. Although some reports of cobalt aluminate spinels ( $\text{CoAl}_2\text{O}_4$ ) are there

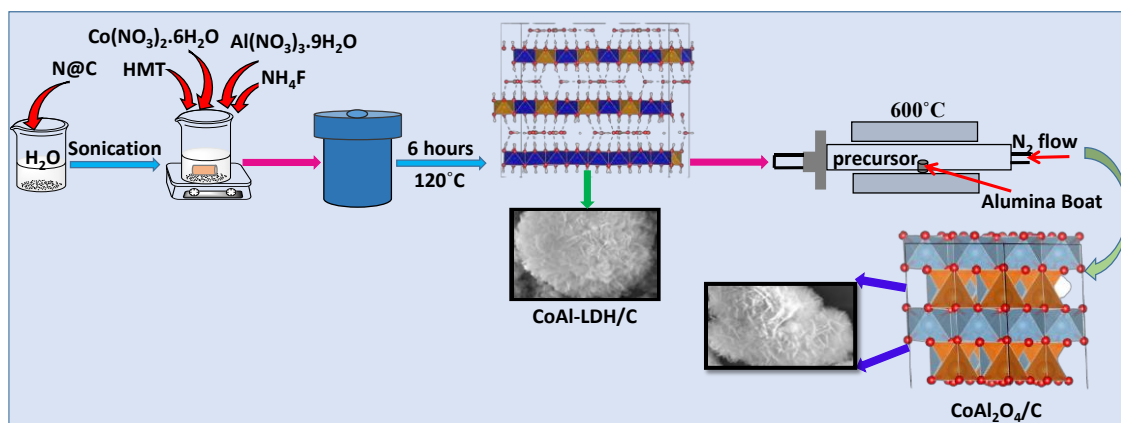
for electrochemical applications such as electrochemical hydrogen storage performance<sup>22</sup> but their application for supercapacitors is limited as per our knowledge.

This chapter demonstrates facile synthesis and assembly for two dimensional (2D) thin nanosheets like Co-Al spinel sheets/C composite in two steps- hydrothermal synthesis of CoAl Layered double hydroxide (LDH) followed by calcination to form  $\text{CoAl}_2\text{O}_4/\text{C}$ . The composite has a very high SSA of  $102.7 \text{ m}^2\text{g}^{-1}$  shows a very high specific capacitance value of  $1394 \text{ F g}^{-1}$  along with good rate capacity confirming the improved catalytic activity of the material as compared to other controlled samples.

### 7.3. EXPERIMENTAL SECTION:

#### 7.3.1. Materials:

Cobalt (II) nitrate hexahydrate ( $\text{Co}(\text{NO}_3)_2 \cdot 6\text{H}_2\text{O}$ ), Formamide ( $\text{HCONH}_2$ ), and Aluminum (III) nitrate nonahydrate ( $\text{Al}(\text{NO}_3)_3 \cdot 9\text{H}_2\text{O}$ ) were bought from Merck (India). Hexamethylene tetramine (HMT) was purchased from ThermoFisher, India. Ammonium fluoride ( $\text{NH}_4\text{F}$ ) was supplied by HI-Media. Potassium hydroxide (KOH) was bought from SigmaAldrich. Deionized (DI) water obtained from the Milli-Q ultrafiltration system was used in all experiments with a resistivity of  $17.9 \text{ M}\Omega \text{ cm}$ .



**Scheme 7.1.** Scheme illustrating synthesis of  $\text{CoAl}_2\text{O}_4/\text{C}$ .

### 7.3.2. Synthesis of Nitrogen doped carbon (N@C)

N@C was prepared using the following method<sup>23</sup>. A three-necked round bottom flask with 20 ml of Formamide was heated at 180 °C for 3 hours under continuous stirring in a microwave synthesizer to produce a brown color solution which was further vacuum-evaporated in a rotary evaporator at 180 °C to get solid N@C. Finally, it was washed multiple times in DI  $\text{H}_2\text{O}$  and dried at room temperature under vacuum.

### 7.3.3. Synthesis of $\text{CoAl}_2\text{O}_4/\text{C}$

The  $\text{CoAl}_2\text{O}_4/\text{C}$  were prepared by two steps process- the 1<sup>st</sup> step is the hydrothermal synthesis of carbon-supported Cobalt Aluminium layered double hydroxide (CoAl-LDH/C) composite and in the second step, the heating of as synthesized LDH at 600 °C for 2 hours in the nitrogen environment to form  $\text{CoAl}_2\text{O}_4/\text{C}$  composite. The heating rate was 5 °C per minute and nitrogen flow was 200 ml/min. The Co and Al precursor ratio were taken 1:2 for the synthesis of  $\text{CoAl}_2\text{O}_4/\text{C}$ . The CoAl-LDH/C was prepared by using our previous report<sup>24</sup>. 35 mg of N@C were dispersed in 20 mL of DI  $\text{H}_2\text{O}$  containing 77.6 mg of  $\text{Co}(\text{NO}_3)_2 \cdot 6\text{H}_2\text{O}$  and 200 mg  $\text{Al}(\text{NO}_3)_3 \cdot 9\text{H}_2\text{O}$  to obtain total molarity of 40 mM. In to this solution, 0.600 g of HMT, and 0.100 g of  $\text{NH}_4\text{F}$  were added and heated

for 6 hours in a 50 mL Teflon-lined autoclave to maintain a constant temperature of 120 °C. It was then cooled and centrifuged at 1000 rpm to obtain solid product. The product was washed with  $\text{H}_2\text{O}$  and ethanol multiple times and this product was named as CoAl-LDH/C. The  $\text{Co}_m\text{Al}_n\text{O}_x/\text{C}$  composites ( $\text{Co}_2\text{Al}_1\text{O}_x/\text{C}$ ,  $\text{Co}_1\text{Al}_1\text{O}_x/\text{C}$ ,  $\text{Co}_1\text{Al}_2\text{O}_x/\text{C}$ , and  $\text{Co}_1\text{Al}_3\text{O}_x/\text{C}$ ) were also prepared by varying Co and Al precursor ratio.

Only  $\text{CoAl}_2\text{O}_4$  spinel without carbon support was synthesized by using the above mentioned method without N@C. The  $\text{Co}_3\text{O}_4/\text{C}$  and  $\text{Al}_2\text{O}_3/\text{C}$  were also synthesized by using the same method without adding Al precursor and Co precursor respectively.

#### 7.3.4. Synthesis of Activated Carbon (AC)

AC was prepared from Formamide by using the following procedure reported previously<sup>25</sup>. 50 mL of Formamide was taken in a 100 mL autoclave and heated for 48 hours at 200 °C to get the polymerized product. The black polymerized product was further heated at 400 °C in a muffle furnace for 1 hour followed by annealing in a tube furnace for 2 hours at 700 °C under  $\text{N}_2$  flow (700 ml/min) and a heating rate of 5 °C/min. Then it was mixed with potassium hydroxide in a weight ratio of 1:2 followed by activation for two hours at 700 °C with  $\text{N}_2$  flow of 700 ml/min with a heating rate of 5 °C/min. The as obtained carbon composite was named as Activated carbon (AC). The product was rinsed with 0.2 M HCl followed by DI  $\text{H}_2\text{O}$  several times and dried to get the desired product. The product obtained was used as anode material for designing the asymmetric device.

#### 7.3.5. Electrode Fabrication:

For the fabrication of the working electrode, a piece of Ni foam of area 1 cm<sup>2</sup> (1 cm × 1 cm) was used. The Ni foam was washed with 3M HCl to remove the oxide layers and then it was rinsed with  $\text{H}_2\text{O}$ , ethanol and finally dried. The AC, conductive carbon (CC),

and polyvinylidene fluoride (PVDF) binder in N-methyl-2-pyrrolidone (NMP) in a weight % of 80:10:10 were mixed to form a homogenous slurry. The slurry was coated over the 1×1 cm<sup>2</sup> Ni foam and it was then dried in an oven. The mass of the CoAl<sub>2</sub>O<sub>4</sub>/C (active material) loaded on the Ni foam was found to be 1mg. For the designing of ASC, the AC was used as the negative electrode (anode) and active material as the positive electrode (cathode), and cellulose paper used as a separator. For positive and negative electrodes, the weight loading ratio was calculated to be 0.3 (weight loading for positive and negative electrodes were 1 mg and 3.5 mg, respectively).

#### 7.3.6. Characterizations:

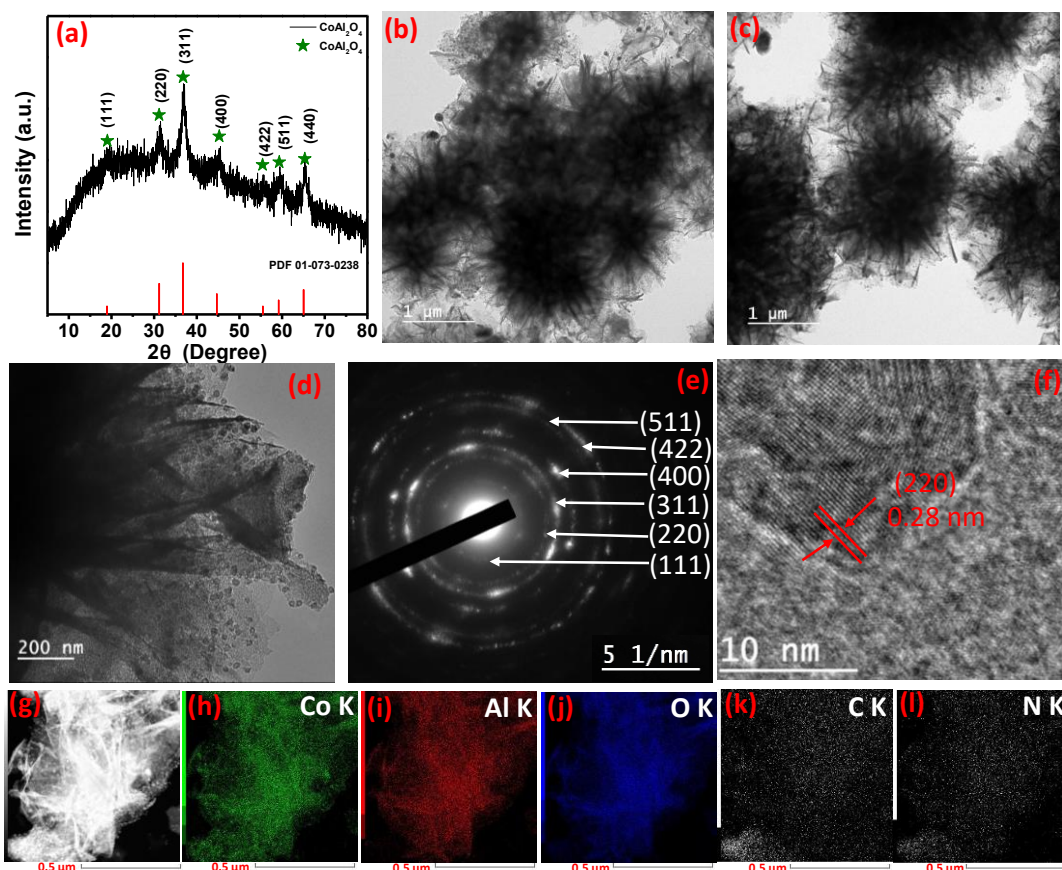
The x-ray diffraction data (p-XRD) of as prepared samples were conducted by Bucker DAVINCI D8 ADVANCE diffractometer equipped with a monochromatic radiation source of Cu K $\alpha$  ( $\lambda$ = 0.15406). The composition and morphology of the material was recorded by Field-emission scanning electron microscope (FESEM) system (Carl Zeiss, Germany make, Model: Sigma) and Transmission Electron Microscopy (TEM, JEOL F200) and High-Resolution TEM (HRTEM). VG Microtech was used to record the XPS data with monochromatic Mg K $\alpha$  X-ray as the source. All electrochemical measurements were performed by using CorrTest Electrochemical Workstation [Model: CS350]. Quantachrome Instruments (AutosorbiQ-XR-XR (2 Stat.)) Viton was used to determine the Specific surface area by N<sub>2</sub> adsorption-desorption isotherm.

### 7.4. RESULTS AND DISCUSSIONS:

#### 7.4.1. Structural and morphological characterizations

The freshly prepared CoAl<sub>2</sub>O<sub>4</sub>/C composite were first characterized by using the powder X-ray diffraction (p-XRD) technique. As displayed in Figure 7.1(a), p-XRD pattern of Co<sub>1</sub>Al<sub>2</sub>O<sub>4</sub>/C show the presence of several diffraction peaks at 18.95, 31.191, 36.752,

44.693, 55.506, 59.20, and 65.054 corresponding to (111), (220), (311), (400), (422), (511), and (440) planes of  $\text{CoAl}_2\text{O}_4$  spinel structure (PDF 01-073-0238)<sup>26-27</sup>. By increasing and decreasing Co/Al molar precursor's ratio, different other  $\text{Co}_m\text{Al}_n\text{O}_x/\text{C}$  composites were also prepared. The p-XRD patterns of  $\text{Co}_2\text{Al}_1\text{O}_x/\text{C}$ ,  $\text{Co}_1\text{Al}_3\text{O}_x/\text{C}$ ,  $\text{Co}_3\text{O}_4/\text{C}$ , and  $\text{Al}_2\text{O}_3/\text{C}$  were given in Figure S7.1. In Figure S7.1(a), p-XRD pattern of  $\text{Co}_2\text{Al}_1\text{O}_x/\text{C}$  shows (220), (311), (400), and (422) reflection planes of  $\text{CoAl}_2\text{O}_4$  spinel and also show the presence of peaks of Cobalt oxide. But, in Figure S7.1(b), in addition to the (311), (400), (422), (511), and (440) reflection of  $\text{CoAl}_2\text{O}_4$  spinel, several diffraction peaks of the  $\text{Al}_2\text{O}_3$  phase were observed in the p-XRD pattern of  $\text{Co}_1\text{Al}_3\text{O}_x/\text{C}$ . This suggests that  $\text{CoAl}_2\text{O}_4$  spinel and either cobalt oxide or aluminum oxide are formed when Co: Al precursor's ratio was taken more or less than 1:2 during synthesis. The p-XRD patterns of only  $\text{Co}_3\text{O}_4/\text{C}$  and  $\text{Al}_2\text{O}_3/\text{C}$  composites are presented in Figure S7.1(c), and S1 (d) respectively. Figure S7.2 displays the FESEM image of  $\text{CoAl}_2\text{O}_4/\text{C}$ . The as-synthesized  $\text{CoAl}_2\text{O}_4/\text{C}$  shows hierarchical 2D nanosheets that are randomly aggregated to form 3D assemble type morphology. FESEM images of only  $\text{Al}_2\text{O}_3/\text{C}$  and  $\text{Co}_3\text{O}_4/\text{C}$  are shown in Figure S7.3(a, b) respectively.



**Figure 7.1.** (a) p-XRD pattern, (b-d) TEM images, (e) SAED pattern, (f) HRTEM image, (g) STEM image of  $\text{CoAl}_2\text{O}_4/\text{C}$ , and corresponding Elemental mapping of elements (h) Co, (i) Al, (j) O, (k) C, and (l) N of  $\text{CoAl}_2\text{O}_4/\text{C}$  showing the uniform distribution of Co, Al, O, C, and N respectively.

The low and high-resolution TEM images of  $\text{CoAl}_2\text{O}_4/\text{C}$  are presented in Figure 7.1(b-d) showing an assembly of thin nanosheets. The 2D thin nanosheets are interconnected to form 3D hierarchical morphology. As shown in Figure 7.1(d), some thin folded sheets of  $\text{CoAl}_2\text{O}_4$  are clearly seen and very small nanoparticles of  $\text{CoAl}_2\text{O}_4$  are also present in some sheets. Figure 7.1(e) displays the SAED pattern and d-spacing are calculated to be 0.28, 0.244, 0.201, 0.165, 0.156, 0.143, and 0.127 nm corresponding to (220), (311), (400), (422), (511), (440), and (620) planes of  $\text{CoAl}_2\text{O}_4/\text{C}$ . This is well consistent with

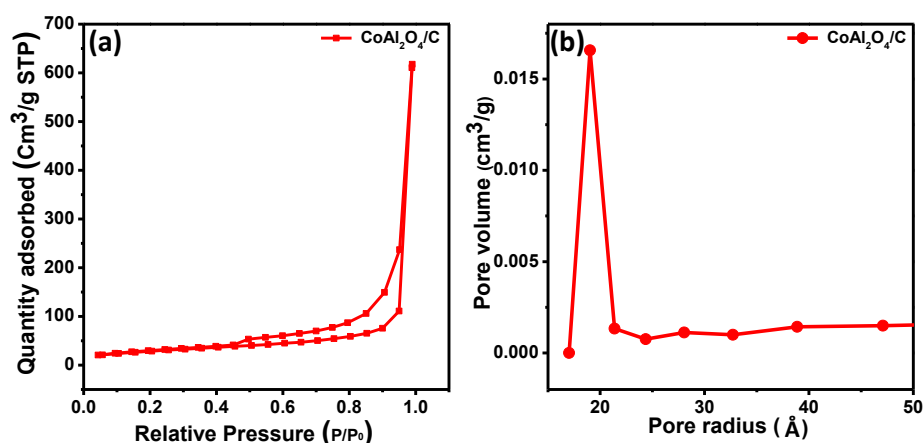
the p-XRD results of CoAl<sub>2</sub>O<sub>4</sub>/C. The HRTEM of the CoAl<sub>2</sub>O<sub>4</sub>/C composite is presented in Figure 7.1(f). The lattice fringes with 0.28 nm interlayer-spacing confirmed the (220) plane of CoAl<sub>2</sub>O<sub>4</sub> spinel in the CoAl<sub>2</sub>O<sub>4</sub>/C composite. Figure 7.1(g-l) displays the STEM image and corresponding elemental mapping showing the presence of Co, Al, O, C, and N, respectively, indicating the uniform distribution of elements over nanosheets.

We also characterized the first step product of the hydrothermal heating when Co/Al precursor ratio was 1:2. The p-XRD pattern, SEM, High and low-resolution TEM of this product were provided in Figure S7.4. The p-XRD peaks corresponding to planes (003), (006), (012), (015), (018), (110), (113), and (116) of CoAl-LDH/C (Figure S7.4(a)) suggest the formation of LDH phases due to the hydrothermal treatment in the 1<sup>st</sup> step of synthesis of CoAl<sub>2</sub>O<sub>4</sub>/C composite<sup>23-24, 28</sup>. As presented in Figure S7.4(b), the SEM image of the 1<sup>st</sup> step product show 3D flower like morphology of CoAl-LDH/C composite. Figure S7.4(c, and d) represents the high and low resolution TEM images of the CoAl-LDH/C composite. The lattice fringe with an inter-planar spacing of 0.24 nm was indexed to (015) planes of CoAl-LDH/C structure. This confirmed presence of LDH phases in the composite. Based on these results, we can conclude that, in the 1st step, CoAl-LDH/C was formed due to the hydrothermal treatment, and in the second step calcination results in the formation of spinel CoAl<sub>2</sub>O<sub>4</sub>/C composite (Scheme 7.1).

The specific surface area (SSA) and average pore size are vital parameters for the enrichment of the electrochemical property of the electrode material for energy storage applications. The porous morphology (SSA and average pore size) of as synthesized composite was evaluated by using N<sub>2</sub> desorption/adsorption isotherms (BET technique). Figure 7.2(a) shows the presence of a typical hysteresis loop of type IV after relative



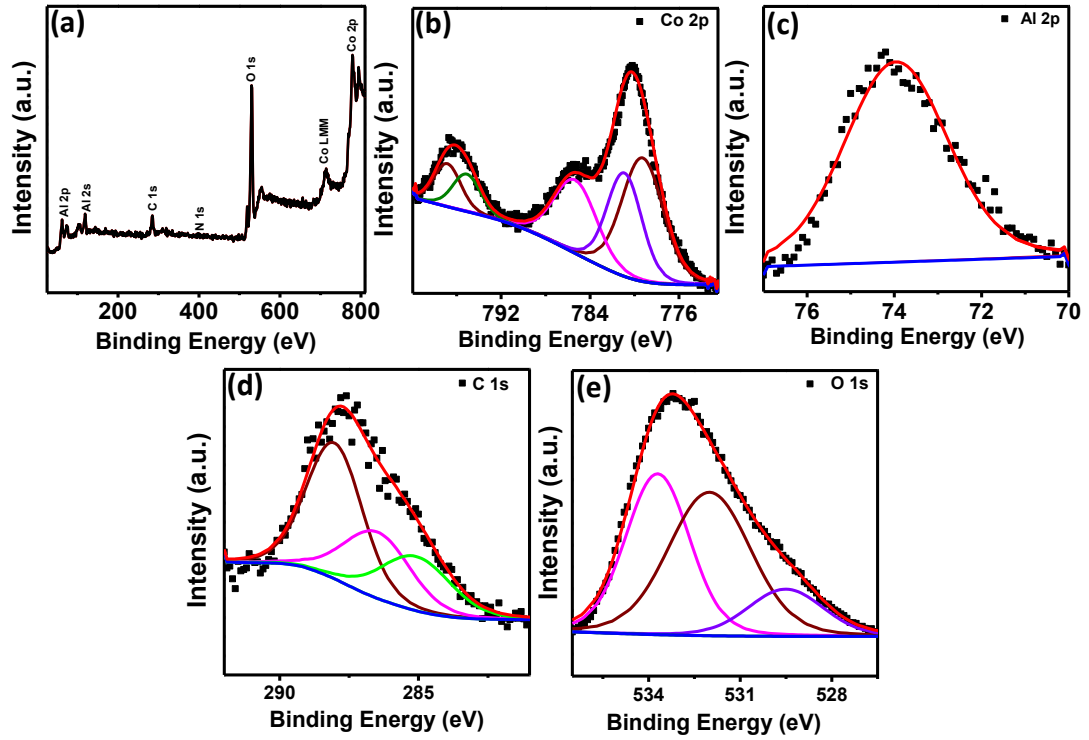
pressure  $P/P_0 > 0.4$  suggesting the presence of mesoporous nature of the material. Multipoint BET SSA values for Co<sub>2</sub>Al<sub>1</sub>O<sub>x</sub>/C, Co<sub>1</sub>Al<sub>1</sub>O<sub>x</sub>/C, CoAl<sub>2</sub>O<sub>4</sub>/C, Co<sub>1</sub>Al<sub>3</sub>O<sub>x</sub>/C, and CoAl-LDH/C were found to be 36.656 m<sup>2</sup>g<sup>-1</sup>, 49.242 m<sup>2</sup>g<sup>-1</sup>, 102.7 m<sup>2</sup>g<sup>-1</sup>, 67.168 m<sup>2</sup>g<sup>-1</sup>, and 84.745 m<sup>2</sup>g<sup>-1</sup> respectively which indicates that the SSA for CoAl<sub>2</sub>O<sub>4</sub>/C is much higher compared to other ratios and CoAl-LDH/C. The N<sub>2</sub> desorption/adsorption isotherms for Co<sub>m</sub>Al<sub>n</sub>O<sub>x</sub>/C and CoAl-LDH/C are shown in Figure S7.5(a-d). Barrett-Joyner-Halenda (BJH) pore size distribution analysis is used for the calculation of average pore radius of the material and for CoAl<sub>2</sub>O<sub>4</sub>/C average pore radius was obtained to be 19.027 Å which is presented in Figure 7.2 (b).



**Figure 7.2.** (a, b) N<sub>2</sub> desorption/adsorption isotherm and pore size distribution of CoAl<sub>2</sub>O<sub>4</sub>/C.

ICP-OES measurement was performed to identify the exact composition of metal ion percentage present in Co<sub>m</sub>Al<sub>n</sub>O<sub>x</sub>/C. Table S7.1 shows the comparison presenting the real composition of materials and the calculated amount of metal ions from the precursor. The Co/Al ratio is found to be 2.93, 1.31, 0.51, and 0.3 for Co<sub>2</sub>Al<sub>1</sub>O<sub>x</sub>/C, Co<sub>1</sub>Al<sub>1</sub>O<sub>x</sub>/C, CoAl<sub>2</sub>O<sub>4</sub>/C, and Co<sub>1</sub>Al<sub>3</sub>O<sub>x</sub>/C composites respectively. The values obtained are very close to the molar ratio of precursors calculated throughout the synthesis process.

The chemical composition and surface oxidation state for CoAl<sub>2</sub>O<sub>4</sub>/C were determined by X-ray photoelectron spectroscopy (XPS) which is shown in Figure 7.3. The wide survey spectrum for CoAl<sub>2</sub>O<sub>4</sub>/C showing the existence of Co, Al, O, C elements, and the presence of a small amount of N is presented in Figure 7.3(a). Figure 7.3(b) shows XPS spectra of Co. Co 2p peak can be deconvoluted into two parts, one for Co 2p<sub>3/2</sub> and the other one is for Co 2p<sub>1/2</sub> along with one satellite peak. The main peaks at 780.23 eV for Co 2p<sub>3/2</sub> and 796.15 eV for Co 2p<sub>1/2</sub> are deconvoluted into two peaks. The peaks at 779.31 eV and 775.8 eV can be assigned to Co (II) and peaks at 781.8 eV and 796.89 eV were indexed to Co (III) respectively along with a satellite peak at 785.57 eV indicating that Co(II) is present in octahedral coordination site<sup>29</sup>. Figure 7.3(c) represents the High resolution XPS spectra for Al 2p which shows a singlet at 74.1 eV indicating the presence of Al (III). As shown in Figure 7.3(d), the C 1s peak can be deconvoluted into three peaks centered at 288.12 eV, 286.61 eV, and 284.9 eV. The peak at 284.9 eV corresponds to sp<sup>2</sup> carbon (C-C) and the peak centered at 286.61 eV and 288.12 eV are due to C-O bond<sup>30-31</sup> and N-C=C bond respectively<sup>29-30</sup>. The O 1s peaks are deconvoluted into three peaks which are presented in Figure 7.3(e). The peak at 529.45 eV corresponds to lattice oxygen (O<sub>latt.</sub>, O<sup>2-</sup>) of CoAl<sub>2</sub>O<sub>4</sub>, peak at 531.9 eV ascribes the surface adsorbed water and oxygen species, and the peak centered at 532.89 eV indicates the presence of adsorbed water within the material<sup>24, 32</sup>. Figure S7.6 represents the N 1s peak which can be deconvoluted into three peaks. The peaks at 399.1 eV, 399.8 eV, and 401.8 eV correspond to graphitic nitrogen, pyridinic nitrogen and pyrrolic nitrogen respectively.



**Figure 7.3.** (a) XPS wide spectrum of CoAl<sub>2</sub>O<sub>4</sub>/C. High resolution XPS spectra of (b) Co 2p, (c) Al 2p, (d) C 1s, and (e) O 1s respectively.

#### 7.4.2. Electrochemical Analysis

The electrochemical performance of Co<sub>m</sub>Al<sub>n</sub>O<sub>x</sub>/C composites were studied using an electrochemical Workstation. Cyclic voltammetry (CV) and Galvanostatic charge-discharge curve (GCD) experiments were performed at ambient temperature in a 2M KOH aqueous solution. For half-cell configuration platinum wire (as counter), Ag/AgCl (as reference) and active material coated on 1×1 cm<sup>2</sup> Ni foam (as working electrode) was used.

Specific capacitance ( $C_s$ ) was computed from CV curve by using equation 7.1<sup>8, 33</sup>

$$C_s = \frac{\int IdV}{2m\Delta V} \quad (7.1)$$

Specific capacitance was computed from the GCD curve by using equation 7.2<sup>8, 34</sup>

$$C_s = \frac{It}{m\Delta V} \quad (7.2)$$

Where  $C_s$  presents the specific capacitance ( $F\ g^{-1}$ ),  $I$  is current (mA),  $\Delta t$  is the discharge time (sec),  $m$  represents mass of active material (mg),  $\Delta V$  is the operating voltage range (V),  $\int I\ dV$  is the area covered by the CV curve and  $v$  denotes the sweep rate ( $mV\ s^{-1}$ ).

For Asymmetric supercapacitor (ASC) cell the as prepared material (active material) acts as cathode and AC acts as an anode. The full cell is represented as CoAl<sub>2</sub>O<sub>4</sub>/C //AC. To balance the charge storage, the mass ratio of CoAl<sub>2</sub>O<sub>4</sub>/C and AC was calculated by using equation 7.3<sup>24, 29, 34</sup>.

$$\frac{m^-}{m^+} = \frac{C^+ \Delta V^+}{C^- \Delta V^-} \quad (7.3)$$

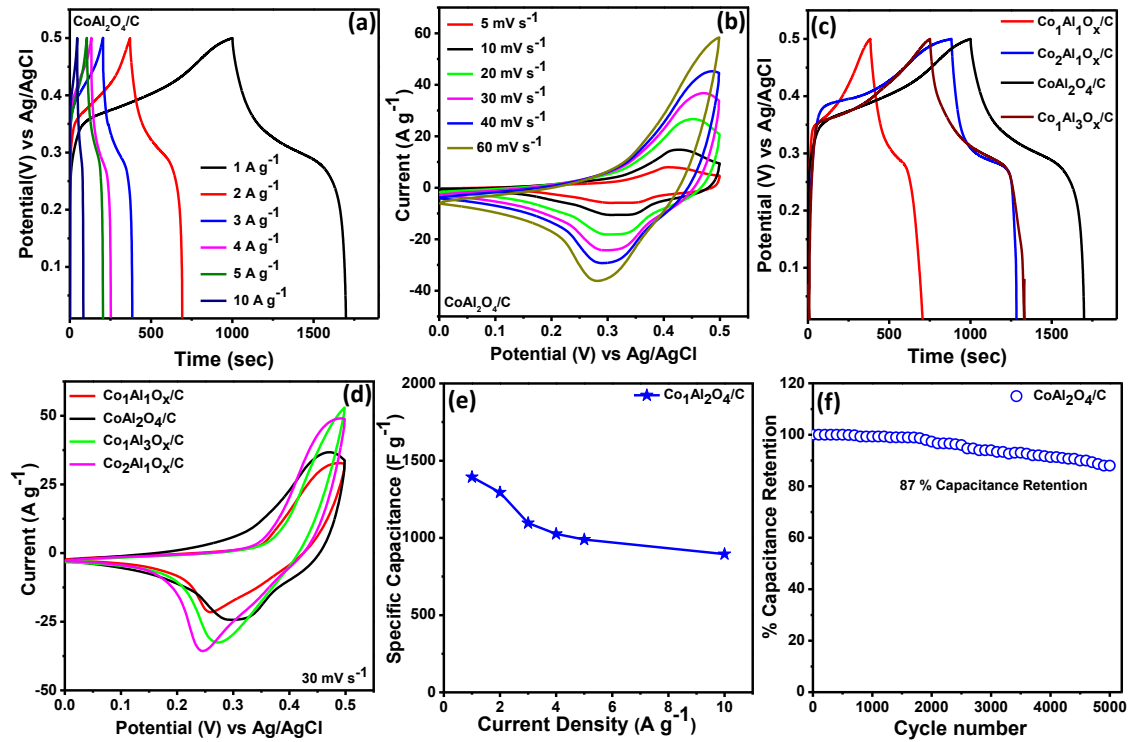
Where  $m^+$  was mass (mg),  $C^+$  and  $C^-$  were  $C_s$  values of active material, and AC respectively,  $\Delta V^+$  and  $\Delta V^-$  are voltage range of cathode and anode electrode respectively and  $m^-$  was mass of anode<sup>24, 35</sup>.

$$E = \frac{C_s (\Delta V)^2}{7.2} \quad (7.4)$$

$$P = \frac{E}{\Delta t} \times 3600 \quad (7.5)$$

Where  $\Delta V$  is the voltage window (V),  $C_s$  is the capacitance of ASC ( $F\ g^{-1}$ ) and  $\Delta t$  is the discharge time (sec).

Nonlinear GCD profiles for CoAl<sub>2</sub>O<sub>4</sub>/C at different current densities are presented in Figure 7.4(a) with potential window ranging from 0-0.5 V<sup>36</sup>. The  $C_s$  values were obtained from the GCD curves by using equation 7.2 and were obtained to be 1394  $F\ g^{-1}$ , 1294  $F\ g^{-1}$ , 1096  $F\ g^{-1}$ , 989.7  $F\ g^{-1}$ , and 895  $F\ g^{-1}$  under 1, 2, 3, 4, and 10 A  $g^{-1}$  current. It shows 64.2 % retention of its capacitance at 10 A  $g^{-1}$  current. For comparison GCD curve of only Ni foam at 1 mA current was performed which is shown in Figure S7.7 indicating negligible contribution towards electrochemical performance.



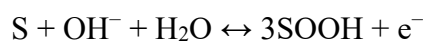
**Figure 7.4.** (a) GCD profile of CoAl<sub>2</sub>O<sub>4</sub>/C composite (1-10 A g<sup>-1</sup>). (b) CV profile of CoAl<sub>2</sub>O<sub>4</sub>/C from 5-60 mV s<sup>-1</sup> scan rate. (c) CD profile of CoAl<sub>2</sub>O<sub>4</sub>/C with other ratios of Co<sub>m</sub>Al<sub>n</sub>O<sub>x</sub>/C at 1 A g<sup>-1</sup> current. (d) Comparison CV profile of CoAl<sub>2</sub>O<sub>4</sub>/C and other ratios at a sweep rate of 30 mV s<sup>-1</sup> (e) Plot of C<sub>s</sub> (F g<sup>-1</sup>) of CoAl<sub>2</sub>O<sub>4</sub>/C with current density (A g<sup>-1</sup>). (f) Plot of cyclic durability of CoAl<sub>2</sub>O<sub>4</sub>/C at 10 A g<sup>-1</sup> current.

**Table 7.1.** Comparison of electrochemical performance of CoAl<sub>2</sub>O<sub>4</sub>/C composite with previously reported literatures.

Electrode material	Specific capacitance of single Electrode	Capacitance retention after cycling stability (%)	No. of cycles	Ref.
CuCo <sub>2</sub> O <sub>4</sub> /MnCo <sub>2</sub> O <sub>4</sub>	1434 F g <sup>-1</sup> (0.5 A g <sup>-1</sup> )	81.4	5000	37
Al <sub>0.2</sub> Cu <sub>0.4</sub> Co <sub>0.4</sub> Fe <sub>2</sub> O <sub>4</sub>	548 F g <sup>-1</sup> (100 mV s <sup>-1</sup> )	88	300	38

Co <sub>3</sub> O <sub>4</sub> nanorods	739 F g <sup>-1</sup> (5 mV s <sup>-1</sup> )	100	50000	<sup>39</sup>
Cr-doped Mn <sub>3</sub> O <sub>4</sub> nanocrystals	272 F g <sup>-1</sup> (0.5 A g <sup>-1</sup> )	100	1000	<sup>40</sup>
Co-doped-NiO nanosheets	1244 F g <sup>-1</sup> (5 A cm <sup>-2</sup> )	86.2	2000	<sup>41</sup>
MnFe <sub>2</sub> O <sub>4</sub> /MoS <sub>2</sub>	2093 F g <sup>-1</sup> (1 A g <sup>-1</sup> )	80	2000	<sup>42</sup>
Ni <sub>0.5</sub> Zn <sub>0.5</sub> Fe <sub>2</sub> O <sub>4</sub> @NF	504 F g <sup>-1</sup> (1 A g <sup>-1</sup> )	-	-	<sup>43</sup>
MOF-derived NiFe <sub>2</sub> O <sub>4</sub>	833 F g <sup>-1</sup> (0.25 A g <sup>-1</sup> )	74	700	<sup>44</sup>
1)				
2D NiCo <sub>2</sub> O <sub>4</sub> /MWCNT hybrid	1396 F g <sup>-1</sup> (1 A g <sup>-1</sup> )	94.3	5000	<sup>45</sup>
CoFe <sub>2</sub> O <sub>4</sub>	777 F g <sup>-1</sup> (0.5 mA cm <sup>2</sup> )	100	1500	<sup>46</sup>
rGO/Ni <sub>0.5</sub> Co <sub>0.5</sub> Fe <sub>2</sub> O <sub>4</sub>	1286 F g <sup>-1</sup> (0.5 A g <sup>-1</sup> )	95	6000	<sup>47</sup>
2D Co <sub>3</sub> O <sub>4</sub> /PANI/graphene hybrid	1063 F g <sup>-1</sup> (1 A g <sup>-1</sup> )	95	2500	<sup>48</sup>
Co <sub>3</sub> V <sub>2</sub> O <sub>8</sub> /CN <sub>x</sub>	1236 F g <sup>-1</sup> (1 A g <sup>-1</sup> )	87	4000	<sup>29</sup>
2D CuCo <sub>2</sub> O <sub>4</sub> /MnO <sub>2</sub> hybrid	416 F g <sup>-1</sup> (1 A g <sup>-1</sup> )	92.1	4200	<sup>49</sup>
CoAl <sub>2</sub> O <sub>4</sub> /C	1394 F g <sup>-1</sup> (1 A g <sup>-1</sup> )	87	5000	This work

Figure 7.4(b) displays the CV profile of CoAl<sub>2</sub>O<sub>4</sub>/C in potential ranging between 0-0.5V vs. Ag/AgCl at different sweep rates varying from 5-60 mV s<sup>-1</sup> to evaluate pseudocapacitance performance<sup>50-51</sup>. The cathodic and anodic peaks were observed at 0.45 V and 0.31 V which originates due to redox reaction occurring in the Co-O/Co-O-OH in spinel type metal oxide in KOH electrolyte<sup>52</sup>. At higher scan rate all the CV curves were almost identical in nature and the cathodic and anodic peaks shift towards lower and higher voltage range respectively indicating slow diffusion of electrolyte ions into electrode interface<sup>52</sup>. The C<sub>s</sub> values for CoAl<sub>2</sub>O<sub>4</sub>/C were obtained by integrating the area under the CV curves. The C<sub>s</sub> values were calculated to be 503.35 F g<sup>-1</sup> under 5 mV s<sup>-1</sup> and 446.3 F g<sup>-1</sup> under 10 mV s<sup>-1</sup> scan rate respectively by using equation 7.1. The possible electrochemical redox reaction can be represented as follows<sup>53-54</sup>



Where “S” represents CoAl<sub>2</sub>O<sub>4</sub>/C composite. A lower capacitance value at a higher sweep rate is because of the slow ion diffusion on the surface of the active material. At a lower sweep rate, the diffusion of ions is not restricted and the ions get sufficient time to diffuse into the surface of the active material resulting higher specific capacitance<sup>55-56</sup>. At a higher scan rate the EDLC predominates over pseudocapacitance and vice versa for slow scan rate cases i.e. sweep rate below 10 mV s<sup>-1</sup>.

Figure 7.4(c) represents the comparison GCD curve of CoAl<sub>2</sub>O<sub>4</sub>/C with other ratios Co<sub>m</sub>Al<sub>n</sub>O<sub>x</sub>/C. The GCD curves of Co<sub>m</sub>Al<sub>n</sub>O<sub>x</sub>/C composites show that the discharge time for CoAl<sub>2</sub>O<sub>4</sub>/C is much higher than other composites resulting highest specific capacitance. The C<sub>s</sub> values were calculated to be 801 F g<sup>-1</sup>, 646 F g<sup>-1</sup>, 1394 F g<sup>-1</sup>, and 1159 F g<sup>-1</sup> for Co<sub>2</sub>Al<sub>1</sub>O<sub>x</sub>/C, Co<sub>1</sub>Al<sub>1</sub>O<sub>x</sub>/C, CoAl<sub>2</sub>O<sub>4</sub>/C, Co<sub>1</sub>Al<sub>3</sub>O<sub>x</sub>/C under 1 A g<sup>-1</sup> current. Figure S7.8 displays the GCD profile of CoAl-LDH/C and only Co<sub>1</sub>Al<sub>2</sub>O<sub>4</sub> and C<sub>s</sub> values

were calculated to be 674 F g<sup>-1</sup> and 744.8 F g<sup>-1</sup> at 1 A g<sup>-1</sup> current showing much lower specific capacitance compared to CoAl<sub>2</sub>O<sub>4</sub>/C. Among all, the superior capacitance value was obtained for CoAl<sub>2</sub>O<sub>4</sub>/C where Co/Al molar ratio was 1:2 and the capacitance value decreases when the Al molar precursor ratio was increased to 3. The reduction of specific capacitance with an increase in Al substitution may be attributed to the prohibition of electrochemical redox reaction occurring at the electrode and electrolyte (increase in Al contain react with KOH resolution primarily resulting decrease in specific capacitance)<sup>52</sup>. Table S7.2 shows the Comparison of electrochemical performance of Co<sub>m</sub>Al<sub>n</sub>O<sub>x</sub>/C composite by varying Co/Al ratio and Table 7.1 displays the Comparison of electrochemical performance of CoAl<sub>2</sub>O<sub>4</sub>/C composite to that of previously reported literatures. Figure 7.4(d) shows comparison CV curve of Co<sub>2</sub>Al<sub>1</sub>O<sub>x</sub>/C, Co<sub>1</sub>Al<sub>1</sub>O<sub>x</sub>/C, CoAl<sub>2</sub>O<sub>4</sub>/C, and Co<sub>1</sub>Al<sub>3</sub>O<sub>x</sub>/C and the current response from CoAl<sub>2</sub>O<sub>4</sub>/C is greater than other materials indicating fast redox reaction kinetics process of CoAl<sub>2</sub>O<sub>4</sub>/C. Figure 7.4(e) presents C<sub>s</sub> (F g<sup>-1</sup>) of CoAl<sub>2</sub>O<sub>4</sub>/C with respect to a current density ranging from 1-10 A g<sup>-1</sup>. For practical capacitor application cycling stability is considered to be a very vital factor. So 5000 cycles GCD curves are carried out under 10 A g<sup>-1</sup> current which is presented in Figure 7.4(f). CoAl<sub>2</sub>O<sub>4</sub>/C spinel maintains capacitance retention of 87 percent of its initial value even after 5k cycles. It implies that CoAl<sub>2</sub>O<sub>4</sub>/C metal oxide is highly stable at 10 A g<sup>-1</sup> in 2M KOH solution. To provide a better clarification for the charge storage mechanism of the electrode material, the CV profile at 5 and 10 mV s<sup>-1</sup> sweep rates are obtained for the three electrode configuration. CV currents are divided into two types. One is capacitive contribution and another one is ion diffusion-controlled current contribution. The former demonstrates non-insertion capacity, which could be related to both the double layer capacity and fast faradaic pseudo-capacity (surface ion

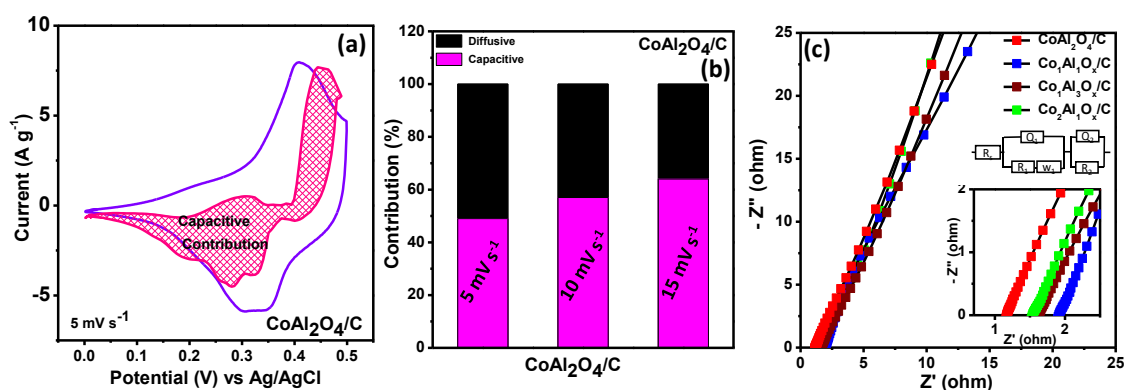


adsorption/desorption process) and varies linearly with  $v$  and the later one is diffusion controlled intercalation process which varies linearly with  $v^{1/2}$ . When we fixed the voltage ( $V$ ), the current ( $i$ ) can be determined by using Dunn's method which is given in equation 7.6<sup>57-60</sup>

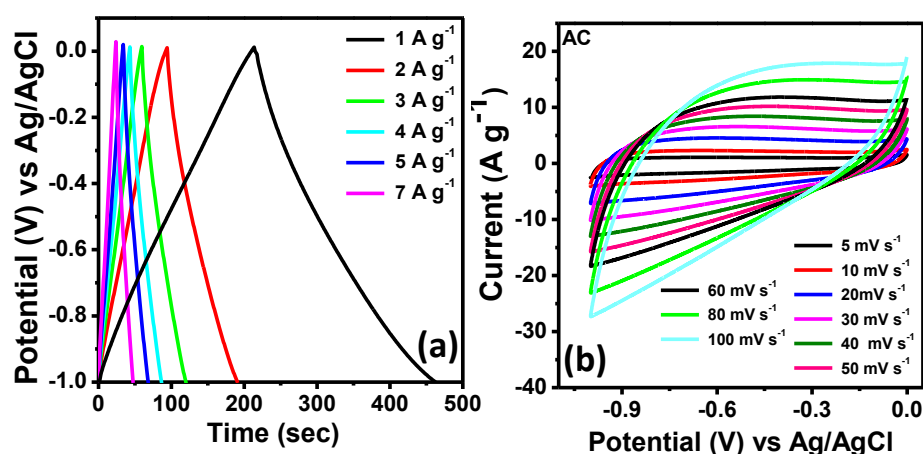
$$i(V) = k_1v + k_2v^{1/2} \quad (7.6)$$

Where  $k_1$  and  $k_2$  are constant and  $v$  is the sweep rate.  $k_2v^{1/2}$  and  $k_1v$  presents the diffusion controlled current and capacitive current.  $k_1$  and  $k_2$  can be calculated by using the CV curve. The slope ( $k_1$ ) can be achieved by plotting  $i$  vs  $v^{1/2}$ . The fraction of capacitance contribution at slow sweep rate was determined by using the above equation. The capacitive contribution for CoAl<sub>2</sub>O<sub>4</sub>/C at 5 mV s<sup>-1</sup> was calculated to be 48.9 and contribution at 10 mV s<sup>-1</sup> and 15 mV s<sup>-1</sup> sweep rate was calculated to be 57 and 64 respectively indicating the a typical battery type faradaic behaviour of the material as presented in Figure 7.5 (a, b)<sup>61</sup>. To elucidate the origin of high electrochemical activity, Electrochemical Impedance spectra (EIS) were performed. Figure 7.5(c) presents the Nyquist spectra for Co<sub>2</sub>Al<sub>1</sub>O<sub>x</sub>/C, Co<sub>1</sub>Al<sub>1</sub>O<sub>x</sub>/C, CoAl<sub>2</sub>O<sub>4</sub>/C, and Co<sub>1</sub>Al<sub>3</sub>O<sub>x</sub>/C composites in 2M KOH electrolyte at frequency ranging from 0.1-100 kHz under open circuit voltage in a three electrode configuration with an AC amplitude of 10 mV. The larger slope of the vertical line at the lower frequency region for CoAl<sub>2</sub>O<sub>4</sub>/C compared to other ratios shows higher specific capacitance value of CoAl<sub>2</sub>O<sub>4</sub>/C. The charge transfer resistance ( $R_{CT}$ ) of CoAl<sub>2</sub>O<sub>4</sub>/C was found to be 2.16  $\Omega$  indicating improved electronic conductivities<sup>62</sup>. The Equivalent series resistance ( $R_s$ ) for all samples were lower than 2  $\Omega$  which were obtained from equivalent circuit fitting of the Nyquist plot illustrating the improved total conductivity of the composite. The impedance spectra of only CoAl<sub>2</sub>O<sub>4</sub> (without support) were also measured. Figure S7.9 shows the EIS spectra of only

$\text{CoAl}_2\text{O}_4$  spinel (without support). The  $R_{CT}$  value of  $\text{CoAl}_2\text{O}_4/\text{C}$ ,  $\text{Co}_2\text{Al}_1\text{O}_x/\text{C}$ ,  $\text{Co}_1\text{Al}_1\text{O}_x/\text{C}$ ,  $\text{Co}_1\text{Al}_3\text{O}_x/\text{C}$  and only  $\text{CoAl}_2\text{O}_4$  were obtained to be  $2.16\ \Omega$ ,  $2.32\ \Omega$ ,  $2.7\ \Omega$ ,  $3.1\ \Omega$ , and  $17\ \Omega$  respectively. The lower  $R_{CT}$  value of  $\text{CoAl}_2\text{O}_4/\text{C}$  compared to other composites and only  $\text{CoAl}_2\text{O}_4$  indicates strong synergistic interaction between carbon support and the  $\text{CoAl}_2\text{O}_4$  spinel<sup>63</sup>.



**Figure 7.5.** (a) CV profile of  $\text{CoAl}_2\text{O}_4/\text{C}$  differentiating diffusive contribution and capacitive at  $5\text{ mV s}^{-1}$  scan rate. (b) Pseudocapacitance contribution of  $\text{CoAl}_2\text{O}_4/\text{C}$  by varying sweep rates. (c) EIS plot profile of  $\text{Co}_m\text{Al}_n\text{O}_x/\text{C}$  in 2M KOH.

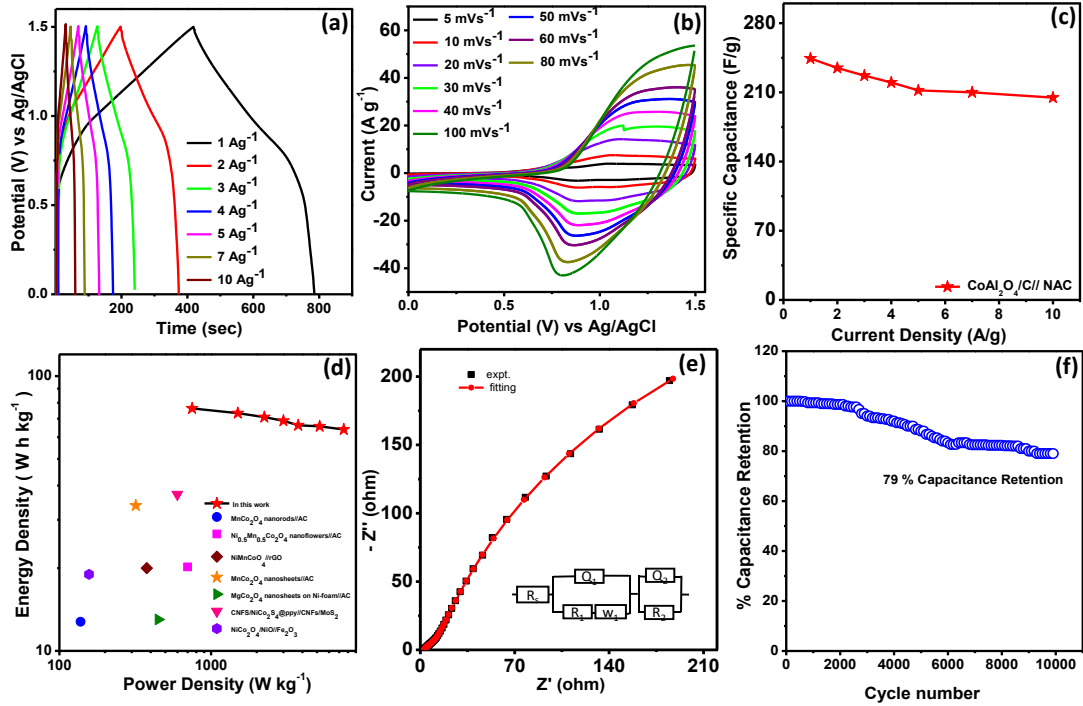


**Figure 7.6.** (a, b) GCD plot of AC from  $1\text{--}7\text{ A g}^{-1}$  current and CV cycles of AC under different sweep rates ( $5\text{--}100\text{ mV sec}^{-1}$ ).

Figure 7.6(a) displays the CD profile at a current density varying from 1 A g<sup>-1</sup> to 7 A g<sup>-1</sup> and Figure 7.6(b) displays CV profile of AC at a different sweep rate in 2M KOH at a voltage range between 0 to -1 V. Using a three electrode setup, the electrochemical performance of AC is performed by using platinum wire, Ag/AgCl, and AC as counter, reference, and working electrode respectively. The symmetrical rectangular nature of the CV curve having no oxidation reduction peaks and the symmetry CD curve indicates the EDLC type nature of the AC. C<sub>s</sub> value for AC were obtained to be 227.72 F g<sup>-1</sup> and 212.53 F g<sup>-1</sup> at a scan rate of 5 mV s<sup>-1</sup> and 10 mV s<sup>-1</sup> respectively and 250 F g<sup>-1</sup> (-1.0 to 0.0 V) under current of 1 A g<sup>-1</sup> with high rate durability as mentioned in our previous reports. This proves that AC can be used as suitable anode material for energy storage applications.

To investigate the ultimate application of CoAl<sub>2</sub>O<sub>4</sub>/C composite, an asymmetric supercapacitor device (CoAl<sub>2</sub>O<sub>4</sub>/C//AC) was designed using CoAl<sub>2</sub>O<sub>4</sub>/C (pseudocapacitive) and AC (EDLC nature) as cathode and anode electrodes respectively. All electrochemical tests of the ASC device were performed in 2M KOH using a two-electrode setup. CV curve for AC and CoAl<sub>2</sub>O<sub>4</sub>/C with voltage window ranging from -1.0 to 0.0 V and 0 to 0.5 V respectively are presented in Figure S7.10. The GCD curve for the CoAl<sub>2</sub>O<sub>4</sub>/C //AC device was performed to confirm the energy storage behaviour in a voltage range of 0 to 1.5 V which is presented in Figure 7.7(a). The symmetrical and non-linear behaviour of the galvanostatic charge discharge curve suggests the faradic reaction taking place during the CD process. The C<sub>s</sub> for CoAl<sub>2</sub>O<sub>4</sub>/C // AC device was measured to be 244.3, 234.67, 227, 220, 212, 210 and 204.67 F g<sup>-1</sup> under applied current of 1, 2, 3, 4, 5, 7, and 10 A g<sup>-1</sup> which shows that nearly 83.6 % of initial capacitance retention when current raised from 1 to 10 A g<sup>-1</sup> indicating excellent rate durability of

$\text{CoAl}_2\text{O}_4/\text{C} // \text{AC}$  device. Figure 7.7(b) represents the CV curve in a cell potential ranging from 0 to 1.5 V at different sweep rates ( $5\text{--}100\text{ mV s}^{-1}$ ). With an increase in sweep rate, the behavior of the CV profile remains unaffected which signifies the capacitive nature generated by the assembly of the battery-type and EDLCs electrodes.



**Figure 7.7.** Electrochemical behavior of asymmetric supercapacitor  $\text{CoAl}_2\text{O}_4/\text{C} // \text{AC}$  device (a) CD profile of  $\text{CoAl}_2\text{O}_4/\text{C} // \text{AC}$  at diff. current 1 to  $10\text{ A g}^{-1}$ . (b) CV profile of device at diff. Scan rate ( $5\text{ to }100\text{ mV s}^{-1}$ ). (c)  $C_s$  at diff. current densities. (d) Ragone plot of  $\text{CoAl}_2\text{O}_4/\text{C} // \text{AC}$  ASC and its comparison with literature. (e) EIS spectra of the ASC (f) cyclic durability of the ASC under  $10\text{ A g}^{-1}$  current.

All CV profiles display a pair of redox peaks at all sweep rates ranging from 5-100 mV s<sup>-1</sup> indicating the capacitive performance of the ASC. Figure 7.7(c) ascribes the C<sub>s</sub> vs. current density plot indicating the increase in C<sub>s</sub> with decrease in current densities. The C<sub>s</sub> for the ASC device was calculated to be 244.3, 234.67, 227, 220, 212, 210, and 204.67 F g<sup>-1</sup> at a current of 1, 2, 3, 4, 5, 7, and 10 A g<sup>-1</sup>. Figure 7.7(d) describes Ragone plot of CoAl<sub>2</sub>O<sub>4</sub>/C //AC ASC device along with the comparison of some ASC reported recent literatures<sup>64-69</sup>. Using equations 7.4 and 7.5, the corresponding energy density and power density values were obtained. The ASC device had an energy density of 76.34 W h kg<sup>-1</sup> at a power density of 750.05 W kg<sup>-1</sup> while the energy density value of 63.96 W h kg<sup>-1</sup> was obtained at power density of 7500.2 W kg<sup>-1</sup> which is significantly higher than Al doped and Co-based spinel ASC devices reported in the literature such as MnCo<sub>2</sub>O<sub>4</sub> nanorods//AC (12.77 W h kg<sup>-1</sup>, 138 W kg<sup>-1</sup>)<sup>64</sup>, Ni<sub>0.5</sub>Mn<sub>0.5</sub>Co<sub>2</sub>O<sub>4</sub> nanoflowers //AC (20.2 W h kg<sup>-1</sup>, 700 W kg<sup>-1</sup>)<sup>65</sup>, NiMnCoO<sub>4</sub> // rGO (20 W h kg<sup>-1</sup>, 377 W kg<sup>-1</sup>)<sup>66</sup>, MnCo<sub>2</sub>O<sub>4</sub> nanosheets //AC (33.8 W h kg<sup>-1</sup>, 318.9 W kg<sup>-1</sup>)<sup>67</sup>, MgCo<sub>2</sub>O<sub>4</sub> nanosheets on Ni-foam // AC (12.99 W h kg<sup>-1</sup>, 448.7 W kg<sup>-1</sup>)<sup>68</sup>, CNFs/NiCo<sub>2</sub>S<sub>4</sub>@ppy // CNFs/MoS<sub>2</sub> (37.15 W h kg<sup>-1</sup>, 598.8 W kg<sup>-1</sup>)<sup>69</sup>, NiCo<sub>2</sub>O<sub>4</sub>/NiO // Fe<sub>2</sub>O<sub>3</sub> (19 W h kg<sup>-1</sup>, 157 W kg<sup>-1</sup>)<sup>70</sup>. To calculate the charge transfer during the charging-discharging process, EIS spectra of the CoAl<sub>2</sub>O<sub>4</sub>/C // AC ASC device were performed which is represented in Figure 7.7(e). EIS test was conducted between 0.1 Hz-100 kHz frequency range under an open circuit potential with an applied AC amplitude of 5mV. From equivalent circuit fit, the R<sub>s</sub> and R<sub>CT</sub> were obtained to be 2.87 Ω and 3.02 Ω respectively. Lower R<sub>s</sub> and R<sub>CT</sub> indicate the lower resistance as well as better conductivity of the ASC. The real application of the electrode active material was determined from the cyclic stability. Repeated GCD cycles were performed for the ASC device at 10 A g<sup>-1</sup> current and the CoAl<sub>2</sub>O<sub>4</sub>/C // AC ASC device

exhibits cyclic durability of 79 % retention of its initial value which is ascribed in Figure 7.7(f).

The high specific capacitance value for CoAl<sub>2</sub>O<sub>4</sub>/C can be due to the following reasons.

- (i) The hierarchical 2D nanosheets are self-assembled and interconnected to form 3D morphology of CoAl<sub>2</sub>O<sub>4</sub>/C composites. The high surface area is generally crucial for adsorption and various catalytic reactions in supercapacitors<sup>2</sup>. With increasing SSA (specific surface area) the electrostatic charge accumulation between electrolyte-electrode interfaces increases. The 3D morphology provides numerous interspaces for rapid electrolyte ion accessibility and shortening the diffusion path and facilitates more redox reactions<sup>2, 52</sup>. The SSA for CoAl<sub>2</sub>O<sub>4</sub>/C composite was much high than that of CoAl-LDH/C and other composites as the LDHs upon calcination undergo phase transformation to metal oxide through sequential dehydration, dehydroxylation, and gasification of interlayer anions resulting in relatively high specific surface Area<sup>71</sup>. The high surface area could be one of the reasons for high supercapacitor behaviour.
- (ii) The synergistic interaction between carbon support and the CoAl<sub>2</sub>O<sub>4</sub> spinel provides more active sites in the CoAl<sub>2</sub>O<sub>4</sub>/C composite compared to only CoAl<sub>2</sub>O<sub>4</sub>. The low R<sub>CT</sub> value for CoAl<sub>2</sub>O<sub>4</sub>/C (2.16 Ω) compared to only CoAl<sub>2</sub>O<sub>4</sub> (17 Ω) suggests the lower electronic and diffusion resistance of CoAl<sub>2</sub>O<sub>4</sub>/C resulting in better charge transfer at electrode/electrolyte interface and good electronic conductivity which increases the electrochemical activity of the CoAl<sub>2</sub>O<sub>4</sub>/C<sup>2</sup>.

## 7.5. CONCLUSIONS

In this chapter three dimensional assembly of CoAl<sub>2</sub>O<sub>4</sub>/C spinel nanosheets derived from CoAl-LDH/C have been successfully synthesized via a two-step method (hydrothermal followed by calcination). The CoAl<sub>2</sub>O<sub>4</sub>/C showed a high SSA of 102.7 m<sup>2</sup>g<sup>-1</sup> as compared

to other composites, prepared by varying Co/Al molar ratios. Among all composites, CoAl<sub>2</sub>O<sub>4</sub>/C displayed maximum specific capacitance of 1394 F g<sup>-1</sup> under an applied current of 1 A g<sup>-1</sup>. The high electrochemical performances of this composite can be attributed to its high SSA and synergistic interaction between carbon support and the CoAl<sub>2</sub>O<sub>4</sub> spinel. The presence of aluminum makes the composite more cost effective with a reduction of the atomic percentage of Co to nearly 33% of the sample. The CoAl<sub>2</sub>O<sub>4</sub>/C electrode showed cyclic stability of 87% after 5k cycles for a single electrode and for CoAl<sub>2</sub>O<sub>4</sub>/C // AC ASC the composite showed a specific capacitance of 244.3 F g<sup>-1</sup> at 1 A g<sup>-1</sup> current density. It showed an energy density value of 76.34 W h kg<sup>-1</sup> at a power density value of 750.05 W kg<sup>-1</sup> and impressive cyclic performance (approx. capacitance retention of 79 %) at 10 A g<sup>-1</sup>. This work may be useful for the advancement and designing of highly efficient electrode material for electrochemical energy storage applications.

## 7.6. REFERENCES

- (1) Hu, B.; DeBruler, C.; Rhodes, Z.; Liu, T. L. *Journal of the American Chemical Society* **2017**, *139*, 1207-1214.
- (2) Bhujun, B.; Tan, M.; Shanmugam, S. *Ceramics International* **2016**, *42*.
- (3) Zhao, X.; Mao, L.; Cheng, Q.; Li, J.; Liao, F.; Yang, G.; Xie, L.; Zhao, C.; Chen, L. *Chemical Engineering Journal* **2020**, *387*, 124081.
- (4) Zhuo, H.; Hu, Y.; Chen, Z.; Zhong, L. *Carbohydrate Polymers* **2019**, *215*, 322-329.
- (5) Song, D.; Zhu, J.; Xuan, L.; Zhao, C.; Xie, L.; Chen, L. *Journal of Colloid and Interface Science* **2017**, *509*.
- (6) Vadivel, S.; Naveen, N.; Jayaraman, T.; Jagannathan, M.; T, S.; Subramanian, B. *Ceramics International* **2016**, *42*.
- (7) Wang, J.; Zhou, C.; Yan, X.; Wang, Q.; Sha, D.; Pan, J.; Cheng, X. *Journal of Materials Science: Materials in Electronics* **2019**, *30*, 6633-6642.
- (8) Chatterjee, M.; Sain, S.; Roy, A.; Das, S.; Pradhan, S. K. *Journal of Physics and Chemistry of Solids* **2021**, *148*, 109733.
- (9) Worku, A. K.; Ayele, D. W.; Habtu, N. G.; Yemata, T. A. *Heliyon* **2021**, *7*, e08076.
- (10) Lienau, K.; Triana, C. A.; Reith, L.; Siol, S.; Patzke, G. R. *Frontiers in Chemistry* **2020**, *8*.
- (11) Chen, M.; Ge, Q.; Qi, M.; Liang, X.; Wang, F.; Chen, Q. *Surface and Coatings Technology* **2019**, *360*, 73-77.
- (12) Wang, P.-p.; Sun, H.; Ji, Y.; Li, W.; Wang, X. *Advanced Materials* **2014**, *26*, 964-969.

- (13) Song, D.; Zhu, J.; Xuan, L.; Zhao, C.; Xie, L.; Chen, L. *J Colloid Interface Sci* **2018**, *509*, 163-170.
- (14) Kumar, R.; Singh, R. K.; Vaz, A. R.; Savu, R.; Moshkalev, S. A. *ACS Applied Materials & Interfaces* **2017**, *9*, 8880-8890.
- (15) Jing, Q.; Li, W.; Wang, J.; Chen, X.; Pang, H. *Inorganic Chemistry Frontiers* **2021**, *8*, 4222-4229.
- (16) Abbasi, L.; Arvand, M. *Applied Surface Science* **2018**, *445*, 272-280.
- (17) Xiao, X.; Wang, G.; Zhang, M.; Wang, Z.; Zhao, R.; Wang, Y. *Ionics* **2018**, *24*, 2435-2443.
- (18) Lv, X.-W.; Liu, Y.; Tian, W.; Gao, L.; Yuan, Z.-Y. *Journal of Energy Chemistry* **2020**, *50*, 324-331.
- (19) Chen, J.; Peng, X.; Song, L.; Zhang, L.; Liu, X.; Luo, J. *Royal Society Open Science* **5**, 180842.
- (20) Wang, H.-Y.; Hung, S.-F.; Chen, H.-Y.; Chan, T.-S.; Chen, H. M.; Liu, B. *Journal of the American Chemical Society* **2016**, *138*, 36-39.
- (21) Kanazawa, T.; Kato, K.; Yamaguchi, R.; Uchiyama, T.; Lu, D.; Nozawa, S.; Yamakata, A.; Uchimoto, Y.; Maeda, K. *ACS Catalysis* **2020**, *10*, 4960-4966.
- (22) Yan, S.-R.; Gholami, T.; Amiri, O.; Salavati-Niasari, M.; Seifi, S.; Amiri, M.; Sabet, M.; Foong, L. K. *Journal of Alloys and Compounds* **2020**, *828*, 154353.
- (23) Bhowmik, T.; Mishra, R.; Barman, S. *Energy & Fuels* **2021**, *35*.
- (24) Panda, P.; Mishra, R.; Barman, S.; Panigrahy, S. *Materials Advances* **2021**.
- (25) Mishra, R.; Prasad, P. R.; Panda, P.; Barman, S. *Energy & Fuels* **2021**, *35*.
- (26) Umapathy, V.; Manikandan, A.; Ramu, P.; Arul Antony, S.; Neeraja, P. *Journal of Nanoscience and Nanotechnology* **2016**, *16*, 987-993.
- (27) Valan, M. F.; Manikandan, A.; Antony, S. A. *Journal of Nanoscience and Nanotechnology* **2015**, *15*, 4580-4586.
- (28) Wang, J.; Li, L.; Chen, X.; Lu, Y.; Yang, W.; Duan, X. *Nano Research* **2017**, *10*, 2508-2518.
- (29) Mishra, R.; Panda, P.; Barman, S. *New Journal of Chemistry* **2021**, *45*.
- (30) Jin, F.; He, X.; Jiang, J.; Zhu, W.; Dai, J.; Yang, H. *Nanomaterials* **2020**, *10*.
- (31) Ganguly, A.; Sharma, S.; Papakonstantinou, P.; Hamilton, J. *The Journal of Physical Chemistry C* **2011**, *115*, 17009-17019.
- (32) Cheng, M.; Fan, H.; Song, Y.; Cui, Y.; Wang, R. *Dalton Transactions* **2017**, *46*, 9201-9209.
- (33) Xu, J.; Gao, L.; Cao, J.; Wang, W.; Chen, Z. *Electrochimica Acta* **2010**, *56*, 732-736.
- (34) Ramesh, S.; Karuppasamy, K.; Kim, H.-S.; Kim, H. S.; Kim, J.-H. *Scientific Reports* **2018**, *8*, 16543.
- (35) Chen, X.; Xie, R.; Li, H.; Jaber, F.; Musharavati, F.; Zalnezhad, E.; Bae, S.; Hui, K. S.; Hui, K. N. *Scientific Reports* **2020**, *10*, 18956.
- (36) Meher, S. K.; Rao, G. R. *The Journal of Physical Chemistry C* **2011**, *115*, 15646-15654.
- (37) Chen, S.; Yang, G.; Jia, Y.; Zheng, H. *Journal of Materials Chemistry A* **2017**, *5*, 1028-1034.
- (38) Bhujun, B.; Tan, M. T. T.; Shanmugam, A. S. *Ceramics International* **2016**, *42*, 6457-6466.
- (39) Cheng, G.; Kou, T.; Zhang, J.; Si, C.; Gao, H.; Zhang, Z. *Nano Energy* **2017**, *38*, 155-166.
- (40) Dong, R.; Ye, Q.; Kuang, L.; Lu, X.; Zhang, Y.; Zhang, X.; Tan, G.; Wen, Y.; Wang, F. *ACS Applied Materials & Interfaces* **2013**, *5*, 9508-9516.
- (41) Xu, H.; Cao, Y.; Li, Y.; Cao, P.; Liu, D.; Zhang, Y.; Li, Q. *Journal of Energy Chemistry* **2020**, *50*, 240-247.
- (42) Sharifi, S.; Rahimi, K.; Yazdani, A. *Scientific Reports* **2021**, *11*, 8378.
- (43) Nawaz, B.; Ali, G.; Ullah, M. O.; Rehman, S.; Abbas, F. *Energies* **2021**, *14*.
- (44) Patil, P. D.; Shingte, S. R.; Karade, V. C.; Kim, J. H.; Dongale, T. D.; Mujawar, S. H.; Patil, A. M.; Patil, P. B. *Journal of Energy Storage* **2021**, *40*, 102821.
- (45) Mondal, A. K.; Liu, H.; Li, Z.-F.; Wang, G. *Electrochimica Acta* **2016**, *190*, 346-353.
- (46) Nikam, S. M.; Sharma, A.; Rahaman, M.; Teli, A. M.; Mujawar, S. H.; Zahn, D. R. T.; Patil, P. S.; Sahoo, S. C.; Salvan, G.; Patil, P. B. *RSC Advances* **2020**, *10*, 19353-19359.



- (47) Hareesh, K.; Rondiya, S. R.; Dzade, N. Y.; Dhole, S. D.; Williams, J.; Sergey, S. *Journal of Science: Advanced Materials and Devices* **2021**, *6*, 291-301.
- (48) Li, S.; Wu, D.; Cheng, C.; Wang, J.; Zhang, F.; Su, Y.; Feng, X. *Angewandte Chemie International Edition* **2013**, *52*, 12105-12109.
- (49) Kuang, M.; Liu, X. Y.; Dong, F.; Zhang, Y. X. *Journal of Materials Chemistry A* **2015**, *3*, 21528-21536.
- (50) Li, L.; He, F.; Gai, S.; Zhang, S.; Gao, P.; Zhang, M.; Chen, Y.; Yang, P. *CrystEngComm* **2014**, *16*, 9873-9881.
- (51) Harilal, M.; Krishnan, S. G.; Yar, A.; Misnon, I. I.; Reddy, M. V.; Yusoff, M. M.; Ojur Dennis, J.; Jose, R. *The Journal of Physical Chemistry C* **2017**, *121*, 21171-21183.
- (52) Huang, J.; Wei, J.; Xiao, Y.; Xu, Y.; Xiao, Y.; Wang, Y.; Tan, L.; Yuan, K.; Chen, Y. *ACS Nano* **2018**, *12*, 3030-3041.
- (53) Kaverlavani, S. K.; Moosavifard, S. E.; Bakouei, A. *Journal of Materials Chemistry A* **2017**, *5*, 14301-14309.
- (54) Zhu, J.; Song, D.; Pu, T.; Li, J.; Huang, B.; Wang, W.; Zhao, C.; Xie, L.; Chen, L. *Chemical Engineering Journal* **2018**, *336*, 679-689.
- (55) Zhang, A.; Wang, C.; Xu, Q.; Liu, H.; Wang, Y.; Xia, Y. *RSC Advances* **2015**, *5*, 26017-26026.
- (56) Shakir, I.; Shahid, M.; Rana, U. A.; Nashef, I. M. A.; Hussain, R. *Electrochimica Acta* **2014**, *129*, 28-32.
- (57) Liu, S.; Ni, D.; Li, H.-F.; Hui, K. N.; Ouyang, C.-Y.; Jun, S. C. *Journal of Materials Chemistry A* **2018**, *6*, 10674-10685.
- (58) Yuan, C.; Li, J.; Hou, L.; Zhang, X.; Shen, L.; Lou, X. W. *Advanced Functional Materials* **2012**, *22*, 4592-4597.
- (59) Yan, W.; Kim, J. Y.; Xing, W.; Donovan, K. C.; Ayvazian, T.; Penner, R. M. *Chemistry of Materials* **2012**, *24*, 2382-2390.
- (60) Cheng, Y.; Wei, Z.; Du, Q.; Liu, F.; Duan, X.; Wang, Y.; Jia, D.; Zhou, Y.; Li, B. *Electrochimica Acta* **2018**, *284*, 408-417.
- (61) Clerici, F.; Fontana, M.; Bianco, S.; Serrapede, M.; Perrucci, F.; Ferrero, S.; Tresso, E.; Lamberti, A. *ACS Applied Materials & Interfaces* **2016**, *8*, 10459-10465.
- (62) Shang, C.; Dong, S.; Wang, S.; Xiao, D.; Han, P.; Wang, X.; Gu, L.; Cui, G. *ACS Nano* **2013**, *7*, 5430-5436.
- (63) Zhu, H.-L.; Zheng, Y.-Q. *Electrochimica Acta* **2018**, *265*, 372-378.
- (64) Haripriya, M.; Ashok, A. M.; Hussain, S.; Sivasubramanian, R. *Ionics* **2021**, *27*, 325-337.
- (65) Mu, H.; Su, X.; Zhao, Z.; Han, C.; Wang, Z.; Zhao, P. *Journal of the American Ceramic Society* **2019**, *102*, 6893-6903.
- (66) Pendashteh, A.; Palma, J.; Anderson, M.; Marcilla, R. *RSC Advances* **2016**, *6*, 28970-28980.
- (67) Saravanakumar, B.; Wang, X.; Zhang, W.; Xing, L.; Li, W. *Chemical Engineering Journal* **2019**, *373*, 547-555.
- (68) Vijayakumar, S.; Nagamuthu, S.; Ryu, K.-S. *Dalton Transactions* **2018**, *47*, 6722-6728.
- (69) Huang, J.; Wei, J.; Xu, Y.; Xiao, Y.; Chen, Y. *Journal of Materials Chemistry A* **2017**, *5*, 23349-23360.
- (70) Gao, H.; Xiao, F.; Ching, C. B.; Duan, H. *ACS Applied Materials & Interfaces* **2012**, *4*, 2801-2810.
- (71) Lee, S.-B.; Ko, E.-H.; Park, J. Y.; Oh, J.-M. *Nanomaterials* **2021**, *11*.

## Appendix E

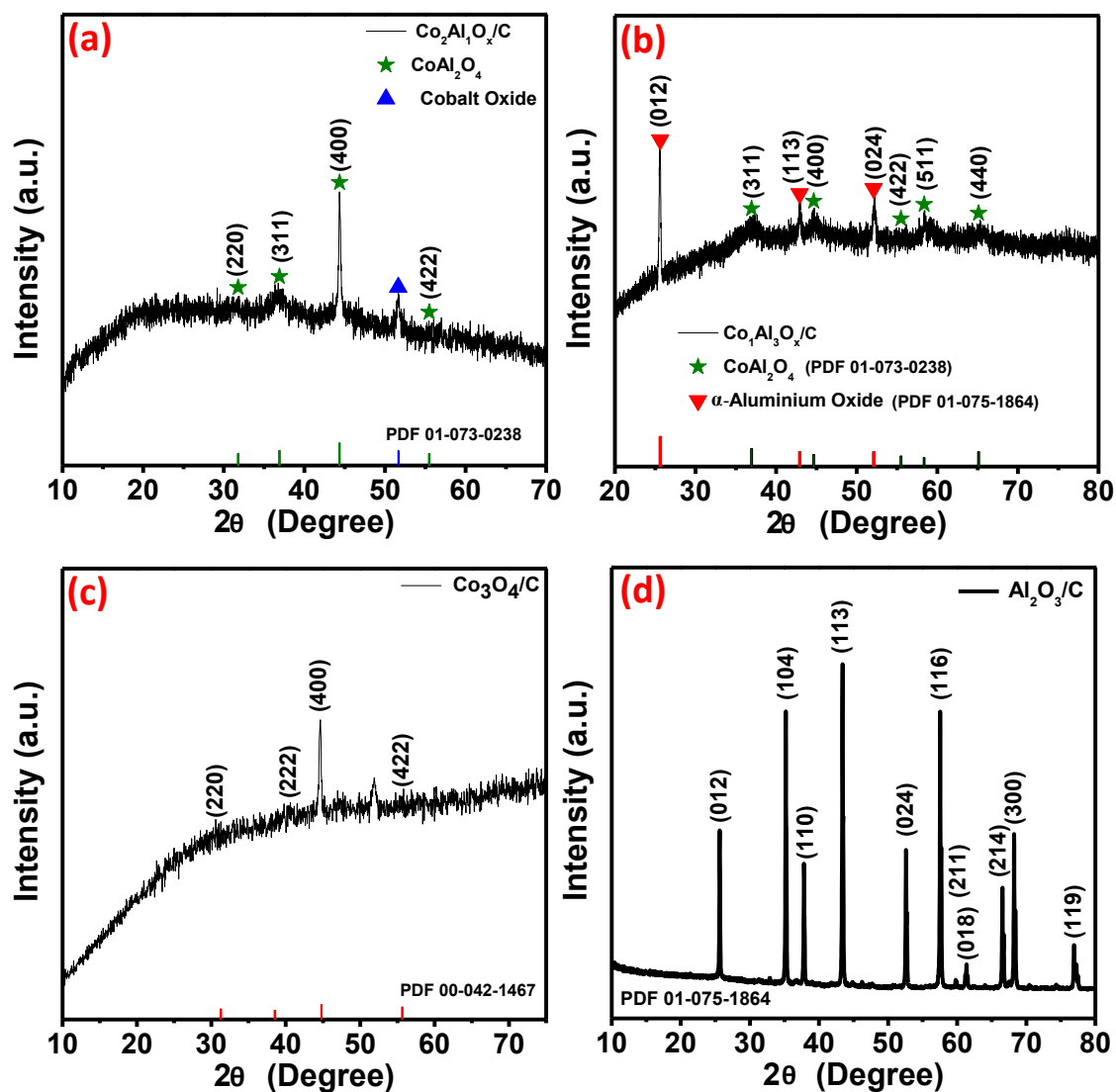
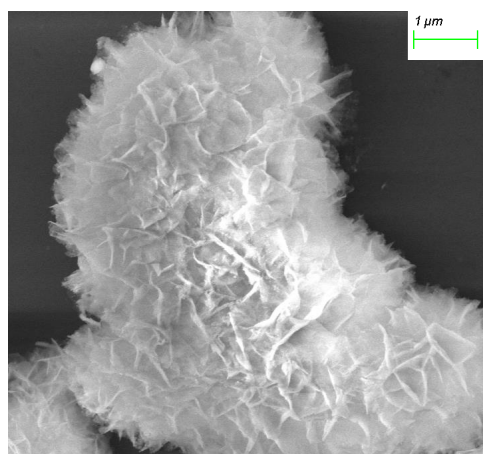
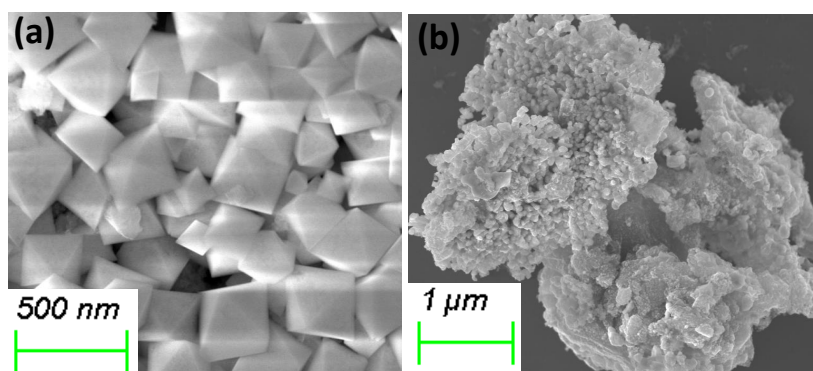


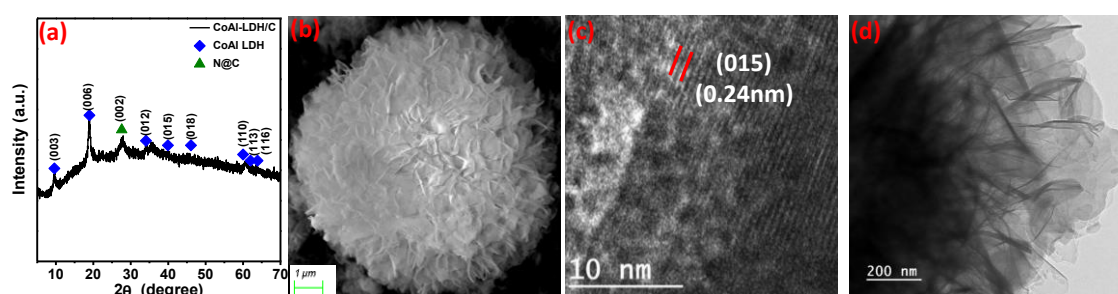
Figure S7.1. p-XRD pattern of (a)  $\text{Co}_2\text{Al}_1\text{O}_x/\text{C}$ , (b)  $\text{Co}_1\text{Al}_3\text{O}_x/\text{C}$ , (c)  $\text{Co}_3\text{O}_4/\text{C}$ , and (d)  $\text{Al}_2\text{O}_3/\text{C}$  composites.



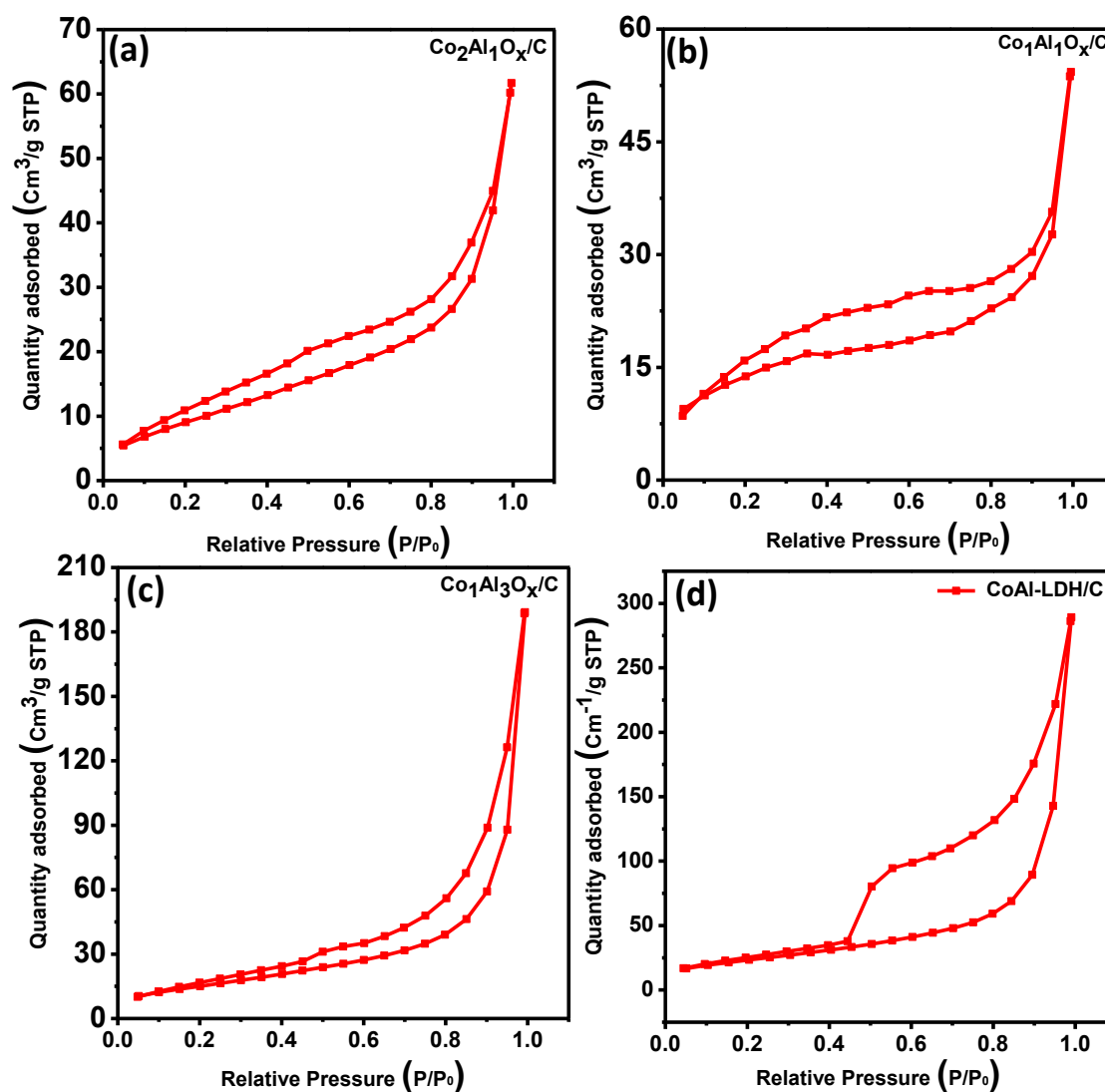
**Figure S7.2.** SEM image of  $\text{CoAl}_2\text{O}_4/\text{C}$  composite.



**Figure S7.3.** SEM image of (a)  $\text{Al}_2\text{O}_3/\text{C}$  and (b)  $\text{Co}_3\text{O}_4/\text{C}$ .



**Figure S7.4.** (a) p-XRD pattern, (b) SEM image, and (c, d) High and low resolution TEM image of  $\text{CoAl-LDH/C}$  respectively.



**Figure S7.5.** N<sub>2</sub> adsorption-desorption isotherm of (a)  $\text{Co}_2\text{Al}_1\text{O}_x/\text{C}$  (b)  $\text{Co}_1\text{Al}_1\text{O}_x/\text{C}$  (c)  $\text{Co}_1\text{Al}_3\text{O}_x/\text{C}$  and (d)  $\text{CoAl-LDH}/\text{C}$  composites.

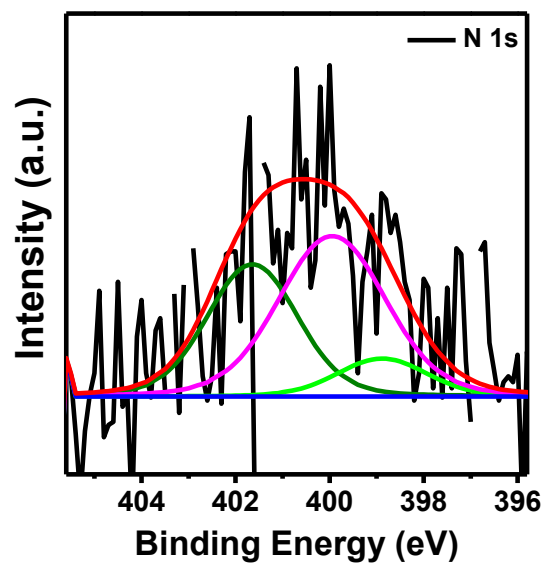


Figure S7.6. High resolution XPS spectra of N 1s.

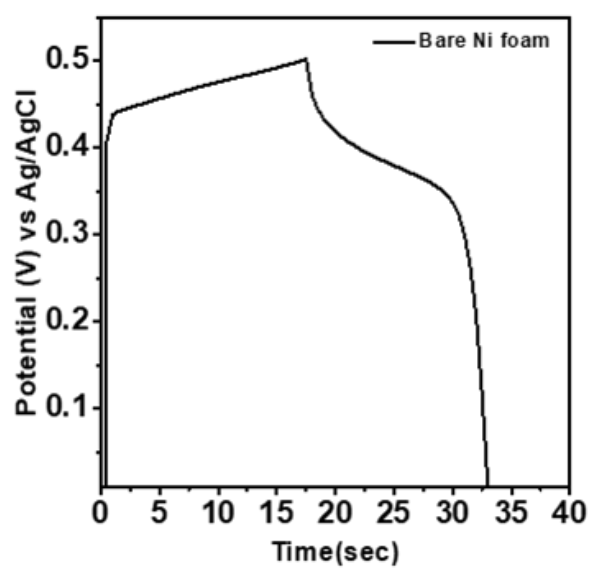
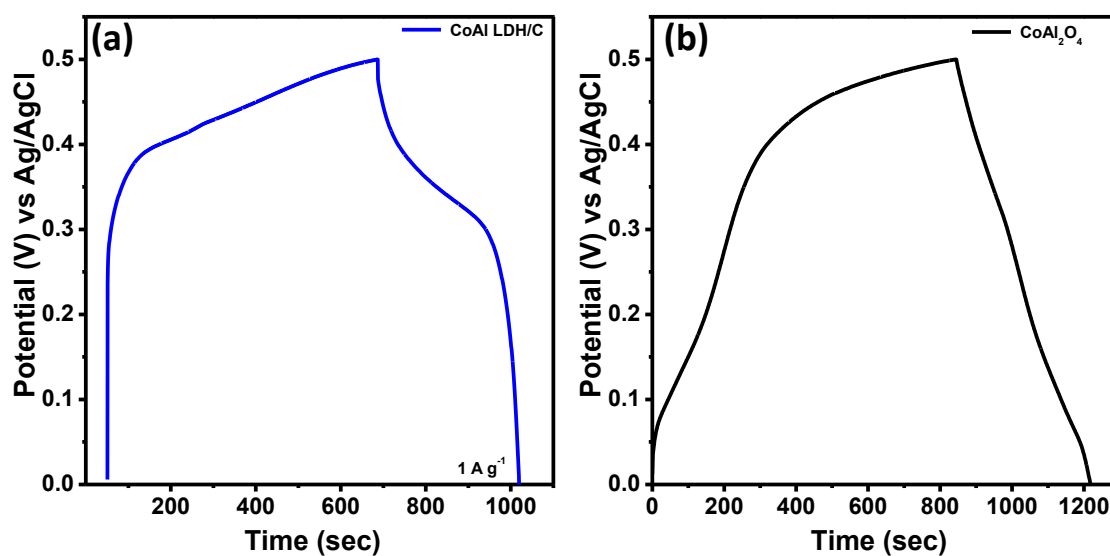
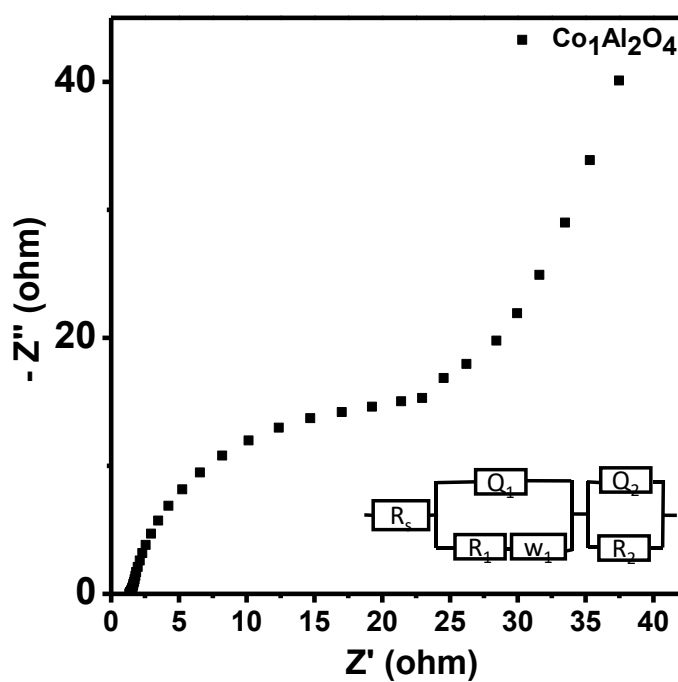


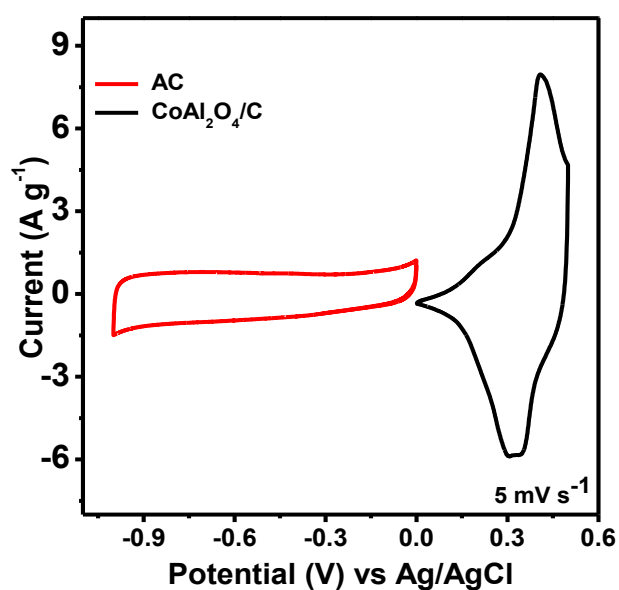
Figure S7.7. GCD curves of bare Ni foam at 1 mA current.



**Figure S7.8.** GCD curves of (a) CoAl-LDH/C, and (b) only  $\text{CoAl}_2\text{O}_4$   $1 \text{ A g}^{-1}$  current density.



**Figure S7.9.** EIS spectra of only  $\text{CoAl}_2\text{O}_4$ .



**Figure S7.10.** CV curves of AC and  $\text{CoAl}_2\text{O}_4/\text{C}$  spinel at a sweep rate of  $5 \text{ mV s}^{-1}$ .

**Table S7.1.** Composition analysis of the  $\text{CoAl}_2\text{O}_4/\text{C}$  and  $\text{Co}_m\text{Al}_n\text{O}_x/\text{C}$  from ICP-OES.

Sample Name	Theoretical stoichiometry of Co and Al (molar ratio)		Actual stoichiometry of Co and Al (ICP-OES)		Ratio from ICP-OES analysis
	Co	Al	Co	Al	Co:Al
$\text{Co}_1\text{Al}_1\text{O}_x/\text{C}$	1	1	1.5	1.14	1.31
$\text{CoAl}_2\text{O}_4/\text{C}$	1	2	1.14	2.2	0.51
$\text{Co}_1\text{Al}_3\text{O}_x/\text{C}$	1	3	1	3.37	0.3
$\text{Co}_2\text{Al}_1\text{O}_x/\text{C}$	2	1	3.23	1.1	2.93

**Table S7.2.** Comparison of electrochemical performance of  $\text{Co}_m\text{Al}_n\text{O}_x/\text{C}$  composite by varying Co/Al ratio.

Sample name	Co percentage	Specific capacitance ( $\text{F g}^{-1}$ )
$\text{Co}_3\text{O}_4/\text{C}$	100	502
$\text{Co}_2\text{Al}_1\text{O}_x/\text{C}$	66.6	801
$\text{Co}_1\text{Al}_1\text{O}_x/\text{C}$	50	646
$\text{Co}_1\text{Al}_2\text{O}_4/\text{C}$	33.33	1394
$\text{Co}_1\text{Al}_3\text{O}_x/\text{C}$	25	1159
$\text{Al}_2\text{O}_3/\text{C}$	0	45.34



## Chapter 8

### One-dimensional RuO<sub>2</sub>-Nitrogen doped Carbon Composite for Energy Storage Application in Alkaline Medium

#### 8.1. ABSTRACT

One-dimensional electrode materials have been the most promising material for supercapacitors because of their unique features such as 1D morphology with large surface area, high mechanical rigidity, excellent cyclic stability, and great electrical conductivity. This chapter demonstrate one-dimensional RuO<sub>2</sub>-N-doped carbon (1D-RuO<sub>2</sub>/C) composite, synthesized by facile thermal method, for super-capacitor application. The 1D-RuO<sub>2</sub>/C composite delivers a specific capacitance ( $C_s$ ) of 671 F/g under a current of 5 A/g with extraordinary capacitance retention of 93.46 % after 5k cycles. The asymmetric supercapacitor (ASC) device, (1D-RuO<sub>2</sub>/C//AC) was constructed by using 1D-RuO<sub>2</sub>/C as positive and activated carbon as negative electrode material. The 1D-RuO<sub>2</sub>/C//AC device shows a  $C_s$  value of 53 F/g under 1A/g current and delivers a power density (PD) of 751.66 W kg<sup>-1</sup> at 16.71 W h kg<sup>-1</sup> energy density (ED). The ASC maintains approximately 98.65 % of its initial value at 10 A/g discharge current. The high electrochemical activity of 1D-RuO<sub>2</sub>/C composite is primarily due to the one-dimensional morphology of RuO<sub>2</sub>, high surface area, synergistic interaction between RuO<sub>2</sub> and carbon support, etc. So this 1D-RuO<sub>2</sub>/C composite will find its application in energy storage systems.

## 8.2. INTRODUCTION

In recent days, more efforts have been dedicated to the rapid development of alternative energy storage and conversion due to the upcoming unavailability of fossil fuels<sup>1</sup>. To resolve the ever-increasing energy issues renewable energy sources are finding great attention as alternatives<sup>2-5</sup>. The researchers had put more attention towards the study of alternative or renewable energy sources such as rechargeable batteries<sup>6-7</sup>, supercapacitors (energy storage), and photo-electrochemical productions (energy conversion). Electrochemical capacitors also known as supercapacitors or ultracapacitors act as the bridge between high-energy batteries and high-power conventional capacitors<sup>8</sup>. Depending on the energy storage mechanism, supercapacitors can be classified into two different categories<sup>9</sup>. Electrical double-layered capacitor (EDLC) storage charge through the accumulation of charge at electrolyte/electrode interface and pseudocapacitor store charge through reversible redox reactions on the surfaces of the active material<sup>10-11</sup>. Compared to the battery, supercapacitors show several advantages such as ultrafast charge/discharge rate, excellent cyclic durability, greater power density, and low environmental impact<sup>12</sup>. These characteristics are desirable for applications like portable electronics to electrical vehicles<sup>12</sup>. However, batteries show higher energy densities compared to supercapacitors. A high energy density can be obtained by increasing either the voltage range or by increasing the specific capacitance. Besides this low energy density, pseudocapacitors face problems like poor cyclic stability<sup>13-14</sup>. To overcome the above-mentioned problems the combination of EDLCs and pseudocapacitors is one of the main challenges to improve the supercapacitor properties<sup>11, 15</sup>.

In recent times, carbon-based materials attracted significant interest as promising electrode materials for supercapacitor applications<sup>16</sup>. But due to its restacking of sheets and aggregation, it restricts its specific capacitance to reach its theoretical value in real applications<sup>17</sup>. Carbon-based composites, as electrode material has attracted the interest of scientist for energy storage applications. Transition metal oxides (TMOs) prevent aggregation and make spaces between the sheets which results in increasing the specific capacitance of the composites<sup>13</sup>. Compared to other platinum group metal oxides ruthenium oxide (RuO<sub>2</sub>) was considered the best electrode material for supercapacitor applications due to its outstanding capacitance value, high specific surface area (SSA), high rate durability as well as high thermal stability, and fast reversible redox processes<sup>18</sup>. However, RuO<sub>2</sub> particles agglomerate and suffer from poor porosity and cyclic durability resulting in a decrease in electrochemical activity owing to its incomplete reaction of RuO<sub>2</sub> during the electrochemical redox process which initiates from the surface of RuO<sub>2</sub> particles and becomes slower as the reaction proceeds<sup>19</sup>. So the development of a hybrid system that consists of a faradic reaction based on the Ru and an EDLC process based on carbon-based composites is needed. RuO<sub>2</sub> along with some carbon-based materials like graphene, reduced graphene oxide, activated carbon nanofibers, carbon nitride, carbon nanotubes, etc. afford an electrode material that prevents the agglomeration and increases the charge transport of RuO<sub>2</sub> during the electrochemical process resulting in an enhanced electrochemical activity of the composites<sup>20</sup>. By tuning the synthesis method and/or morphology and support (like several carbon-based materials such as graphene, mesoporous carbon, activated carbon, and carbon nanotubes) over which the RuO<sub>2</sub> grew up, the property of ruthenium-based materials like RuO<sub>2</sub> and RuO<sub>2</sub> based perovskites can be changed<sup>13, 21-23</sup>. Ismail et al. Synthesized ruthenium oxide nanoparticles on nickel

foam via Aspalathus linearis process confirming the formation of spherical RuO<sub>2</sub> nanoparticles of nearly 5nm size with long-term cyclic stability of 97% capacitance retention after 500 charge-discharge cycles<sup>18</sup>. R. Thangappan et. al reports the synthesis of RuO<sub>2</sub> nanoparticles on graphene nanosheets showing a C<sub>s</sub> value of 441.1 F/g under 0.1 A/g current in 1M Na<sub>2</sub>SO<sub>4</sub> electrolyte<sup>24</sup>. Furthermore, the characteristic properties of TMOs are remarkably improved by 1D and 1D-analogue nanostructure materials. 1D nanostructure materials provide direct current pathways, shorten the ion diffusion distance, provide high electrode-electrolyte contact area, accommodate volume expansion, and limit mechanical degradation. 1D nanostructure includes nanowires<sup>25</sup>, nanorods<sup>26</sup>, nanotubes<sup>27</sup>, and nanobelts<sup>28</sup>. Wei et al. reported the advantages of 1D nanostructure in the field of electrochemical energy storage applications<sup>29</sup>. 1D nanostructures with higher SSA facilitated direct electron transport pathways. Higher SSA offers more electroactive sites and allows efficient contact with the electrolyte, resulting in a higher discharge/ charge capacity at a higher current.

This chapter demonstrate one-dimensional ruthenium oxide nanorods-N-doped carbon nanosheets (1D-RuO<sub>2</sub>/C) composite, synthesized by a thermal method, for supercapacitor application. The composite shows a high C<sub>s</sub> value of 671 F/g at 5A/g current in 2M KOH solution compared to pure RuO<sub>2</sub>. In addition, the as-synthesized composite exhibits high cyclic rate durability of 93.46 % after 5k cycles. The ASC 1D-RuO<sub>2</sub>/C// AC shows an ED of 16.71 W h/Kg at PD of 751.66 W/Kg. The device can archive an operating potential of 1.5 V with an outstanding cyclic stability of 98.65 % even after 5k cycles in alkaline electrolyte. The outstanding electrochemical activity of the 1D-RuO<sub>2</sub>/C composite is mainly due to the high SSA and 1D morphology of RuO<sub>2</sub>,

the low internal resistance/charge transfer resistance resulting from the strong synergistic interaction of RuO<sub>2</sub> and N-doped carbon support, etc.

### **8.3. EXPERIMENTAL SECTION:**

#### **8.3.1. Materials:**

Formamide (HCONH<sub>2</sub>), Ruthenium chloride hydrate (RuCl<sub>3</sub>.xH<sub>2</sub>O), Potassium hydroxide (KOH), Sodium borohydride (NaBH<sub>4</sub>) were purchased from Sigma Aldrich. All the reagents were used without further purification. In all the experiments Milli-Q water (DI H<sub>2</sub>O) was used, obtained from ultra-filtration system.

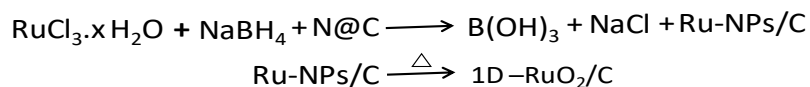
#### **8.3.2. Preparation of Nitrogen-doped Carbon (N@C)**

N@C was prepared from HCONH<sub>2</sub> as reported before by our group<sup>30-31</sup>. In brief 30 ml of HCONH<sub>2</sub> was taken in a 100 ml three-neck round bottom flask and heated in a microwave synthesizer for 3 h at 180 °C maintaining a constant power of 300 W. A brown coloured solution was obtained which was evaporated in a rotary evaporator at 180 °C to obtain a black coloured product. The product obtained was then washed with DI H<sub>2</sub>O multiple times followed by ethanol and oven dried at 70°C overnight to get the N@C.

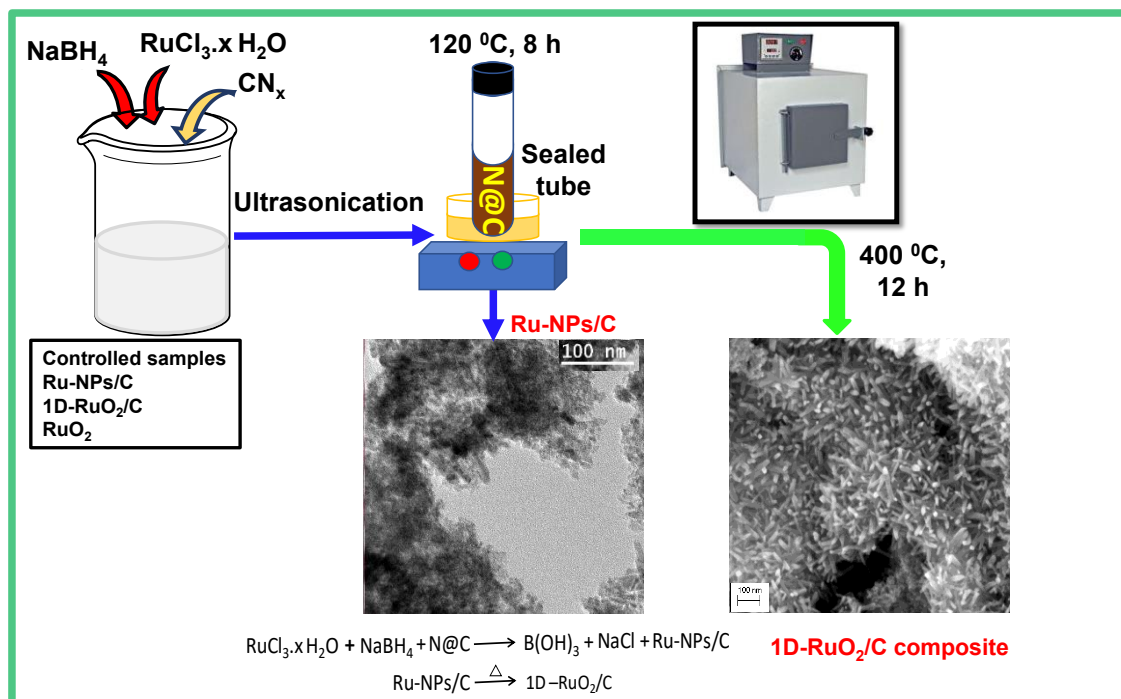
#### **8.3.3. Synthesis of One-Dimensional Ruthenium oxide/C nanorods (1D-RuO<sub>2</sub>/C)**

The 1D-RuO<sub>2</sub>/C composite synthesis was done by a two steps thermal method<sup>31</sup>. In the first step synthesis of Ruthenium nanoparticles supported on N@C (Ru-NPs/C) was carried out by NaBH<sub>4</sub> mediated hydrothermal reduction of RuCl<sub>3</sub>.xH<sub>2</sub>O and in the second step Ru-NPs/C composite was thermally heated at 400 °C for 12 hours to form 1D-RuO<sub>2</sub>/C. In brief, the Ru-NPs/C composite was prepared by the reduction of RuCl<sub>3</sub> in presence of N@C. A 5 mg of as-prepared N@C was dispersed in 2 ml of DI H<sub>2</sub>O. In

another glass vial, RuCl<sub>3</sub>.xH<sub>2</sub>O was dispersed in 4 ml of DI H<sub>2</sub>O to obtain a total molarity of 0.12 mmol. Then the two solutions were mixed and sonicated in a bath sonicator at 60 Hz operating frequency to form a homogeneous suspension. The suspension was then transferred into a 100 ml glass tube and heated at 65 °C. A 2 ml of 1.58 mmol aqueous solution of NaBH<sub>4</sub> was added once the oil bath temperature touched 65 °C followed by constant heating at 120 °C for 8 hours with constant stirring at 450 rpm. It was then naturally cooled to room temperature and centrifuged at 16000 rpm followed by washing in DI H<sub>2</sub>O and ethanol and vacuum drying. The obtained product was named as Ru-NPs/C. 1D-RuO<sub>2</sub>/C was synthesized by thermal heating of Ru-NPs/C at 400 °C for 12 hours. Scheme 8.1 represents the detailed synthesis method and the mechanism for the formation of 1D-RuO<sub>2</sub>/C is as follows<sup>32</sup>:



Only RuO<sub>2</sub> was also prepared by using the similar method mentioned above without N@C and named RuO<sub>2</sub>.



**Scheme 8.1.** Schematic representation for the Synthesis of 1D-RuO<sub>2</sub>/C composite.

### 8.3.4. Characterizations:

The x-ray diffraction data (p-XRD) of as prepared samples were conducted by Buker DAVINCI D8 ADVANCE diffractometer equipped with a monochromatic radiation source of Cu  $\alpha$  ( $\lambda = 0.15406$ ). The composition and morphology of the material was recorded by Field-emission scanning electron microscope (FESEM) system (Carl Zeiss, Germany make, Model:  $\Sigma$ igma) and Transmission Electron Microscopy (TEM, JEOL F200) and High-Resolution TEM (HRTEM). VG Microtech was used to record the XPS data with monochromatic Mg K $\alpha$  X-ray as the source. All electrochemical measurements were performed by using CorrTest Electrochemical Workstation [Model: CS350]. Quantachrome Instruments (AutosorbiQ-XR-XR (2 Stat.)) Viton was used to determine the Specific surface area by N<sub>2</sub> adsorption-desorption isotherm.

### **8.3.5. Fabrication of electrodes:**

A piece of Ni foam of area  $1 \times 1 \text{ cm}^2$  was used for the fabrication of working electrode. Oxide layers were removed by washing Ni foam in 3M HCl for 30 min followed by washing in water and ethanol and dried. AC (activated carbon), conductive carbon (CC) and polyvinylidene fluoride (PVDF) binder in N-methyl-2-pyrrolidone (NMP) in 80:10:10 weight % were used for the preparation of homogenous slurry and the slurry was coated on the  $1 \times 1 \text{ cm}^2$  Ni foam followed by oven drying. The mass of active material loaded on the Ni foam was found to be 1mg. For ASC designing, AC and active material were used as negative and positive electrode respectively and cellulose paper as separator. For positive and negative electrodes the weight loading ratio was calculated to be 0.5 (weight loading for positive and negative electrodes were 1 mg and 2 mg respectively).

The electrochemical characteristics of the synthesized composites were analysed by cyclic voltammetry (CV) and Galvanostatic charge discharge curve (GCD) in 2M KOH aqueous solution at room temperature. For the half-cell configuration platinum wire, Ag/AgCl and active material coated on  $1 \times 1 \text{ cm}^2$  Ni foam were used as counter, reference and working electrode respectively.

Specific capacitance ( $C_s$ ) can be calculated from the CV curve by using the equation 8.1<sup>33-34</sup>

$$C_s = \frac{\int I dV}{2m\Delta V_v} \quad (8.1)$$

$C_s$  can be calculated from GCD curve by using equation 8.2<sup>34-35</sup>

$$C_s = \frac{I\Delta t}{m\Delta V} \quad (8.2)$$

Where  $C_s$ ,  $I$ ,  $\Delta t$ ,  $m$ , and  $\Delta V$  accounts for the specific capacitance (F/g), current applied (mA), discharge time (sec), mass of active material (mg), and operating potential



window (V), respectively.  $\int I dv$  Stands for area under the CV curve , and  $v$  represents the scan rate ( $\text{mV s}^{-1}$ ).

For Asymmetric supercapacitor (ASC) cell the as prepared material (1D-RuO<sub>2</sub>/C) act as cathode and commercial Activated Carbon (AC) act as anode. The full cell is represented as 1D-RuO<sub>2</sub>/C //AC. To balance the charge storage the mass ratio of and AC were calculated by using equation 8.3<sup>35-37</sup>.

$$\frac{m_-}{m_+} = \frac{C_+ \Delta V_+}{C_- \Delta V_-} \quad (8.3)$$

where  $m_+$  was the mass (mg),  $C_+$  and  $C_-$  were the specific capacitance of 1D-RuO<sub>2</sub>/C and AC respectively,  $\Delta V_+$  and  $\Delta V_-$  is the voltage window of cathode and anode electrode respectively and  $m_-$  was the mass of anode<sup>4, 37-38</sup>.

$$E = \frac{C_s (\Delta V)^2}{7.2} \quad (8.4)$$

$$P = \frac{E}{\Delta t} \times 3600 \quad (8.5)$$

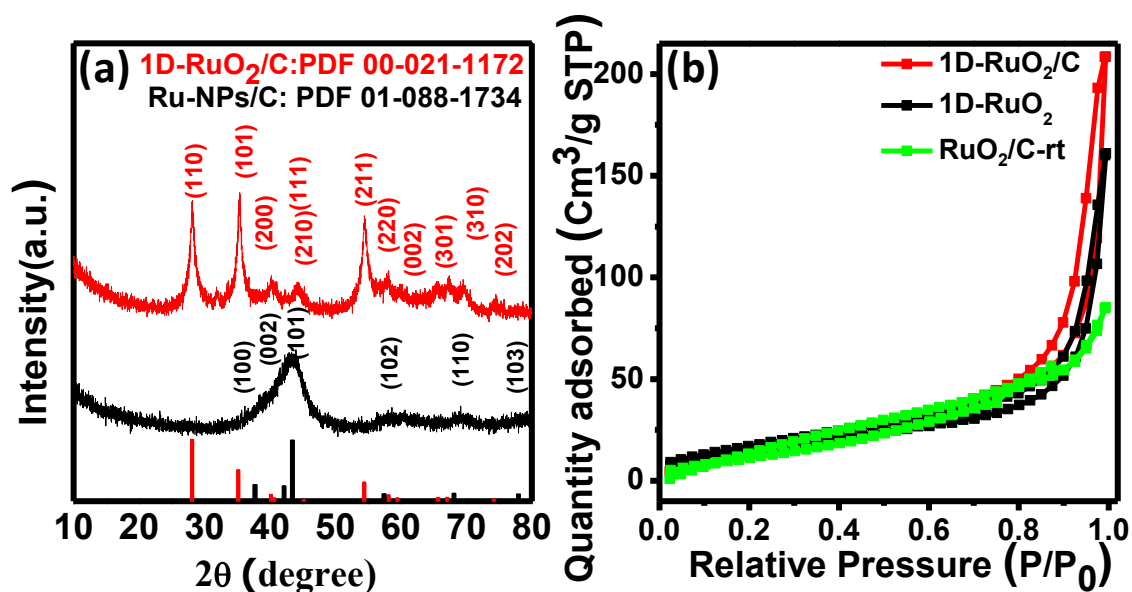
Where  $\Delta V$  is the voltage window (V),  $C_s$  is the capacitance of ASC ( $\text{Fg}^{-1}$ ) and  $\Delta t$  is the discharge time (sec).

## **8.4. RESULTS AND DISCUSSIONS:**

### **8.4.1. Results and discussion**

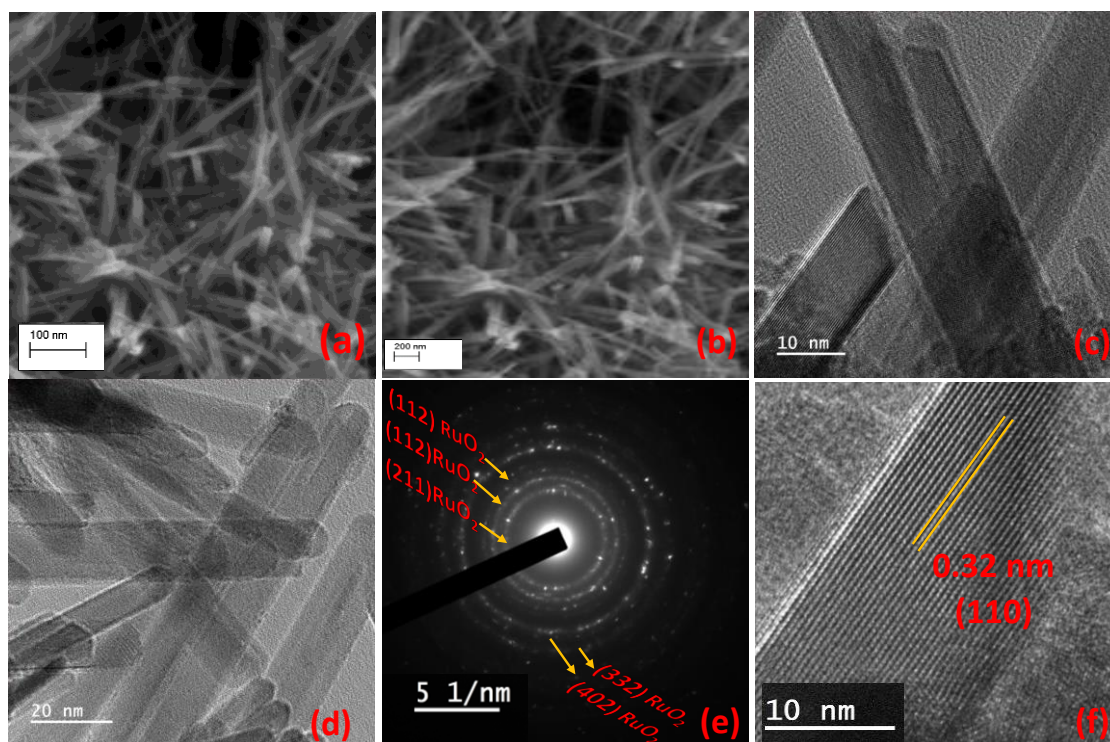
The X-ray diffraction (XRD) is first used to characterize 1D-RuO<sub>2</sub>/C, and Ru-NPs/C as provided in Figure 8.1(a). As shown in Figure 8.1(a), the diffraction peak at  $2\theta$  values 28.02°, 35.06°, 40.03°, 40.54°, 45.09°, 54.24°, 58.10°, 59.38°, 65.55°, 66.98°, and 74.20° correspond to the lattice planes of (110), (101), (200), (111), (210), (211), (220), (002), (310), (301), and (202) of ruthenium oxide respectively (PDF 00-021-1172). The p-XRD pattern of Ru-NPs/C shows the diffraction peaks at 37.73 °, 42.17 °, 43.43 °, 57.86 °, and 77.97 ° corresponding to the (100), (002), (101), (110), and (103) planes of metallic

ruthenium which are presented in Figure 8.1(a) (PDF 01-088-1734). This suggests the presence of metallic Ru nanoparticles in Ru-NPs/C. The XRD studies (Figure 8.1(a)) suggest that the crystalline RuO<sub>2</sub> is formed due to the thermal treatment of Ru-NPs/C 400°C. The Surface area was analyzed by BET (Brunauer–Emmett–Teller) technique. All samples show type IV with a hysteresis loop between 0.5 and 1 (after relative pressure  $1 < P/P_0 < 0.5$ ), indicating the existence of mesopores (Figure 8.1(b)). The composites 1D-RuO<sub>2</sub>/C, RuO<sub>2</sub> (without carbon support), and Ru-NPs/C show an SSA of 55.5, 51.4, and 47.8 m<sup>2</sup>/g respectively showing the SSA for 1D-RuO<sub>2</sub>/C is higher than the RuO<sub>2</sub> (without carbon support) and Ru-NPs/C composite. This result suggests that annealing Ru-NPs/C composite at 400 °C increases the SSA which offers more electroactive sites and enables efficient contact with the electrolyte, resulting in a higher electrochemical activity.



**Figure 8.1.** p-XRD pattern of (a) 1D-RuO<sub>2</sub>/C composite, and Ru-NPs/C, (b) N<sub>2</sub> desorption/adsorption isotherm of 1D-RuO<sub>2</sub>/C, RuO<sub>2</sub>, and Ru-NPs/C composites.

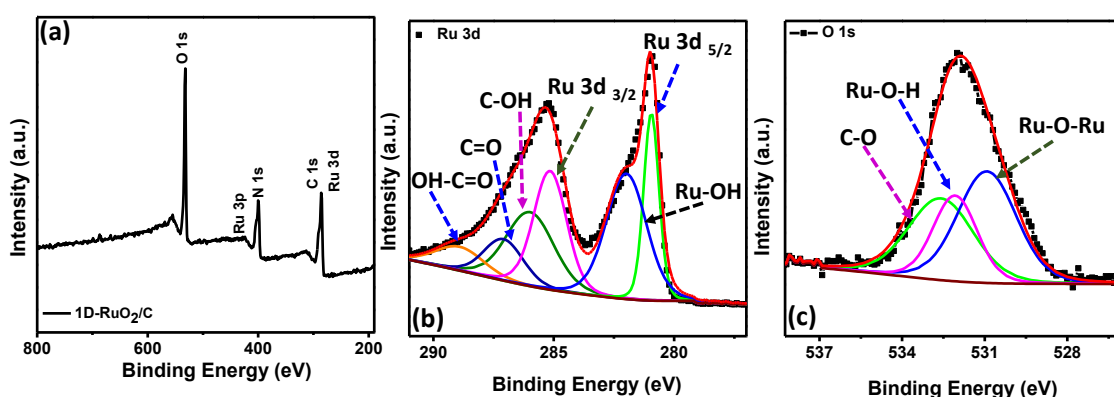
The XRD pattern of RuNPs/C (Figure 8.1(a)) suggests the formation of Ru nanoparticles on N@C. N@C is used to support nucleation and the growth of ruthenium nanoparticles. The Ru-NPs/C are heated at 400 °C in presence of air to form 1D-RuO<sub>2</sub>/C. Figure S8.1 represents the SEM images of 1D- RuO<sub>2</sub>/C. It is observed that the 1D nanorods of RuO<sub>2</sub> formed on the surface of the carbon nanosheets when Ru-NPs/C was calcined at 400 °C. The 1D nanostructure provides large SSA which promotes the access of electrolyte ions to the electrode materials<sup>39</sup>. The weight percent of Ru, O, C, and N in the 1D-RuO<sub>2</sub>/C composite was determined from the EDX spectrum and is presented in Table S8.1. The SEM-EDX (presented in Figure S8.2(a-e)) analysis confirms the uniform distribution of Ru, C, N, and O. Figure S8.3 represents the SEM image of only N@C showing nanosheet-like morphology. The Transmission electron microscopic (TEM) technique was used to analyze the detailed crystal structure and surface morphology of the prepared composite. Low-resolution SEM images of 1D-RuO<sub>2</sub>/C composite reveal the RuO<sub>2</sub> nanorods are randomly grown over the carbon sheets with an average length of nearly 600 to 800 nm, as presented in Figure 8.2 (a, b). The TEM images of 1D-RuO<sub>2</sub>/C composite as shown in Figure 8.2 (c-d), one-dimensional nanorods of RuO<sub>2</sub> are seen. The SEAD (Selected Area Electron Diffraction) pattern of the 1D-RuO<sub>2</sub>/C composite is presented in Figure 8.2 (e). The d-spacing from the SEAD image corresponds to the (211), (112), (332), and (402) planes of RuO<sub>2</sub>. This is in good agreement with the p-XRD studies. In the HRTEM image, the lattice fringes with an interplanar distance of 0.32 nm corresponding to the (110) plane of RuO<sub>2</sub> confirm the presence of RuO<sub>2</sub> in the 1D-RuO<sub>2</sub>/C composite (Figure 8.2(f)). For a better understanding, the TEM images of only N@C are presented in Figure S8.4.



**Figure 8.2.** (a, b) Low-resolution SEM images, (c, d) TEM images, (e) SAED pattern, and (f) HRTEM images of 1D-RuO<sub>2</sub>/C Composites.

The XPS measurements have performed to identify the elements present in 1D-RuO<sub>2</sub>/C, their chemical state, and chemical composition in the composite material. Figure 8.3(a) represents the presence of Ru, O, C, and N elements confirmed from the XPS survey scan of 1D-RuO<sub>2</sub>/C composites. The high-resolution XPS spectrum of Ru 3d shows the overlapping of Ru 3d<sub>3/2</sub> peak with C 1s peak appearing at a binding energy of 284.6 eV (Figure 8.3(b)). Moreover, Ru 3d spectrum can be deconvolution into three peaks centered at 280.98, 282.46, and 285.93 eV corresponding to Ru-O-H, Ru 3d<sub>5/2</sub>, and Ru 3d<sub>3/2</sub> respectively. The XPS results confirmed the 1D-RuO<sub>2</sub>/C composites formed were partially hydrated RuO<sub>2</sub> as RuO<sub>2</sub> could absorb moisture when exposed to an ambient (with H<sub>2</sub>O or -OH content inside the structure)<sup>40</sup>. The peaks at binding energy 286.1, 287.2, and 289.2 eV correspond to C-OH, C=O, and OH-C=O respectively<sup>41</sup>. The

existence of RuO<sub>2</sub> in the nanocomposite was confirmed from the XPS spectrum of O 1s. Figure 8.3(c) presents the O 1s spectrum which can be deconvoluted into two peaks, Ru–O–Ru centred at 529.5 eV and Ru–O–H centred at 530.5 eV can be assigned to RuO<sub>2</sub><sup>22, 40, 42</sup>. The C–O peak centred at 531.6 eV mainly originates from the surface, oxygenated groups.



**Figure 8.3.** (a) Survey scan; XPS spectra of (b) Ru 3d + C 1s and (c) O 1s of 1D-RuO<sub>2</sub>/C composite.

#### 8.4.2. Electrochemical Analysis

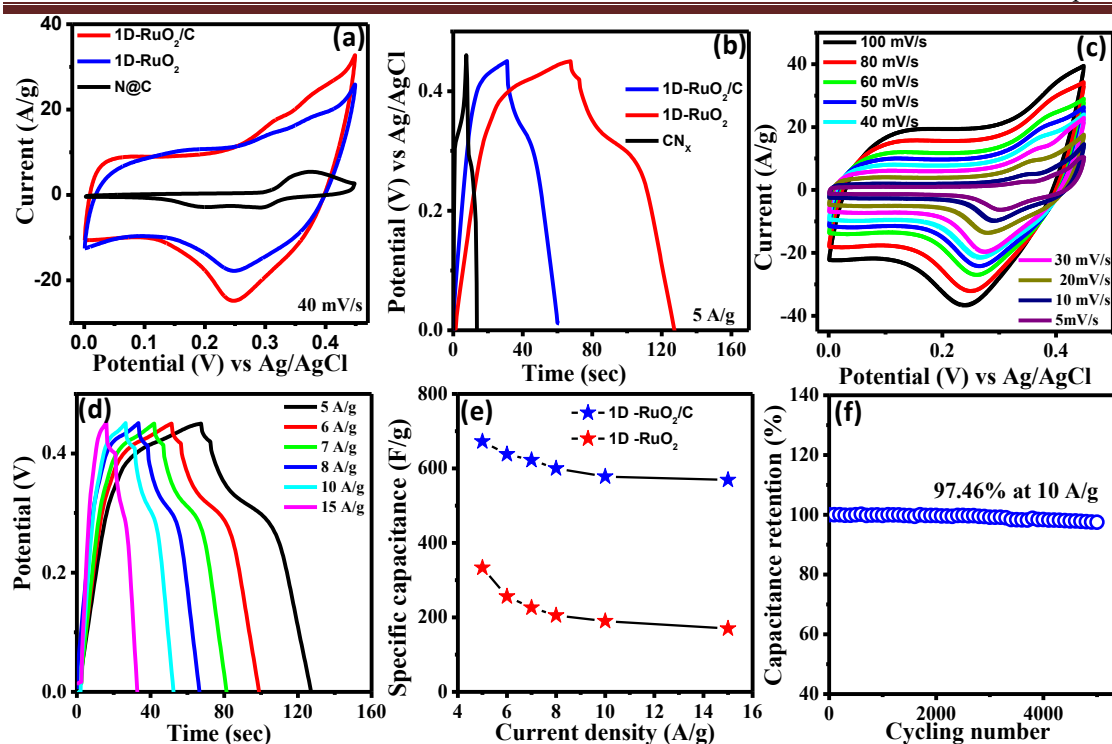
Figure 8.4 shows the electrochemical performance of 1D-RuO<sub>2</sub>/C, RuO<sub>2</sub> (without support), and N@C. Comparison CV profiles of 1D-RuO<sub>2</sub>/C, RuO<sub>2</sub>, and N@C at 40 mV/sec scan rate and a potential window ranging from 0-0.45V in 2M KOH electrolyte are presented in Figure 8.4(a). The CV profile showing the redox peaks indicates the charge storage process is pseudocapacitive in nature. A pair of redox peaks appeared around 0.35 V and 0.30 V for 1D-RuO<sub>2</sub>/C due to the adsorption/desorption of electrolyte cations (K<sup>+</sup>) at ruthenium oxide (RuO<sub>2</sub>) surface according to the following equation<sup>18</sup>:



The specific capacitance values for 1D-RuO<sub>2</sub>/C, RuO<sub>2</sub>, and N@C was obtained by integrating the area under the CV curves using equation 8.1 and are obtained to be 310, 260, and 32.76 F/g indicating poor specific capacitance value of RuO<sub>2</sub> and N@C compared to 1D-RuO<sub>2</sub>/C, which is attributed to the higher SSA, and synergistic interaction between carbon support and RuO<sub>2</sub> composites. In addition, to demonstrate the application potential of the 1D-RuO<sub>2</sub>/C electrode, GCD measurement was performed at 5 A/g current density. Comparison of GCD curves for these three composites are presented in Figure 8.4(b) and the specific capacitance are calculated by using equation 8.2 and are found to be 671, 338, and 66 F/g at 5 A/g current density, presented in Figure 8.4(b) showing better specific capacitance value of 1D-RuO<sub>2</sub>/C compared to RuO<sub>2</sub> and N@C which is consistent with the calculated  $C_s$  value. The CV plots of 1D-RuO<sub>2</sub>/C at different sweep rate is illustrated in Figure 8.4(c). At a higher scan rate (moving from 5-100 mV/s) there is no obvious change in the nature of the CV curves indicating the capacitive behaviour of the electrode material. With a rise in scan rate the current response increases. The CV profiles of 1D-RuO<sub>2</sub>/C indicate redox reaction process confirming the 1D-RuO<sub>2</sub>/C is based on the charge storage mechanism of ruthenium oxide in aqueous 2M KOH electrolyte owing to the fast intercalation of K<sup>+</sup> into the surface of the electrode material during the electrochemical process. Further GCD measurements of 1D-RuO<sub>2</sub>/C were carried out at different current densities in a voltage window of 0-0.45V and the corresponding GCD profiles are presented in Figure 8.4(d). The  $C_s$  values of the 1D-RuO<sub>2</sub>/C composite were calculated to be 671, 638, 622, 600, 578, and 569 F/g at 5, 6, 7, 8, 10, and 15 A/g current densities. For comparison purposes, the electrochemical performance of N@C was studied. Figure S8.5 represents the CV curve at different scan rates (5-100 mV/s) and GCD curves of N@C at different current

densities (1-5 A/g). The GCD measurement for bare Ni-foam was conducted at 1 mA current and 0-0.45V voltage range, showing a negligible contribution of capacitance from the current collector (Figure S8.6). Upon increasing the current density the gradual decrease in capacitance may be because of the insufficient involvement of the active material in the redox process and the incremental potential drop at higher current density<sup>18</sup>. Table 8.1 presents the comparison of the electrochemical activity of 1D-RuO<sub>2</sub>/C with other recently reported values. Figure 8.4(e) shows the specific capacitance depending on the current density plot indicating that with an increase in current density, C<sub>s</sub> values gradually decrease because of insufficient active material and the incremental voltage drop being involved in the redox reaction at a higher current density<sup>43</sup>. A cyclic stability test was performed showing 93.46 % retention of its initial C<sub>s</sub> after 5k Galvanostatic charge/discharge cycles recorded under a constant current of 10 A/g, indicating long-term durability and extraordinary stability of the composite compared to other recently reported literature<sup>39</sup>. The high electrochemical activity and a cyclic lifetime of the 1D-RuO<sub>2</sub>/C composite were attributed to the strong interaction between carbon support and ruthenium oxide which provides structural stability. The post-electrochemical stability characterization of 1D-RuO<sub>2</sub>/C composite was carried out by SEM measurements as presented in Figure S8.7 showing no significant change in 1D morphology. This indicates the morphology of the composite remains unaltered after a long-term cyclic test.





**Figure 8.4.** (a, b) CV and charging/discharging curves of 1D-RuO<sub>2</sub>/C, RuO<sub>2</sub>, and N@C composites at a scan rate of 40 mV/s and 5 A/g current. (c) CV curves of 1D-RuO<sub>2</sub>/C at sweep rate 5-100 mV s<sup>-1</sup>. (d) charging/discharging curves of 1D-RuO<sub>2</sub>/C at 5-15 A/g current. (e) Specific capacitance depends on the current density for 1D-RuO<sub>2</sub>/C and RuO<sub>2</sub> composites. (f) A cyclic lifetime of 1D-RuO<sub>2</sub>/C under 10 A g<sup>-1</sup> current.

**Table 8.1.** Electrochemical properties of different composites with 1D-RuO<sub>2</sub>/C composite as electrode materials with previously reported literature.

Electrode material	C <sub>s</sub> (F g <sup>-1</sup> ) of single Electrode	Cycling stability (%)	No. of cycles	Ref.
Ru/mesoporous carbon	287 (0.05 A/g) 6 M KOH	96.4	1000	19
NiF/RuO <sub>2</sub>	750 (10 A/g)	97.5	500	18



2 M KOH				
<b>RuO<sub>2</sub> and Activated carbon composite</b>	180 (1 mA/cm <sup>2</sup> )	-	-	44
	6 M KOH			
<b>Mulberry like RuO<sub>2</sub></b>	400 (0.2 A/g) 1 M H <sub>2</sub> SO <sub>4</sub>	84.7	6000	39
<b>RuO<sub>2</sub>-CNF(220)</b>	188 (1mA/cm <sup>2</sup> )	93	3000	2
	6 M KOH			
<b>RuO<sub>2</sub>/carbon nanofibers composites</b>	220 (5 mV/s) 2 M H <sub>2</sub> SO <sub>4</sub>	98.9	1000	45
<b>RuO<sub>2</sub>-G nanocomposite</b>	444 (0.1 A/g) 1 M Na <sub>2</sub> SO <sub>4</sub>	94	1000	24
<b>1D-RuO<sub>2</sub>/C</b>	671 (5 A/g) 2M KOH	93.46	5000	Present work

The storage mechanism of the electrode material was analysed by studying the relationship between peak current (*i*) and sweep rate (*v*) using equations 8.7 and 8.8<sup>46</sup>:

$$i = kv^b \quad (8.7)$$

$$\log i = \log k + b \log v \quad (8.8)$$

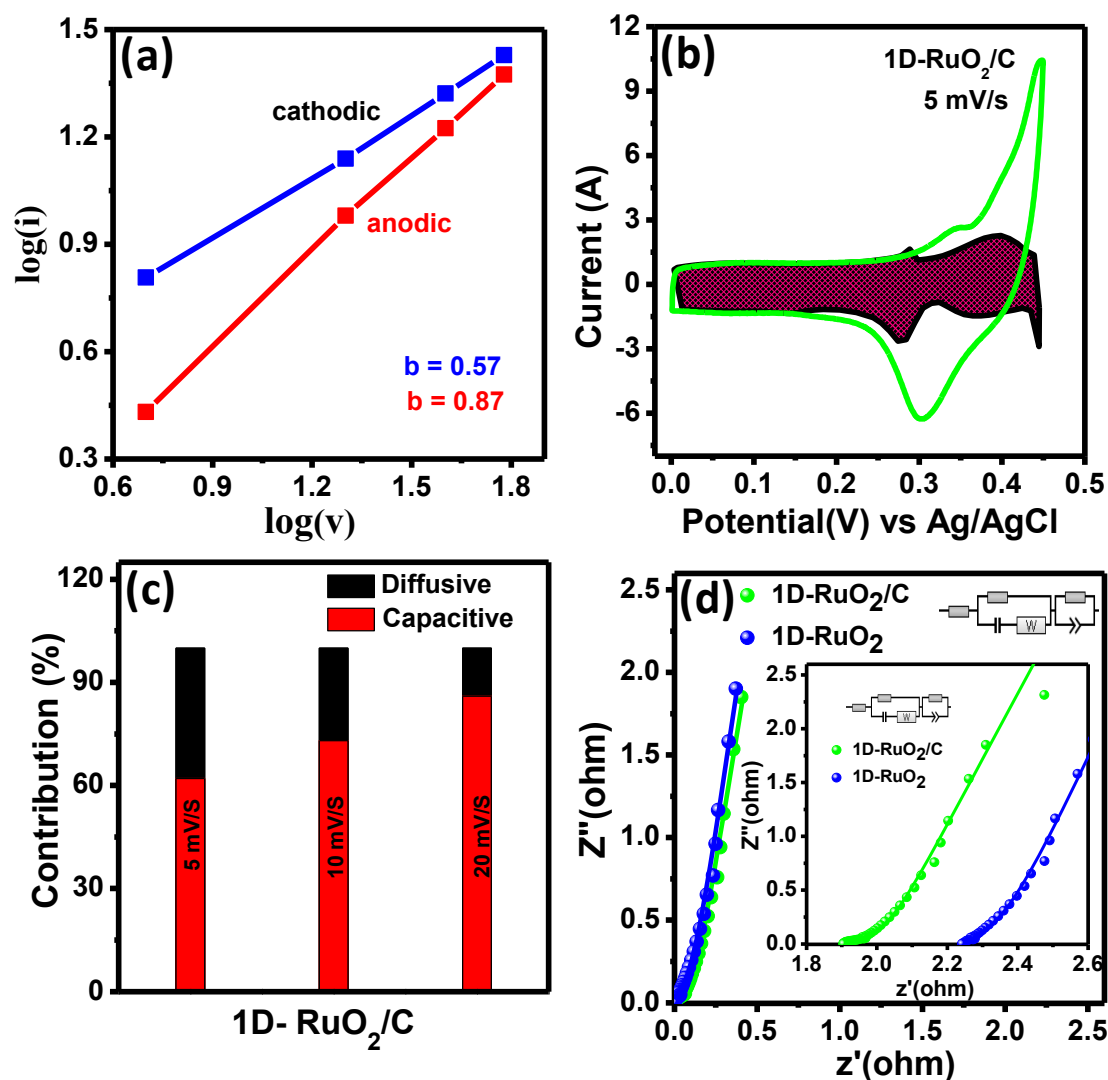
Here *i* and *v* represent the current density (A g<sup>-1</sup>) and sweep rate (mV s<sup>-1</sup>) respectively and *k* and *b* are constants. The values of *b* can be obtained from the slope and used to determine the control mechanism of the electrode. Log *i* was plotted against log *v* to obtain the values of *b*. The *b* values 0.5 and 1 indicate the diffusion-controlled (battery) process and pseudocapacitive process respectively<sup>47</sup>. As shown in Figure 8.5(a) the *b* value for anodic and cathodic peaks are obtained to be 0.87 and 0.57 respectively

suggesting the specific capacitance of the 1D-RuO<sub>2</sub>/C is controlled by a mixed controlled mechanism of the charge storage electrode. The CV curves are used to investigate the pseudocapacitive contribution of the electrode by using equation 8.9<sup>48-51</sup>.

$$i(V) = k_1v + k_2v^{1/2} \quad (8.9)$$

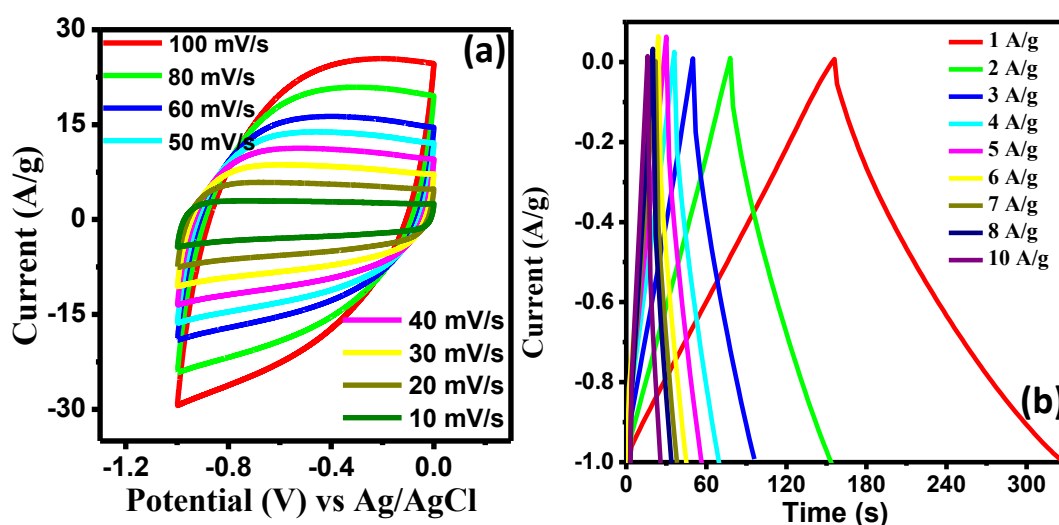
Where  $k_1$  and  $k_2$  stand for the changeable parameters and  $v$  is the sweep rate.  $k_1$  and  $k_2$  are obtained from the slope and y-intercept respectively.  $k_1v$  and  $k_2v^{1/2}$  give information about the capacitive and diffusion-controlled current respectively. Figure 8.5(b) despite the pseudocapacitive contribution of the 1D-RuO<sub>2</sub>/C electrode at 5 mV s<sup>-1</sup> and the overflow of the capacitance contribution from the original CV curve is due to the relationship of polarization, the voltage will move at different scan rate<sup>46</sup>. At the same potential,  $i$  value will be different near the peak current. This might be the reason for the overflow of the capacitive curve from the original CV profile<sup>46</sup>. The capacitive contribution for 1D-RuO<sub>2</sub>/C composites was calculated under 5, 10, and 20 mV s<sup>-1</sup> scan rate and are obtained to be 62 and 73 and 86 % respectively suggesting a typical mixed controlled mechanism behaviour of the electrode material<sup>52</sup>. With the increase in scan rate the pseudocapacitive charge storage behaviour increases indicating a fast ion deintercalation/intercalation process resulting in good rate capability and reversibility of the electrode<sup>53</sup>. The bar plot for 1D-RuO<sub>2</sub>/C composites distinguishing the diffusion-controlled process and pseudocapacitive contribution at a sweep rate of 5, 10, and 20 mV s<sup>-1</sup> are presented in Figure 8.5(c). Figure 8.5(d) depicts the Nyquist plot of 1D-RuO<sub>2</sub>/C and RuO<sub>2</sub> composites at a frequency ranging from 0.1-100 kHz with a 10 mV AC amplitude. The charge transfer resistance ( $R_{CT}$ ) for 1D-RuO<sub>2</sub>/C composite and RuO<sub>2</sub> are found to 0.026 and 0.25  $\Omega$  respectively and the solution resistance ( $R_s$ ) are obtained to be 1.9 and 1.74  $\Omega$ . The lowest equivalent series resistance for 1D-RuO<sub>2</sub>/C composite

than RuO<sub>2</sub> without support results excellent conductivity of the 1D-RuO<sub>2</sub>/C composite electrode material indicates strong synergistic interaction between carbon support and the RuO<sub>2</sub>.



**Figure 8.5.** (a) Log (v) vs. log (i) plot for cathodic and anodic peaks. (b) CV curve of 1D-RuO<sub>2</sub>/C showing capacitive and diffusive contribution at 5 mV s<sup>-1</sup> scan rate. (c) Pseudocapacitive contribution of 1D-RuO<sub>2</sub>/C (%) at different sweep rates. (d) Nyquist plots the profile of 1D-RuO<sub>2</sub>/C composites and RuO<sub>2</sub> in 2 M KOH.

CV and GCD measurements were done to check the electrochemical activity of AC as an anode electrode material. CV plots for AC at various scan rates and GCD curves at different current densities in 2M KOH at 0 to -1 V potential window are presented in Figure 8.6. The CV curves have no redox peaks (symmetrical behaviour of curve) and the triangular GCD curve indicates the EDLC-type nature of AC. The  $C_s$  value was



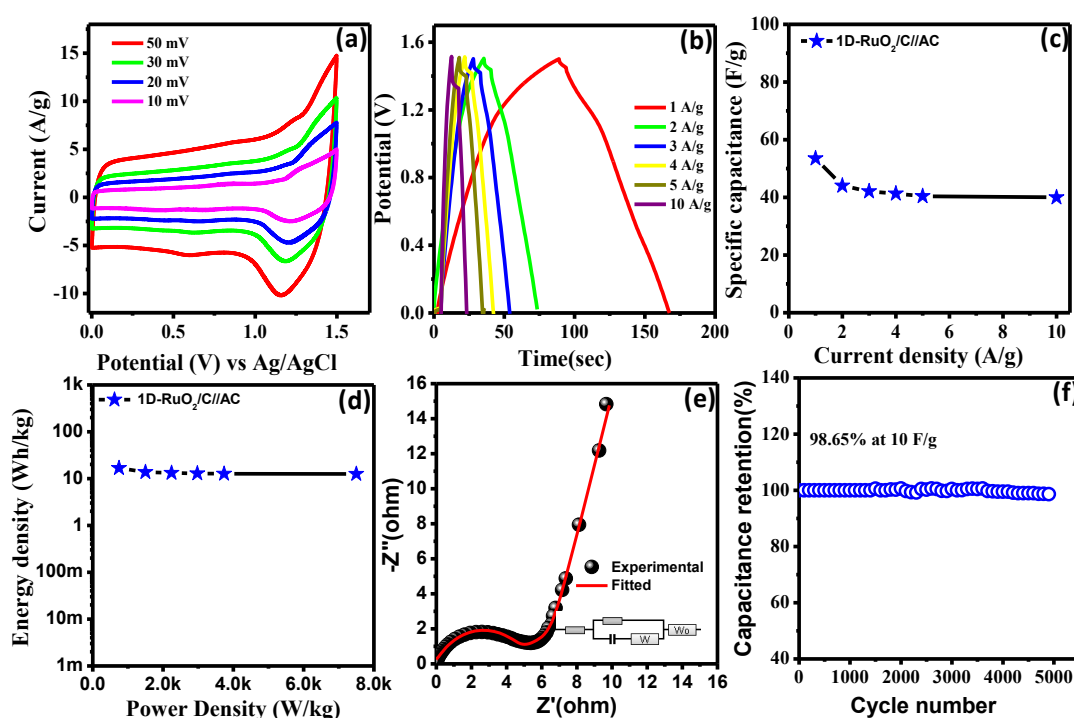
**Figure 8.6.** (a and b) CV profiles at a sweep rate of 10-100 mV s<sup>-1</sup> and GCD cycle under 1-10 A g<sup>-1</sup> current for AC.

calculated from the area under the CV profile and was obtained to be 266 F g<sup>-1</sup> 10 mV s<sup>-1</sup> sweep rate and the  $C_s$  value 170.68 F g<sup>-1</sup> was calculated from the GCD curve under 1 A g<sup>-1</sup> current. This demonstrates that AC is suitable for negative electrode material in the energy storage device.

To better reflect the practical application of the 1D-RuO<sub>2</sub>/C electrode, a two-electrode system (complete supercapacitor device) was designed. To assemble an ASC device, the 1D-RuO<sub>2</sub>/C electrode was chosen as positive and the AC electrode was chosen as negative electrode material. The device was denoted as 1D-RuO<sub>2</sub>/C //AC. Figure S8.8

displays the CV plots of 1D-RuO<sub>2</sub>/C and AC under a scan rate of 10 mV s<sup>-1</sup> potential window ranging from 0-0.45 V and -1.0-0.0 V respectively. CV cycles for the 1D-RuO<sub>2</sub>/C //AC device were recorded at varied potential rang 1.2-1.6 V (Figure S8.9), displaying no such change in nature of the curve up to 1.5 V. This indicates the maximum potential range for the asymmetric device can be sustained up to 0 to 1.5 V, presented in Figure S8.9. The CV curves for 1D-RuO<sub>2</sub>/C //AC device at varied sweep rates (10-50 mV s<sup>-1</sup>) in a cell voltage range of 0-1.5 V are presented in Figure 8.7(a) and the capacitance was calculated from the CV curves at 10 mV/s scan rate and was obtained to be 149.42 F/g. Figure 8.7(b) shows the GCD curves to confirm the energy storage behaviour of the asymmetric device performed in a 0-1.5 V potential range. The device 1D-RuO<sub>2</sub>/C //AC offered a C<sub>s</sub> value of 53.5, 44.04, 42.04, 41.30, 40.37, and 40 F g<sup>-1</sup> under an applied current of 1, 2, 3, 4, 5, and 10 A g<sup>-1</sup> resulting ~98.65 % retention of initial capacitance after 10 A g<sup>-1</sup> current indicating good rate capability of the system. Plot 8.7(c) represents the C<sub>s</sub> vs. current density for the 1D-RuO<sub>2</sub>/C //AC ASC device. Figure 8.7(d) shows the Ragone plots for the 1D-RuO<sub>2</sub>/C //AC ASC device and the energy density and power density values are calculated by using equations 8.4 and 8.5 respectively. The assembled device offered a high energy density of 16.71 W h kg<sup>-1</sup> at 751.66 W kg<sup>-1</sup> power density. EIS analysis is used as a principal method to examine the fundamental behavior of the asymmetric device. The corresponding equivalent circuit was presented inset of Figure 8.7 (e). The interfacial charge transfer resistance (R<sub>CT</sub>) and solution resistance (R<sub>s</sub>) for the asymmetric device were obtained to be 4.34 and 3.84 respectively from the circuit fitting. The EIS result mated with the electrochemical performance of the asymmetric device by providing high capacitance value, exceptional energy, and power density. For the practical use of a supercapacitor, a long cyclic lifetime

is a vital requirement. The Cyclic lifetime of the 1D-RuO<sub>2</sub>/C//AC asymmetric device was examined by 5k charging/discharging cycles at 10 A/g current and the device maintains a 39.46 F/g capacitance after 5k cycles. The device shows a 98.65 % capacitance retention ensuring excellent cyclic stability of the device presented in Figure 8.7(f). From the above-obtained results, it was confirmed that the 1D-RuO<sub>2</sub>/C //AC asymmetric device with high electrochemical active sites not only results in high electrical conductivity but also results in fast diffusion of electrons.



**Figure 8.7.** Electrochemical behavior of asymmetric supercapacitor (a) CV plots of 1D-RuO<sub>2</sub>/C //AC ASC device, (b) GCD plots of 1D-RuO<sub>2</sub>/C //AC at different current density, (c)  $C_s$  vs. current density, (d) Ragone plot for a-1D-RuO<sub>2</sub>/C //AC device, (e) Nyquist plot of the ASC, (f) Cyclic lifetime of 1D-RuO<sub>2</sub>/C //AC asymmetric device at a current of 10 A g<sup>-1</sup>.

## 8.5. CONCLUSIONS

In summary, a simple and facile thermal synthesis method was used to grow one-dimensional RuO<sub>2</sub> nanorods over N@C. The 1D-RuO<sub>2</sub>/C composite displays a high C<sub>s</sub> value of 671 F g<sup>-1</sup> at 5 A g<sup>-1</sup> current (two times higher than 1D-RuO<sub>2</sub> without support) with excellent cyclic durability of 93.46 % after 5k cycles at 10 A/g current density. An ASC device (1D-RuO<sub>2</sub>/C//AC) was assembled showing a specific capacitance of 53.5 F g<sup>-1</sup> under 1 A g<sup>-1</sup> current. An energy density of 16.71 W h kg<sup>-1</sup> was achieved with an impressive cyclic performance (approx. 98.65 % capacitance retention after 5k cycles) at 10 A g<sup>-1</sup>. The superior electrochemical activity of the 1D-RuO<sub>2</sub>/C composite was attributed to the 1D nanorods morphology, synergistic interaction between carbon support and RuO<sub>2</sub>, low charge transfer resistance, and high surface area. The excellent specific capacitance with long-term cyclic stability hopefully makes the 1D-RuO<sub>2</sub>/C as a promising electrode material for energy storage devices.

## 8.6. REFERENCES

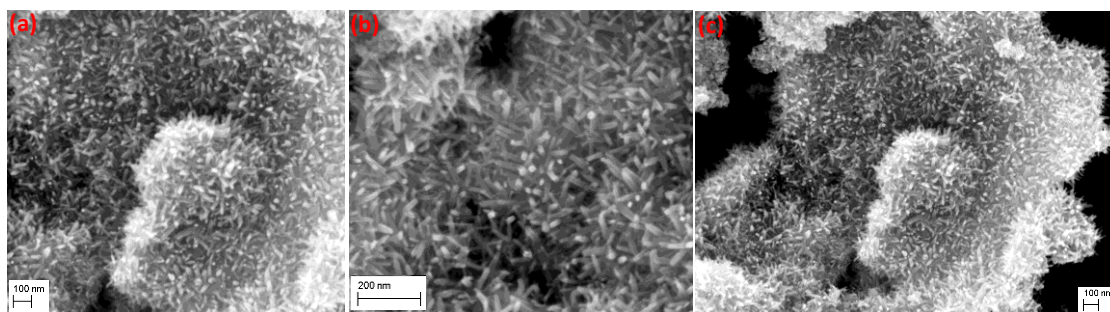
- (1) Yue, L.; Ma, C.; Yan, S.; Wu, Z.; Zhao, W.; Liu, Q.; Luo, Y.; Zhong, B.; Zhang, F.; Liu, Y.; Alshehri, A. A.; Alzahrani, K. A.; Guo, X.; Sun, X. *Nano Research* **2022**, *15*, 186-194.
- (2) Jeon, S.; Jeong, J. H.; Yoo, H.; Yu, H. K.; Kim, B.-H.; Kim, M. H. *ACS Applied Nano Materials* **2020**, *3*, 3847-3858.
- (3) Shekhawat, A.; Samanta, R.; Barman, S. *ACS Applied Energy Materials* **2022**, *5*, 6059-6069.
- (4) Liang, J.; Zhao, H.; Yue, L.; Fan, G.; Li, T.; Lu, S.; Chen, G.; Gao, S.; Asiri, Abdullah M.; Sun, X. *Journal of Materials Chemistry A* **2020**, *8*, 16747-16789.
- (5) Theerthagiri, J.; Lee, Seung J.; Karuppasamy, K.; Arulmani, S.; Veeralakshmi, S.; Ashokkumar, M.; Choi, M. Y. *Journal of Hazardous Materials* **2021**, *412*, 125245.
- (6) Yue, L.; Wang, D.; Wu, Z.; Zhao, W.; Ren, Y.; Zhang, L.; Zhong, B.; Li, N.; Tang, B.; Liu, Q.; Luo, Y.; Asiri, A. M.; Guo, X.; Sun, X. *Chemical Engineering Journal* **2022**, *433*, 134477.
- (7) Zhao, W.; Ma, X.; Yue, L.; Zhang, L.; Luo, Y.; Ren, Y.; Zhao, X.-E.; Li, N.; Tang, B.; Liu, Q.; Liu, Y.; Gao, S.; Alshehri, A. A.; Sun, X. *Journal of Materials Chemistry A* **2022**, *10*, 4087-4099.
- (8) Yue, L.; Liang, J.; Wu, Z.; Zhong, B.; Luo, Y.; Liu, Q.; Li, T.; Kong, Q.; Liu, Y.; Asiri, A. M.; Guo, X.; Sun, X. *Journal of Materials Chemistry A* **2021**, *9*, 11879-11907.

- (9) Panda, S.; Deshmukh, K.; Khadheer Pasha, S. K.; Theerthagiri, J.; Manickam, S.; Choi, M. Y. *Coordination Chemistry Reviews* **2022**, 462, 214518.
- (10) Panda, P.; Mishra, R.; Panigrahy, S.; Barman, S. *ACS Applied Nano Materials* **2022**, 5, 5176-5186.
- (11) Thiagarajan, K.; Balaji, D.; Madhavan, J.; Theerthagiri, J.; Lee, S. J.; Kwon, K.-Y.; Choi, M. Y. Cost-Effective Synthesis of Efficient CoWO<sub>4</sub>/Ni Nanocomposite Electrode Material for Supercapacitor Applications *Nanomaterials* [Online], 2020.
- (12) Simon, P.; Gogotsi, Y. *Nature Materials* **2008**, 7, 845-854.
- (13) Lin, N.; Tian, J.; Shan, Z.; Chen, K.; Liao, W. *Electrochimica Acta* **2013**, 99, 219-224.
- (14) Theerthagiri, J.; Durai, G.; Tatarchuk, T.; Sumathi, M.; Kuppusami, P.; Qin, J.; Choi, M. Y. *Ionics* **2020**, 26, 2051-2061.
- (15) Li, Z.; Wang, J.; Liu, S.; Liu, X.; Yang, S. *Journal of Power Sources* **2011**, 196, 8160-8165.
- (16) Lee, S. J.; Theerthagiri, J.; Nithyadharseni, P.; Arunachalam, P.; Balaji, D.; Madan Kumar, A.; Madhavan, J.; Mittal, V.; Choi, M. Y. *Renewable and Sustainable Energy Reviews* **2021**, 143, 110849.
- (17) Hassan, H. K.; Atta, N. F.; Hamed, M. M.; Galal, A.; Jacob, T. *RSC Advances* **2017**, 7, 11286-11296.
- (18) Ismail, E.; Khamlich, S.; Dhlamini, M.; Maaza, M. *RSC Advances* **2016**, 6, 86843-86850.
- (19) He, X.; Xie, K.; Li, R.; Wu, M. *Materials Letters* **2014**, 115, 96-99.
- (20) Stoller, M. D.; Ruoff, R. S. *Energy & Environmental Science* **2010**, 3, 1294-1301.
- (21) He, X. J.; Geng, Y. J.; Oke, S.; Higashi, K.; Yamamoto, M.; Takikawa, H. *Synthetic Metals* **2009**, 159, 7-12.
- (22) Hwang, J. Y.; El-Kady, M. F.; Wang, Y.; Wang, L.; Shao, Y.; Marsh, K.; Ko, J. M.; Kaner, R. B. *Nano Energy* **2015**, 18, 57-70.
- (23) Leng, X.; Zou, J.; Xiong, X.; He, H. *Journal of Alloys and Compounds* **2015**, 653, 577-584.
- (24) Thangappan, R.; Arivanandhan, M.; Dhinesh Kumar, R.; Jayavel, R. *Journal of Physics and Chemistry of Solids* **2018**, 121, 339-349.
- (25) Xu, X.; Yan, M.; Tian, X.; Yang, C.; Shi, M.; Wei, Q.; Xu, L.; Mai, L. *Nano Letters* **2015**, 15, 3879-3884.
- (26) Li, R.; Wang, Y.; Zhou, C.; Wang, C.; Ba, X.; Li, Y.; Huang, X.; Liu, J. *Advanced Functional Materials* **2015**, 25, 5384-5394.
- (27) Niu, C.; Meng, J.; Wang, X.; Han, C.; Yan, M.; Zhao, K.; Xu, X.; Ren, W.; Zhao, Y.; Xu, L.; Zhang, Q.; Zhao, D.; Mai, L. *Nature Communications* **2015**, 6, 7402.
- (28) Cheng, C.; Fan, H. J. *Nano Today* **2012**, 7, 327-343.
- (29) Wei, Q.; Xiong, F.; Tan, S.; Huang, L.; Lan, E. H.; Dunn, B.; Mai, L. *Advanced Materials* **2017**, 29, 1602300.
- (30) Sadhukhan, M.; Barman, S. *Journal of Materials Chemistry A* **2013**, 1, 2752-2756.
- (31) Bhowmik, T.; Kundu, M. K.; Barman, S. *ACS Applied Materials & Interfaces* **2016**, 8, 28678-28688.
- (32) Patharkar, R. G.; Nandanwar, S. U.; Chakraborty, M. *Journal of Chemistry* **2013**, 2013, 831694.
- (33) Xu, J.; Gao, L.; Cao, J.; Wang, W.; Chen, Z. *Electrochimica Acta* **2010**, 56, 732-736.
- (34) Chatterjee, M.; Sain, S.; Roy, A.; Das, S.; Pradhan, S. K. *Journal of Physics and Chemistry of Solids* **2021**, 148, 109733.
- (35) Ramesh, S.; Karuppasamy, K.; Kim, H.-S.; Kim, H. S.; Kim, J.-H. *Scientific Reports* **2018**, 8, 16543.
- (36) Mishra, R.; Panda, P.; Barman, S. *New Journal of Chemistry* **2021**, 45.
- (37) Panda, P.; Mishra, R.; Barman, S.; Panigrahy, S. *Materials Advances* **2021**.
- (38) Chen, X.; Xie, R.; Li, H.; Jaber, F.; Musharavati, F.; Zalnezhad, E.; Bae, S.; Hui, K. S.; Hui, K. N. *Scientific Reports* **2020**, 10, 18956.
- (39) Yu, F.; Pang, L.; Wang, H.-X. *Rare Metals* **2021**, 40, 440-447.

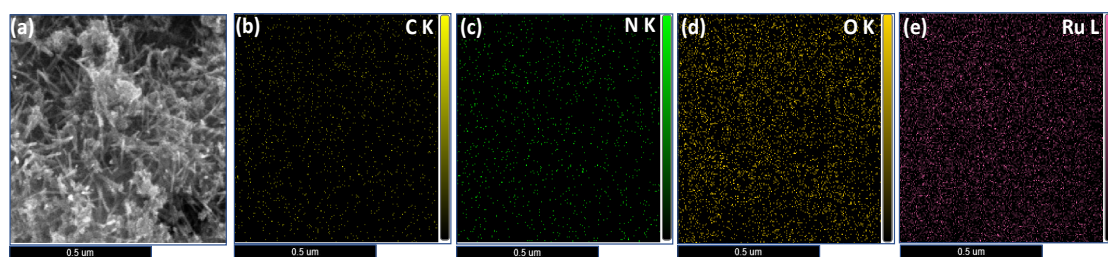


- (40) Han, Z. J.; Pineda, S.; Murdock, A. T.; Seo, D. H.; Ostrikov, K.; Bendavid, A. *Journal of Materials Chemistry A* **2017**, *5*, 17293-17301.
- (41) Hosseini, M. G.; Shahryari, E. *Ionics* **2019**, *25*, 2383-2391.
- (42) Wang, W.; Guo, S.; Lee, I.; Ahmed, K.; Zhong, J.; Favors, Z.; Zaera, F.; Ozkan, M.; Ozkan, C. S. *Scientific Reports* **2014**, *4*, 4452.
- (43) Ma, X.-J.; Zhang, W.-B.; Kong, L.-B.; Luo, Y.-C.; Kang, L. *RSC Advances* **2015**, *5*, 97239-97247.
- (44) Yang, K. S.; Kim, B.-H. *Electrochimica Acta* **2015**, *186*, 337-344.
- (45) Chuang, C.-M.; Huang, C.-W.; Teng, H.; Ting, J.-M. *Composites Science and Technology* **2012**, *72*, 1524-1529.
- (46) Jiang, J.; Hu, Y.; He, X.; Li, Z.; Li, F.; Chen, X.; Niu, Y.; Song, J.; Huang, P.; Tian, G.; Wang, C. *Small* **2021**, *17*, 2102565.
- (47) Abdelaal, M. M.; Hung, T.-C.; Mohamed, S. G.; Yang, C.-C.; Huang, H.-P.; Hung, T.-F. *Nanomaterials* **2021**, *11*.
- (48) Liu, S.; Ni, D.; Li, H.-F.; Hui, K. N.; Ouyang, C.-Y.; Jun, S. C. *Journal of Materials Chemistry A* **2018**, *6*, 10674-10685.
- (49) Yuan, C.; Li, J.; Hou, L.; Zhang, X.; Shen, L.; Lou, X. W. *Advanced Functional Materials* **2012**, *22*, 4592-4597.
- (50) Yan, W.; Kim, J. Y.; Xing, W.; Donovan, K. C.; Ayvazian, T.; Penner, R. M. *Chemistry of Materials* **2012**, *24*, 2382-2390.
- (51) Cheng, Y.; Wei, Z.; Du, Q.; Liu, F.; Duan, X.; Wang, Y.; Jia, D.; Zhou, Y.; Li, B. *Electrochimica Acta* **2018**, *284*, 408-417.
- (52) Ma, F.-X.; Yu, L.; Xu, C.-Y.; Lou, X. W. *Energy & Environmental Science* **2016**, *9*, 862-866.
- (53) Ning, J.; Xia, M.; Wang, D.; Feng, X.; Zhou, H.; Zhang, J.; Hao, Y. *Nano-Micro Letters* **2020**, *13*, 2.

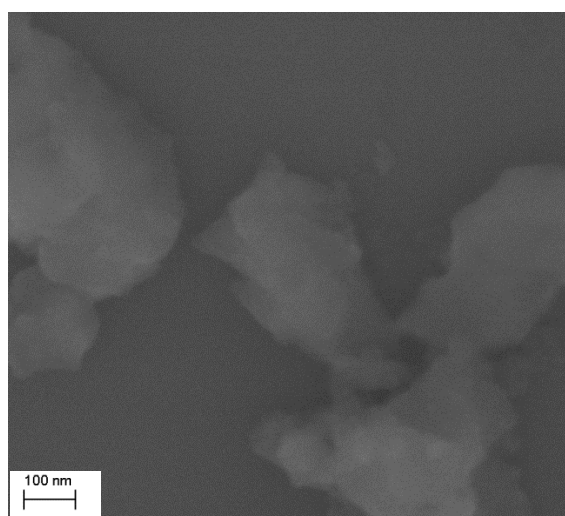
## Appendix F



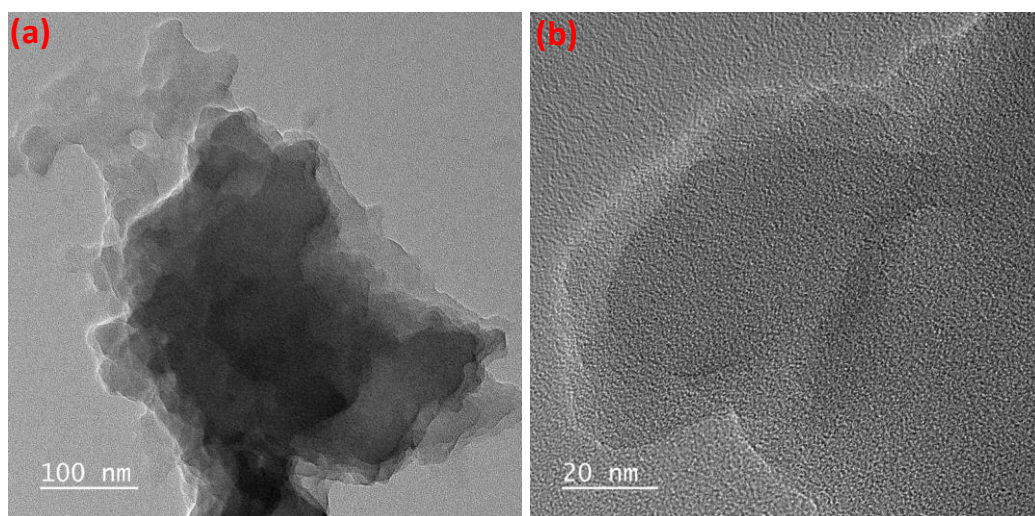
**Figure S8.1.** FESEM image of 1D-RuO<sub>2</sub>/C.



**Figure S8.2.** (a) SEM image and corresponding elemental mapping of elements (b) C, (c) N, (d) O, and (e) Ru respectively indicating uniform distribution of elements in 1D-RuO<sub>2</sub>/C.



**Figure S8.3.** SEM image of N@C.



**Figure S8.4.** TEM image of N@C.

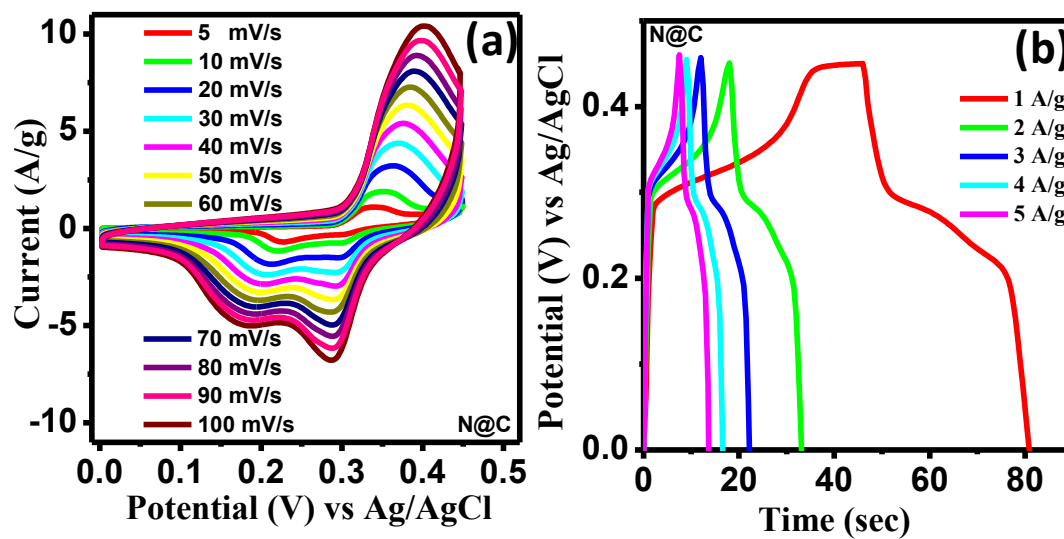


Figure S8.5. (a, b) CV and charging/discharging curves of N@C.

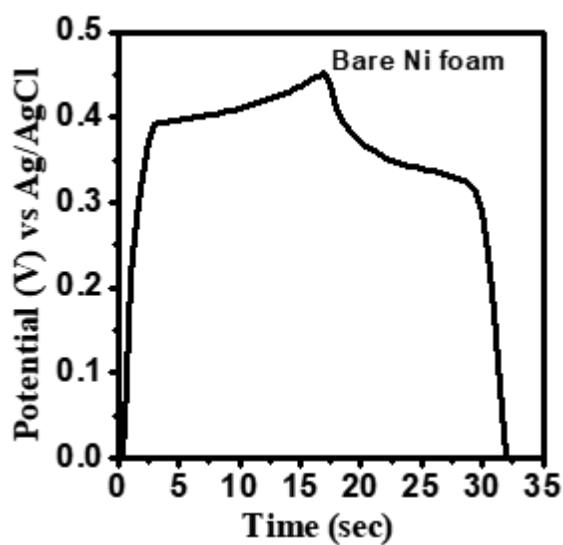
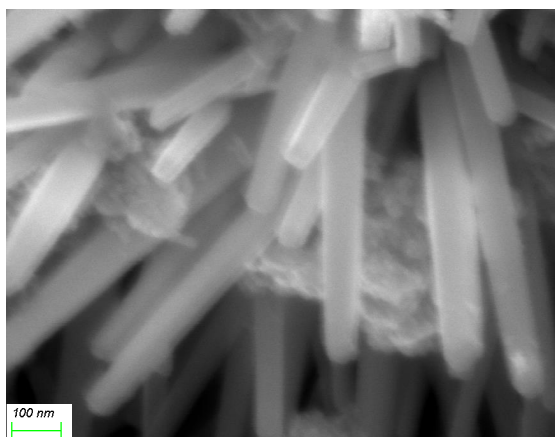
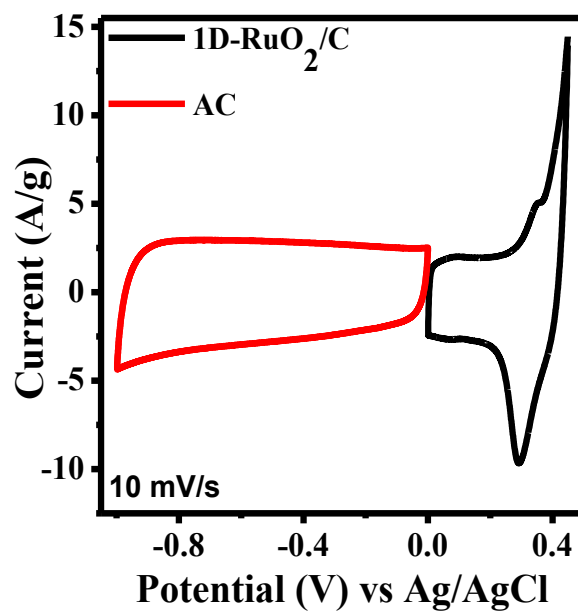


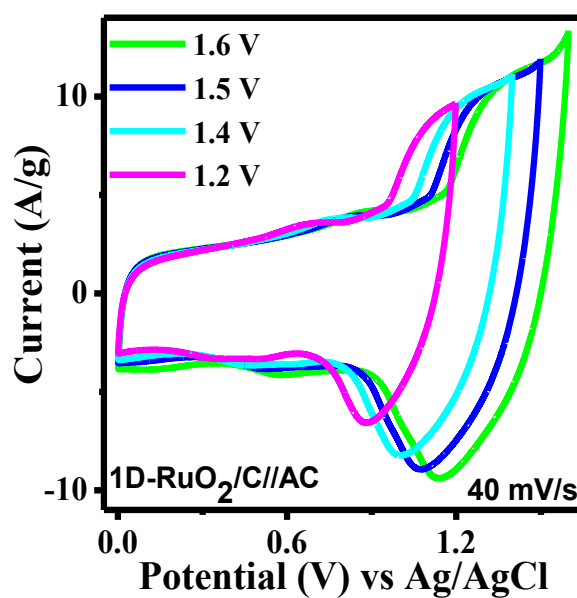
Figure S8.6. GCD curve of bare Ni foam at 1 mA current.



**Figure S8.7.** FESEM image of 1D-RuO<sub>2</sub>/C after capacitance retention test.



**Figure S8.8.** CV curves of AC and 1D-RuO<sub>2</sub>/C at a scan rate of 10 mV s<sup>-1</sup>.



**Figure S8.9.** CV curves for ASC (1D-RuO<sub>2</sub>/C// AC) device at potential ranging from 1.2 V to 1.6 V.

**Table S8.1.** Weight % of Ru, O, C, and N present in 1D-RuO<sub>2</sub>/C samples calculated from SEM EDX analysis.

Sample Name	Ru (%)	O (%)	C (%)	N (%)
1D-RuO <sub>2</sub> /C	52.9	41.5	3.3	2.3

## Chapter 9

### **In-situ Nano-engineering of Amorphous MoS<sub>2</sub> Nanosheets with Carbon Dots for enhanced Supercapacitor performances**

#### **9.1. ABSTRACT**

Amorphous materials have snatched special attention for electrochemical energy storage applications owing to the presence of plenty of activate sites for energy storage. Herein, the microwave-assisted-hydrothermal synthesis of amorphous MoS<sub>2</sub> with some 1T phase and *in-situ*-nano-engineering with C-dots for energy storage application was reported. The specific capacitance ( $C_s$ ) of a-MoS<sub>2</sub>/C-dots was found to be 1368 F g<sup>-1</sup> (at 1 A g<sup>-1</sup>), which is ~2.9 and 1.65 times higher than a-MoS<sub>2</sub> (without C-dots) and crystalline c-MoS<sub>2</sub>/C-dots. Capacitance is also strongly dependent on synthesis methods:  $C_s$  of a-MoS<sub>2</sub>/C-dots is 2.15 times higher than h-MoS<sub>2</sub>/C-dots produced by the normal-hydrothermal method. The Asymmetric supercapacitor was designed using a-MoS<sub>2</sub>/C-dots as cathode and activated-carbon as anode showing  $C_s$  180.82 F g<sup>-1</sup> at a maximum potential of 1.5 V. Energy density (ED) of 56.5 W h kg<sup>-1</sup> at a power density (PD) of 750 W kg<sup>-1</sup> with excellent capacitance retention were observed. The high  $C_s$  of a-MoS<sub>2</sub>/C-dots can be attributed to amorphous MoS<sub>2</sub>, formation of metallic 1T phase, good charge transport, and strong catalyst support interaction. This synthesis and *in-situ* nano engineering method of MoS<sub>2</sub> may provide a promising technique for developing a high-performance supercapacitor for energy storage applications.



## 9.2. INTRODUCTION

The recent development of renewable energy storage devices has received enormous attention towards the growth of electrochemical energy storage and energy conversion system. Compared to conventional capacitors and batteries, supercapacitors (also named electrochemical capacitors or ultra-capacitors) are able to fulfil the gap between capacitors and batteries, which play an essential role in the field of energy storage devices providing great potential owing to their high PD, great ED, quick charging-discharging process and long life operation which makes them superior for power storage device<sup>1-3</sup>. According to the energy storage mechanism ultra-capacitors are categorized into two types. One is electrical double layer capacitors (EDLC), that store charge on the electrolyte-electrode interface and other one is pseudocapacitor whose charge storage mechanism is based on the reversible oxidation/reduction reaction taking place on the electrode surface<sup>4</sup>. Carbon material has been the preferred material for EDLC type capacitors, while materials such as metal oxides, nitrides, sulphides, phosphides are extensively studied for Pseudocapacitors. Among above materials, synthesis of transition metal dichalcogenides (TMD) and their hybrids, i.e., mixing carbon-based electrode materials with TMD have been beneficial for Pseudocapacitors owing to their higher electrical conductivity and mechanical stability<sup>3</sup>. Notable research has been investigated on TMD (MoS<sub>2</sub>, MoTe<sub>2</sub>, VSe<sub>2</sub>, WS<sub>2</sub>, etc.) along with carbon-based materials and explored their activity towards energy storage applications owing to their specific area, high ED as well as PD, and excellent rate durability<sup>2, 5</sup>. Compared to other transition metal-based chalcogenides, two-dimensional (2D) MoS<sub>2</sub> have gained an aroused attention owing to its morphological flexibility, unique chemical and physical properties, and its high intrinsic conductivity<sup>6</sup> and have various application in catalysis such as

batteries, nano-electronics, and supercapacitors. 2D layered structure of MoS<sub>2</sub> not only provides high SSA for charge accumulation but also diffusion of ions into the interlayer of the MoS<sub>2</sub> nanostructures provides redox property. However, its lower electrical conductance, possible aggregation, poor rate performance, and its lower cyclic stability limit its practical application<sup>7</sup> demanding an alternative way of preparation. To solve the above-mentioned issues, recent studies focus on different forms of MoS<sub>2</sub> having different morphology, such as hollow sphere<sup>8</sup>, nanochains<sup>9</sup>, nanorods<sup>10</sup> etc. by mixing with carbon based materials that are widely used for energy storage devices to increase its conductivity, surface wettability and SSA of molybdenum sulfide.

There are several methods to enhance electrochemical activities of materials, such as the change of composition of materials, morphology change, dimensionality change, crystal phase modification of the materials, etc<sup>11</sup>. In the amorphous phase of a material with no long-range order arrangement of atoms, only several atomic short-range order has generally no grain boundary, isotropic property but has plenty of defects. Amorphous two-dimensional materials (ATMs) has several advantages over crystalline materials: – ATMs have high specific surface area and large number of defects which can act as active sites. They have favourable distance and diffusion paths for reactants and products. The absence of grain boundary and covalent in-plane bond enhances mechanical properties for shape/volume change. In recent times, amorphous materials owing to the presence of a number of active sites, have gained much attention as electrode materials in energy storage applications which can efficiently enhance the storage capacity of the electrode. *In-situ*-nano-engineering is an effective approach to completely utilize the advantages of the amorphous structure to boost electrochemical activity<sup>11</sup>. The electrochemical activity



of electrode materials depends on the structure of the materials, and 2D materials with high electrochemical surface area allow easy diffusion of ions leading to high electrochemical properties<sup>12</sup>. The confinement of electron in two dimension of these materials helps to enhance electron transfer and electrode reactions. It is thus interesting to develop amorphous 2D electrode materials for energy applications. Although the 2D amorphous carbon<sup>13</sup>, amorphous phosphorous<sup>14</sup>, etc., for energy storage and conversion applications are reported in literature, very few reports are available for other amorphous materials<sup>15-17</sup>.

According to the theoretical prediction, depending upon the arrangement of 'S'-atoms, MoS<sub>2</sub> exists in two different symmetries i.e., 2H and 1T having trigonal prismatic (D<sub>3h</sub>) and octahedral (O<sub>h</sub>) geometry, respectively<sup>18</sup>. The most common phase is 2H which is semiconducting with a monolayer having band gap of 1.67 eV, whereas 1T phase is metallic with a conductivity 10<sup>7</sup> times greater than 2H phase and is highly attractive as an electrode material in electrochemical energy conversion as well as storage applications, for instance, electrocatalysts, hydrogen-evolution reaction (HER), supercapacitors, and dye-sensitized solar cells<sup>19</sup>. Acerce et al. reported metallic 1T phase molybdenum disulfide electrode material in an aqueous electrolyte which displays twenty times higher volumetric capacitance than 2H phase<sup>20</sup>. The promising electrochemical activity of 1T phase are owing to their excellent electrical conductivity, intercalation of various ions, and hydrophilicity nature<sup>20</sup>. In the case of HER, higher catalytic activity of 1T molybdenum sulfide is due to the basal plane of 1T MoS<sub>2</sub>, which act as the main active site resulting in the enhancement of the activity of the catalyst<sup>21</sup>. Metallic 1T-MoS<sub>2</sub> shows excellent electronic conductivity, large number of

electrochemical active sites along the basal plane offers intriguing benefits for energy storage applications compared to its semiconducting 2H-MoS<sub>2</sub> phase. Crystalline MoS<sub>2</sub> showing very limited specific capacitance have paid great attention by the researcher, but still, a few research have been made on amorphous MoS<sub>2</sub><sup>3</sup>. Amorphous MoS<sub>2</sub> material shows unique chemical as well as physical properties with isotropic nature and more active sites. Compared to 2H-MoS<sub>2</sub>, shorter Mo-Mo and Mo-S bonds are observed in 1T MoS<sub>2</sub> as well as amorphous MoS<sub>2</sub> thin-film electrode, which is vital for the enhancement of electrochemical property of both 1T and amorphous phase MoS<sub>2</sub> catalyst<sup>22</sup>. The disordered structure in the case of amorphous MoS<sub>2</sub> facilitates the easy diffusion of ions and faradic process. As a result, the SSA of the composite is increased during the electrochemical process, which facilitates the diffusion of K<sup>+</sup> ions into the electrode material. L. Wu et al. reported that 2D amorphous MoS<sub>2</sub> showed much better hydrogen evolution reaction activity than that of crystalline 2H MoS<sub>2</sub> phase<sup>22</sup>. Carbon dots (C-dots) are novel zero-dimensional (0D) carbon-nanoparticles, which have been widely used in applications, for instance, sensors bioimaging and photocatalysis<sup>7</sup>. In recent days C-dots have snatched more attention owing to their cost-effectiveness compared to other carbon nanoparticles, more flexibility, good hydrophilicity, photoluminescence, and stability after doping with other hetero atoms. So, to increase the conductivity and electrochemical activity of the material, utilization of C-dots in composites with other materials provide more pathways and interface for transfer of ions and volume change. The addition of carbon dots into TMD not only improve the cyclic stability, but also enhance the electrical conductivity and wettability of the fabricated composites upon their use as electrode materials<sup>7</sup>. However, the synthesis strategies to develop amorphous 2D materials, especially amorphous MoS<sub>2</sub>, are still very few, and their applications are also

limited due to low conductivity and poor stability. Gao et al. adopted a microwave-assisted synthesis method for the preparation of edge-terminated crystalline molybdenum disulfide for electrochemical hydrogen production<sup>23</sup>. Although both hydrothermal and microwave synthesis strategies have been separately reported for the preparation of MoS<sub>2</sub> but microwave-assisted-solvothermal method for the single-step synthesis of amorphous MoS<sub>2</sub> and in-situ generation/functionalization with C-dots to form a-MoS<sub>2</sub>/C-dots composite is not reported to the best of our knowledge.

Here this chapter present an amorphous MoS<sub>2</sub>/C-dots (a-MoS<sub>2</sub>/C-dots) composite prepared by a facile microwave-assisted hydrothermal heating method that exhibits a high C<sub>s</sub> value of 1368 F g<sup>-1</sup>, which is much greater than the only amorphous MoS<sub>2</sub> or h-MoS<sub>2</sub>/C-dots prepared by simple hydrothermal method. The microwave-assisted hydrothermal method produces amorphous MoS<sub>2</sub> and *in-situ* nano-engineering of a-MoS<sub>2</sub> with C-dots. The a-MoS<sub>2</sub>/C composite was heated at 400 °C to form a more crystalline c-MoS<sub>2</sub>/C-dots composite. The specific capacitance of a-MoS<sub>2</sub>/C-dots is also higher than its crystalline counterpart (c-MoS<sub>2</sub>/C-dots). The high supercapacitor performance and cycling durability of a-MoS<sub>2</sub>/C-dots can be ascribed to the amorphous phase of MoS<sub>2</sub>, allowing easy diffusion of ions, formation of 1T phase, synergetic interaction between a-MoS<sub>2</sub> and C-dots resulting from *in-situ* nano-engineering process, and high SSA, etc.

### **9.3. EXPERIMENTAL SECTION:**

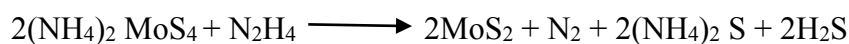
#### **9.3.1. Materials:**

(NH<sub>4</sub>)<sub>2</sub>MoS<sub>4</sub>, 99.97% (Ammonium tetrathiomolybdate), and KOH (potassium hydroxide) was purchased from Sigma-Aldrich. N<sub>2</sub>H<sub>4</sub>·4H<sub>2</sub>O (hydrazine hydrate) and

N, N dimethylformamide (DMF) were purchased from Spectrochem, India. All the chemicals used were without any purification. Deionized (DI) water was obtained from an ultrafiltration system (Milli-Q) at room temperature with a resistivity of 18.2 MΩ cm.

### **9.3.2. Synthesis of a-MoS<sub>2</sub>/C-dots, a-MoS<sub>2</sub>, c-MoS<sub>2</sub>/C, and h-MoS<sub>2</sub>/C-dots**

A total of 35 mg of (NH<sub>4</sub>)<sub>2</sub>MoS<sub>4</sub> was added to a 1:1 mixture of DMF and H<sub>2</sub>O and sonicated for 1 h. Then, 1 ml of hydrazine hydrate was mixed with this solution by sonicating for another 1 h. The whole solution was then transferred into a 50 mL autoclave and heated at 150 °C for 150 minutes under microwave-hydrothermal conditions. The product obtained was washed with H<sub>2</sub>O and ethanol multiple times to get the final product and named a-MoS<sub>2</sub>/C-dots. The (NH<sub>4</sub>)<sub>2</sub>MoS<sub>4</sub> reacts with N<sub>2</sub>H<sub>4</sub> at high temperatures to form MoS<sub>2</sub>.



Amorphous MoS<sub>2</sub> without C-dots (a-MoS<sub>2</sub>) was synthesized under the same microwave-hydrothermal heating condition of (NH<sub>4</sub>)<sub>2</sub>MoS<sub>4</sub> in water solvent; no DMF was used. The (NH<sub>4</sub>)<sub>2</sub>MoS<sub>4</sub> in a 1:1 mixture of DMF and H<sub>2</sub>O was heated under the normal hydrothermal condition at 150 °C for 6 h to form an h-MoS<sub>2</sub>/C-dots composite. The Carbon-dots (C-dots) were synthesized by heating a 1:1 mixture of DMF and water solution at the same temperature for the same duration. The resulting product was dispersed into water for characterization of C-dots. The c-MoS<sub>2</sub>/C-dots composite was formed by the heating of a-MoS<sub>2</sub>/C-dots at 400 °C for 1.5 h with 2 °C/min heating rate under an N<sub>2</sub> atmosphere.

### **9.3.3. Electrode Fabrication:**

A piece of Ni foam of area  $1 \times 1 \text{ cm}^2$  was used for the fabrication of the working electrode. Oxide layers were removed by washing Ni foam in 3M HCl for 30 min, followed by washing in water and ethanol and dried. AC (activated carbon), conductive carbon (CC), and polyvinylidene fluoride (PVDF) binder in N-methyl-2-pyrrolidone (NMP) in 80:10:10 weight % were used for the preparation of homogenous slurry, and the slurry was coated on the  $1 \times 1 \text{ cm}^2$  Ni foam followed by oven drying. The mass of active material loaded on the Ni foam was found to be 1 mg. For the designing of asymmetric supercapacitor (ASC), AC and active material were used as negative and positive electrodes, respectively, and cellulose paper as a separator. For positive and negative electrodes, the weight loading ratio was calculated to be 0.24 (weight loading for positive and negative electrodes were 1 mg and 4.1 mg, respectively).

### **9.3.4. Characterizations:**

The x-ray diffraction data (p-XRD) of as prepared samples were conducted by Bucker DAVINCI D8 ADVANCE diffractometer equipped with a monochromatic radiation source of  $\text{Cu K}\alpha$  ( $\lambda = 0.15406$ ). The composition and morphology of the material was recorded by Field-emission scanning electron microscope (FESEM) system (Carl Zeiss, Germany make, Model: Sigma) and Transmission Electron Microscopy (TEM, JEOL F200) and High-Resolution TEM (HRTEM). VG Microtech was used to record the XPS data with monochromatic  $\text{Mg K}\alpha$  X-ray as the source. All electrochemical measurements were performed by using CorrTest Electrochemical Workstation [Model: CS350]. Quantachrome Instruments (AutosorbIQ-XR (2 Stat.)) Viton was used to determine the Specific surface area by  $\text{N}_2$  adsorption-desorption isotherm.

## **9.4. RESULTS AND DISCUSSIONS:**

### **9.4.1. Morphology and characterization**

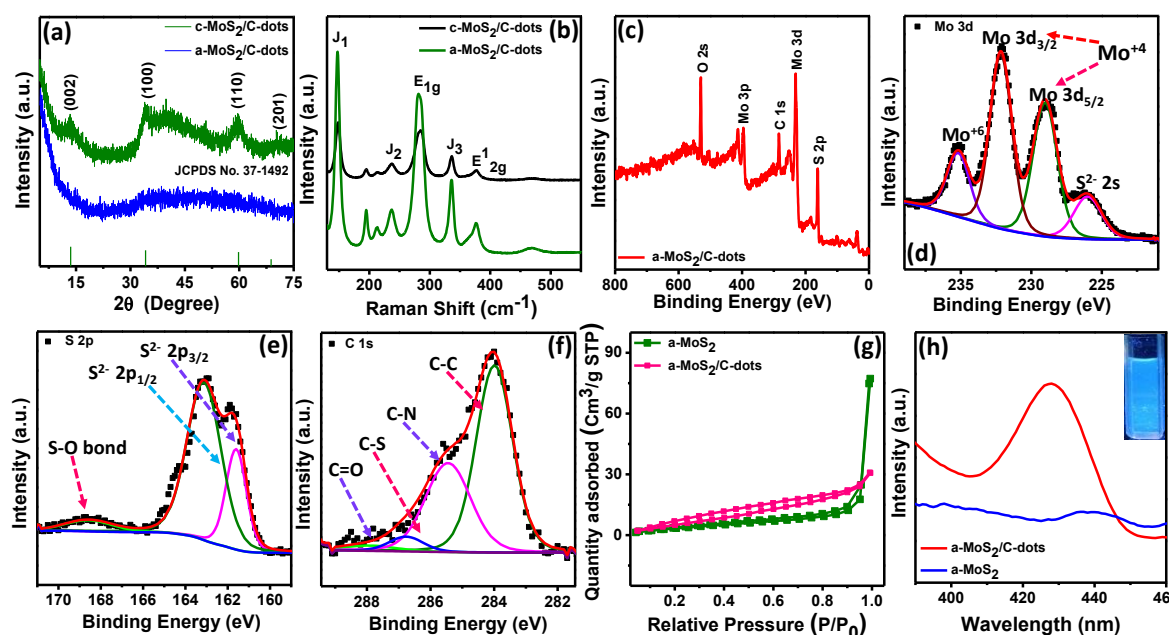
The a-MoS<sub>2</sub>/C-dots was produced by microwave-assisted hydrothermal treatment of (NH<sub>4</sub>)<sub>2</sub>MoS<sub>4</sub> in DMF-water solvent. Calcination of this a-MoS<sub>2</sub>/C-dots composite was done at 400 °C in an N<sub>2</sub> atmosphere to form c-MoS<sub>2</sub>/C-dots composite. The characterization of these two composites was done by using p-XRD (powder X-ray diffraction) technique. Figure 9.1(a) displays the comparison of the p-XRD patterns of a-MoS<sub>2</sub>/C-dots and c-MoS<sub>2</sub>/C-dots composites. In the XRD pattern, a-MoS<sub>2</sub>/C-dots show that there is no prominent peak and only one broad peak indicating the formation of amorphous phase in a-MoS<sub>2</sub>/C-dots. However, XRD pattern of c-MoS<sub>2</sub>/C-dots shows the presence of characteristic peaks at 2θ values 13.9°, 33.5°, 59.3°, and 69.1°, corresponding to (002), (100), (110), and (201) planes of crystalline MoS<sub>2</sub>. These two p-XRD patterns were compared with standard p-XRD data (JCPDS No. 37-1492). This suggested the formation of crystalline phase of MoS<sub>2</sub> in c-MoS<sub>2</sub>/C-dots composite on calcinations at 400 °C in an N<sub>2</sub> atmosphere. These two composites were then characterized by Raman Spectroscopy, presented in Figure 9.1(b). The Raman spectra of these two composites show several peaks – three peaks at 148, 236, and 333 cm<sup>-1</sup> are assigned to J<sub>1</sub>, J<sub>2</sub>, and J<sub>3</sub> vibration of MoS<sub>2</sub>, respectively, indicating the development of the metallic 1T phase of MoS<sub>2</sub>. The peak centered at 376 cm<sup>-1</sup> and 282 cm<sup>-1</sup> corresponds to E<sub>12g</sub>, and E<sub>1g</sub> Raman modes, respectively. These Raman characteristic peaks of 1T-MoS<sub>2</sub> phase in spectra of both the composite suggested the presence of 1T-MoS<sub>2</sub> phase in a-MoS<sub>2</sub>/C-dots and c-MoS<sub>2</sub>/C-dots composites. The valance state, chemical composition, and bonding information of a-MoS<sub>2</sub>/C-dots composite was studied by XPS (X-ray photoelectron spectroscopy) technique. The XPS survey scan for a-MoS<sub>2</sub>/C-dots

composite is presented in Figure 9.1(c), showing the presence of different elements such as Mo, S, C, N, and O. Figure 9.1(d) presents the High-resolution XPS plot for Mo 3d in a-MoS<sub>2</sub>/C-dots. The Mo3d/S2s XPS spectrum can be deconvoluted into four peaks; the 3d<sub>5/2</sub> and 3d<sub>3/2</sub> XPS peaks appeared at 228.94 and 232.176 eV, confirming Mo is in +4 oxidation state (Mo(IV)) at 1T form. The S2s XPS appears at binding energy 226.024 eV is due to S<sup>2-</sup> whereas the peak at a high binding energy of 235.8 eV is due to the presence of Mo<sup>+6</sup> in octahedral configuration<sup>24</sup> indicating the presence of oxides which arises from the surface oxidation during sample preparation and storage. The S2p XPS spectrum was deconvoluted into three peaks. The peaks centered at 161.64 and 162.872 eV corresponds to the presence of S2p<sub>3/2</sub> and S2p<sub>1/2</sub> of S<sup>2-</sup> components of MoS<sub>2</sub><sup>25-26</sup>. The peak at 168.65 eV indicates the S-O bond arises due to partial oxidation of a-MoS<sub>2</sub>/C-dots, which is presented in Figure 9.1(e)<sup>27</sup>. The stoichiometry of a-MoS<sub>2</sub>/C-dots was determined from XPS spectra and is calculated to be MoS<sub>2.4</sub>. Figure 9.1(f) illustrates the high-resolution XPS spectrum of C1s, deconvoluted into 4 peaks. The peaks centered at 284.2, 285.74, 286.84, and 287.94 eV are ascribed to C-C, C-N, C-S, and C=O bonds, respectively. Figure S9.1 displays a high-resolution XPS spectrum of N1s/Mo3p. The peaks at 394.8 eV, 396.9 eV, 398.7 eV, and 401.5 eV can be assigned to Mo 3p, pyridinic N, pyrrolic N, and graphitic N, respectively<sup>28</sup>. BET (Brunauer-Emmett-Teller) SSA (Specific surface area), and average pore size distribution of a-MoS<sub>2</sub>/C-dots and a-MoS<sub>2</sub> composites are investigated by using N<sub>2</sub> adsorption and desorption isotherms at 77K. Figure 9.1(g) depicts the N<sub>2</sub> desorption/adsorption profile of a-MoS<sub>2</sub>/C-dots and a-MoS<sub>2</sub> composites. The a-MoS<sub>2</sub>/C-dots composite shows type IV isotherm with a typical H3 hysteresis loop after pressure P/P<sub>0</sub> > 0.8, suggesting the material is mesoporous<sup>29</sup>. BET SSA for a-MoS<sub>2</sub>/C-dots and a-MoS<sub>2</sub> composites are obtained to be 25.36 m<sup>2</sup>g<sup>-1</sup> and

12.7 m<sup>2</sup>g<sup>-1</sup> respectively. a-MoS<sub>2</sub>/C-dots showing higher SSA compared to a-MoS<sub>2</sub> composites could provide more reaction sites for the energy storage application. The presence of C-dots was confirmed by photoluminescence (PL) studies. The PL spectrum of these two composites is given in Figure 9.1(h). The strong fluorescence peak of a-MoS<sub>2</sub>/C-dots appeared at 428 nm, and PL emission intensity is very low in case of a-MoS<sub>2</sub>. The inset of Figure 9.1(h) shows the photograph of a-MoS<sub>2</sub>/C-dots under UV light. The a-MoS<sub>2</sub>/C-dots showed intense blue emission, confirming the presence of C-dots in the a-MoS<sub>2</sub>/C-dots composite. The excitation-dependent fluorescence emission of C-dots produced from DMF under the same microwave-hydrothermal condition (Figure S9.2 (a-c)) also confirmed in-situ formation of C-dots from solvent (DMF) during the synthesis of MoS<sub>2</sub>.

The surface morphology of a-MoS<sub>2</sub>/C-dots composite was examined by Transmission electron microscopy (TEM) and Scanning electron microscopy (SEM) studies. The low-resolution TEM image of a-MoS<sub>2</sub>/C-dots composite is provided in Figure 9.2(a, b), which shows the formation of thin nano-sheets, and these thin sheets are interconnected to each other. The selected area electron diffraction (SAED) image of a-MoS<sub>2</sub>/C-dots as presented inset of Figure 9.2(c), show weak diffraction ring suggesting formation of amorphous phase. The high magnified TEM image shows that the absence of ordered phase confirmed the two-dimensional, amorphous MoS<sub>2</sub> structure. In addition, very few lattice fringes with d value of 0.62 nm end edge corresponding to plane (002) of MoS<sub>2</sub> are observed, which is presented in Figure 9.2(d).





**Figure 9.1.** XRD pattern of (a) a-MoS<sub>2</sub>/C-dots, and c-MoS<sub>2</sub>/C-dots, (b) Raman spectra of a-MoS<sub>2</sub>/C-dots, and c-MoS<sub>2</sub>/C-dots, (c) Wide XPS spectrum of a-MoS<sub>2</sub>/C-dots, High-resolution XPS spectra of (d) Mo 3d, (e) S 2p, and (f) C 1s respectively, (g) N<sub>2</sub> desorption/adsorption isotherm of a-MoS<sub>2</sub>/C-dots and a-MoS<sub>2</sub> composites, and (h) photoluminescence spectra of a-MoS<sub>2</sub>/C-dots and a-MoS<sub>2</sub> excited at 240 nm.

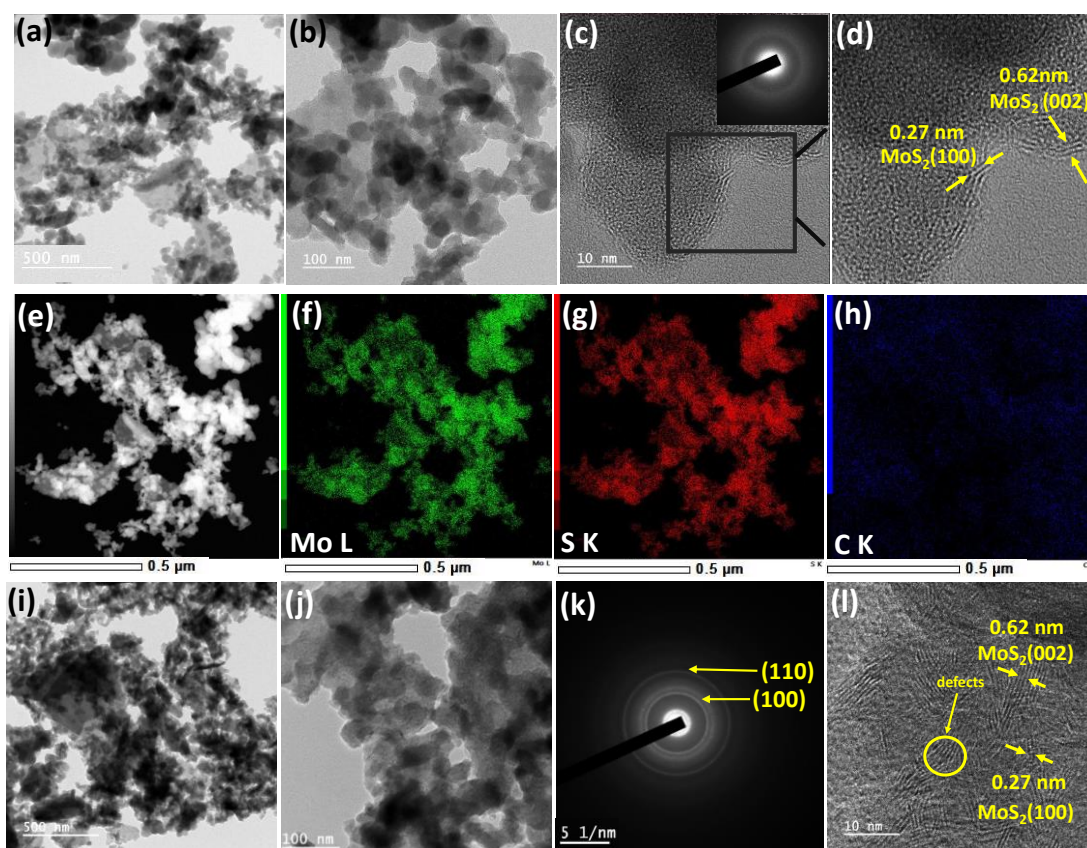
Figure 9.2(e) presents the STEM image of a-MoS<sub>2</sub>/C, while Figure 9.2(f-h) shows STEM mappings showing presence of Mo, S, and C, respectively, with a uniform distribution of all the elements. Mo: S ratio was calculated from the TEM EDX data and was found to be 1: 2.46 (Stoichiometry of MoS<sub>2.46</sub>), which matches with Mo: S calculated from the XPS analysis (Table S9.1). Table S9.1 represents the stoichiometry of Mo and S as determined by XPS and TEM EDX in a-MoS<sub>2</sub>/C-dots composite. Annealing is a process to improve crystallinity of amorphous materials. The annealing of a-MoS<sub>2</sub>/C-dots was done in N<sub>2</sub>-atmosphere at 400 °C for 1.5 h to form c-MoS<sub>2</sub>/C-dots composite. The low-resolution TEM show that size of two-dimensional sheets is increased as shown in

Figure 9.2 (i, j). The SAED image of c-MoS<sub>2</sub>/C-dots is presented in Figure 9.2 (k). It shows that, on calcination at 400 °C for 1.5 h, the diffraction patterns (rings) got more intense and discrete suggesting significant improvement of crystallinity of two-dimensional sheets in c-MoS<sub>2</sub>/C-dots. The HRTEM image of c-MoS<sub>2</sub>/C-dots (Figure 9.2 (l)) shows the presence of lattice fringes with *d* values of 0.62 nm and 0.27 nm corresponding to the (002) and (100) planes of MoS<sub>2</sub>. These results indicate that calcination of a-MoS<sub>2</sub>/C-dots helped to improve crystallinity of two-dimensional MoS<sub>2</sub> sheets significantly. But the discontinuous and twisted lattice fringes defects are observed in Figure 9.2 (l), suggesting low crystallinity of these sheets even after heating at 400 °C. Figure S9.3 represents the STEM image and corresponding elemental mapping of Mo, S, and C in c-MoS<sub>2</sub>/C-dots composites showing uniform distribution of elements.

Figure S9.4 (a-d) represents the SEM image of a-MoS<sub>2</sub>/C-dots, c-MoS<sub>2</sub>/C-dots, h-MoS<sub>2</sub>/C-dots and a-MoS<sub>2</sub>. The a-MoS<sub>2</sub>/C-dots show the presence of 2D nano-sheet-like morphology of MoS<sub>2</sub> as presented in Figure S9.4(a). The 2D MoS<sub>2</sub> layers are folded to form 3D flower-like morphology for c-MoS<sub>2</sub>/C and h-MoS<sub>2</sub>/C-dots composites (Figure S9.4(b) and (c)). Figure S9.4(d) shows the aggregation of particles without carbon support in a-MoS<sub>2</sub> composite. The a-MoS<sub>2</sub>/C-dots composite shows better electrochemical performances. The 2D nanosheets provide high accessible surface area that increases the contact between the electrolyte and their surface-active sites, facilitating the fast electron; hence the electrical conductivity and electrochemical performance of a-MoS<sub>2</sub>/C-dots are enhanced<sup>30</sup>.

The h-MoS<sub>2</sub>/C-dots, synthesized by a simple hydrothermal method, was also characterized by p-XRD and TEM analysis. The p-XRD and TEM images of h-MoS<sub>2</sub>/C-dots and a-MoS<sub>2</sub> (without C-dots) were given in Figure S9.5. The absence of diffraction

peaks in the p-XRD pattern of a-MoS<sub>2</sub>, and the presence of diffraction peaks corresponding to (100) and (110) planes of MoS<sub>2</sub> indicate h-MoS<sub>2</sub>/C-dots is more crystalline than a-MoS<sub>2</sub> and a-MoS<sub>2</sub>/C-dots. The TEM image shows the assembly of thin MoS<sub>2</sub> sheets in h-MoS<sub>2</sub>/C-dots, whereas aggregated nanostructures are formed in a-MoS<sub>2</sub> without C-dots. The presence of diffraction peaks in p-XRD pattern of h-MoS<sub>2</sub>/C-dots suggested more crystallinity as compared to that of a-MoS<sub>2</sub>/C-dots.



**Figure 9.2.** (a, b) Low-resolution TEM and, (c) HRTEM images (inset shows the SAED pattern), (d) Enlarged view of HRTEM image, (e) STEM image and corresponding elemental mapping of (f) Mo, (g) S, and (h) C in a-MoS<sub>2</sub>/C-dots Composites. (i, j) Low-resolution TEM images, (k) SAED pattern, and (l) HRTEM image of c-MoS<sub>2</sub>/C-dots Composites showing defects.

### 9.4.2. Electrochemical Analysis

The electrochemical behaviour of synthesized composites was analysed by CV (cyclic voltammetry) and GCD (Galvanostatic charge-discharge) curve using electrochemical analyser in 2M KOH aqueous electrolyte at room temperature. For three-electrode (half-cell) configuration platinum wire, Hg/HgO, and a-MoS<sub>2</sub>/C-dots coated on 1 cm × 1 cm Ni foam were used as counter, reference, and working electrode, respectively.

Specific capacitance ( $C_s$ ) can be obtained from the CV curve by using the equation 9.1<sup>31</sup>

$$C_s = \frac{\int I dV}{2m\Delta Vv} \quad (9.1)$$

$C_s$  can be calculated from GCD curve by using equation 9.2<sup>31</sup>

$$C_s = \frac{I\Delta t}{m\Delta V} \quad (9.2)$$

Here  $C_s$ ,  $I$ ,  $\Delta t$ ,  $m$ , and  $\Delta V$  account for capacitance ( $F\ g^{-1}$ ), current applied (mA), discharge duration (sec), weight of a-MoS<sub>2</sub>/C-dots Composites (mg), and operating voltage range (V), respectively.  $\int I\ dv$  stands for area under CV curve, and  $v$  represents the sweep rate ( $mV\ s^{-1}$ ).

For ASC cell, the as-prepared material (a-MoS<sub>2</sub>/C-dots) acts as cathode, and commercial Activated Carbon (AC) acts as anode, assembled in a CR2032 coin cell. The full cell is represented as a-MoS<sub>2</sub>/C-dots //AC. The weight ratio of a-MoS<sub>2</sub>/C-dots and AC was calculated so as to balance the charge storage by using equation 9.3<sup>31</sup>.

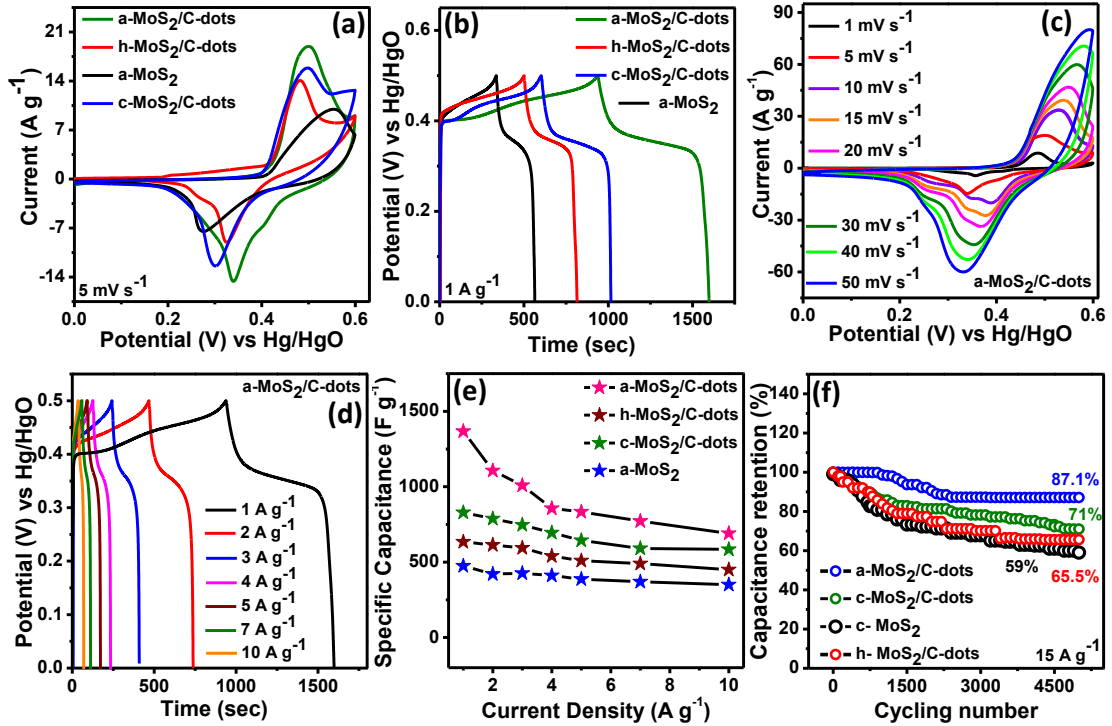
$$\frac{m^-}{m^+} = \frac{C^+\Delta V^+}{C^-\Delta V^-} \quad (9.3)$$

Here  $m^+$  was the mass (mg),  $C^+$  and  $C^-$  were the specific capacitance of a-MoS<sub>2</sub>/C-dots and AC, respectively,  $\Delta V^+$  and  $\Delta V^-$  were the potential range of positive (a-MoS<sub>2</sub>/C-dots) and negative (AC) electrode respectively and  $m^-$  was the weight of anode<sup>31</sup>.

$$ED = \frac{C_s(\Delta V)^2}{7.2} \quad (9.4)$$

$$PD = \frac{E}{\Delta t} \times 3600 \quad (9.5)$$

Here  $\Delta V$  and  $C_s$  stand for voltage range in Volt and specific capacitance of ASC in  $F\ g^{-1}$ , respectively and  $\Delta t$  is the discharge duration in sec.



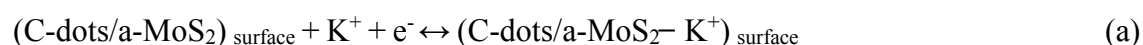
**Figure 9.3.** (a, b) Comparison of CV and GCD plot profiles for a-MoS<sub>2</sub>/C-dots, a-MoS<sub>2</sub>, c-MoS<sub>2</sub>/C-dots, and h-MoS<sub>2</sub>/C-dots composites at sweep rate of 5 mV s<sup>-1</sup> and 1 A g<sup>-1</sup> current. (c) CV profile of a-MoS<sub>2</sub>/C-dots at different scan rates (1-50 mV s<sup>-1</sup>). (d) GCD profile of a-MoS<sub>2</sub>/C-dots (1-10 A g<sup>-1</sup>). (e) C<sub>s</sub> Comparison Plot of a-MoS<sub>2</sub>/C-dots, a-MoS<sub>2</sub>, c-MoS<sub>2</sub>/C-dots, and h-MoS<sub>2</sub>/C-dots composites w.r.t current. (f) Percentage capacitance retention (%) w.r.t cycling number for a-MoS<sub>2</sub>/C-dots, c-MoS<sub>2</sub>/C-dots, h-MoS<sub>2</sub>/C-dots, and a-MoS<sub>2</sub> composites at current of 15 A g<sup>-1</sup>.

**Table 9.1.** Comparison of electrochemical performance of a-MoS<sub>2</sub>/C-dots electrode material with previously reported literature.

Electrode material	C <sub>s</sub> (F g <sup>-1</sup> ) of single Electrode	C <sub>s</sub> retention after cycling performance (%)	cycling number	Ref.
MoS <sub>2</sub> /PPy nanocomposites	654 (10 mV s <sup>-1</sup> )	95	500	32
MoS <sub>2</sub> @G/AC nanofibers	334 (0.5 A g <sup>-1</sup> )	83.8	5000	33
MoS <sub>x</sub> /GCNT/CP	414 (0.67 A g <sup>-1</sup> )	80	500	34
3D NiS-rGO aerogel	852 (2 A g <sup>-1</sup> )	82	1000	3
MoS <sub>2</sub> /NG	245 (0.25 A g <sup>-1</sup> )	91.3	1000	35
defective MoS <sub>2</sub>	379 (1 A g <sup>-1</sup> )	92	3000	36
Oxygen incorporated MoS <sub>2</sub> nanosheets	246 (0.5 A g <sup>-1</sup> )	60	20000	37
MoS <sub>2</sub> /rGO nanohybrids	850 (1 A g <sup>-1</sup> )	95.3	10000	38
MoS <sub>2</sub> nanosheets petal-like MoS <sub>2</sub>	811 (0.1 A g <sup>-1</sup> )	82.7	1000	39
1T-MoS <sub>2</sub> hydrogel	147 (1 A g <sup>-1</sup> )	90	5000	40
a-MoS <sub>2</sub> /C-dots	1368 (1 A g <sup>-1</sup> )	87.1	5000	This work

Figure 9.3(a) displays the comparison CV profiles of a-MoS<sub>2</sub>/C-dots, a-MoS<sub>2</sub>, c-MoS<sub>2</sub>/C-dots, and h-MoS<sub>2</sub>/C-dots obtained in 2M KOH aqueous electrolyte at 5 mV s<sup>-1</sup> in a potential ranging from 0-0.6 V to investigate the capacitive response of the composites. All the CV profiles show redox peaks demonstrating the pseudocapacitive charge storage process. Among all the three CV curves, area under the CV curve and intense redox peaks for a-MoS<sub>2</sub>/C-dots is highest compared to other composite showing excellent faradic behaviour and highest capacitance value. The CV curve area of a-MoS<sub>2</sub>/C-dots is higher than that of the other composites, indicating a-MoS<sub>2</sub>/C-dots possess excellent electrochemical activity. Moreover, the more or less shifting of the redox peak position for different electrodes can be ascribed to the changed morphology of these samples that influences the ion transfer rate between the electrode and electrolyte. 2D nanosheets of a-MoS<sub>2</sub>/C-dots provide high accessible surface area that increases the contact between the electrolyte and their surface-active sites, enhanced electrical conductivity, and facilitates the fast electron. The morphologies of these catalysts are different. It is reported that electrochemical performance is affected by the morphologies of the composites<sup>30</sup>. The C<sub>s</sub> values were calculated by integrating the area under the CV profiles for a-MoS<sub>2</sub>/C-dots, a-MoS<sub>2</sub>, c-MoS<sub>2</sub>/C-dots, and h-MoS<sub>2</sub>/C-dots by using equation 9.1 and were obtained to be 667.98, 355.97, and 530.1, and 359.3 F g<sup>-1</sup> respectively under a sweep rate of 5 mV s<sup>-1</sup>.

The lower peak separation in a-MoS<sub>2</sub>/C-dots compared to other composites was because of the charge transfer process, which confirms the superior performance of a-MoS<sub>2</sub>/C-dots in 2M KOH electrolyte. Two kinds of non-faradic and faradic reactions in a-MoS<sub>2</sub>/C-dots were possible which is represented as follows<sup>41</sup>:







The Faradic process is favored by Mo atoms whereas the non-faradic reaction is associated with the desorption/adsorption of electrolyte ions ( $\text{K}^+$ ) on the surface of the active material. The comparison of non-linear GCD profiles is presented in Figure 9.3(b) for a-MoS<sub>2</sub>/C-dots, a-MoS<sub>2</sub>, c-MoS<sub>2</sub>/C-dots, and h-MoS<sub>2</sub>/C-dots. The  $C_s$  values were calculated from the GCD curves by using equation 9.2 and were found to be 1368, 475, 829, and 635 F g<sup>-1</sup> under 1 A g<sup>-1</sup> current density in a voltage range of 0-0.5V. This suggests that the specific capacitance of a-MoS<sub>2</sub>/C-dots is strongly dependent on synthesis method, presence of C-dots, and crystal phase of MoS<sub>2</sub>. The in-situ nano-engineering played an important role in improving supercapacitor performances: the  $C_s$  values for a-MoS<sub>2</sub>/C-dots (1368 F g<sup>-1</sup>) were ~2.9 times greater than that of a-MoS<sub>2</sub> (without C-dots) suggesting that *in-situ* modification of amorphous MoS<sub>2</sub> with C-dots helps to improve the supercapacitor performance. The C-dots are formed from solvent DMF during microwave-hydrothermal synthesis, and then, nano-engineering of MoS<sub>2</sub> sheets with C-dots during synthesis leads to formation of a-MoS<sub>2</sub>/C-dots. The enhanced activity of a-MoS<sub>2</sub>/C-dots as compared to a-MoS<sub>2</sub> could be due to strong synergistic interaction between MoS<sub>2</sub> and C-dots. As discussed in the previous section that the a-MoS<sub>2</sub>/C-dots was produced by microwave-hydrothermal method, whereas h-MoS<sub>2</sub>/C-dots is formed during normal hydrothermal heating. The  $C_s$  value of a-MoS<sub>2</sub>/C-dots is also 1.65 times higher than that of crystalline c-MoS<sub>2</sub>/C-dots. a-MoS<sub>2</sub>/C-dots were calcinated at 400 °C to form c-MoS<sub>2</sub>/C-dots. The size of sheets as well as crystalline nature of MoS<sub>2</sub> sheets was increased in c-MoS<sub>2</sub>/C-dots. This indicates that amorphous MoS<sub>2</sub> is better compared to crystalline MoS<sub>2</sub> for energy storage applications. As discussed in the previous section that the a-MoS<sub>2</sub>/C-dots were produced by microwave-



hydrothermal method, whereas h-MoS<sub>2</sub>/C-dots is formed by normal hydrothermal heating. The C<sub>s</sub> value for a-MoS<sub>2</sub>/C-dots is ~2.15 times higher than that of h-MoS<sub>2</sub>/C-dots suggesting that capacitor performance of these catalysts is strongly dependent on synthesis method. Microscopic and fluorescence studies showed that size, crystallinity of MoS<sub>2</sub> sheets are higher, and presence of C-dots is less in h-MoS<sub>2</sub>/C-dots than that of a-MoS<sub>2</sub>/C-dots. Table S9.2 represents the comparison of electrochemical performance of the as-prepared materials. The enhanced C<sub>s</sub> values for a-MoS<sub>2</sub>/C-dots can be attributed to (i) disordered structure, which provides large number of active sites for the passage of electrolyte (OH<sup>-</sup>) across the core region, (ii) the redox reaction occurring both on the surface and inside the core of the material<sup>42</sup>. Figure 9.3(c) represents the CV profile of a-MoS<sub>2</sub>/C-dots at sweep rate of 1-50 mV s<sup>-1</sup> at a voltage range of 0-0.6V. The good reversibility of the composite was confirmed by the regularity in reduction and oxidation peaks in CV curves. CV curves have similar type of nature and strong redox peaks showing pseudocapacitive characteristics of the composite. For fast potential sweep rate (i.e., with increase in sweep rate), the oxidation peaks shift to more positive voltage side (during charging), corresponding to higher energy supply, and the reduction peaks shift to more negative voltage side (during discharging) corresponding to the chemical reaction taking place between a-MoS<sub>2</sub>/C-dots and electrolyte<sup>41</sup> indicating more charge diffusion polarization within the electrode material owing to enhanced charge storage property<sup>43</sup>. The enhancement in current response with sweep rate confirms the enhancement of area under the CV profile<sup>41</sup>. Another reason for the shift of oxidation peak towards higher and reduction peak at lower voltage with increase in sweep rate from 1 to 50 mV s<sup>-1</sup> may be due to the change in internal resistance, better charge, and mass transfer, and improved electron conduction in a-MoS<sub>2</sub>/C-dots composites. The GCD curves of a-MoS<sub>2</sub>/C-dots at different currents (1-10 A g<sup>-1</sup>) having non-linear profile are

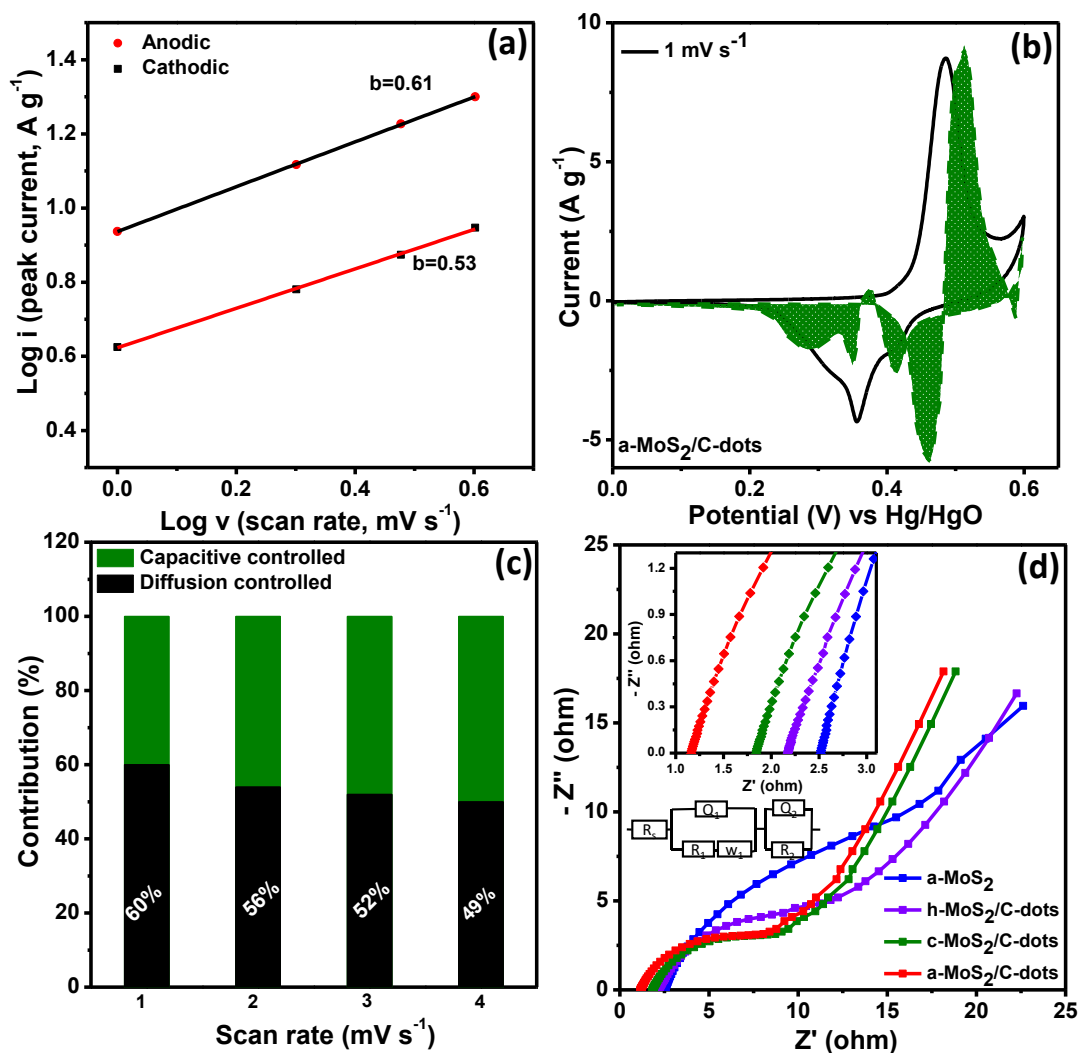
presented in Figure 9.3(d) indicating the Faradic behavior of the composite. A  $C_s$  value of 1368 F g<sup>-1</sup> was obtained under 1 A g<sup>-1</sup> current. At higher current of 5 A g<sup>-1</sup>, a  $C_s$  value of 833.03 F g<sup>-1</sup> is obtained suggesting 60.89 % rate retention of its initial capacitance indicating a good rate capability maintained of a-MoS<sub>2</sub>/C-dots electrode. At lower current density, a higher specific capacitance value indicates the easy diffusion of electrolyte ions across the electrode surface and opposite phenomena was noticed as the effective interaction between the electrode-electrolyte decreases at higher current density. Comparison of electrochemical performance of a-MoS<sub>2</sub>/C-dots, a-MoS<sub>2</sub>, h-MoS<sub>2</sub>/C-dots, and c-MoS<sub>2</sub>/C-dots composites are presented in tabular form (Table S9.2). Figure 9.3(e) displays the  $C_s$  (F g<sup>-1</sup>) plot with respect to current (A g<sup>-1</sup>) for a-MoS<sub>2</sub>/C-dots, a-MoS<sub>2</sub>, c-MoS<sub>2</sub>/C-dots, and h-MoS<sub>2</sub>/C-dots composites.  $C_s$  of a-MoS<sub>2</sub>/C-dots are greater than that of other MoS<sub>2</sub> composites, and the high  $C_s$  values of a-MoS<sub>2</sub>/C-dots composites correlate with the CV results. GCD curve for bare Ni foam was carried out at 1 mA current in a potential range of 0-0.5V, showing almost no capacitance contribution (quite negligible) of the current collector in 2M KOH (Figure S9.6). Figure 9.3(f) illustrates the cyclic durability for a-MoS<sub>2</sub>/C-dots single electrode, which exhibits an excellent 87.1 % cyclability of the initial value at the end of 5000 GCD cycles under a current of 15 A g<sup>-1</sup>. The cyclic durability of c-MoS<sub>2</sub>/C-dots, h-MoS<sub>2</sub>/C-dots, and a-MoS<sub>2</sub> were also performed, showing 71, 65.5, and 59% retention of initial  $C_s$  values after 5k cycles. High cyclic durability for a-MoS<sub>2</sub>/C-dots can be explained on the basis of isotropic nature in amorphous phase than crystalline phase<sup>42</sup> and strong synergetic interaction between the a-MoS<sub>2</sub> and C-dots stabilize amorphous MoS<sub>2</sub> composite in a-MoS<sub>2</sub>/C-dots. The presence of some high purity of metallic 1T phase and *in-situ*-nano-

engineering with C-dots improved the cyclability, wettability, and conductivity of MoS<sub>2</sub> in a-MoS<sub>2</sub>/C-dots.

The post electrochemical stability characterization of a-MoS<sub>2</sub>/C-dots catalyst was carried out by p-XRD and SEM measurements. As presented in Figure S9.7 (a), the post-stability XRD pattern shows absence of any peaks for MoS<sub>2</sub>, which shows that the material still remains in the amorphous phase even after 5K durability test. The additional peaks correspond to the electrolyte (KOH), and substrate (Ni foam) used for the stability performance. The SEM image of the electrode material after electrochemical stability test is presented in Figure S9.7 (b), showing no such significant change in the morphology of the a-MoS<sub>2</sub>/C-dots composite, indicating that the structure and chemical composition of the composite remains unaltered after a long-term cyclic test. For a better understanding of the storage mechanism, kinetic analyses of the a-MoS<sub>2</sub>/C-dots electrode were further carried out. Figure S9.8 shows the CV curves from 1-4 mV s<sup>-1</sup> showing pair of redox peaks indicating battery like behaviour of the electrode material. The peak currents (*i*) are plotted as a function of square root of sweep rate (*v*<sup>b</sup>) plotted based on the following equation<sup>44</sup>:

$$i = kv^b$$

Here *i* stands for current (A g<sup>-1</sup>), *v* is sweep rate (mV s<sup>-1</sup>), and *k* and *b* are constants. Value of *b* gives information about charge storage kinetics. When *b* approaches to 1, the storage kinetics is capacitive controlled, and when *b* approaches to 0.5 diffusion-controlled behaviour is dominant. The value of *b* can be obtained by plotting to log *i* vs. log *v*<sup>45</sup> i.e., log *i* = log *k* + *b* log *v*.



**Figure 9.4.** (a) Plot of  $\log i$  w.r.t  $\log v$ . (b) CV profile of a-MoS<sub>2</sub>/C-dots differentiating diffusive contribution and capacitive contribution at 1 mV s<sup>-1</sup> sweep rate. (c) Pseudocapacitive contribution of a-MoS<sub>2</sub>/C-dots by varying scan rates. (d) EIS plot profile of a-MoS<sub>2</sub>/C-dots, a-MoS<sub>2</sub>, c-MoS<sub>2</sub>/C-dots, and h-MoS<sub>2</sub>/C-dots composites in 2M KOH.

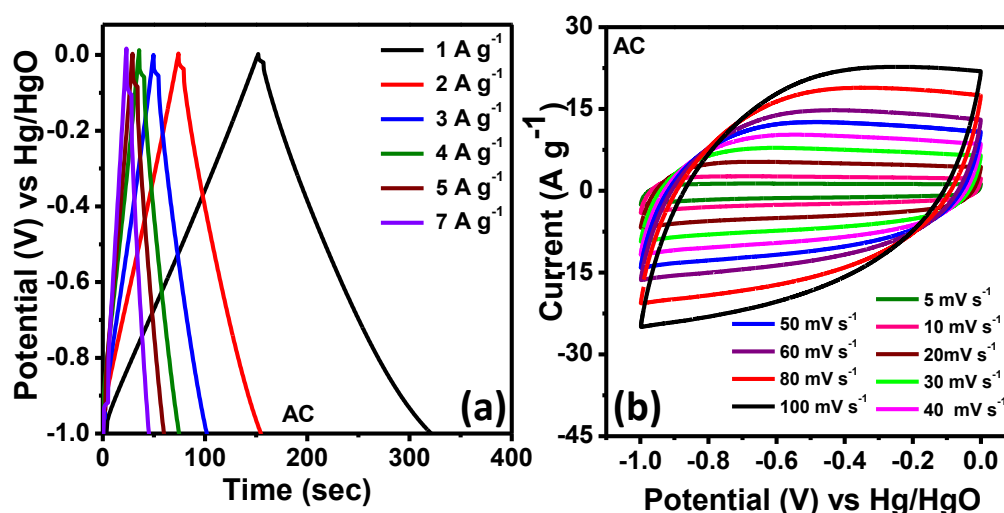
The  $b$  value for a-MoS<sub>2</sub>/C-dots are obtained to be 0.61 and 0.53, respectively, indicating the charge storage process is dominant by diffusion-controlled process i.e., battery-type nature of the electrode which is shown in Figure 9.4(a). CV currents are classified into 2 types, ion diffusion-controlled current contribution ( $k_2v^{1/2}$ ) and capacitive contribution

( $k_1v$ ). Capacitive contribution demonstrates non-insertion capacity, related to both EDLC contribution and fast faradaic pseudocapacity (surface ion desorption/adsorption process) and varies linearly with sweep rate ( $v$ ), and diffusion contribution is due to the diffusion-controlled intercalation process, which varies linearly with  $v^{1/2}$ . In order to quantify the capacitive and diffusion contributions, the following equation is used at a certain scan rate which is presented below in equation 9.6<sup>31</sup>

$$i(V) = k_1v + k_2v^{1/2} \quad (9.6)$$

Where  $k_1$  and  $k_2$  are constant, and  $v$  represents the sweep rate.  $k_2v^{1/2}$  and  $k_1v$  present the diffusion-controlled and capacitive current, respectively.  $k_1$  and  $k_2$  can be evaluated by using the CV curve at lower sweep rate. The slope ( $k_1$ ) can be achieved by plotting  $i$  vs.  $v^{1/2}$ . At slow sweep rate, the fraction of capacitance contribution was obtained by using the equation mentioned above. A CV curve at  $1 \text{ mV s}^{-1}$  and capacitive contribution curve is presented in Figure 9.4 (b), showing overflow of the capacitive contribution curve. We think that this overflow of the capacitive contribution curve from original CV curve is due to the relationship of polarization, the potential will move at different sweep rates<sup>44</sup>. In the near peak current, the value of  $i$  will be different at same potential. This could be the reason of capacitive contribution curve is overflowing from original CV curve<sup>44</sup>. The diffusion contribution for a-MoS<sub>2</sub>/C-dots composites at  $1 \text{ mV s}^{-1}$  was calculated to be 60%, and contribution at 2, 3, and  $4 \text{ mV s}^{-1}$  scan rates were obtained to be 56, 52, and 49 %, respectively, showing a typical battery type faradic behaviour<sup>46</sup> of a-MoS<sub>2</sub>/C-dots composites as shown in Figure 9.4 (c). Electrochemical Impedance Spectroscopy (EIS) was performed to demonstrate the ion transport and conductivity for the as-synthesized composites in 2M KOH electrolyte at a frequency range of 100 kHz to 0.1Hz under OCP (open circuit potential). The experiment was carried out in a 3 electrode setup with an AC amplitude of 10 mV. The equivalent series resistance ( $R_s$ ) includes the material

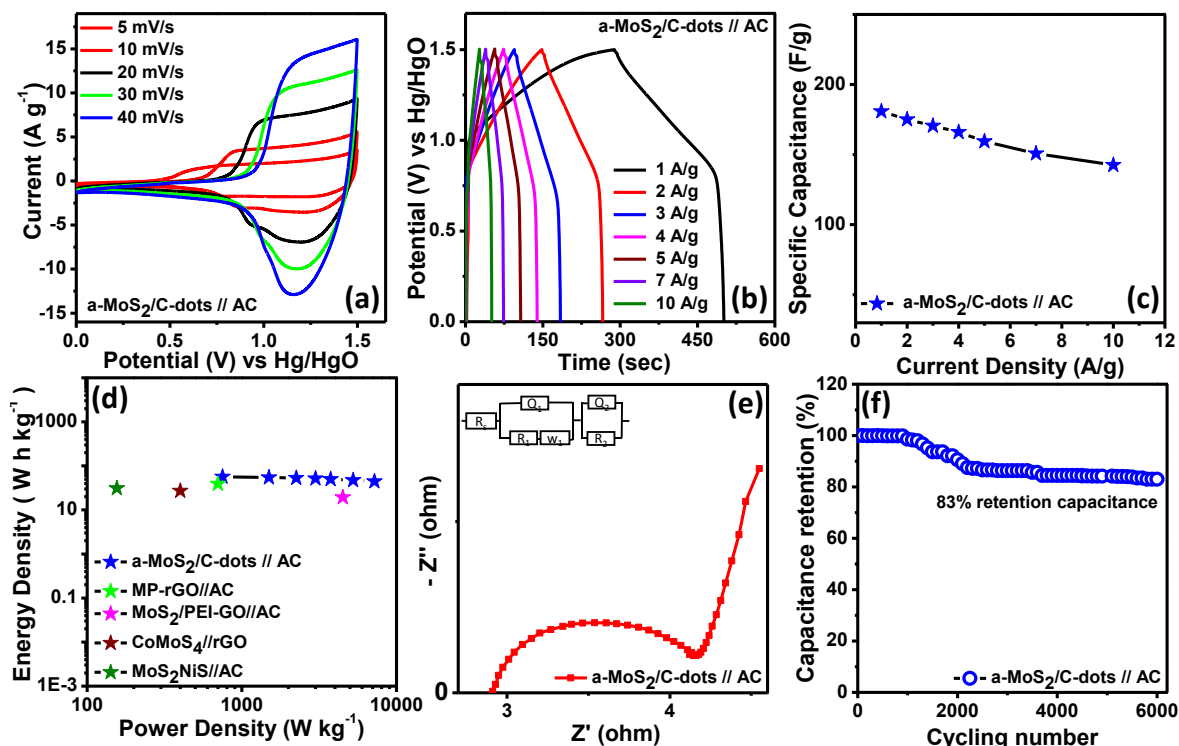
resistance, i.e., current collector, electrolyte, and electrode material, and the contact resistance between current collector and electrode.  $R_s$  for a-MoS<sub>2</sub>/C-dots, a-MoS<sub>2</sub>, c-MoS<sub>2</sub>/C-dots, and h-MoS<sub>2</sub>/C-dots are measured to be 1.18, 2.54, 1.86, and 2.2  $\Omega$  (Figure 9.4 (d)) suggesting lower resistance and enhanced conductivity for a-MoS<sub>2</sub>/C-dots compared to other electrode materials. The vertical line at the lower frequency range for a-MoS<sub>2</sub>/C-dots compared to other MoS<sub>2</sub> composites shows faster electron transfer. The charge transfer resistance ( $R_{CT}$ ) for a-MoS<sub>2</sub>/C-dots, a-MoS<sub>2</sub>, c-MoS<sub>2</sub>/C-dots, and h-MoS<sub>2</sub>/C-dots are found to be 7.16, 15.6, 13.5, and 9.23  $\Omega$  respectively. Lower  $R_{CT}$  for a-MoS<sub>2</sub>/C-dots indicates rapid electron transfer on the surface during the electrochemical reaction and excellent rate capability<sup>24</sup>. The  $R_s$  values for all composites were lesser than 3  $\Omega$ .  $R_s$  values were obtained from Nyquist plot by fitting the equivalent circuit. Lower  $R_{CT}$  value of a-MoS<sub>2</sub>/C-dots compared to other MoS<sub>2</sub> composites are due to strong synergistic contribution of a-MoS<sub>2</sub> and carbon support.



**Figure 9.5.** (a-b) GCD profiles under 1-7 A g<sup>-1</sup> current and CV profiles at of 5-100 mV s<sup>-1</sup> sweep rate for AC.

So as to use AC as anode, we have also measured CV and GCD measurements of AC. Figure 9.5 (a, b) shows the GCD curve at different current and CV curve of AC at different scan rates with voltage ranging from 0 to -1 V. The electrochemical performance of AC is done by using platinum rod (counter), Hg/HgO (reference), and AC (working electrode) in a three-electrode setup configuration. The CV curve shows a symmetrical rectangular nature having no reduction-oxidation peaks, and the triangular GCD profiles indicate the EDLC-type behaviour of AC.  $C_s$  values for AC were calculated to be 248.3 F g<sup>-1</sup> at voltage rate of 5 mV s<sup>-1</sup> and 166.8 F g<sup>-1</sup> (-1.0-0.0 V) under current of 1 A g<sup>-1</sup> indicating AC can be used as appropriate anode material for supercapacitor applications.

To further research the practicability of a-MoS<sub>2</sub>/C-dots electrode material, a-MoS<sub>2</sub>/C-dots electrode (used as cathode) and AC electrode (anode material) were assembled into ASC device denoted as a-MoS<sub>2</sub>/C-dots //AC in a CR2032 coin cell configuration, while aqueous solution of 2 M potassium hydroxide was used as electrolyte and glass microfiber filter paper used as a separator. Figure S9.9 represents the CV profiles of AC and a-MoS<sub>2</sub>/C-dots at a sweep rate of 5 mV s<sup>-1</sup> in a voltage ranging from 0.0 to -1.0V and 0-0.6 V, respectively. CV cycles for the ASC device were carried out at voltage ranging from 1 to 1.5 V, showing no obvious change in the nature of the curve, indicating final maximum potential window for ASC device can be expanded to 0 ~1.5 V, which was determined based on the CV curves as shown in Figure S9.10.



**Figure 9.6.** Electrochemical behavior of ASC for a-MoS<sub>2</sub>/C-dots //AC device (a) CV profiles ASC at a sweep rate of 5-40 mV s<sup>-1</sup>, (b) GCD profile of a-MoS<sub>2</sub>/C-dots //AC (1-10 A g<sup>-1</sup>), (c) C<sub>s</sub> vs. current density, (d) Ragone plot for a-MoS<sub>2</sub>/C-dots //AC ASC, (e) EIS curve of the ASC (f) Cycling stability of ASC over 6000 GCD cycles.

Figure 9.6 (a) presents the CV curve for a-MoS<sub>2</sub>/C-dots //AC device at different sweep rates from 5-40 mV s<sup>-1</sup> in a cell voltage ranging from 0-1.5 V. With increase in scan rate, shape of the CV curves remains unaffected indicating capacitive nature caused by the assembly of a-MoS<sub>2</sub>/C-dots and EDLC (AC) electrodes. The GCD curve for the as-prepared device was performed to confirm the energy storage behaviour in a potential range of 0-1.5 V which is presented in Figure 9.6(b). The specific capacitance for ASC device (a-MoS<sub>2</sub>/C-dots // AC) was obtained to be 180.8, 175.04, 170.61, 166, 150, and 142.52 F g<sup>-1</sup> under an applied current of 1, 2, 3, 4, 7 and 10 A g<sup>-1</sup> which displays nearly



78 % of initial capacitance was retained when current raised from 1 to 10 A g<sup>-1</sup> suggesting good rate capability of a-MoS<sub>2</sub>/C-dots //AC device. Plot 6(c) represents the C<sub>s</sub> vs current density for a-MoS<sub>2</sub>/C-dots //AC ASC device. ED and PD for ASC device was obtained by using equation 9.4 and 9.5, respectively. The Ragone plot for ASC device was presented in Figure 9.6(d). An ED of 56.5 W h kg<sup>-1</sup> was obtained at 750 W kg<sup>-1</sup> PD which is much higher than the previously reported literature such as MP-rGO//AC (39.1 W h kg<sup>-1</sup>, 0.7 kW kg<sup>-1</sup>)<sup>43</sup>, MoS<sub>2</sub>/PEI-GO//AC (19 W h kg<sup>-1</sup>, 4500 kW kg<sup>-1</sup>)<sup>24</sup>, CoMoS<sub>4</sub>//rGO (27.2 W h kg<sup>-1</sup> at 400 W kg<sup>-1</sup>)<sup>47</sup>, and MoS<sub>2</sub>/NiS//AC (31 W h kg<sup>-1</sup>, 155.7 W kg<sup>-1</sup>)<sup>48</sup> are presented in Figure 9.6(d). EIS measurements are done in the frequency ranging from 100 kHz -0.1 Hz, and Figure 9.6 (e) depicts the EIS profile of a-MoS<sub>2</sub>/C-dots //AC ASC along with the equivalent circuit fit. R<sub>s</sub> represents the solution resistance, a time constant involving R<sub>1</sub>, and Q<sub>2</sub> is associated with the charge-transfer (CT) process taking place at the interface of solution and electrode. R<sub>2</sub> is the CT resistance, and Q<sub>2</sub> is the constant phase element modelling the capacitance of the double-charge layer. W represents the Warburg constant which arises from a diffusion-controlled process respectively. The R<sub>s</sub> and R<sub>CT</sub> values for ASC were found to be 2.8 and 4.14 Ω, obtained by fitting the experimental data with an equivalent circuit. The lower R<sub>CT</sub> value implies the low resistance and high CT property of the material. Long term Cyclic durability test of the ASC device evaluated after 6k cycles at 10 A g<sup>-1</sup> current and the device exhibits 83% initial retention of capacitance showing good reversibility of the ASC device which is presented in Figure 9.6(f).

The specific capacitance of a-MoS<sub>2</sub>/C-dots (1368 F g<sup>-1</sup>) is greater than that of more crystalline c-MoS<sub>2</sub>/C, a-MoS<sub>2</sub>, and h-MoS<sub>2</sub>/C. The supercapacitor performance of these

MoS<sub>2</sub> compounds strongly depends on synthesis methods. The high specific capacitance value for a-MoS<sub>2</sub>/C-dots can be due to several reasons:

- (i) Microwave-assisted hydrothermal method produces amorphous two-dimensional MoS<sub>2</sub>/C-dots composite whereas simple hydrothermal treatment of same precursors at same temperature lead to formation of more crystalline h-MoS<sub>2</sub>/C-dots composite. The amorphous 2D MoS<sub>2</sub> compound has several advantages over its crystalline counterpart. In case of crystalline MoS<sub>2</sub> for supercapacitor, the charge storage takes place through the charging of double layer on the external surface or through ions diffusion of inter-layer space of MoS<sub>2</sub>. Since crystalline MoS<sub>2</sub> is anisotropic, ions diffusion into interlayer-space of MoS<sub>2</sub> happens via open edge sites of MoS<sub>2</sub>. On the other hand, amorphous MoS<sub>2</sub> is isotropic. Diffusion of ions can occur thorough entire surface of amorphous MoS<sub>2</sub>. It is also known that the coefficient for lithium ions diffusion for amorphous MoS<sub>2</sub> was much higher than that of crystalline MoS<sub>2</sub>. The supercapacitor performance of a-MoS<sub>2</sub>/C-dots was found to decrease when this amorphous compound was heated at 400 °C to form crystalline MoS<sub>2</sub>/C-dots. The amorphous MoS<sub>2</sub>/C-dots produced by microwave-assisted hydrothermal synthesis method could be the main reason for its high supercapacitor performance.
- (ii) The in-situ nano-engineering of amorphous MoS<sub>2</sub> with C-dots could be another main reason for its high performance. When the mixture of DMF and H<sub>2</sub>O solvent is used for synthesis of MoS<sub>2</sub>, C-dots produced during synthesis of MoS<sub>2</sub> and *in-situ* modify the whole surface of amorphous MoS<sub>2</sub>, enhancing its performance. The amorphous MoS<sub>2</sub>, formed when only H<sub>2</sub>O was used as solvent, showed much lower supercapacitor performance and stability as

compared to C-dots modified amorphous MoS<sub>2</sub> composite. The strong synergetic interaction between the a-MoS<sub>2</sub> and C-dots not only enhances its electrochemical activity but helps to stabilize amorphous MoS<sub>2</sub> (Figure 9.3(f)). The EIS spectra of a-MoS<sub>2</sub>/C-dots, a-MoS<sub>2</sub>, and c-MoS<sub>2</sub>/C were presented in Figure 9.4(d). The low R<sub>CT</sub> value of a-MoS<sub>2</sub>/C-dots (7.1  $\Omega$ ) in comparison to a-MoS<sub>2</sub> (15.6  $\Omega$ ) and c-MoS<sub>2</sub>/C-dots (13.5  $\Omega$ ) suggested the lower electronic resistance of a-MoS<sub>2</sub>/C-dots. Low R<sub>CT</sub> and R<sub>S</sub> values for a-MoS<sub>2</sub>/C-dots confirmed strong synergic interaction between a-MoS<sub>2</sub> and C-dots. It is reported that electrical conductivity of amorphous MoS<sub>2</sub> was two orders of magnitude higher than crystalline MoS<sub>2</sub><sup>49</sup>. The a-MoS<sub>2</sub>/C-dots composite displays better charge transfer at electrode/electrolyte interface, and good electronic conductivity due to strong synergetic interactions significantly contributed to enhancing supercapacitor performance and cycling stability of a-MoS<sub>2</sub>/C-dots composite.

- (iii) In addition, amorphous MoS<sub>2</sub>/C-dots have plenty of defect sites. It is also reported that defect sites in two-dimensional materials such as graphite, MoS<sub>2</sub> are more electrochemically active than other atoms<sup>50</sup>. Therefore, defects in MoS<sub>2</sub>/C-dots may also contribute to enhance supercapacitor performance. The presentence of 1T phase of MoS<sub>2</sub> in a-MoS<sub>2</sub>/C-dots may also help to improve the supercapacitor performance.

## 9.5. CONCLUSION

In summary, a composite of amorphous MoS<sub>2</sub> with 1T phase/C-dots was synthesized by a facile microwave-assisted-hydrothermal method which was helpful for the in-situ

formation of C-dots for composite formation with MoS<sub>2</sub>. A series of both crystalline and amorphous materials was prepared for comparison of electrochemical behavior, and the a-MoS<sub>2</sub>/C-dots showed better capacitance performance as compared to other prepared materials (C-dots free a-MoS<sub>2</sub>, more crystalline c-MoS<sub>2</sub>/C and normal hydrothermal method synthesized h-MoS<sub>2</sub>/C-dots). The a-MoS<sub>2</sub>/C-dots display a highest C<sub>s</sub> value of 1368 F g<sup>-1</sup> under 1 A g<sup>-1</sup> current with retention of 87.1 % capacitance under 15 A g<sup>-1</sup> after 5k cycles. The high supercapacitor performance of a-MoS<sub>2</sub>/C-dots composite was result of the 2D amorphous MoS<sub>2</sub> phase with plenty of defects, presence of some 1T-MoS<sub>2</sub> and its strong synergistic interaction between MoS<sub>2</sub> and C-dots, etc. The ASC device for a-MoS<sub>2</sub>/C-dots//AC exhibits a C<sub>s</sub> value of 180.8 F g<sup>-1</sup> under 1 A g<sup>-1</sup> current. An energy density of 56.5 W h kg<sup>-1</sup> was obtained with an impressive cyclic performance (approx. 83% retention of capacitance after 6k cycles) at 10 A g<sup>-1</sup>. Hopefully, *in-situ* nano-engineering method due to microwave-hydrothermal treatment may find application in electrochemical energy storage technologies.

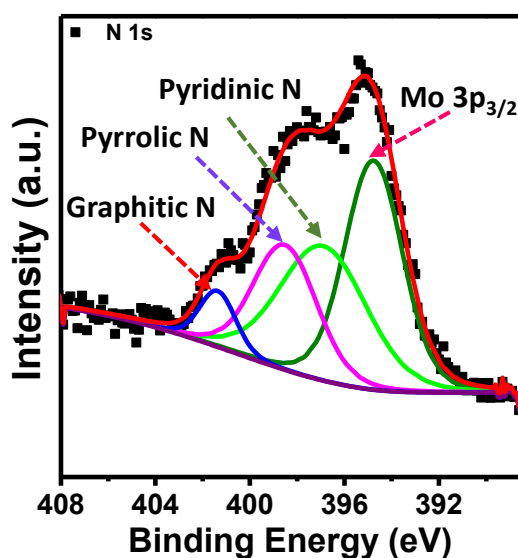
## 9.6. REFERENCES

- (1) Bello, I. T.; Adio, S. A.; Oladipo, A. O.; Adedokun, O.; Mathevula, L. E.; Dhlamini, M. S. *International Journal of Energy Research* **2021**, *45*, 12665-12692.
- (2) Zhang, W.-J.; Huang, K.-J. *Inorganic Chemistry Frontiers* **2017**, *4*, 1602-1620.
- (3) Cai, F.; Sun, R.; Kang, Y.; Chen, H.; Chen, M.; Li, Q. *RSC Advances* **2015**, *5*, 23073-23079.
- (4) Manikandan, R.; Raj, C. J.; Nagaraju, G.; Pyo, M.; Kim, B. C. *Journal of Materials Chemistry A* **2019**, *7*, 25467-25480.
- (5) Pedico, A.; Lamberti, A.; Gigot, A.; Fontana, M.; Bella, F.; Rivolo, P.; Cocuzza, M.; Pirri, C. F. *ACS Applied Energy Materials* **2018**, *1*, 4440-4447.
- (6) Zheng, N.; Bu, X.; Feng, P. *Nature* **2003**, *426*, 428-432.
- (7) El Sharkawy, H. M.; Dhmees, A. S.; Tamman, A. R.; El Sabagh, S. M.; Aboushahba, R. M.; Allam, N. K. *Journal of Energy Storage* **2020**, *27*, 101078.
- (8) Wang, Q.; Jiao, L.; Du, H.; Si, Y.; Wang, Y.; Yuan, H. *Journal of Materials Chemistry* **2012**, *22*, 21387-21391.
- (9) Zhou, W.; Chen, W.; Nai, J.; Yin, P.; Chen, C.; Guo, L. *Advanced Functional Materials* **2010**, *20*, 3678-3683.

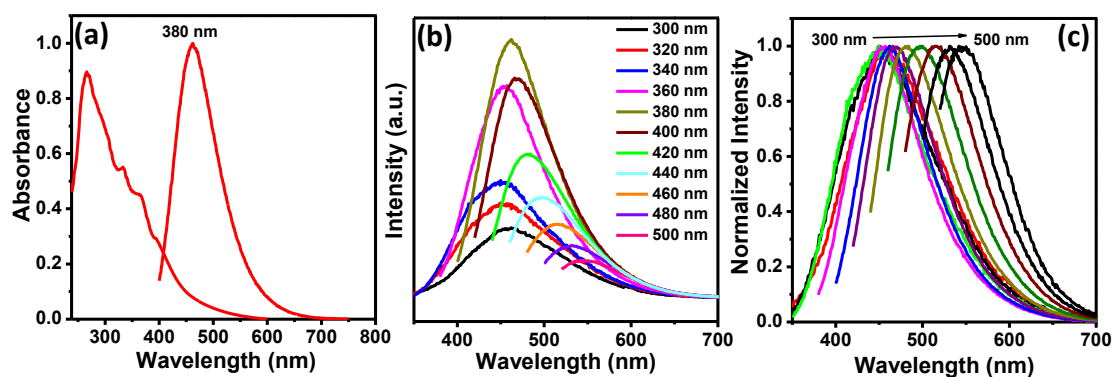
- (10) Zhou, W.; Cao, X.; Zeng, Z.; Shi, W.; Zhu, Y.; Yan, Q.; Liu, H.; Wang, J.; Zhang, H. *Energy & Environmental Science* **2013**, *6*, 2216-2221.
- (11) Li, Q.; Xu, Y.; Zheng, S.; Guo, X.; Xue, H.; Pang, H. *Small* **2018**, *14*, 1800426.
- (12) Liu, J.; Hao, R.; Jia, B.; Zhao, H.; Guo, L. *Nanomaterials* **2021**, *11*.
- (13) Sarkar, S.; Roy, S.; Hou, Y.; Sun, S.; Zhang, J.; Zhao, Y. *ChemSusChem* **2021**, *14*, 3693-3723.
- (14) Wu, Y.; Liu, Z.; Zhong, X.; Cheng, X.; Fan, Z.; Yu, Y. *Small* **2018**, *14*, 1703472.
- (15) Liu, W.; Liu, H.; Dang, L.; Zhang, H.; Wu, X.; Yang, B.; Li, Z.; Zhang, X.; Lei, L.; Jin, S. *Advanced Functional Materials* **2017**, *27*, 1603904.
- (16) Liu, J.; Ji, Y.; Nai, J.; Niu, X.; Luo, Y.; Guo, L.; Yang, S. *Energy & Environmental Science* **2018**, *11*, 1736-1741.
- (17) Yan, S.; Abhilash, K. P.; Tang, L.; Yang, M.; Ma, Y.; Xia, Q.; Guo, Q.; Xia, H. *Small* **2019**, *15*, 1804371.
- (18) Ambrosi, A.; Sofer, Z.; Pumera, M. *Chemical Communications* **2015**, *51*, 8450-8453.
- (19) Ejigu, A.; Kinloch, I. A.; Prestat, E.; Dryfe, R. A. W. *Journal of Materials Chemistry A* **2017**, *5*, 11316-11330.
- (20) Acerce, M.; Voiry, D.; Chhowalla, M. *Nature Nanotechnology* **2015**, *10*, 313-318.
- (21) Voiry, D.; Salehi, M.; Silva, R.; Fujita, T.; Chen, M.; Asefa, T.; Shenoy, V. B.; Eda, G.; Chhowalla, M. *Nano Letters* **2013**, *13*, 6222-6227.
- (22) Wu, L.; Longo, A.; Dzade, N. Y.; Sharma, A.; Hendrix, M. M. R. M.; Bol, A. A.; de Leeuw, N. H.; Hensen, E. J. M.; Hofmann, J. P. *ChemSusChem* **2019**, *12*, 4383-4389.
- (23) Gao, M.-R.; Chan, M. K. Y.; Sun, Y. *Nature Communications* **2015**, *6*, 7493.
- (24) Liu, M.-C.; Xu, Y.; Hu, Y.-X.; Yang, Q.-Q.; Kong, L.-B.; Liu, W.-W.; Niu, W.-J.; Chueh, Y.-L. *ACS Applied Materials & Interfaces* **2018**, *10*, 35571-35579.
- (25) Wang, H.; Lu, Z.; Xu, S.; Kong, D.; Cha, J. J.; Zheng, G.; Hsu, P.-C.; Yan, K.; Bradshaw, D.; Prinz, F. B.; Cui, Y. *Proceedings of the National Academy of Sciences* **2013**, *110*, 19701.
- (26) Lin, Q.; Dong, X.; Wang, Y.; Zheng, N.; Zhao, Y.; Xu, W.; Ding, T. *Journal of Materials Science* **2020**, *55*, 6637-6647.
- (27) Li, B.; Jiang, L.; Li, X.; Ran, P.; Zuo, P.; Wang, A.; Qu, L.; Zhao, Y.; Cheng, Z.; Lu, Y. *Scientific Reports* **2017**, *7*, 11182.
- (28) Mei, Y.; Li, T.-T.; Qian, J.; Li, H.; Wu, M.; Zheng, Y.-Q. *Chemical Communications* **2020**, *56*, 13393-13396.
- (29) Gao, Y.; Chen, C.; Tan, X.; Xu, H.; Zhu, K. *Journal of Colloid and Interface Science* **2016**, *476*, 62-70.
- (30) Mohanty, B.; Bhanja, P.; Jena, B. K. *Materials Today Energy* **2022**, *23*, 100902.
- (31) Panda, P.; Mishra, R.; Panigrahy, S.; Barman, S. *ACS Applied Nano Materials* **2022**, *5*, 5176-5186.
- (32) Niaz, N. A.; Shakoor, A.; Imran, M.; Khalid, N. R.; Hussain, F.; Kanwal, H.; Maqsood, M.; Afzal, S. *Journal of Materials Science: Materials in Electronics* **2020**, *31*, 11336-11344.
- (33) Fu, H.; Zhang, X.; Fu, J.; Shen, G.; Ding, Y.; Chen, Z.; Du, H. *Journal of Alloys and Compounds* **2020**, *829*, 154557.
- (34) Pham, K.-C.; McPhail, D. S.; Wee, A. T. S.; Chua, D. H. C. *RSC Advances* **2017**, *7*, 6856-6864.
- (35) Xie, B.; Chen, Y.; Yu, M.; Sun, T.; Lu, L.; Xie, T.; Zhang, Y.; Wu, Y. *Carbon* **2016**, *99*, 35-42.
- (36) Joseph, N.; Muhammed Shafi, P.; Chandra Bose, A. *New Journal of Chemistry* **2018**, *42*, 12082-12090.
- (37) Zhou, J.; Fang, G.; Pan, A.; Liang, S. *ACS Applied Materials & Interfaces* **2016**, *8*, 33681-33689.
- (38) Baig, M. M.; Pervaiz, E.; Yang, M.; Gul, I. H. *Frontiers in Materials* **2020**, *7*.
- (39) Mishra, R. K.; Manivannan, S.; Kim, K.; Kwon, H.-I.; Jin, S. H. *Current Applied Physics* **2018**, *18*, 345-352.
- (40) Liu, C.; Zhao, X.; Wang, S.; Zhang, Y.; Ge, W.; Li, J.; Cao, J.; Tao, J.; Yang, X. *ACS Applied Energy Materials* **2019**, *2*, 4458-4463.

- (41) Nandi, D. K.; Sahoo, S.; Sinha, S.; Yeo, S.; Kim, H.; Bulakhe, R. N.; Heo, J.; Shim, J.-J.; Kim, S.-H. *ACS Applied Materials & Interfaces* **2017**, *9*, 40252-40264.
- (42) Zhang, Y.; Sun, W.; Rui, X.; Li, B.; Tan, H. T.; Guo, G.; Madhavi, S.; Zong, Y.; Yan, Q. *Small* **2015**, *11*, 3694-3702.
- (43) Hao, J.; Liu, H.; Han, S.; Lian, J. *ACS Applied Nano Materials* **2021**, *4*, 1330-1339.
- (44) Jiang, J.; Hu, Y.; He, X.; Li, Z.; Li, F.; Chen, X.; Niu, Y.; Song, J.; Huang, P.; Tian, G.; Wang, C. *Small* **2021**, *17*, 2102565.
- (45) Abdelaal, M. M.; Hung, T.-C.; Mohamed, S. G.; Yang, C.-C.; Huang, H.-P.; Hung, T.-F. *Nanomaterials* **2021**, *11*.
- (46) Ma, F.-X.; Yu, L.; Xu, C.-Y.; Lou, X. W. *Energy & Environmental Science* **2016**, *9*, 862-866.
- (47) Xu, X.; Song, Y.; Xue, R.; Zhou, J.; Gao, J.; Xing, F. *Chemical Engineering Journal* **2016**, *301*, 266-275.
- (48) Qin, Q.; Chen, L.; Wei, T.; Liu, X. *Small* **2019**, *15*, 1803639.
- (49) Miki, Y.; Nakazato, D.; Ikuta, H.; Uchida, T.; Wakihara, M. *Journal of Power Sources* **1995**, *54*, 508-510.
- (50) Pumera, M.; Sofer, Z.; Ambrosi, A. *Journal of Materials Chemistry A* **2014**, *2*, 8981-8987.

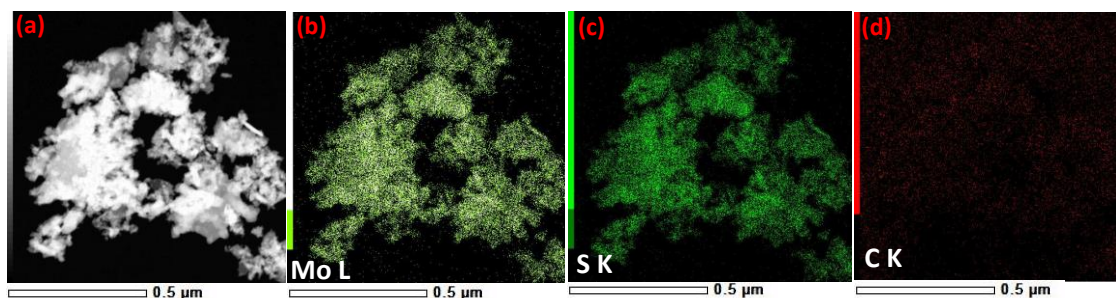
## Appendix G



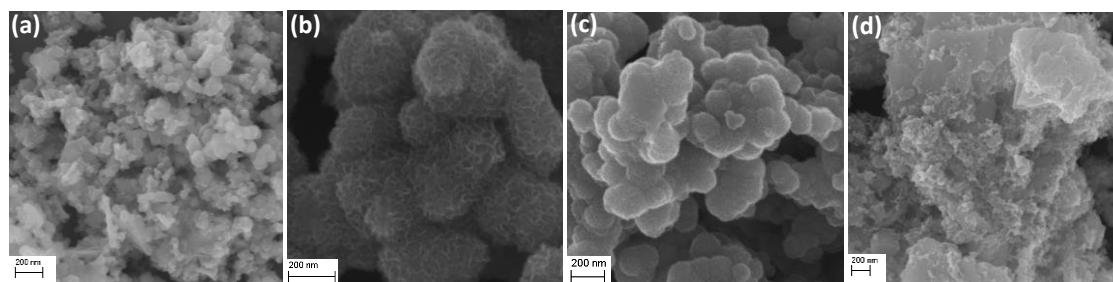
**Figure S9.1.** High resolution XPS spectra of N1s/Mo3p in a-MoS<sub>2</sub>/C-dots.



**Figure S9.2.** UV–visible spectrum, (b) PL spectra at different wavelengths, and (c) Normalized PL spectra of C-dots excited at different wavelengths.

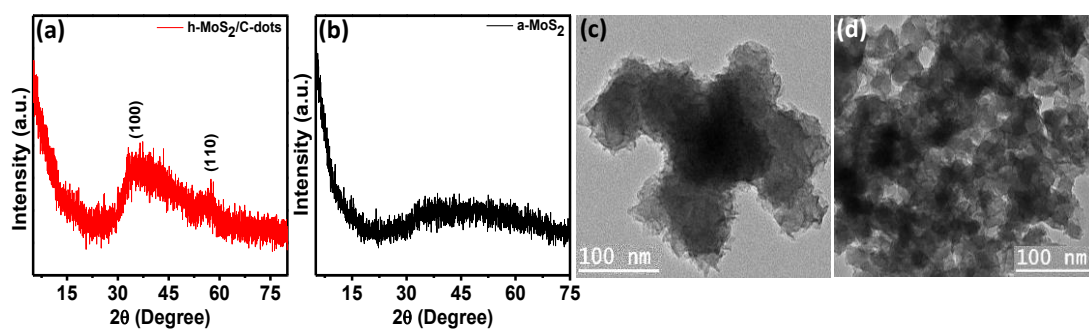


**Figure S9.3.** STEM image and corresponding elemental mapping of (a) Mo, (b) S, and (c) C in c-MoS<sub>2</sub>/C-dots Composites.

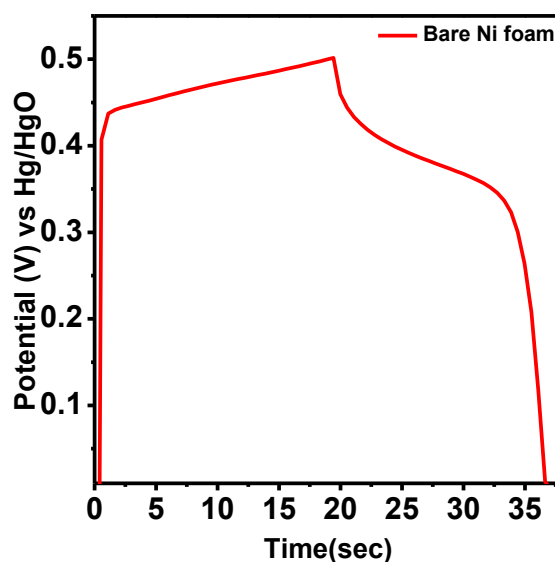


**Figure S9.4.** FESEM image of (a) a-MoS<sub>2</sub>/C-dots, (b) c-MoS<sub>2</sub>/C-dots, (c) h- MoS<sub>2</sub>/C-dots, and (d) a-MoS<sub>2</sub>.



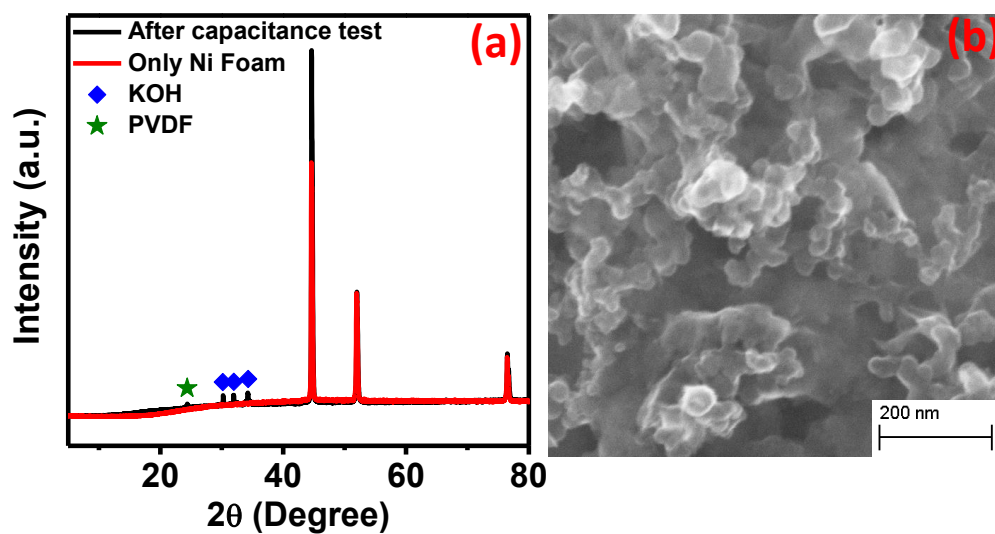


**Figure S9.5.** XRD pattern of (a) h-MoS<sub>2</sub>/C-dots, and (b) a-MoS<sub>2</sub>, low resolution TEM image of (c) h-MoS<sub>2</sub>/C-dots, and (d) a-MoS<sub>2</sub>.

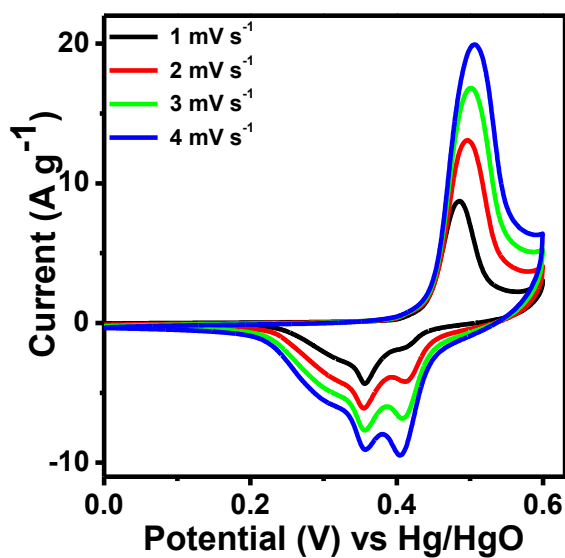


**Figure S9.6.** GCD curves of bare Ni foam at 1 mA current.

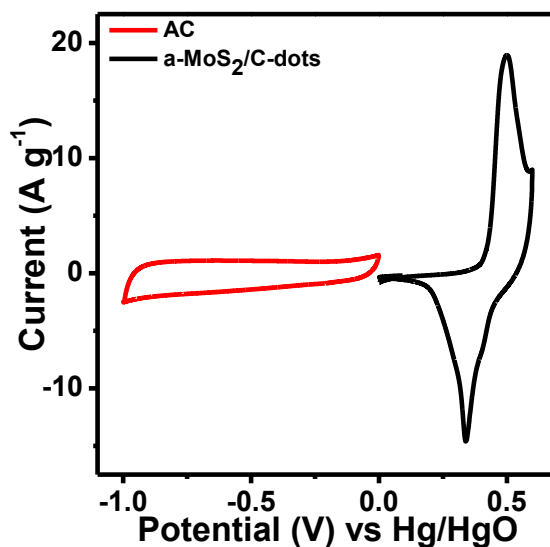




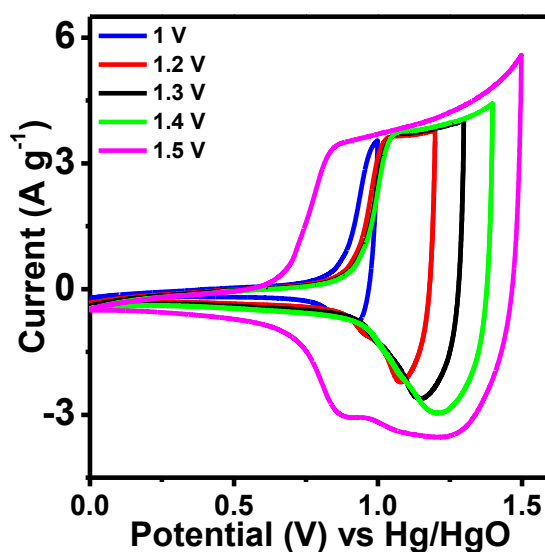
**Figure S9.7.** (a) XRD and (b) FESEM image of a-MoS<sub>2</sub>/C-dots after capacitance retention test.



**Figure S9.8.** Comparison CV profiles of a-MoS<sub>2</sub>/C-dots at scan rate 1-4 mV s<sup>-1</sup>.



**Figure S9.9.** CV curves of AC and a-MoS<sub>2</sub>/C-dots at a scan rate of 5 mV s<sup>-1</sup>.



**Figure S9.10.** CV curves for ASC device at potential ranging from 1-1.5 V.

**Table S9.1.** Stoichiometry of MoS<sub>2</sub> as determined by TEM EDX and XPS in a-MoS<sub>2</sub>/C-dots composite.

a-MoS <sub>2</sub> /C-dots	Mo	S
Stoichiometry (XPS)	1	2.4
Stoichiometry (EDX)	1	2.46

**Table S9.2.** Comparison of electrochemical performance of a-MoS<sub>2</sub>/C-dots, a-MoS<sub>2</sub>, c-MoS<sub>2</sub>/C-dots, and h-MoS<sub>2</sub>/C-dots composites.

Sample name	Specific capacitance (F g <sup>-1</sup> ) at 1 A g <sup>-1</sup> current density
a-MoS <sub>2</sub> /C-dots	1368
a-MoS <sub>2</sub>	475
h-MoS <sub>2</sub> /C-dots	635
c-MoS <sub>2</sub> /C-dots	829

## Chapter 10

### Ultrathin Ni-Co Bimetallic Metal-Organic Framework Nanobelts for High-Performance Energy Storage

#### 10.1. ABSTRACT

The design and advancement of nanostructured composite materials in one-dimensional (1D) configuration have garnered significant interest in the pursuit of high-performance supercapacitor applications. Herein, the synthesis of ultrathin 1D NiCo metal-organic framework (MOF) nanobelts via solvothermal process was presented. The resulting nanobelts exhibit a unique and uniformly distributed 1D morphology characterized by high specific surface area (SSA) and exceptional structural stability. The electrochemical investigations reveal that the optimized 1D NiCo-MOF-31 composite shows a high specific capacitance ( $C_s$ ) of  $1697.5 \text{ F g}^{-1}$  under  $1 \text{ A g}^{-1}$  current and  $696.43$  under  $10 \text{ A g}^{-1}$ , with superior cyclic performance over 5000 charging-discharging cycles. Furthermore, an asymmetric supercapacitor (ASC) device (1D NiCo-MOF-31//SNAC) was constructed by using sulfur and nitrogen co-doped activated carbon (SNAC) as anode and 1D NiCo-MOF-31 as cathode material. The device demonstrates an impressive energy density (ED) of  $26.56 \text{ W h kg}^{-1}$  at a power density (PD) of  $750 \text{ W kg}^{-1}$  with remarkable cyclic stability. The exceptional electrochemical activity is owing to its one-dimensional nanobelt morphology which offer notable advantages such as high specific surface area, rapid ion and electron transport, etc. These inherent benefits position nanobelt as highly promising candidates for advancing the field of high-performance supercapacitors.

## 10.2. INTRODUCTION

Nowadays the escalating environmental challenges stemming from current energy resources encourage researchers to explore alternate energy storage technologies<sup>1</sup>. Supercapacitors (SCs) have garnered significant attention in this domain owing to their notable features, including high  $C_s$ , moderate ED and high PD, and long-term cyclic stability<sup>2</sup>. However, the applicability of SCs is limited due to their specific energy being constrained<sup>3-4</sup>. To address this limitation, carbonaceous materials are extensively used as electrode materials for SC applications. Nonetheless, their use in energy storage applications is restricted by their low SSA. Recently, MOFs have emerged as highly versatile materials widely utilized in a multitude of applications<sup>5</sup>, including catalysis, energy storage devices, drug delivery, gas storage, and separation. MOFs possess intriguing properties such as high porosity, tunable functionalities, coordination of unsaturated metal sites, regulatable nanospace, and functional organic ligands<sup>6-7</sup>. The flexibility exhibited by MOFs is manifested through localized structural changes, such as linker rotation, as well as correlated structural changes, including volume expansion and subunit displacement. Furthermore, the presence of defects and disorder is frequently linked to the flexibility observed in MOFs, indicating a combination of characteristics found in both crystalline frameworks and soft materials<sup>8-12</sup>. The incorporation of both ordered and disordered regions, along with localized and correlated structural dynamics, has propelled solid-state chemistry into new frontiers of research. The benefits of defects and disorders in MOFs have often been undervalued due to the difficulty of accessing these features using commonly used characterization techniques. Exploring the intricate interplay between flexibility, disorder, and defects in hybrid solids like MOFs necessitates the use of various techniques and strategies. Moreover, MOFs are

convenient to prepare using transition metal salt as starting materials. Transition metals such as Co, Fe, Ni, etc. are used for the synthesis of different kinds of MOFs for pseudocapacitive redox centre<sup>13</sup>. The application of MOFs for energy storage applications includes two cases: (i) MOFs can be directly used as supercapacitor electrodes and (ii) MOFs are used as a template for fabricating porous carbons, metal chalcogenides, metal oxides, and their composites via ion exchange method or one step calcination method. The pyrolysis of MOFs more or less destroys the framework of the MOFs and hence decreases the SSA as well as the active redox sites which results in lowering the electrochemical activity of the material.

In recent times, researchers have increasingly focused on utilizing SCs for energy storage applications. Several studies have reported the utilization of MOFs as electrode materials for SC devices. For instance, W. Chaikittisilp et al. synthesized nonporous carbons by direct carbonizing zeolitic imidazolate framework (ZLF-8) for electrode materials in electric double-layer capacitors (EDLCs)<sup>14</sup>. Similarly, a hierarchically porous three-dimensional (3D) carbon framework with both micro- and mesopores was synthesized from the ZIF-8 material by Amali et al., demonstrating excellent performance in energy storage devices<sup>15</sup>. The distinctive structures of MOFs offer an abundant supply of pseudocapacitive redox centers, making them suitable for direct use in SC applications. However, certain drawbacks such as inadequate pore sizes for ion transportation, poor electrical conductivity impeding electron transfer, and poor cyclic stability during the charging/discharging process resulting in low specific capacitance, and low rate performance of MOFs compared to transition metal oxides. Nevertheless, tunable morphology, pore size, and organic functionality for MOFs make them highly desirable

for energy storage applications. Consequently, various approaches have been explored to address these challenges. According to previous reports layered structure MOFs exhibits high specific capacitance as the layered structure offers sufficient space for OH<sup>-</sup> deintercalation/intercalation process and functions as an electron transport pathway, thereby enhancing the electrochemical performance<sup>16</sup>. Furthermore, the synthesis of MOFs with high SSA can be achieved by tuning the metal ions and organic ligands, which in turn enhance the  $C_s$  value of the electrode materials<sup>17</sup>. The electrochemical activity of MOF can be improved by doping with different metals<sup>18</sup> or with polymers<sup>19</sup>. 1D materials such as nanoribbons<sup>20</sup>, nanotubes<sup>21</sup>, nanorods<sup>22</sup>, nanowires<sup>23</sup>, nanobelt<sup>24</sup> and nanofiber<sup>25</sup> find extensive use in various applications like catalysis, energy storage device, sensors, membrane, and electronics.

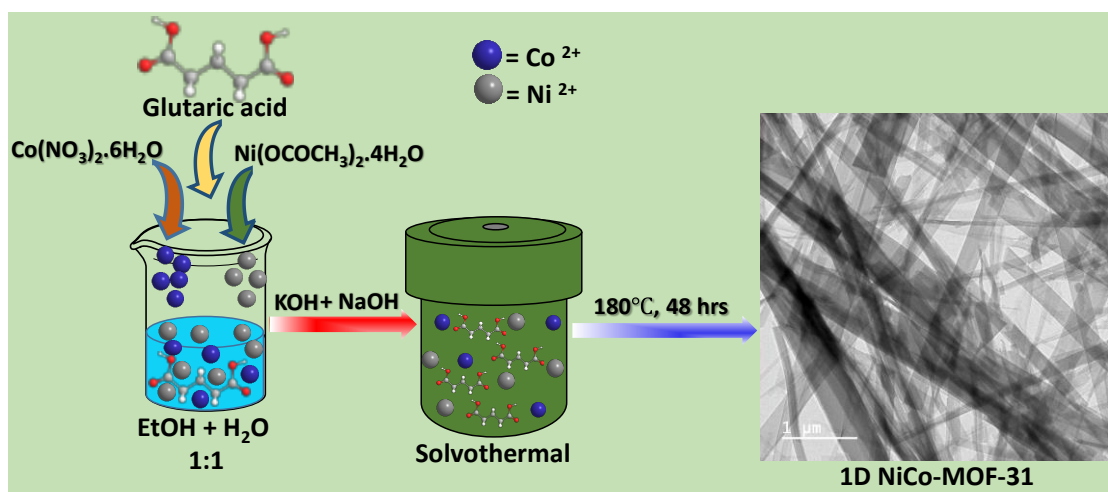
Herein, the energy storage application of ultrathin 1D NiCo metal-organic framework (MOF) synthesized by a simple one-step solvothermal process was reported. By tuning the amount of Ni and Co ratio, the optimized 1D NiCo-MOF-31 exhibits a high  $C_s$  value of 1697.4 F g<sup>-1</sup> under 1 A g<sup>-1</sup> current with superior cyclic performance over 5000 charge/discharge cycles. In addition, to assess the practical applicability an ASC device (1D NiCo-MOF-31//SNAC) was fabricated using SNAC as the negative and 1D NiCo-MOF-31 as the positive electrode materials. The device delivers an impressive ED of 26.56 W h kg<sup>-1</sup> at a PD of 750 W kg<sup>-1</sup> with outstanding cyclic stability over 5000 cycles.

### **10.3. EXPERIMENTAL SECTION:**

#### **10.3.1. Materials:**

Glutaric acid (HOOC(CH<sub>2</sub>)<sub>3</sub>COOH), Cobalt (II) nitrate tetrahydrate (Co(NO<sub>3</sub>)<sub>2</sub>·4H<sub>2</sub>O), and Nickel acetate tetrahydrate (Ni(CH<sub>3</sub>COO)<sub>2</sub>·4H<sub>2</sub>O). Ethanol was bought from

Thermo Scientific (India). Sodium hydroxide (NaOH) and Potassium hydroxide (KOH) were purchased from Merk. Formamide was purchased from Merck, India. Thiourea was purchased from Spectrochem PVT. LTD. Mumbai (India). Hydrochloric acid (HCl) was purchased from CDH chemicals, India. PVDF binder was purchased from MTI corporation. All of these chemicals were used without any additional purification. Deionized (DI) water obtained from the Milli-Q ultrafiltration system was used in all experiments with a resistivity of 17.9 MΩ cm.



**Scheme 10.1.** Scheme illustrating synthesis of 1D NiCo-MOF-31.

### 10.3.2. Synthesis of 1D NiCo-MOF-x, Ni-MOF, and Co-MOF

1D NiCo-MOF-x was synthesized through a facile hydrothermal method by a route described in our previous study, with slight modification<sup>26</sup>. In a typical synthesis method 0.79g Glutaric acid, 0.64g potassium hydroxide, Cobalt (II) nitrate tetrahydrate and Nickel acetate tetrahydrate were dissolved in 1:1 DI water and ethanol solution (40 ml) followed by addition of 0.4M NaOH (4ml) to form a homogeneous solution under continuous stirring. Then the solution was transferred into a 100 ml autoclave and kept at 180 °C for 48 h. And the product obtained was washed multiple times with DI water



and ethanol and dried in a vacuum oven to get the solid product. The product obtained was named as 1D NiCo-MOF-x (where x= molar ratio of Ni/Co) i.e. 1D NiCo-MOF-11 (Ni/Co molar ratio 1:1), 1D NiCo-MOF-21 (Ni/Co molar ratio 2:1), 1D NiCo-MOF-31 (Ni/Co molar ratio 0.75:1), 1D NiCo-MOF-41 (Ni/Co molar ratio 0.5:1) and 1D NiCo-MOF-13 (Ni/Co molar ratio 1:3). A detailed method for the synthesis of 1D NiCo-MOF-x is presented in Scheme 10.1.

Similarly, Ni-MOF was synthesized by using the above-mentioned method by using  $\text{Ni}(\text{CH}_3\text{COO})_2 \cdot 4\text{H}_2\text{O}$  at 180 °C for 48 h and denoted as Ni-MOF.

Co-MOF was synthesized by using the above-mentioned method by using  $\text{Co}(\text{NO}_3)_2 \cdot 4\text{H}_2\text{O}$  at 140 °C for 24 h and denoted as Co-MOF.

### **10.3.3. Synthesis of Sulphur (S) and Nitrogen (N) co-doped Activated Carbon (SNAC)**

S, N co-doped activated carbon (SNAC) was prepared from Formamide and thiourea by using a two-step method reported by our group<sup>27</sup>. In brief, 4g of thiourea was mixed with 30 ml of Formamide to form a homogeneous solution. The solution was transferred into a 100 ml autoclave and heated at 220 °C for 48 h. After the heating was done the autoclave was allowed to cool to room temperature. The black colour product obtained was calcinated at 700 °C in a tube furnace for 2 h followed by activation at 800 °C for 1h under  $\text{N}_2$  atmosphere (keeping C: KOH ratio 1:2). The black colour product obtained was washed multiple times with DI water and 0.3 M HCl and dried under vacuum to get the desired product and was denoted as SNAC.

### **10.3.4. Electrode Fabrication:**

For the fabrication of the working electrode, a piece of Ni foam of area 1 cm<sup>2</sup> (1 cm × 1 cm) was used. The Ni foam was washed with 3M HCl to remove the oxide layers and

then it was rinsed with H<sub>2</sub>O, ethanol and finally dried. The 1D NiCo-MOF-31, conductive carbon (CC), and polyvinylidene fluoride (PVDF) binder in N-methyl-2-pyrrolidone (NMP) in a weight % of 80:10:10 were mixed to form a homogenous slurry. The slurry was coated over the 1×1 cm<sup>2</sup> Ni foam and it was then dried in a oven. The mass of the 1D NiCo-MOF-31 (active material) loaded on the Ni foam was found to be 1mg. For the designing of ASC, the SNAC was used as the negative electrode (anode) and active material as the positive electrode (cathode), and cellulose paper used as a separator. For positive and negative electrodes, the weight loading ratio was calculated to be 0.27 (weight loading for positive and negative electrodes were 1 mg and 3.72 mg, respectively).

Specific capacitance ( $C_s$ ) was computed from CV curve by using equation 10.1 <sup>1,3</sup>

$$C_s = \frac{\int I dV}{2m\Delta Vv} \quad (10.1)$$

Specific capacitance was computed from the GCD curve by using equation 10.2 <sup>4</sup>

$$C_s = \frac{I\Delta t}{m\Delta V} \quad (10.2)$$

where  $C_s$  presents the specific capacitance (F g<sup>-1</sup>),  $I$  is current (mA),  $\Delta t$  is the discharge time (s),  $m$  represents mass of active material (mg),  $\Delta V$  is the operating voltage range (V),  $\int I dV$  is the area covered by the CV curve, and  $v$  denotes the sweep rate (mV s<sup>-1</sup>).

For asymmetric supercapacitor (ASC) cell, the as-prepared material (active material) acts as a cathode and AC acts as an anode. The full cell is represented as 1D NiCo-MOF-31//SNAC.

To balance the charge storage, the mass ratio of 1D NiCo-MOF-31 and SNAC was calculated by using equation 10.3 <sup>1,3</sup>

$$\frac{m^-}{m^+} = \frac{C^+\Delta V^+}{C^-\Delta V^-} \quad (10.3)$$

In this equation,  $m^+$  is mass (mg),  $C^+$  and  $C^-$  are  $C_s$  values of active material and AC, respectively,  $\Delta V^+$  and  $\Delta V^-$  are voltage range of cathode and anode electrodes, respectively, and  $m^-$  is the mass of anode. Energy density and power density of the device were calculated by using the following equations.<sup>1,3</sup>

$$E = \frac{C_s(\Delta V)^2}{7.2} \quad (10.4)$$

$$P = \frac{E}{\Delta t} \times 3600 \quad (10.5)$$

Here,  $\Delta V$  is the voltage window (V),  $C_s$  is the capacitance of ASC ( $F\ g^{-1}$ ), and  $\Delta t$  is the discharge time (s).

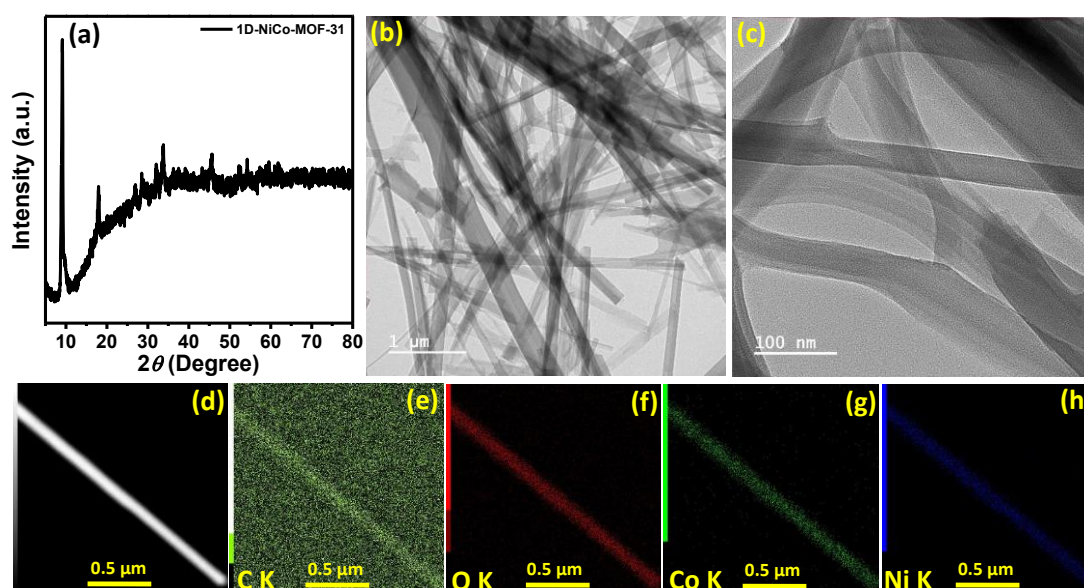
#### **10.3.5. Characterizations:**

The x-ray diffraction data (p-XRD) of as prepared samples were conducted by Bruker DAVINCI D8 ADVANCE diffractometer equipped with a monochromatic radiation source of  $Cu\ K\alpha$  ( $\lambda = 0.15406$ ). The composition and morphology of the material was recorded by Field-emission scanning electron microscope (FESEM) system (Carl Zeiss, Germany make, Model: Sigma) and Transmission Electron Microscopy (TEM, JEOL F200) and High-Resolution TEM (HRTEM). VG Microtech was used to record the XPS data with monochromatic  $Mg\ K\alpha$  X-ray as the source. All electrochemical measurements were performed by using CorrTest Electrochemical Workstation [Model: CS350]. Quantachrome Instruments (Autosorb-iQ-XR-XR (2 Stat.)) was used to determine the Specific surface area by  $N_2$  adsorption-desorption isotherm.

## 10.4. RESULTS AND DISCUSSIONS:

### 10.4.1. Structural and morphological characterizations

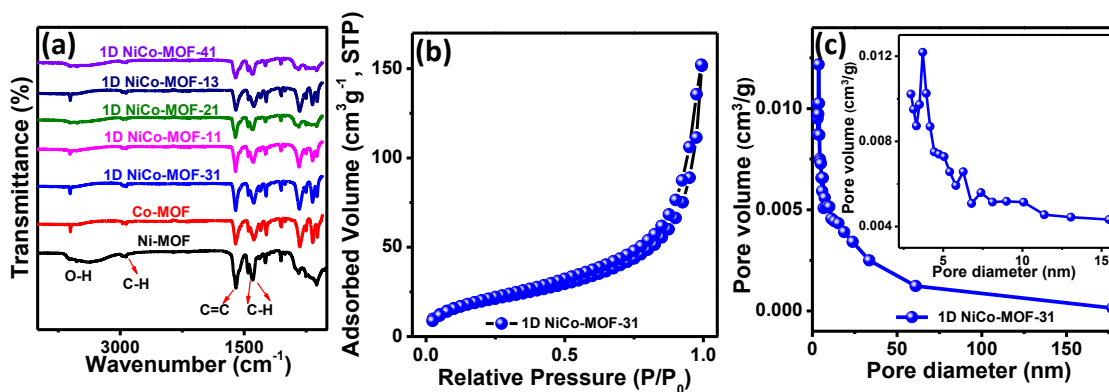
The 1D Cobalt Nickel-MOF-x has garnered substantial interest owing to its unique structural properties and promising catalytic performance. The phase purity and crystallographic structure of the synthesized MOFs were tested by using powder X-ray diffraction (p-XRD) pattern. Figure 10.1(a) and Figure S10.1 represents the p-XRD pattern of all the MOFs. The p-XRD pattern shows a sharp diffraction peaks at  $2\theta$  value  $9.2^\circ$  signifying the formation of the MOF<sup>28</sup>. All the composites show same type of XRD pattern indicating the same crystal phase. This observation confirms the successful synthesis of the product, affirming its accurate structural formation.



**Figure 10.1.** (a) p-XRD pattern, (b, c) TEM images of 1D NiCo-MOF-31, (d-h) STEM image and elemental mapping of 1D NiCo-MOF-31.

The morphology and nanostructure of the 1D NiCo-MOF-x were further inspected by Field emission Scanning Electron Microscope (FESEM) and Transmission Electron Microscope (TEM). The SEM image of 1D NiCo-MOF-31 shows uniform growth of smooth 1D nanobelt (Figure S10.2). Figure S10.3 represents the SEM image of 1D NiCo-MOF-11, 1D NiCo-MOF-13, 1D NiCo-MOF-21, 1D NiCo-MOF-41, Co-MOF, and Ni-MOFs revealing 1D nanobelt morphology and with increase in Ni content, the nanobelt becomes thinner and longer. The MOF with Ni/Co molar ratio 0.75:1 (i.e. for 1D NiCo-MOF-31) exhibits the best morphology. However, the structure of the nanobelt eventually disintegrates as the Ni content decreases. Figure S10.3 (e) represents the FESEM image of Co-MOF where the structure of the nanobelt are broken up. The TEM images of 1D NiCo-MOF-31 confirm the formation of 1D nanobelt with a mean diameter of ~90-105 nm. The higher and lower magnification TEM images are presented in Figure 10.1 (b, c). The TEM image suggests that the nanobelts had empty space on all sides. This indicates the ions can be transferred quickly from the surface of nanobelts to another. Figure S10.4 (a, b) and Figure S10.4 (c) presents the High Resolution TEM (HRTEM) image and enlarged HRTEM images respectively revealing the crystalline nature of 1D NiCo-MOF-31. The Energy Dispersive Spectroscopy (EDS) mapping of all the elements are presented in Figure 10.1(d-h) showing uniform distribution of C, O, Co, and Ni with no other impurity in the MOF. The percentage of Ni and Co ratio obtained was 0.77:1 in 1D NiCo-MOF-31 (presented in Table S10.1), which is very close to the molar ratio of Ni and Co precursor used during synthesis (i.e. 0.75:1). The molecular structure of all the seven MOFs are determined from Fourier transform infrared spectrometer (FT-IR) depicted in Figure 10.2(a). A broad peak positioned at  $3598\text{ cm}^{-1}$  can be due to the presence of stretching mode of O-H groups. A small peak

around  $2937\text{ cm}^{-1}$  is attributed to C-H (saturated hydrocarbon) vibration. Two peaks at  $1450$  and  $1391\text{ cm}^{-1}$  are due to stretching vibration of COOH group from glutaric acid. A peak at  $1603\text{ cm}^{-1}$  is because of the characteristic mode of alkene (C=C).

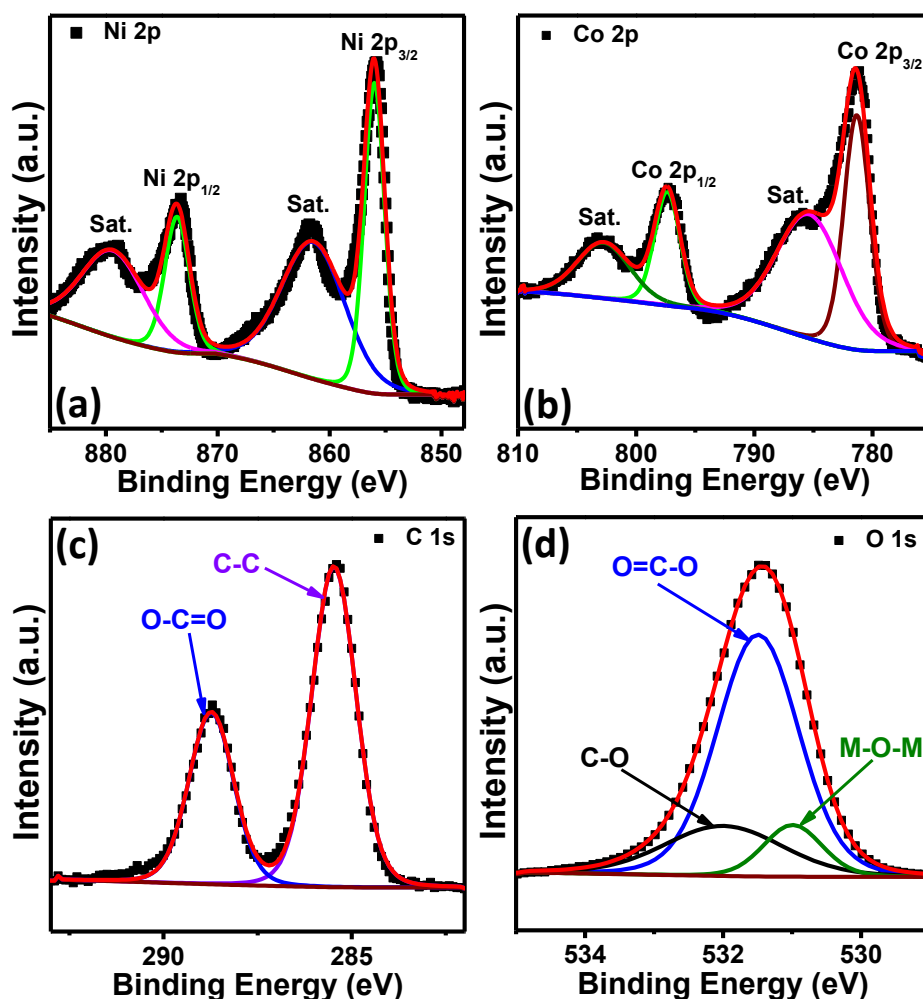


**Figure 10.2.** (a) FT-IR spectrum of all the seven MOFs, (b)  $\text{N}_2$  desorption/adsorption isotherm, and (c) PSD of 1D NiCo-MOF-31.

$\text{N}_2$  sorption isotherm was performed to examine the SSA and porosity of all the MOFs. Figure 10.2(b and c) represents the Brunauer–Emmett–Teller (BET) isotherm and pore size distribution (PSD) of 1D NiCo-MOF-31. Also the SSA and PSD of other 1D NiCo-MOF-x were presented in Figure S10.5. This shows type II isotherm with H4-type hysteresis loop. The 1D NiCo-MOF-31, 1D NiCo-MOF-41, 1D NiCo-MOF-11 and 1D NiCo-MOF-21 show SSA of 73, 44, 41, and  $12.27\text{ m}^2\text{ g}^{-1}$  with pore diameter 3.71, 3.13, 3.31, and 2.97 nm respectively (calculated through BJH PSD method). The SSA of the 1D NiCo-MOF-31 is remarkably higher than the other prepared MOFs. The large SSA and well defined porous structure result in exposure of high active site, leading to a significant improvement in the electrochemical performance of the material.

X-ray photoelectron spectroscopy (XPS) was employed to acquire a comprehensive comprehension of the effects of the bimetallic composite. Figure S10.6 represents the

XPS survey scan of 1D NiCo-MOF-31 affirming the presence of Ni, Co, C, and O elements. The high-resolution XPS spectrum of Ni 2p peaks having binding energy 856.1 and 873.6 eV were separately assigned to Ni 2p<sub>3/2</sub> and Ni 2p<sub>1/2</sub> respectively with a characteristic binding energy difference of 17.5 eV. This indicates the existence of Ni (II) in 1D NiCo-MOF-31. The peaks at binding energy 861.7 and 879.6 eV were indexed to the satellite peaks associated with Ni 2p<sub>3/2</sub> and Ni 2p<sub>1/2</sub> respectively (Figure 10.3(a)). Figure 10.3(b) represents the high-resolution XPS spectrum of Co 2p deconvoluted into two peaks centered at 781.4 and 797.4 eV corresponding to the Co 2p<sub>3/2</sub> and Co 2p<sub>1/2</sub> respectively with a spin-energy interval of 16.1 eV, indicating the dominance of the Co(II) oxidation state in 1D NiCo-MOF-31. The C 1s peak can be indexed into three peaks (Figure 10.3(c)). The peak centered at 285.1, and 288.4 eV refer to C-C, and O-C=O respectively<sup>28</sup>. The O spectrum can be deconvoluted into three peaks centered at 530.9, 531.5 and 532.4 eV attributed to M-O-M (metal-oxygen-metal), O=C-O and C-O respectively (Figure 10.3(d))<sup>28</sup>. XPS findings indicate the successful formation of 1D NiCo-MOF-31. The metal ratio was determined by the inductively coupled optical emission spectroscopy (ICP-OES). The Ni and Co ratio in 1D NiCo-MOF-31 compound is calculated to be 0.71:1 which is in well agreement with the TEM EDS findings (0.77:1) and the amount of precursor taken during the synthesis (0.75:1). The Ni and Co ratio in 1D NiCo-MOF-x composites are presented in Table S10.2.



**Figure 10.3.** High-resolution XPS spectra of (a) Ni 2p, (b) Co 2p, (c) C 1s, and (d) O 1s of 1D NiCo-MOF-31.

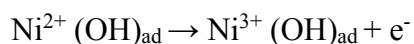
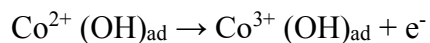
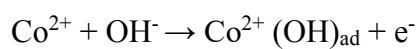
## 10.4.2. Electrochemical Analysis

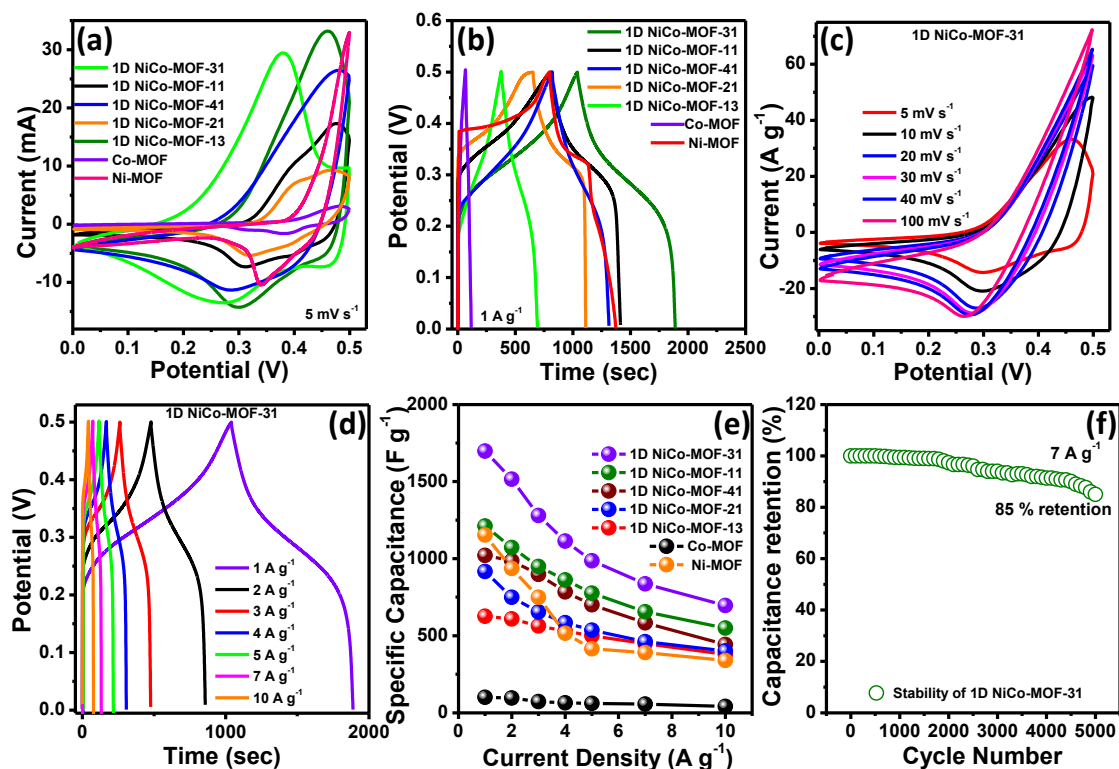
### 10.4.2.1. Electrochemical behavior in three electrode system

The SC performance of all the MOFs are assessed by using using techniques such as CV (Cyclic voltammetry), GCD (galvanostatic charge/discharge), and EIS (electrochemical impedance spectra) employing a 3M KOH electrolyte (in a three electrode system). For this study, Hg/HgO was served as reference, Pt wire as counter and active material coated



on Ni foam as working electrode. The voltage was varied within the range of 0 to 0.5 V. Figure 10.4(a) represents the comparison CV plots at 5 mV s<sup>-1</sup> sweep rate for all samples. The 1D NiCo-MOF-31 shows highest current response and highest area under the CV curves indicating higher charge storage compared to all other prepared MOFs. A pair of well separated faradic redox peak was observed for all the CV curves indicating the pseudocapacitive behavior (battery type property)<sup>29</sup>. These peaks are mainly due to the surface redox reaction and ion exchange, which is consistent with the OH<sup>-</sup> intercalation/deintercalation in the electrode materials. The intercalation of OH<sup>-</sup> ions from the electrolyte to the surface of the electrode takes place during the charging process and de-intercalation was taking place throughout discharging process. This phenomenon can be elucidated by the following mechanism<sup>30-31</sup>:





**Figure 10.4.** (a, b) Comparison CV and GCD profiles of all the MOFs under  $5 \text{ mV s}^{-1}$  sweep rate and  $1 \text{ A g}^{-1}$  current respectively. (c, d) CV ( $5$  to  $100 \text{ mV s}^{-1}$ ) and GCD ( $1$ – $10 \text{ A g}^{-1}$ ) profile of  $1\text{D NiCo-MOF-31}$ , (e) Comparison of  $C_s$  plot w.r.t current for all the MOFs. (f) Cyclic durability test of  $1\text{D NiCo-MOF-31}$  under  $7 \text{ A g}^{-1}$  current.

The  $C_s$  values can be calculated using area under the CV curves with equation 10.1 and are obtained to be  $1368.9$ ,  $800.5$ ,  $997.1$ ,  $664.6$ ,  $464.2$ ,  $93.1$ , and  $420.3 \text{ F g}^{-1}$  under  $5 \text{ mV s}^{-1}$  sweep rate for  $1\text{D NiCo-MOF-31}$ ,  $1\text{D NiCo-MOF-11}$ ,  $1\text{D NiCo-MOF-13}$ ,  $1\text{D NiCo-MOF-41}$ ,  $1\text{D NiCo-MOF-21}$ ,  $\text{Co-MOF}$  and  $\text{Ni-MOF}$  respectively. The corresponding comparison GCD curves of all the MOFs were presented in Figure 10.4(b) at  $1 \text{ A g}^{-1}$  current. All the GCD plot exhibit a nonlinear curve showing redox reaction rather than EDLCs process, which is in excellent concordance with the CV results. The  $1\text{D NiCo-}$

MOF-31 exhibits highest discharge time i.e. highest charge storage capacity compared to other MOFs samples under the same current density, accordance with CV findings. The  $C_s$  were calculated to be 1697.4, 1211.8, 1020.8, 916, 626.7, 100.1, and 1153.3 F g<sup>-1</sup> under 1 A g<sup>-1</sup> for 1D NiCo-MOF-31, 1D NiCo-MOF-11, 1D NiCo-MOF-13, 1D NiCo-MOF-41, 1D NiCo-MOF-21, Co-MOF and Ni-MOF respectively which was obtained from the discharge time of GCD curves using equation 10.2 (Table S10.3). This finding indicates that the electrochemical activity of the 1D NiCo-MOF-x samples can be optimized by tuning the Ni/Co molar ratio. Ni/Co molar ratio of 0.75 and 1 are the best optimized ratio and when the Ni/Co molar ratio was further lowered to 0.5 and 1, the electrochemical activity of the sample got degrade. In addition, compared to monometallic MOFs (Co MOF and Ni MOF) multicomponent MOFs shows higher electrochemical property owing to the synergistic interaction between the metal cations. Combination of Ni<sup>2+</sup> and Co<sup>2+</sup> not only increases redox reaction sites, but also enhances the conductivity of the electrode materials<sup>32</sup>. Figure 10.4(c) display the CV profile of 1D NiCo-MOF-31 at different sweep rate varying from 5-100 mV s<sup>-1</sup>. With rise in scan rate the current response increases with no such change in nature of the CV curves suggesting a remarkable rate capability. With increase in scan rate, the redox peaks exhibit a gradual shift towards both sides. This behaviour arises from insufficient diffusion reactions, leading to an elevated internal diffusion resistance at higher sweep rates. To provide a comparative analysis, GCD curve was generated for Ni foam under a current of 1 mA, as depicted in Figure S10.7. The results of this analysis revealed a minimal impact on the overall electrochemical performance, indicating negligible contribution from Ni foam. Figure 10.4(d) shows the nonlinear shape GCD curves of 1D NiCo-MOF-31 at different current densities represent the Faradic performance of the electrode material. The  $C_s$  for 1D NiCo-MOF-31 was calculated to be 1697.4, 1515.8, 1280.1, 1113.5, 986, 836 and

696.4 at 1, 2, 3, 4, 5, 7 and 10 A g<sup>-1</sup> respectively. The C<sub>s</sub> of 1D NiCo-MOF-31 decreases to 41% after 10 A g<sup>-1</sup> current. Furthermore, the C<sub>s</sub> value decreases with increasing current density, which could be ascribed to limitations of migration of ion within the active materials. At high current densities, it is crucial for a significant influx of OH<sup>-</sup> ions to rapidly intercalate at the electrolyte /electrode interface. However, the limited charging time, low concentration, and restricted accessibility of OH<sup>-</sup> ions hinder their ability to fulfil this requirement effectively<sup>33</sup>. Table 10.1 represents the comparison electrochemical performance of 1D NiCo-MOF-31 with recently reported literature. Figure S10.8, S10.9, S10.10, and S10.11 represents the CV and GCD plots for 1D NiCo-MOF-11, 1D NiCo-MOF-13, 1D NiCo-MOF-41, and 1D NiCo-MOF-21 respectively. The energy storage properties of optimized Co-MOF and Ni-MOF were studied as shown in Figure S10.12 and S10.13. Figure 10.4(e) shows the changes of C<sub>s</sub> value of 1D NiCo-MOF-31, 1D NiCo-MOF-x, Co-MOF and Ni-MOF electrodes under various current densities. It can be shown that 1D NiCo-MOF-31 displays highest specific capacitance compared to monometallic Co-MOF, Ni-MOF and bimetallic 1D NiCo-MOF-x. When the Ni/Co molar ratio was 0.5:1 the C<sub>s</sub> value decreases to 1020.8 F g<sup>-1</sup>. Nickel and cobalt have their own reaction potentials. The active material is Ni. The incorporation of small amount of Co into the Ni-MOF matrix improves the electrochemical properties of the pure Ni-MOF. When the Ni amount is increased by keeping Co molar ratio constant, the electrochemical properties also degraded. Design of multicomponent MOF electrode materials is conducive to enhance the electrochemical activity owing to its synergistic interaction between different metal cations. The highest electrochemical activity of the 1D NiCo-MOF-31 may be due to optimal mixed metallic components and 1D morphology which provide large SSA for easy transportation of electrons and diffusion of electrolyte ions in the redox reaction process. The introduction of an optimal amount

of Co and Ni results in higher redox activity, improved conductivity, and a synergistic effect between multiple components. Figure 10.4(f) shows the cyclic stability of 1D NiCo-MOF-31 at 7 A g<sup>-1</sup> current. A continuous 5000 cycles was carried out displaying 85% capacitance retention after 5000 cycles.

The energy storage capacity of an electrode material is quantified through the assessment of both non-diffusion and diffusion processes. The kinetic behavior and energy storage mechanism of the electrode was analyzed by the following equation:

$$i = av^b \quad (10.6)$$

$i$  denotes the redox peak current,  $v$  is the corresponding scan rate,  $a$  and  $b$  are variables of intercept and slope of  $\log i$  vs.  $\log v$  at a given voltage respectively. Figure 10.5(a) presents the plot of  $\log(i)$  vs.  $\log(v)$ . If the  $b$  value lies 0.5 to 1, the electrode material shows the property of battery and pseudocapacitance.  $b=1$  indicates process to be controlled by surface ion adsorption/desorption and  $b=0.5$  indicates faradic-dominant charge storage process of the material. For cathodic reaction,  $b=0.51$  and for anodic reaction  $b=0.4$  revealing the charge storage involves diffusion controlled process (battery type). To quantify the capacitive and diffusive controlled contribution, the ratio of two contribution can be calculated by using Dunn's method by using the following equation:

$$i = k_1v + k_2v^{1/2} \quad (10.7)$$

Here  $i$ ,  $k_1v$ , and  $k_2v^{1/2}$  represents the peak current at a fix potential, capacitive current and diffusion-controlled current respectively. Slope and intercept can be obtained from the plot of  $i/v^{1/2}$  vs.  $v^{1/2}$ .

Figure 10.5(b) represents the CV profile of 1D NiCo-MOF-31 at 5 mV s<sup>-1</sup> scan rate differentiating capacitive and diffusive contribution plot. The shaded area in the CV profile represents the capacitive contribution. The capacitive contribution of

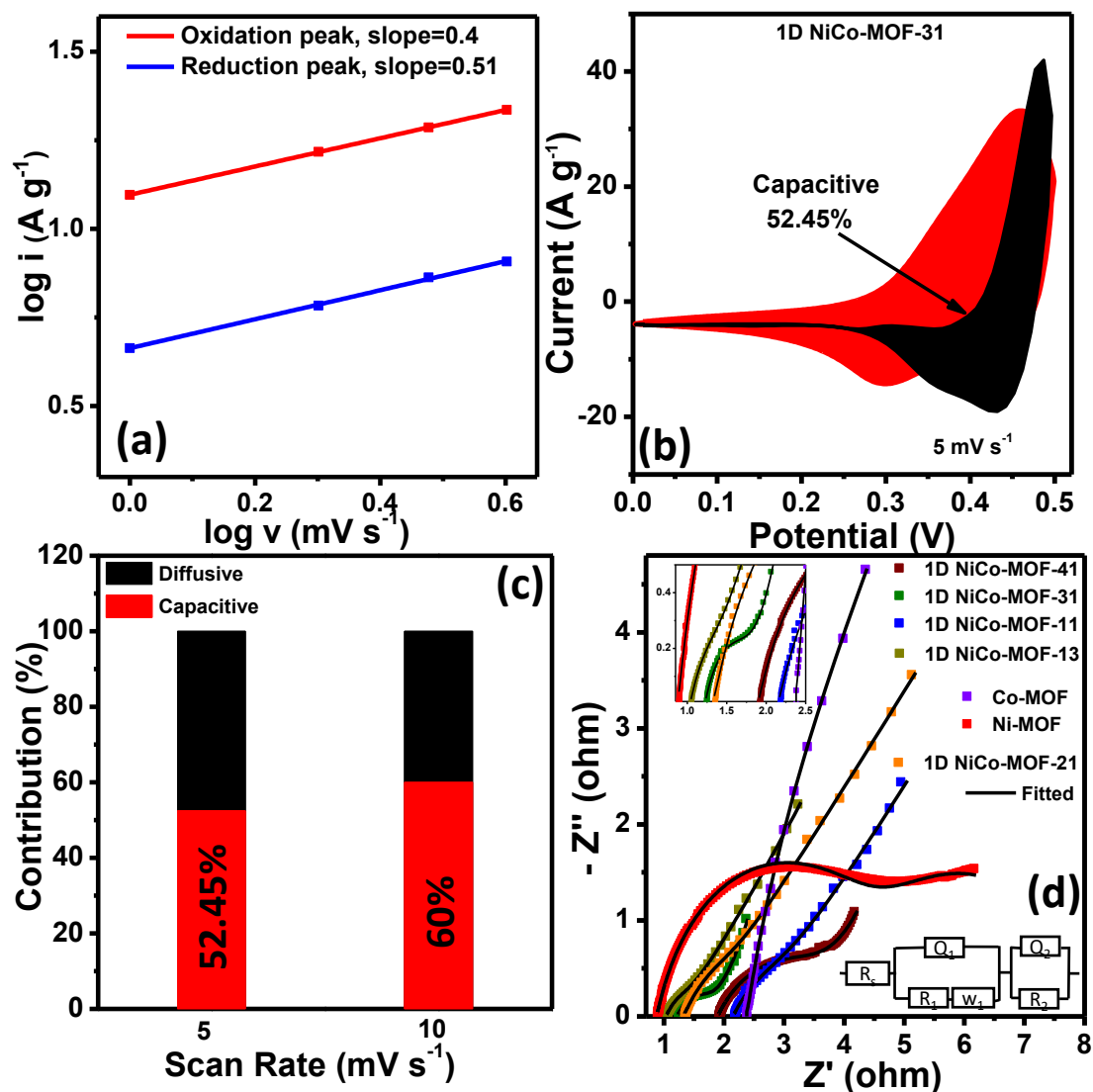
1D NiCo-MOF-31 at 1, 2, 5 and 10  $\text{mV s}^{-1}$  scan rates are calculate to be 15.8, 23, 52.45 and 60% respectively. Figure 10.5(c) represents the bar plot showing capacitive and diffusive contribution at 5 and 10  $\text{mV s}^{-1}$  sweep rate. To study the conductivity properties of electrode materials, EIS spectra was performed for all the materials. Figure 10.5(d) represents the EIS plot with open circuit potential 10 mV (frequency ranging from 0.01 Hz - 10 kHz). The Nyquist plot shows a semicircle at higher frequency range and a line at lower frequency range. The inset shows the corresponding equivalent circuit for the fitted EIS plot.  $R_s$  represents the contact resistance of the electrode and substrate (nickel foam), the electrode resistance and the electrolyte resistance. The  $R_s$  value was determined from the intersection of  $Z'$  axis and the semicircle arc.  $R_{ct}$  denotes the charge transfer resistance due to the faradic reaction taking place on the surface of the electrode materials. The  $R_{ct}$  can be obtained from the diameter of the semicircle at higher frequency. Both  $R_s$  and  $R_{ct}$  for 1D NiCo-MOF-31 is relatively small compared to other materials. The  $R_{ct}$  values for 1D NiCo-MOF-31, 1D NiCo-MOF-11, 1D NiCo-MOF-21, 1D NiCo-MOF-13, 1D NiCo-MOF-41, Co-MOF, and Ni-MOF were 0.02, 0.52, 0.33, 0.22, 1.75, 6.91, and 0.12  $\Omega$  respectively and the  $R_s$  values were found to be 0.003, 2.14, 1.32, 1.03, 1.89, 2.37, and 0.87  $\Omega$  respectively. All the above result confirms that bimetallic 1D NiCo-MOF-31 exhibits better electrical conductivity than other synthesized materials.

**Table 10.1.** Electrochemical performance of 1D NiCo-MOF-31 with recently reported MOF materials.

Material	C <sub>s</sub> of single Electrode (F g <sup>-1</sup> )	Capacitance retention (%)	No. of cycles	Ref.
Ni/Co-MOF-5	1220.2 (1 A g <sup>-1</sup> )	87.8	5000	34
Ni/Co-MOF- NPC-2:1	1214 (1 A g <sup>-1</sup> )	98.8	6000	31
Ni-Co-S/NF	1406.9 (0.5 A g <sup>-1</sup> )	88.6	1000	35
NCM 2:1	1385 (4 mA cm <sup>-2</sup> )	88.4	3000	33
Ni/Co-MOF	980 (2.5 A g <sup>-1</sup> )	73	5000	36
Ni/Co-MOF	1049 (1 A g <sup>-1</sup> )	97.4	5000	37
Ni/Co-MOF	758 (1 A g <sup>-1</sup> )	75	5000	6

<b>NiMo-</b>	1536	-	-	
<b>LDH@NiCo-</b>	(1 A g <sup>-1</sup> )			38
<b>MOF</b>				
<b>CoNi<sub>0.5</sub>-MOF</b>	663.6	96	10000	
	(1 A g <sup>-1</sup> )			30
<b>Ultrathin NiCo-</b>	1202.1	89.5	5000	
<b>MOF nanosheets</b>	(1 A g <sup>-1</sup> )			13
<b>CoNi-MOF</b>	1044	94	5000	
	(2 A g <sup>-1</sup> )			39
<b>NiCo-MOF-3</b>	639.8	89.7	7000	
	(1 A g <sup>-1</sup> )			40
<b>1D NiCo-MOF-</b>	1697.4	85	5000	This
<b>31</b>	(1A g <sup>-1</sup> )			work





**Figure 10.5.** (a)  $\log$  (peak current) vs.  $\log$ (sweep rate) plot. (b) CV profile of 1D NiCo-MOF-31 displaying contribution area of the pseudocapacitance at a scan rate of  $5 \text{ mV s}^{-1}$ . (c) Pseudocapacitive contribution of 1D NiCo-MOF-31 at a scan rate of 5 and  $10 \text{ mV s}^{-1}$ . (d) EIS profile of all MOFs in 3 M KOH.

The high electrochemical performance of the 1D NiCo-MOF-31 is due to the following reasons:

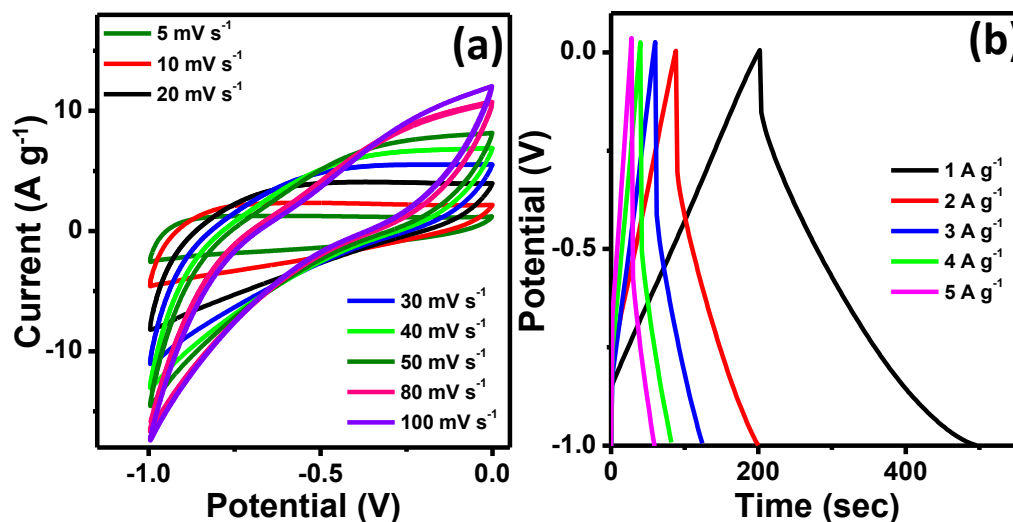
- 1) One-dimensional nanobelt materials exhibit a high surface-to-volume ratio, facilitating efficient ion adsorption and desorption processes. This unique

structural characteristic results in superior electrochemical performance, characterized by a high  $C_s$  and excellent rate capability.

- 2) The elongated morphology of nanobelt enables rapid diffusion of ions and efficient electron transport throughout the electrode material. The unidirectional nature of nanobelt facilitates unimpeded ion migration, leading to enhanced charge-discharge kinetics and elevated power density.
- 3) The inherent stability of nanobelts stems from their elongated geometry, which mitigates the risk of structural collapse or degradation during prolonged charge-discharge cycling. This exceptional structural robustness ensures long-term cycling stability and prolongs the operational lifespan of the supercapacitor.
- 4) Nanobelts offer the advantage of precise control over their size and aspect ratio during synthesis. This tunability allows researchers to optimize the electrochemical properties by tailoring the SSA and porosity of the nanobelts, thereby influencing the overall capacitance and energy storage performance of the supercapacitor.

Using a three-electrode setup, electrochemical performance of SNAC was evaluated with a platinum wire, Hg/HgO, and SNAC serving as the counter, reference, and working electrodes, respectively. The CV curve displayed a symmetrical rectangular shape without any oxidation or reduction peaks, indicating the electrochemical double-layer capacitor (EDLC) nature of the AC material (Figure 10.6). Under a sweep rate of  $5 \text{ mV s}^{-1}$ , the  $C_s$  value for SNAC was measured to be  $227.72 \text{ F g}^{-1}$ , while under  $10 \text{ mV s}^{-1}$  it was  $212.53 \text{ F g}^{-1}$ . Under  $1 \text{ A g}^{-1}$  current, the  $C_s$  value was found to be  $291 \text{ F g}^{-1}$  (potential

ranging from -1.0 to 0.0 V), demonstrating excellent high-rate durability, as reported in our previous studies<sup>27</sup>. These findings substantiate the suitability of SNAC as an ideal anode material for energy storage applications.



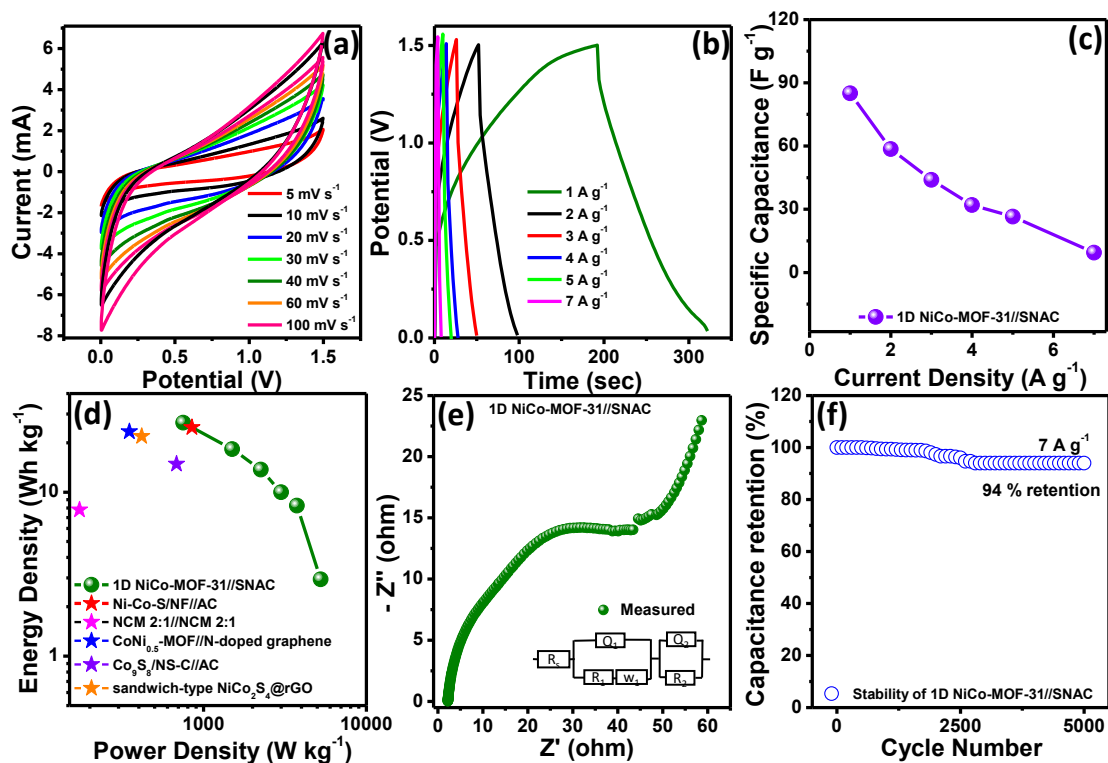
**Figure 10.6.** (a, b) CV profile of SNAC at different sweep rates and GCD profile of SNAC at different current.

#### 10.4.2.2. Electrochemical Performance of the Asymmetric Supercapacitor

The practical suitability of 1D NiCo-MOF-31 material was further assessed by fabricating an ASC device 1D NiCo-MOF-31//SNAC where 1D NiCo-MOF-31 (pseudocapacitive) act as cathode and SNAC (EDLC) act as anode. All the electrochemical performance were conducted using a two electrode setup in 3M KOH electrolyte. Figure S10.14 represents the CV cycle of 1D NiCo-MOF-31 and SNAC at potential 0-0.5 V and -1-0 V respectively under 5 mV s<sup>-1</sup>. The combined contribution of cathode and anode electrode material were used to determine the potential range of 1D NiCo-MOF-31//SNAC device. The above findings (according to the CV curves of 1D NiCo-MOF-31 and SNAC) illustrate that the voltage window of the device can be extended to be 1.5 V. To further confirm the voltage window for the device, CV cycles

were performed at different potential gaps. By extending the voltage window to 1.5 V, a substantial polarization of the cyclic voltammetry (CV) curve was observed during the measurement. (Figure S10.15). In Figure 10.7(a), the cyclic voltammetry (CV) curve of the ASC device is depicted, demonstrating variations at different scan rates (5-100 mV s<sup>-1</sup>) within a potential window of 0 to 1.5 V. The CV curves exhibit a pair of indistinct redox peaks, suggesting that the energy storage mechanism of the assembled device is governed by a combination of battery behaviour and double electric layer behaviour. Figure 10.7(b) displays the GCD curves of the device across various current densities (1-7 A g<sup>-1</sup>). The nonlinear and symmetrical nature of the GCD curve indicates exceptional electrochemical reversibility and rate performance. The C<sub>s</sub> of the device was determined from the discharge time of the GCD curves and are obtained to be 85, 58.56, 43.9, 32, 26.5 and 9.4 at 1, 2, 3, 4, 5, and 7 A g<sup>-1</sup> as shown in Figure 10.7(c). Figure 10.7(d) represents the Ragone plot of 1D NiCo-MOF-31//SNAC with some reported recent literatures. ED and PD of the 1D NiCo-MOF-31//SNAC device was calculated by using equation 10.4 and 10.5. The 1D NiCo-MOF-31//SNAC possess an ED of 26.56 Wh kg<sup>-1</sup> at 750 W kg<sup>-1</sup> PD and 3 Wh kg<sup>-1</sup> at 5250 W kg<sup>-1</sup> PD which is higher than NiCo MOF based devices which are previously reported, such as Ni-Co-S/NF//AC (24.8 W h kg<sup>-1</sup>, 849.5 W kg<sup>-1</sup>)<sup>35</sup>, NCM 2:1//NCM 2:1 (7.8 Wh kg<sup>-1</sup>, 173.07 W kg<sup>-1</sup>)<sup>33</sup>, CoNi<sub>0.5</sub>-MOF//N-doped graphene (23.44 Wh kg<sup>-1</sup>, 350 W kg<sup>-1</sup>)<sup>30</sup>, Co<sub>9</sub>S<sub>8</sub>/NS-C//AC (14.85 Wh kg<sup>-1</sup> at 681.82 W kg<sup>-1</sup>)<sup>41</sup>, sandwich-type NiCo<sub>2</sub>S<sub>4</sub>@rGO (21.9 W h kg<sup>-1</sup> at 417.1 W kg<sup>-1</sup>)<sup>42</sup>. In Figure 10.7(e), the EIS spectra of the ASC device with a small semicircle and the inset illustrates the equivalent circuit with R<sub>s</sub> and R<sub>ct</sub> values 1.9 and 27.9 Ω respectively. The practical performance of a device was evaluated from cyclic performance. To evaluate the cycling performance of the ASC device, repeated GCD cycles were conducted at a current of 7 A g<sup>-1</sup>. Remarkably, the device exhibited a capacitance

retention of 94% of its initial value after 5000 charging/discharging cycles presented in Figure 10.7(f).



**Figure 10.7.** (a, b) CV and GCD curves at different scan rates and different current densities. (c) Plot of  $C_s$  vs. current. (d) Plot of ED vs. PD and comparison to recently reported SC devices. (e) EIS plot. (f) Cyclic stability performance for 5000 cycles under 7 A g<sup>-1</sup> for the ASC device.

## 10.5. CONCLUSION

In summary, bimetallic 1D NiCo-MOF-31 was synthesized through a facile one-step solvothermal method, resulting in a significant high SSA of 73 m<sup>2</sup> g<sup>-1</sup>. The as synthesized nanobelts electrode material exhibits a notable high  $C_s$  of 1697.5 F g<sup>-1</sup> under 1 A g<sup>-1</sup> current and 696.43 under 10 A g<sup>-1</sup>, indicating exceptional rate performance of 41 % with superior cyclic stability over 5000 charging-discharging cycles. Furthermore, an ASC

device (1D NiCo-MOF-31//SNAC) was assembled by using SNAC as anode and 1D NiCo-MOF-31 as cathode material. The device exhibits an impressive ED of 26.56 W h kg<sup>-1</sup> at a PD of 750 W kg<sup>-1</sup> accompanied by outstanding cyclic stability. This result validates the efficacy of tuning the metal ratio is an effective approach to optimizing the morphology and augmenting the electrochemical activity of MOFs. This outcome exhibits significant potential for application in energy storage systems.

## 10.6. REFERENCES

- (1) Yan, Y.; Li, K.; Chen, X.; Yang, Y.; Lee, J.-M. *Small* **2017**, *13*, 1701724.
- (2) Jayakumar, A.; Antony, R. P.; Wang, R.; Lee, J.-M. *Small* **2017**, *13*, 1603102.
- (3) Tan, Y. B.; Lee, J.-M. *Journal of Materials Chemistry A* **2013**, *1*, 14814-14843.
- (4) Pan, Z.; Jiang, Y.; Yang, P.; Wu, Z.; Tian, W.; Liu, L.; Song, Y.; Gu, Q.; Sun, D.; Hu, L. *ACS Nano* **2018**, *12*, 2968-2979.
- (5) Zhang, L.; Lu, C.; Ye, F.; Pang, R.; Liu, Y.; Wu, Z.; Shao, Z.; Sun, Z.; Hu, L. *Advanced Materials* **2021**, *33*, 2007523.
- (6) Gao, S.; Sui, Y.; Wei, F.; Qi, J.; Meng, Q.; Ren, Y.; He, Y. *Journal of Colloid and Interface Science* **2018**, *531*, 83-90.
- (7) Zhou, H.-C. J.; Kitagawa, S. *Chemical Society Reviews* **2014**, *43*, 5415-5418.
- (8) Bennett, T. D.; Cheetham, A. K.; Fuchs, A. H.; Coudert, F.-X. *Nature Chemistry* **2017**, *9*, 11-16.
- (9) Cairns, A. B.; Goodwin, A. L. *Chemical Society Reviews* **2013**, *42*, 4881-4893.
- (10) Bennett, T. D.; Cheetham, A. K. *Accounts of Chemical Research* **2014**, *47*, 1555-1562.
- (11) Ehrling, S.; Reynolds, E. M.; Bon, V.; Senkovska, I.; Gorelik, T. E.; Evans, J. D.; Rauche, M.; Mendt, M.; Weiss, M. S.; Pöpl, A.; Brunner, E.; Kaiser, U.; Goodwin, A. L.; Kaskel, S. *Nature Chemistry* **2021**, *13*, 568-574.
- (12) Xu, X.; Yang, J.; Hong, Y.; Wang, J. *ACS Applied Nano Materials* **2022**, *5*, 8382-8392.
- (13) Wang, Y.; Liu, Y.; Wang, H.; Liu, W.; Li, Y.; Zhang, J.; Hou, H.; Yang, J. *ACS Applied Energy Materials* **2019**, *2*, 2063-2071.
- (14) Chaikittisilp, W.; Hu, M.; Wang, H.; Huang, H.-S.; Fujita, T.; Wu, K. C. W.; Chen, L.-C.; Yamauchi, Y.; Ariga, K. *Chemical Communications* **2012**, *48*, 7259-7261.
- (15) Amali, A. J.; Sun, J.-K.; Xu, Q. *Chemical Communications* **2014**, *50*, 1519-1522.
- (16) Yang, J.; Ma, Z.; Gao, W.; Wei, M. *Chemistry – A European Journal* **2017**, *23*, 631-636.
- (17) Srimuk, P.; Luanwuthi, S.; Krittayavathananon, A.; Sawangphruk, M. *Electrochimica Acta* **2015**, *157*, 69-77.
- (18) Mandal, A.; Rissanen, K.; Mal, P. *CrystEngComm* **2019**, *21*, 4401-4408.
- (19) Jiao, Y.; Chen, G.; Chen, D.; Pei, J.; Hu, Y. *Journal of Materials Chemistry A* **2017**, *5*, 23744-23752.
- (20) Sarkar, D.; Mandal, M.; Mandal, K. *ACS Applied Materials & Interfaces* **2013**, *5*, 11995-12004.
- (21) Niu, C.; Meng, J.; Wang, X.; Han, C.; Yan, M.; Zhao, K.; Xu, X.; Ren, W.; Zhao, Y.; Xu, L.; Zhang, Q.; Zhao, D.; Mai, L. *Nature Communications* **2015**, *6*, 7402.
- (22) Li, F.-L.; Shao, Q.; Huang, X.; Lang, J.-P. *Angewandte Chemie International Edition* **2018**, *57*, 1888-1892.

- (23) Li, W.-H.; Lv, J.; Li, Q.; Xie, J.; Ogiwara, N.; Huang, Y.; Jiang, H.; Kitagawa, H.; Xu, G.; Wang, Y. *Journal of Materials Chemistry A* **2019**, *7*, 10431-10438.
- (24) Shinde, S. K.; Jalak, M. B.; Karade, S. S.; Majumder, S.; Tamboli, M. S.; Truong, N. T.; Maile, N. C.; Kim, D.-Y.; Jagadale, A. D.; Yadav, H. M. A Novel Synthesized 1D Nanobelt-like Cobalt Phosphate Electrode Material for Excellent Supercapacitor Applications *Materials* [Online], 2022.
- (25) Wang, C.; Kaneti, Y. V.; Bando, Y.; Lin, J.; Liu, C.; Li, J.; Yamauchi, Y. *Materials Horizons* **2018**, *5*, 394-407.
- (26) Panigrahy, S.; Panda, P.; Shekhawat, A.; Barman, S. *ACS Applied Nano Materials* **2023**, *6*, 3825-3834.
- (27) Panda, P.; Barman, S. *Sustainable Energy & Fuels* **2023**, *7*, 2441-2454.
- (28) Xiao, X.; Li, Q.; Yuan, X.; Xu, Y.; Zheng, M.; Pang, H. *Small Methods* **2018**, *2*, 1800240.
- (29) Yang, P.; Wu, Z.; Jiang, Y.; Pan, Z.; Tian, W.; Jiang, L.; Hu, L. *Advanced Energy Materials* **2018**, *8*, 1801392.
- (30) Zhang, W.; Guo, X.; Wang, Y.; Zheng, Y.; Zhao, J.; Xie, H.; Zhang, Z.; Zhao, Y. *Energy & Fuels* **2022**, *36*, 1716-1725.
- (31) Zhou, P.; Wan, J.; Wang, X.; Xu, K.; Gong, Y.; Chen, L. *Journal of Colloid and Interface Science* **2020**, *575*, 96-107.
- (32) Wang, J.; Zhong, Q.; Zeng, Y.; Cheng, D.; Xiong, Y.; Bu, Y. *Journal of Colloid and Interface Science* **2019**, *555*, 42-52.
- (33) Salunkhe, A. D.; Pagare, P. K.; Torane, A. P. *Journal of Electronic Materials* **2023**, *52*, 3472-3487.
- (34) Chen, C.; Wu, M.-K.; Tao, K.; Zhou, J.-J.; Li, Y.-L.; Han, X.; Han, L. *Dalton Transactions* **2018**, *47*, 5639-5645.
- (35) Tao, K.; Han, X.; Ma, Q.; Han, L. *Dalton Transactions* **2018**, *47*, 3496-3502.
- (36) Radhika, M. G.; Gopalakrishna, B.; Chaitra, K.; Bhatta, L. K. G.; Venkatesh, K.; Sudha Kamath, M. K.; Kathyayini, N. *Materials Research Express* **2020**, *7*, 054003.
- (37) Gholipour-Ranjbar, H.; Soleimani, M.; Naderi, H. R. *New Journal of Chemistry* **2016**, *40*, 9187-9193.
- (38) Cheng, C.; Zou, Y.; Xu, F.; Xiang, C.; Sun, L. In Situ Growth of Nickel&ndash;Cobalt Metal Organic Frameworks Guided by a Nickel&ndash;Molybdenum Layered Double Hydroxide with Two-Dimensional Nanosheets Forming Flower-Like Structures for High-Performance Supercapacitors *Nanomaterials* [Online], 2023.
- (39) Deng, T.; Lu, Y.; Zhang, W.; Sui, M.; Shi, X.; Wang, D.; Zheng, W. *Advanced Energy Materials* **2018**, *8*, 1702294.
- (40) Zhang, W.; Shahnavaz, Z.; Yan, X.; Huang, X.; Wu, S.; Chen, H.; Pan, J.; Li, T.; Wang, J. *Inorganic Chemistry* **2022**, *61*, 15287-15301.
- (41) Zhang, S.; Li, D.; Chen, S.; Yang, X.; Zhao, X.; Zhao, Q.; Komarneni, S.; Yang, D. *Journal of Materials Chemistry A* **2017**, *5*, 12453-12461.
- (42) Li, H.; Chen, L.; Jin, P.; Li, Y.; Pang, J.; Hou, J.; Peng, S.; Wang, G.; Shi, Y. *Nano Research* **2022**, *15*, 950-958.



## Appendix H

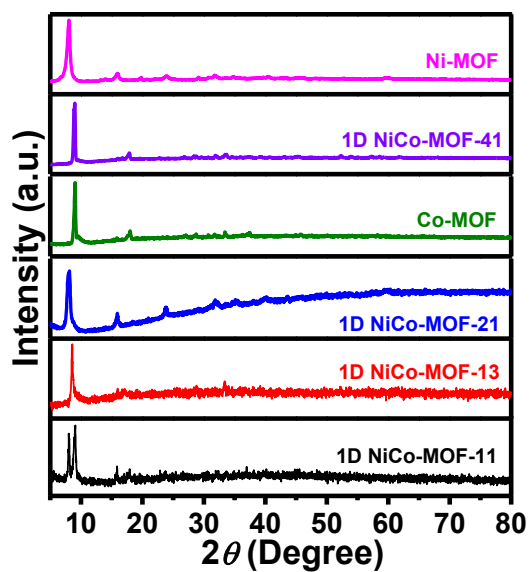


Figure S10.1. p-XRD pattern of all the MOFs.

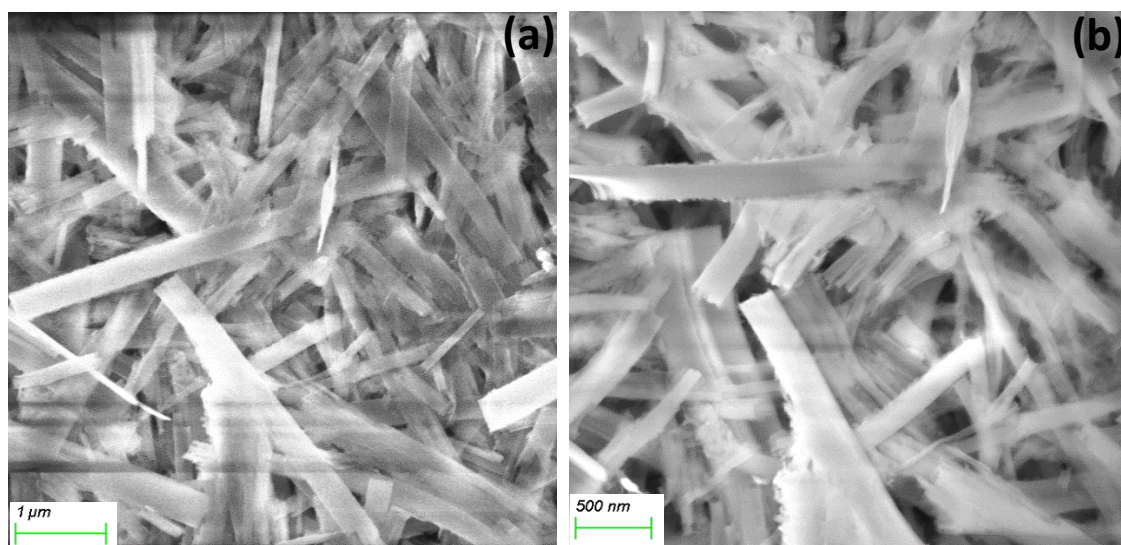
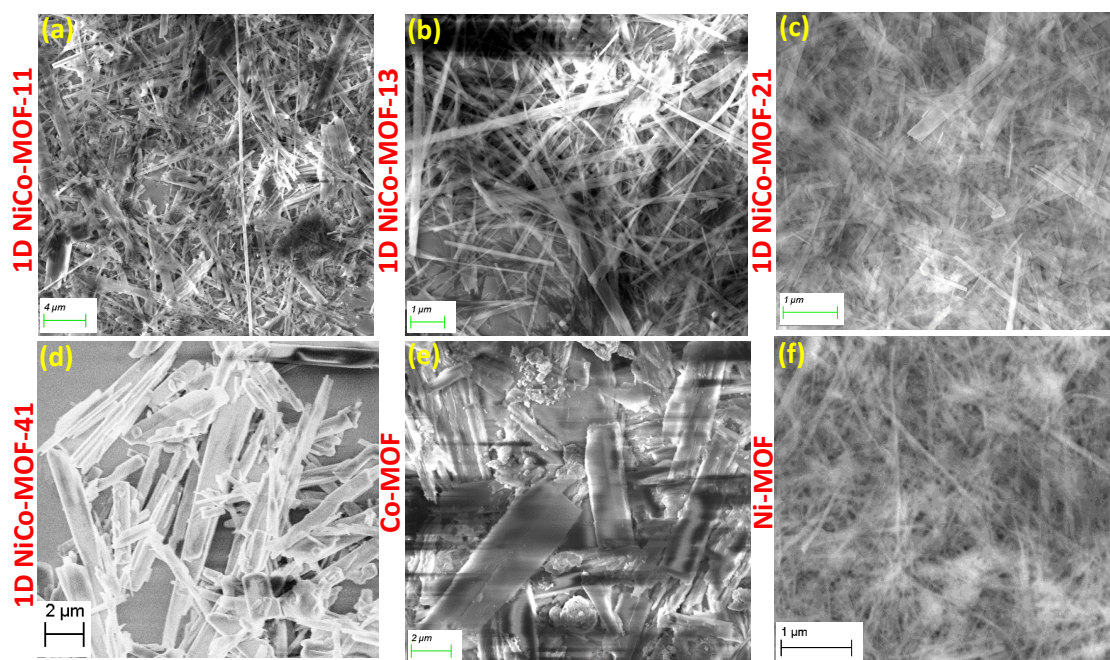
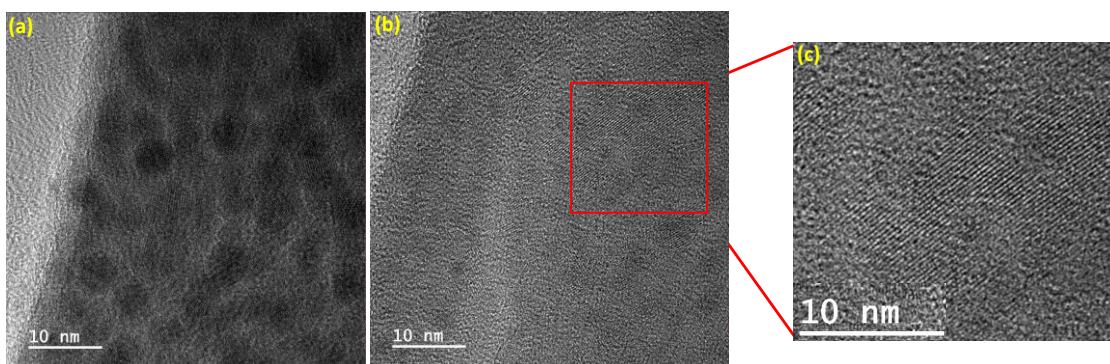


Figure S10.2. FESEM image of (a, b) 1D NiCo-MOF-31.





**Figure S10.3.** FESEM image of (a) 1D NiCo-MOF-11, (b) 1D NiCo-MOF-13, (c) 1D NiCo-MOF-21, (d) 1D NiCo-MOF-41, (e) Co-MOF, and (f) Ni-MOF.



**Figure S10.4.** (a, b) HRTEM images and (c) enlarged HRTEM images of 1D NiCo-MOF-31.

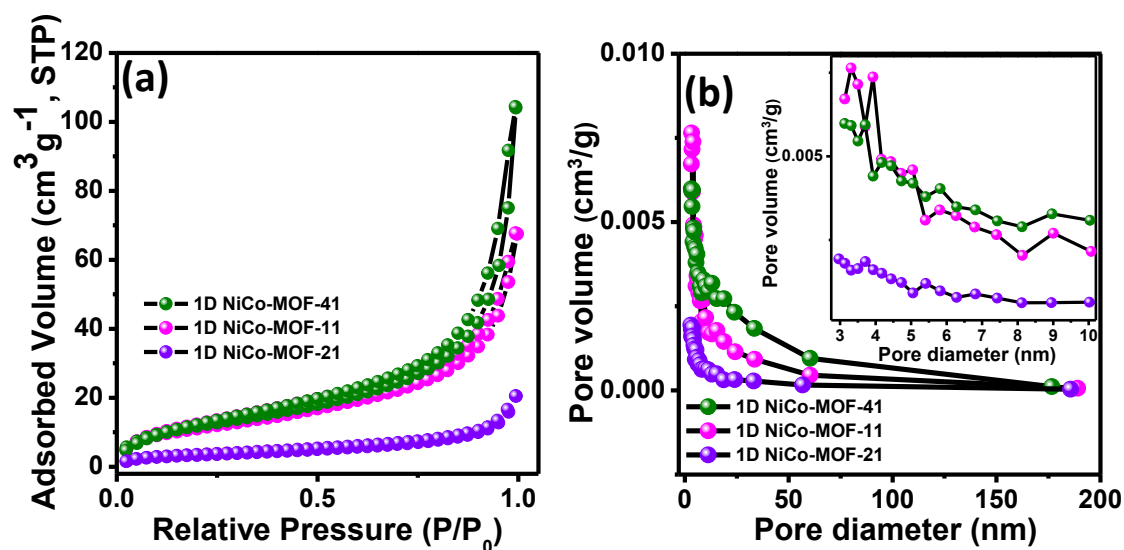


Figure S10.5. (a)  $N_2$  desorption/adsorption isotherm, and (b) PSDs of 1D NiCo-MOF-x.

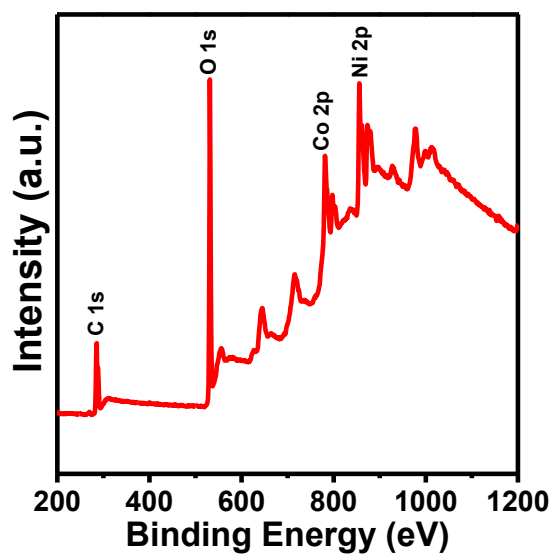


Figure S10.6. XPS survey scan of 1D NiCo-MOF-31.

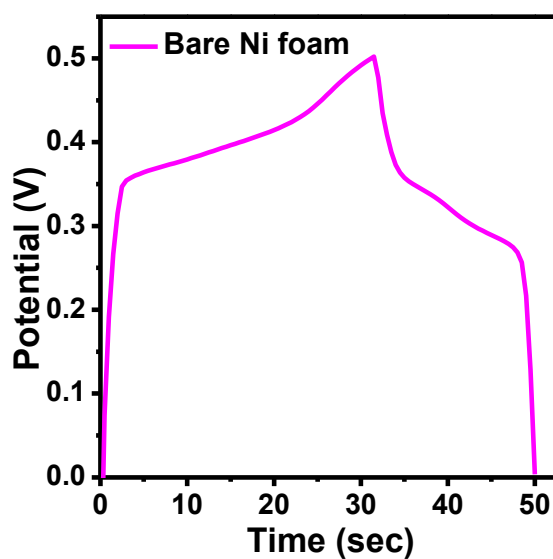


Figure S10.7. GCD curve of bare Ni foam at 1 mA current.

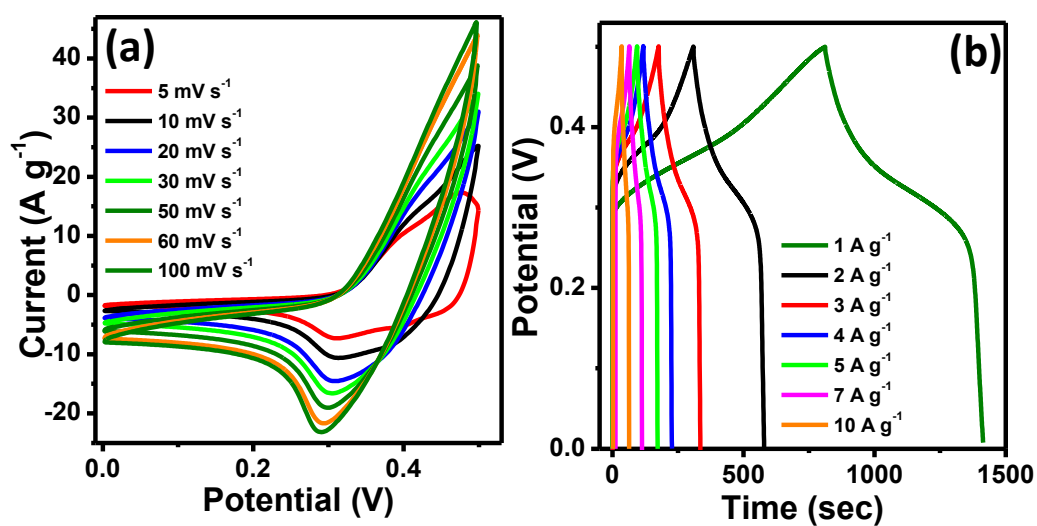


Figure S10.8. (a) CV and (b) GCD profiles of 1D NiCo-MOF-11.

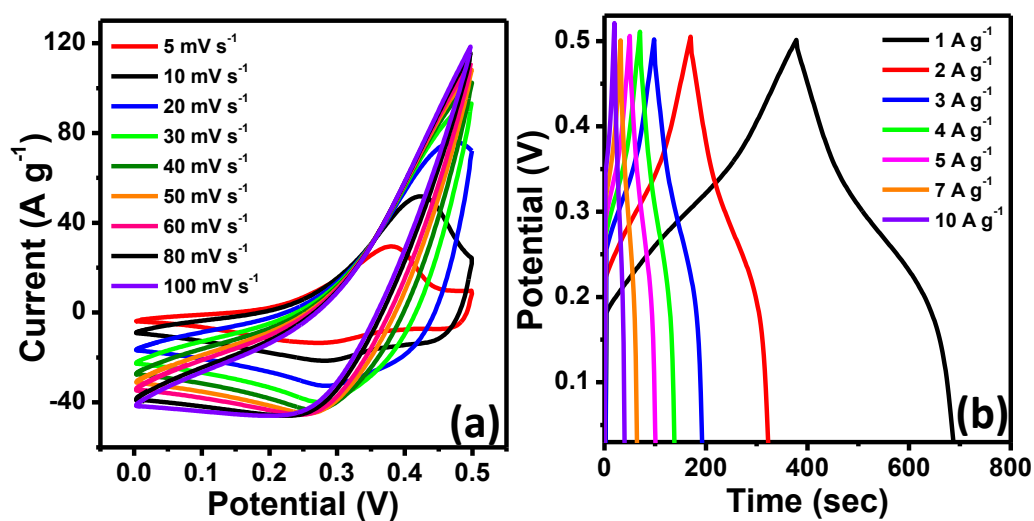


Figure S10.9. (a) CV and (b) GCD profiles of 1D NiCo-MOF-13.

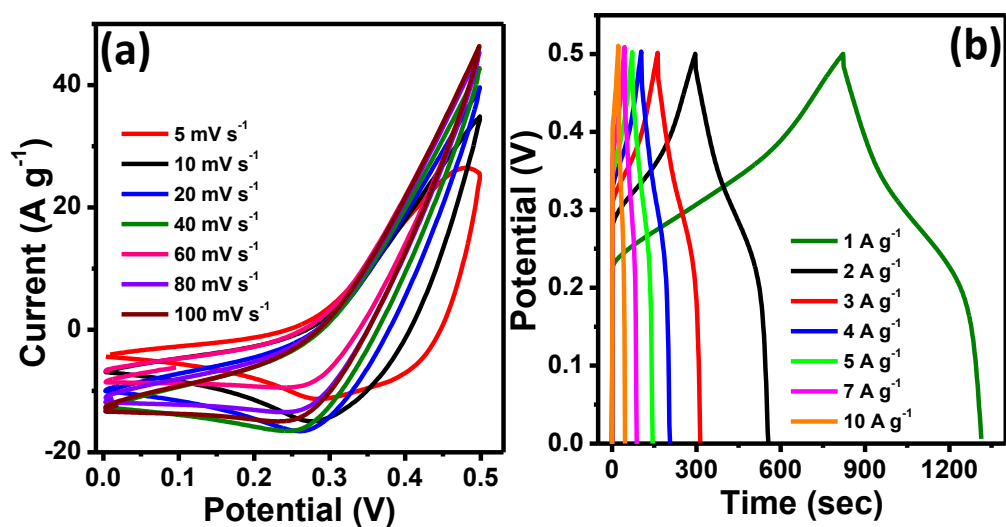


Figure S10.10. (a) CV and (b) GCD profiles of 1D NiCo-MOF-41.

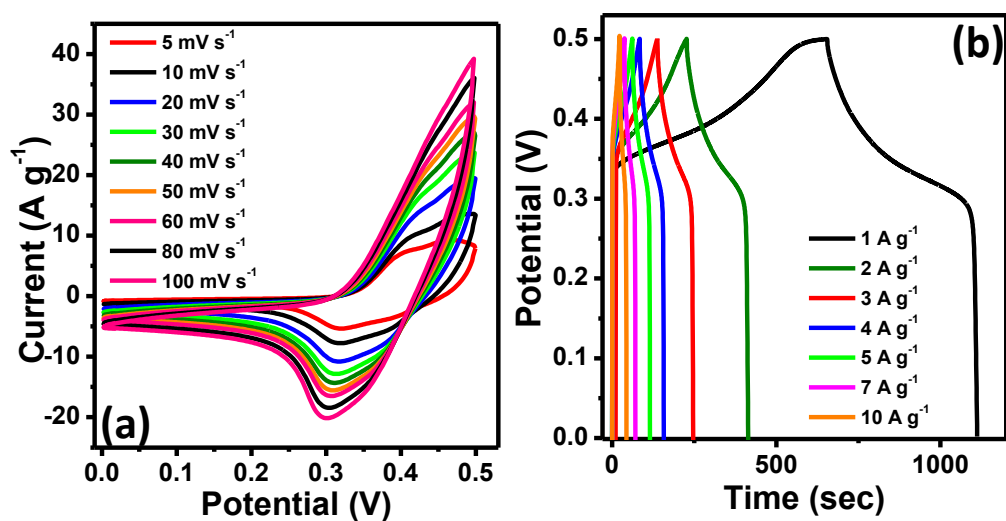


Figure S10.11. (a) CV and (b) GCD profiles of 1D NiCo-MOF-21.

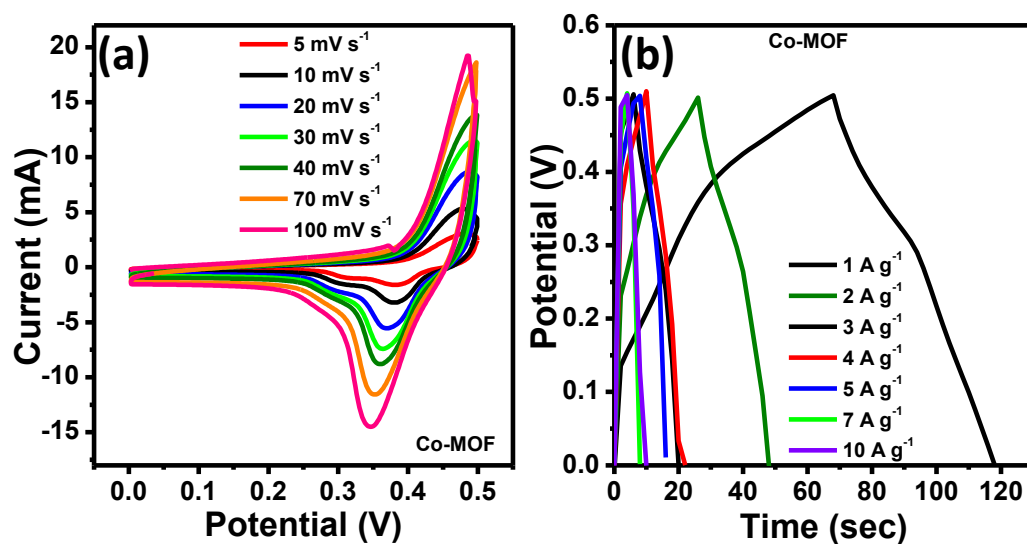


Figure S10.12. (a) CV and (b) GCD profiles of Co-MOF.

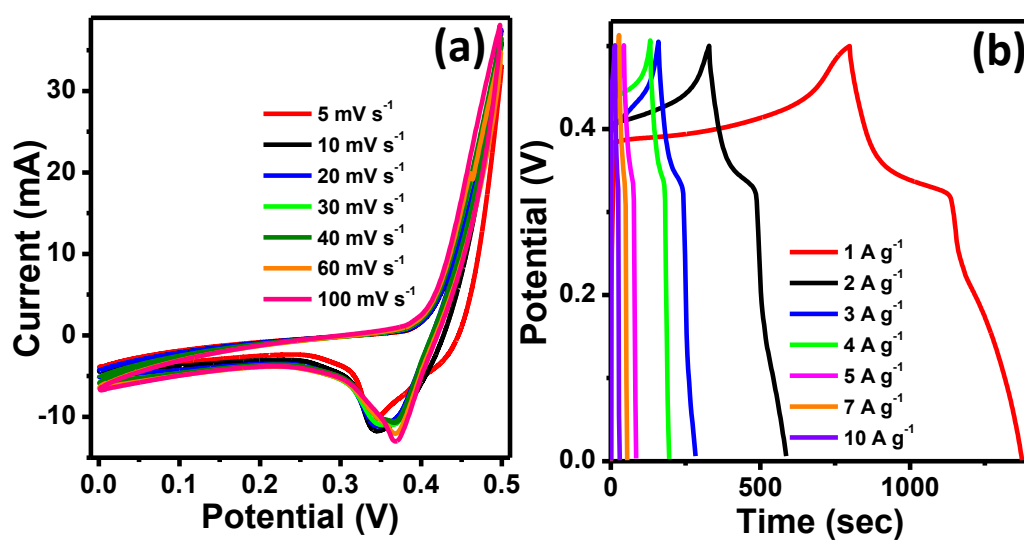


Figure S10.13. (a) CV and (b) GCD profiles of Ni-MOF.

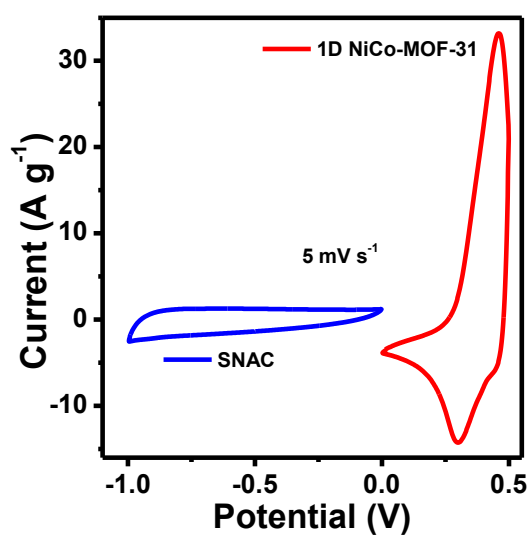
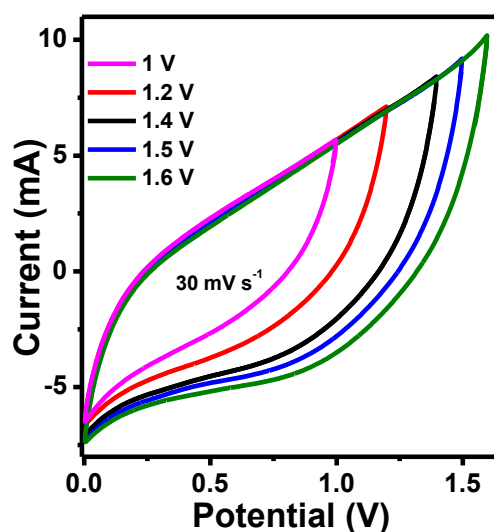


Figure S10.14. CV curves of SNAC and 1D NiCo-MOF-31 at a scan rate of 5 mV s<sup>-1</sup>.



**Figure S10.15.** CV curves for ASC (1D NiCo-MOF-31// SNAC) device at potential ranging from 1 V to 1.6 V.

**Table S10.1.** 1D NiCo-MOF-31 in terms of atomic percentage obtained from TEM EDS.

Catalyst	C (%)	O (%)	Co (%)	Ni (%)	Ni:Co
1D NiCo-MOF-31	95.91	0.92	1.79	1.38	0.77:1

**Table S10.2.** Weight percentage of Co and Ni calculated from ICP-OES.

Catalyst	Ni (%)	Co (%)	Ni:Co
1D NiCo-MOF-11	20.23	18.88	1.07:1
1D NiCo-MOF-21	30.81	16.1	1.9:1
1D NiCo-MOF-13	12.94	40.14	0.3:1
1D NiCo-MOF-31	17.49	24.56	0.71:1

**Table S10.3.** Comparison of electrochemical performance of all the MOFs in 3M KOH electrolyte.

Sample Name	Specific capacitance ( F g <sup>-1</sup> ) at 1 A g <sup>-1</sup> current density
1D NiCo-MOF-11	1211.8
1D NiCo-MOF-21	626.7
1D NiCo-MOF-31	1697.4
1D NiCo-MOF-13	1020.8
1D NiCo-MOF-41	916
Co-MOF	100.1
Ni-MOF	1153.3